WATEREUSE

U.S. DEPARTMENT OF THE INTERIOR
BUREAU OF RECLAMATION

Analysis of Parameters Affecting Process Efficiency, Energy Consumption, and Carbon Footprint in Water Reuse

Full Scale Microfiltration, Reverse Osmosis, and UV/H_2O_2 at Orange County's Groundwater Replenishment System

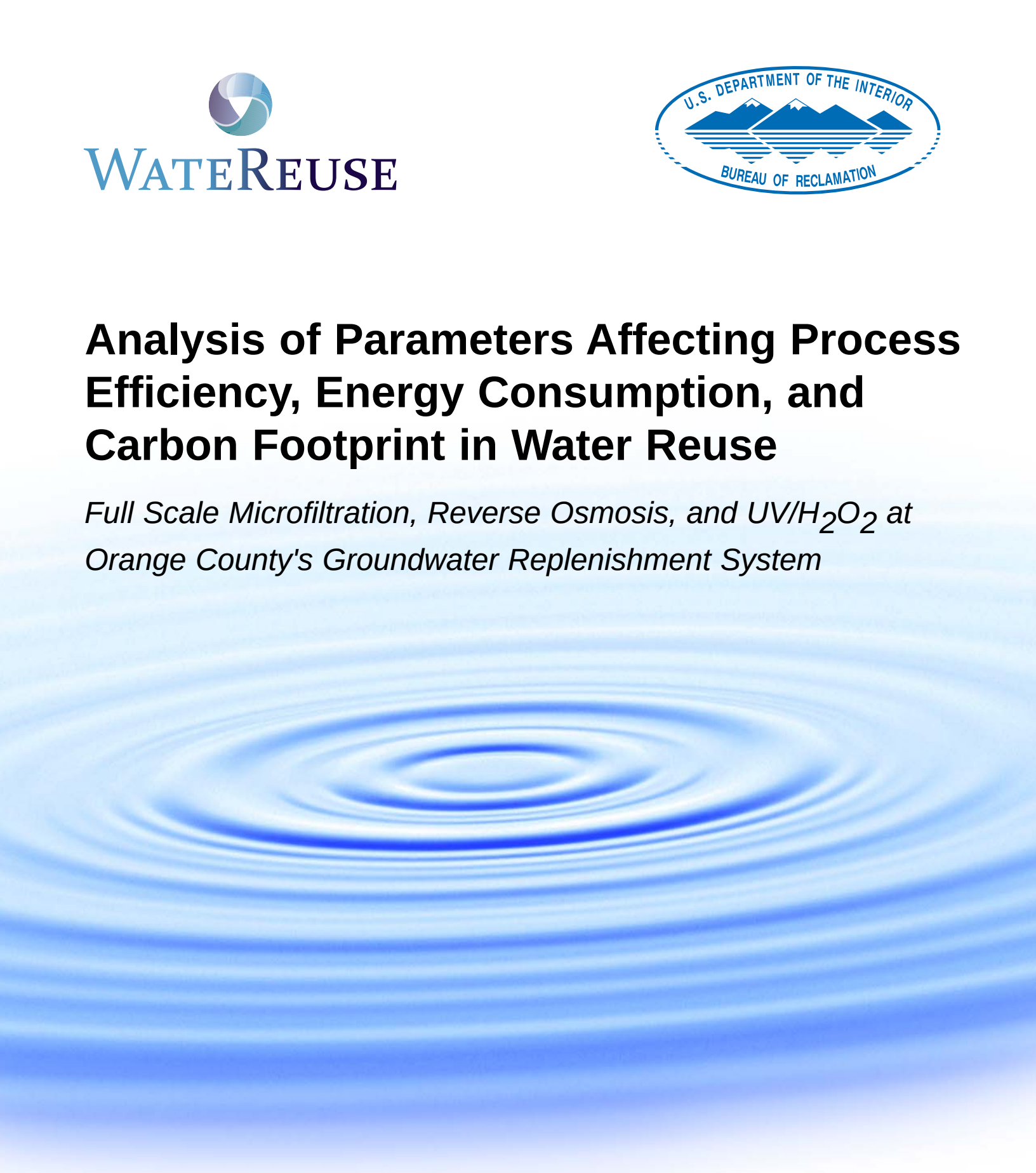

WateReuse Research Foundation

Analysis of Parameters Affecting Process Efficiency, Energy Consumption, and Carbon Footprint in Water Reuse

About the WateReuse Research Foundation

The mission of the WateReuse Research Foundation is is to build support for water reuse through research and education.The Foundation's research advances the science of water reuse and supports communities across the United States and abroad in their efforts to create new sources of high quality water for various uses through reclamation, recycling, reuse, and desalination while protecting public health and the environment.

The Foundation sponsors research on all aspects of water reuse, including emerging chemical contaminants, microbiological agents, treatment technologies, reduction of energy requirements, concentrate management and desalination, public perception and acceptance, economics, and marketing. The Foundation's research informs the public of the safety of reclaimed water and provides water professionals with the tools and knowledge to meet their commitment of providing a reliable, safe product for its intended use.

The Foundation's funding partners include the supporters of the California Direct Potable Reuse Initiative, Water Services Association of Australia, Pentair Foundation, and Bureau of Reclamation. Funding is also provided by the Foundation's Subscribers, water and wastewater agencies, and other interested organizations.

Analysis of Parameters Affecting Process Efficiency, Energy Consumption, and Carbon Footprint in Water Reuse

Full Scale Microfiltration, Reverse Osmosis, and UV/H_2O_2 at Orange County's Groundwater Replenishment System

Kenneth P. Ishida, Ph.D.
Orange County Water District

William J. Cooper, Ph.D.
University of California, Irvine

Cosponsors
Bureau of Reclamation
Orange County Water District

WateReuse Research Foundation
Alexandria, VA

Disclaimer

This report was sponsored by the WateReuse Research Foundation and cosponsored by the Bureau of Reclamation and the Orange County Water District. The Foundation, its Board Members, and the project cosponsors assume no responsibility for the content of this publication or for the opinions or statements of facts expressed in the report. The mention of trade names of commercial products does not represent or imply the approval or endorsement of the WateReuse Research Foundation, its Board Members, or the cosponsors. This report is published solely for informational purposes.

For more information, contact:

WateReuse Research Foundation
1199 North Fairfax Street, Suite 410
Alexandria, VA 22314
703-548-0880
703-548-5085 (fax)
www.WateReuse.org/Foundation

WateReuse Research Foundation Project Number: 08-11
ISBN: 978-1-941242-29-2

Contents

Figures

Tables

Acronyms

%T	percent transmittance
^{1}H NMR	proton nuclear magnetic resonance
14DIOX	1,4-dioxane
AFM	atomic force microscopy
ANN	artificial neural network
AOC	assimilable organic carbon
AOP	advanced oxidation process
ASE	activated sludge effluent
ATR-FTIR	attenuated total reflection-Fourier transform infrared
AWPF	Advanced Water Purification Facility
AWQA	Advanced Water Quality Assurance
BOD	biological oxygen demand
BPL	ballast power level
BSA	bovine serum albumin
CBOD	carbonaceous biological oxygen demand
CDPH	California Department of Public Health
CDOM	chromophoric dissolved organic matter
CF4	carbon tetra fluoride
CHO	carbohydrate
CHOS	carbon, hydrogen, oxygen, sulfur atom formula
CI	cleaning interval
CID	collision-induced dissociation
CIP	cleaning-in-place
CL2	total titrimetric chlorine
CLA	total amperometric chlorine
COSY	correlation spectroscopy
Da	dalton
DAPI	4',6-diamido-2-phenylindole
DATS	dialkyl tetralin sulfonates
DATSI	dialkyl tetralin sulfonate intermediates
DBE	double bond equivalency
DDW	Division of Drinking Water
delta-P	differential pressure
DLS	dynamic light scattering
DOC	dissolved organic carbon
DOM	dissolved organic matter
DPD	N,N-diethyl-*p*-phenylenediamine
DPW	decarbonated UV product water
DTGS	deuterated triglycine sulfate
EDCs	endocrine disrupting compounds
EDS	energy dispersive X-ray spectrometry
EDX	energy dispersive X-ray
EED	electrical energy dose

EEM	excitation-emission matrix
EfOM	effluent organic matter
Em	emission
EOLL	end-of-lamp-life
EPS	extracellular polymeric substances
ESI	electrospray ionization
Ex	excitation
FAS	ferrous ammonium sulfate; $(NH_4)_2(SO_4)_2 \cdot 6H_2O$
FASE	filtered activated sludge effluent
FPW	final product water
FT-ICR	Fourier transform ion cyclotron resonance
FY	fiscal year
GA	genetic algorithm
GC	gas chromatography
gfd	gallon per square foot per day
GHG	greenhouse gas
gpm	gallons per minute
GWR	Groundwater Replenishment
GWRS	Groundwater Replenishment System
H/C H:C	hydrogen-to-carbon ratio
HFP	hexafluoropropene
$HO^{\bullet}$	hydroxyl radical
HSDB	hazardous substance database
IMAC	immobilized metal affinity chromatography
IDL	instrument detection limit
IRIS	Integrated Risk Information System
ISO-LAS	isomers of LAS
kVA	total power
LAS	linear alkyl benzene sulfonates
LIMS	Laboratory Information Management System
LC-MS	liquid chromatography mass spectrometry
LPHO	low-pressure high-output
MALDI	matrix-assisted laser desorption ionization
MBAS	methylene blue active substances
MDL	minimum detection limit
MDLT	material derived from linear terpenoids
MF	microfiltration
MFBW	membrane filtered backwash
MFC	microfiltration backwash or microfiltration concentrate
MFE	microfiltration effluent
MFF	microfiltration feedwater
MG	million gallons
mgd	million gallons per day
MIMS	membrane introduction mass spectometry

MLR	multiple linear regression
MRM	multiple-reaction monitoring
MS	mass spectrometry
MWCO	molecular weight cutoff
NDMA	N-nitrosodimethylamine
NDN	nitrification-dentrification
NFP	normalized feed pressure
NIH	National Institute of Health
NIST	National Institute of Standards and Testing
NL	notification level
NLM	National Library of Medicine
NMR	nuclear magnetic resonance
NOESY	Nuclear Overhauser effect spectroscopy
NOM	natural organic matter
NTU	nephelometric turbidity units
OCH_3	methoxy functional group
OCSD	Orange County Sanitation District
OCWD	Orange County Water District
OFCB	octafluorocyclobutane
OH	hydroxyl functional group
P^3	persistent popular pollutants
PES	polyethersulfone
PF	power factor
PFIB	perfluoroisobutane
PLC	programmable logic controller
PLFA	phospholipid fatty acid
PP	polypropylene
PPCPs	pharmaceutical and personal care products
PPL	styrene-divinyl-benzene-polymer
PSI	pounds per square inch
PTEDSB	phosphatidylethanolamine, dipalmitoyl-sulforhodamine B
QSE	quinine sulfate equivalents
RC	research center
RDL	reportable detection limit
RMS	root mean square
RO	reverse osmosis
ROC	reverse osmosis concentration or brine
ROF	reverse osmosis feedwater
ROP	reverse osmosis permeate (without hydrogen peroxide)
SASE	simulated activated sludge effluent
SCADA	supervisory control and data acquisition
SCN	thiocyanate
SDI	silt density index
SEM	scanning electron microscopy
SiF4	silicon tetrafluoride

SPC	sulfophenyl carboxylic acids
SPE	solid phase extraction
SRNOM	Suwanee River natural organic matter
STP	standard temperature pressure
TDS	total dissolved solids
TFA	trifluoroacetic acid
TFE	tetrafluoroethylene
TFE	trickling filter effluent
TMP	transmembrane pressure
TOC	total organic carbon
TOF	time of flight
TOTCL2	total titrimetric chlorine
TOTCLA	total amperometric chlorine
TSS	total suspended solids
UF	ultrafiltration
UPLC	ultra performance liquid chromatography
UV	ultraviolet
UVF	feedwater to the UV/AOP facility
UVP	product water from the UV/AOP facility
UVT	percent transmittance
VOC	volatile organic compound

Foreword

The WateReuse Research Foundation, a nonprofit corporation, sponsors research that advances the science of water reclamation, recycling, reuse, and desalination. The Foundation funds projects that meet the water reuse and desalination research needs of water and wastewater agencies and the public. The goal of the Foundation's research is to ensure that water reuse and desalination projects provide sustainable sources of high-quality water, protect public health, and improve the environment.

An Operating Plan guides the Foundation's research program. Under the plan, a research agenda of high-priority topics is maintained. The agenda is developed in cooperation with the water reuse and desalination communities including water professionals, academics, and Foundation subscribers. The Foundation's research focuses on a broad range of water reuse and desalination research topics including:

- Defining and addressing emerging contaminants, including chemicals and pathogens
- Determining effective and efficient treatment technologies to create 'fit for purpose' water
- Understanding public perceptions and increasing acceptance of water reuse
- Enhancing management practices related to direct and indirect potable reuse
- Managing concentrate resulting from desalination and potable reuse operations
- Demonstrating the feasibility and safety of direct potable reuse

The Operating Plan outlines the role of the Foundation's Research Advisory Committee (RAC), Project Advisory Committees (PACs), and Foundation staff. The RAC sets priorities, recommends projects for funding, and provides advice and recommendations on the Foundation's research agenda and other related efforts. PACs are convened for each project to provide technical review and oversight. The Foundation's RAC and PACs consist of experts in their fields and provide the Foundation with an independent review, which ensures the credibility of the Foundation's research results. The Foundation's Project Managers facilitate the efforts of the RAC and PACs and provide overall management of projects.

The Advanced Water Purification Facility at Orange County Water District utilizes a multiple-barrier approach to recycle secondary-treated wastewater for indirect potable reuse. The purification process consists of microfiltration (MF), reverse osmosis (RO), and a UV/hydrogen peroxide advanced oxidation process (AOP). An investigation was conducted to identify the mechanisms of MF and RO fouling, characterize the foulants, and characterize the AOP. This project also included a carbon and energy footprint analysis of the purification facility. The ultimate goal of these ongoing studies is to optimize the purification process and improve the quality of the product.

Doug Owen
Chair
WateReuse Research Foundation

Melissa Meeker
Executive Director
WateReuse Research Foundation

Acknowledgments

This project was funded by the WateReuse Research Foundation in cooperation with the U.S. Bureau of Reclamation and the Orange County Water District.

The principal investigators would like to thank the Project Advisory Committee and the Project Team that contributed to the success of this project.

Principal Investigators
Kenneth P. Ishida, *Orange County Water District*
William J. Cooper, *University of California Irvine*

Project Team
Don Phipps, Jr., *Orange County Water District*
Menu Leddy, *Orange County Water District*
Jana Safarik, *Orange County Water District*
Grisel Rodriguez, *Orange County Water District*
Richard Bold, *Orange County Water District*
Christine Pham, *Orange County Water District*
Leticia Villarreal, *Orange County Water District*
Tom Knoell, *Orange County Water District*
Dave Dubry, *Orange County Water District*
Robert Raley, *Orange County Water District*
Water Production Department, *Orange County Water District*
Advanced Water Quality Assurance Laboratory, *Orange County Water District*

Dr. Diego Rosso, *University of California, Irvine*
Dr. Reza Sobhani, *University of California, Irvine*
Dr. Barbara Cottrell, *University of California, Irvine*
Mathew Zwartjes, *University of California, Irvine*
Dr. Donald Blake, *University of California, Irvine*
Yu-Hsin Hung, *University of California, Irvine*

Dr. Michael Gonsior, *University of Maryland*
Dr. Weihua Song, *Fudan University*
Dr. Eunha Ho, *San Diego State University*
Dr. Andre Simpson, *University of Toronto*

Participating Agencies
Orange County Water District
University of California, Irvine
San Diego State University
University of Toronto

Project Advisory Committee
Greg Bradshaw, *AECOM*
Katie Guerra, *U.S. Bureau of Reclamation*
Jim Lozier, *CH2M HILL*
Dr. Ben Stanford, *Hazen and Sawyer*
Dr. Pei Xu, *New Mexico State University*

Executive Summary

On January 10, 2008, Orange County Water District (OCWD) commissioned the 70 mgd Groundwater Replenishment (GWR) System that replaced the 5 mgd Water Factory 21 that began service in October 1976. The GWR System is an indirect potable reuse project jointly operated by OCWD and Orange County Sanitation District (OCSD). The Advanced Water Purification Facility (AWPF) is the main component of the GWR System. The AWPF produces highly treated recycled wastewater for direct injection into a seawater intrusion barrier and for groundwater recharge. The treatment train is comprised of microfiltration (MF) and reverses osmosis (RO) and utilizes ultraviolet (UV) light for disinfection and distruction of N-nitrosodimethylamine (NDMA). With the addition of hydrogen peroxide (H_2O_2) to the UV process, removal of trace contaminants is achieved by an advanced oxidation process (AOP). Although the AWPF produces high-quality recycled wastewater, measures can be taken to improve or optimize its performance and potentially reduce the operating costs, which currently exceed $31.6 million per year (FY 2012–2013).

Improvements can be made throughout the entire treatment process. The clarified secondary effluent possesses a significant load of biological detritus, such as microparticulates, nanoparticulates, and effluent organic matter (EfOM), which contribute to rapid fouling of the hollow fiber MF membranes with consequent loss of performance and increase in operational costs. Accumulation of foulants on the RO membrane surface often leads to a rapid decline in membrane performance in terms of decreased water flux and increased salt passage. A UV/H_2O_2-based AOP was added to the treatment process as a barrier to trace organic and inorganic compounds of public health concern. However, there are no data to indicate that the 3 mg/L peroxide dose is the optimum concentration to apply to the RO permeate feedwater to the UV/AOP. Understanding how the soluble chemical constituents in the feedwaters affect and are affected by the MF and RO separation processes and the extent to which the trace organic compounds are modified by the UV/AOP process are vital to the development of a more cost-effective, energy-efficient treatment process. Investigation into the application of advanced oxidation for the removal of pharmaceuticals and personal care products (PPCPs) from RO concentrate (ROC) and the development of a surrogate for AOP has significant implications from an environmental and public health point of view. And finally, for the first time, an assessment of the carbon and energy footprint of the AWPF was performed.

The focus of this research project was on the characterization of each unit processes, the source waters that feed them, the mechanisms of fouling, the foulants, and the performance of the AOP, followed by an assessment of the carbon and energy footprint of each unit. Results from these studies were used to identify specific areas where monitoring and control strategies can be implemented to improve on the performance of the MF, RO, and UV/H_2O_2 AOP and potentially reduce the carbon and energy footprint.

A number of standard and nonstandard analytical methods were used in the characterization process including light and scanning electron microscopy (SEM), energy dispersive X-ray (EDX) spectroscopy, gas chromatography (GC), electrospray ionization Fourier transform ion cyclotron resonance (ESI-FT-ICR) and time of flight (TOF) mass spectrometry (MS), excitation-emission matrix (EEM) fluorescence spectroscopy, attenuated total reflection

Fourier transform infrared (ATR-FTIR) spectroscopy, and proton nuclear magnetic resonance (^{1}H NMR) spectroscopy.

Characterization of EfOM in Secondary-Treated Wastewater

The source water to the AWPF consists of a blend of trickling filter effluent (TFE) and activated sludge effluent (ASE) from the OCSD, which operates a nitrification denitrification process. EfOM in TFE and ASE were isolated by solid-phase extraction (SPE) and characterized by ^{1}H NMR and ESI-FT-ICR mass spectrometry. The analysis revealed the presence of mass fragments containing a single sulfur atom (CHOS molecular formula) associated with anthropogenic surfactants. More specifically, these fragments were linked to linear alkyl benzene sulfonates (LAS), dialky tetralin sulfonate (DATS), dialkyl tetralin sulfonate intermediate (DATSI), and sulfophenyl carboxylic acid (SPC). Among compounds common to both ASE and TFE, the highest abundances of any mass occurred for those whose formula corresponded exactly with those of SPC, LAS, and DATS. The SPE and mass spectrometry did not provide information on the quantity of these fragments in the ASE and TFE.

Characterization of MF Fouling Mechanism

Laboratory bench-scale experimental studies to evaluate fouling of the polypropylene MF membranes indicated two mechanisms of MF fouling: (1) classical pore blocking via surface cake formation by particulates >0.2 µm nominal pore size that are largely alleviated by backwashing and air scouring, and (2) pore plugging that is due to intercalation of EfOM (nanoparticulates) with dimensions <0.2 µm into the membrane matrix that is difficult to mitigate with regular backwashing.

The use of fluorescent nanobeads and a bench-scale reactor demonstrated that the accumulation of membrane foulants occurs from the top of the fibers (where suction is applied) and progresses toward the bottom. This observation was supported by autopsies of MF membranes recovered from the full-scale pilot unit. Carbohydrate (CHO) and protein concentrations also were highest on the top portion of the membranes, suggesting that these microconstituents were deposited in a manner similar to the nanobeads.

Nanoparticulates that enter the membrane matrix and fill the void space accounted for 80% of the flux reduction during MF operation. These nanoparticulates have a higher potential to foul the membrane than the microparticles and are most likely responsible for irreversible fouling that necessitates a chemical clean-in-place (CIP). The size of the nanoparticles in the clarified secondary effluent responsible for MF fouling was determined by differential filtration using a graded series of microfilters and ultrafilters (down to 10 kDa MWCO). These results suggested that the size of the fouling particles start between 2.5–3.5 nm and ranges up to the effective MF cutoff of 0.2 µm.

Much of the material responsible for MF fouling appears to be biological debris. CHO, protein, and lipids were all identified on the surface of fouled membranes from the bench-scale test cell and full-scale pilot units. Energy dispersive X-ray (EDX) analysis revealed evidence of biological elements not native to the polypropylene membrane, such as phosphorus, sulfur, carbon, and oxygen.

MF Precoagulation

Successful MF fouling mitigation strategies must reduce the accumulation of nanomaterials within the MF matrix either by removing the materials from the feedwater or by reducing their interaction with the membrane surface so that they can be dislodged during the backwash. Nanoparticulate preaggregation experiments with the coagulant Sumaclear 700 (S700) were performed. The S700 coagulant was shown to aggregate nanoparticles into microparticles larger than the average MF 0.2 μm pore size. This reduced the concentration of nanoparticles in solution and the rate at which the nanoparticles adsorbed to the membrane matrix and eventually clogged the pores. The overall effect of this pretreatment was to extend the time between cleanings and improve membrane performance.

MF pretreatment with 10 mg/L of S700 coagulant increased the cleaning interval (CI) from 21 days to 82 days (291%), improved the removal of CHO and protein from the feedwater, and reduced the total CHO and protein load on the RO process. However, application of the coagulant also resulted in aluminum (Al) bleed-through into the MF effluent (MFE), thereby increasing the total RO feedwater Al concentration, which may increase the potential for aluminum silicate scaling in the third stage of the RO process.

MF pretreatment with 5 mg/L S700 increased the CI from 21 days to 54 days (157%). The addition of 5 mg/L S700 resulted in a slight increase of Al in MFE, which could potentially result in alumina scaling further downstream in the RO process. The addition of 2.5 mg/L of S700 increased the CI from 21 days to 36 days (71%) and did not result in an increase of Al in MFE. In addition to increasing the CI, the S700 pretreated membranes operated at a much lower transmembrane pressure (TMP) at all three coagulant concentrations, resulting in lower overall energy costs while producing the same quantity of MF product water.

The quality of the MF effluent has a direct affect on the RO performance downstream and, thus, coagulant bleed-through is a concern. The results of the coagulant bleed-through studies suggested that the presence of low doses (2.5 mg/L) of S700 at the feed end of the RO process does not have a significant effect on RO performance, although SEM of the feed end RO membranes showed a layer of nanoparticulates on both coagulant pretreated and untreated membranes. However, the effect of adding the equivalent of 5 mg/L of coagulant to the RO feedwater led to heavy fouling and loss of membrane flux in the third stage where feedwater constituents are concentrated six times. SEM analysis showed a thick precipitate covering the membrane surface and membrane spacer. Results from these studies demonstrated that MF performance can be improved by preventing nanoparticles from entering the membrane matrix, but coagulant that passes through the membrane into the MFE may have adverse effects on the RO performance downstream. Therefore, strict polymer control is needed to prevent coagulant bleed-through, which otherwise could lead to severe fouling in the third-stage RO treatment process.

Isolation and Characterization of MF Foulants

MF foulants were isolated by solid-phase extraction (SPE) followed by elution with different solvents. Eluates were analyzed by EEM fluorescence spectroscopy, ^{1}H NMR spectroscopy, and GC×GC−TOF MS. The ^{1}H NMR spectra of the raw MFF and MFE samples showed the presence of (1) carbohydrate, (2) carbohydrate-rich alicyclic, (3) aliphatic, and (4) aromatic compounds in both source waters. This analysis also revealed that the compounds, present in the MFF, were small enough to pass through the 0.2 μm pores of the polypropylene

membrane into the effluent and, thus, the MF is not a complete barrier to the EfOM of the wastewater. The results were consistent with differential filtration studies that showed that MFE still posseses the potential to foul and clog the pores of an MF membrane and restrict the flow of water. Fractionation of the EfOM by SPE with different solvent elutions of the MFF and MFE showed small variations in the type or class of compounds that were adsorbed to the membrane surface. The MFF extracts contained more hydrophobic lipids, fatty acids, and aromatic compounds. This would be expected for wastewaters treated with a hydrophobic membrane material like polypropylene. Microorganisms retained at the membrane surface likely contribute to much of the lipid and fatty acid content of the EfOM from the MFF eluate. The results from the ^{1}H NMR spectroscopic analysis were consistent with the results of the EEM fluorescence spectroscopic analysis of MFF and MFE. Whereas this aromatic and hydrophobic lipid-like class of EfOM appeared to foul the membrane surface to a greater extent, these compounds were not removed completely, were small enough to pass through the membrane, and could foul the cartridge filters and RO membranes downstream.

Reverse Osmosis Membrane Autopsy

An autopsy was conducted on a lead element of one of the 5 mgd three-stage RO units that was performing poorly. The foulant on the surface of the RO membrane was mostly biomass and nanoparticulate. Much of the material was composed of whole bacterial cells and organic EPS (i.e. CHO), proteins, and other bacterial debris. The biofilm appeared to be the heaviest at the feed end of the membrane and lightest on the brine end. The biofilm was a network of cells imbedded in a thick coat of EPS. The cells were “glued” together by EPS, making a total bacterial count impossible.

Visualization of the gram stained biofilm through a series of focal planes revealed a layered network of bacteria. Open spaces between the layers and bacteria were visible. The presence of these void spaces allow for nutrient transport into the biofilm structure. The biofilm did not appear to be diverse in bacterial species. The majority of the bacteria present may be an endospore forming bacterium of the genus *Bacillus*, which allow a bacterium to survive harsh environmental conditions. These endospores may be left behind after membrane cleaning and remain on the membrane surface, and when conditions become favorable, they may be reactivated, restarting the biofouling process.

The foulant material appeared to be multilayered with a top layer taking the form of a biofilm and the bottom layer composed of nanoparticulates. A portion of the nanoparticles were of biological origin, which was evidenced by the presence of CHO smaller than 0.2 µm. The hypothesis is that the nanoparticulate fouling is the primary fouling layer and the bacteria are the secondary fouling layer. Nanoparticles are the first component the membrane comes in contact with when the formation begins. Biofilm development occurs over time as conditions at the membrane surface become favorable.

Elemental mapping of the membrane surface by environmental SEM revealed a small presence of aluminum and silicon, which was attributed to aluminum silicate scaling. An EDX spectroscopic analysis of the fouled membrane revealed the presence of the elements C, O, S, Si, Al, P, N, Na, Mg, Cl, and Ca. Analysis of the fouled feed spacer revealed the presence of similar elements.

Fouling of the feed spacer may have a significant impact on biofouling and membrane performance. The feed spacer had the same double layer of foulants as observed on the membrane surface. Nanoparticles were in direct contact with the spacer, and bacteria

appeared to be in contact with the nanoparticles. Biofilm accumulation on and around the feed spacer may result in an increase in membrane fouling and redirect the flow of the feedwater through the membrane module. Although these autopsies provide information on the nature of the foulants and their distribution on and within the RO element, they do not provide information that directly correlates to the reduction of membrane performance, in other words, water flux and salt rejection (see discussion following on the impact of foulants on RO performance).

Artificial Neural Network (ANN) Models of Full-Scale RO Fouling

Overall, it was possible, on the basis of historical data from the AWPF operating from April 2008 through February 2010, to explain first-stage RO membrane lifetime (defined as the time between CIP) using just six inputs involving only four ROF water quality parameters by employing an ANN-based multivariate model. The predictive ability of this model was further tested using 8 months of data obtained from March 2010 through December 2010 with mixed success.

Input parameters identified as predictive of first-stage RO membrane lifetime included the maximum observed ammonia nitrogen (NH_3-N) value, the average NH3-N, the maximum calcium (Ca), the average Ca, the average sulfate (SO_4), and the maximum total chlorine (amperometric) observed during each membrane's lifetime between cleanings (all in mg/L).

Whereas the original ANN model performance suggested a highly explanatory and predictive model, the validation study yielded mixed results. Eight of the 15 RO units exhibited a close fit with the model, which accurately predicted their membrane lifetime performance, whereas the model failed to predict membrane lifetimes of the other seven RO units from the validation set. In these cases, the observed membrane lifetimes were significantly less than that predicted by the model.

Because the ANN model was quite capable in more than half of the cases of predicting the validation exemplar responses of the membranes, it does appear generally to be valid. One hypothesis as to why it failed to predict the behavior of the other units' membrane lifetime may lie in changes specific to those units that occurred between when the ANN model was constructed and when the validation lifetime data were obtained. It is hoped that further historical data can be obtained on the particular RO units where the model failed, and if those units now have a history disparate from the others, it may be possible to identify a quantifiable factor or factors that will allow inclusion of their behavior in a new membrane lifetime model. With time, new exemplars will be added to the data set to strengthen the ANN, which has shown that it may be possible to use basic water quality data to predict lifetimes between RO cleanings.

Bench-Scale Investigation of the Impact of Biological and EfOM Fouling on RO Performance

The relationship between the accumulation of biological and organic matter on the RO membrane surface and loss of normalized specific membrane product water flux (i.e., membrane fouling) was investigated using linear correlation analysis for each stage of a three-stage AWPF RO unit. RO stage performance was characterized by the behavior of membranes at the leading end (feed end) of the stage and at the tail end (brine end) of each

stage using sets of five 4 × 6 in. flat sheet test cells fed with water from both ends of the RO stage.

Correlation was ranked on the basis of statistical significance of the observed relationship using the 95% confidence level, $p \leq 0.05$, as the criterion, as well as on the percentage of the observed variability in fouling that could be explained by the observed variability in the accumulation of material on the membrane surface (percent R-squared, % R^2).

Based on this approach, the results of the study suggest that factors related to membrane fouling change significantly along the RO feed channel from stage to stage. In the first AWPF RO stage, fouling was best related to the accumulation of protein material on the membrane surfaces. In the second RO stage, this relationship transitioned from accumulation of protein to accumulation of viable aerobic heterotrophic bacteria. And finally, in the third RO stage, fouling initially was influenced by the presence of viable bacteria at the beginning of the stage but transitioned toward an "uncharacterized factor" that influenced fouling at the end of the stage. This uncharacterized factor may possibly be associated with mineral scaling.

Bench-Scale Investigation of the Impact of Elemental Fouling on RO Performance

SEM-EDX spectroscopy provides a means of identifying the presence of atomic elements on the surface of a specimen. Although it is possible to obtain the raw area counts related to the intensity of the signal from atoms under the electron beam, variations in the properties of the beam and specimen make direct use of the data for comparison of the elemental concentration from sample to sample difficult. To overcome this limitation, normalization of the elemental EDX signal to carbon by calculation of the element/carbon signal ratio was performed. Carbon is ubiquitously present in the RO membrane and spacer material, and, thus, it presents a consistent background for comparison of other, less concentrated elements.

Using this approach, the relationship between the element/C ratios determined for RO membrane swatches exposed to feedwaters from RO Unit E01 corresponding to those at the beginning of the first, second, and third RO stages and the end of the third RO stage were regressed against the observed normalized specific product water flux. Elemental analysis of the membrane surface and the Vexar spacer material were determined by EDX spectroscopy. Elements incorporated into fouling matter were anticipated to show a negative relationship between their element/C ratios and membrane normalized specific water flux. The strength of the relationships was determined using the linear regression % R^2 (the percent of the variance in the normalized specific water flux that could be explained by variations in the element/C ratio) and the statistical significance of the relationships evaluated using the regression model p-values, where $p \leq 0.05$ corresponds to significance at the 95% confidence level.

Fouling of Membrane Surface

Examination of elements on the RO membrane surface representative of the front end of the RO train (i.e., the lead end of the first element) revealed that more than 90% of the observed decline in normalized specific water flux could be explained by the increase in iron/C and copper/C ratios alone. The element/C ratios of the other elements were not significantly related to the normalized specific water flux.

At the end of the first RO stage and beginning of the second RO stage, the increase in silicon/C ratio on the membrane surface could explain > 98% of the observed decline in the

normalized specific water flux. Observed variances in element/C ratios of O, Na, Mg, Al, P, S, Cl, Ca, and K each corresponded to half or more of the variations in the normalized specific water flux. This suggests that each of these elements also played a role in the composition of surface fouling material on the membrane in this region of the RO train.

At the end of the second RO stage and beginning of the third RO stage, an increase in no element/C ratio accounted for > 38% of the observed decline in the normalized specific product flux, suggesting that another factor was primarily responsible for membrane fouling in this region of the RO train.

At the end of the third RO stage, several element/C ratios were fairly strongly negatively related to the observed decline in the normalized specific water flux, although not to the degree seen in other regions of the RO train. These elements included (in order of apparent influence) the following:

phosphorus	(% R^2 = 77.65%, p = 0.1188)
iron	(% R^2 = 77.65%, p = 0.1188)
copper	(% R^2 = 77.65%, p = 0.1188)
calcium	(% R^2 = 67.79%, p = 0.1766)
sulfur	(% R^2 = 60.31%, p = 0.2234)

All of these elements can combine to form potentially insoluble mineral compounds, so higher ratios of these elements on the membrane surface should be linked to loss of membrane water flux.

Fouling of Vexar Spacer

Accumulation of material on the polypropylene Vexar spacer was hypothesized to have the potential to partially or completely occlude the feed channel and cause a loss of normalized specific membrane water flux. This would cause a disruption in the cross flow over the RO membrane surface. The resulting increase in the polarization layer would result in an increase in the membrane surface osmotic pressure, resulting in a decrease of the net hydraulic pressure available for solute separation.

Examination of element/C ratios on the Vexar spacer revealed that at the lead end of the first RO element in the first RO stage, several element ratios were strongly and significantly negatively related (at the 95% confidence level, $p \leq 0.05$) to the membrane normalized specific water flux. These included the following (in order of the strength of the relationship):

silicon	(% R^2 = 98.15%, p = 0.0093)
chlorine	(% R^2 = 97.20%, p = 0.0141)
potassium	(% R^2 = 95.38%, p = 0.0234)
sodium	(% R^2 = 94.92%, p = 0.0257)
nitrogen	(% R^2 = 93.17%, p = 0.0348)
magnesium	(% R^2 = 92.42%, p = 0.0386)
copper	(% R^2 = 91.74%, p = 0.0422)
fluorine	(% R^2 = 91.69%, p = 0.0425)
calcium	(% R^2 = 91.43%, p = 0.0438)
oxygen	(% R^2 = 90.31%, p = 0.0497)

In addition, aluminum (% R^2 = 74.56%, p = 0.1365) also was strongly negatively related to the membrane normalized specific water flux. In addition, all of these element/C ratios were strongly cross-correlated with each other, suggesting that they all may have been incorporated into the same suite of foulant material. Aluminum and silicon also were strongly interrelated, which suggests that aluminum silicate may have formed on the Vexar spacer. Taken together, these data strongly suggest the possibility that fouling of the Vexar spacer may have even more influence on the loss of RO membrane water flux at the front end of the first RO stage than foulants deposited on the membrane surface.

No other strong (% R^2 > 90%), statistically significant ($p \leq 0.05$), negative relationships were observed between any of the Vexar spacer element/C ratios and the normalized specific water flux at any of the other points examined (end of the first and beginning of the second, end of the second and beginning of the third, or end of the third RO stages) in the RO train. However, strong positive relationships were observed between ratios for sodium, chlorine, and potassium at the end of the first RO stage and beginning of the second RO stage, for aluminum at the end of the second RO stage and beginning of the third RO stage, and for iron and phosphorus at the end of the third stage.

The positive relationships between element/C ratios on the Vexar spacers and normalized specific water flux was much more difficult to explain but may have to do with an increase in Vexar surface charge that improved hydrodynamic flow over the spacer by decreasing the hydrophobicity of the polypropylene spacer. Dehydrating the spacer then would result in counter ions associating with the adsorbed charged surface molecules and detection by the EDX spectroscopy.

In the tail part of the third RO stage, the chlorine/C ration on the Vexar spacer was the only spacer element/C ratio observed to be fairly strongly negatively associated with the normalized specific membrane water flux. The copper/C ratio also appeared to exhibit a weak negative relationship (% R^2 = 56.26%, p = 0.2500).

In many cases, the element/C ratios calculated from EDX spectroscopic data on the membrane surfaces and on the Vexar spacer were found to be negatively related to membrane performance. This was consistent with their correlation with the accumulation of foulant material directly on the RO membranes or on the Vexar spacer in a fashion that disrupted operation of the membrane swatches.

One difficulty encountered in the study was the lack of experimental exemplars with which to define the linear regression model. Although five membrane swatches were exposed to each RO feed type, experimental difficulties associated with the operation of the RO facility limited the study to only four exemplars, and in many cases this became reduced to only three, which made establishing statistically significant relationships very challenging. In addition, in a number of cases, clustering of the data was seen, with a lack of exemplars in mid-points of the model relationships. In many cases, conclusions were based on the behavior of a single data point, which greatly weakened the statistical significance of many of the models.

EDX spectroscopic data are relatively simple to obtain for both RO membranes and the Vexar spacers. Therefore, it is intended that this study will be repeated with another set of membranes with the hope that all five swatches can be harvested for analysis.

Characterization of the UV/H_2O_2 Advanced Oxidation Process

A series of pilot-scale reactor experiments were conducted to mimic the performance of the full-scale UV/AOP reactors. Data from these experiments along with historical data from the full-scale reactor trains of the AWPF were used to characterize and optimize the performance of the UV/H_2O_2 AOP.

The limited availability of reportable 1,4-dioxane data from the UV feed (UVF) and UV product (UVP) source waters of the AWPF UV/AOP facility over a 5-year period between January 2008 and December 2012 made accurate assessment of the performance of the AOP difficult. Eighteen samples (of 279 total) with a UVF 1,4-dioxane concentration above the RDL of 1 μg/L were used to determine the removal efficiency by the hydroxyl radical-based AOP. Seventeen of these sample pairs had a UVP concentration below the reportable detection limit (RDL), but were still used to obtain an estimate of the performance of the UV/H_2O_2 AOP. An average 0.45-log reduction (n = 18) of the 1,4-dioxane concentration in UVF was measured, which meet the minimum removal criterion approved by the California Department of Public Health.[1] A linear regression line fit to the data (R^2 = 0.89) indicate 70% reduction or 0.52-log of 1,4-dioxane was achieved under the normal operating conditions of an applied EED of 0.24–0.32 kWh/kgal, an H_2O_2 concentration in the feedwater of 2.6–3.3 mg/L, a total chlorine (chloramines) concentration of 3–4 mg/L, and a UVT of 97–98 %T. The average EE/O for 1,4-dioxane of the full-scale UV/AOP facility of the AWPF was 0.658 ± 0.132 kWh/kgal/log (n = 18).

The UV dose (mJ/cm^2) associated with the normal operation of a reactor train was estimated using a combination of collimated beam NDMA photolysis data (Sourshian et al., 2001) and the NDMA photolysis data from full-scale reactor studies (Brown, 2008). One-log reduction of NDMA from an RO permeate was achieved at an EED of 0.168 kWh/kgal by the Trojan UVPhox (containing 72 lamps per reactor). An equivalent 1-log reduction of NDMA from the RO permeate was achieved with a UV dose of 550 mJ/cm^2 with a collimated beam of UV light in the absence of hydrogen peroxide. Therefore, it was estimated that a UVPhox reactor train operating at an EED of 0.168 kWh/kgal was approximately equivalent to delivering a UV dose of 550 mJ/cm^2. The actual equivalent UV dose delivered by the UVPhox to achieve 1-log reduction of NDMA is slightly high than 550 mJ/cm^2 at the EED of 0.168 kWh/kgal because there was ~3 mg/L of H_2O_2 present in the UV feedwater when the full-scale study was conducted and an undetermined amount of NDMA was presumably removed by hydroxyl radical-mediated advanced oxidation. The effect of each individual reactor was assumed to be additive and the combined EED associated with the number of reactors in service was used to estimate the UV dose that is delivered to the feedwater. The delivered UV dose of the 72-lamp UVPhox of the AWPF was estimated to be slightly more than 3274 mJ/cm^2 per kWh/kgal for a source water that contains 2.5–3.0 mg/L of chloramines, 2.6–3.0 mg/L of H_2O_2 and a UVT of 97–98 %T at pH 5.3–5.5. And thus, under normal operating conditions (0.26–0.32 kWh/kgal), the UV/AOP facility is believed to deliver between 850 and 1050 mJ/cm^2.

[1] Pacifico, O. C. System No. 309001–Characterization of NDMA and 1,4-Dioxane Oxidation at the Full Scale Advanced Water Purification Facility. California Department of Public Health, Southern California Drinking Water Field Operations Branch, Santa Ana District, correspondence letter dated August 28, 2009.

A model of H_2O_2 photolysis from the pilot reactor indicated that 0.2 mg/L is consumed from an RO permeate feedwater with a UVT of 97 %T, containing 2.6 mg/L H_2O_2 in the presence of 2.6 mg/L of total residual chlorine (that consisted of 50% (w/v) monochloramine and 50% dichloramine) at a flow rate of 6 gpm. The consumption of 0.2 mg/L H_2O_2 across the pilot reactor running at a flow rate of 6 gpm and was consistent with the quantity of 0.2 mg/L H_2O_2 consumed across the full-scale UV/AOP of the AWPF with a similar average 2.6 mg/L H_2O_2 feed operating at an average 0.289 kWh/kgal.

Through the work of the AOP pilot studies, it was discovered that a significant amount of 1,4-dioxane is removed in the absence of H_2O_2 and presence of ~2.6 mg/L total chlorine. A total of 0.14–0.21 log (28–38%) reduction of the 1,4-dioxane concentration was achieved in the absence of H_2O_2. Whereas the presence of mono- and dichloramine (molar absorptivity 388 and 142 $M^{-1}cm^{-1}$, respectively) would appear to hinder the AOP by scavenging photons and reducing the UVT at 254 nm, the combined chlorine appears to contribute significantly to the AOP.

A series of linear regression models were generated from the pilot data that mimicked the performance of the full-scale reactor train at different rates of flow. Based on the model representative of the normal operating conditions of the UV/AOP facility, the application of a measured 2.6 mg/L of H_2O_2 in the RO permeate feedwater to reactor train operating at an EED of 0.290 kWh/kgal, containing 2.6 mg/L total residual chlorine with a UVT of 97% T would result in a measured 0.51-log reduction of 1,4-dioxane. Furthermore, the model projected the reactor train would achieve an additional 0.15-log 1,4-dioxane removal for each additional 1 mg/L of H_2O_2 added to the feedwater under these operating conditions.

Characterization of VOCs in RO Permeate and UV/AOP Product Water

A purging or degassing system for the GC/MS analysis of atmospheric VOCs was modified to measure VOCs in water samples. This study showed that very small amounts (μg/L) of the alkyl nitrates (methyl, ethyl, and isopropyl) are present in the ROF, ROP, and UVP source waters of the AWPF. The amount recovered by a helium purge and GC/MS analysis varied from day to day. Quenching of residual chlorine (chloramines) in ROF samples with sodium thiosulfate resulted in a slight reduction in the recovery of all three alkyl nitrates. The sodium thiosulfate quenching agent did not appear to affect the recovery of the alkyl nitrates from the ROP and UVP water samples.

The RO process removed a portion of the alkyl nitrates from the feedwater—methyl nitrate 0.1–0.4-log (21–60%) reduction, ethyl nitrate 0.10–0.27-log (21–46%) reduction, and isopropyl nitrate 0.48–0.78-log (67–80%) reduction. However, a significant increase in the methyl nitrate concentration was measured across the UV/H_2O_2 AOP. The methyl nitrate concentration increased by a factor of 34 to 41times in the unquenched UVP water samples and by 33 to 47 times in the quenched UVP samples. The ethyl nitrate concentration increased 17% to 75% in the quenched samples and 50% to 100% in the unquenched UVP samples. The isopropyl nitrate concentration increased four-fold across the UV/H_2O_2 AOP in both the quenched and unquenched samples. Although these observed changes in alkyl nitrate concentration were consistent on each sampling date, the variation in concentrations reflected differences in the quality of the source water on different days. Currently there are no human or environmental health water quality standards established for these alkyl nitrates.

Application of AOP to Remove of Trace Organics in RO Concentrate

The results of radiolytic oxidation studies indicated that AOPs can effectively remove PPCPs from RO concentrates. This was the first attempt to evaluate the kinetics of a hydroxyl radical-mediated oxidation of PPCPs and to model their degradation in RO concentrate. The biomolecular reaction rate constants of individual PPCP and RO concentrate (EfOM) were employed to predict the removal rate of PPCPs, and the calculated results were in accordance with the experimental results. In addition, the removal of PPCPs was well correlated with the reduction of protein-like fluorescence of RO concentrate, suggesting that monitoring the changes of this fluorescence peak may provide a rapid and inexpensive method for the quantitative estimation of PPCPs degradation under treatment plant conditions.

Carbon and Energy Footprint Analysis

Pumps utilized by the MF process were responsible for 62% of the entire MF footprint. Of this, 30% is utilized by filtration pumps, 14% for backwashings, and 18% for transfer of the MF backwash (MFC) to the OCSD. Blowers employed for air scouring during the backwash process are responsible for the remaining 38% of the total energy footprint. The MF represents 14% of the total energy usage of the AWPF. The normalized energy footprint of the MF process was 272 kWh/MG of water production. A slightly larger amount of energy, 286 kWh/MG, is required to transfer MF effluent from the 2 MG break tank to the RO facility.

In the RO process, 1000 hp feedwater pumps dominate the energy footprint of the plant and make the footprint of the rest of the equipment (e.g., chemical transfer pumps and CIP pumps) negligible. The RO process accounts for 63% of the entire AWPF energy footprint. The normalized energy footprint of the RO process is 1180 kWh/MG.

The UV/AOP facility consists of eight trains that each contains 432 UV lamps for a total of 3888 low-pressure high-output 257 watt mercury lamps. The energy footprint of this process is dominated by the UV lamps that have a nominal energy footprint of 148 kWh/MG and represents 8% of the total energy usage by the AWPF.

A dynamic energy footprint model of the MF/RO/UV/AOP was generated. This model represented a diurnal variation of input parameters (e.g., hydraulic load and pollution concentration) their effects on electricity consumption, and the amplitude of variation. The results showed the benefit of an adaptive MF backwash cycling (determined from the dynamic influent load) and revealed the significant variation in required power for RO pumping in a regular diurnal period. Furthermore, an analysis of the indirect greenhouse gas emission associated with the operation of the AWPF was completed. The results indicated that these emissions are dominated by those associated with electricity consumption (i.e., 95–97%) contribution, compared to the emission associated with chemical transportations (i.e., 3–5%) contribution.

The principal greenhouse gases (GHGs) emitting to the atmosphere are carbon dioxide (CO_2), methane (CH_4), nitrous oxide (N_2O), and chlorofluorinated gases. Each gas has a global warming potential, which quantifies the molecular potential to accumulate heat relative to that of carbon dioxide. Therefore, GHGs reported in this study are in terms of the equivalent amount of carbon dioxide (CO_2eq).

Generally, during the carbon footprint analyses of an operating facility, the GHG emissions are categorized into direct and indirect emissions. Moreover, a special category is defined for indirect emission associated with imported electrical power. For reporting purposes (e.g., when using an accounting and reporting protocol, such as the LGOP, 2010) direct emission can be labeled as Tier I, indirect emissions for power importation as Tier II, and all other indirect emissions as Tier III. The boundary we considered in this study includes all tiers.

Because of their small contributions, direct CO_2, CH_4, and N_2O emissions of treatment processes (i.e., MF, RO, and AOP) are considered negligible. This is because the unit operations employed in the AWPF are largely relying on electrical power and do not emit directly carbon- or nitrogen-based gases.

The energy-associated CO_{2eq} emission of main AWPF's treatment processes were calculated based on the energy (kWh) consumed by the AWPF's treatment processes during 2011 and the published data for Southern California carbon emission of 236 gr CO_{2eq}/kWh (PG&E, 2013). The customary units for carbon footprint are metric tons (1 metric ton = 1 tonne = 1000 kg = 1 t). The results indicate that RO has the highest monthly emission of 909 tonne/month, following by MF and AOP with monthly emissions of 439 tonne/month and 138 tonne/month, respectively.

The water purification processes are chemical intensive. AWPF uses the chemicals for different treatment stages including operating and clean-in-place (CIP) stages of the MF process, operating and posttreatment stages of the RO process, and operating stage of the AOP process. There is almost no chemical use for the MF backwash. The chemicals are carried to the treatment plant mostly by trucks and stored appropriately for diurnal or periodic (e.g., the chemicals required for MF CIP stage) consumption.

A comparison between the quantitative truckloads associated with the AWPF's treatment processes revealed that the RO process had the highest associated monthly truckload count with 79.3 truckloads/month. This was mainly because of the lime consumption required for the RO posttreatment stage that required 62.4 average monthly truckloads. The MF process accounted for an average of 39.1 monthly loads. AOP had the lowest monthly truckloads with an average of 2.2 monthly loads. Overall, of the monthly average 120 truckloads entering the AWPF, half of them were related to the lime chemical consumption.

The results of GHG emission analysis indicated that the AWPF's total carbon footprint is dominated by the energy associated carbon emission (i.e., 97% contribution). Meanwhile, the carbon emissions associated with the chemical transportation are responsible for a small 3% contribution among the studied components. The results are based on 50 mi of chemical transportation. If this parameter is doubled by considering an average 100 mi of transportation for the consumed chemicals, the contribution of this component would increase by ~2% (i.e., overall 5% contribution), and thus it shows that the total carbon footprint for this parameter is low in sensitivity.

In the state of California, the carbon emission for unit energy generation is higher during the summer season compared to the winter. The main reason is because there is a greater contribution of fossil fuel sources in power generation during the peak hours of hot summer days. Currently, California is facing gradual changes in the portfolio of energy sources employed for power generation. A greater contribution from renewable sources with lower carbon emission compared with traditional fossil fuel power sources is expected in the future. Thus, because of the massive contribution of energy consumption, any variation among the

unit energy GHG emissions can significantly change the total carbon footprint of the AWPF and make this parameter significantly sensitive.

Recommendations

1. Develop more hydrophilic membrane materials that are more resistant to fouling by protein, carbohydrate, and lipid EfOM associated with municipal wastewater, which could be accomplished through the development of new materials or possibly through the application of membrane coatings.

2. Analyze chemical and energy costs associated with the purchase and use of coagulants and reduction in cleaning chemical use, which was not done as part of the coagulant study and should be done.

3. Investigate the impact of coagulant bleed-through on the performance of a three-stage RO pilot unit operating at 20–30 gpm when the system is available.

4. Minimize the extent to which nanoparticulate EfOM passes through the MF membrane, as it exerts a significant potential to fouling the surface of the RO membranes downstream and negatively impacts performance.

5. Repeat RO fouling studies using the coupon test array to confirm previous observed relationships between deposition of the various components on the membrane surface and spacers.

6. Expand the development of RO membrane performance predictive modeling using more extensive data manipulation and numerical process model construction reported in this study.

7. Undertake a greater understanding of the role chloramines play in the UV/H_2O_2 AOP. More specifically, determine if the complete removal of chloramines from the feedwater to the UV/H_2O_2 AOP will result in a significant improvement to the process. Determine if the increase in the UVT and increase in the H_2O_2 photolysis, (i.e., hydroxyl radical production) outweigh the loss of AOP resulting from the production of chlorine and chloramine radicals.

Chapter 1

The Advanced Water Purification Facility at the Orange County Water District

1.1 Background, Introduction, and Problem Definition

On January 10, 2008, the Orange County Water District (OCWD) commissioned the 70-mgd Groundwater Replenishment System (GWRS) that replaced the 5-mgd Water Factory 21 that began service in October 1976. The GWR System is an indirect potable reuse project jointly operated by OCWD and Orange County Sanitation District (OCSD). The Advanced Water Purification Facility (AWPF) is the main component of the GWR System. The AWPF produces highly treated recycled water for direct injection into a seawater intrusion barrier and for groundwater recharge. The treatment train is comprised of microfiltration (MF), reverse osmosis (RO), UV disinfection, and a UV/hydrogen peroxide advanced oxidation process (AOP). Although the AWPF produces high-quality recycled water, measures can be taken to improve or optimize its performance and reduce operating costs, which currently exceed $31.6 million/year (FY 2012–2013).

Improvements can be made throughout the entire treatment process. The clarified secondary effluent possesses a significant load of biological detritus, such as microparticulates, nanoparticulates, and dissolved organic matter (DOM), which contribute to rapid fouling of the hollow fiber MF membranes with consequent loss of performance and increase in operational costs. Despite advancements made in low-fouling, thin-film composite RO membranes, the occurrence of biotic and abiotic (colloidal) fouling limits the efficient operation of this process. Accumulation of foulants on the membrane surface often leads to a rapid decline in membrane performance in terms of decreased water flux and increased salt passage. Reduction in the rate of biological and colloidal accumulation on the membrane surface is critical to the efficient operation of both MF and RO separation processes. A UV/hydrogen peroxide-based AOP was added to the treatment process as a barrier to organic and inorganic compounds of public health concern that happen to get past the RO process. The California Department of Public Health (CDPH) [2] mandated a dose of 3 mg/L H_2O_2. However, there was no scientific evidence to indicate that this was the optimum concentration to apply to a feedwater with 50–75 μg/L (ppb) of total organic carbon (TOC).[3] Understanding how the soluble chemical constituents in the feedwaters affect and are affected by the MF and RO separation processes and the extent to which the trace organic compounds are modified by the UV/AOP process are vital to the development of a more cost-effective, energy-efficient treatment process.

[2] On July 1, 2014, the Drinking Water Program transferred from the CDPH to the State Water Resources Control Board, Division of Drinking Water.

[3] TOC concentrations measured with a Ge Sievers 900 online analyzer are 50–75 μg/L as compared to a Ge Sievers 5310 C analyzer measurements of 150–200 μg/L for open air RO permeate grab samples returned to the laboratory for analysis. The sampling point is the same.

1.2 Treatment Overview

The AWPF of the GWRS utilizes a multiple-barrier approach to recycle secondary-treated wastewater that would otherwise be discharged to the ocean (Figure 1.1). Each step in the treatment process has unique operational demands. Each can be individually addressed to improve on the overall performance of the treatment process.

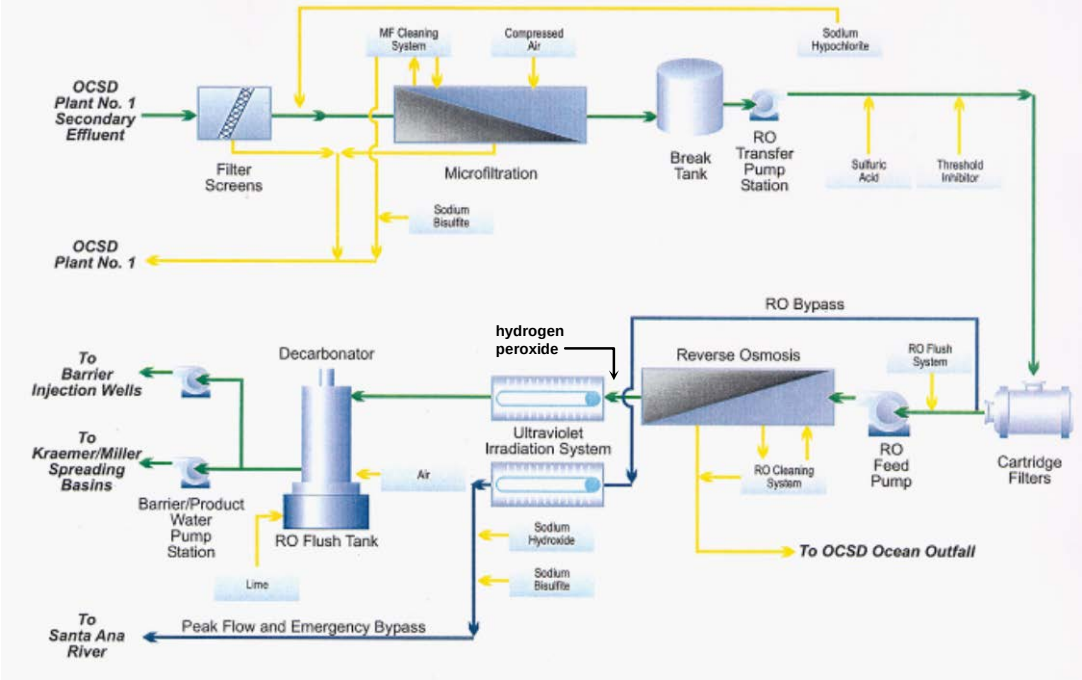

Figure 1.1. Schematic drawing of the Orange County Water District Advanced Water Purification Facility of the Ground Water Replenishment System.

1.2.1 Microfiltration (MF)

The MF system utilized Siemens' CMF-S technology, which is an induced flow process where water is drawn through the membrane module using the pressure differential developed from the suction side of the filtrate pump. The modules are submerged in a process feedwater tank, which is open to the atmosphere. Each module consists of approximately 14,500 hollow fibers constructed of polypropylene material. The design flux for each module is 20 gfd (or 4.5 gpm). The MF system consists of 26 Siemens/Memcor CMF-S units (cells). The cells are grouped into three large trains with eight cells in each train and a fourth train of two cells. Each cell contains 684 modules that operate at a recovery rate of 88% to 90%. The nominal pore size of the membrane material is 0.2 µm; therefore, particulates larger than 0.2 µm remain on the outside of the membrane fiber, and particles smaller than 0.2 µm are free to lodge in the interstices in the membrane. Every 22 min the membranes are backwashed and air scoured, and in spite of these cleaning cycles, fouling continues to slowly progress, reducing membrane performance. The components of the clarified secondary effluent (microbial detritus, nanoparticulates, and DOM) contribute to membrane fouling resulting in increased hydrodynamic resistance (i.e., flux loss), thereby increasing the need for frequent chemical cleanings, reducing water production efficiency, and driving up operational costs. Laboratory studies at OCWD suggest there are two mechanisms of MF

fouling: (1) classical pore blocking via surface cake formation by particulates greater than the 0.2 µm nominal pore size, which may be removed by backwashing and air sparging, and (2) pore plugging that is due to intercalation of DOM and nanoparticulates with dimensions less than 0.2 µm into the membrane matrix, which are more difficult to remove with regular backwashing. Nanoparticles that enter the membrane matrix and clog the pores can account for 80% of the flux reduction during MF operation. The nanoparticles may eventually be responsible for irreversible fouling that necessitates a chemical clean in place (CIP). The nanoparticle foulants in secondary-treated wastewater have been sized by differential filtration using a graded series of microfilters and ultrafilters down to 10kDa molecular weight cut off (MWCO). Filtrates were assessed for MF fouling potential with hollow fiber 0.2 µm pore size polypropylene MF membranes using a bench-scale MF test cell. The 10kDa MWCO filtrate had no effect on membrane flux, but the 20kDa MWCO filtrate did cause a slight decrease in MF flux, indicating fouling particle size started between 2.5 and 3.5 nm (Safarik and Phipps, 2005). Commercially available coagulants were used to aggregate nanoparticles smaller than 0.2 µm into larger (>0.2 µm) microparticles. Increasing the size of the fouling material prevented them from entering the membrane matrix and resulted in improved membrane performance. Although the size of the particulate foulants has been identified, less is known about the chemical composition of the foulants. Initial characterization studies suggest proteins, carbohydrates, and phospholipids (or phospholipid-fatty acids). However, a more detailed characterization has not been made nor is it known to what extent these materials are removed by the MF membrane. A more thorough investigation of the exact chemical composition and molecular weight distribution of the soluble organic component of the feedwater and effluent will aid in ongoing MF and RO fouling studies at OCWD.

1.2.2 Reverse Osmosis (RO)

Proprietary advancements have resulted in a wide variety of thin-film composite (TFC) membranes with distinct surface chemistries, some of which slow biological fouling. The AWPF utilizes the Hydranautics ESPA2 (Nitto Denko, Oceanside, CA) high flux, high salt rejection membrane. There are a total of 15 RO treatment units, with 150 vessels per unit at a ratio of 78:48:24 vessels per RO unit (3.25:2:1 ratio) operated in three passes or stages. Each vessel houses seven membrane elements. Each unit has a rated capacity of 5 mgd, operating over a range of recovery from 80–85 %. The reject stream (concentrate) from the RO process is sent back to OCSD for mixing with secondary effluent prior to discharge to the exiting OCSD ocean outfall. The RO permeate is directed to the UV/H_2O_2 AOP for further treatment.

RO membrane fouling is described by the accumulation of organic matter (i.e., bacteria, macromolecules), inorganic colloidal particulates (i.e., silica, scale), and other debris on the membrane surface that have a negative impact on performance (Ridgway, 1987; Ridgway and Flemming, 1996; Byrne, 2002; Encyclo. Membr. Sci. Technol., 2013). Membrane cleaning processes become necessary as normalized feed pressure (NFP) increases. Application of cleaning agents continues to be a critical factor in reducing the effects and economic impacts of membrane fouling. Cleaning practices are now dictated to a significant extent by chemical composition of the fouling layer and the type of membrane in operation. Understanding the chemical composition of the organic and inorganic constituents in the feedwater will improve our understanding of fouling at the membrane surface. Understanding of the molecular interactions between chemical cleaning agents, the surface foulants, and the RO membranes, and their influence on membrane performance are vital to the development and implementation of cost-effective treatment processes. There is still a lack of the basic understanding of how adsorbed macromolecules affect membrane performance. This research

project will help to identify soluble organic components in the feedwater to the RO separations process and will lay some of the groundwork for understanding the complex interactions between inorganic and organic foulants, chemical cleaning agents and the polymer RO membranes and their direct impact on membrane performance. This knowledge will help in the development of more effective membrane cleaning chemicals while minimizing the compromising effect they might have on membrane performance. Although both MF effluent and RO permeate will be characterized, the primary focus will be toward understanding the changes in chemical processes across the MF and AOP and the optimization of their performance. The characterization of the organic constituents in the RO feedwater (i.e., MF effluent), and RO permeate (i.e., AOP feedwater), resulting from these studies will support ongoing RO fouling studies at OCWD.

1.2.3 UV/Hydrogen Peroxide Advanced Oxidation Process (AOP)

During the design process of the GWRS, the CDPH mandated the addition of UV for removal or destruction of NDMA, which had been detected in drinking water in a number of wells in California (CDPH, 2006). The system was designed to achieve greater than 4-log inactivation of MS2 phage and greater than 1.2-log reduction of NDMA at greater than 50 mJ/cm^2 outlined in the 2003 National Water Research Institute / American Water Works Association Research Foundation UV guidelines (NWRI/AWWARF, 2003). Incorporation of UV photolysis into the treatment process meant that a chloramination step could be eliminated from the final product water (FPW) because of the high number of credits received in association with the large quantity of UV light needed to remove NDMA. Later the CDPH mandated the application of an AOP for the destruction of trace inorganic and organic contaminants (more specifically 1,4-dioxane that had been detected in the GWRS source waters). Because the application of UV light for disinfection and NDMA removal was in place, a hydroxyl radical-mediated advanced oxidation process was chosen. An H_2O_2 concentration as high as 5 mg/L had been considered; however, the CDPH and OCWD eventually settled on a dose of 3 mg/L in the feedwater to the UV/AOP reactor train. It is not known if 3 mg/L H_2O_2 is the most effective concentration, nor is it known how effective AOP is at removing trace levels (low ppb and ppt) of organic contaminants from feedwaters that have a total organic carbon load of 50–75 μg/L. The electrical energy dose (EED) of 0.203 kWh/kgal was initially established to assure adequate disinfection and removal of NDMA. However, it was later increased to 0.230 kWh/kgal to ensure adequate removal of 1,4-dioxane.

The Trojan UVPhox system (Trojan Technologies, London, ON) consists of three vertically stacked chambers. Each chamber contains two reactors. Each reactor contains 72 257-watt low-pressure high-output (LPHO) mercury amalgam lamps. Each reactor consumes 18.5 kW, running at ballast power level (BPL) of 100%. Trojan's logic system adjusts the BPL and number of reactors turned on based on five operational parameters: water temperature, flow rate, UVT at 254 nm, lamp age, and a UV fouling index.

In the presence of UV light at wavelengths less than ~270 nm, hydrogen peroxide can undergo photolysis to form a hydroxyl free radical. Hydroxyl radicals are highly reactive and readily oxidize organic (or inorganic) compounds on contact. Under the right conditions, organic compounds can be completely mineralized to carbon dioxide.

Unfortunately, hydrogen peroxide has a very low molar absorptivity (19.6 $M^{-1}cm^{-1}$) at the 254-nm output of the LPHO lamps. This renders the AOP process inefficient because the production of hydroxyl radicals is small at this wavelength. Dosing the 70 mgd AWPF with

3 mg/L of H_2O_2 also adds significant cost to the treatment process. The cost of H_2O_2 for the 2011–2012 fiscal year was $373,000, equivalent to $124,000 per mg/L H_2O_2 per year.

Both microbial disinfection and NDMA photolysis occur by direct interaction with the UV light. Both processes work well and are not an issue with the operation of the AWPF. However, much less is known about how effective the AOP is at oxidizing trace organic and inorganic constituents that get past the RO process. Early measurements from the AWPF indicate 21% of the hydrogen peroxide feed is routinely consumed by the Trojan UVPhox running at an EED between 0.25 and 0.35 kWh/kgal. However, the extent to which the AOP occurs by hydroxyl radical-mediated oxidation has never been determined in the Trojan reactors and 2.2 mg/L of H_2O_2 of the 2.7 mg/L average feed remains in the UV product water. At the time of this study, there were no online monitors for the measure of H_2O_2 concentration, consumption, or hydroxyl radical generation, nor were there any monitors for any specific trace organic or inorganic molecules (including NDMA). There are currently no persistent organic pollutants in the RO permeate that require advanced oxidation to be transformed and eliminated from the RO effluent. Initially 1,4-dioxane was a target compound; however, OCSD was able to reduce its presence in the plant influent (typically 2–4 μg/L) through source control to the point where it is rarely measured at a reportable concentration in the UV feedwater (RO permeate). One-log reduction of 1,4-dioxane is typically achieved across the RO process. Concentrations of 1,4-dioxane in the effluent from the AOP have been well below the original 3 μg/L notification level set by the CDPH and below the revised notification level of 1 μg/L established in November 2010 (CDPH, 2011). However, this still leaves in question the exact chemical composition of the 50–75 μg/L of TOC that is present in the RO permeate and to what extent the compounds are oxidized by the UV/H_2O_2 AOP.

1.2.4 Carbon and Energy Footprint

With increased awareness of climate change, a paradigm shift in treatment is occurring. That is, for every process that is being considered, it will be necessary to evaluate the carbon footprint or the contribution of the process (and associated infrastructure) to GHG emissions. No carbon and energy studies have been conducted to evaluate the footprint of the MF, RO, and UV/AOP processes at full scale.

The carbon and energy footprints of each operational unit, sub-train, and whole process train will be calculated according to our method previously published (Rosso and Stenstrom, 2008). The total carbon footprint will include the direct carbon footprint (i.e., the carbon in the water) and the indirect footprint (i.e., the carbon emissions produced to generate the power drawn by the process). The carbon footprint includes the equivalent carbon emissions of carbon influent and effluent fluxes, of direct energy consumption, and of production and in situ storage of H_2O_2. Site specific fluxes of carbon and energy will be included in both footprint analyses. The calculation of the energy footprint includes the energy consumption of each unit during its operational time, thus accounting for fouling and the potential decrease in process efficiency over time.

It is crucial to perform the footprint analysis on the integrated optimization over the entire process, as it will return the minimum footprint result. The operating points corresponding to the minimum footprint will be recommended to the operators for full-scale implementation, physical limitations permitting. The footprint analyses will yield scenarios for the whole process and its sub-units for different process control and optimization strategies.

1.2.5 Summary

Measures can be taken throughout the entire AWPF treatment process to improve or optimize its performance and potentially reduce the operating costs. Reduction in the rate of biological and colloidal accumulation on the membrane surface is critical to the efficient operation of both MF and RO separation processes. Understanding how the soluble chemical constituents in the feedwaters affect and are affected by the MF and RO separation processes and the extent to which the trace organic and inorganic compounds are removed or degraded by the UV/AOP process are vital to the development of a more cost-effective, energy-efficient treatment process. To this end, we employed a number of standard and non-standard analytical techniques to determine both detailed and gross characteristics of organic constituents of the treatment stream throughout the process and carried out experiments designed to improve or identify measures to reduce the impact of dissolved organics on membrane performance. In addition, we analyzed the efficiency of the AOP to develop process and control strategies that will maximize efficiency as it minimizes H_2O_2 use. In improving overall efficiency of the process, we aimed to evaluate the carbon footprint of each optimization scenario so as to choose those that offer the greatest combined benefit of improved water quality and reduced carbon footprint.

1.3 Project Goal

The overarching goal of this project was to minimize energy utilization and maximize treatment efficiency. The treatment efficiency metric is defined as the quality of the product water. This project captures the first 3 to 5 years of operation of the plant and obtains data on changes in the quality of the water for each process in the early phases of operation. Furthermore, this was a unique opportunity to study the carbon and energy footprints of a MF, RO, and UV/AOP of the AWPF.

1.4 Objectives

This research project was divided into five major objectives with tasks outlined to achieve them:

1. Microfiltration (MF) – Characterize the organic and inorganic constituents in the feedwater, the effluent, and the membrane foulants. Determine the mechanism of fouling and identify ways to optimize the microfiltration process.
2. Reverse osmosis (RO) – Characterize the organic and inorganic constituents in the feedwater, permeate, and those on the membrane surface. Identify the membrane foulants specifically responsible for water flux decline and the initiation of a chemical cleaning. Identify ways to optimize the reverse osmosis process.
3. UV/H_2O_2 advanced oxidation process (AOP) – Characterize the dissolved organic compounds in feedwater to the UV/AOP and identify oxidation products. Determine the optimum concentration of H_2O_2 for a feedwater containing 100–200 μg/L of TOC operating at minimum electrical energy dose (EED) of 0.230 kWh/kgal.
4. Monitoring and control strategies development based on the characterization of organic and inorganic constituents in the different process waters.
5. Alternatives evaluation, which leads to minimization of the carbon (energy) footprint of the advanced water purification facility.

Chapter 2

Characterization of Effluent Organic Matter (EfOM) in Secondary-Treated Wastewater[4]

2.1 Introduction

Water quality has a significant impact on the performance of membrane separation processes. Although colloidal matter is readily removed or rejected at the surface of MF membranes, effluent dissolved organic matter (EfOM) in the source waters has a tendency to accumulate on or foul membrane surfaces, rendering them less efficient. Characterization of the source waters and MF foulants, in particular, has been limited to gross molecular characterization (Shon et al., 2006; Jarusutthirak et al., 2002). A detailed chemical analysis of the wastewater effluent is critical to the understanding of chemical dynamics of membrane fouling and performance. Chemical characterization of natural organic matter (NOM) and its impact on the water treatment process and resulting water quality has been studied extensively (Haarhoff et al., 2010; Baghoth et al, 2009; Chow et al., 2004), but a detailed molecular understanding has not been established. The chemical composition of EfOM has been compared to and believed to be similar to NOM (Drewes and Croue, 2002); it also was determined that EfOM contains many organic compounds, such as soluble microbial products and synthetic organic compounds, which all have different chemical characteristics compared to NOM (Jarusutthirak and Amy, 2007). These constituents ultimately have an impact on the membrane treatment process (in terms of fouling and removal of dissolved organic materials) and the overall performance of the purification facility.

In the past, characterization of EfOM has been focused on bulk chemical properties, such as molecular size, aromaticity, elemental composition, functional group composition, and spectrophotometric properties (Shon et al., 2006; Jarusutthirak et al., 2002; Ahmad and Reynolds, 1999; Frimmel and Abbt-Braun, 1999; Imai et al., 2002; Sirivedhin and Gray, 2005; Nam and Amy, 2008; Pernet-Coudrier et al., 2008). Because of the complex mixture of dissolved organic molecules in EfOM and a lack of appropriate analytical techniques in the past to analyze such complexity, a detailed description of the molecular composition of EfOM has not been established. In this study, a non-targeted approach using a technique referred to as ultra-high resolution electrospray ionization Fourier transform ion cyclotron resonance mass spectrometry (ESI-FT-ICR-MS) was used to reveal the detailed molecular composition of EfOM collected from trickling filter effluent (TFE) and activated sludge effluent (ASE) from the OCSD. A blend of TFE and ASE serves as the feedwater to OCWD's advanced water purification facility. The microfiltration effluent (MFE) also was characterized. These spectra were compared to an international natural organic matter reference isolate from the Suwannee River (SRNOM).

[4] A major portion of this chapter is reprinted with the permission from Gonsior, M.; Zwartjes, M.; Cooper, W.J.; Song, W.; Ishida, K.P.; Tseng, L.Y.; Jeung, M.K.; Rosso, D.; Hertkorn, N.; Schmitt-Kopplin, P. Molecular Characterization of Effluent Organic Matter Identified by Ultrahigh Resolution Mass Spectrometry. *Water Res.* **2011**, *45*, 2943–2953. Copyright 2011 Elsevier Ltd.

Electrospray ionization-based FT-ICR-MS has been used in recent years to determine the molecular composition of NOM. Unambiguous molecular formula assignments for masses up to ~600 Da can be calculated using an ESI-FT-ICR-MS at high magnetic fields (≥12 Tesla). The technique recently has been used to identify parent and intermediate breakdown products of a pharmaceutical wastewater (Sirtori et al., 2009) and disinfection byproducts of a treatment plant (Heffner et al., 2007). Through this non-targeted analysis, it is possible to assess the complexity of organic molecules in EfOM.

2.2 Materials and Methods

A detailed description of the materials and methods used to isolate and characterize the effluent organic matter can be found in the publication by Gonsior et al. (2011). The methods are described in brief following. OCSD utilizes two separate treatment processes, which result in two effluent streams—TFE and ASE. At OCSD it was observed that the activated sludge process outperforms the trickling filter process in every measure of effluent quality (Wade, 2010). The residence time of the effluent in the activated sludge was 1.1 days during both sampling periods. The AWPF treated a blend of 80% ASE and 20% TFE at the time this study was conducted. This blended effluent is identified as Q1.

The water quality of the Q1 secondary wastewater effluent to the AWPF is monitored on a regular basis. A list of the parameters and frequency of tests by standard methods performed by OCWD's AWQA laboratory are displayed in Table 2.1. The data were tabulated on a yearly basis.

Table 2.1. Q1 Water Quality Test Parameters (23) and Sample Schedule

Parameter	Sample Schedule	Parameter	Sample Schedule
Turbidity (TURB)	2WG	Total alkalinity (TOTALK)	MC
Suspended solids (SUSSOL)	DC	Calcium (Ca)	MC
Total dissolved solids (TDS)	2WG	Magnesium (Mg)	MC
Total organic carbon (TOC)	DC	Manganese (Mn)	MC
Electrical conductivity (EC)	2WG	Iron (Fe)	MC
Silica (SIO2)	MC	Chloride (Cl)	MC
Ammonia-nitrogen (NH3-N)	WG	Sulfate (SO4)	MC
Nitrite (NO2-N)	2WG	Ortho-phosphate (PO4-P)	WC
Nitrate (NO3-N)	2WG	pH	2WG
Organic nitrogen (ORG-N)	WG	Methylene blue active substances (MBAS)	MC
Total Kjeldal nitrogen (TKN)	WG	Total coliforms (TCOLIM)	2WG
Biological oxygen demand (BOD)[a]	QC	Fecal coliforms (FCOLIM)	2WG

Notes: [a]Analysis outsourced; 2WG–twice-a-week grab; WG–weekly grab; DC–daily composite; MC–monthly composite; QC–quarterly composite.

ASE and TFE were collected on three sampling days separated by 6 months and 1 year when OCSD's activated sludge process was operated in carbonaceous biochemical oxygen demand (CBOD) mode. All samples were filtered through Millipore GV 0.22-µm filters. In addition, the chloraminated MFE from the AWPF was sampled. All samples were extracted within 4 h using a solid-phase extraction (SPE) procedure. For the purpose of comparison with NOM, SRNOM also was analyzed by ESI-FT-ICR-MS using the same technique. The SRNOM

sample was obtained using a combination of RO and cation exchange resin. A detailed description of the procedure can be found at International Humic Substances Society: http://www.ihss.gatech.edu/ro_nom.html.

Effluent samples were acidified to pH 2 and extracted using Varian Mega Bond Elut PPL SPE cartridges filled with 1 g of a functionalized styrene-divinylbenzene polymer (PPL) resin. The cartridges were gravity fed and extraction was typically completed within 10 h. The SPE cartridges were rinsed with acidified (pH 2) high purity grade water (Water LC-MS, Fluka Chromasolv), dried, and eluted with methanol (LC-MS Fluka Chromasolv). A detailed description of the SPE method and extraction efficiencies for NOM is given elsewhere (Dittmar et al., 2008). Dissolved organic carbon (DOC) measurements before and after extraction were undertaken on 0.22 µm filtered, acidified and filtered effluent samples using a GE Sievers 5310C TOC analyzer. The extraction efficiency of this SPE procedure was measured on all effluent samples.

2.2.1 ESI-FT-ICR-MS Analysis

SRNOM, the wastewater samples, and the MFE sample were diluted with methanol and analyzed at the Helmholtz Zentrum in Munich, Germany, using a Bruker Apex QE 12 Tesla ESI-FT-ICR-MS. Electrospray ionization (ESI) was used in negative and positive ion mode to generate largely intact ions at atmospheric pressure. Additional information about the ESI-FT-ICR-MS technique used in this study is given elsewhere (Hertkorn et al., 2007). The molecular formula assignments were based on the following elements: $^{1}H_{0-\infty,}$ $^{12}C_{0-\infty}$, $^{16}O_{0-\infty}$, $^{32}S_{0-2}$, $^{14}N_{0-2}$, as well as $^{13}C_{1}$ and $^{34}S_{1}$.

Van Krevelen diagrams were generated to aid in the interpretation of the mass data (Kim et al., 2003). In these diagrams, dots represent the molar ratio of oxygen-to-carbon (O/C) of the molecular formula plotted on the x-axis and the molar ratio of hydrogen-to-carbon (H/C) on the y-axis. Molecular formula with the same elemental ratios cannot be distinguished using these diagrams. As major chemical classes typically found in NOM have characteristic H/C and O/C ratios, they cluster within a specific region of the diagram. Thus, patterns in Van Krevelen diagrams of NOM (Hertkorn et al., 2008) can reflect the source material, as well as changes in bulk NOM composition that is due to degradation. In this study, Van Krevelen diagrams were used to demonstrate the contribution of SRNOM to wastewater EfOM and to show molecular differences between these different types of organic matter. A useful parameter in the characterization of the unsaturation and aromaticity of molecular formula arising from ESI-FT-ICR-MS analysis include the degree of unsaturation or double bond equivalency (DBE).

2.2.2 Nuclear Magnetic Resonance (NMR) Spectroscopy

The solid-phase-extracted samples were dried (vacuum and nitrogen atmosphere) and re-dissolved in CD_3OD (Merck, 99.95 ^{2}H). In this study, all NMR spectra were acquired using a Bruker DMX 500 MHz spectrometer at 283 K and a 5-mm $^{1}H/^{13}C/^{15}N$ TXI cryogenic probe (90° pulse: 10 µs). One dimensional ^{1}H NMR spectra were recorded using the first increment of the preset nuclear Overhauser effect spectroscopy (NOESY) sequence: solvent suppression with presaturation and spin-lock; 5 s acquisition time; 15 s relaxation delay; between 160 and 512 scans; 1 ms mixing time and 1 Hz exponential line broadening. The gradient enhanced (1 ms length; 450 µs recovery) absolute value correlation spectroscopy (COSY) NMR spectrum was acquired using acquisition times of 747 ms at a spectral width of 5482 Hz and 64 scans at

285 increments. The achieved data were visualized using an 8k × 512 matrix applying a 2.5 Hz exponential multiplication in F2 and an unshifted sine bell in F1.

2.3 Results and Discussion

2.3.1 Secondary Wastewater Effluent Water Quality

The Q1 water quality data were tabulated on a yearly basis and represent a blend of TFE and ASE (see Table 2.2). The AWPF initially (January 2008) operated solely on ASE. However, in early June 2008, 20% TFE was blended into the ASE. The data for 2008 were not segregated. In early November 2009, OCSD switched from a CBOD treatment process to NDN treatment. It took approximately 2 months for the NDN process to stabilize. In late November 2009, the TFE fraction of the blended wastewater effluent was increased to 30%, and by January 2010 the NDN method of processing wastewater stabilized. A reduction in the ammonia and an increase in nitrate are reflected in the tabulated data.

Table 2.2. Blended Secondary-Treated Wastewater Effluent (Q1) Water Quality[a]

	Units	2008[b]	2009	2010[c]	2011	2012
pH		7.7±0.1	7.6±0.1	7.40.1	7.5±0.1	7.3±0.1
MBAS	mg/L	0.23±0.11	0.20±0.07	0.27±0.09	0.23±0.04	0.19±0.04
TURB	NTU	2.9±1.2	3.4±1.6	2.8±1.2	2.3±1.2	2.3±0.8
SUSSOL	mg/L	6.4±4.1	8.9±6.0	9.8±7.0	7.3±4.3	8.0±5.9
TDS	mg/L	920±70.7	950±90	1016±83.4	955±85	901±57
EC	µS/cm	1660.7±136.8	1650±165	1559±140	1503±131	1477±100
SiO2	mg/L	21.3±1.08	22.2±1.6	21.1±0.9	21.2±1.8	21.4±1.4
TOC	mg/L	14.1±0.2	13.6±1.3	10.6±1.1	10±0.8	9.48±0.63
BOD	mg/L	11±2	13±2	15±9	11±4	31±3
NH3-N	mg/L	24.7±3.8	20.3±5.6	2.2±1.7	2.4±1.2	3.6±1.7
NO2-N	mg/L	0.3±0.34	0.58±1.09	0.40±0.10	0.52±0.15	0.59±0.19
NO3-N	mg/L	1.81±0.74	2.8±2.3	9.7±1.6	9.2±1.6	9.0±1.2
ORG-N	mg/L	2.1±0.5	2.3±0.6	0.95±0.48	1.0±0.4	0.57±0.32
TKN	mg/L	26.7±3.8	22.8±5.6	3.1±1.9	3.1±1.5	4.1±1.7
TOTALK	mg/L	292±22.3	287±37	190±15.1	175±21	180±22
Ca	mg/L	78.4±3.3	84.6±5.7	82.2±5.9	78.7±4.8	76.9±4.2
Mg	mg/L	22.8±2.0	25.7±1.6	26.7±2.0	28.2±2.3	26.4±3.5
Fe	mg/L	248±118	451±212	509±225	276±66	415±161
Mn	mg/L	47.4±4.8	42.1±5.7	35.6±6.2	34.2±9.9	47.5±7.8
PO4-P	mg/L	0.79±0.22	0.57±0.17	0.30±0.13	0.32±0.12	0.7±0.3
SO4	mg/L	226±26.3	231±34	241±24	213±30	206±19
Cl	mg/L	241±26.3	258±31.9	238±13.9	230±16	247±30

Notes: [a]-average ± standard deviation. [b]-CBOD treatment of wastewater until early November 2009. [c]-NDN method of wastewater treatment stabilized in January 2010 to present.

2.3.1 Molecular Composition Differences Between SRNOM and EfOM

Constituents in EfOM have been reviewed (Shon et al., 2006). It was shown that wastewater compounds smaller than 1000 Da included carbohydrates, amino acids, vitamins, and chlorophyll. The higher molecular weight fraction was associated with humic and fulvic acid-

like compounds presumably arising from the source water. However, little was mentioned in the review about highly polar surface-active substances. Another study by Knepper et al. (2004) showed that persistent polar pollutants (P^3) including linear alkyl benzene sulfonates (LAS) were not efficiently removed by activated sludge treatment.

The extraction efficiency was lower and the initial DOC level higher for the TFE, 9.89 mg/L DOC and 43% carbon extraction efficiency, compared to ASE and MFE with 5.26 mg/L and 5.47 mg/L DOC, respectively, and 57% carbon extraction efficiency observed in both cases (Table 2.3). The 57% extraction efficiency of ASE and MFE was practically the same as for NOM samples (Dittmar et al., 2008).

Table 2.3. Carbon-Based Solid-Phase Extraction Efficiency for All Effluent Organic Matter Samples

Sample	DOC Before Extraction (mg/L)	DOC After Extraction (mg/L)	Efficiency (%)
ASE	5.26	2.25	57.2
TFE	9.89	5.61	43.3
MFE	5.47	2.31	57.8

The mass spectra of EfOM (ASE) and SRNOM revealed pronounced differences between the SRNOM and the EfOM present in the OCSD effluent (Figure 2.1). The differences in the extraction procedures for the SRNOM (RO) and the EfOM (SPE) samples have an influence on the fraction extracted from the dissolved organic matter pool but were not mainly responsible for the molecular differences observed using ESI-FT-ICR-MS. Other NOM samples extracted the same way as the EfOM using the SPE method also were evaluated and showed very similar results. For comparison reasons and the convenience of easily available SRNOM samples, all data analyses in this study were referred to this SRNOM reference material.

The different appearance in the SRNOM and EfOM mass spectra was manifested in the intense peaks associated with formulas containing a single sulfur atom (CHOS: carbon, hydrogen, oxygen, sulfer atom formula) in the EfOM sample in contrast to the intense peaks associated with CHO formulas in the SRNOM sample. For example, at nominal mass 305, several intense CHO masses represented members of a homologous series with a spacing of 0.0364 Da (CH_4 vs. oxygen) in the SRNOM sample (Stenson et al., 2003). In contrast, these peaks showed very low abundance or were absent in the EfOM and the intense peaks were dominated by CHOS formulas (Figure 2.1). These observations reflected the generally lower numbers of CHO formulas in the EfOM samples and the absence of CHO formulas of higher molecular weight.

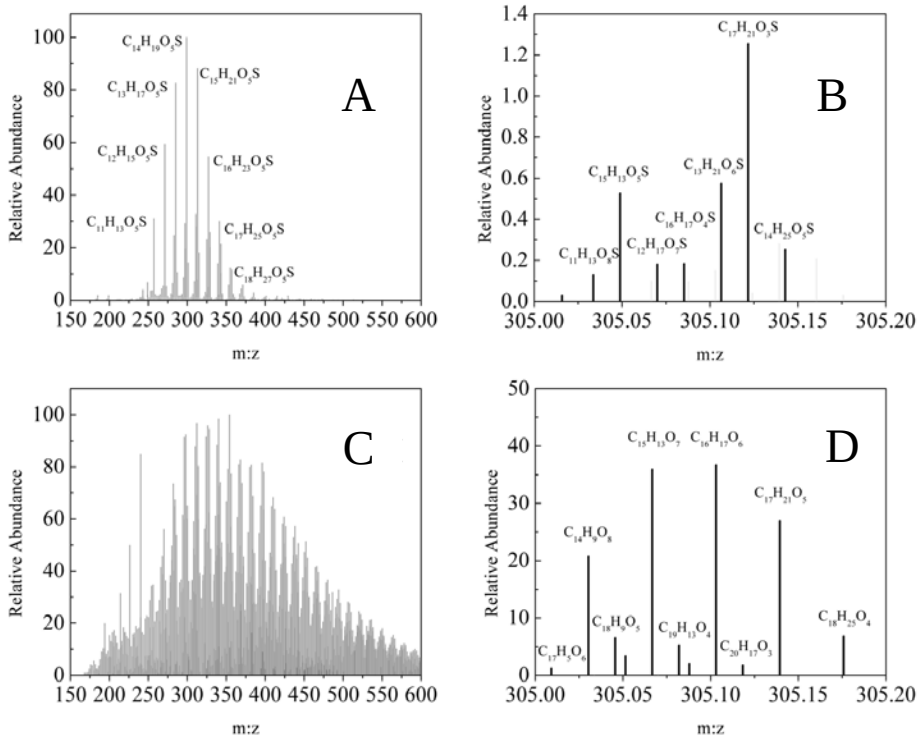

Figure 2.1. Ultra-high resolution mass spectra of [A, B] EfOM (OCSD ASE) and [C, D] SRNOM.

The mass spectra demonstrated the irregular distribution of masses in EfOM compared with SRNOM and the skewing of the distribution toward lower mass. Furthermore, the m/z peaks with highest relative abundances were associated with molecular formula identical to those of sulfophenyl carboxylic acids (SPC), a known biodegradation product of the alkyl LAS (Ramon-Azcon et al., 2005). These LAS are a major class of surfactants, and concentrations of reasonable high levels have been found in wastewater, as well as in ocean environments (Knepper et al., 2003). The most common isomers for LAS, their coproducts, and metabolites are shown in Figure 2.2.

In the negative ion mode, the SRNOM sample contained 75% CHO formulas, in contrast to EfOM which contained only 34% CHO formulas (Figure 2.3). EfOM was dominated by compounds containing a single sulfur atom (41%). CHOS formulas represented less than 5% of all formulas in the SRNOM. The differences between CHO and CHOS formulas in SRNOM and EfOM were even more pronounced when the intensity-weighted distribution were calculated. EfOM was then dominated by 90% of CHOS formulas, whereas SRNOM was dominated by 90% of CHO formulas. However, the intensity-weighted results were most likely biased toward the sulfur-containing molecular formulas, because sulfonic acids are known to ionize very easily in negative ESI. This implies that a quantitative evaluation of ionization efficiencies in such complex mixtures is not practical.

The negative ESI Van Krevelen diagrams arising from the mass spectrometric analysis of the SRNOM and EfOM samples showed distinct distribution differences in the H/C and O/C ratios for both CHO and CHOS formulas (Figure 2.4) indicating different origins for both types of organic matter. Comparison of molecular formulas common to both the SRNOM and EfOM and unique to each sample described the differences in composition not evident from

simple observation of the mass spectra. Characteristics of all assigned formulas for the comparison between SRNOM and EfOM are summarized in Table 2.4.

Linear alkyl benzene sulfonates (LAS)
$C_{18}H_{29}O_3S$

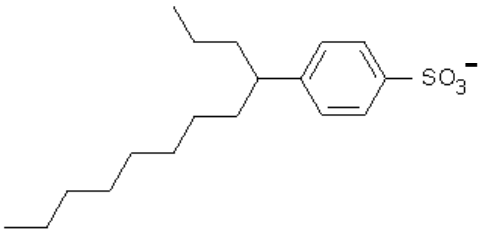

Dialkyl tetralin sulfonate (DATS)
$C_{16}H_{23}O_3S$

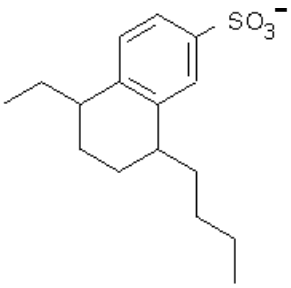

Dialkyl tetralin sulfonate intermediate (DATSI) $C_{16}H_{23}O_3S$

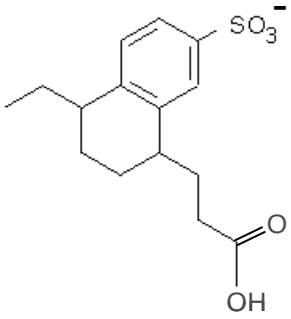

Sulfophenyl carboxylic acid (SPC)
$C_{14}H_{19}O_3S$

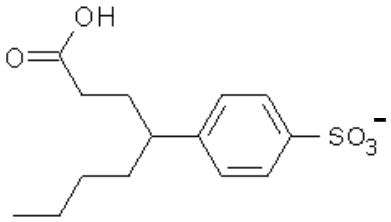

Figure 2.2. The most common isomers of linear alkyl benzene sulfonate (LAS), dialkyl tetralin sulfonate (DATS), dialkyl tetralin sulfonate intermediates (DATSI), and sulfophenyl carboxylic acids (SPC).

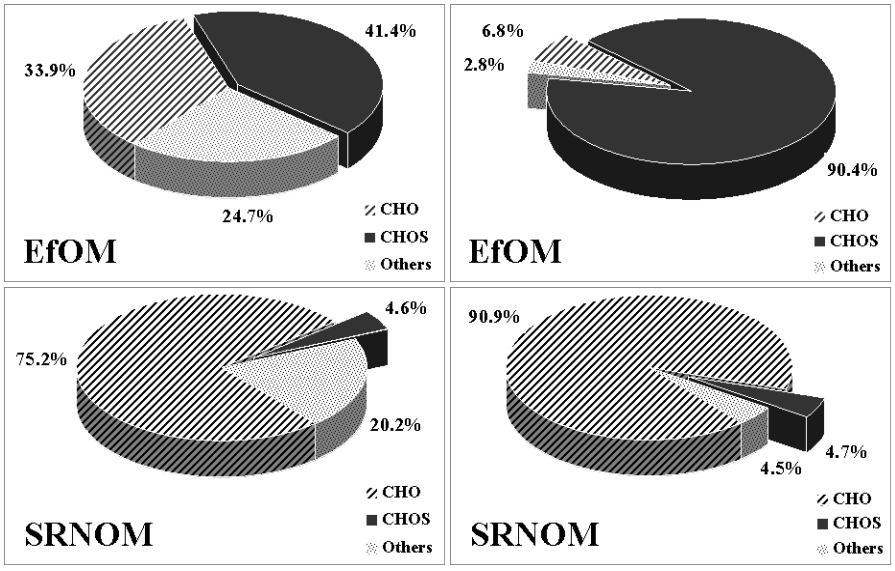

Figure 2.3. Comparison of the elemental composition based on number of formulas (left) and intensity-weighted elemental composition (right) associated with EfOM and SRNOM.

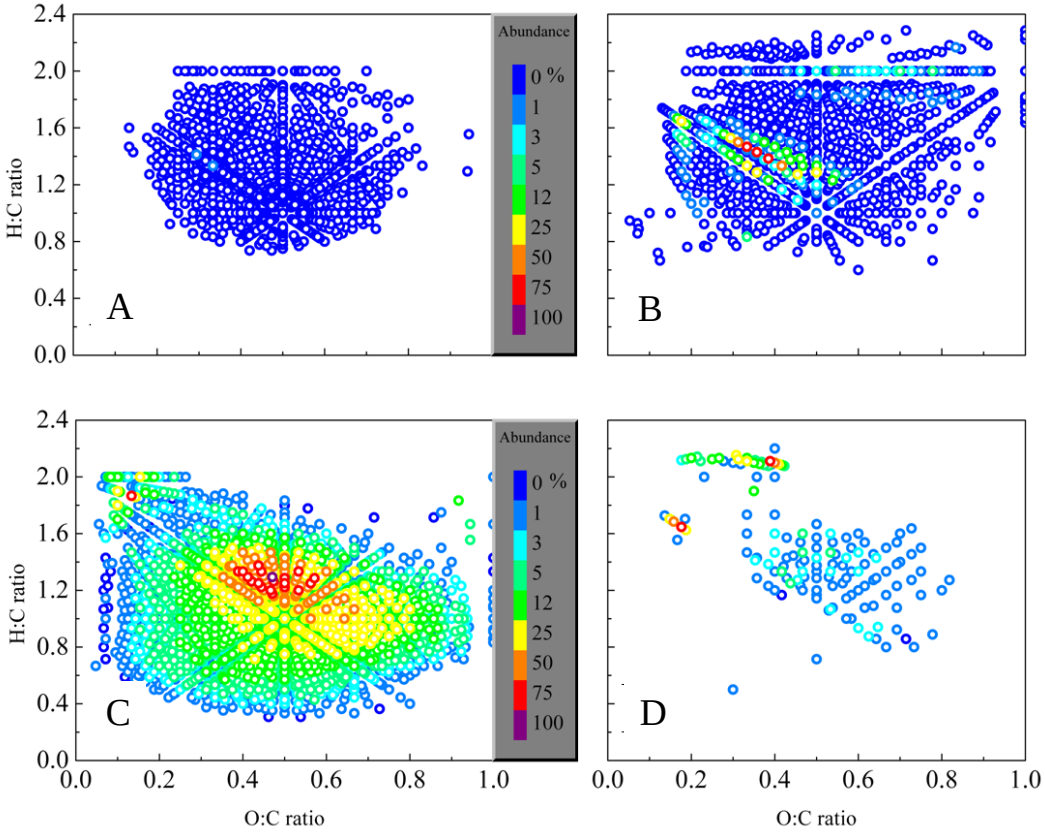

Figure 2.4. Van Krevelen diagrams of (A) CHO and (B) CHOS elemental formulas for EfOM and (C) CHO and (D) CHOS elemental formulas for SRNOM.

Table 2.4. Differences Between Suwannee River NOM and Activated Sludge EfOM Identified by ESI-FT-ICR-MS

	Sample	n[a]	Center of Mass	Unique	Shared	ΔO/C	ΔH/C	DBE
CHO formula	NOM	2503	379.3	1651	852	0.45	1.19	8.6
	EfOM	979	356.4	127	852	0.47	1.23	7.0
CHOS formula	NOM	152	339.7	22	130	0.34	1.93	4.3
	EfOM	1197	314.4	1067	130	0.40	1.48	4.7

Note: [a]n = number of ^{13}C referenced exact molecular formula.

About 63% and 54% of formulas of SRNOM and EfOM were unique to each type, respectively. The majority (66%) of CHO formulas in SRNOM was unique, whereas only 13% of CHO formulas in EfOM were unique to it. The opposite was true for CHOS formulas, with nearly all (89%) of CHOS formulas found in EfOM being unique and only 14% of CHOS formulas in SRNOM being unique.

The decreased number of CHO molecular assignments in the EfOM suggested that these compounds were either removed during drinking water treatment or intensively suppressed in

the electrospray by sulfur-containing compounds. However, the observation that the CHOS compounds dominated in EfOM suggested that these were introduced from anthropogenic sources (detergents and surface-active substances). It should be noted that 44% of the CHO formulas found in SRNOM also were present in EfOM indicating a common pool of dissolved organic molecules.

Overall, formulas unique to SRNOM showed a higher degree of unsaturation than EfOM. The fact that unique CHO formulas were found in the EfOM was rather interesting and unexpected and suggested the presence of a new and previously not described source of CHO compounds. Unique CHO formulas of EfOM had lower O/C ratios and much higher H/C ratios than those unique to SRNOM. The differences in these parameters between EfOM and SRNOM also were observed for CHOS formulas. The very high H/C ratios and low O/C ratios of the EfOM set it apart from SRNOM samples. The ratios were more extreme than those of estuary, river, mudbelt-porewater, and continental shelf porewater samples (Koch et al., 2005; Schmidt et al., 2009; Sleighter and Hatcher, 2008). One possible explanation is that the contribution of synthetic CHO compounds were discharged into the wastewater via anthropogenic sources. A possible fit in terms of H/C and O/C ratios were alkylphenol ethoxylates and/or alcohol ethoxylates, which are widely used as surfactants. However, the origin of these unique CHO formulas in EfOM remained uncertain.

2.3.2 EfOM Molecular Characteristics Analyzed by NMR Spectroscopy

^{1}H NMR spectra of the effluent samples were well resolved and shared common signal envelopes (Figure 2.5), which also were reflected in the rather narrow bandwidth of the NMR section integrals (Table 2.5). Near equal amounts of aliphatic and functionalized protons (approximately 35%) were accompanied by 20% of oxygenated units (**H**CO) and less than 10% aromatic protons. Aliphatics present in EfOM were commonly branched as deduced from the near absence of polymethylene (δ_H ~ 1.2 ppm) and the considerable fraction of methyl resonances (δ_H < 1.1 ppm) observed (Figure 2.5). Methyl groups terminated various branched aliphatic chains (COSY cross peak A_1), were adjacent to carbonyl (**H**$_3$C-CH-C=O) derivatives (COSY cross peak A_2) and showed interactions analogous to methylated carbohydrates (COSY cross peak A_3) and oxygenated aliphatics (Figure 2.6). Intra-aliphatic correlations (C-C**H**-C**H**-C) were common (COSY cross peak B), again reflecting the occurrence of branched aliphatics. COSY cross peaks indictive of O-C**H**-C**H**-C units were scarce, whereas those representing double oxygenated units (XO-C**H**-C**H**-OY), such as carbohydrates, were abundant (COSY cross peak D). The strong resonances at δ_H ~ 3.6 and 3.7 ppm did not show appreciable COSY cross peaks, and therefore, were likely to represent methoxy (OCH_3) groups.

Table 2.5. ^{1}H NMR Section Integrals (Exclusion of Residual Water and Methanol)

δ^1H (ppm)	Main Substructure	ASE (%) 02/2009	TFE (%) 02/2009	MFE (%) 02/2009	ASE (%) 07/2008	TFE (%) 07/2008	MFE (%) 07/2008
10 – 5	H_{ar}	8.9	8.5	7.7	8.8	7.8	7.8
5 – 3.1	OCH	20.8	20.1	20.4	20.3	20.4	19.7
3.1 – 1.95	X*CCH	38.0	36.5	38.3	34.5	35.3	34.9
1.95 – 0.5	CCH	32.3	34.9	33.7	36.4	36.5	37.6

Note: X* denotes hetero atoms.

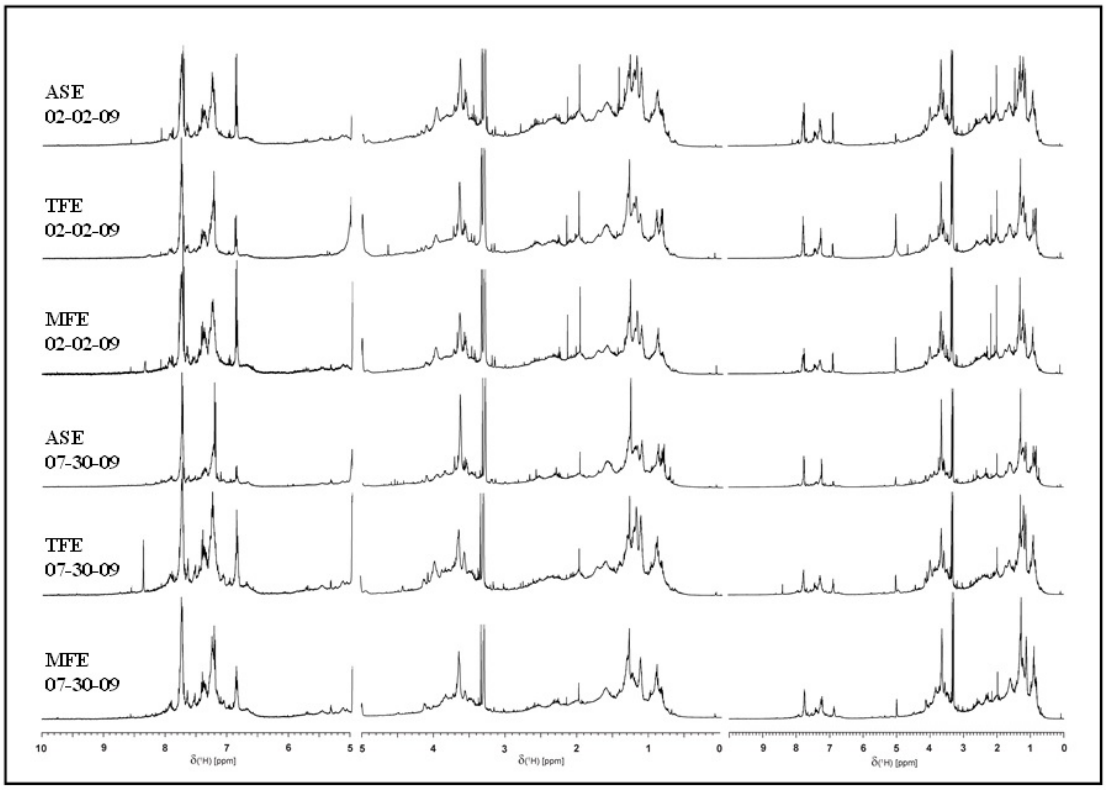

Figure 2.5. ^{1}H NMR spectra of effluent organic matter in ASE, TFE, and MFE with downfield aromatic section (left), upfield aliphatic section (middle), and full spectrum (right).

Aromatic protons showed four major signal regions denoted a, b, c, and d in Figure 2.6 including major intensity variations across the six samples. The absence of clear intensity correlations between NMR resonances "a-d" already implied contributions of several aromatic EfOM constituents resulting in superimposed NMR peaks. Branched aliphatic attached to aromatic rings (C_{ar}-C**H**-C**H**-C_{al}) would resonate in section "C" (COSY cross peak C), similar to carboxyl-rich alicyclic compounds (Hertkorn et al., 2006).

On the basis of chemical shift considerations, NMR resonance "a" represented ortho- and para- substituted oxygenated aromatics, typically adjacent to carbon and hydrogen substituted aromatics, that is, the COSY cross peak "a-b" (see Figure 2.6). The aromatic protons of peak "b" were positioned ortho and para to neutral substituents (hydrogen and carbon, respectively) and showed additional COSY cross peaks "b, c-d". Peak "d" represented aromatics with several carbonyl derivative substituents. However, sulfonyl substituted aromatics (C_{ar}-SO_2-O-R) would produce NMR resonances at both positions "b" (meta position: δ_H ~ 7.3 ppm) and "d" (ortho position: δ_H ~ 7.8 ppm) with corresponding COSY cross peak "b" and "c-d". These NMR resonances were distinct features within all EfOM samples and supported the suggested important influence of sulfonated aromatic components in EfOM.

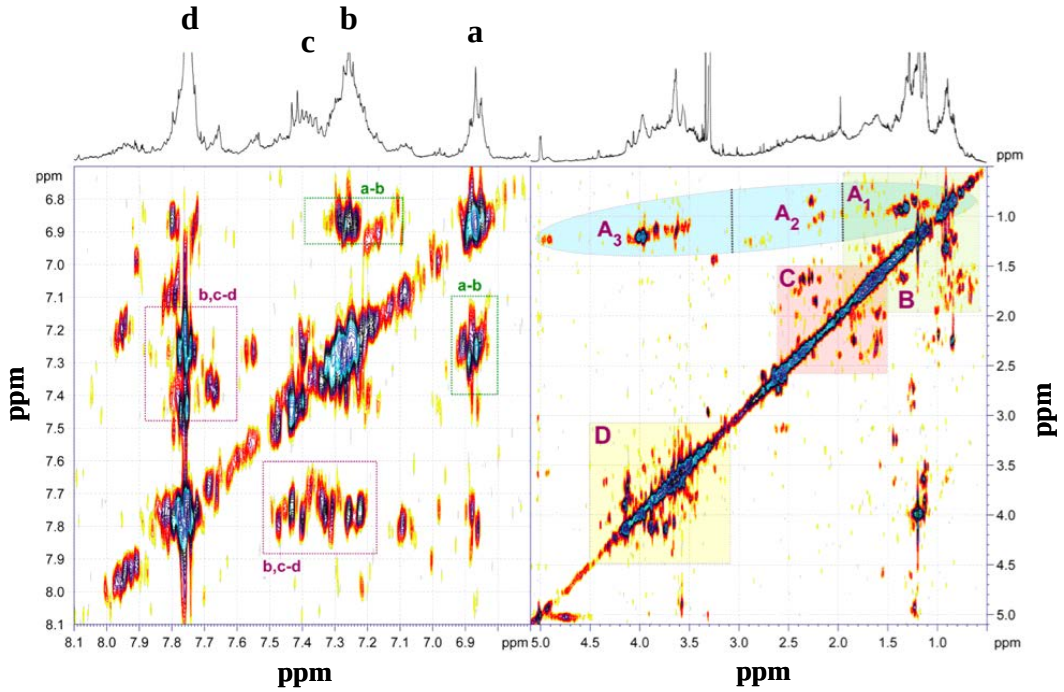

Figure 2.6. Correlation spectroscopy (COSY) ^{1}H NMR spectrum of EfOM with aromatic cross peaks (left) and aliphatic cross peaks (right).

2.3.3 Sulfur Content of EfOM

LAS are among the most common groups of anionic surfactants and, after soaps (mostly linear alkyl sulfates, e.g., sodium dodecyl sulfate or sodium lauryl sulfate), the most widely used surfactants in domestic detergents (Smulders et al., 2007). The presence of surfactants negatively affects oxygen transfer in wastewater aerated processes, thus increasing the treatment's energy footprint (Rosso et al., 2006). Commercial LAS mixtures usually contain about 15% coproducts. The molecular formulas were consistent with commercially used surfactants, and the black dots in Figure 2.7 emphasize abundant formulas in the investigated EfOM. Major LAS coproducts were dialkyl tetralin sulfonates (DATS) and methyl-branched isomers of LAS (iso-LAS). Biodegradation of LAS lead to long chain SPCs, LAS, DATS, and their metabolites have been detected in sewage treatment (Di Corcia et al., 1999a), in surface waters (Gonzalez-Mazo et al., 1997), and in coastal waters (Riu et al., 1999).

Previous studies showed that LAS and DATS concentrations in wastewater treatment influents ranged from 1.8 to 15.1 mg/L (Matthijs et al., 1999; McAvoy et al., 1998; Trehy et al., 1996; Waters and Feijtel, 1995) and 0.15 to1.2 mg/L (Trehy et al., 1996; Crescenzi et al., 1996), respectively, and that activated sludge processes removed more LAS than trickling filters, with removal efficiencies ranging from 95 to greater than 99% and 73 to 90%, respectively (Matthijs et al., 1999; McAvoy et al., 1998; De Henau et al., 1986; McAvoy et al., 1993; Rapaport and Eckhoff, 1990; Woltering, 1987). Activated sludge treatment also removed more DATS than trickling filters, with 95% removal compared to 63% removal (Trehy et al., 1996). It was suggested that the higher hydraulic- and solids-retention times were associated with these higher LAS and DATS removal percentages (McAvoy et al., 1993). DATSI concentrations were usually higher in the treatment effluent than in the influent. It was previously shown that DATSI concentrations were 1.6 times

higher in activated sludge treatment and 1.7 times higher in trickling filter treatment (Trehy et al., 1996) suggesting a production and/or release internal to the treatment process.

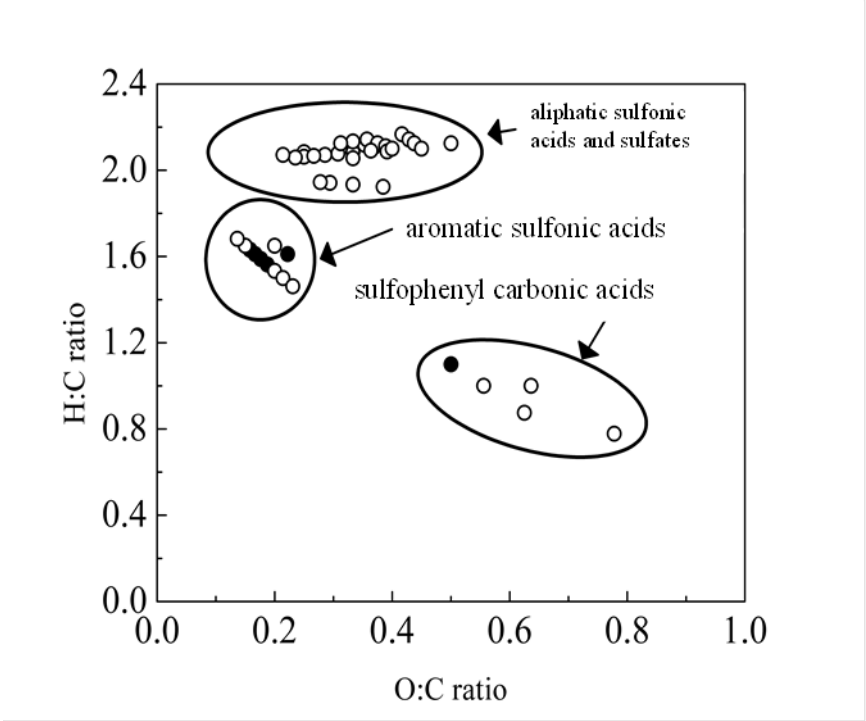

Figure 2.7.Van Krevelen diagram of the same molecular formulas found in commercial sulfur-containing surfactants and CHOS formulas in EfOM.

Note: The black dots indicate a high abundance (up to 28%) of peaks in the EfOM.

The findings on LAS chain length in our study were consistent with findings of others, averaging from $C_{11.8}$–$C_{12.0}$ (McAvoy et al., 1998; McAvoy et al., 1993; Rapaport and Eckhoff, 1990). Sorption to activated sludge biomass and biodegradation were demonstrated to be the main removal pathways of LAS in wastewater treatment (McAvoy et al., 1993; Rapaport and Eckhoff, 1990; Painter and Zabel, 1989; Takada and Ishiwatari, 1987) with SPCs as the major products of biodegradation in aerobic conditions at approximately 50 µg/L and 10 µg/L in activated sludge and trickling filter effluents, respectively (Trehy et al., 1996; Gonzalez-Mazo et al., 1998).

Among compounds common to both ASE and TFE, the highest abundances of any mass occurred for those whose formula corresponded exactly with those of SPC, LAS, and DATS (Figure 2.8). Collision-induced dissociation (CID) tandem mass spectrometry was undertaken with selected masses to confirm the suggested surfactant classes associated with each homologous series and the fragmentation pattern strongly supported the existence of SPC, LAS, and DATS homologous molecules (Figure 2.9). However, it should be noted that ESI-FT-ICR-MS cannot be used as a quantitative tool.

In both ASE and TFE, the highest abundances of SPC formulas occurred for those of side chain lengths C_7 to C_9 (see Figures 2.1 and 2.2) with steady decreasing abundances at lower and higher masses (range C_2–C_{17}). This result was in agreement with a study in which the highest SPC concentrations in a littoral environment were those of length C_6 to C_8 (Leon et al., 2002).

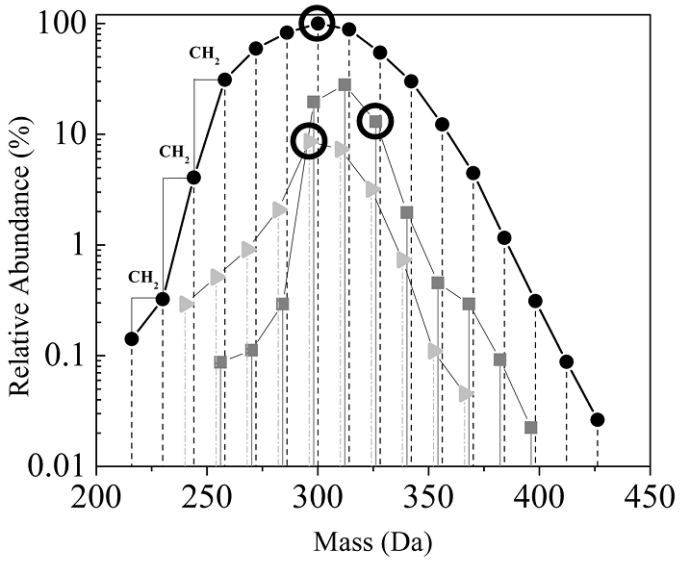

Figure 2.8. Relative abundance of classes of surfactants.

Note: Sulfophenyl carboxylic acids (SPC) (circle), linear alkyl benzene sulfonates (LAS) (square), and dialkyl terralin sulfonates (DATS) (triangle) in the activated sludge sample. Circles correspond to mass used for MS-MS analysis (see Figure 2.9).

Intact LAS formulas with the highest abundances were those of the chain length of C_{10} to C_{12}, with relative abundances steady decreasing for smaller and longer chain lengths (range C_7–C_{17}) similar to the trend observed for SPC formulas (Figure 2.8). The close relationship between the relative abundances of LAS and SPC molecular formulas was not surprising if a similar biodegradation of LAS of different chain lengths was assumed. For example, the C_{12}-LAS biodegradation resulted in two acetic acid molecules and the addition of the carboxylic acid group to form C_7-SPC (Di Corcia et al., 1999b). This degradation pathway was in agreement with the observed relative abundances of LAS and SPC in this study. The high abundance of SPC formulas suggests that a further biodegradation of these compounds was relatively slow and, therefore, these accumulated during the wastewater treatment process.

In addition, major coproducts of commercial LAS, such as DATS and iso-LAS, have been found to be resistant to biodegradation by microorganisms populating an activated sludge of a treatment plant (Trehy et al., 1996; Di Corcia et al., 1999b). In our study, similar to the LAS and SPCs, molecular formulas fitting DATS molecules also were present in high abundances in the EfOM although less than the abundances found for LAS and SPC compounds. The distribution pattern of the suggested DATS homologous series (side chain C_1–C_{10}, highest at C_5) followed the trend in relative abundances observed in LAS and SPCs (Figure 2.8).

The laboratory biodegradation experiment of LAS and coproducts conducted in a previous study (Di Corcia et al., 1999b) also showed that the ω/β-oxidation mechanism produced, in addition to expected monocarboxylated metabolites, significant quantities of dicarboxylated metabolites. Likewise, formulas matching dicarboxylated metabolites were abundant in our samples. Furthermore, the distribution pattern of the relative abundances of different chain lengths of dicarboxylated DATS or DATS intermediates (DATSI) also matched the DATS compounds if an addition of four oxygen and the loss of two hydrogen and two carbon was

considered during the biodegradation as suggested in an earlier study (Di Corcia et al., 1999b). Unlike LAS, DATS, and sulfophenyl alkyl monocarboxylated-LAS, aquatic toxicity data and long-term effects of DATSI on aquatic life are still unknown (Di Corcia et al., 1999b).

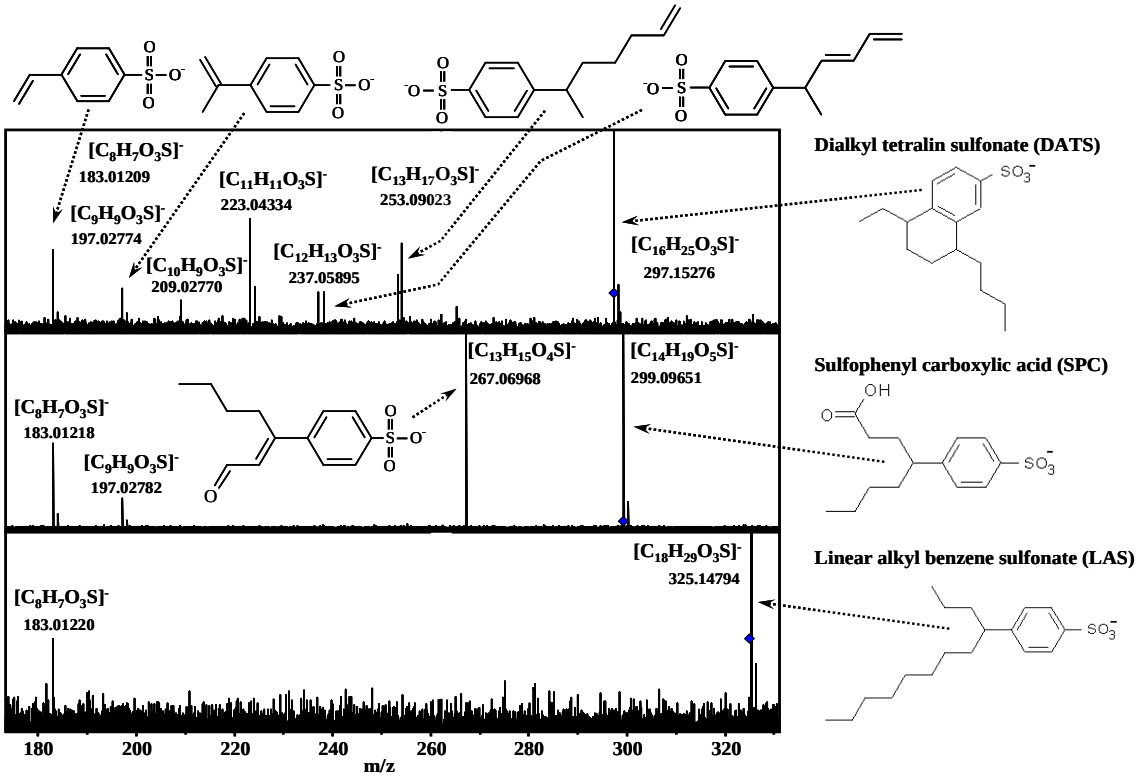

Figure 2.9. The MS-MS fragmentation pattern of the highest abundant peaks of SPC-, LAS-, and DATS-type masses.

It is well known that major components of the wastewater influent are surface active substances and that these organic molecules and metabolites also are found in high quantities in treated effluent. A close relationship between commercially used surfactants, their coproducts, and their biodegradation products was found and evaluated using ultra-high resolution ESI-FT-ICR-MS. In addition to the surfactants and their metabolites being responsible for the highly abundant CHOS formulas present, the presence of several hundreds of additional CHOS formulas with high oxygen content were very difficult to explain using solely surfactants as a source for sulfur. One possible explanation was that under anaerobic conditions, H_2S reacted with CHO compounds to form high molecular weight mercaptans and other sulfur-containing molecules. The possible reactions of H_2S with organic matter have been previously described (Vairavamurthy and Mopper, 1987). Overall, the ESI-FT-ICR-MS technique detected sulfur-containing molecular formulas that were expected, but showed in detail an unexpected large diversity of these compounds in EfOM.

2.3.4 Molecular Composition Differences Between EfOM in ASE and TFE

Very subtle differences existed between the characteristics of the formulas found in both sample sets (different dates) in either ASE, TFE, or MFE, as evident in Table 2.3. The DBE, H:C ratios, O:C ratios, and average masses were very similar for formulas of ASE, TFE, and MFE that were detected on both sampling dates with one exception of the ASE sample

collected on July 30, 2008, showing a higher degree of saturation (DBE = 5.5) among the CHO formulas. This result also was reflected in the MFE sample (DBE = 5.7) of the same date.

Table 2.6. Characteristics of Activated Sludge (ASE), Trickling Filter (TFE), and Microfiltration (MFE) Effluents

	Sample	Date	n*	Center of Mass	ΔO/C	ΔH/C	DBE
CHO formula	ASE	02/02/09	979	356.4	0.47	1.23	7.0
	ASE	07/30/08	1112	333.6	0.39	1.48	5.5
	TFE	02/02/09	836	358.9	0.47	1.29	7.2
	TFE	07/30/08	1029	352.2	0.44	1.35	6.8
	MFE	02/02/09	1055	351.6	0.46	1.34	6.8
	MFE	07/30/08	1013	341.1	0.40	1.47	5.7
CHOS formula	ASE	02/02/09	1197	314.4	0.40	1.48	4.7
	ASE	07/30/08	1065	314.7	0.40	1.49	4.7
	TFE	02/02/09	1114	312.1	0.38	1.49	4.6
	TFE	07/30/08	1187	317.3	0.37	1.57	4.2
	MFE	02/02/09	1236	313.4	0.41	1.47	4.8
	MFE	07/30/08	1129	316.8	0.40	1.52	4.4

Note: n^*-number of ^{13}C referenced exact molecular formulas.

Sulfur formulas in the TFE sample collected on the July 30, 2008, were slightly more saturated than those of ASE and the later sampling for the TFE. However, the similarity of the CHOS formulas found in all EfOM samples was very high and, in fact, the samples looked almost identical in terms of CHOS formulas. Within the coarse regions of the ^1H NMR spectra, considerable differences also were observed between the sampling periods but little between treatments, suggesting that temporal differences between samples of the same treatment process appear to be greater than those between the two processes. As a result, characteristics of the wastewater influent have more of an impact on EfOM than does the process itself. Further studies are being conducted to determine the potential effect of these sulfur-containing compounds on treatment in water for indirect potable use.

2.4 Conclusions

The non-target analysis of EfOM using FT-ICR-MS revealed the presence of sulfur-containing molecular formulas with an unexpected wide ranging molecular diversity. Anthropogenic surface-active compounds, their coproducts and metabolites were responsible for the highest abundant peaks in the analyzed FT-ICR-MS data. The origin of several hundreds of low abundant sulfur-containing molecular formulas unique to EfOM remains uncertain. This study also demonstrated the very different composition of EfOM compared with NOM.

NMR spectroscopy and FT-ICR mass spectrometry are invaluable techniques to evaluate complex organic mixtures such as EfOM. This study has shown detailed information about the organic content of EfOM and the importance of qualitative analysis of such complex matrices. Future studies can now be designed to further investigate the different components of EfOM and their environmental fates. In addition, FT-ICR-MS and 2D-NMR can be applied to investigate degradation pathways and reactivity of specific components of EfOM.

Chapter 3

Microbial and Water Quality Survey

3.1 Introduction

Four microbiological and general water quality surveys of the Advanced Water Purification Facility were conducted in 2010. Two nighttime and two daytime surveys were conducted, as the AWPF operated on a diurnal cycle with lower plant flows between 2:00 a.m. and 7:00 a.m. During the night the flow of secondary effluent (Q1) from the OCSD drops and the AWPF only produces 50 to 55 mgd of FPW. Normal daytime AWPF production rates are 65 to 68 mgd. Samples were analyzed to determine if the biological and chemical composition of the secondary effluent from OCSD differ between the nighttime and daytime conditions. All four plant surveys were collected when the OCSD was operating in NDN mode of treatment.

During the period from January 2008 to November 2009, OCWD received Q1 effluent from OCSD that was processed by carbonaceous biological oxygen demand (CBOD). In June 2008, the AWPF began treating a blend of 20% TFE and an 80% ASE. In early November 2009, OCSD switched to a nitrification-denitrification (NDN) treatment process and increased the blend of TFE to 30%. The NDN process and Q1 water quality stabilized in January 2010.

3.2 Materials and Methods

The date, start time, source water condition, and plant flow for each microbiological and water quality survey are listed in Table 3.1. Grab samples for the survey were collect at eight locations throughout the AWPF (Figure 3.1). The sampling was timed to capture representative samples as the water flowed through the purification plant. The timing of each grab sample and the associated AWPF plant flow rate are displayed in Table 3.2. The general minerals (Level II) analysis was performed by OCWD's Advanced Water Quality Assurance (AWQA) Laboratory (see Table 3.3). The microbiological analysis and micro-constituent analysis were performed by OCWD's Research and Development Department.

Table 3.1. AWPF Microbiological and Water Quality Surveys

Date	Start Time	Source Water Condition	AWPF Flow (MGD)
March 30, 2010	7:00 a.m.	Night Flow	50
May 20, 2010	1:00 p.m.	Day Flow	65
July 21, 2010	6:00 a.m.	Night Flow	45
September 23, 2010	10:00 a.m.	Day Flow	70

Total protein was determined by the Lowery method (Lowery et al., 1951) and total carbohydrate determined by the phenol-sulfuric acid method (Dubois et al., 1956). Both unfiltered and samples filter through a 0.22 μm cellulose acetate (CA) membrane (Costar, Cambridge, MA) were analyzed for total protein and total carbohydrate. The filtered samples represented the dissolved portions of protein and carbohydrate in the source waters free of

bacterial cells. Excitation-emission matrix (EEM) spectroscopic analysis was preformed at University of California Irvine and recorded using a FluoroMax (Horiba-Jobin Yvon, Edison, NJ). The excitation wavelength was incrementally increased from 240 nm to 500 nm in 5-nm intervals, with emission monitored from 280 to 600 nm at 5-nm intervals for each excitation wavelength. The total chlorine concentration was determined by the DPD colorimetric assay (Hach Company, Program 1485).

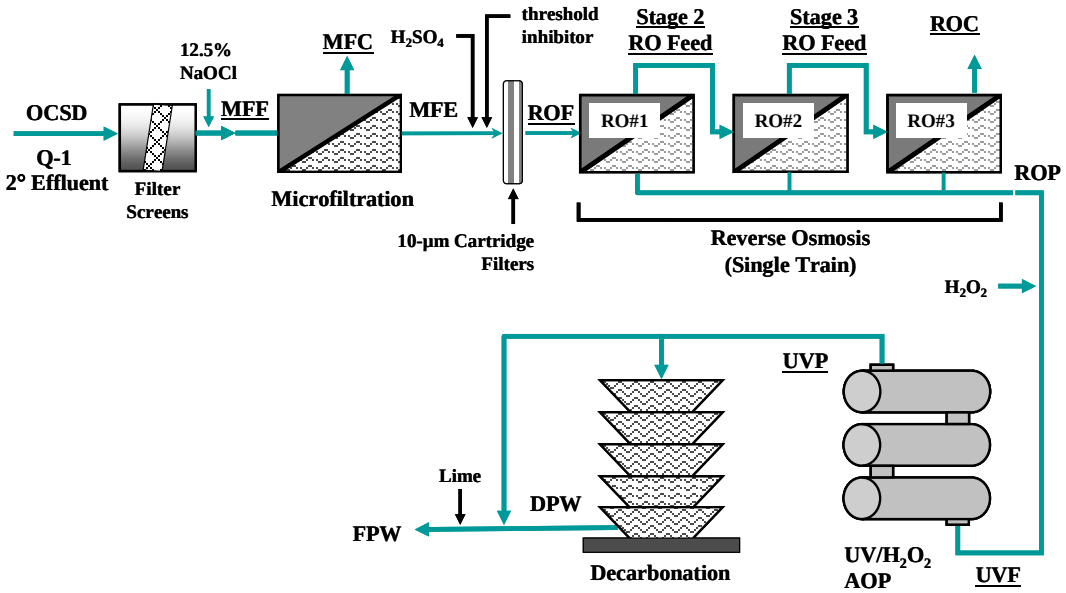

Figure 3.1. AWPF plant survey diagram with sample stations representing MFF, MFE, ROF, Stage 2 RO feed (STG2 ROF), Stage 3 RO feed (STG3 ROF), ROC, ROP, UV feedwater (UVF), UV product water (UVP), decarbonated product water (DPW), and FPW.

Note: Stations sampled for the survey are underlined.

Table 3.2. Sample Grab Time in Conjunction with Total Flow of the AWPF

	Relative Collection Time from First Grab Sample			
Sample Station	**45 mgd (Night)**	**50 mgd (Night)**	**65 mgd (Day)**	**70 mgd (Day)**
MFF	0 min	0 min	0 min	0 min
MFC	8 min	7 min	6 min	5 min
RO Transfer Pump Station Residence Time	~46 min	~41 min	~35 min	~33 min
ROF	54 min	41 min	35 min	33 min
ROC/STG1	56 min	43 min	36 min	35 min
ROC/STG2	57 min	44 min	37 min	36 min
ROC/STG3	58 min	45 min	38 min	37 min
UVF	1 h 7 min	52 min	45 min	44 min
UVP	1 hr 14 min	58 min	50 min	48 min

Table 3.3. Analysis Preformed on AWPF Source Waters

General Minerals (Level II) Analysis	
Aluminum (Al)	Manganese (Mn)
Alkalinity phenolphthalein (ALKPHE)	Mercury (Hg)
Antimony (Sb)	Nickel (Ni)
Arsenic (As)	Nitrate (NO3)
Barium (Ba)	Nitrite (NO2)
Beryllium (Be)	Nitrogen (N)
Bicarbonate as CaCO3 (HCO3Ca)	pH
Boron (B)	Phosphate (PO4)
Cadmium (Cd)	Potassium (K)
Calcium (Ca)	Selenium (Se)
Carbonate as CaCO3 (CO3Ca)	Silica (SiO2)
Chloride (Cl)	Silver (Ag)
Chromium (Cr)	Sodium (Na)
Cobalt (Co)	Sulfate (SO4)
Copper (Cu)	Suspended solids (SUSSOL)
Electrical conductivity (EC)	Thalium (Tl)
Hydroxide as CaCO3 (OHCa)	Total dissolved solids (TDS)
Iron (Fe)	Total hardness as CACO3 (TOTHRD)
Lead (Pb)	Total organic carbon (TOC)
Magnesium (Mg)	Zinc (Zn)
Microbiological analysis	
Total bacterial counts (EPI)	
Aerobic / Heterotrophic plate counts (HPC)	
Total carbohydrate (colorimetric)	
Total protein (colorimetric)	
Total chlorine (DPD colorimetric)	
Assimilable organic carbon (AOC/bioluminescence)	
Other analytical analysis	
Excitation-emission matrix (EEM) fluorescence spectroscopy	

Assimilable organic carbon (AOC) was determined by rapid non-growth-based assay using a naturally occurring luminous strain *Vibrio harveyi* BB721 to determine the fraction of low molecular weight organic carbon in the water samples (Ma et al., 2012).

3.3 Results and Discussion

The water quality data for the secondary wastewater effluent (Q1) from OCSD were tabulated on a yearly basis. The average and standard deviation for each test parameter dating back to January 2008 through December 2012 are displayed in Table 2.1 in Chapter 2. Further discussion of the Q1 water quality is included here. Initially the AWPF treated an ASE processed by CBOD. Starting in June 2008, the Q1 effluent was composed of a mixture of 20% TFE and 80% ASE. All data from 2008 were tabulated and averaged. The data were not tabulated separately. In early November 2009, OCSD switched from CBOD treatment of the wastewater to an NDN mode of treatment that took approximately 2 months to stabilize. In late November 2009 the TFE composition was increased from 20% to 30% of the total makeup of the blended secondary effluent. The most significant changes in the secondary effluent were a reduction in the concentration of ammonia-N, organic-N, and total Kjeldahl-N, and an increase in the nitrate-N. The concentration of the total alkalinity also dropped noticeably in the blended effluent upon switching from the CBOD process to the

NDN mode of treatment. In 2008 and 2009 the average total alkalinity was ~290 mg/L under the CBOD process, and following the transition to the NDN mode of treatment, the average total alkalinity dropped to ~180 mg/L. It was not known why this happened. Also for unknown reasons, in 2012 the BOD increased three-fold to 31 ± 4 mg/L over the 11 ± 3 mg/L average measured in 2011. The 2012 BOD data is well removed from the November 2009 date when the TFE contribution was increased to 30%. Finally, there has been gradual year-to-year decrease in the TOC concentration in the blended Q1 secondary effluent.

The measured concentrations for each of the 47 parameters from the eight sample stations representing MFF to UVP for the four microbiological and water quality surveys of the AWPF are displayed in Figures 3.2–3.38.

At the beginning of the purification process, sodium hypochlorite (12.5%) is added Q1 wastewater by means of a Water Champ placed in the center of the 96 in. pipeline. Chloramines rapidly form because of the presence of ~0.5 mg/L of ammonia-N. There is ~1 min of reaction time before the blend of TFE and ASE reaches the first sample station (i.e. MFF). Following the MF process, the hold time of the MFE in the 2 million gallon break tank ranged from 41 to 46 min under low-flow (40–50 mgd) nighttime conditions and from 30 to 35 min under normal (65–70 mgd) daytime conditions. The targeted residual chlorine concentration in the RO feedwater (ROF) was 4 mg/L except for the March 30 50 mgd nighttime sampling of the AWPF (Figure 3.28). For 14 days in late March and early April 2010, the target ROF residual chlorine level was set at 5 mg/L as a treatment to mitigate biological fouling on the RO membranes. This RO membrane chlorination study was not initiated as part of the RO foulant characterization study of this project, and thus the findings from this Water Production Department study were not presented within this report.

The targeted ROF chlorine concentration varied from the high of 5 mg/L that lasted for 2 weeks in March 2010 to a low of 1.5 mg/L that lasted for 5 days in May 2010. The majority of the time the ROF total residual chlorine target concentration was 3 to 4 mg/L.

During the process of characterizing the MF, RO, and UV/AOP of the AWPF, it was discovered that the reporting of total residual chlorine by online amperometric analyzers did not agree with other methods of total chlorine analysis, including standard methods. The online amperometric total chlorine analyzer routinely reported out a higher concentration of chlorine than grab samples analyzed by the amperometric and DPD-FAS titration standard methods, as well as the DPD spectrophotometric method (HACH Company, Program 1485). Further discussion of the issues associated with the measurement of total residual chlorine in source waters of the AWPF are presented in Appendix A.

3.3.1 General Minerals

3.3.1.1 Microfiltration

There was little change in the concentration of cationic and anionic minerals across the MF process as would be expected. However, there was a small increase in the concentration of the ortho-phosphate in the MFC, which was presumably associated with the removal of bacterial cells during the backwash cycle (every 22 min). There also was a significant increase in the concentration of iron and aluminum in the MFC. Both increased greater than four-fold in the MF backwash relative to the concentration in the MFF. The aluminum was likely associated with silicates trapped in the cake layer, whereas the iron was presumed to

take the form of insoluble oxides and hydroxides. Both were removed by the backwash. Further measures were not taken to characterize the aluminum and iron constituents.

3.3.1.2 Reverse Osmosis

In general, the feedwater constituents were concentrated six-fold across the three-stage (three-pass) RO process that is operated at 80 to 85% recovery. There was a two-fold concentration of rejected constituents across the first stage, a four-fold concentration across the second stage (relative to the concentration of the constituents in the feedwater), and finally a six-fold concentration of constituents by the end of the third stage.

The aluminum and iron that passed through the MF membranes were concentrated in the brine of the RO process by 2.2, 4.6, and 4.9 times on average for aluminum for Stage 1, 2, and 3, respectively, and 2.2, 5.0, and 6.0 times on average for iron. The sodium and calcium concentrations in the brine increased 2.3, 5.1, and 6.1times across the three stages. The anions were removed similarly with both the sulfate and chloride concentrations increasing 2.3 times across Stage 1, 5.1 times relative to the ROF in Stage 2, and 6.5 times across Stage 3.

The six-fold concentration also was reflected in the EC and TDS data. The EC from the Stage 1 effluent increased by a factor of 2.1, the Stage 2 effluent by a factor of 4.4, and the Stage 3 effluent by a factor of 5.3. The TDS concentration increased by factors of 2.2, 5.1, and 6.1, respectively, in the brine samples across the RO process.

3.3.1.3 UV/H_2O_2 Advanced Oxidation Process

The vast majority of the minerals were reduced below the detection limit by the RO process that produced a very low electrical conductivity permeate to be treated by the UV/H_2O_2 AOP. The mineral levels that were measurable in the RO permeate (UVF feedwater) were mostly unaffected by the AOP. A small reduction (0.2 mg/L) in the total Kjehldahl nitrogen was measured in each of the four AWPF samplings. The UV/H_2O_2 AOP had the greatest impact on the total chlorine concentration with 65 to 75% reduction occurring in both daytime samples and the second 50-mgd nighttime samples. Up to 90% of the total chlorine was removed from the RO permeate (UVF) across the UV/AOP in the samples grabbed during the first nighttime sampling of the AWPF. The removal occurred by a combination of direct photolysis by UV light and oxidation by hydroxyl radicals (see Chapter 11 for a more detailed discussion).

3.3.2 Micro-Constituents

3.3.2.1 Microfiltration

The EEM fluorescence spectra indicated the presence of protein (excitation/emission wavelength, Ex/Em 280/331 nm) and humic acid-like compounds (Ex/Em 342/436 nm) (Chen et al., 2003). Only one representative set of EEM spectra is displayed in Figures 3.29 and 3.30, as the spectra from each sampling of the AWPF were similar. A plot of the fluorescence peak intensity associated with protein and humic acid-like matter from each sample station is displayed in Figures 3.31 and 3.32, respectively. The intensity of the protein peak increased by a factor of two in the MFC. This was indicative of the removal of “cake” material from the inner pores and membrane surface during the backwash cycle. Removal of protein from the membrane was confirmed through analysis of the samples by the colorimetric protein assay (Figure 3.33). There was a three-to-four-fold increase in the

concentration of total protein in the unfiltered MFC samples, which was presumably associated with bacterial cells that were a part of the dislodged cake. Forty percent of the MFC total protein was removed by filtration of the water sample at 0.22 μm prior to running the Lowry protein assay, and this fraction is believed to represent the bacterial cell component of the MF backwash (Figure 3.34).

The unfiltered total protein content of the ROF (MFE with acid and antiscalants) was reduced by 63% on average from 1.83 mg/L in MFF to 0.67 mg/L in ROF by the MF process (Figure 3.33), and the protein content of the filtered MFF effluent dropped 58% across the MF process (Figure 3.34). The slightly greater fraction (5%) of protein removed from the unfiltered MF water samples was attributed to the removal of bacterial cells by the MF process.

The fluorescent proteinaceous matter was not as extensively removed by the MF. The average fluorescence intensity only dropped 14% across the MF process (Figure 3.31) as compared to a 63% drop in the total unfiltered protein content (Figure 3.33). This indicated that the soluble fraction of protein contained more of the fluorescent components.

The fluorescent humic acid-like matter was not adsorbed or concentrated in the cake layer, as equal fluorescence intensities were measured in all three MFF, MFC, and MFE samples. These results also indicate that humic acids are not closely associated with the microbial fraction of the MFF and are more strongly associated with the soluble constituents in the MF feedwater.

A significant amount of carbohydrate matter was measured in the unfiltered MFC samples as compared to the unfiltered MF feedwater. The unfiltered MFC samples contained approximately 3 to 5 times more carbohydrate than the unfiltered MFF samples. Slightly more carbohydrate was measured in the unfiltered MFC samples (15.5 μg/L on average; Figure 3.35) as compared to the filtered MFC samples (13.47 μg/L; Figure 3.36). This small difference (~10%) represented the fraction of carbohydrate associated with bacteria and large macromolecules incapable of passing through the 0.22 μm filter present in the MF concentrate or backwash. The removal of carbohydrate by the MF process was mixed. In two cases (i.e. the 45-mgd and 70-mgd surveys), the carbohydrate content was reduced by 50% across the MF process. In the other two cases (i.e. the 50-mgd and 65-mgd surveys), the carbohydrate concentration in the ROF was 30 to 60% higher than the concentration in the MFF.

Greater than 5.5 logs removal of bacteria by MF have been reported by Oliveri et al. (1991) and 2 to 6 logs reduction by Willingham et al. (1993) from wastewater effluents (USEPA, 2001). A 3 to 3.5 log reduction of total bacteria was measured across the MF process from the two nighttime samplings of the AWPF (Figure 3.37). However, only ~1-log reduction of reduction in the total bacterial counts was observed for the two daytime samplings. MFE is retained in a 2 million gallon break tank with a residence time of 30 to 45 min before it passes on to the RO process. The walls of the transfer pipeline and walls of the break tank are hypothesized to be covered with a biofilm that periodically release bacterial cells into the MFE. Thus, the true removal efficiency of the AWPF MF process is undoubtedly greater than 3 to 3.5 logs.

The polypropylene cartridge filters downstream of the MF, whose main function is to remove particulate matter from the MFE so as not to damage the RO membranes, also provides a

large surface area for bacterial colonization and a surface on which nanoparticles can adhere. An autopsy of a used cartridge filter confirmed this hypothesis (see Chapter 5).

3.3.2.2 Reverse Osmosis

The protein (Figures 3.31, 3.33, and 3.34), humic substances (Figure 3.32), and carbohydrate matter (Figures 3.35 and 3.36) were concentrated in the RO brine (ROC). Total protein, both unfiltered and filtered, were concentration by a factors of 2.0, 4.3, and 4.9, respectively, across the first, second, and third stages of the RO process. The fluorescence emission intensity associated with the humic substances increased by factors of 2.2, 5.5, and 6.5, respectively (Figure 3.32). The unfiltered carbohydrate increased by factors of 1.8, 3.1, and 3.6, and the filtered samples increased by factors of 1.3, 2.8, and 3.3 across the first, second, and third stages of the RO process, respectively (Figure 3.35 and 3.36). The fact that some of the macromolecular constituents did not concentrate precisely at the theoretical 2, 4, and 6 orders of magnitude in the brine of each stage suggests that the deposition on the membrane surface may have occurred.

Small amounts of protein, humic acids, and carbohydrate were detected in the RO permeate. These likely resulted from the shedding of biofilm from the backside of the surface of the RO membranes and the surface of the pipelines. Theoretically, none of the protein, carbohydrate, or humic substance should pass through the RO membrane (see further discussion following).

On average, there was 140 ± 25 μg/L AOC as glucose-C in the MFF samples from the four water quality surveys. A significant amount (60–85%) of AOC was removed by the MF process and presumably more by the RO membrane filtration processes (Figure 3.27). The AOC concentration increased two-to-six-fold in the first-stage brine samples, between seven-to-12-fold (nine-fold on average) in the second-stage brine, and 10-to-20-fold in the third-stage brine.

The total chlorine level of the AWPF was set unusually high (ROF target: 5 mg/L) during the second nighttime sampling because of an attempt to attenuate microbial fouling at the membrane surface (Figure 3.28). Chloramines readily passed through the RO membrane with little measurable chorine demand (~0.2 mg/L) across the RO process.

3.3.2.3 UV/H_2O_2 AOP

Bacteria were enumerated in the RO permeate. The total bacterial counts varied from 250 cells/mL to more than 1000 cells/mL for the four AWPF surveys (Figure 3.37). The RO membranes act as a complete barrier to bacteria. However, it is hypothesized that bacteria present during manufacturing of the membranes, construction of the RO facility, small leakage of the RO product tube o-rings, and servicing of the RO trains leads to bacterial colonization of the surfaces of collection pipes post-RO. Over time, biofilms are established that routinely shed bacterial cells. Therefore, measurable quantities of bacteria are often detected downstream of the RO process. Total bacterial counts ranged from 270 to 1230 cells/mL in the RO permeate (UVF feedwater) for the four AWPF surveys.

Total bacterial counts of the UV product water from the two nighttime samplings revealed higher numbers—more than a 115% increase across the UV/AOP for the 45-mgd survey and more than a 150% increase for the 50-mgd survey (Figure 3.37). A release of bacterial cells from the walls of the pipeline apparently occurred, leading to higher total bacterial counts in the UVP product water. The two daytime microbial surveys indicated that there was a 0.16-

log (31.5%) reduction of total bacteria across the UV/AOP for the 65-mgd survey and a 0.28-log (47.7%) reduction for the 70-mgd survey. These results suggest that the UV/AOP process was not energetic enough to completely lyse all the bacterial cells in the feedwater.

Approximately 2% of the total bacteria in the UVF feedwater from the 45-mgd nighttime sampling were viable on R2A agar medium, whereas less than 0.1% were viable from the remaining three UVF samples (see Figures 3.37 and 3.38). A high of 14,500 viable bacteria per 1000 mL were detected in the UVF of the 45-mgd nighttime survey that were reduced to 53 viable cells per 1000 mL in the UVP product. The 50-mgd survey showed higher viable counts in the UVP sample with 10 viable cells per 1000 mL in the UVF and 25 viable cells per 1000 mL in the UVP. The two daytime samplings across the UV/AOP revealed a 0.6 to 1-log reduction of viable bacterial cells. The small number of bacteria that are able to survive presumably possess a DNA repair mechanism to reverse the damaging effects of UV irradiation and catalase to neutralize the effects of hydrogen peroxide. Overall, between 25 and 120 viable bacterial cells per 1000 mL were detected in the samples of UV product water from the four microbial surveys of the AWPF.

Analysis of AOC in the ROP was not included in the survey. The quantity of AOC in the UVF and UVP water samples was not determined at the time of the study because of the presence of H_2O_2, which interfered with the assay[5]. No detectable change in the total organic carbon was measured across the UV/AOP, indicating no measurable breakdown of organic constituents all the way to carbon dioxide.

[5] Currently bovine catalase is added to the sample to quench the hydrogen peroxide in source waters from the AWPF (Liu, et al., 2003).

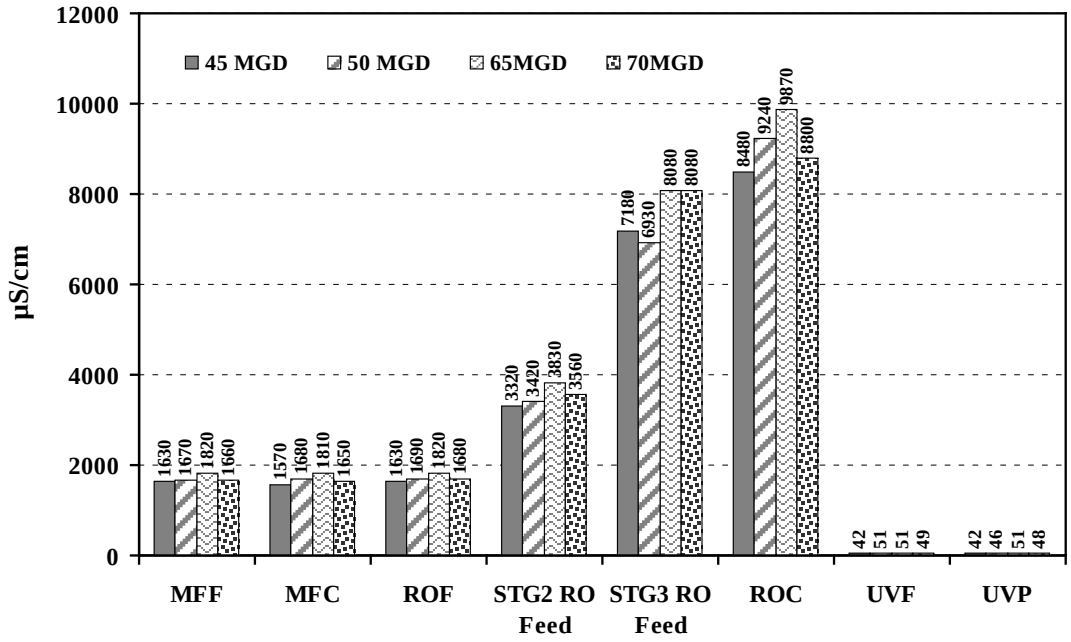

Figure 3.2. Plot of electrical conductivity (µS/cm) content.

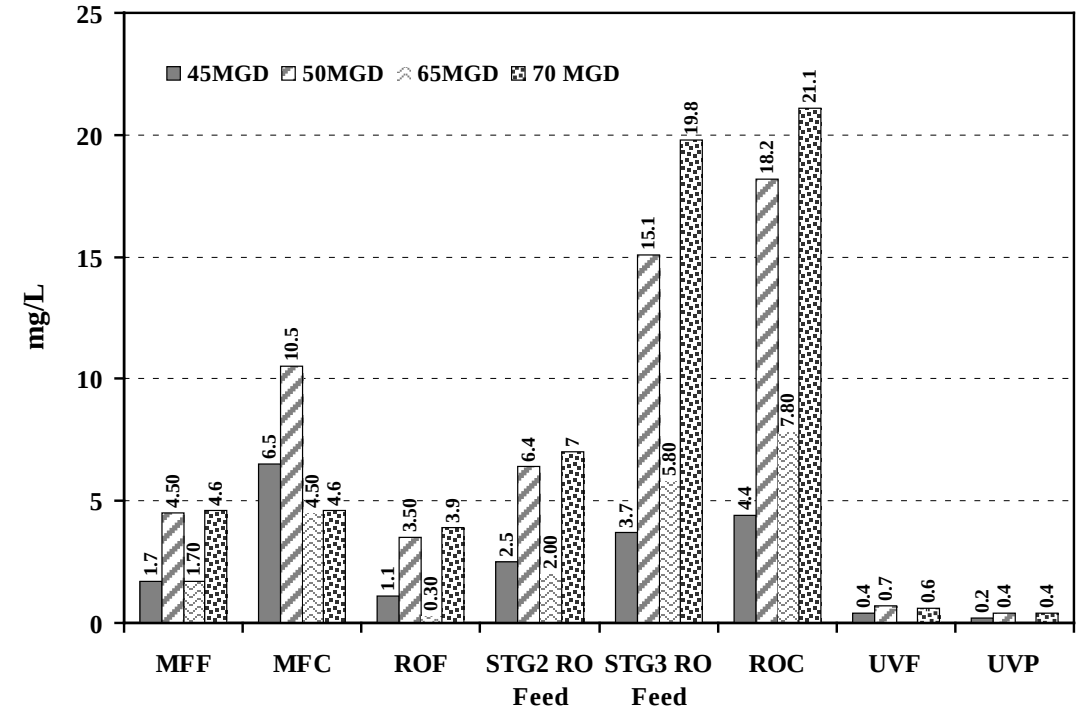

Figure 3.3. Plot of total Kjeldahl nitrogen (mg/L) content.

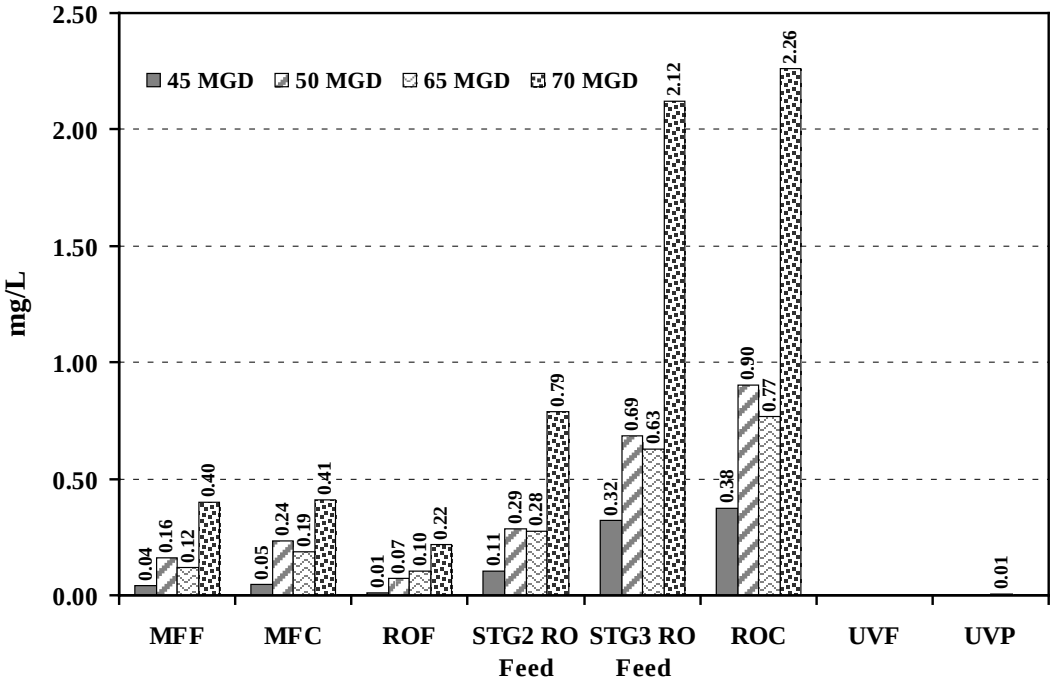

Figure 3.4. Plot of nitrite-nitrogen (mg/L) content.

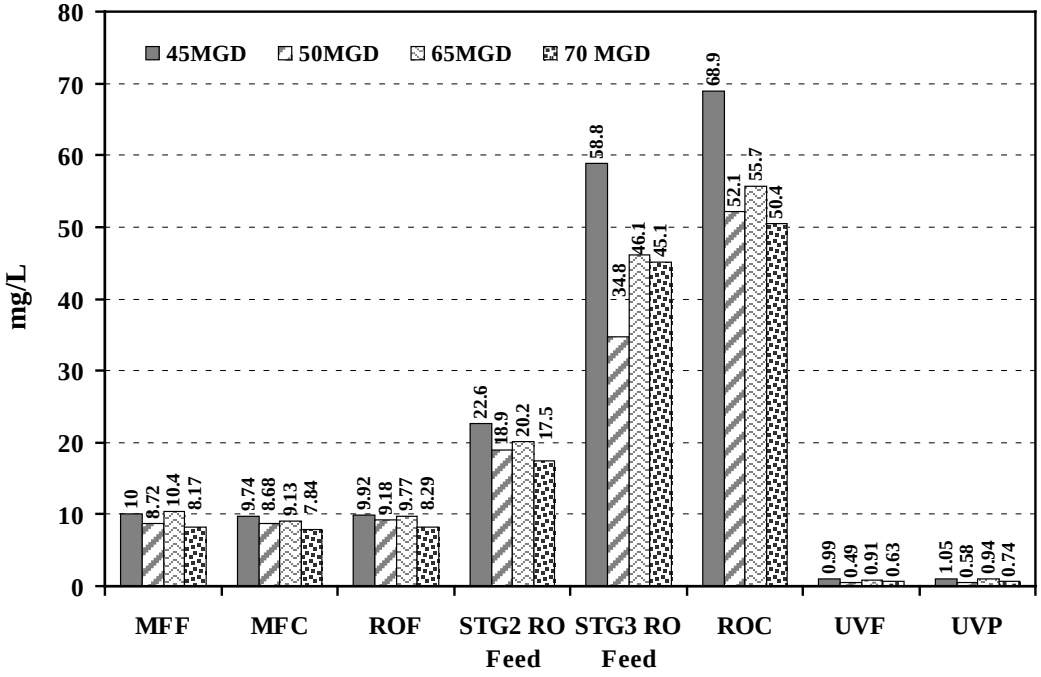

Figure 3.5. Plot of nitrate-nitrogen (mg/L) content.

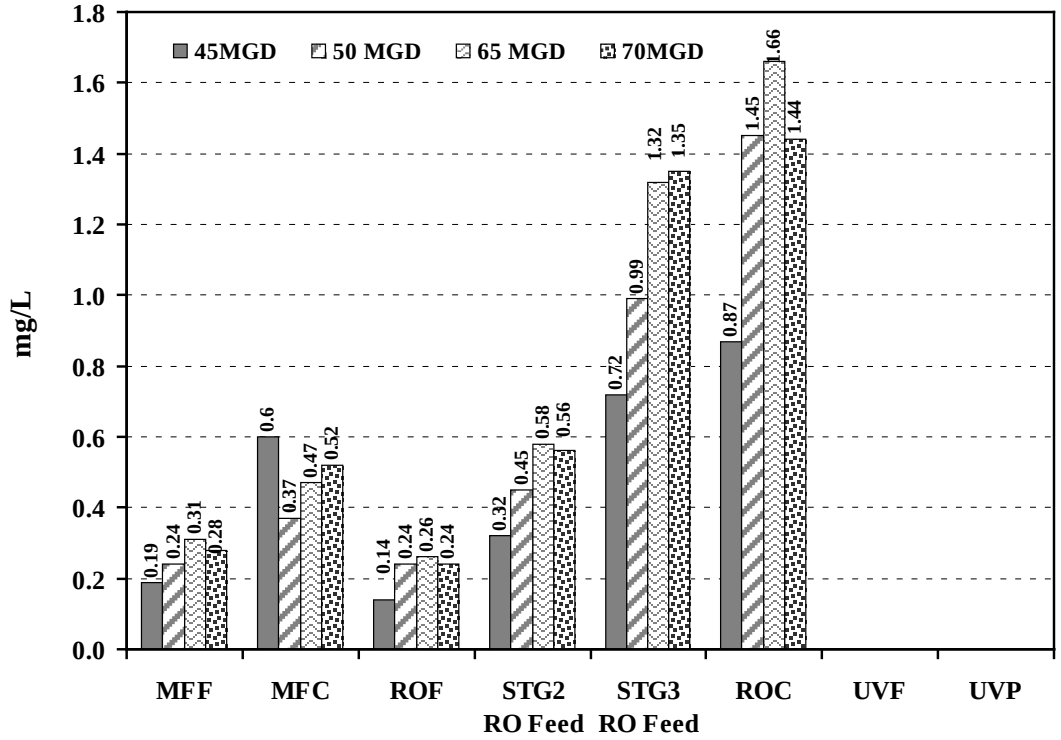

Figure 3.6. Plot of phosphate (mg/L) content.

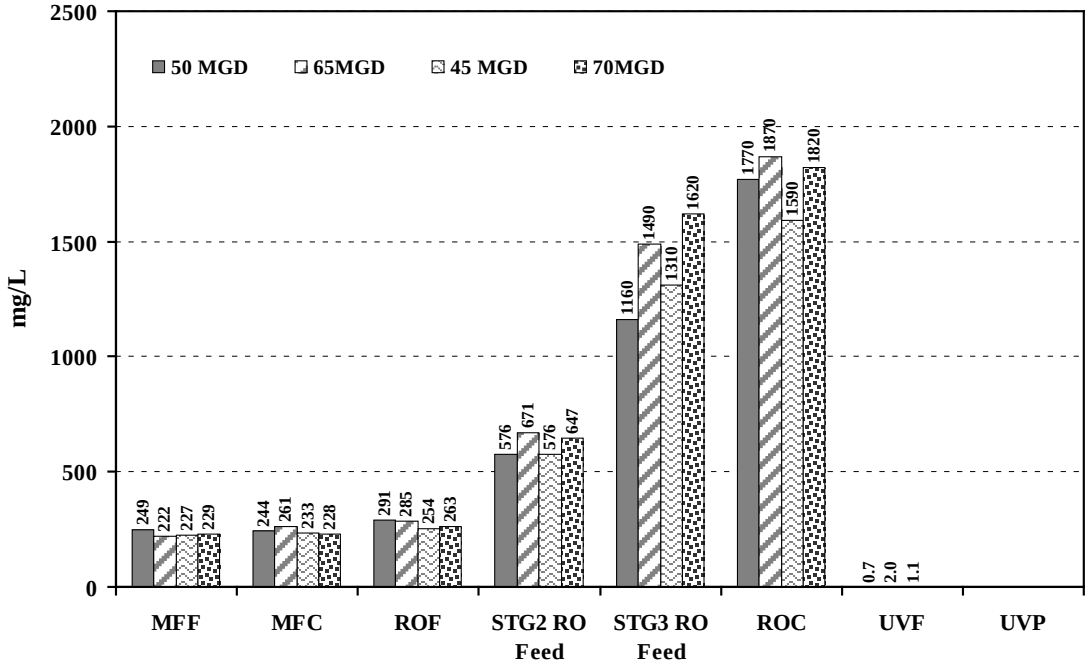

Figure 3.7. Plot of sulfate (mg/L) content.

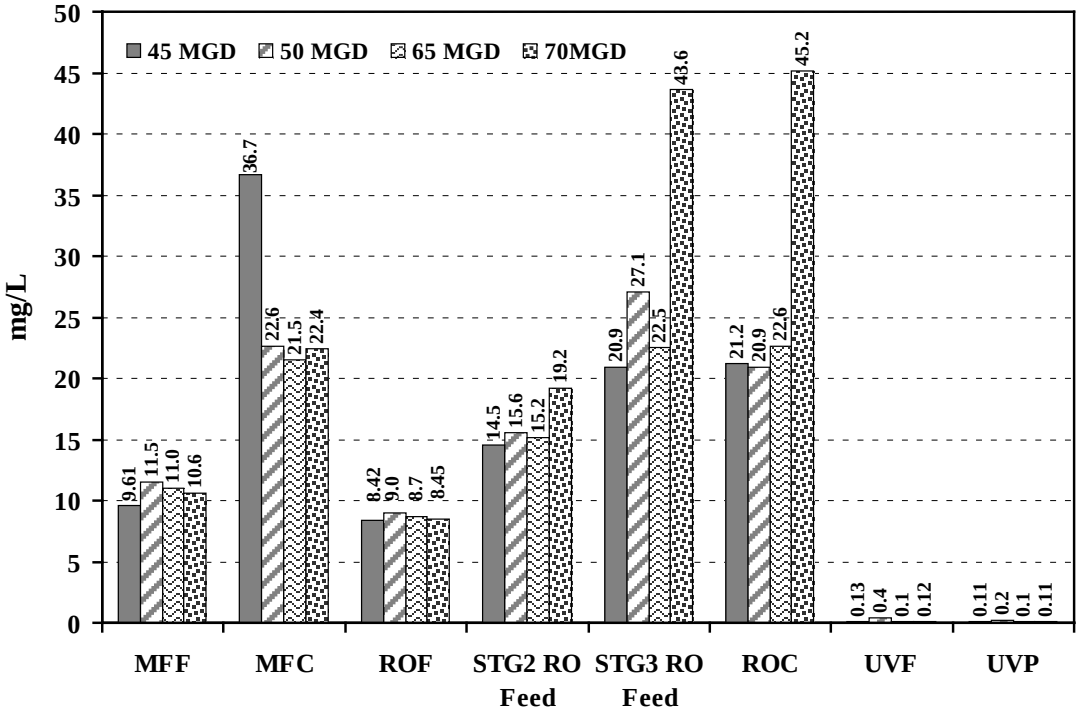

Figure 3.8. Plot of total organic carbon (mg/L) content.

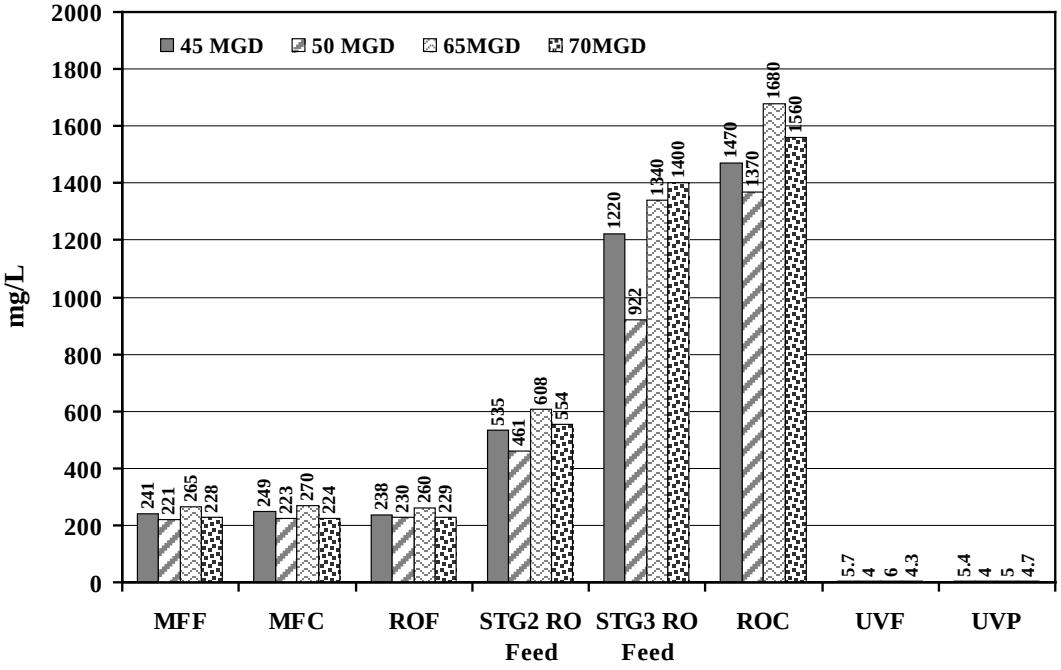

Figure 3.9. Plot of chloride (mg/L) content.

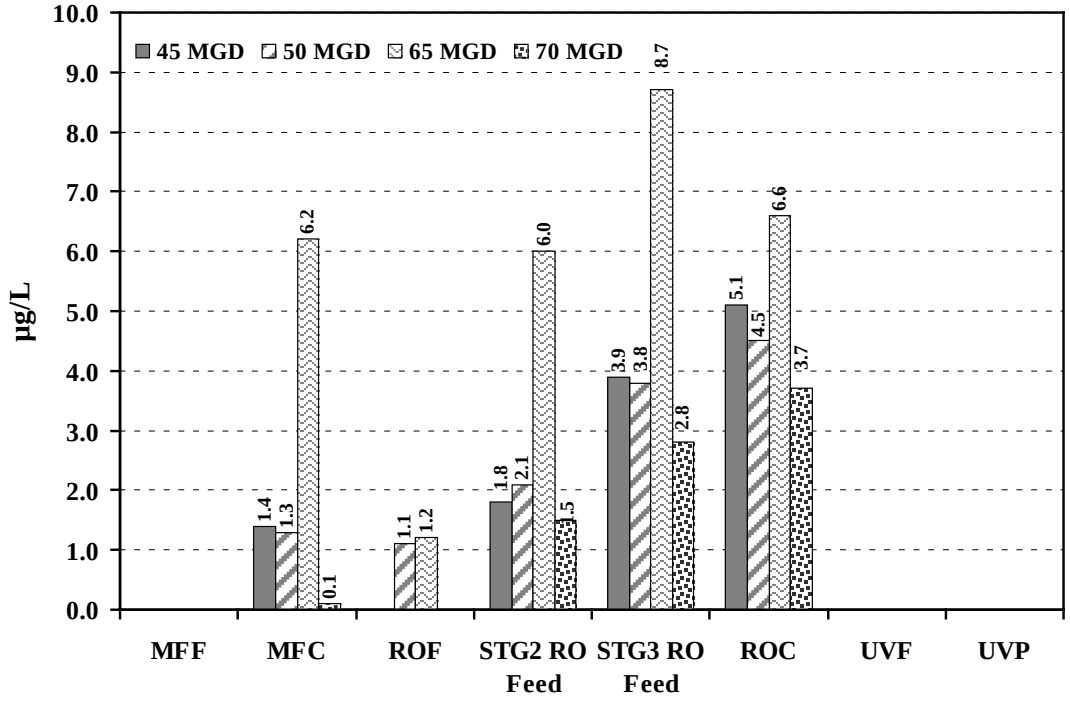

Figure 3.10. Plot of arsenic (µg/L) content.

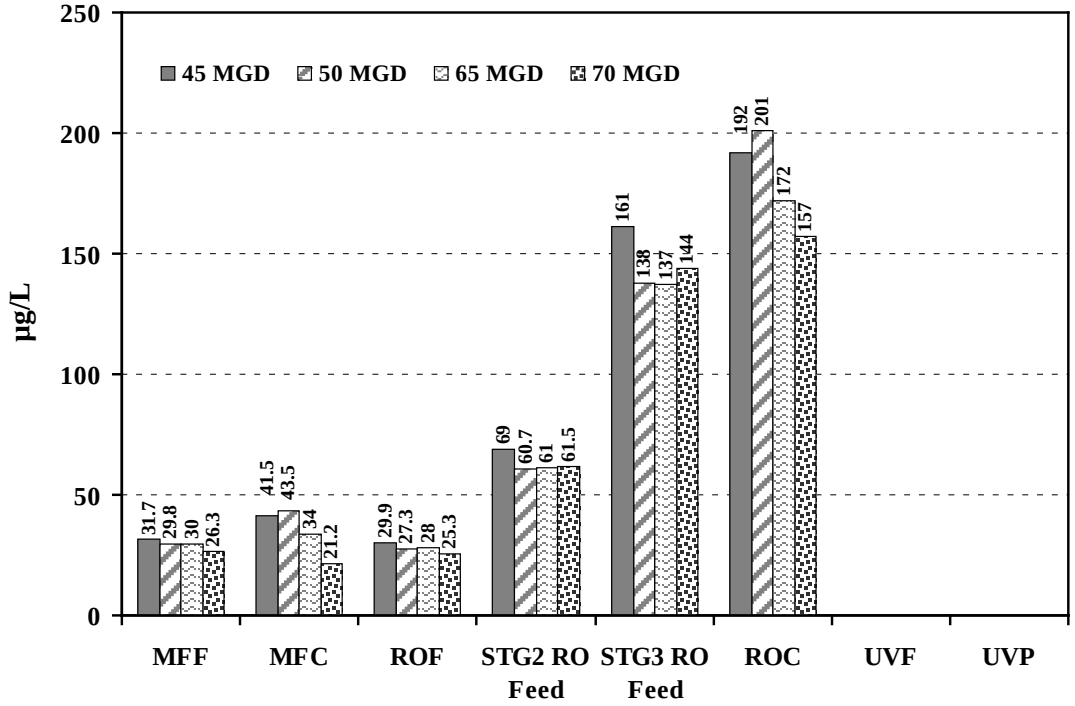

Figure 3.11. Plot of barium (mg/L) content.

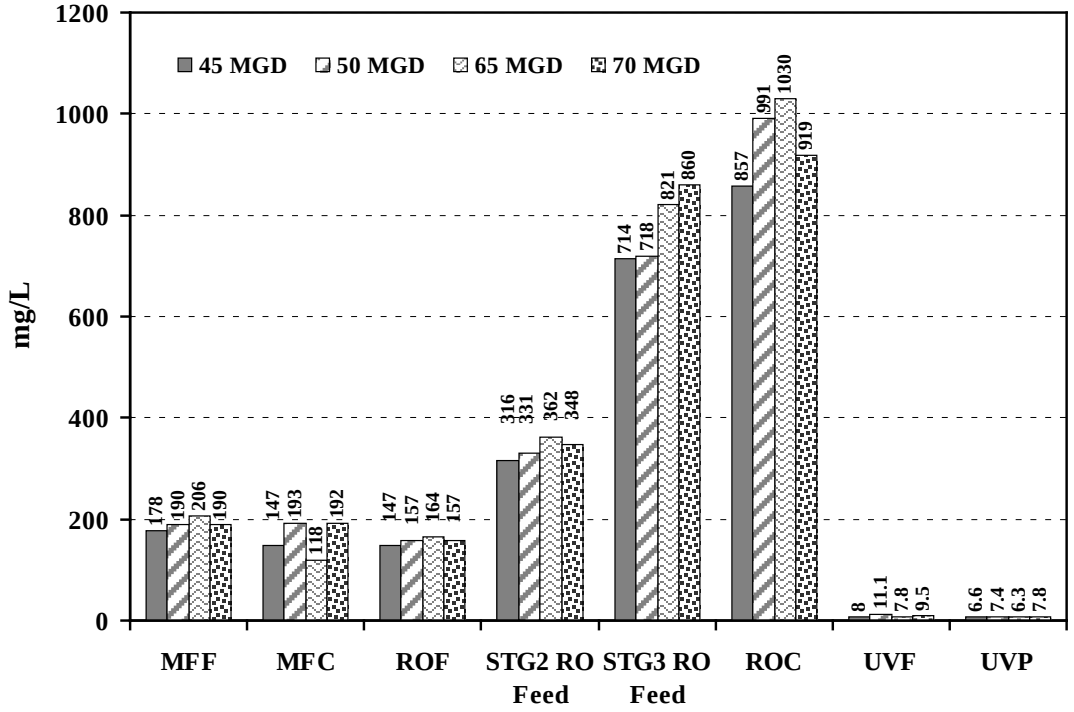

Figure 3.12. Plot of bicarbonate as HCO3Ca (mg/L) content.

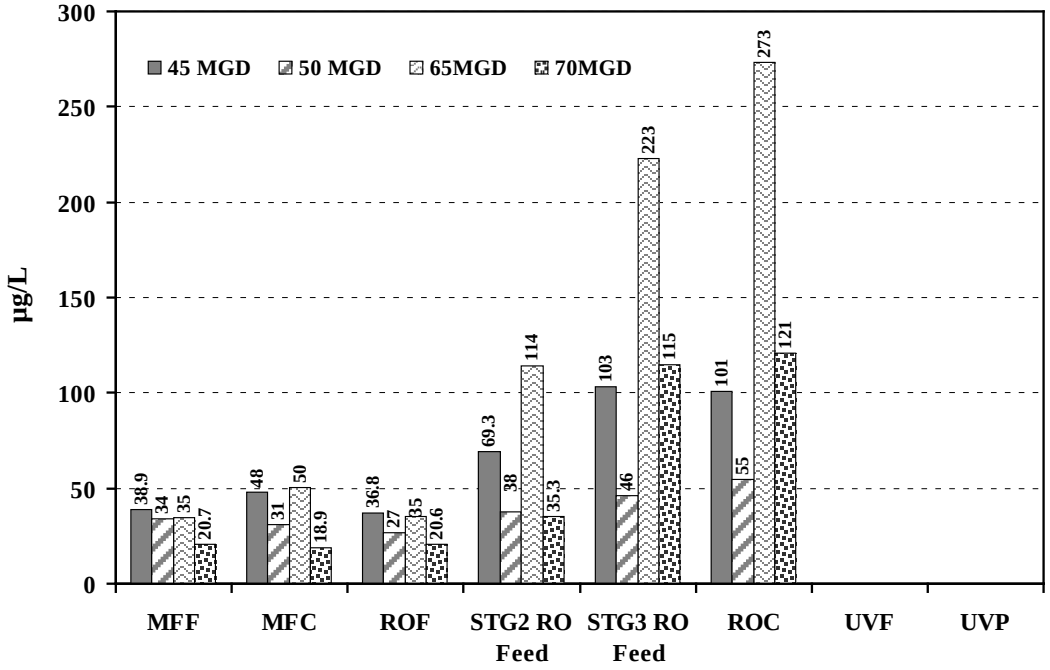

Figure 3.13. Plot of manganese (µg/L) content.

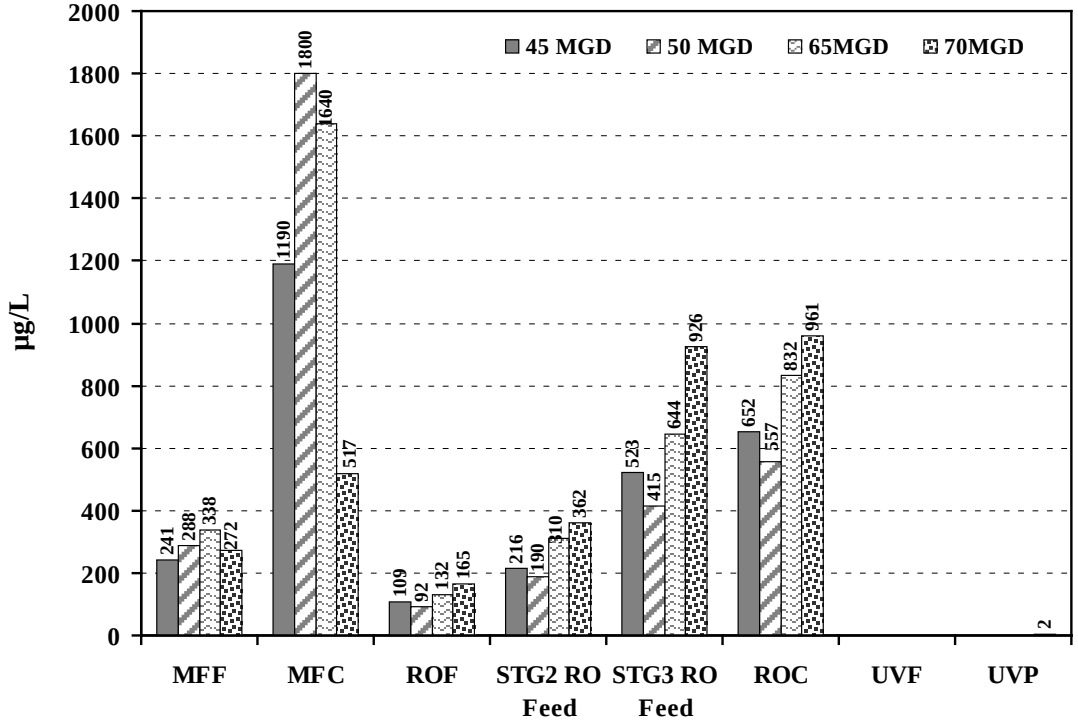

Figure 3.14. Plot of iron (µg/L) content.

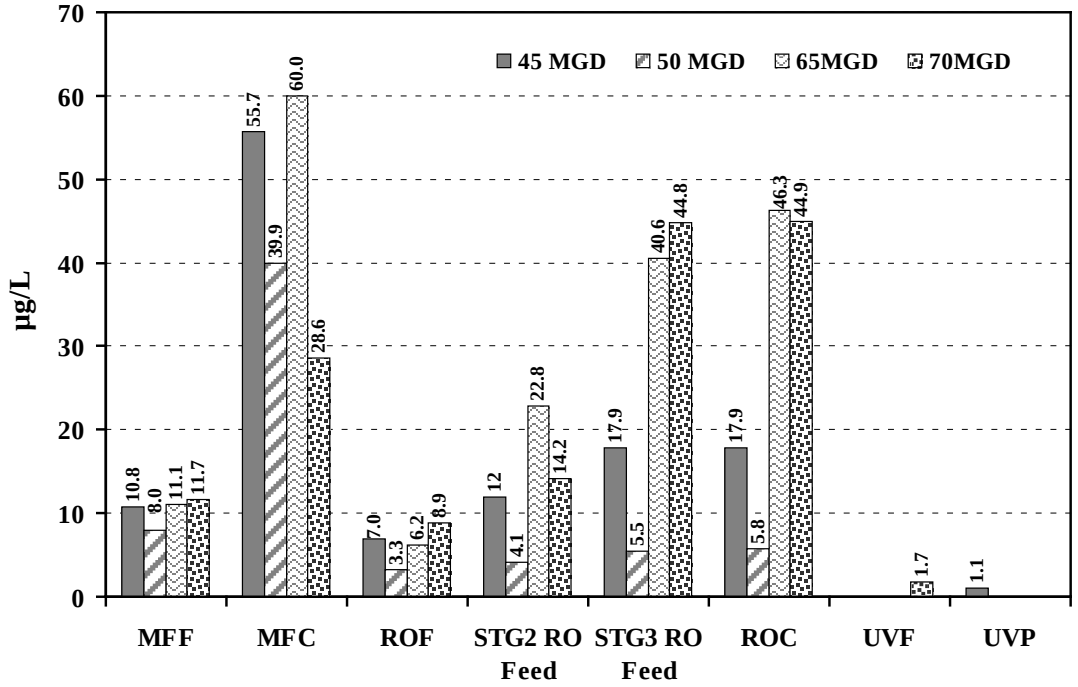

Figure 3.15. Plot of aluminum (µg/L) content.

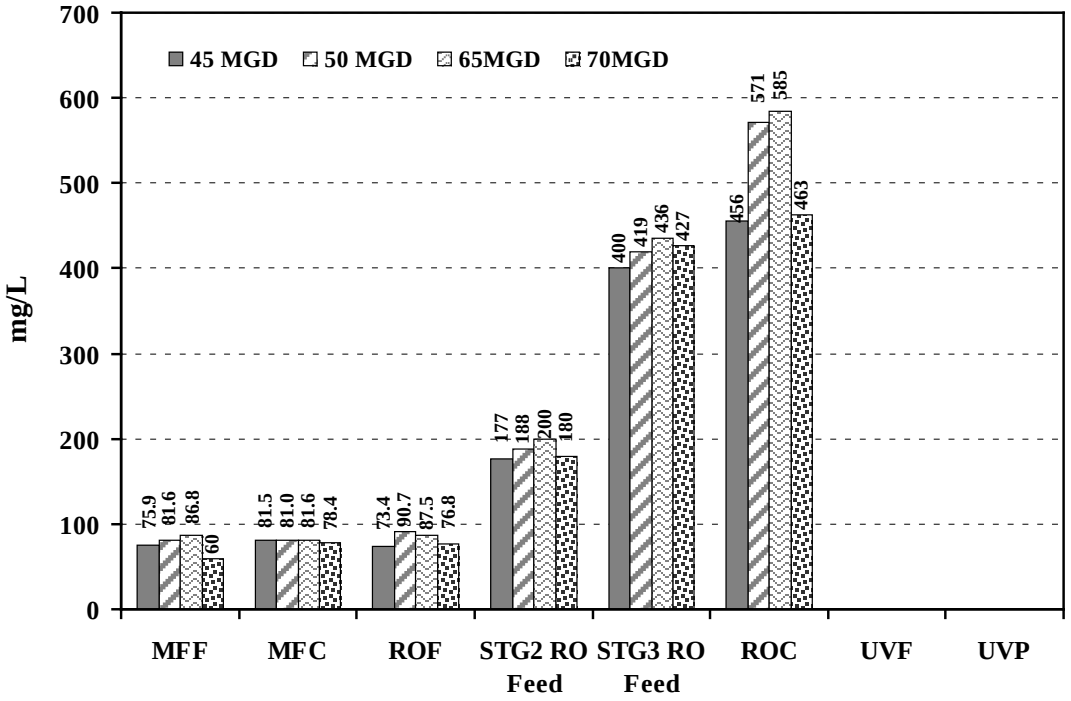

Figure 3.16. Plot of calcium (mg/L) content.

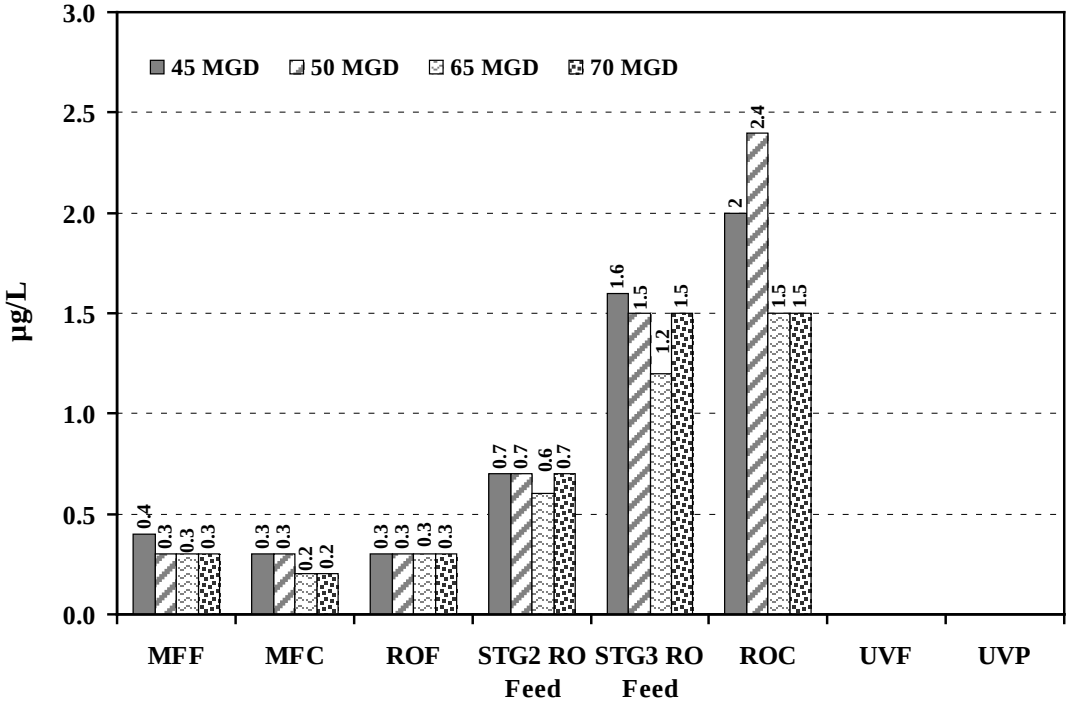

Figure 3.17. Plot of mercury (mg/L) content.

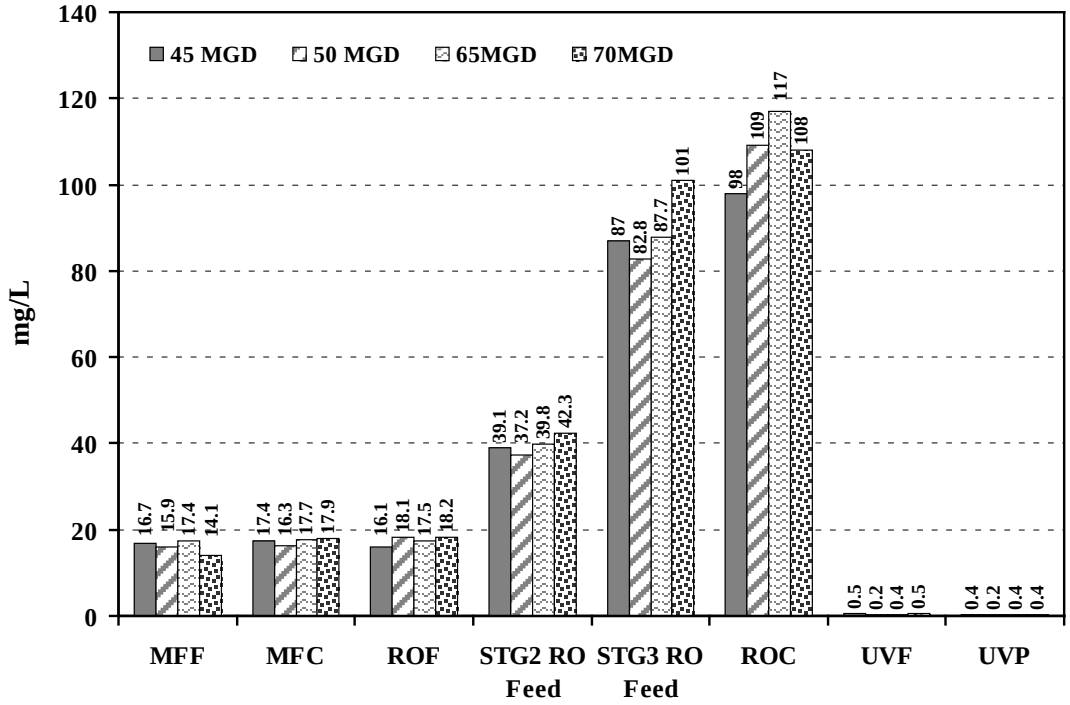

Figure 3.18. Plot of potassium (mg/L) content.

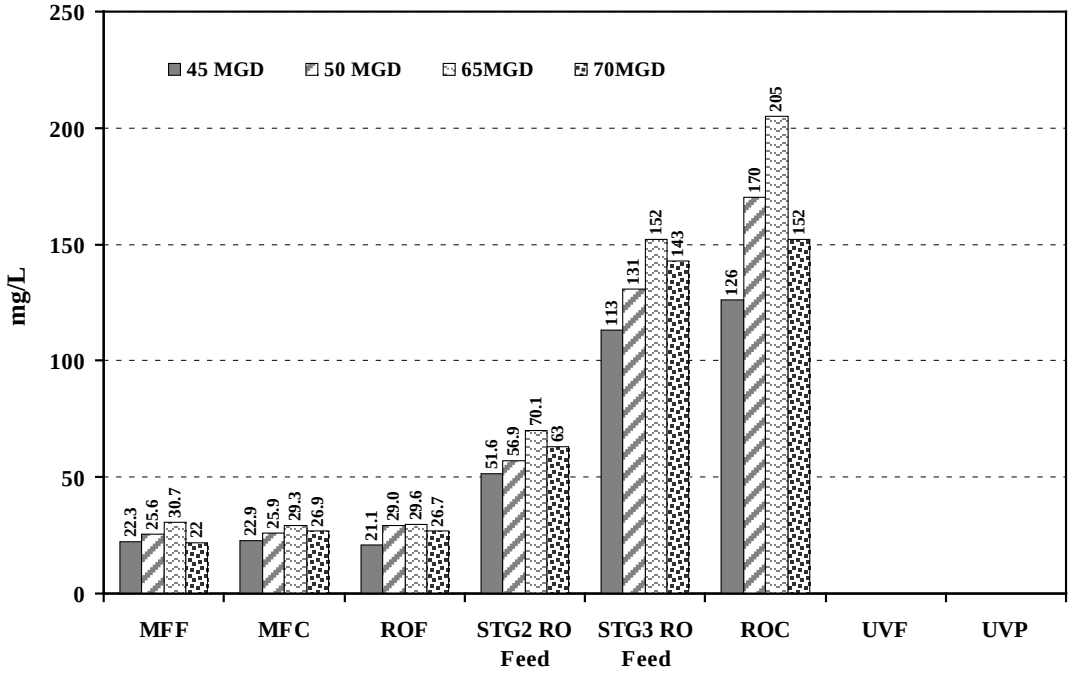

Figure 3.19. Plot of magnesium (mg/L) content.

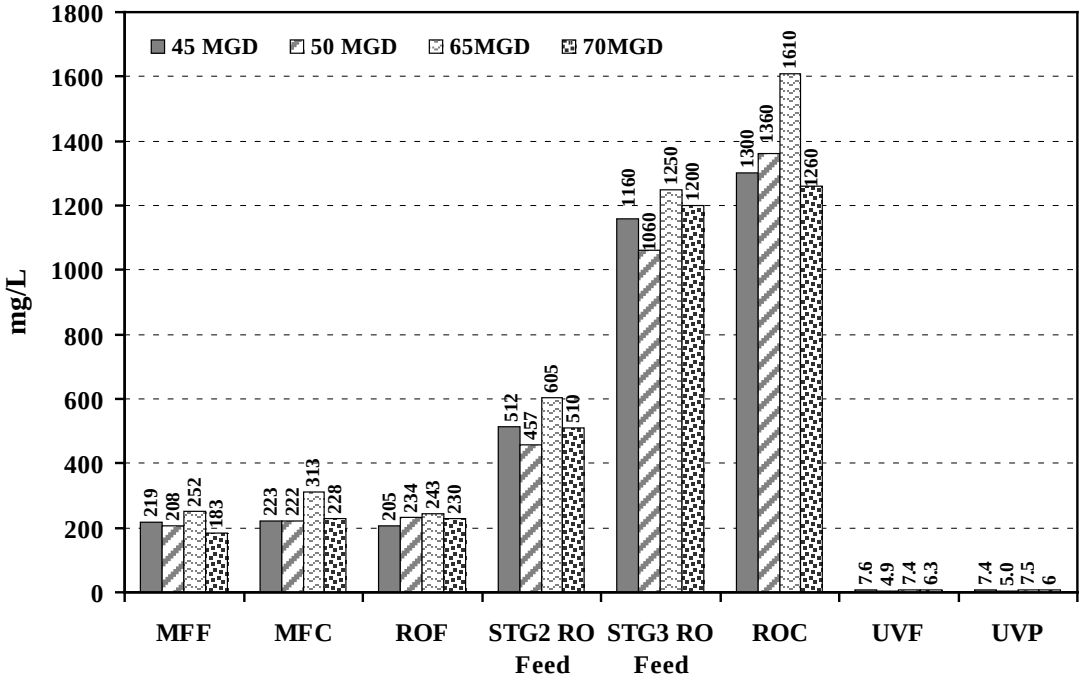

Figure 3.20. Plot of sodium (mg/L) content.

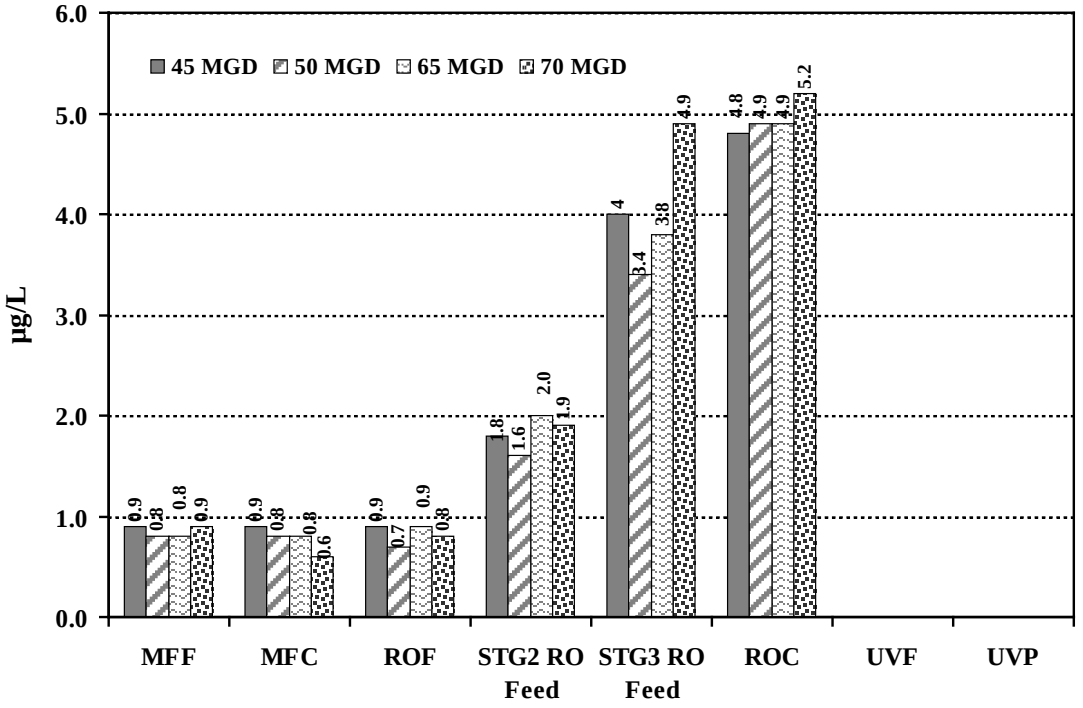

Figure 3.21. Plot of antimony (µg/L) content.

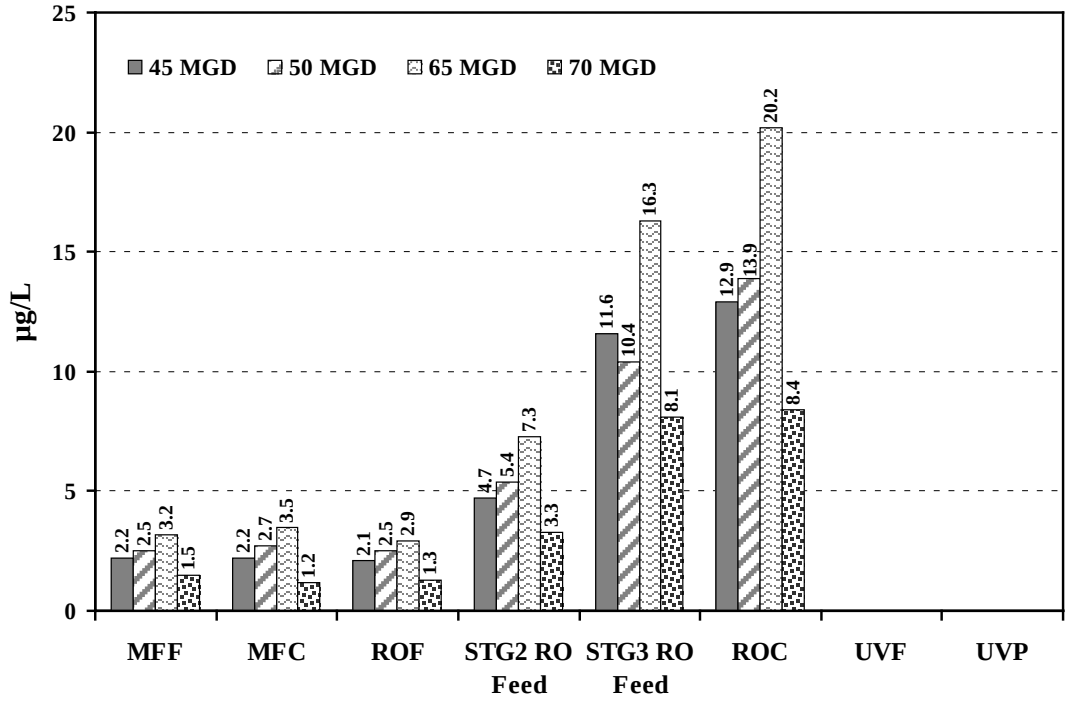

Figure 3.22. Plot of selenium (µg/L) content.

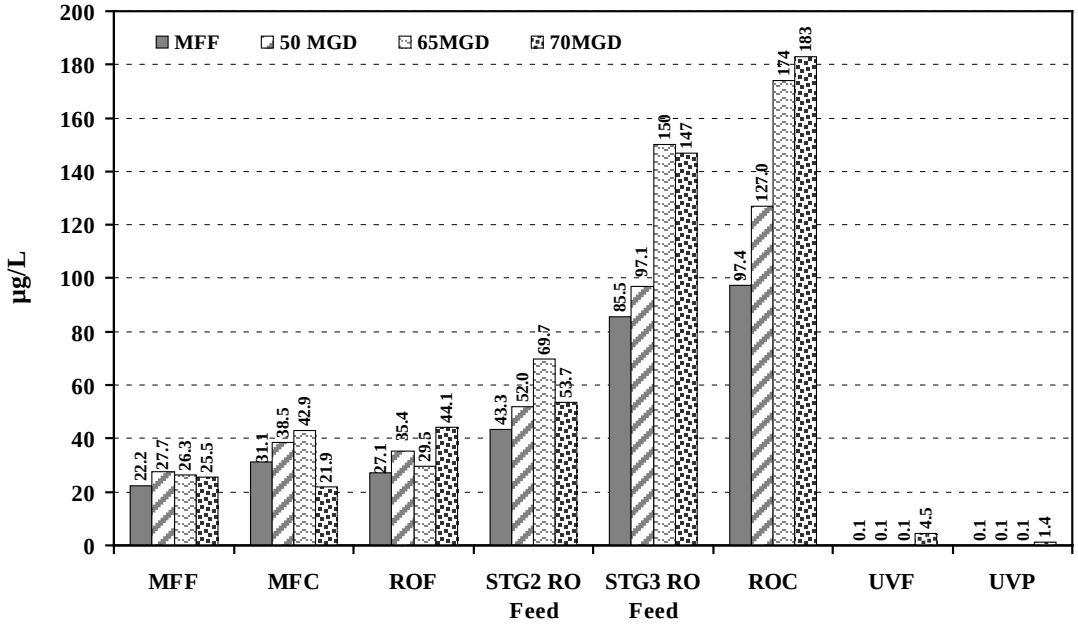

Figure 3.23. Plot of zinc (µg/L) content.

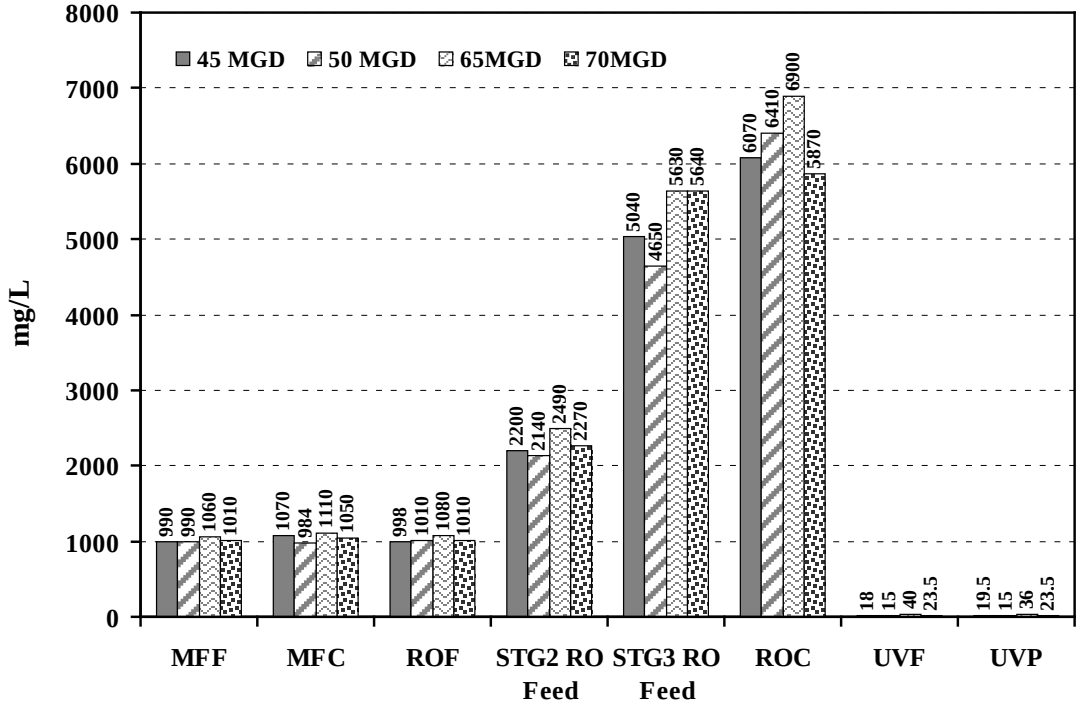

Figure 3.24. Plot of total dissolved solids (mg/L) content.

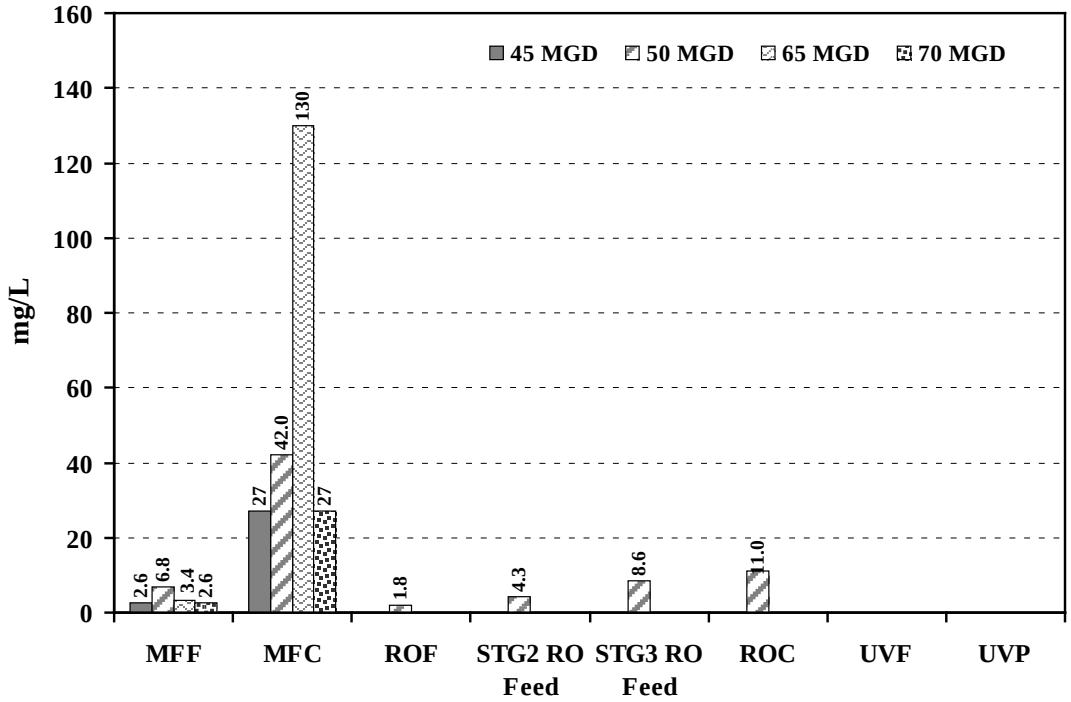

Figure 3.25. Plot of suspended solids (mg/L) content.

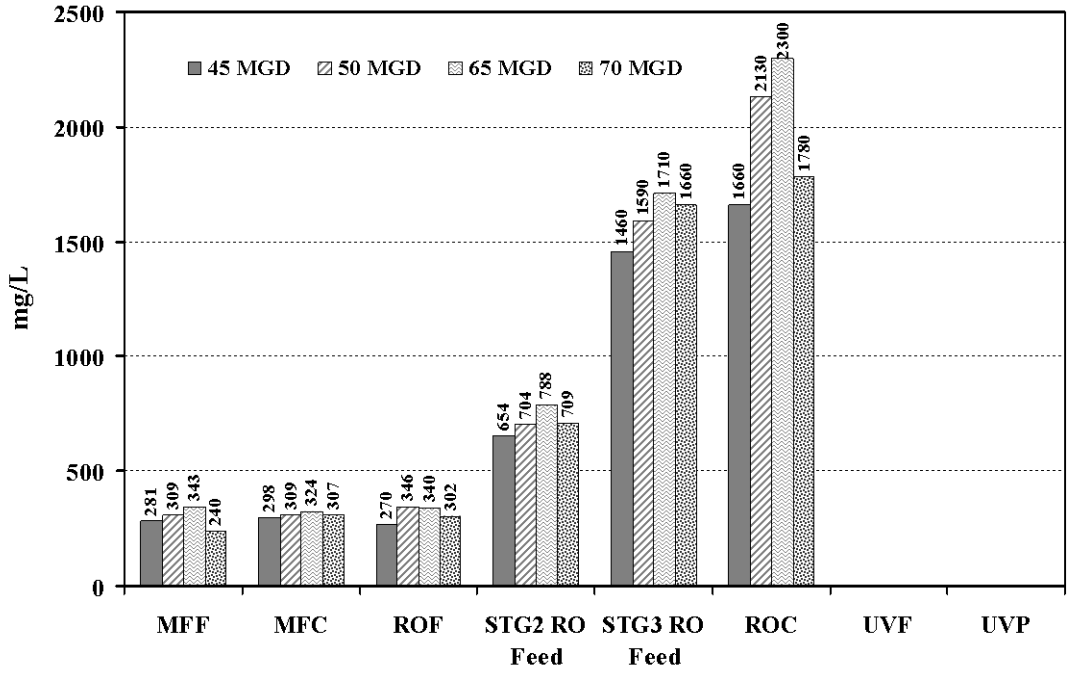

Figure 3.26. Plot of total hardness (mg/L) content.

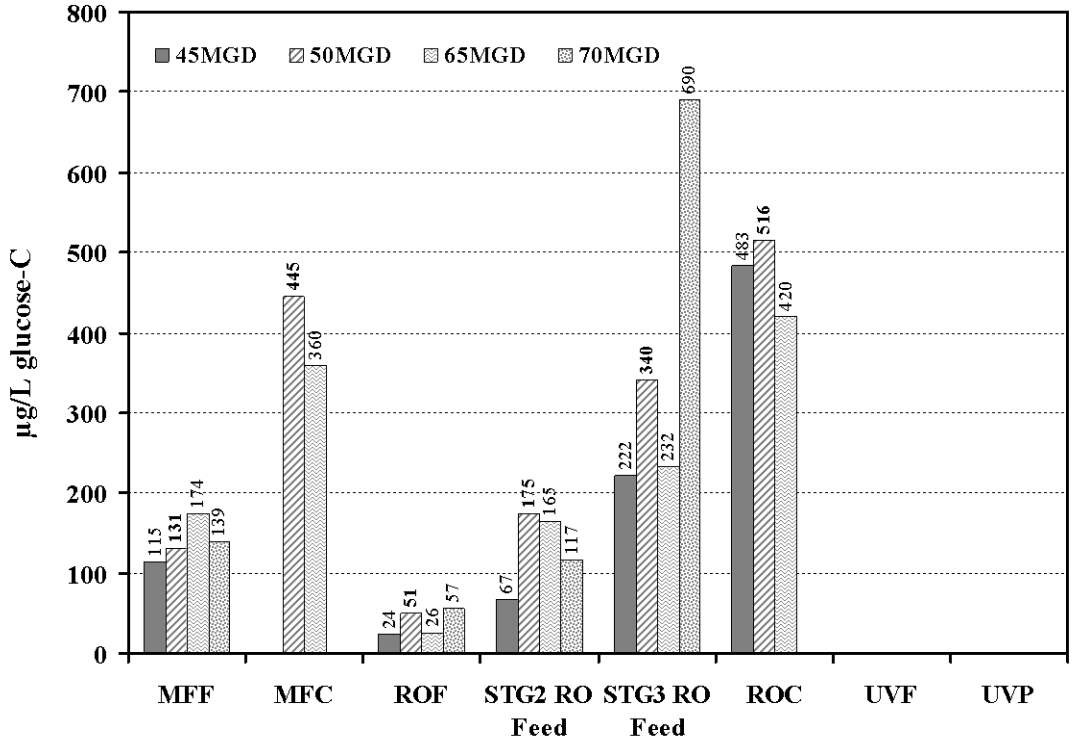

Figure 3.27. Assimilable organic carbon (AOC) as glucose-C (µg/L).

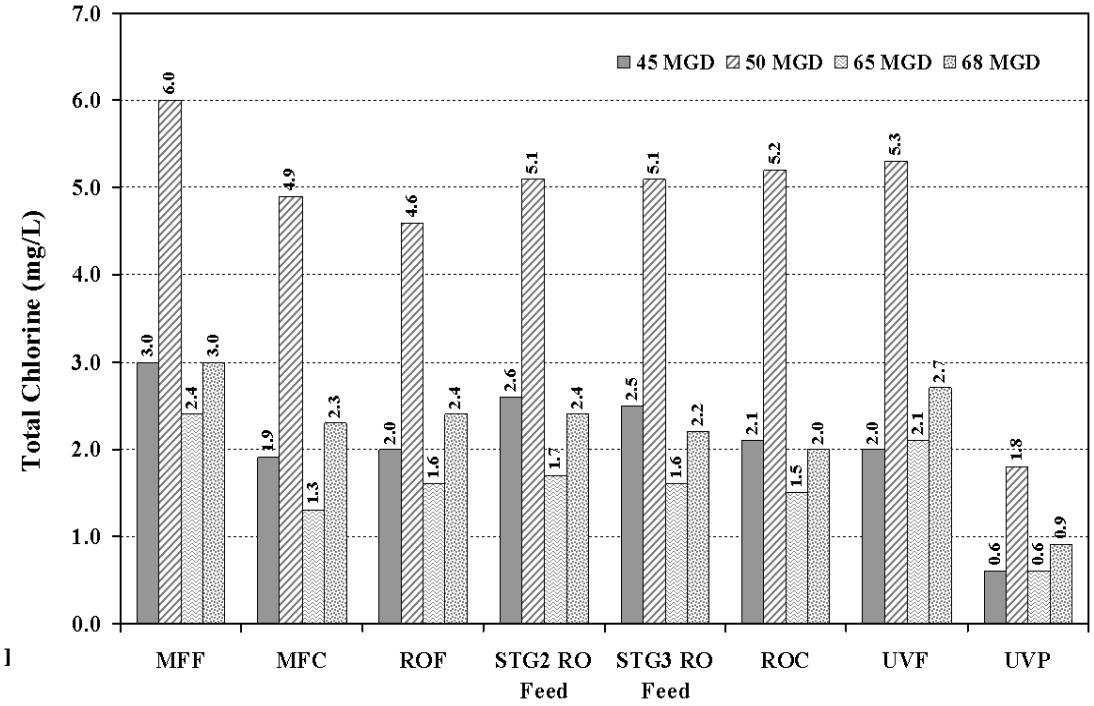

Figure 3.28. Total residential chlorine (mg/L) determined by HACH DPD colorimetric method.

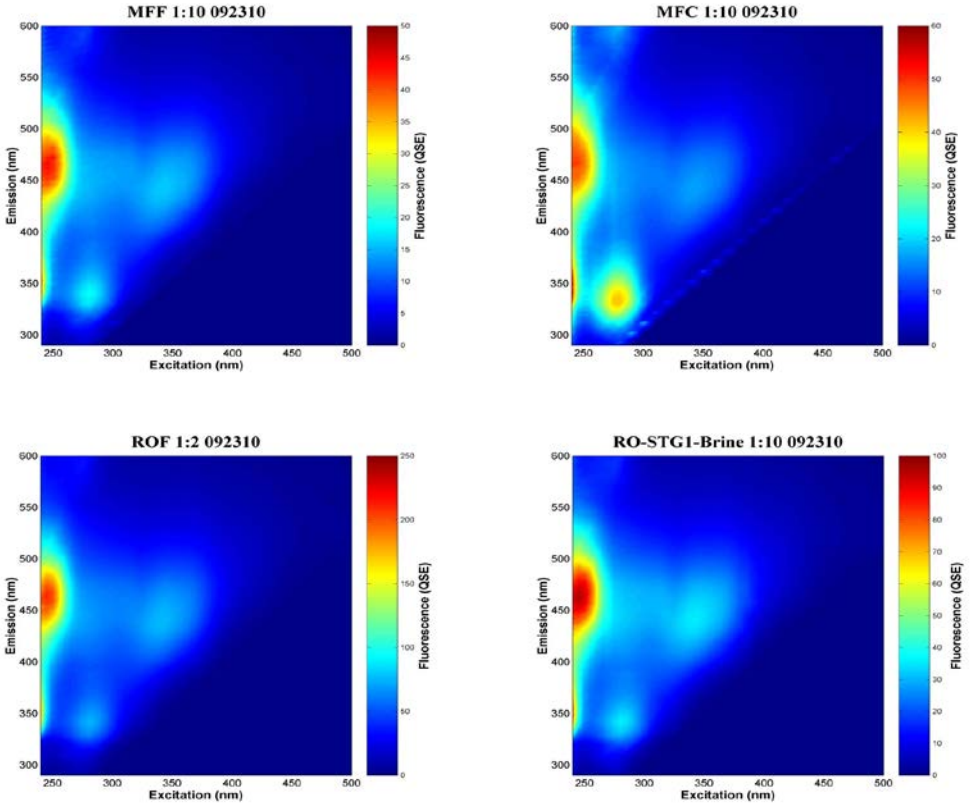

Figure 3.29. EEM fluorescence spectra from AWPF Survey No. 4, September 23, 2010, daytime flow (70 mgd).

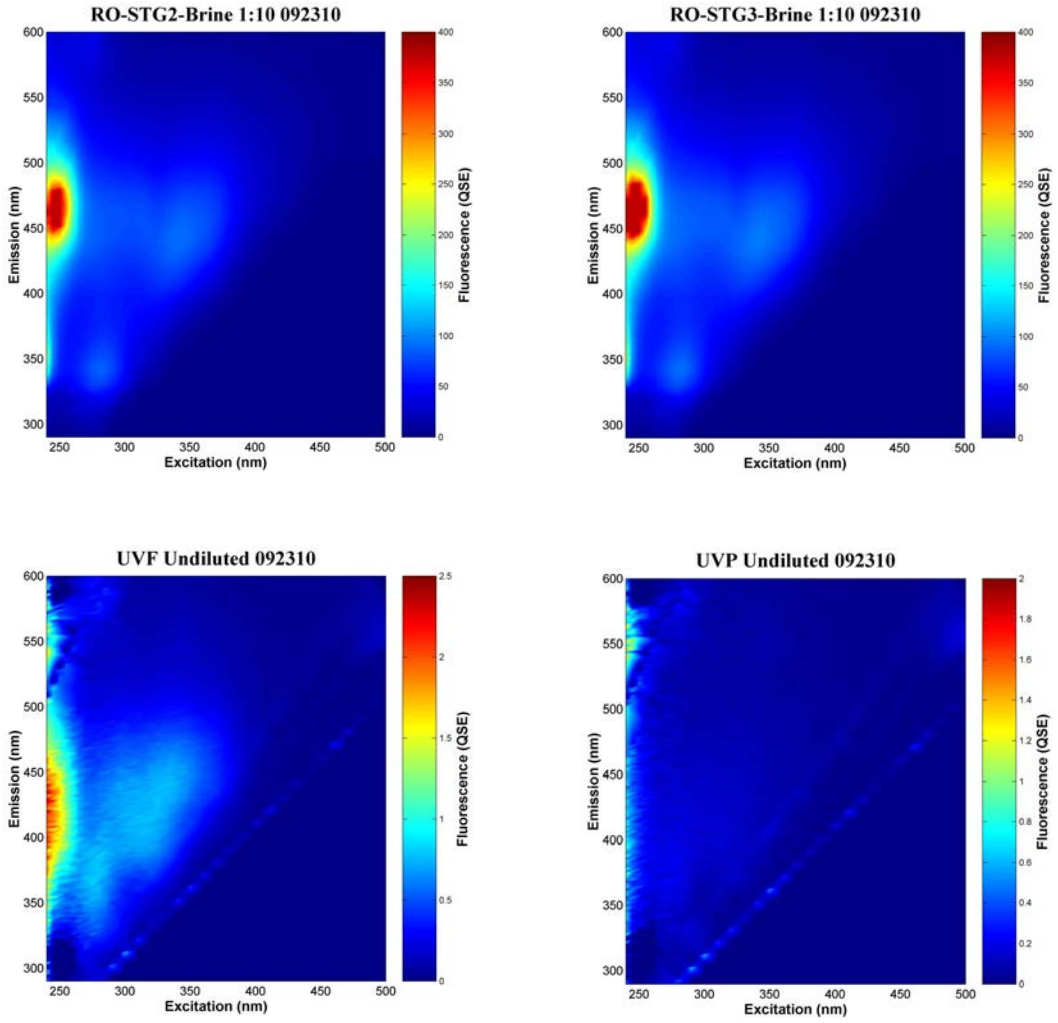

Figure 3.30. EEM fluorescence spectra from AWPF Survey No. 4, September 23, 2010, daytime flow (70 mgd).

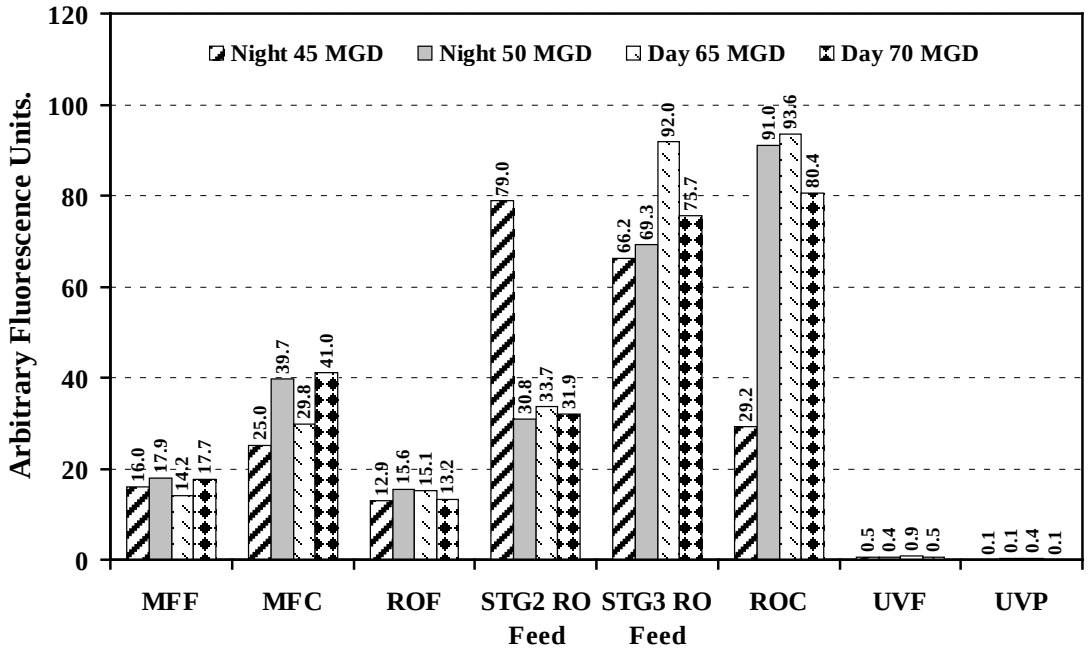

Figure 3.31. Plots of normalized fluorescence intensity of protein in MFF, MFC, ROF, RO Stage 2 Feed, Stage 3 RO Feed, ROC, UVF, and UVP.

Note: The UVF and UVP were analyzed undiluted. All other samples were diluted 10 times.

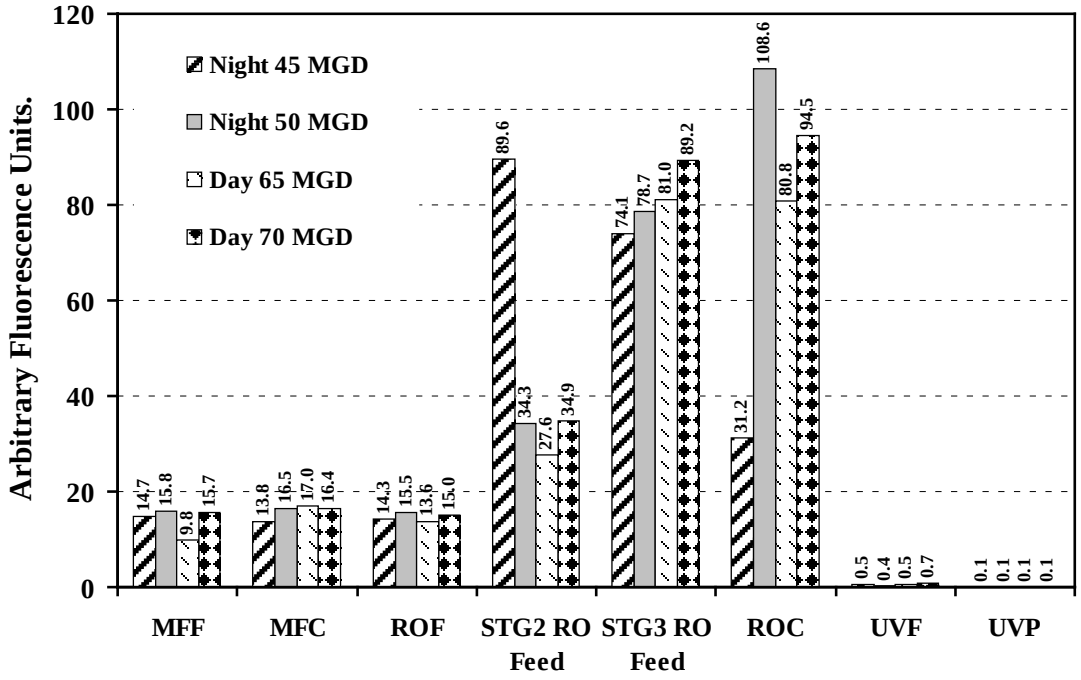

Figure 3.32. Plots of normalized fluorescence intensity of humic acid-like matter in MFF, MFC, ROF, Stage 2 RO Feed, Stage 3 RO Feed, ROC, UVF, and UVP.

Note: The UVF and UVP were analyzed undiluted. All other samples were diluted 10 times.

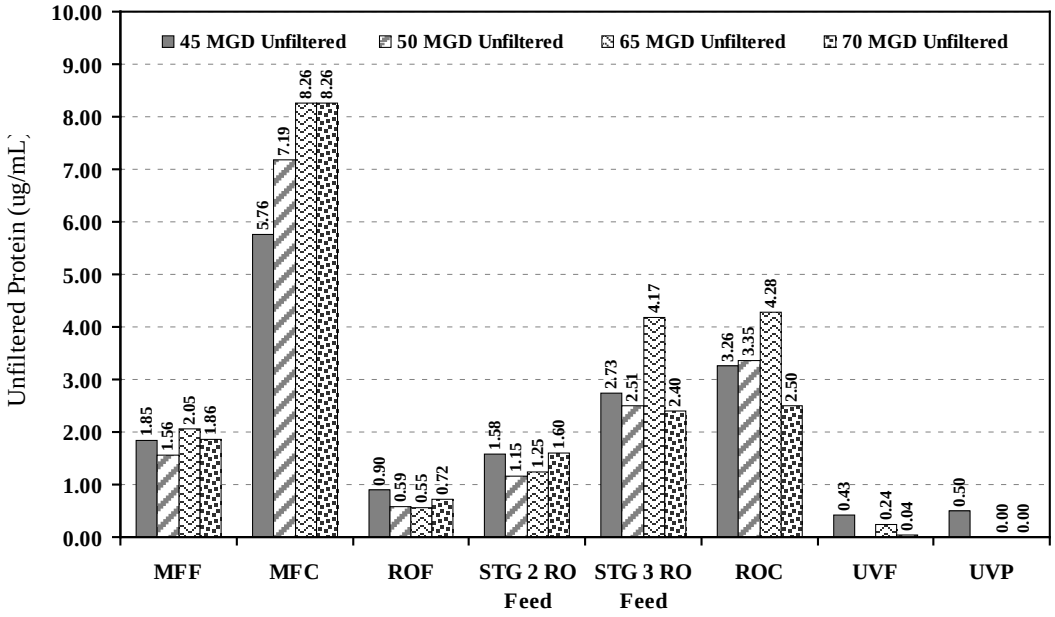

Figure 3.33. Total protein (µg/mL) in unfiltered water samples.

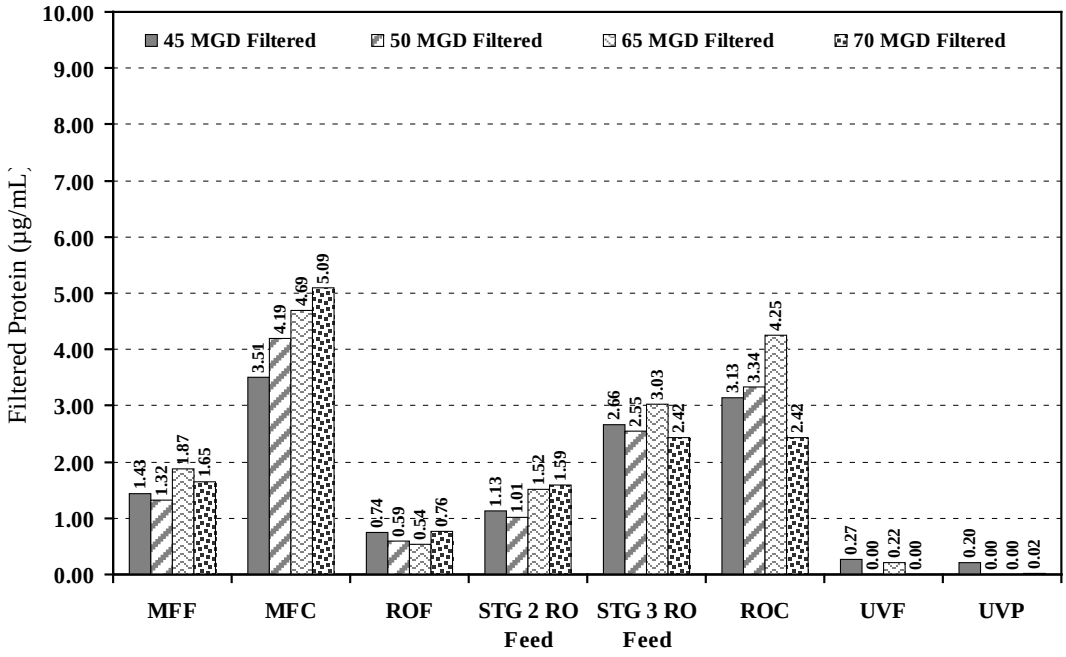

Figure 3.34. Total protein (µg/mL) in 0.22 µm-filtered water sample.

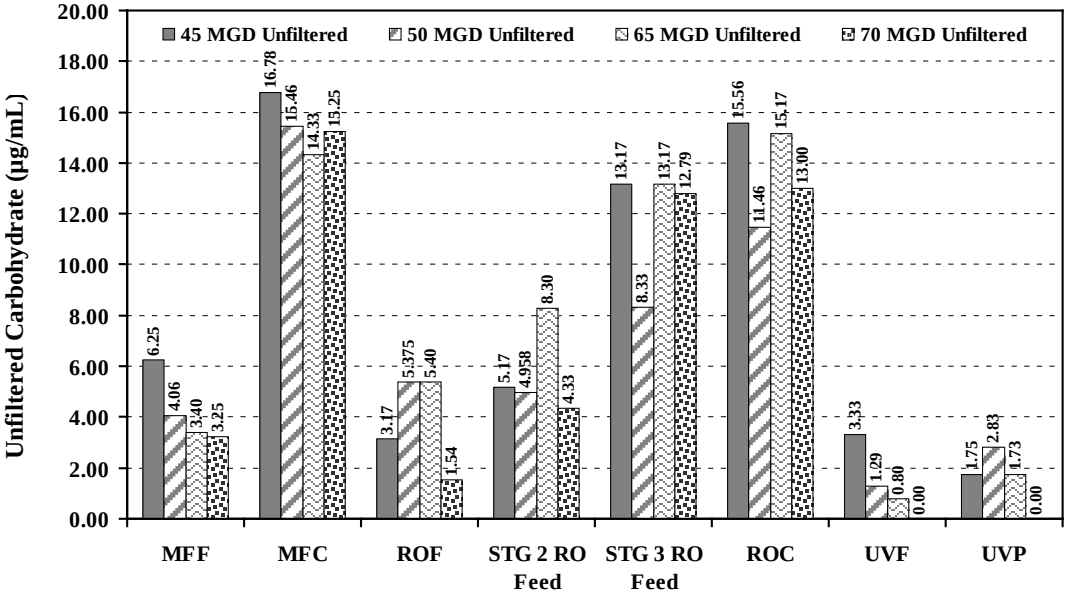

Figure 3.35. Total carbohydrate (µg/mL) in unfiltered water samples.

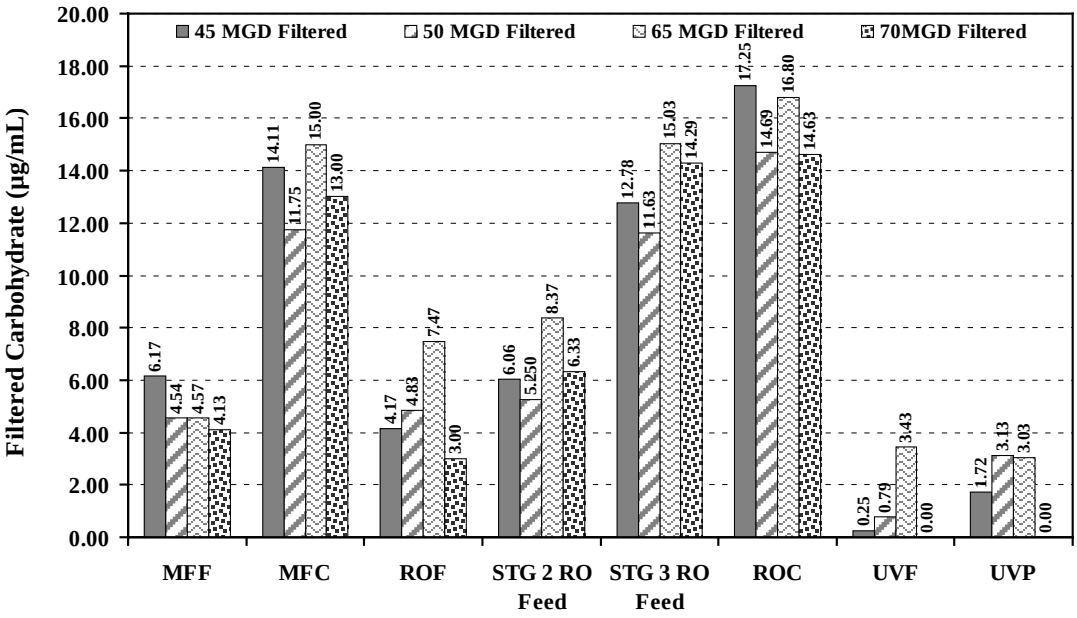

Figure 3.36. Total carbohydrate (µg/mL) in 0.22 µm-filtered water sample.

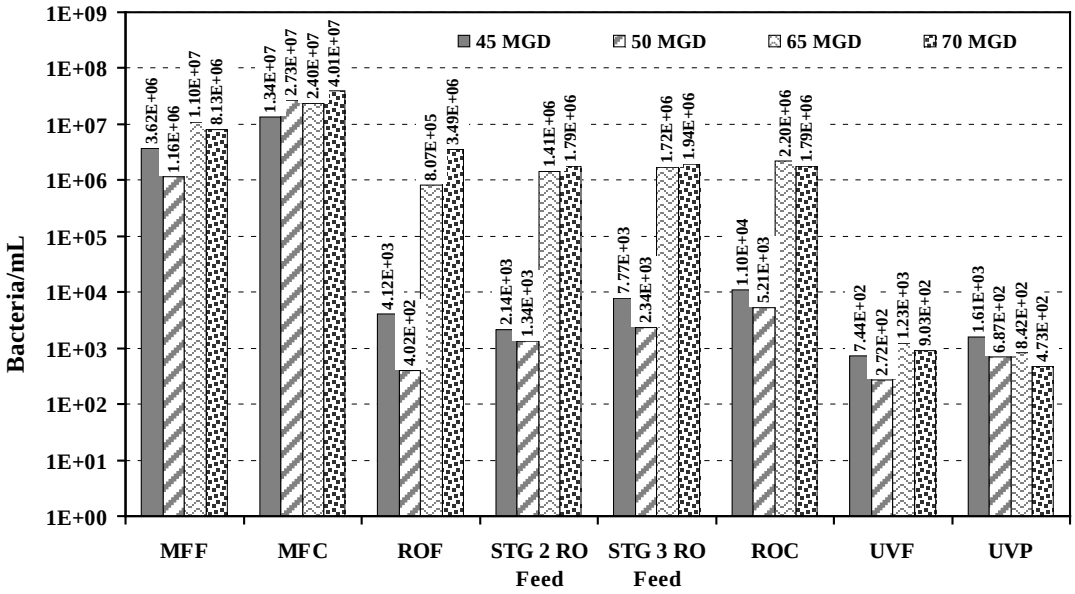

Figure 3.37. Total bacterial counts/DAPI epifluorescence counts (bacterial cells/mL).

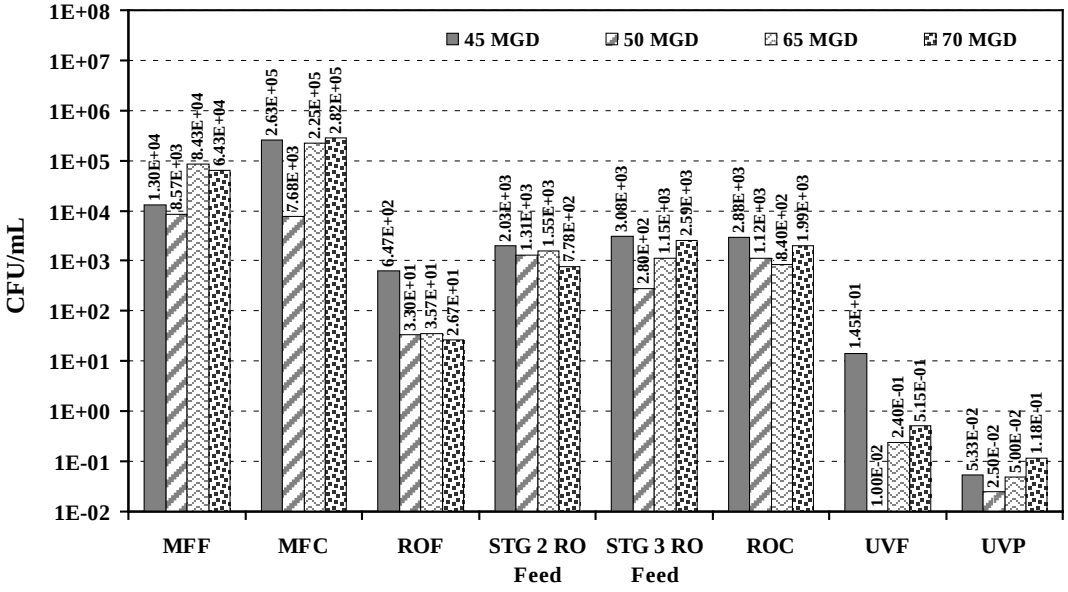

Figure 3.38. Heterotrophic plate counts/viable bacterial counts (cells/mL).

3.4 Summary and Conclusions

General water quality data associated with the secondary-treated wastewater effluent (Q1) were tabulated over a 5-year period from 2008 to 2010. In early November 2009, OCSD switched from CBOD treatment of the wastewater to an NDN mode of treatment that took approximately 2 months to stabilize. The most significant changes in the secondary effluent were a reduction in the concentration of ammonia-N, organic-N, and total Kjeldahl-N, and an increase in the nitrate-N. The concentration of the total alkalinity also dropped noticeably in the Q1 wastewater effluent upon switching to the NDN treatment process. In 2008 and 2009, the average total alkalinity was ~290 mg/L under the CBOD process and following the transition to the NDN method of treatment, the average dropped to ~180 mg/L.

In 2010, two nighttime and two daytime microbial and water quality surveys of the AWPF were conducted. Feed and product water from each of the three unit processes, MF, RO, and UV/H_2O_2 AOP, were sampled and analyzed for general minerals and total and viable bacteria.

Cations and anions readily passed through the MF membranes. Only iron and aluminum were noticeably concentrated in the MF backwash (MFC). At times there were significantly high bacterial loads measured in the MFE, which made it appear that the MF was not effective in removing bacteria from the secondary effluent (MFF). However, these high bacterial counts were attributed to the presence of the 2 million gallon MFE break tank that serves as a source of microorganisms that are periodically released into the effluent and pass downstream to the RO process.

Generally speaking, the RO process was effective at removing minerals from the MF effluent feedwater with a two-fold increase in concentration of the minerals in the Stage 1 reject, four-fold concentration, relative to the feedwater, in the Stage 2 reject, and a five-to-six-fold increase in minerals concentration in the RO concentrate (ROC).

Significant quantities of total and viable bacteria were detected in the RO permeate. However, these were believed to be related to the release of microbial cells growing in biofilms on the backside of RO membranes and on the surface of transfer pipes throughout the RO facility as bacteria cannot pass through the RO membrane. Removal of total and viable bacteria across the UV/H_2O_2 AOP was inconsistent with total bacterial counts actually increasing across the UV/AOP on two occasions. These increases in total bacteria were attributed to sloughing of bacterial cells from the walls of transfer pipes, whereas the presence of viable bacteria in the UV/AOP product water was attributed to microbial DNA repair mechanisms and hydrogen peroxide degrading catalase activity that enable the bacteria to survive the UV and AOP.

Little change in the general minerals occurred across the UV/H_2O_2 AOP. The total organic carbon concentration was unaffected. However, UV fluorescence associated with protein and humic acid-like substances was attenuated across the UV/AOP. The total chlorine was the most severely affected constituent, typically dropping 65 to 75% and 90% at the most upon exposure to the UV/H_2O_2 AOP. Assimilable organic carbon (AOC) was not measure in the UVF and UVP source waters as a suitable protocol for neutralizing the hydrogen peroxide was not available at the time the surveys were conducted.

Chapter 4

Microfiltration Fouling: Mechanism and Potential Mitigation Strategies

4.1 Background

4.1.1 Microfiltration at the Advanced Water Purification Facility

The AWPF microfiltration (MF) system is designed to produce 86 mgd of MF filtrate as feed to the RO system at a design flux of 20 gallons per square foot per day (gfd). It consists of 26 Siemens/Memcor CMF-S units (cells), that are grouped into three trains of eight cells each and a fourth train of two cells. Each cell can hold up to 684 0.2 µm polypropylene hollow fiber membrane modules and operates at a recovery rate between 88% and 90%. The MF feedwater receives upstream chloramination of 3 to 5 mg/L through the addition of 12.5% sodium hypochlorite to the secondary-treated wastewater effluent that contains sufficient ammonia to form chloramines. The MF system produces a low turbidity (<0.1 NTU) product water with a silt density index (SDI) below 3. The backwash from the system is routed back to OCSD Plant No. 1 in Fountain Valley.

The feedwater for the facility is activated sludge effluent (ASE), which possesses significant particulate loading and biological activity. These factors contribute to rapid fouling (i.e., cake formation) of the MF membranes with consequent loss of performance. MF fouling is associated with increased hydrodynamic resistance (i.e., flux loss) and necessitates frequent chemical cleaning of the MF membranes, thereby increasing operational costs. Better understanding of MF fouling and dynamics is needed to improve the efficiency of the MF/RO process of the AWPF and other reclamation facilities.

4.1.2 Published Mechanisms of MF Fouling

Membrane fouling is characterized by a reduction of permeate flux through the MF membrane matrix as a result of increased flow resistance that is due to pore blocking, pore plugging, concentration polarization, and cake formation (Bai and Leow, 2002; Iritani, 2013). The extent of fouling on flux decline depends on membrane pore size, solute loading and distribution, membrane polymer material, source water quality, and operating conditions. Fouling causes a reduction in permeate flux; the long-term effects of fouling may be irreversible, resulting in the reduction of membrane performance and the reduction of membrane lifetime. To reduce operational and maintenance costs, membrane facilities strive to keep membrane fouling to a minimum. Various strategies have been developed to reduce costs and membrane life span, such as the development of new membrane polymers, improved module engineering, modification of feed-flow pattern, improved backwashing techniques, and application of pretreatments, such as flocculation or coagulation (Brink et al., 1993; Leow and Bai, 2001; Wang et. al., 2002).

Classical models of MF cake fouling have suggested that the accumulation of particles close to the membrane surface results in the covering of membrane pores and membrane flux reduction. Previous studies (Safarik and Phipps, 2005; Huang and Morrisey, 1998) demonstrated that there are two mechanisms of MF fouling: (1) the classical MF cake

formation, which may result in a minor reduction of hydraulic conductivity, and (2) deposition of microbial detritus (proteins, carbohydrates, phospholipids, and nanoparticulates (e.g., liposomes), which are responsible for the majority of the observed fouling. The cake layer (bacterial and large particulate layer) is easily removed with regular backwashing and air sparging. Microbial residues, such as colloidal organic matter and nanoparticulates (<0.2 µm), are more difficult to remove with regular backwashing. It was shown that the presence of organic materials adsorbed at the membrane surface was responsible for a large part of the observed flux reduction. This form of fouling occurs simultaneously with cake formation but also can occur without application of transmembrane pressure by the process of diffusion. This adsorption phenomenon may eventually become irreversible.

MF fouling may be mitigated by removal of the cake in situ with transmembrane pressure pulsing or backwashing. Backwashing is an effective way of reducing fouling in membranes, improving the overall filtration rate and extending the cleaning interval (Zhao, 2002; Sondhi and Bhave, 2001). Backwashing involves a temporary reverse at the flow of the MF permeate and introduction of a low pressure air scour. The process forces the MF foulant from the membrane surface, which is then flushed away by the retentate flow. MF backwashing works well in removing the buildup of MF cake, which is composed of bacteria and larger particles at the membrane surface but is less effective in dislodging foulants from within the membrane matrix. In spite of regular intervals of backwashing, membrane fouling continues to slowly progress, resulting in a slow increase in transmembrane pressure (TMP).

4.1.3 "Role of Microfiltration Cake Layer Composition and Stability in Desalination Efficiency"—Previous OCWD Studies

At the onset of the study, it was presumed that the fouling components of MF cakes were comprised mostly of bacteria and large particulates (>0.2 µm), and this would be the major contributor to decreased MF performance. Cake structure was proposed to be studied by using mass by weight measurements and cake stability by light scattering (optical density) and by particle counting and sizing using a Coulter Multisizer. In addition, protein assay, carbohydrate assay, epifluorescence microscopy, and light microscopy were used to study the nature of microbial material accumulating on the membrane surface during cake formation and flux reduction. Through experimentation it was discovered that MF fouling was principally influenced by factors other than microparticulates. A hypothesis was formed that material smaller than bacteria were primarily responsible for the flux decline observed during MF cake formation through treatment of secondary activated sludge effluent (ASE). To test the theory, microparticulate solids larger than the membrane mean occlusion size were removed from the feedwater by passage through a 0.2 µm filter. To confirm the filtered ASE (FASE) was free of these particles equal volumes of ASE and FASE feedwaters were filtered onto black 25 mm diameter, 0.2 µm membranes, stained with 4',6-diamido-2-phenylindole (DAPI) and examined by fluorescence microscopy to confirm that FASE was bacteria free. Filtering ASE through the 0.2 µm filter removed bacteria and presumably particles greater than 0.2 µm. The two feedwaters (ASE with microparticulates and FASE without microparticulates) generated similar permeate flux decay curves, suggesting that flux decay kinetics were not principally influenced by the microparticulate fraction of ASE. The permeate flux difference between the ASE and FASE curves were attributed to the bacteria and other larger particulates present in ASE. This demonstrated that bacterial or particulate fouling (MF cake) is responsible for a far smaller portion of the overall fouling than was previously thought (Safarik and Phipps, 2005; Safarik and Phipps, 2013).

ASE and FASE foulants deposited on polypropylene (PP) membranes also were examined by atomic force microscopy (AFM). AFM images showed fouling on both ASE and FASE membranes. The ASE fouling appeared to be thick and multilayered, and composed of bacteria and other particulates. FASE-fouled membranes did not have bacteria or particles but still were fouled with what appeared to be an amorphous material that covered the membrane pores. AFM showed pores of the PP membrane were blocked. The dissolved foulants or nanoparticulates (<0.2 µm) seemed to enter the membrane matrix and block the pores from within, indicating pore clogging occurs along with pore blocking. The AFM results supported the observation that the most significant amount of MF fouling is not due to bacteria and other microparticulates but to colloidal organic matter and nanoparticulates.

To further characterize MF fouling, ATR-FTIR spectrometry was employed to analyze the ASE and FASE fouling layers left on the membrane surface. Vibrational bands designating protein and carbohydrate foulants were represented in both ASE and FASE spectra, providing additional evidence that the primary MF foulant may be the result of mostly biological detritus as opposed to whole bacteria and other particles larger than 0.2 µm.

To further characterize the OCWD FASE cake, protein and carbohydrate analyses of the bacterial-free (FASE) feedwater, ASE, FASE permeate, and fouling layer were performed. A significant concentration of carbohydrates (64%) remained following removal of bacteria from ASE and FASE. Carbohydrates appeared to be strongly deposited on the PP membrane, representing approximately 71% of the cellular carbohydrate in the feed.

An experiment was performed to test adsorption and removal of a pure protein from the PP membrane surface by exposure of an MF membrane to 0.01 wt% gelatin protein. Upon protein introduction into the system, permeate flux dropped within seconds of exposure. Washing the protein-fouled MF membrane with 5 mg/L Proteinase K reversed the fouling and restored the MF flux. However, when Proteinase K was used to remove protein from ASE and FASE fouled membranes, the results were not as positive as with gelatin alone, indicating other factors also are involved in the fouling process besides simply protein deposition.

Cell debris may contain fragments of cell membranes that anneal to form nanoparticulates (liposomes). The material fragments are largely made up of phospholipids. Of the lipids, the phopholipid fatty acids (PLFAs) represent the major component of cell membranes. PLFA, when exposed to hydrophobic membrane surfaces, such as PP, may attach and actually intercalate into the membrane matrix. An analysis to determine the presence of PLFA was conducted at various stages of the MF process.

ASE-fouled membrane had a 60% higher concentration of PLFAs than FASE fouled membranes. The ASE foulant is comprised of the total PLFAs (microbial plus nanoparticulate). The FASE foulant contains phospholipids that were present in solution (colloidal organic matter and nanoparticulates), because all microparticualtes (bacteria) were removed by filtration using a 0.2 µm filter. This supports the hypothesis that PLFAs are deposited on the membrane surface during microfiltration and affecting membrane performance.

The adhesion to the PP, movement through the membrane matrix, and effect on permeate flux by a pure phospholipid was investigated using phosphatidylethanolamine, dipalmitoyl-sulforhod-amine B (PTEDSB). A PP membrane was exposed to 1.0 µg/mL of PTEDSB and permeate flux loss was measured as a function of time. As soon as the PTEDSB was added to

the system, permeate flux dropped and continued to drop as more PTEDSB was drawn through the membrane.

Lipase was investigated for its potential effect on flux recovery. PP membranes were fouled with FASE and then treated with lipase (100 µg/mL, pH 7.7 for 1 h). Lipase did not restore flux in these fouled membranes. It is unclear why lipase failed to affect MF water flux as lipids are an integral part of the MF fouling; however, it is known that lipases require an oil/water interface for maximum activity, and binding of lipids to polypropylene may disrupt this interface. Alternatively, monoglycerides formed by lipase activity also may effectively foul PP membranes, resulting in continued water flux reduction.

A membrane pretreatment experiment with lipase was conducted. A PP membrane was pretreated with 100 µg/mL of lipase at pH 7.7 for 1.5 h. After pretreatment, the membrane was exposed to FASE. A control (no lipase) was exposed to a phosphate buffer solution for 1.5 h concurrently. The lipase pretreated membranes started at a lower flux, but the performance appeared to drop at a slower rate, compared to the untreated membranes. Although lipase did not restore the flow of the fouled membrane, pretreating the membrane surface slowed the formation of the MF fouling layer.

A commercially available cleaning agent (Memclean C, Siemens) was tested for its effectiveness at restoring membrane flux. A fouled membrane was exposed to Memclean C, which was heated to 40 °C and stirred at 250 rpm (2 mm magnetic stir rod above the membrane surface) for 15 min. The cleaning solution was removed and permeate flux was measured using DI water. Flux was restored but not to the original level seen before the membrane was fouled.

PLFAs are soluble in polar organic sovlvents, such as ethanol and acetone. Ethanol was used as a cleaning agent to restore flux after membranes were fouled with ASE and FASE. Ethanol restored the flux for both ASE- and FASE-fouled membranes. The FASE-fouled membranes recovered better than ASE-fouled membrane. More than 80% removal of PLFAs from the FASE-fouled membrane was observed (61% of TerBrSats, 73% of Monos, 100% or BrMonos and MiBrSats, and 64% of Nsats phospholipids) using ethanol. This suggests that polar organic molecules or nanoparticles are perhaps responsible for a large part of the observed flux reduction driving microfiltration of secondary-treated wastewater. Ethanol cleaning recovered the membrane performance to its original permeate flux and thus may have more efficiently removed foulant material than Memclean C cleaning solution (Safarik and Phipps, 2005).

Fouling by colloidal organic matter occurs rapidly as the feedwater contacts the membrane surface with no driving pressure required, as opposed to microparticulate cake formation that is pressure driven. Static adsorption was investigated in the laboratory by exposing PP membranes to ASE without applied pressure. Flux was reduced significantly compared to untreated membranes. This result also was observed in the field with a 5 mgd MF facility at OCWD, where new PP hollow fiber membranes were immersed in the same ASE used in laboratory experiments for 7 days with periodic ASE replacement. A decrease in the membrane performance was observed requiring an earlier than planned cleaning.

In conclusion, classical models of MF cake fouling suggest the accumulation of particles close to the membrane surface covering membrane pores are primarily responsible for water flux reduction. The implication from this work is that there are actually two mechanisms of MF fouling, the classical MF cake formation, which may result in moderate reduction of

hydraulic conductivity, and deposition of microbial cell residue (proteins, carbohydrates and phospholipids) and nanoparticulates (e.g., liposomes), which results in the majority of the observed MF fouling.

4.2 MF Fouling Hypotheses

Materials greater than 200 nm that accumulate on the surface of the MF membrane (including microscopic materials, such as whole bacteria) are effectively cleared away by the backwash/air scouring mechanism and do not significantly contribute to long-term membrane fouling. The majority of the long-term MF fouling observed at the AWPF is from the accumulation (by adsorptive and entrainment mechanisms) of colloidal foulant materials less than 200 nm in size (nanoscopic materials, nanoparticulates) within the MF matrix. These nanoparticulate colloidal materials appear to be mostly of a biological nature, consisting largely of proteins and carbohydrates (either as individual colloidal macromolecules), virus particles, or as fragments of disrupted organisms such as liposomes. MF fouling of a hollow fiber will occur wherever there is contact with feedwater but will be greatest where the particulate load is greatest (e.g., at the suction end), and as the fiber operates, foulant material will accrue toward the end where load is the least (the closed end). Reducing the interaction of these nanomaterials with the MF matrix, either through exclusion by filtration, by aggregation into micromaterials that are effectively removed at the membrane surface, or by modification of the MF membrane matrix to reduce adsorption, should result in the mitigation MF fouling.

4.3 Modeling MF Fouling Using Surrogate Nanoscopic Materials

4.3.1 Experimental Methodology

4.3.1.1 Laboratory Bench-Scale Single-Fiber Test Cell

A laboratory bench-scale single-fiber test cell was developed to investigate PP MF-fouling under controlled conditions (Figure 4.1A). Components of the test cell included a feedwater reservoir, MF fiber test cell, permeate reservoir, and electronic balance. The reservoir fed the MF fiber test cell that was designed to accommodate a short-length (20 cm) MF fibers or a full-length (111.8 cm) MF fiber. The feedwater was supplied into the MF test cell in dead-end mode. The permeate reservoir sat on top of a four-place balance, which read permeate mass electronically.

The membrane used in the study was the same used in the AWPF, a 0.2 µm pore size PP hollow fiber (Siemens Water Technologies, Warrendale, PA). This PP membrane has a highly hydrophobic surface that is initially impermeable to water. Therefore, prior to each experiment, 10 mL of 100% ethanol were pulled through the new PP MF membrane followed by flushing with ASTMI deionized (18 Mohm-cm) water to hydrate the membrane material. The hydrated PP fiber was then placed in the short (Figure 2.1B) or long (Figure 2.1C) bench-scale MF test cell. The test cell was filled with feed solution and sealed. A vacuum of -5 psi was applied, and membrane permeate flux at constant pressure was gravimetrically measured continuously with an electronic balance (BP 610, Sartorius, Goettingen, Germany) connected to a computer (Dell Inspirion 8200, Round Rock, TX) through an RS-232 interface using data acquisition software (WinWedge v1.2, TALtech, Philadelphia, PA).

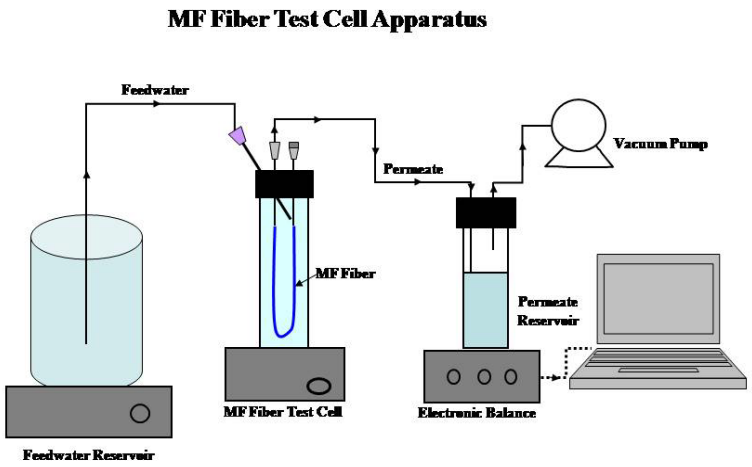

(A)

(B)

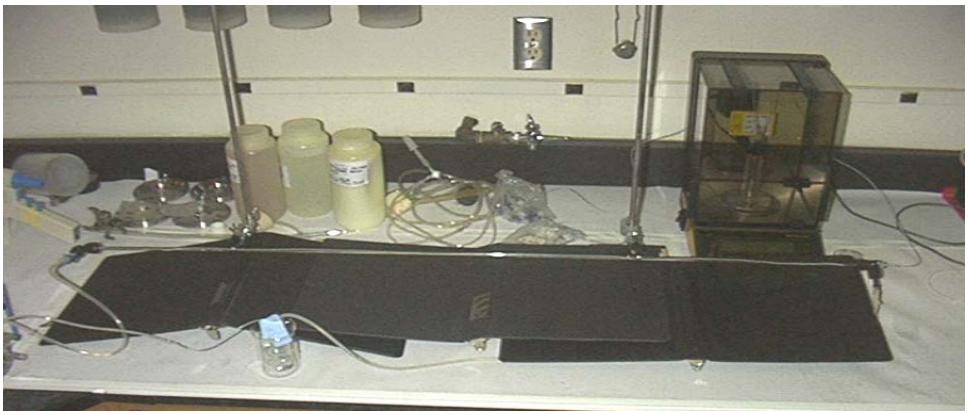

(C)

Figure 4.1. Laboratory bench-scale single-fiber test cell diagram(A), photograph of 20 cm MF fiber experimental setup(B), and photograph of 111.8 cm MF fiber experimental setup (C).

Prior to membrane fouling, a baseline membrane permeate flux was measured using 18 Mohm-cm water using the method described earlier. MF membranes were fouled by

passing feedwater through the membrane at a constant transmembrane pressure of -5 psi for 22 min. Permeate flux was automatically calculated at 5 s intervals.

Source water used for the study was ASE obtained from OCSD, Fountain Valley, CA. MF fouling began immediately upon introduction of the source water, and the progression of deposition of fouling materials was quantified by monitoring the rate of decrease in hydraulic conductivity (flow/pressure) through the membrane.

4.3.1.2 Simulated Activated Sludge Effluent

A simulated activated sludge effluent (SASE) feedwater was developed to mimic ASE chemistry. A chemical analysis of ASE conducted by the OCWD's AWQA laboratory was used as the basis of the SASE formula (Table 4.1). Only average concentrations of metals and ions found in ASE were used in the SASE formulation; organics were omitted. SASE by itself did not influence membrane performance.

Table 4.1. Simulated Activated Sludge Effluent Formula Adjusted to pH 7.5.

Molecular Constituent	Concentration (mg/L)
NaCl	533.83
$NaHCO_3$	767.40
$MgSO_4 \cdot 7H2O$	622.79
$CaCl_2$	209.21
NH4Cl	488.61
$MgCl_2 \cdot 6H_2O$	0.40
KCl	0.02
$NaNO_3$	0.03
Na_2HPO_4	7.70
$FeCl_2 \cdot 4H_2O$	0.81
$MnCl_2 \cdot 4H_2O$	0.39
$ZnCl_2$	0.042
$BaCl_2 \cdot 2H_2O$	0.067
$CuCl_2$	0.029
$CrCl_2$	0.0087
$CoCl_2 \cdot 6H_2O$	0.0012
$CdCl_2 \cdot 5H_2O$	0.0003

4.3.1.3 Fluorescent Carboxylated Nanobeads

Carboxylated, fluorescent nanobeads (100 nm and 500 nm, Invitrogen, Oceanside, CA) were used as surrogates for biodebris to visualize the movement of nanoparticles through the membrane matrix. SASE was spiked with a known concentration of the fluorescent nanobeads and used as feedwater to foul a PP MF membrane. Nanobead fouled membranes

were imaged using an Olympus AX-70 microscope equipped with a color camera (Dage DC 330T, Dage MTF, Michigan City, IN), excitation filter (B390) and emission (Y50).

4.3.1.4 10K MWCO Ultrafiltered ASE Feedwater

Feedwater of 10K-ultrafiltered ASE (10K FASE) was made by passing ASE through a 10K MWCO ultrafilter (Osmonics, Oceanside, CA). The filtrate was used as feedwater and diluent to demonstrate the ability of nanoparticles to reduce MF permeability.

4.3.1.5 MF Membrane Cryosectioning

A 2 in. MF membrane fiber was submerged in an aqueous medium in a glass tube (6×50 mm^2) previously scored using a glass file for easy manual fracturing. The tube was placed into an ultra-low freezer (-150 °C) for 1 h. Following freezing the glass tube was removed and immediately fractured at the score yielding two pieces of membrane. The pieces were allowed to thaw and membranes were allowed to dry. Once completely dried, the membrane sample was examined perpendicular to the cut plane by light microscopy or SEM (Ferlita, et al., 2008).

4.3.2 100-nm and 500-nm Nanobead Exposure Studies

Movement of nanoparticles through PP MF membrane was measured using 100 nm and 500 nm carboxylated, polystyrene fluorescent nanobeads. SASE was used as nanobead diluents and feedwater. After nanobead exposure using the short MF fiber test cell, the MF fiber was cryosectioned and examined with a fluorescent microscope. The 100 nm nanobeads are smaller than the 0.2 µm pore size of the membrane and thus they pass across the membrane surface into the matrix. Some passed through to the permeate side, but many remained lodged in the membrane matrix (Figure 4.2A). The 500 nm nanobeads are larger than the 200 nm pore size of the membrane; therefore, they could not penetrate the membrane and remained at the membrane surface (Figure 4.2B).

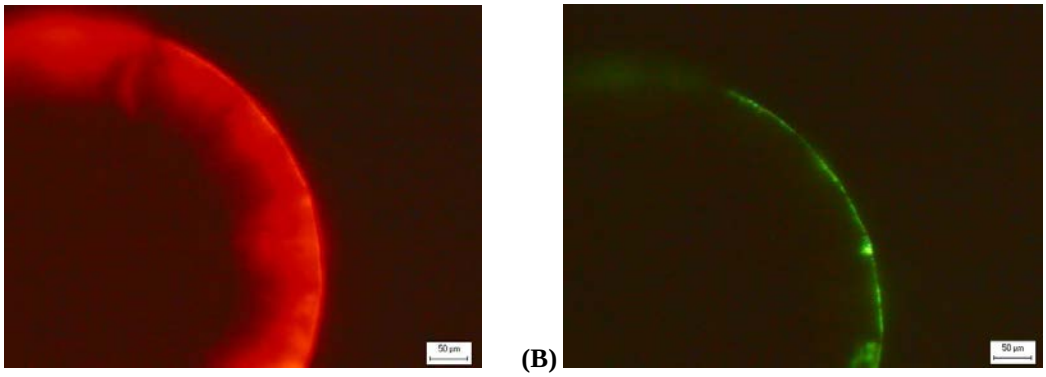

Figure 4.2. Movement of nanoparticles in presence of SASE: (A) 100 nm nanobeads penetrated and lodged in the membrane matrix, (B) 500 nm nanobeads remained on the membrane surface.

Nanobeads (100 nm) also were used to demonstrate the ability of nanoparticles to reduce MF water flux. MF membranes were exposed to three feedwaters (DI water, SASE, 10K-FASE) spiked with 100 nm nanobeads. SASE was composed of salts only (no organics), 10K-ultrafiltered ASE was composed of salts and organics. These three feedwaters alone did not

reduce membrane flux. Figure 4.3 shows that 100 nm nanobeads by themselves (DI water + nanobeads) can reduce membrane permeability. Membrane performance was affected further by the addition of salts (SASE) and organics (10K-FASE). At the end of the experiment, the fouled MF membrane fibers were cryosectioned and microscopically examined using the AX-70 Olympus microscope (Figure 4.4). The DI water membrane had nanobeads both on the membrane surface and inside the membrane lumen, suggesting beads formed a fouling cake on the surface (pore blocking), as well as passed through the membrane matrix. The presence of salts in SASE feedwater resulted in some pore blocking and pore plugging, but most of the nanobeads appeared to pass through without sticking to the MF fiber. The nanobeads mixed with the 10K-FASE feedwater penetrated the membrane matrix resulting in an even nanobead distribution throughout the membrane. Brighter fluorescent signal coupled with significant decline in MF flux suggested that greater nanobead binding occurred with both SASE and 10K-FASE.

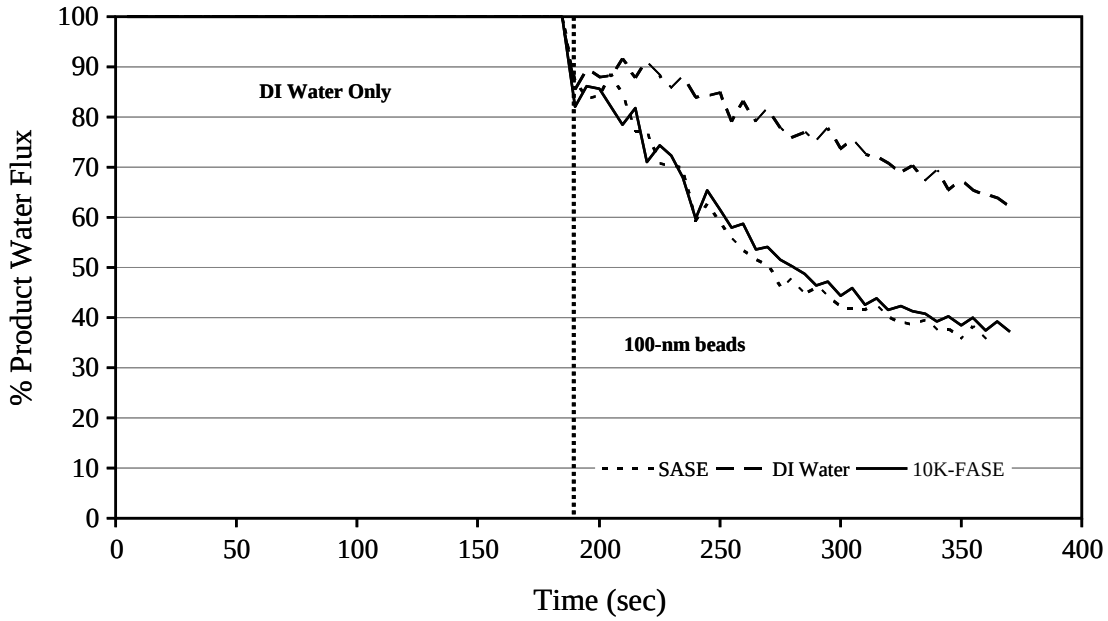

Figure 4.3. The addition of surrogate 100 nm nanobeads to SASE, DI water, and 10K-FASE feedwaters reduced MF flux demonstrating that the chemical makeup of feedwaters does influence membrane performance.

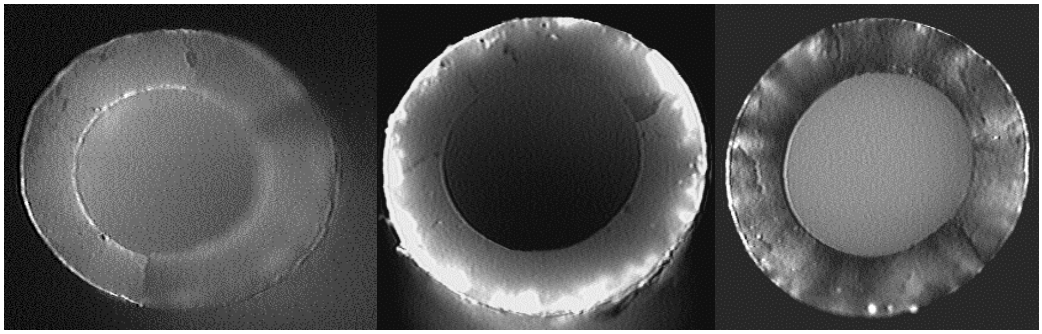

DI Water **SASE** **10K-FASE**

Figure 4.4. Cryosectioned MF membranes exposed to DI water, SASE, or 10K-FASE containing 100 nm nanobeads.

The 100 nm and 500 nm nanobead exposure studies support the hypothesis that particles greater than 200 nm remain on the MF surface, while particles less than 200 nm can accumulate within the MF matrix and result in water flux reduction without forming a surface cake.

4.3.3 Bench-Scale Simulation of MF Fouling Dynamics

Accumulation of membrane foulants occurs from the top of the fibers (where suction is applied) to the bottom of the fibers. Using the long single MF fiber bench-scale test cell, fluorescent microbeads (500 nm) were used to foul a 41 in. MF PP fiber for 2.3 min at -5 psi. The fluorescence of the microbeads was measured by illuminating the fiber with a UV light (Ex filter: B390, Em filter: Y50). Images were taken with a Nikon 8700 camera. The top 8.5 in. of the fiber were the brightest indicating the highest accumulation of microbeads. Microbead fluorescence decreased substantially near the bottom sections of the fiber (Figure 4.5). This demonstrated that accumulation of nanomaterials in the MF fiber proceeds as hypothesized from the suction-end top to the closed-end bottom of the fiber.

0-8.5” 8.5-20” 20-30” 30-41”

Figure 4.5. PP MF fiber fouled for 2.3 min at -5 psi. Microbeads are visualized as green fluorescence on the fiber surface.

4.4 Analysis of MF Hollow Fibers Fouled by Activated Sludge Effluent (ASE) and Filtered Activated Sludge Effluent (FASE)

4.4.1 Experimental Methodology

4.4.1.1 Nanoparticle Size and Size Distribution Using Zetasizer Nano

Nanoparticle sizes and size distributions were evaluated using a Zetasizer Nano (Malvern Instruments, UK) operated with a high power laser (50 mW, 532 nm) (Carl, 2010). The Zetasizer Nano utilizes dynamic light scattering (DSL) to measure particle size and is capable of measuring the size of molecules and particles typically in the submicron region (down to 1 nm). The principal measurement is based on Brownian motion of a particle in a suspension, which is the motion induced by the bombardment by solvent molecules that are moving because of their thermal energy. Illumination of the particles with a laser causes the intensity of the scattered light to fluctuate at a rate that is dependent on the size of the particle as smaller particles are “kicked” farther by the solvent molecules and move more rapidly than larger particles. Analysis of these intensity fluctuations yields the velocity of the Brownian motion and hence the particle size using the Stokes-Einstein relationship (Carl, 2012). Measurements are taken in the native matrix and the mean size calculation only requires knowledge of the liquid viscosity. Typical applications are the measurement of the size and size distribution of proteins, polymers, micelles, carbohydrates, nanoparticles, colloidal dispersions, emulsions, and microemulsions dispersed or dissolved in a liquid.

4.4.1.2 Differential Filtration Method

Size range of the nanoparticulate foulants was determined by differential filtration by passing ASE sequentially through three membranes: (1) 0.2-µm hydrophilic polyethersulfone (PES) filter (<200 nm, Supor 200, Pall Corp., Port Washington, NY, (2) 20K MWCO (ultrafilter <3.5 nm, 20K FASE, Osmonics, Oceanside, CA), and (3) 10K MWCO (ultrafiltered <2.5 nm, 10K FASE, Osmonics, Oceanside, CA). The filtrate from each filter was used as feedwater to test PP membrane performance to determine its fouling potential.

4.4.1.3 Protein Assay

Membrane fibers were cut into 2 in. pieces, weighed, and placed into scintillation vials containing 15 mL of mineral salts buffer. Samples were sonicated for 5 min to dislodge foulants from the membrane surface into the buffer solution, and the assays were performed on serial dilutions of sonicated samples in buffer solution. The protein content was analyzed by the Bio-Rad Protein Assay (Bio-Rad Laboratories, Hercules, CA) using bovine serum albumin (BSA) as a standard.

4.4.1.4 Carbohydrate Assay

The total carbohydrate analysis was performed by a phenol-sulfuric acid assay (Dubois et al., 1956). A carbohydrate standard curve was generated using glucose.

4.4.2 Characterization of Nanomaterials in ASE and FASE by Zetasizer Nano Analysis

Nanoparticle size distributions of MFF, MFE, and MFC (backwash) were evaluated using the Malvern Zetasizer Nano. The MF feed and MF backwash samples were very turbid, with a high concentration of particles greater than 0.2 µm. The large particles and high turbidity of these samples interfered with the Zetasizer analysis. To reduce the interference both samples were prefiltered using a 0.22 µm sterile cellulose acetate syringe filter (Costar, Cambridge, MA). The MF effluents did not require prefiltration. The nanoparticulate profiles of the control feed and MFC from the MF pilot unit were very similar (Figure 4.6). The MF effluent had a slight higher proportion of nanoparticles in the 80 to 100 nm range.

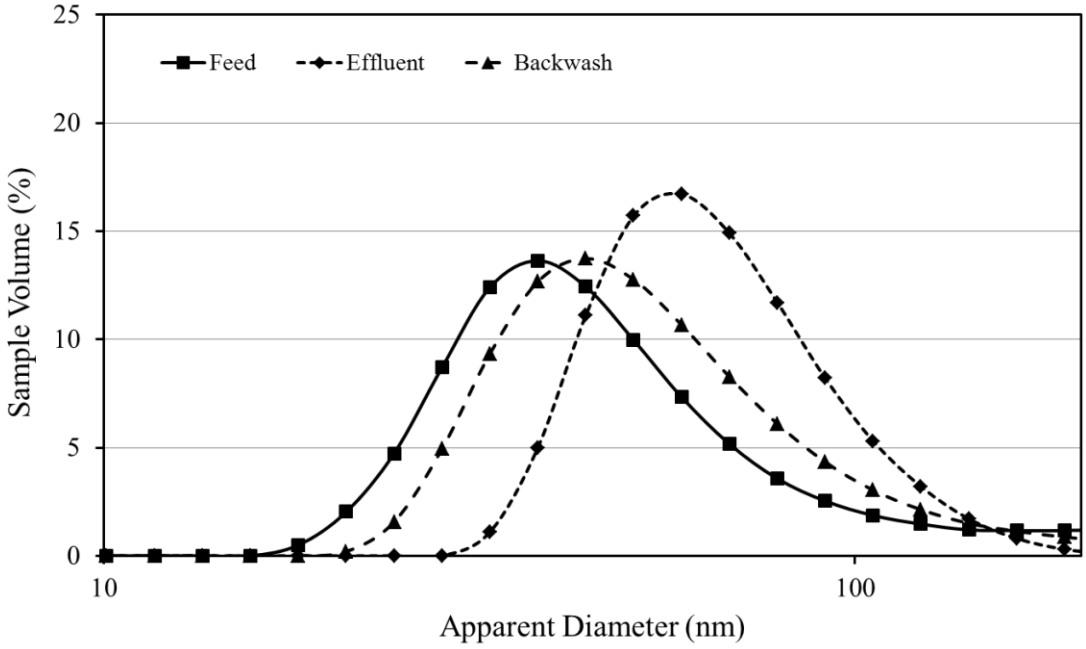

Figure 4.6. Nanoparticulate profiles of MF feed, MF effluent, and MF backwash.

Note: Feedwater and backwash were prefiltered through 0.2 µm filter to reduce microparticulate interference.

4.4.3 Differential Filtration Study

The single-fiber test cell was used to foul MF PP membrane with ASE. Within 2 min of ASE exposure, the permeate flux decreased by 80% (Figure 4.7).

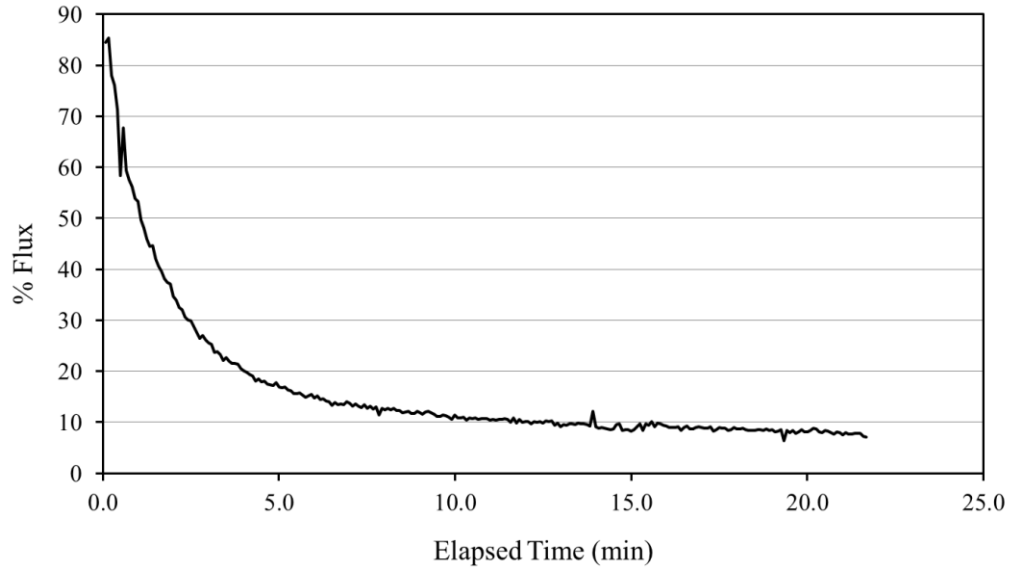

Figure 4.7. Single-fiber PP membrane permeate flux decline with ASE.

Note: Membrane performance declined within seconds of feedwater exposure.

To determine if the majority of the fouling was due to pore blocking by particulates (>0.2 µm), these particulates were removed from ASE using a 0.2 µm PES filter, and the kinetics of the ASE and FASE were compared. Removal of particles greater than 200 nm from the feedwater only improved membrane performance by 20% (Figure 4.8). It was concluded that membrane fouling by pore blocking from deposited particulates greater than 0.2 µm, originally presumed to be responsible for the majority of MF fouling was only responsible for 20% of the observed flux reduction. The principal MF water flux reduction was caused by pore plugging that was due to nanoparticles smaller than 0.2 µm.

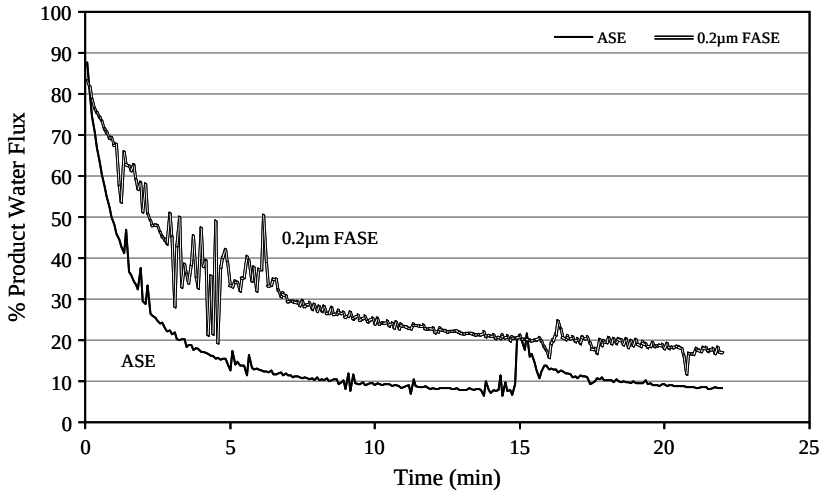

Figure 4.8. Single-fiber PP membrane permeate flux decline on ASE and 0.2 µm filtered ASE.

The lower size range of the nanoparticulate foulants was determined by differential filtration by passing ASE sequentially through three membranes: (1) 0.2 µm PES filter (<200 nm), (2) 20K MWCO ultrafiltered (<3.5 nm, 20K UF-ASE), and (3) 10K MWCO ultrafiltered (<2.5 nm, 10K UF-ASE). Filtrate from each filter was used as feedwater to test PP membrane performance to determine its fouling potential.

After 10 min of filtration, the unfiltered ASE reduced membrane flux by more than 80% (Figure 4.9). Removal of particles greater than 200 nm reduced membrane flux 70% (30% improvement in membrane performance). Removal of nanoparticles greater than 3.5 nm reduce membrane flux 40% (60% improvement in membrane performance). However, no loss in water flux was observed when nanoparticles greater than 2.5 nm were removed (10K MWCO filter), demonstrating the majority of MF membrane fouling is largely due to nanoparticles in the 2.5 to 200 nm range, with most of the foulants in the 2.5 to 3.5 nm range.

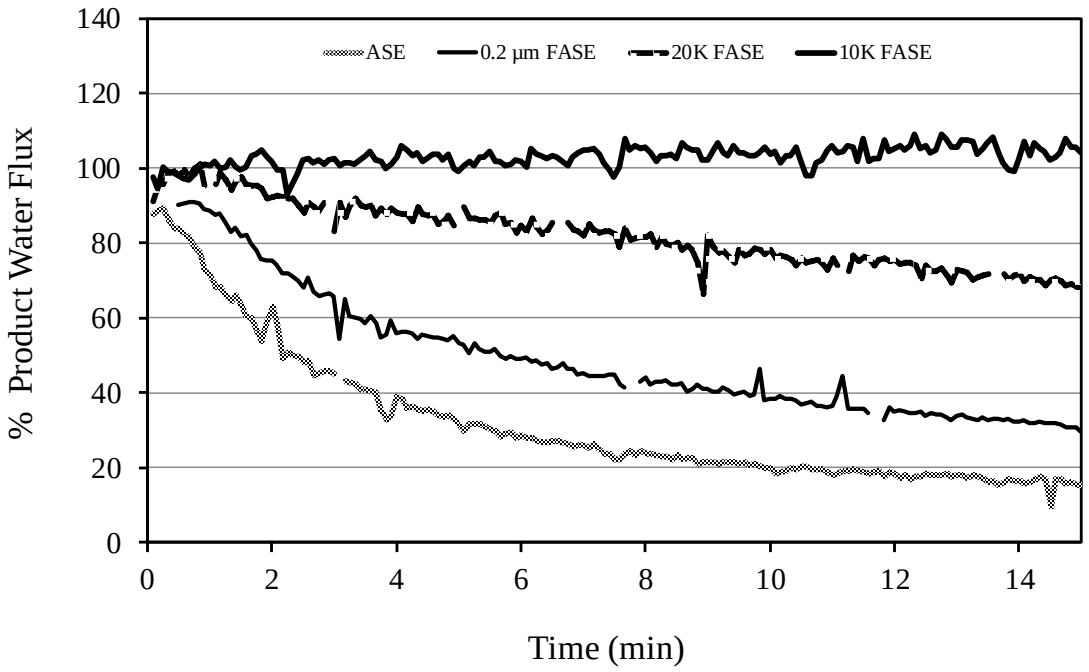

Figure 4.9. Single-fiber MF performance curves demonstrating nanoparticles >2.5 nm are responsible for flux loss.

Protein and carbohydrate analysis (Figures 4.10 and 4.11) indicate that some of the nanoparticulates responsible for fouling are likely biological in nature. Protein concentrations appeared to increase from 1.7 µg/mL to 2.0 µg/mL when filtered through a 0.22 µm filter. The increase may be because of the shearing of large proteins by the filtration process or a majority of the proteins are less than 0.2 µm and freely pass through the filter. Approximately 45% of the protein was removed with the 20K MWCO ultrafilter (UF), and 79% were removed by the 10K MWCO UF filter. The removal of proteins correlates with the flux decline curves, where 10K FASE feedwater did not affect membrane performance and 20K FASE feedwater decreased performance by 40%. This suggests that much of the nanoparticles fouling the MF contain protein.

Unlike protein, 88% of the carbohydrate was removed by filtration at 0.2 µm, whereas the 20K (~3.5 nm) and 10K (~2.5 nm) UF filters removed the remaining carbohydrates below the detection point of the assay. This suggests most of the carbohydrate portion is held up in the MF cake, with only ~12 to 13% was able to penetrate the MF matrix, suggesting that most of the MF nanopartiulate foulants do not contain a significant amount of carbohydrate.

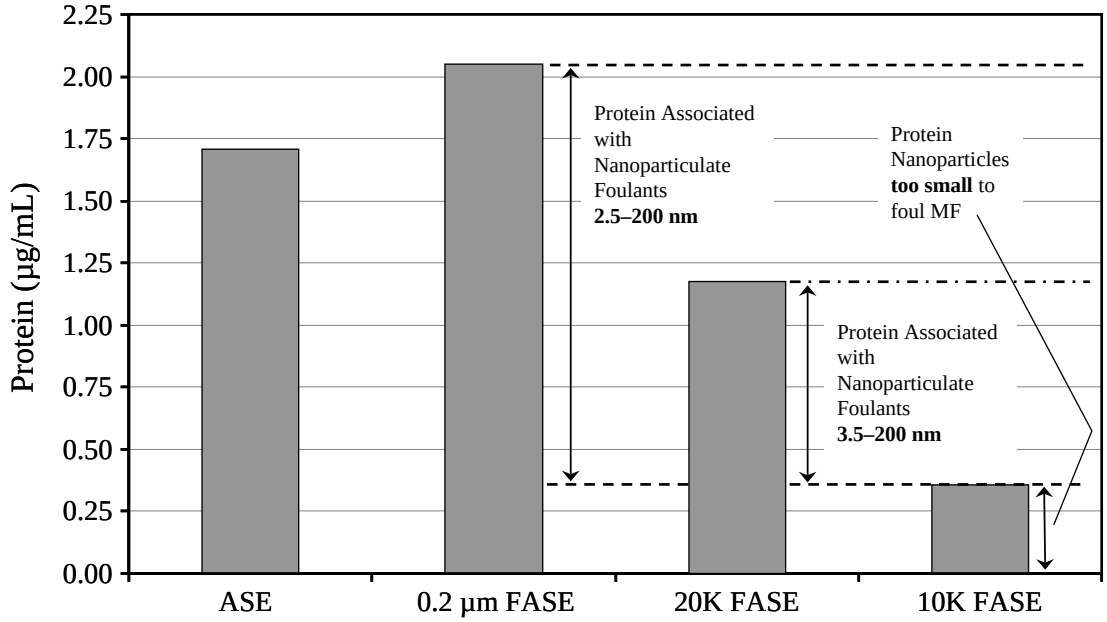

Figure 4.10. Protein analysis of filtered ASE.

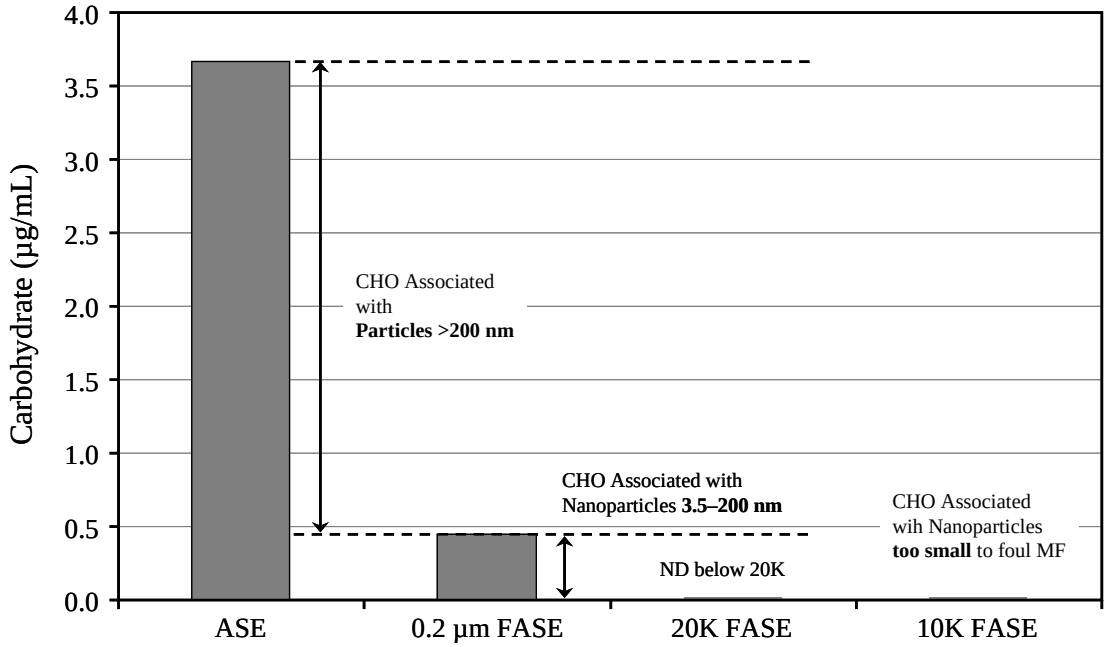

Figure 4.11. Carbohydrate analysis of ASE.

4.5 Autopsy of Fouled MF Element from Pilot System

4.5.1 MF Pilot System

Two direct filtration Siemens 4S10V CS pilot units (Figure 4.12) were used in this study. Each unit was capable of holding up to four MF elements, arranged in a clover configuration

identical to the GWRS MF process. For this test, each pilot unit was fitted with two PP MF elements (the same elements used in AWPF). Each unit operated in direct filtration at 20 gfd (9 gpm). Every 22 min the membranes were automatically backwashed and air scoured. The TMP was automatically logged via a system data logger. Additional measurements also were taken manually, once in the morning and once in the afternoon. When the TMP levels exceeded 12.5 psi (the preset terminal TMP level), the unit automatically shut down for chemical cleaning. Chemical cleaning was conducted in accordance with current AWPF standard operating procedures.

Figure 4.12. Direct filtration 4S10V CS MF pilot units used for MF studies.

The pilot tests were carried out at the OCWD AWPF Research Center. ASE from the OCSD was used as the feed to each unit. Chlorine (sodium hypochlorite) was added to the MF feedwater, and the residual combined chlorine levels were maintained between 2 and 4 mg/L.

4.5.2 Materials and Methods

4.5.2.1 MF Membrane Autopsy

The physical condition of membrane components and deposition of foulants on the surfaces of the MF membrane were evaluated by autopsy. The membranes were removed from the pilot units and visually inspected. Because of the cost of sample analysis, only one membrane from each pilot unit was autopsied. The plastic case of the element was cut away, and fibers were exposed. Fouled fibers were cut from the membrane with sterile scissors and placed into sterile vials for analysis. The membranes were divided into nine sections: front/top, middle/top, back/top, middle/top, middle/middle, middle/bottom, back/top, back/middle, and back/bottom. The hollow fibers were analyzed for carbohydrate and protein deposition, examined by light and SEM microscopy.

4.5.2.2 MF Membrane Cryofracture

MF fibers were cryofractured as described in Section 4.3.1.5 (Ferlita, et al., 2008). The fractured membranes were allowed to thaw, and membranes were allowed to dry. Once

completely dried, the membrane sample was examined perpendicular to the cut plane by light microscopy or SEM.

4.5.2.3 Scanning Electron Microscopy

SEM analysis was done using a Philips XL-30 FEG SEM equipped with energy dispersive X-ray spectroscopy (EDS) system at the MC2 laboratory at University of California, Irvine under the direction of Dr. Jian-Guo Zheng.

4.5.2.4 Light Microscopy

Light microscopy was performed using an Olympus AX-70 microscope equipped with a color camera (Dage DC 330T, Dage MTF, Michigan City, IN).

4.5.2.5 Nanoparticulate Size Distribution

Nanoparticle size distributions of MFF, MFE, and MFC were evaluated using the Malvern Zetasizer Nano, as described in Section *4.4.1.1*.

4.5.3 Distribution of Foulant Materials on a Fouled MF Element

After 25 days of operation on ASE, the MF element or module showed visual evidence of external fouling. The casing was covered with a thick brown slimy layer which appeared to be a combination of EPS, bacteria, and algae (Figure 4.13A). Compared to a new module the discoloration and foulant deposition were very evident (Figure 4.13B).

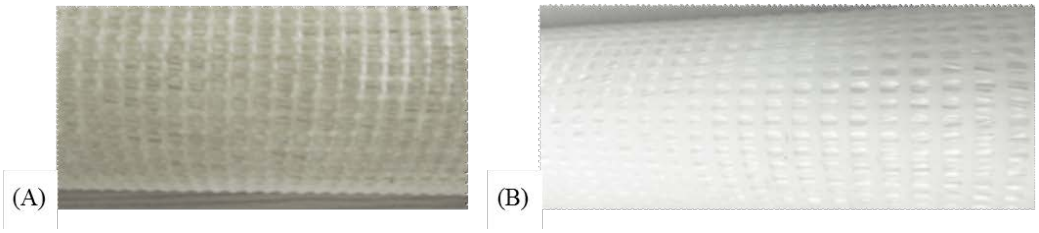

Figure 4.13. Images of (A) fouled MF membrane after 25 days of operation, and (B) clean MF element.

The discoloration of MF fibers was even more evident after the casing was removed. The fibers were discolored with a brownish green tint (Figure 4.14). The discoloration was very evident when compared to clean MF fibers. The heaviest fouling was observed at the top of the bundle where the vacuum is applied (Figure 4.14A). The middle of the membrane element appeared to be the least fouled (Figure 4.14B). Heavy fouling also was observed at the bottom, where fibers are imbedded into the casing of the module. (Figure 4.14C).

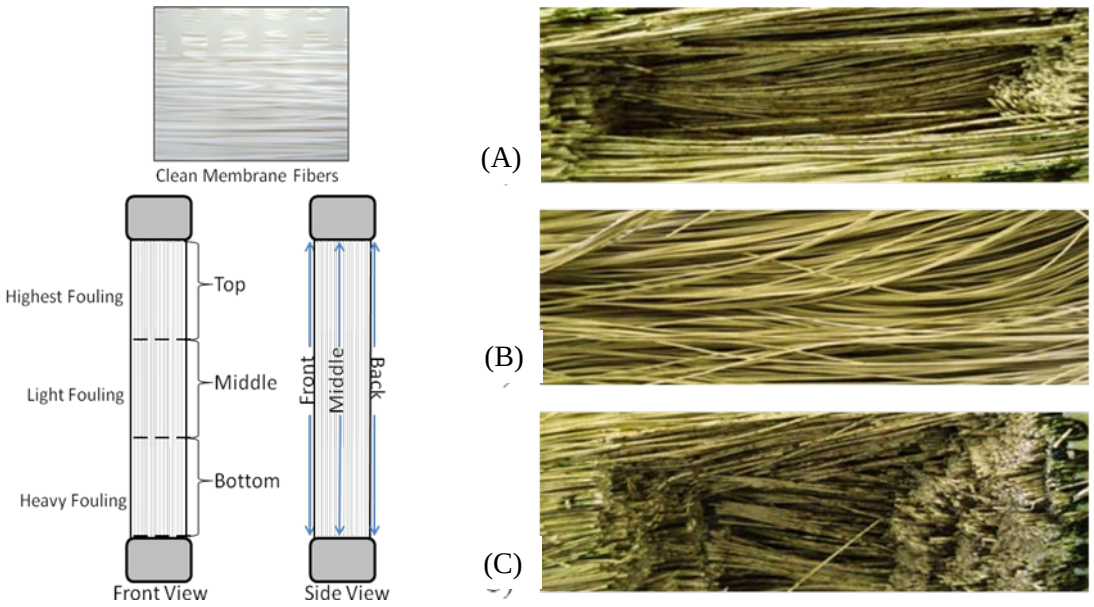

Figure 4.14. Fouled MF membranes: (A) top/middle, (B) middle/middle, and (C) bottom/middle.

Surface microscopy images revealed the hollow fibers of a clean MF membrane surface to be white (Figure 4.15D). The fouling across the used membrane varied over the length of the fiber, with the fouled membrane's top portion contained the thickest layer (Figure 4.15A). Moving down the membrane towards the middle, the fouling was lighter in color and less dense (Figure 4.15B). The bottom of the membrane (Figure 4.15C) appeared slightly more fouled than the middle but not as fouled as the top.

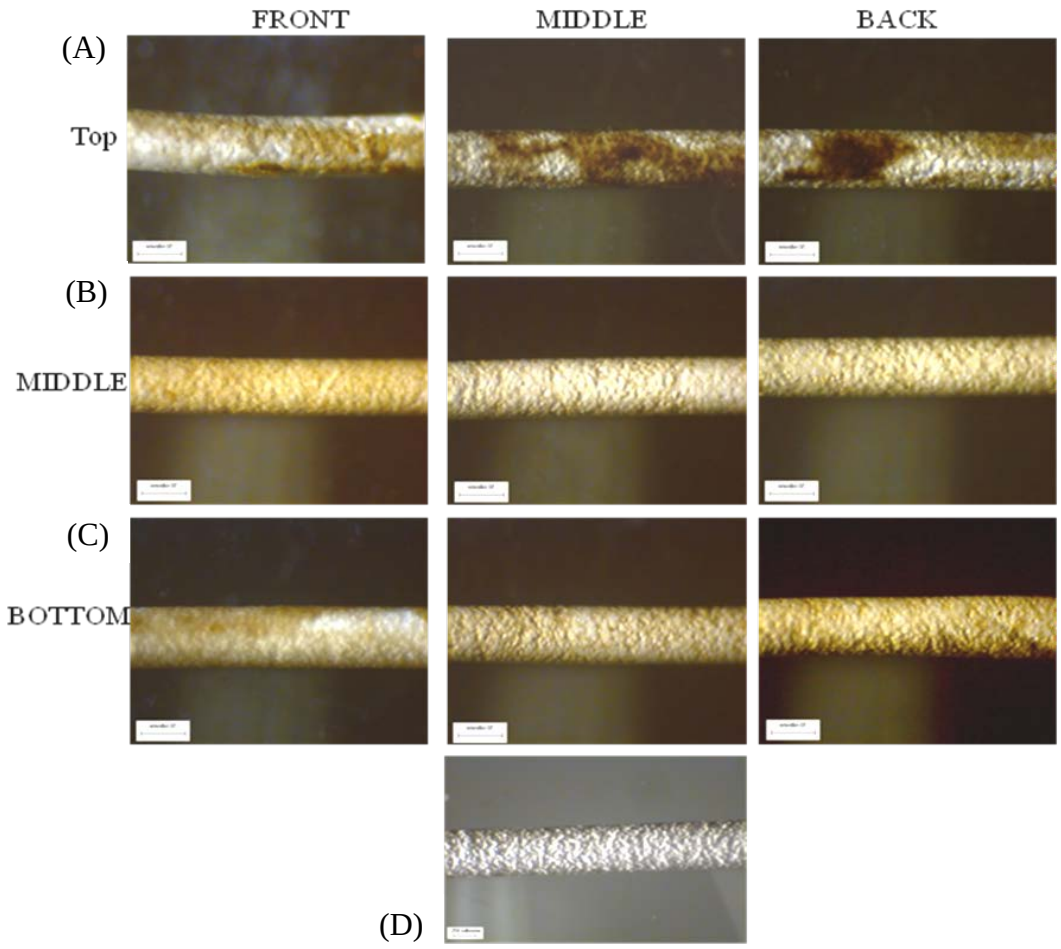

Figure 4.15. Surface microscopy of MF hollow fibers from the top, middle, and bottom sections of a fouled element: (A) front section from top to bottom, (B) middle section from top to bottom, (C) back section from top to bottom, and (D) clean MF membrane.

SEM analysis of the fouled MF membrane showed nanoparticles embedded in the MF matrix (Figure 4.16). Foulant was visible at the membrane surface (pore blocking) and inside the membrane porous structure (pore plugging). EDX analysis indicated the presence of C, O, F, Na, Si, P, S, Cl, and Ca. The detection of C, O, P, and S is consistent with the presence of biological material.

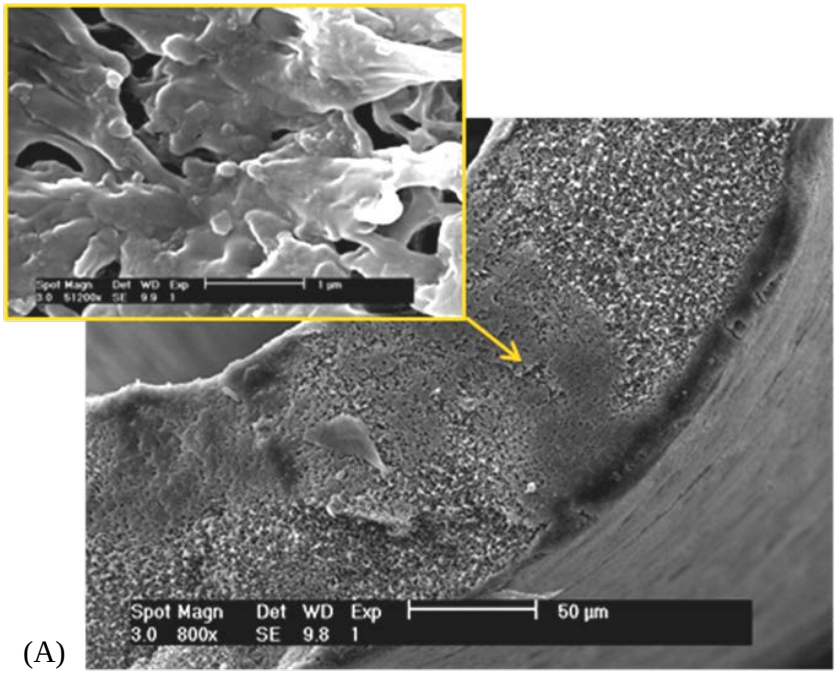

(A)

(B)

EDS Element
C
O
F
Na
Si
P
S
Cl
Ca

Figure 4.16. SEM images of (A) a fouled MF membrane showing natural nanoparticles embedded in the MF matrix, and (B) EDX analysis of MF membrane cross section.

All membrane sections were analyzed for total carbohydrate (CHO) and protein (Figures 4.17 and 4.18). The data indicated that both carbohydrate and protein concentrations were highest at the top portion of the membrane where the CHO ranged between 2.03 and 4.30 µg/cm. The deposition of CHO in the middle and bottom portions of the membrane was between 0.19 and 0.79 µg/cm. The protein content also was highest at the top of the membrane with the middle and bottom portions of the membrane having much lower protein coverage. Both CHO and protein depositions were more variable at the top as seen from the higher standard deviations.

Analysis of the fouled elements from the pilot units revealed an uneven distribution of foulants from top to bottom as evidenced by carbohydrate and protein accumulation that conforms to the loading pattern demonstrated with fluorescent nanoparticles on a whole fiber in the laboratory.

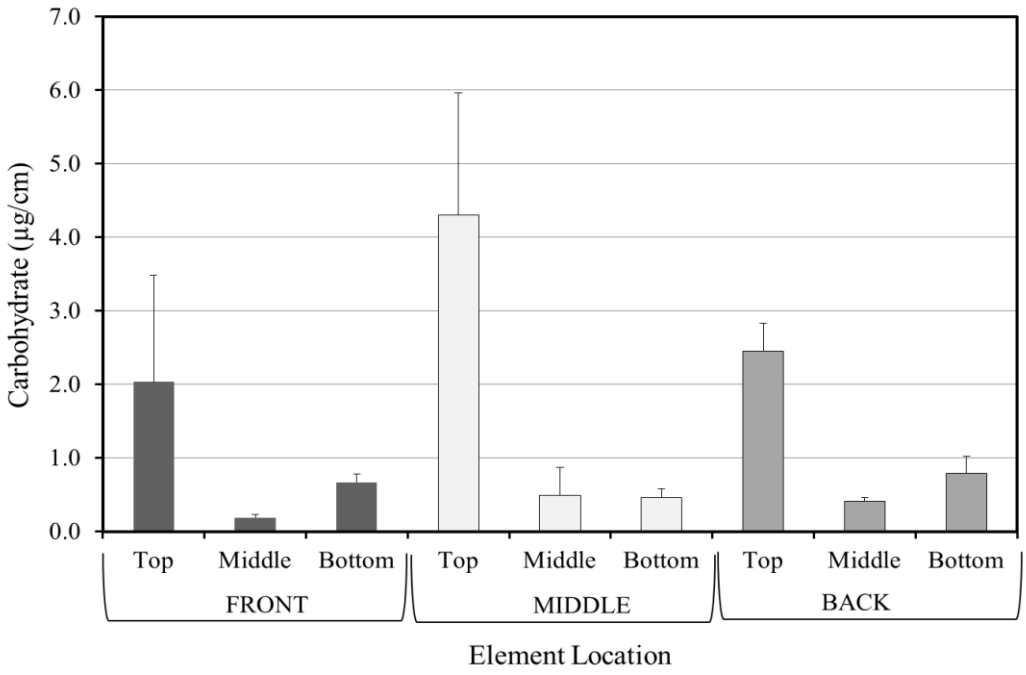

Figure 4.17. Carbohydrate analysis of fouled MF hollow fibers.

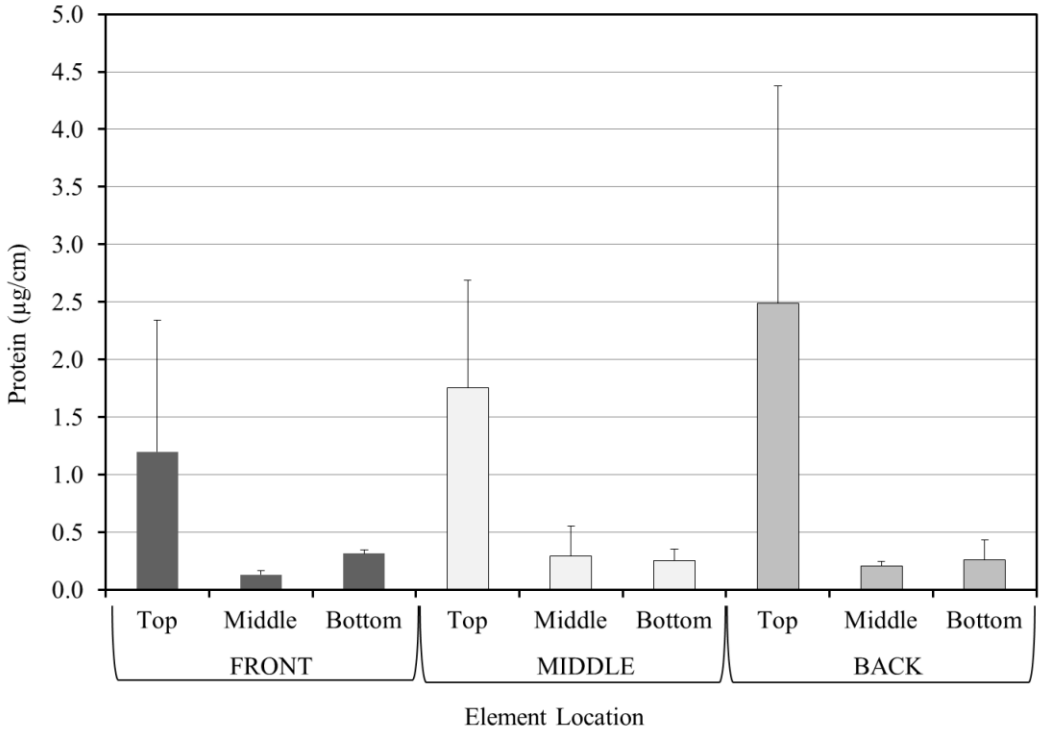

Figure 4.18. Protein analysis of fouled MF hollow fibers.

4.6 Pilot Study of the MF Fouling Mitigation by Precoagulation—Impact of Coagulant Concentration on MF Performance

4.6. Introduction

This pilot study tested the hypothesis that precoagulation of nanoparticles less than 200 nm into particles greater than 200 nm could lead to improved MF performance by keeping material at the surface of the membrane, where it can be effectively removed by backwashing.

Coagulation is the most commonly used chemical pretreatment in MF treatment facilities (Farahbaksh and Smith, 2002). The primary purpose of coagulation is to remove nano- and microparticulates, such as microsomes, large proteins, viruses, and biodebris derived from degraded biological materials. Coagulation agglomerates these small particles into larger particles that are kept from entering the MF membrane matrix.

4.6.2 Materials and Methods

Sumaclear 700 (S700, Summit Labs, New Jersey), a cationic polymerized aluminum compound (Al content ~12%), with a molecular weight of approximately 10,000 daltons was used to coagulate nanoparticles in ASE into particles greater than 0.2 µm in order to keep them from entering the matrix or pores of the PP membrane.

This study utilized the two direct filtration 4S10V CS pilot units described in Section 4.5.1. One unit received ASE feedwater without precoagulation, and the other unit received ASE feedwater that was precoagulated with 2.5, 5, or 10 mg/L of S700. For this investigation, each unit was fitted with two PP MF modules and was operated in direct filtration at 20 gfd (9 gpm), and every 22 min the membranes were automatically backwashed and air scoured. When the TMP levels exceeded 12.5 psi, the unit automatically shut down for chemical cleaning. The CIPs were conducted in accordance with current AWPF standard operating procedure.

ASE from the OCSD was used as the feed to each unit. During the time these studies were conducted, the blended secondary effluent consisted of 20% TFE and 80% ASE. Chlorine (sodium hypochlorite) was added to the MF feedwater and residual combined chlorine levels were maintained between 3 to 5 mg/L.

Control of coagulant dosage was achieved via a precision digital dosing pump (Grundfos, Olathe, KS). A 1 in. PVC inline static mixer (Cole-Parmer Instruments, IL) was installed to ensure adequate mixing, and a 550 ft length of 1.5 in. J-series hose was installed upstream of the MF unit to simulate a 5.3 min contact time of S700 with the ASE (Figure 4.19). At the end of the experiment, membranes were removed and autopsied.

Figure 4.19. S700 coagulant dosing apparatus with 550 ft of 1.5-in. J series hose upstream of the MF pilot unit to simulate 5.3 min of contact time.

4.6.3 Results and Discussion

4.6.3.1 Impact of S700 Coagulant on Nanoparticles in MF Feedwater

Nanoparticle size distributions in the MFF control, Sumaclear 700 (S700) dosed MFF, and MFE were evaluated using the Malvern Zetasizer Nano. The MFF samples were very turbid with high concentration of particles greater than 0.2 µm. The large particles and high turbidity of these samples interfered with the Zetasizer analysis. To reduce the interference the samples were prefiltered using a 0.22 µm sterile CA syringe filter to reduce the interference. The MF effluents did not require prefiltration.

The nanoparticles from the MFF treated with 2.5 mg/L of S700 ranged from 10 to 459 nm, whereas the MFE nanoparticles separated into two distinct population sizes of 1 to 3 nm and 7.5 to 28 nm (Figure 4.20). Increasing the concentration of S700 in the MFF to 5 mg/L removed the nanoparticles from MFE larger than 21 nm, leaving only nanoparticles between 6 and 24 nm (Figure 4.21). A further increase in S700 to 10 mg/L did not result in a measurable difference in the nanoparticulate profile (Figure 4.22). At the 10 mg/L S700 concentration, the nanoparticles that passed through the membrane all ranged between 6 and 20 nm.

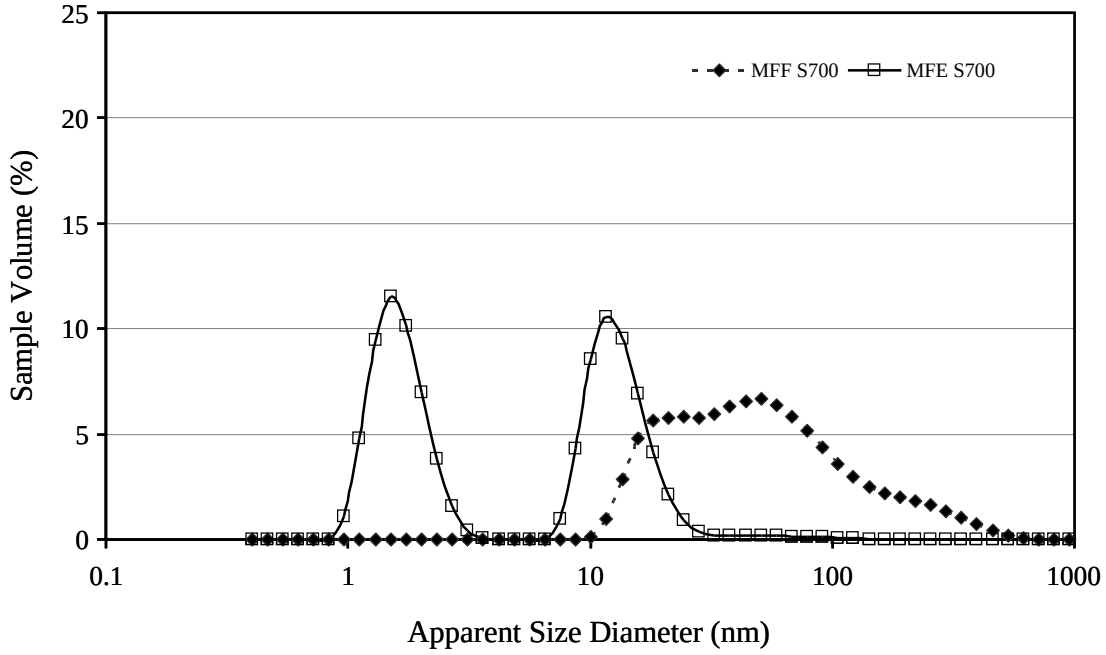

Figure 4.20. S700-pretreated (2.5 mg/L) MF feedwater pilot unit nanoparticulate profiles of MFF (diamonds) and MFE (squares).

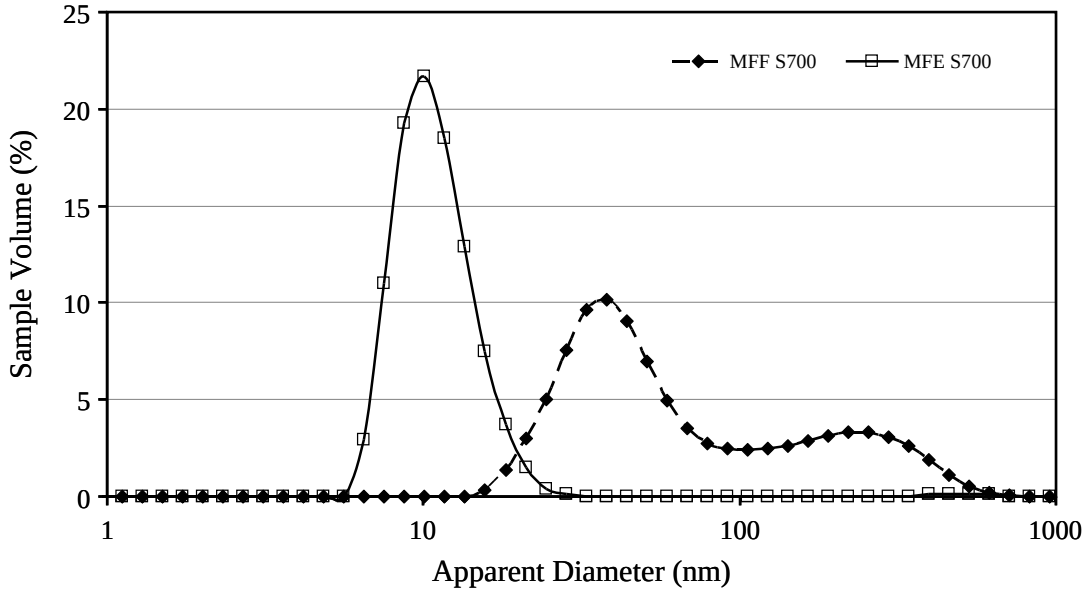

Figure 4.21. S700-pretreated (5 mg/L) MF feedwater pilot unit nanoparticulate profiles of MFF (diamonds) and MFE (squares).

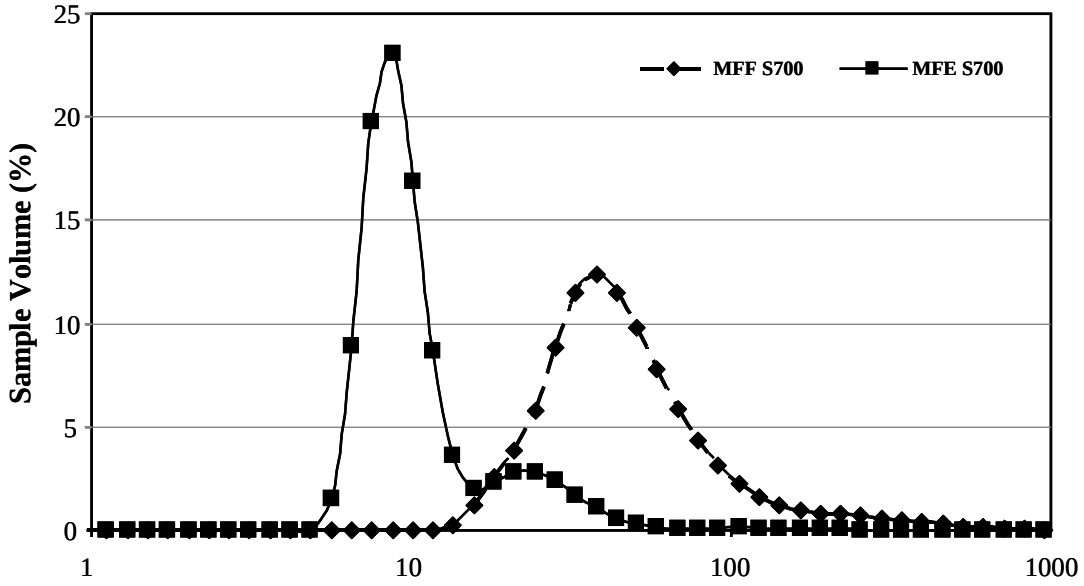

Figure 4.22. S700-pretreated (10 mg/L) MF feedwater pilot unit nanoparticulate profiles of MFF and MFE.

4.6.3.2 Impact of S700 Coagulant on Cleaning Interval of MF Process

Comparison of MF pilot performance at 10 mg/L S700 pretreatment showed the cleaning interval (CI) was increased from 21 days to greater than 82 days (Figure 4.23) with the maximum TMP only reaching 8 psi. TMP levels remained below 12.5 psi and never triggered an automatic shutdown prompting a CIP. The experiment was terminated because of time constraints; therefore, the true CIP interval with 10 mg/L of S700 was never determined. However, the parallel control MF unit that received the same feedwater without the S700 coagulant required a CIP two times during same time period of operation. The first CIP was conducted on the control unit after 21 days of operation when the TMP increased to 12.5 psi. At the start up of the second run of the control unit, both MF units received feedwater with unusually high turbidity (>20 NTU). During the high turbidity event, the TMP in the S700 spiked to 11.3 psi. However, as the high turbidity feedwater moved through the system, the S700 membrane performance returned back to TMP conditions observed prior to the event. This event apparently caused the control membranes to load up with microparticulates and nanoparticulates, resulting in the shorter CI of 17 days. Pretreatment with 10 mg/L of S700 appeared to protect the MF membrane from fouling even with excess nanoparticles present in the high turbidity (>20 NTU) feedwater.

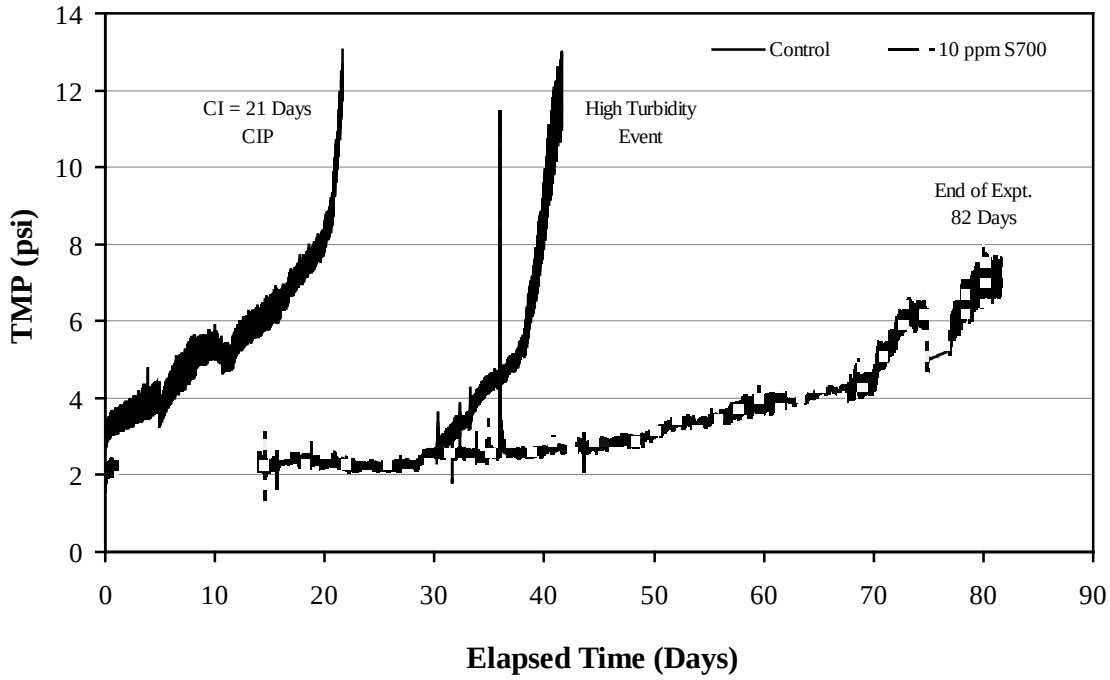

Figure 4.23. Performance of MF pilot unit operated on 10 mg/L of S700 coagulant in the feedwater.

For the next study, the S700 coagulant was reduced to from 10 mg/L to 5 mg/L. Within the first 4 h of operation, both units received high-turbidity feedwater (>12 NTU). During the high-turbidity event the TMP in both units increased slightly. However, the control unit never returned to the pre-event pressure. The TMP continued to rise, resulting in a shorter CI to CIP of 15 days (Figure 4.24). The S700 pilot unit TMP dropped back to the pre-event pressure and unit performance continued at less than 4 psi for 24 days. During this time the main pump of the control pilot unit malfunctioned and took 6 weeks to repair. Therefore, a second control test run in parallel to the 5-mg/L S700 unit could not be performed. A second high-turbidity event (12–30 NTU) occurred on Day 24, resulting in higher TMP (5.4 psi) but as the turbidity returned to normal (~2–4 NTU), the TMP dropped back to less than 4 psi. Two days after this turbidity event, the TMP started to rise. On Day 36 the feedwater color changed from light brown to a red, rusty color. The turbidity did not increase during the "color event," but an increase in TMP was observed (Figure 4.24). The red color was likely the result of textile dye release into the sewer system. The dyes are composed of nanoparticulates that are not well removed by the secondary-treatment settling facilities at OCSD. These dyes increased nanoparticulate loading, which resulted in an increase in TMP. Even with the multiple high-turbidity events, the 5-mg/L S700 pilot unit CI was extended to 50 days (Figure 4.24). Of further interest, the TMP decreased after the turbidity spike with 5 mg/L of S700, but the same decrease was not observed in the MF without coagulant, suggesting that the coagulant prevented long-term deposition of foulant material.

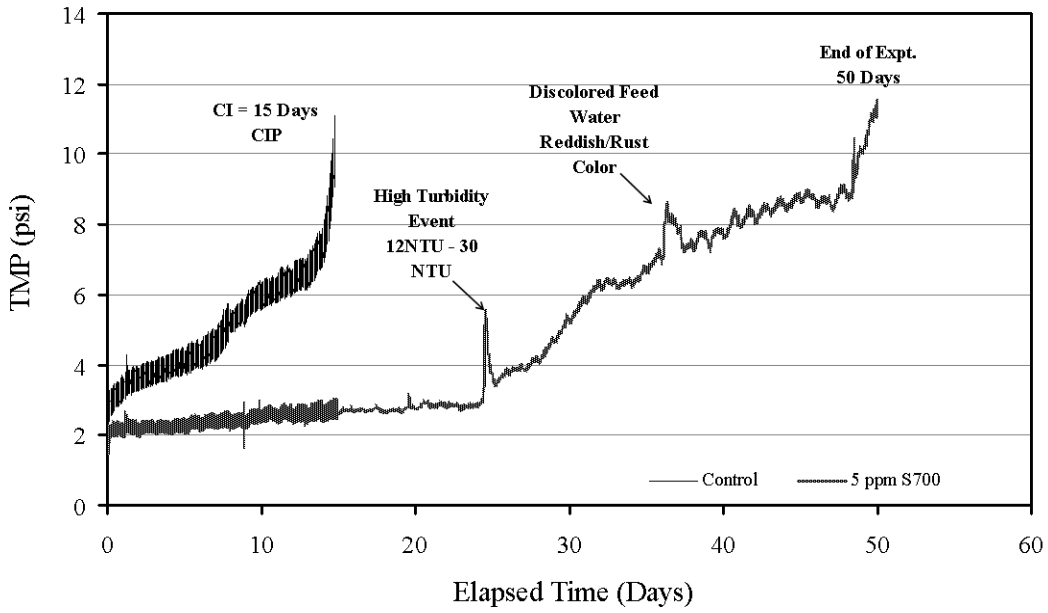

Figure 4.24. Performance of MF pilot unit with 5 mg/L of S700 coagulant in the feedwater.

The final study was completed with 2.5 mg/L of S700 coagulant added to the MF feedwater. The 2.5 mg/L S700 concentration was less effective in extending the CI compared to the 5 and 10 mg/L concentrations, but it was effective in decreasing the overall operational TMP requiring less energy to produce the same volume of water (Figure 4.25). During the 2.5-mg/L S700 testing period, the control unit CI was 25 days, whereas the S700 pilot unit CI increased to 38 days, which represented a 13-day (52%) increase in CI.

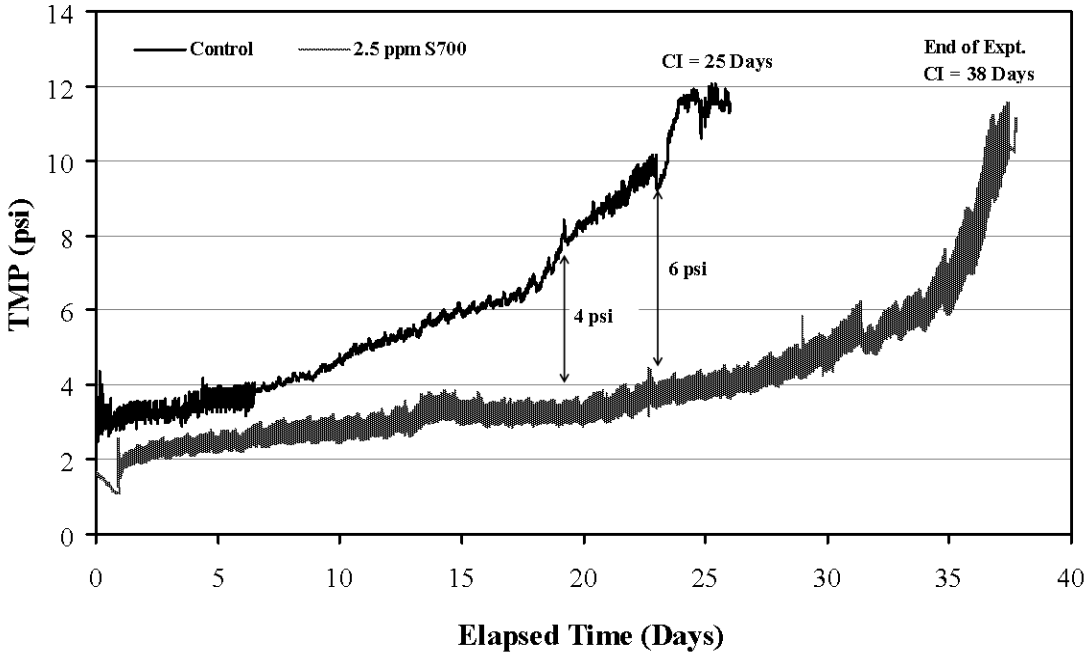

Figure 4.25. Performance of MF pilot unit with 2.5 mg/L of S700 coagulant in the feedwater.

4.6.3.3 Impact of Aluminum Coagulant Bleedthrough on Downstream RO Process

Coagulant S700 is aluminum based; therefore, there was concern that the presence of excess aluminum in the MFE (i.e., RO feedwater) could contribute to aluminum silicate scale formation on the RO membranes. The total aluminum concentrations in the MFF, MFE, and MFC were measured during each S700 MF pilot study and compared to control values (Figure 4.26). Addition of 2.5 mg/L S700 as a pretreatment did not increase the total aluminum concentration in MFF, MFE, or MFC compared to the control. At 5 mg/L S700 pretreated MFF, the aluminum concentration increased from 22 µg/L in the control to 337 µg/L in the MFF after S700 addition. The aluminum in the MFE increased from 11 mg/L in the control to 58 mg/L in the pretreated feedwater. And finally, the aluminum concentration increased from 27 mg/L in the control to 1310 mg/L in the MFC of the pretreated water. The 10 mg/L S700 pretreated MFF aluminum concentration increased from 14 mg/L in the control to 402 mg/L when S700 was added, MFE increased from 9 mg/L to 57 mg/L, and MFC increased from 45 mg/L to 1540 mg/L. This data revealed that not all of the coagulant was tied up in the MF filter cake when the dosing concentration exceeded 5 mg/L. Although it is alarming to see an increase of the total aluminum concentration in the MFE in both the 5 and 10 mg/L pretreated tests, the majority of the total aluminum added in the MFF was removed by the MF process. The 5-mg/L S700 MFF total aluminum concentration decreased by 83% in the MFE, and the 10-mg/L S700 MFF total aluminum concentration decreased by 86% in the MFE. The exact form of the aluminum is not known. Because aluminum ion can form silicates, they are unlikely to form from the polymerized aluminum compound found in the S700 coagulant.

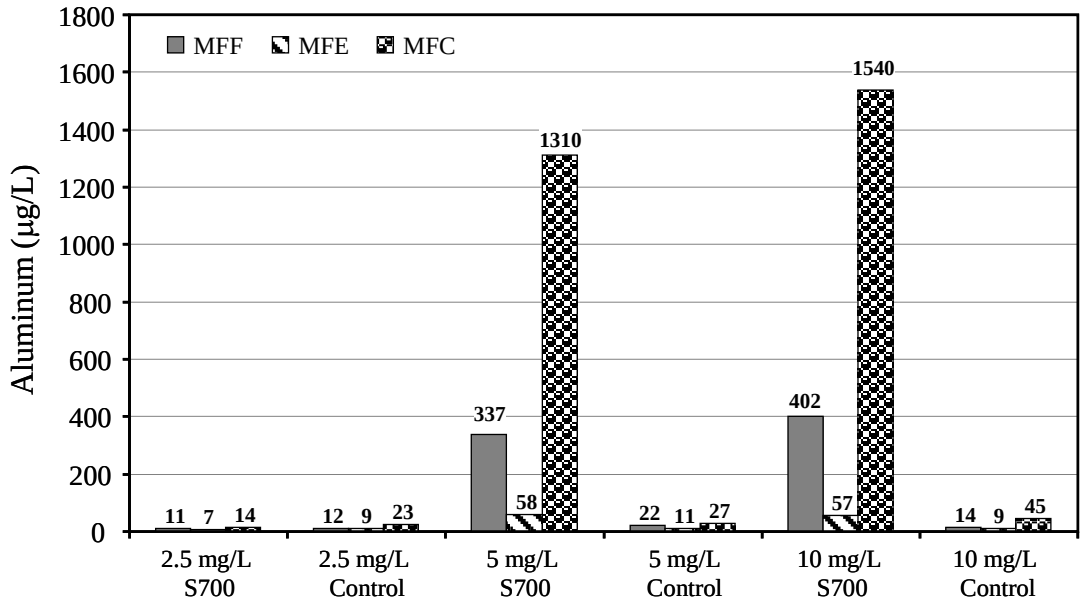

Figure 4.26. Aluminum concentration in MFF, MFE, and MFC with and without S700.

4.6.3.4 MF Membrane Autopsy Following S700 Dosing Experiment

At the end of the 2.5 mg/L S700 pilot test, one membrane from each MF pilot unit was removed and autopsied. The outside casings of both MF elements were inspected for integrity and were found to be in good condition. The outside casings of the 2.5 mg/L S700-treated elements appeared much cleaner compared to the control membranes (Figures 4.27, 4.28,

and 4.29). The casing of the control element that faced the window was covered with a thick, brown, slimy layer that appeared to be a combination of EPS and algae (Figure 4.29A). The back of the element facing the inside of the pilot reservoir did not have the same appearance (Figure 4.29B). The S700-pretreated element appeared much cleaner with some algae growing at the very top of the module, but the casing did not have the same slimy brown growth found on the control (Figures 4.28, 4.29C, and 4.29D). A black precipitate was found inside the end caps of the control element (Figure 4.27C) but not in the S700-treated element (Figure 4.28C). Overall, external appearance of the S700-pretreated MF element was much cleaner than the control MF element.

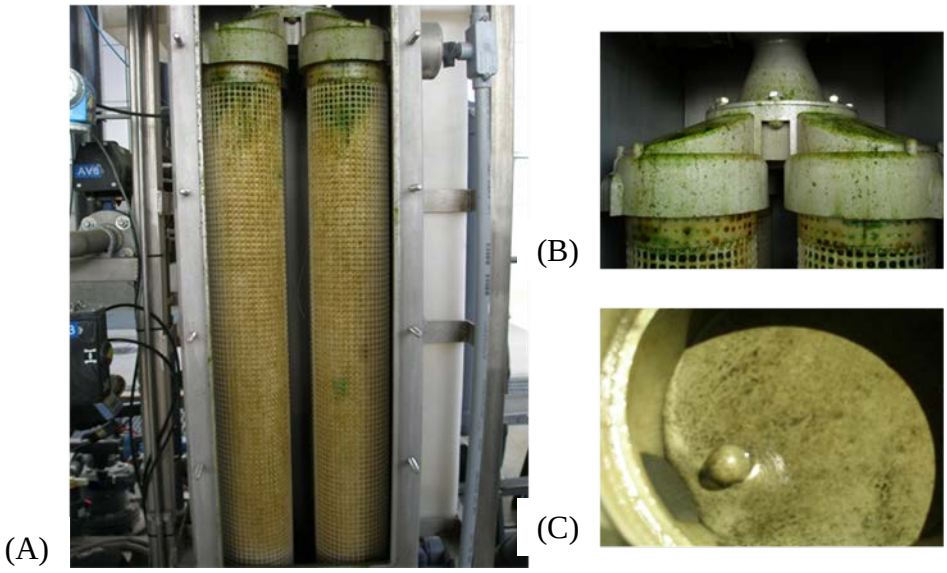

Figure 4.27. MF control elements after 25 days of operation: (A) fouled control membranes, (B) fouled element caps, and (C) inside of fouled MF cap.

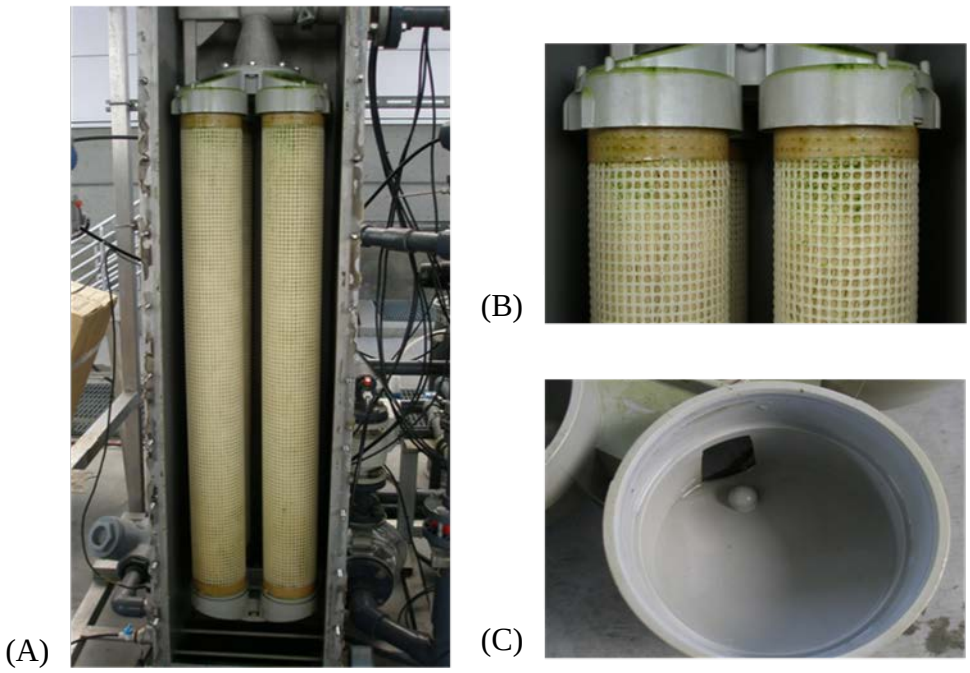

Figure 4.28. MF elements operated with 2.5 mg/L S700-pretreated MF feedwater after 36 days: (A) fouled membranes, (B) fouled MF caps, and (C) inside of fouled MF cap.

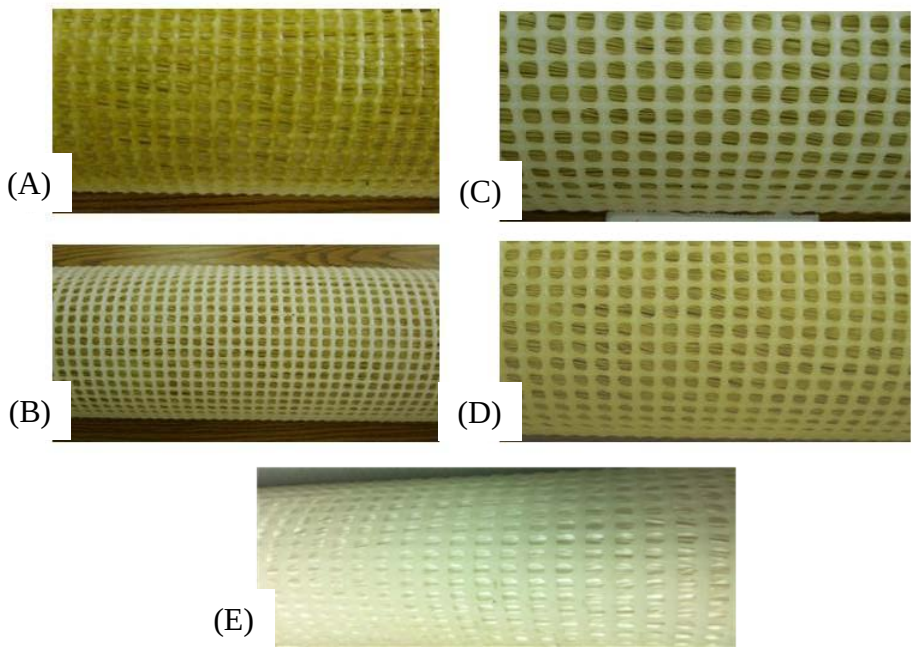

Figure 4.29. Fouled MF element: (A) control facing the window, (B) control facing away from the window, and 2.5 mg/L S700-pretreated MF element: (C) facing window, (D) facing away from the window, and (E) clean unused MF element.

The casings were removed from both elements, and membrane fibers were cut for analysis. Both control and S700 membranes were discolored with a brownish green tint (Figure 4.30). The discoloration is very evident when compared to a clean MF membrane. As observed in Section 4.5.3, heaviest fouling was observed on the top and bottom sections of the control element (Figures 4.30A and 4.30C). The S700 membrane fouling also was heaviest at the top (Figure 4.30) with the middle and bottom sections having similar coverage (Figures 4.30E and 4.30F).

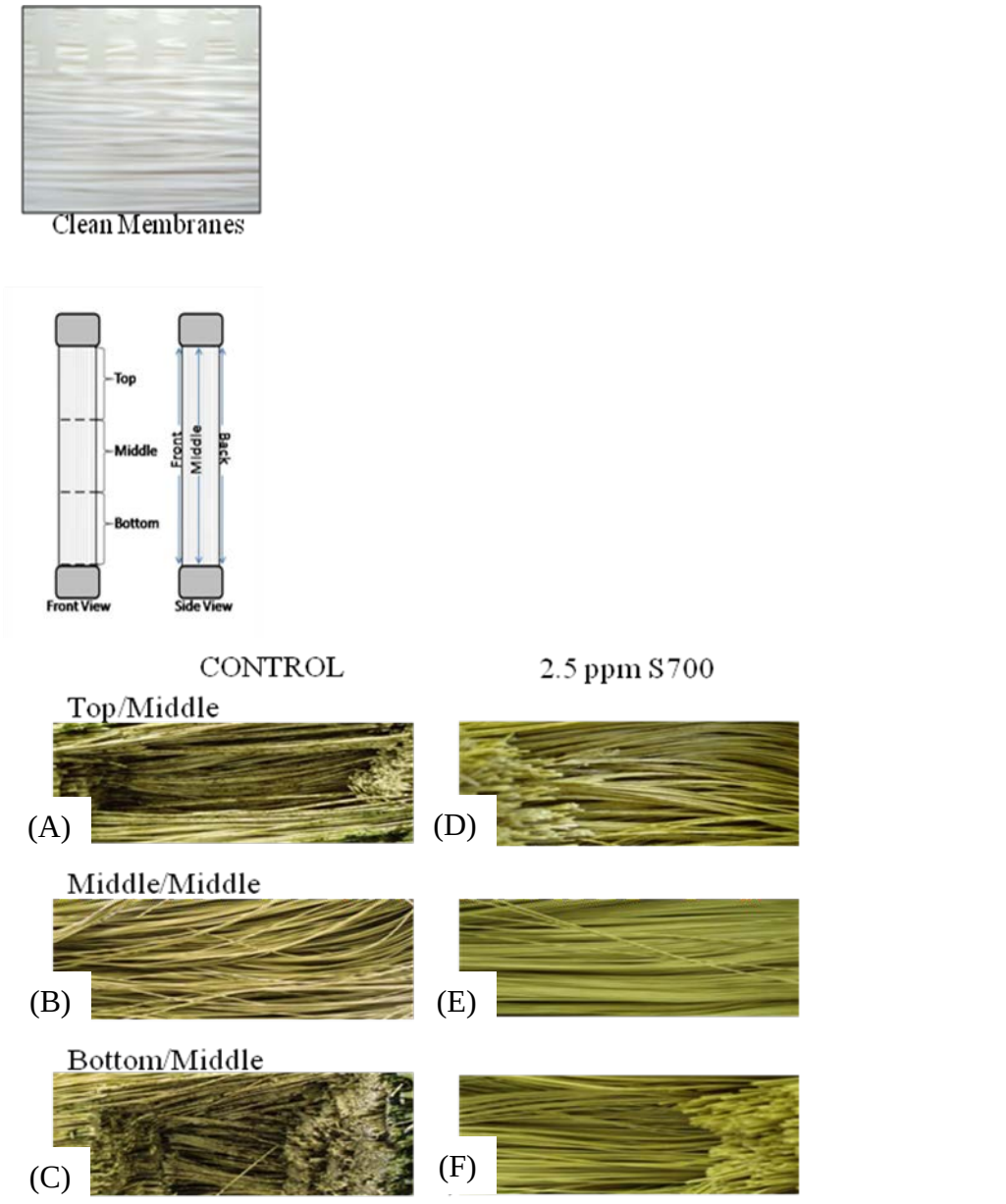

Figure 4.30. Fouled MF control element: (A) control top/middle, (B) control middle/middle, (C) control bottom/middle, and fouled 2.5 mg/L S700-pretreted MF element: (D) top/middle, (E) middle/middle, and (F) bottom/middle.

Surface microscopy images showed both S700-pretreated and control membrane surfaces were fouled, but the density and thickness of the fouling layer varied. The control membrane

appeared to have heavier fouling compared to the S700-pretreated membrane (Figures 4.15 and 4.31). The top portion of the control membrane contained the thickest fouling layer (Figure 4.15A). Toward the middle, the fouling was lighter and less dense (Figure 4.15B). Fouling of the bottom of the membrane (Figure 4.15C) appeared slightly heavier than the middle but not as heavy as the top.

The S700 membrane appeared to be less fouled, and fouling was more evenly distributed across the fiber surface (Figure 4.31). Fibers of the S700-pretreated membrane were not covered with the dark thick patches of foulant observed on the control fibers. The membrane also appeared to be more heavily fouled at the top but less than the fibers of the control.

All membrane sections were analyzed for total CHO and protein (Figures 4.32 and 4.33). The data indicated that both carbohydrate and protein concentrations were highest at the top portion of the membranes for both control and S700 membranes, and both CHO and protein deposition was higher in the control membrane as compared to the S700-pretreated membrane. At the top of the control membrane, the CHO and protein accumulation was higher in the middle and back of the MF membrane bundle. At top of the 2.5 mg/L S700-pretreated membrane, the CHO and protein accumulation varied (indicated by the higher standard deviation). The variability in the lower sections of the membrane was much less compared to the top. These data support earlier laboratory results (Section 4.4.3) that accumulation of foulants proceeds from the top end of the membrane element to the bottom. CHO and protein accumulated at higher rates at the top of both the control and S700-pretreated membranes, but the presence of S700 appeared to attenuate their accumulation.

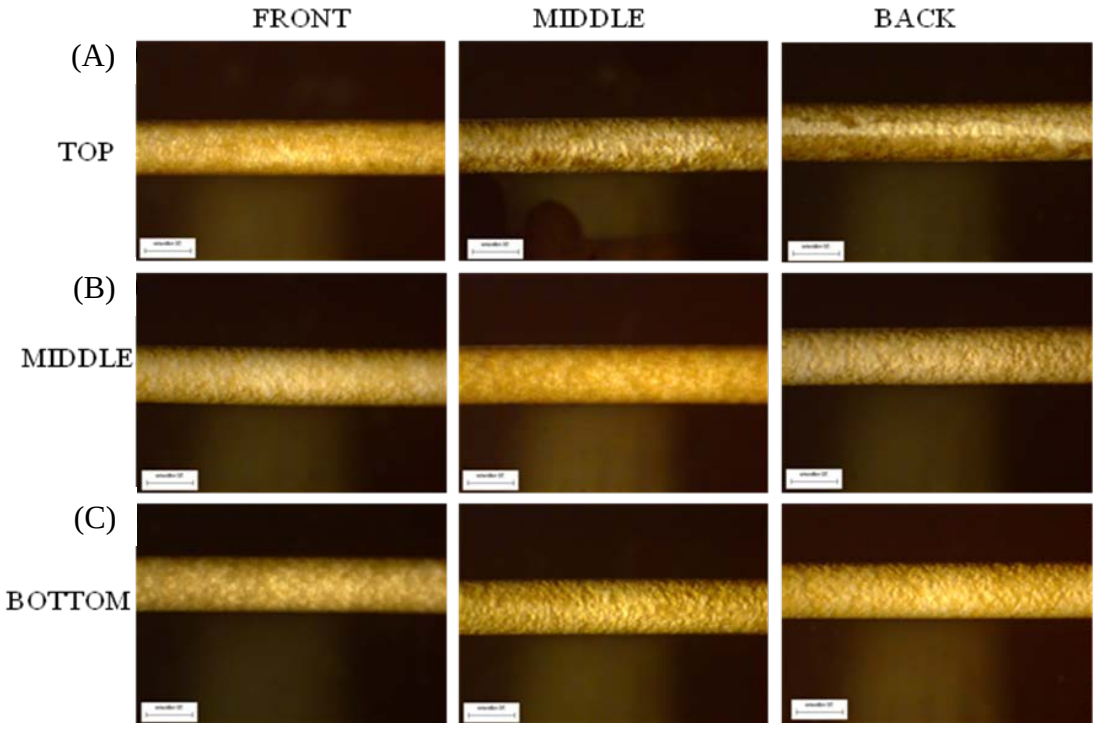

Figure 4.31. Surface microscopy of fouled 2.5 mg/L S700-pretreated MF membrane fiber: (A) top section from front to back, (B) middle section from front to back, and (C) bottom section from front to back.

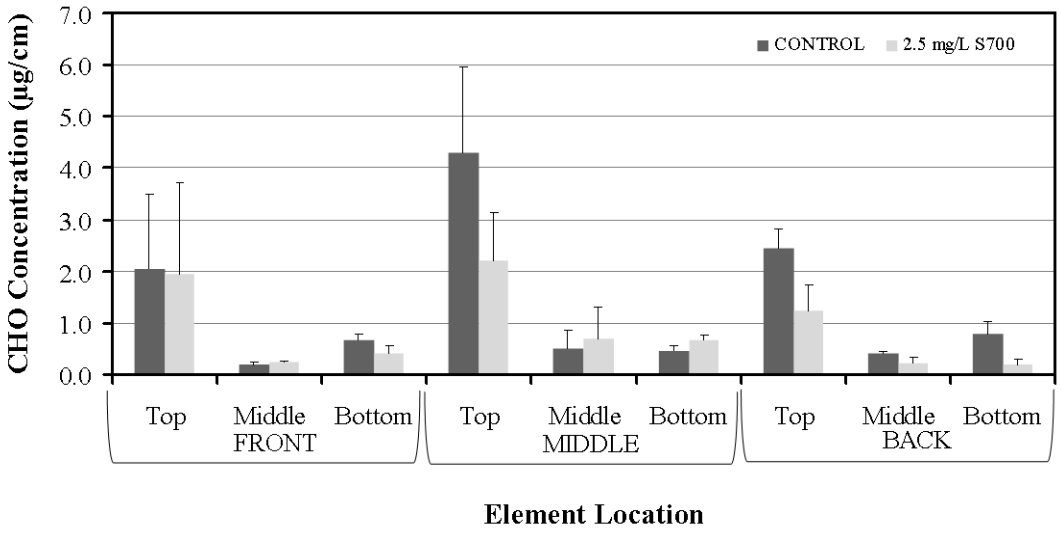

Figure 4.32. Carbohydrate analysis of control and 2.5 mg/L S700-pretreated MF membrane.

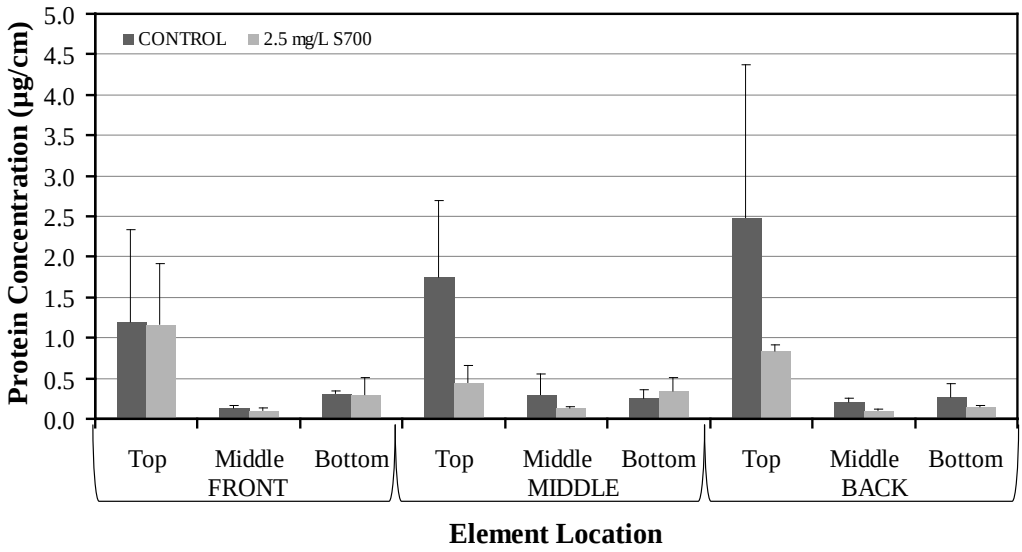

Figure 4.33. Protein analysis of control and 2.5 mg/L S700-pretreated MF membrane.

SEM analysis was performed on the top, middle, and bottom sections of the control and S700-pretreated membranes. Surfaces of the fouled membranes were compared to a clean PP MF membrane (Figure 4.34). The clean PP MF membrane SEM cross section revealed multiple layers of intricately woven voids and pockets with smooth walls and surfaces (Figures 4.34A and 4.34B). The polymer surface appeared smooth with an average pore diameter of 0.2 µm (Figures 4.34C and 4.34D).

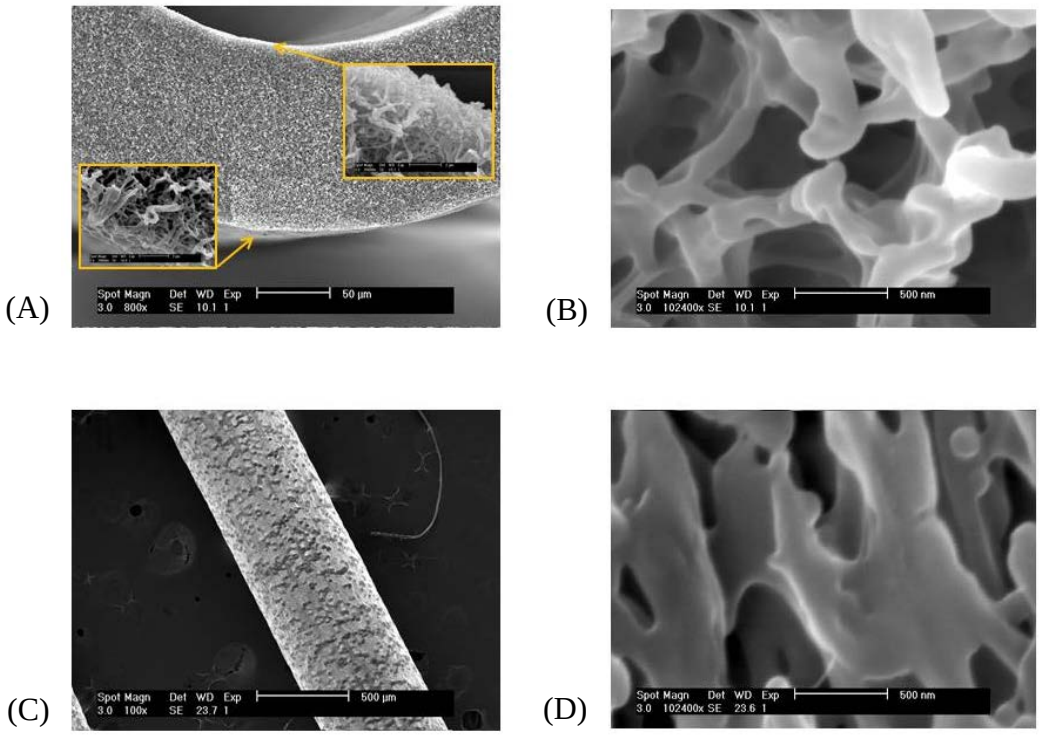

Figure 4.34. SEM of clean PP MF membrane: (A) low magnification at 800 times cross section of clean PP MF membrane, (B) membrane cross section at 102,400 times magnification with clean and smooth voids, (C) low magnification of the surface of a clean MF hollow fiber membrane, and D) outer surface of membrane fiber at 102,400 times magnification.

The fouled membranes exhibited nanoparticulate fouling on the surface and inside the membrane matrices. Top sections of the membrane bundles accumulated heavier fouling than the middle and bottom sections, which was consistent with the visual data and protein and CHO data. Overall, the control membrane fouling appeared to be more abundant than the S700-pretreated membrane, which also was consistent with previously observed results. The control cross section displayed heavy fouling at the surface with nanoparticulates that deeply penetrated into the MF matrix (Figures 4.35, 4.36, and 4.37). However, although the S700 membrane fouling also was concentrated at the surface, fewer nanoparticles penetrated into the matrix (Figures 4.38, 4.39, and 4.40).

SEM cross sections of the untreated MF membrane showed heaviest fouling at the top of the element from front to back. The middle of the control module also was heavily fouled with most of the fouling in the middle of the module. The bottom of the control module was heavily fouled in the front, which faced the window of the pilot unit. Less fouling was observed in the middle and back of the module. From top to bottom of the control membrane, the cross section showed evidence of nanoparticualte fouling (Figures 4.35B, 4.36B, and 4.37B). The presence of these nanoparticulate foulants are presumed to impede water passage, hence, increasing membrane TMP.

The S700-pretreated membrane, as with the control membrane, showed heavy fouling at the top of the membrane module (Figures 4.38A, 4.39A, 4.40A), but most of the foulant remained at the membrane surface and did not enter the membrane matrix. The void spaces

also appeared to be coated with nanoparticulates but not to the extent observed in the untreated membrane. The overall nanoparticulate load in the bottom part of the S700-pretreated membrane appeared to be less than the top and the middle membrane areas.

The cross sections of the S700-pretreated membrane, top to bottom and front to back, show a thick fouling layer on the outside edge of the membrane with less fouling inside the membrane matrix compared to the untreated membrane.

The surfaces of both membranes were covered with a coalescent lawn of nanoparticles obstructing the PP membrane topography (Figures 4.35C, 4.36C, 4.37C, 4.38C, 4.39C, and 4.40C). However, the control nanoparticulate topography appeared rougher compared to the S700-pretreated surface.

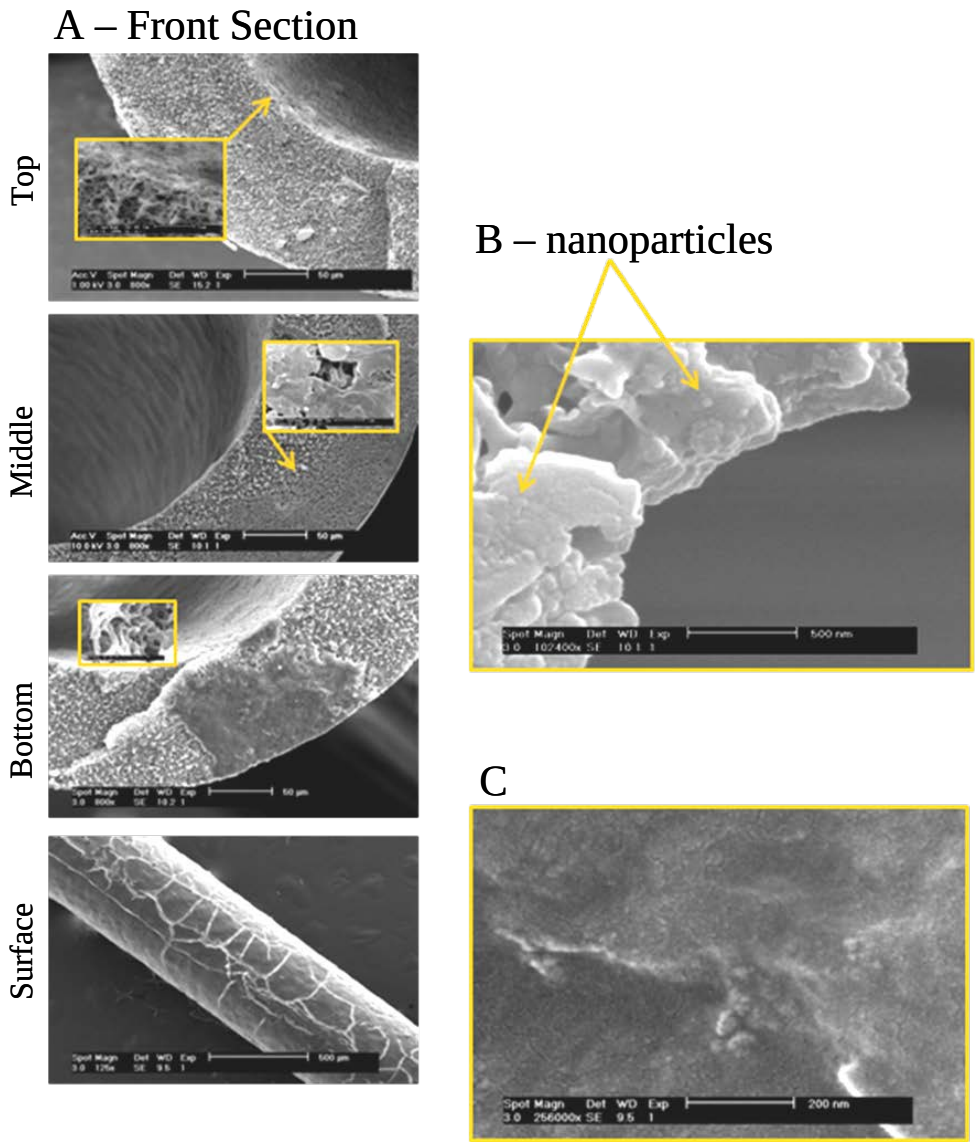

Figure 4.35. SEM of the front section of the fouled control MF membrane: (A) surface and membrane cross sections with nanoparticles penetrating the membrane matrix, (B) nanoparticles deposited inside the voids of the membrane matrix (102,400 times magnification), and (C) fiber surface covered with foulant (256,000 times magnification).

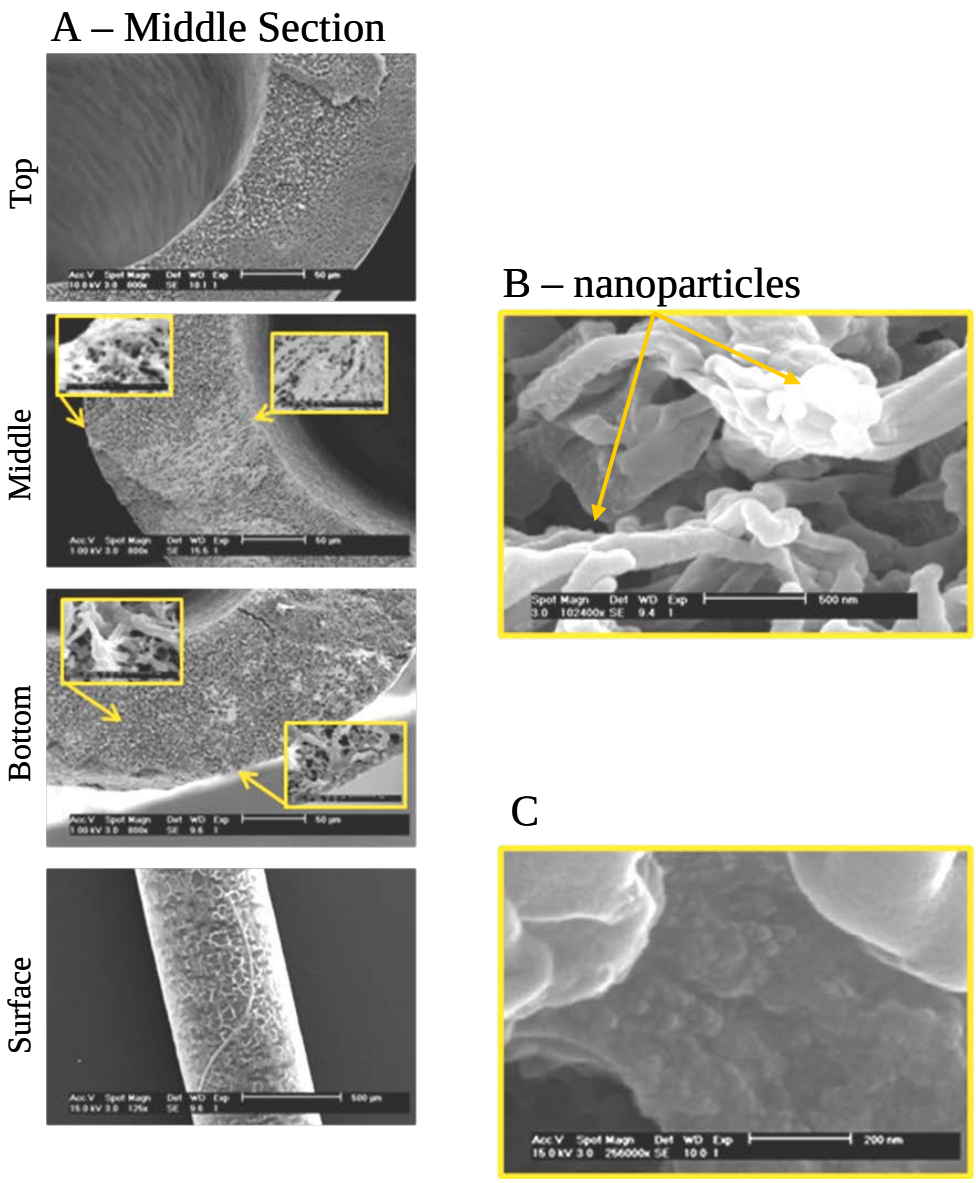

Figure 4.36. SEM of the middle section of the fouled control MF membrane: (A) surface and membrane cross sections with nanoparticles penetrating the membrane matrix, (B) nanoparticles deposited inside the membrane voids (102,000 times magnification), and (C) fiber surface covered with foulant (260,000 times magnification).

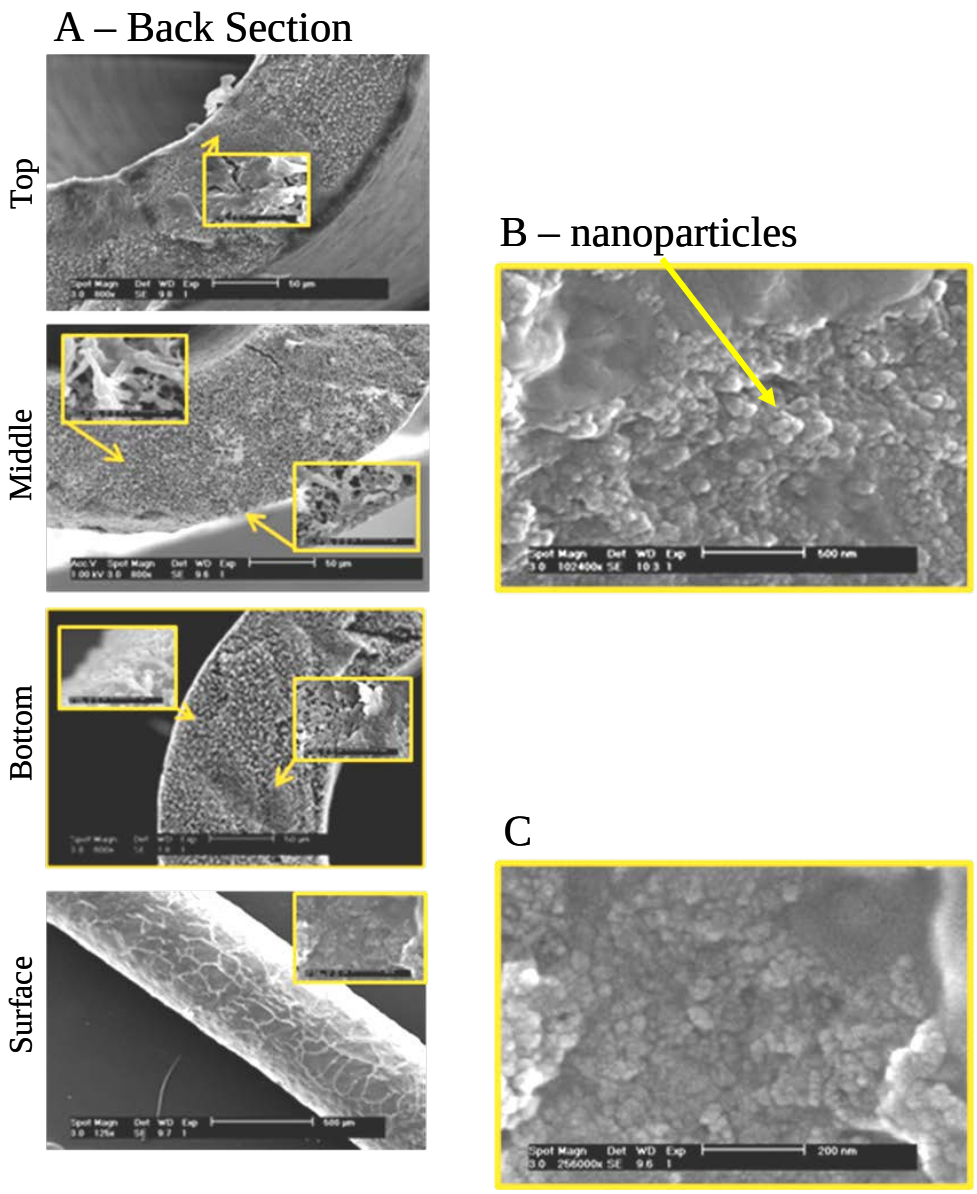

Figure 4.37. SEM of the back section of the fouled control MF membrane: (A) surface and membrane cross sections with nanoparticles penetrating the membrane matrix, (B) nanoparticles deposited inside the membrane voids (102,000 times magnification), and (C) fiber surface covered with nanoparticulate foulant (200,000 times magnification).

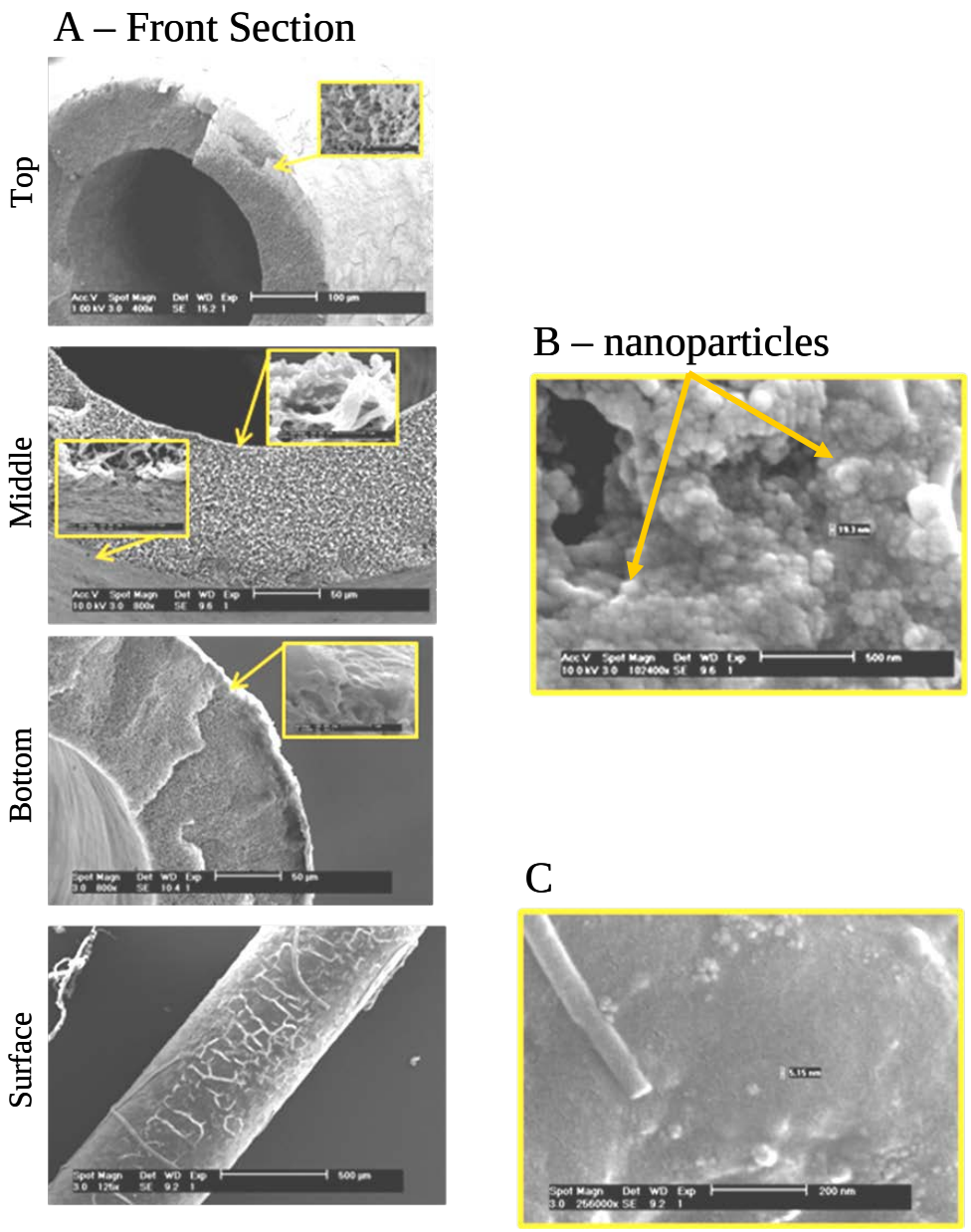

Figure 4.38. SEM of front section from 2.5 mg/L S700-fouled MF membrane: (A) surface and membrane cross sections with nanoparticles penetrating the membrane matrix, (B) nanoparticles deposited inside the membrane voids (102,000 times magnification), and (C) fiber surface covered with nanoparticulate foulant (200,000 times magnification).

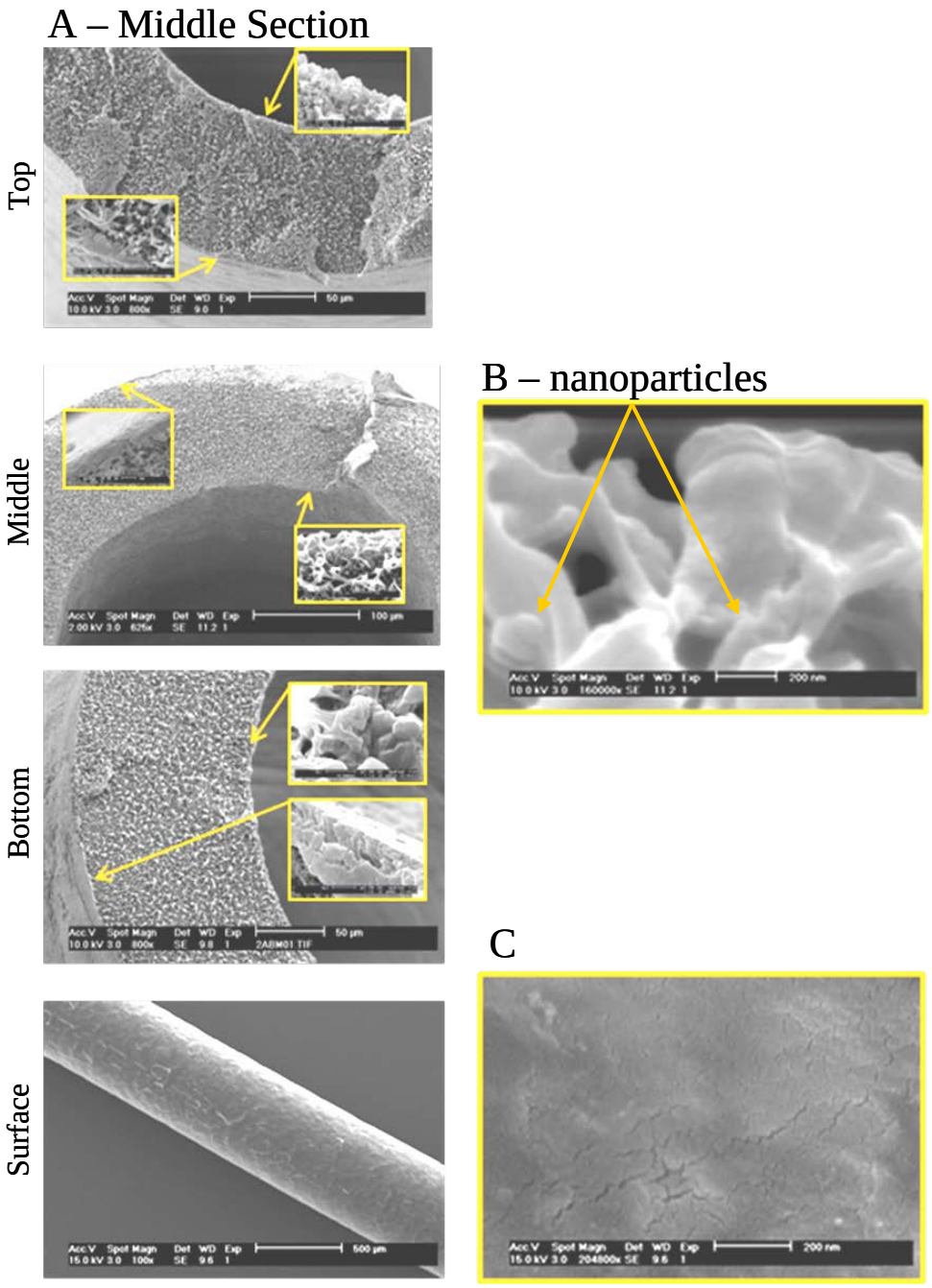

Figure 4.39. SEM of middle section from 2.5 mg/L S700-fouled MF membrane: (A) surface and membrane cross sections with nanoparticles penetrating the membrane matrix, (B) nanoparticles deposited inside the voids of the membrane matrix (160,000 times magnification), and (C) fiber surface revealing nanoparticulate-covered surface (204,000 times magnification).

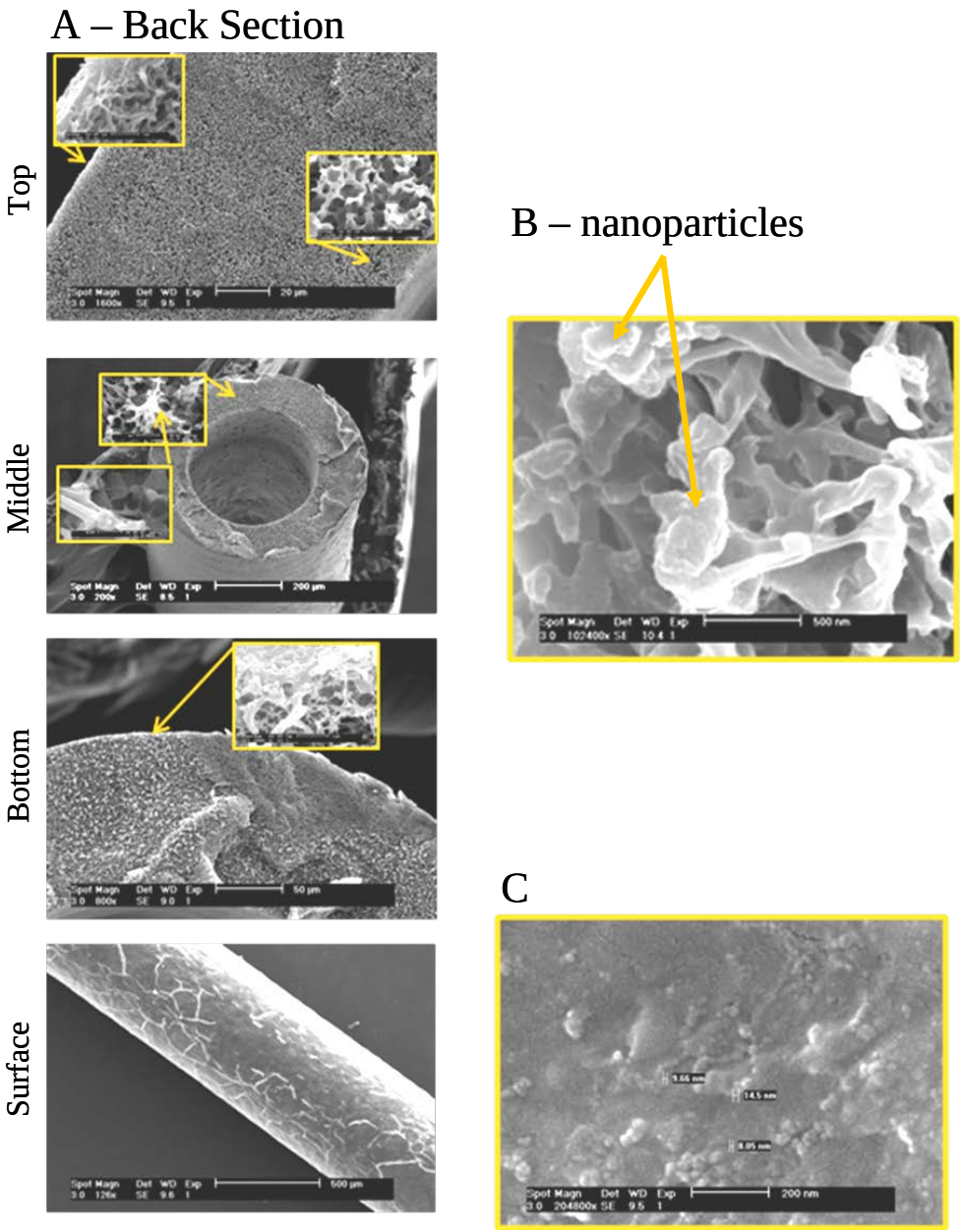

Figure 4.40. SEM of back section from 2.5 mg/L S700-fouled MF membrane: (A) surface and cross sections with nanoparticles penetrating the membrane matrix, (B) nanoparticles deposited inside the voids of the membrane matrix (102,400 times magnification), and (C) membrane surface covered with thick layer of nanoparticles (204,000 times magnification).

The polypropylene membrane is composed of C and H exclusively. Other elements detected were most likely associated with compounds that adhered to the PP membrane material (as foulants or adhering to the foulants). The following elements were identified throughout the membrane matrix (cross sections) and on the membrane surfaces on both the untreated and S700-pretreated MF membranes: C, O, F, Na, Si, P, S, Cl, Ca, Al, K, Fe, and Mg. There was little difference between the control and S700-pretreated MF fibers (Table 4.2).

Table 4.2. EDS Analysis of Top Section of Control and 2.5-mg/L S700-Pretreated Membranes

	Top Cross Section		Top Surface	
Element	**0 mg/L**	**2.5 mg/L**	**0 mg/L**	**2.5 mg/L**
C	+	+	+	+
O	+	+	+	+
F	+	+	+	+
Na	+	+	+	+
Si	+	+	+	+
P	+	+	+	+
S	+	+	+	+
Cl	+	+	+	-
Ca	+	+	+	+
Al	+	+	+	+
K	+	+	-	-
Fe	-	-	+	+
Mg	-	+	+	-

4.6.4 MF Precoagulation Conclusions

The Sumaclear 700 coagulant successfully aggregated nanoparticles present in MFF into microparticles greater than 0.2 µm. At the highest concentration of S700 tested, 10 mg/L, the run time between CIP was in excess of 82 days compared to the 21 days for the control MF—greater than 3.9 times longer. At a concentration of 5 mg/L, the CI was increased from 21 to 54 days. At the lowest concentration tested, 2.5 mg/L, the CI increased from 25 days for the control to 36 days—1.4 times longer. At all three concentrations for all three experiments, the delta-P for the S700-pretreated membranes was significantly lower. Results from this study demonstrated that coagulants added to the MF feedwater can bind nanoparticles into larger microparticles, which prevent them from entering the membrane matrix. Coagulation of these nanoparticles improved the performance of the hollow fiber polypropylene membrane by increasing the cleaning interval and decreasing the operating differential pressure (delta-P).

4.7 Impact of MF Precoagulant Breakthrough on RO Performance

Coagulant that passes through the MF membrane into the effluent has the potential to undergo further reaction downstream. The coagulant is aluminum-based; therefore, the potential exists for it to react with other constituents to form aluminum silicates. The coagulant also may concentrate in the reject or brine of the RO process, fall out of solution, i.e. precipitate, foul the membrane surface, and significantly restrict membrane water flux. A

series of tests were conducted to determine the potential for the S700 coagulant in the MFE to form aluminum silicate and foul the first stage and third stage RO membranes.

4.7.1 Experimental Methods

4.7.1.1 Simulated First Stage S700 RO Exposure—2.5 mg/L Precoagulation Breakthrough

Two identical RO test cells were connected to the effluent from the 2.5 mg/L S700-pretreated MF pilot unit, and two RO test cells were connected to the product of the control MF pilot unit (Figure 4.41). Each test cell was equipped with a 4 × 6 in. flat sheet Hydranautics ESPA2 RO membrane and operated at 0.4 gpm (12 gfd). Performance measurements were taken manually twice a day (morning and afternoon) and included feed and product conductivity (µS/cm), influent turbidity (NTU), total dissolved solids (TDS), and feed and product pressure (psi). RO membranes were removed and analyzed by SEM/EDS.

Figure 4.41. RO flat sheet test cells.

4.7.1.2 Simulated Third Stage S700 RO Exposure—30 mg/L RO Concentrate

The same flat sheet RO test cell cells were set up and fed with RO brine amended with 30 mg/L S700 coagulant, which simulated an ~5 mg/L MF breakthrough into the feedwater of an three-stage RO train operating at 88% recovery. The S700 membrane performance was compared to a membrane that did not receive coagulant pretreatment (control). Both membranes were operated under identical conditions simulating the 0.4 gpm (2 gfd) third-stage RO process. Membrane performance parameters were measured twice a day and included conductivity, total dissolved solids, and feed and product pressure. At the end of the experiment, membranes were removed and SEM/EDS and light microscopy were used to evaluate surface fouling.

4.7.2 Results and Discussion

4.7.2.1 RO Membrane Performance—2.5-mg/L S700 First Stage Breakthrough

The specific flux of the control and S700-pretreated membranes fluctuated between 0.104 and 0.120 gfd/psi for approximately 14 days (Figure 4.42). On Day 14 the specific flux for both membranes dropped below 0.106 gfd/psi and did not recover. On Day 18 the pressure of the control membrane began to rise and the rejection started to drop, but at the same time the pressure and rejection of the S700-pretreated unit remained constant. On Day 20 the TMP of the control MF unit started to affect the feedwater supply to the RO test cells. To prevent damage to the RO feed pumps due to inadequate water supply, the RO performance test of the control membrane was terminated.

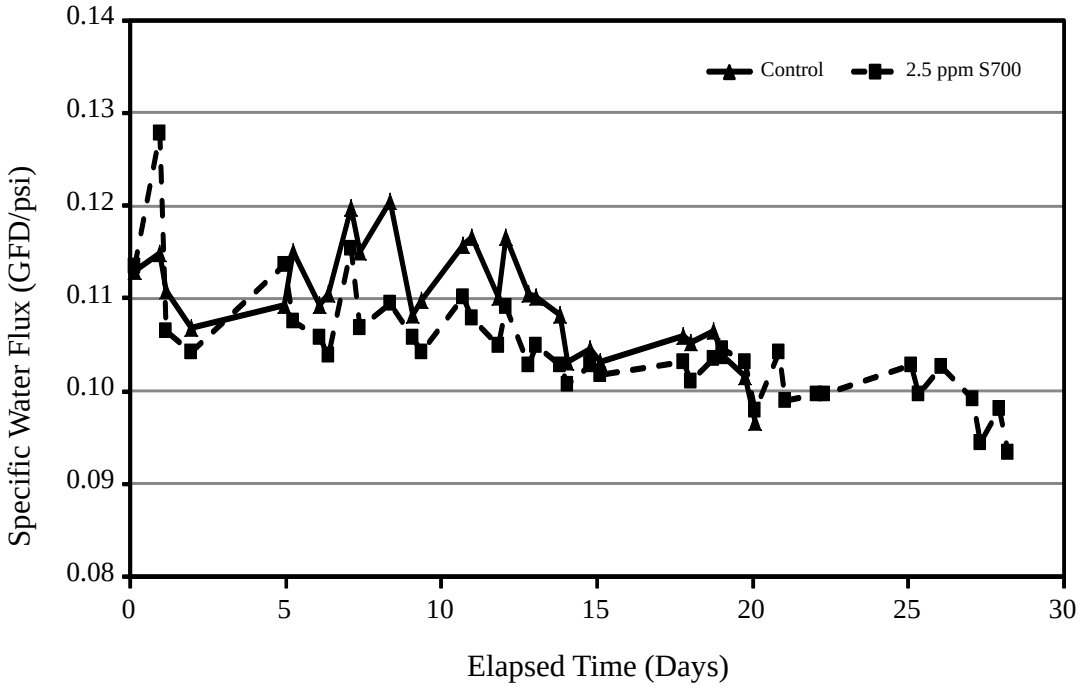

Figure 4.42. Specific flux (gfd/psi) of flat sheet RO membranes operated on MFE from the 2.5 mg/L S700 treated MF pilot unit and control.

On Day 22, the pressure of the S700-pretreated RO unit started to climb and then stabilized over the next 4 days. On Day 26 the pressure began to rise and the specific flux started to decline, and after 28 days the S700-pretreated MF pilot unit was shut down because of increased TMP. As in the control unit, a continuous supply of feedwater to the RO test cells could not be guaranteed; therefore, the test was terminated to prevent pump malfunction.

The salt rejection remained near 98.8% for the first 10 days for both flat sheet RO test units (Figure 4.43). Between Days 10 and 15, the rejection in both units began to fluctuate, with the control dropping to 98.7% by Day 20. During the same time period, the S700 unit rejection improved reaching as high as 99%. On Day 20 the control unit was taken out of service due to insufficient feedwater supply from the MF pilot unit, while the rejection of the S700-pretreated membrane remained at 98.9%. The morning of Day 25, the rejection of the

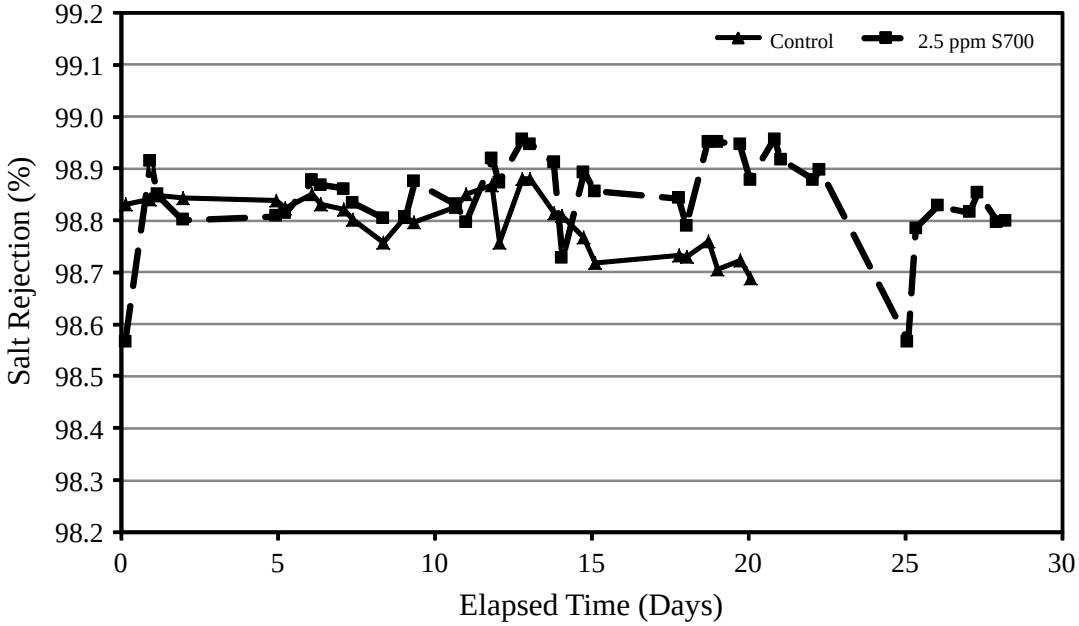

Figure 4.43. Percentage (%) salt rejection of flat sheet RO membranes.

S700-pretreated membrane dropped to 98.6%, but by the afternoon it returned to 98.8% and remained at or above 98.8% until the test was completed on Day 28. The results suggest that pretreating the MF feedwater with as much as 2.5 mg/L of S700 coagulant will not have an adverse effect on first-stage RO performance when compared to a control membrane. However, RO units in the AWPF often run as long as 6 months before a CIP is required. It is not known if adsorbed S700 coagulant will respond to the standard cleaning protocol associated with RO membranes.

The TDS concentrations (Figure 4.44) in the RO feedwater, RO control effluent, and S700-pretreated RO effluent remained consistent during the testing period with no significant fluctuations. Both RO membranes produced effluents with similar water quality.

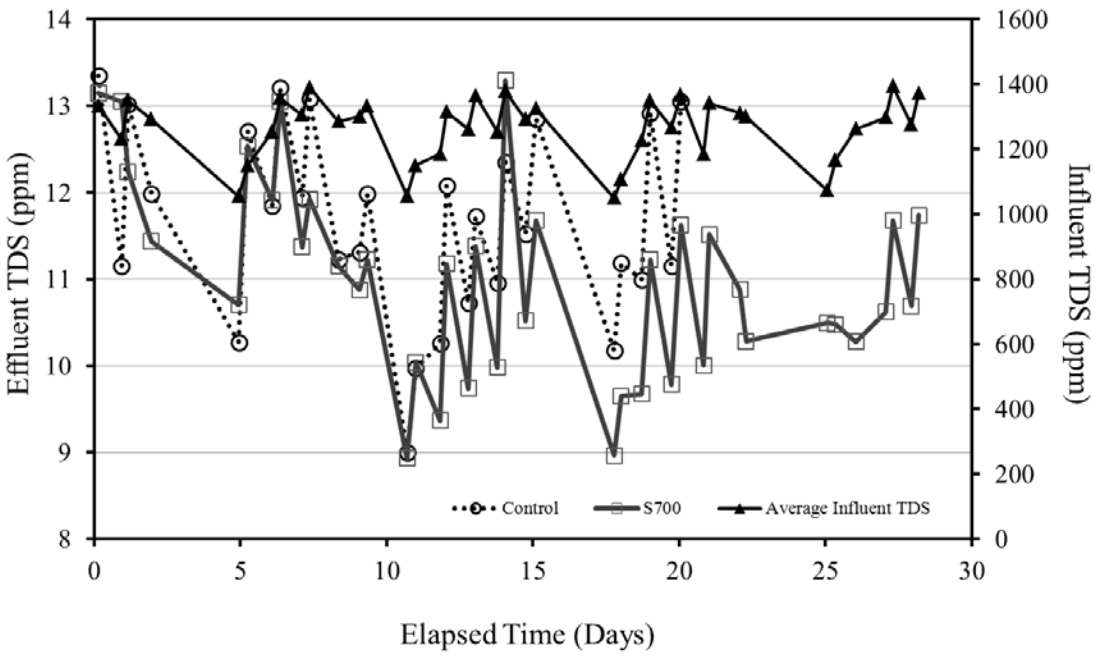

Figure 4.44. TDS concentration (mg/L) in RO feedwater, control RO effluent, and 2.5 mg/L S700-pretreated RO effluent.

4.7.2.2 RO Membrane Surface Analysis—2.5-mg/L S700 First Stage Breakthrough

Fouled ESPA2 RO membranes were removed for SEM and EDS analysis. The test membranes did not have a thick biofilm or any macroscopic fouling. Both control and S700-pretreated test membranes appeared similar to a clean new membrane.

Scanning electron microscopy of a clean ESPA2 membrane revealed a polyamide polymer topography that was rough with peaks and valleys where nanoparticles could deposit and firmly attach (Figure 4.45). SEM images of the surfaces of the test membranes revealed that both membranes were coated with a uniform layer of nanoparticles (Figures 4.45). The lawn of nanoparticles occluded the membrane surface, and by doing so, presumably affected molecular interactions between the feedwater and membrane. The EDS analysis detected the presence of C, O, Na, P, S, Ca, and Cl on both the control and S700 membranes (Table 7.13). Neither Al nor Si were detected on either the control or test membranes. Therefore, at a concentration of 2.5 mg/L, the S700 coagulant did not appear to contribute to the formation of aluminum silicates. The presence of P and S is indicative of biological fouling. However, whole bacteria were not observed in large quantities on the surface of either membrane.

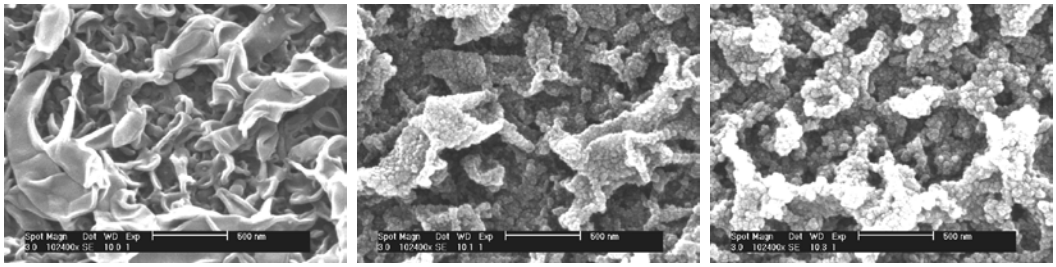

Figure 4.45. SEM of ESPA2 RO membranes, clean (left), fouled control (middle), and 2.5 mg/L S700-pretreated MFF (right).

Table 4.3. EDS Analysis of Control and 2.5 mg/L Exposed RO Membranes

Element	Control	2.5 mg/L S700
C	+	+
O	+	+
Na	+	+
P	+	+
S	+	+
Cl	+	+
Ca	+	+
Si	-	-
Al	-	-

4.7.2.3 Third Stage RO Performance with Simulated 5 mg/L S700 Breakthrough

A 5-mg/L S700 coagulant breakthrough into the MF effluent would theoretically concentrate six-fold by the time the RO feedwater reached the third stage. Therefore, the flat sheet membrane was exposed to a 30-mg/L concentration of S700 in order to simulate a 5-mgL coagulant breakthrough. The performance of the control membrane steadily declined for the first 2 days of operation (Figure 4.46). A significant loss in specific flux occurred on Day 2. After Day 2 the control membrane stabilized and operations remained steady. The presence of S700 coagulant in the RO feedwater had an adverse affect on the membrane performance. A steady decline in membrane specific flux occurred over a 6-day period.

The salt rejection for the two membranes is displayed in Figure 4.47. The control salt rejection fluctuated between 96.1 to 98.6% over the first 24 h. Between Day 2 and Day 6, the salt rejection continued to improve with the best reading of 98.6% on Day 6. The rejection of the S700-amended membrane varied between 96.4% (at start up) to 97.9% on the morning of Day 2. Between Day 2 and Day 3, the salt rejection dropped from 97.9% to 97.3%, and by Day 6 it decreased to 95.4%. As the salt rejection dropped, the feed pressure rose to 165 psi. The test was stopped because of an increase in pressure and decrease in salt rejection in the S700-amended RO cells. Membranes were then visually inspected, removed, and examined by SEM and light microscopy.

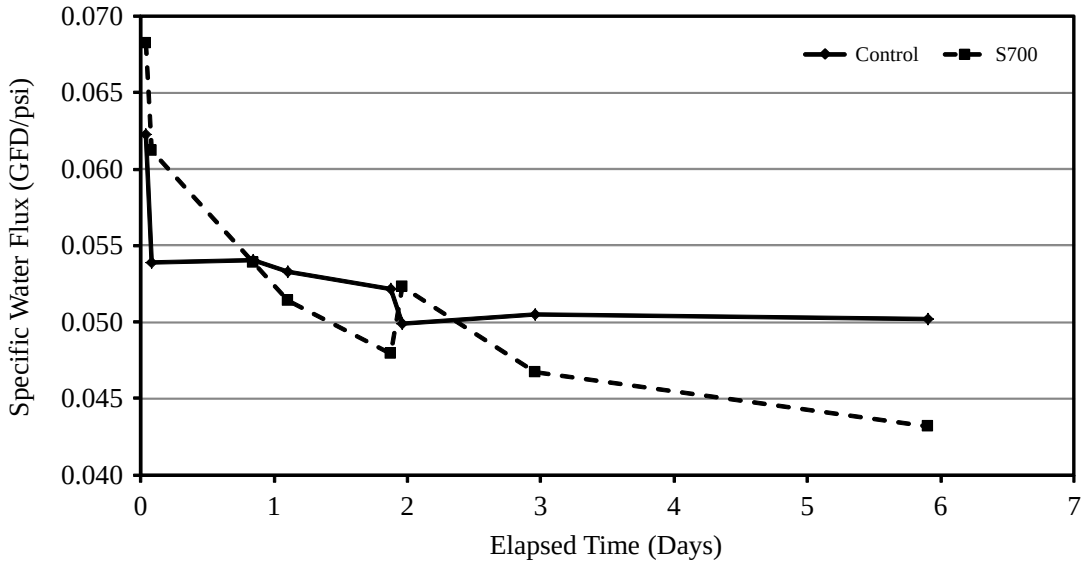

Figure 4.46. Impact of 30 mg/L S700 coagulant on RO membrane specific flux (gfd/psi).

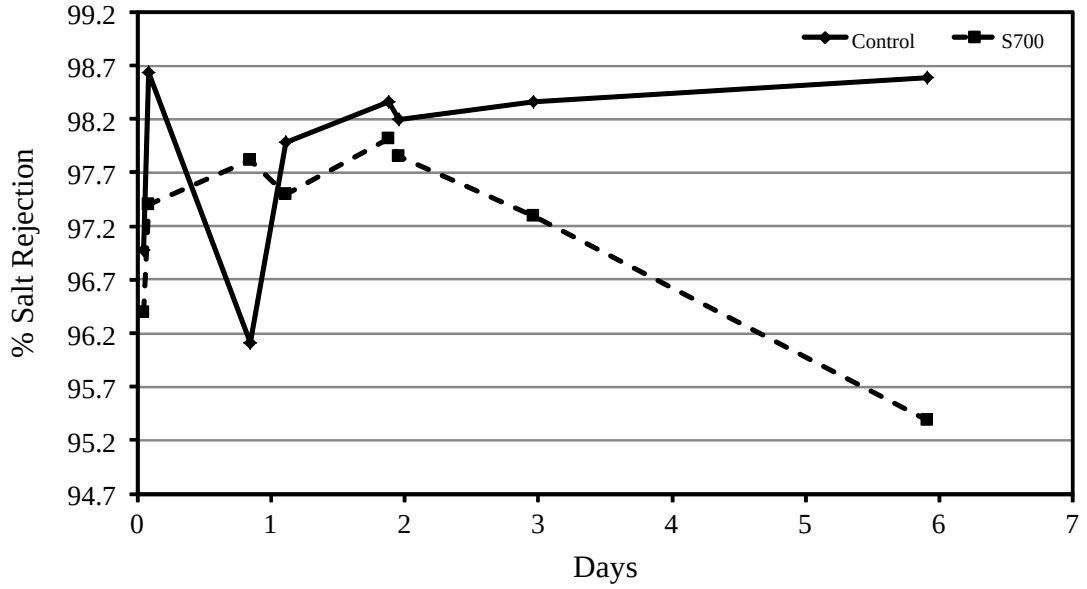

Figure 4.47. Impact of 30 mg/L S700 coagulant on the RO membrane salt rejection (%).

4.7.2.4 RO Membrane Surface Analysis after 5 mg/L S700 Breakthrough Exposure

Images of the control and S700-pretreated membranes are displayed in Figure 4.48. The control membrane appeared clean with no obvious macroscopic fouling. The S700-pretreated membrane was covered in a thick precipitate on the membrane surface and Vexar feed spacer.

Figure 4.48. Images of fouled ESPA2 control membrane (left) and membrane operated on RO concentrate/brine amended with 30 mg/L of S700 coagulant (right).

Light microscopy of the control membrane and control spacer did not reveal significant evidence of chemical or biological fouling (Figures 4.49A and 4.49B). However, images of the membrane and spacer exposed to S700 revealed a thick coating of precipitates on both surfaces (Figures 4.49C and 4.49D).

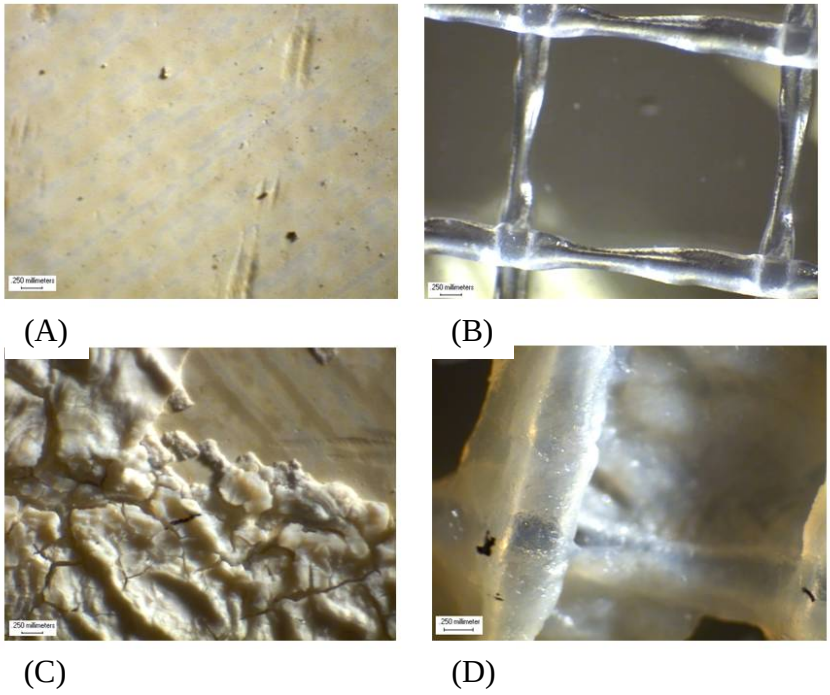

Figure 4.49. Images of ESPA2 RO membranes and feed channel spacers removed from RO test cells operated on RO concentrate with no coagulant pretreatment: (A) membrane surface, (B) spacer, (C) fouled membrane, and (D) fouled spacer from RO membrane operated on RO concentrate/brine amended with 30 mg/L S700 coagulant.

Figure 4.50 shows SEM and EDS results of the fouled control membrane. The membrane surface was covered with crystal formations that contained calcium and sulfur. Also scattered across the membrane surface were Na, Mg, S, Ca, and Cl. The Vexar feed spacer did not appear to be heavily fouled (Figure 4.50C).

Aluminum and silicon were found on the test membranes but did not appear to be crystallized. If in elemental form, they may be easily removed through standard membrane cleaning procedures.

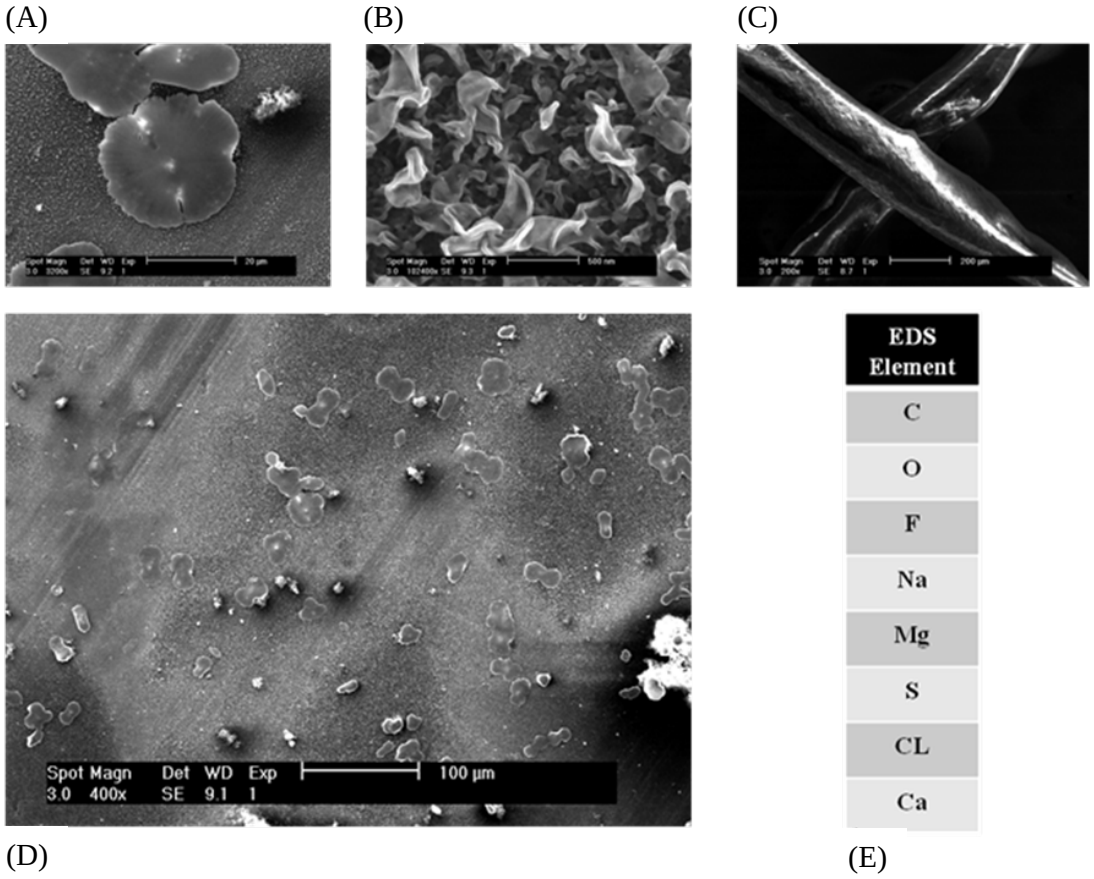

Figure 4.50. Fouled control ESPA2 membrane and spacer removed from RO test cell operated on RO concentrate with (A) crystal formation found on membrane surface, (B) membrane surface covered with nanoparticles, (C) membrane spacer, (D) membrane surface covered with crystal formations, and (E) EDS analysis of foulants covering the membrane.

SEM analysis of 30-mg/L S700-pretreated ESPA2 membrane (Figure 4.51) confirmed the presence of a thick molecular fouling layer on the membrane surface. The membrane surface topography was completely obstructed by a precipitate. EDS analysis identified Ca, Al, and Si as the major elements in the precipitate. Also, P, F, Na, Cl, and Mg were identified. An increase in Al and Si was troubling since the formation of alumina silicate crystals is known to reduce membrane performance. However, the form of Al was undetermined by the EDS analysis and might only represent S700 polymer deposited on the membrane surface.

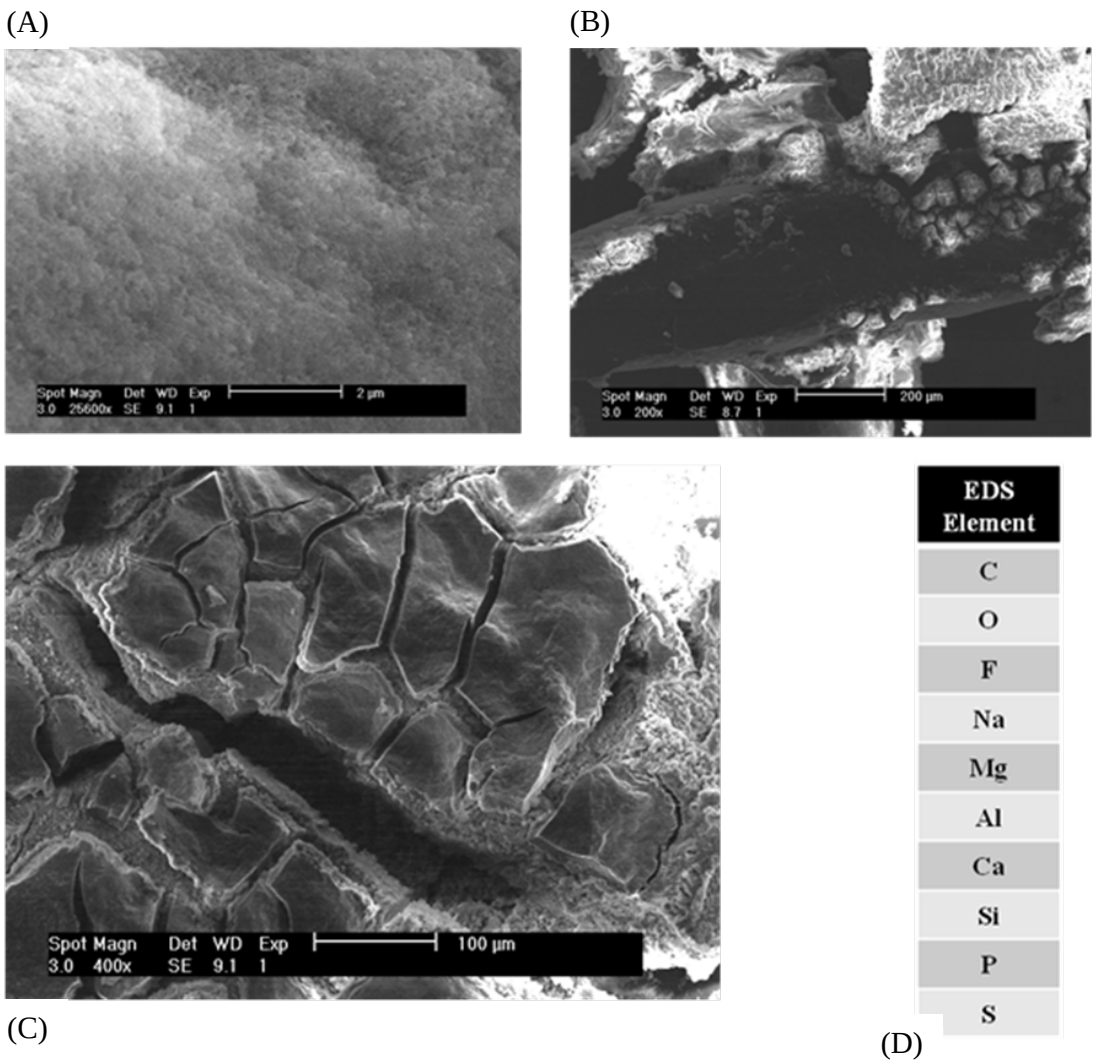

Figure 4.51. Fouled ESPA2 membrane removed from RO test cell operated on RO concentrate amended with 30 mg/L S700 coagulant. SEM images of (A) Al and Si precipitate, (B) membrane spacer covered precipitate, (C) membrane surface covered with thick precipitate composed mostly of Ca, Al, and Si, and (D) EDS analysis of precipitate on membrane surface.

4.7.2.5 Third Stage RO Membrane Protein Analysis after a Simulated 5 mg/L S700 Breakthrough into the RO Feedwater

Protein was not detected on the control membranes (Figure 4.52). However, elevated concentrations of protein were detected on the S700-pretreated membrane, which may have been trapped by the coagulant at the membrane surface.

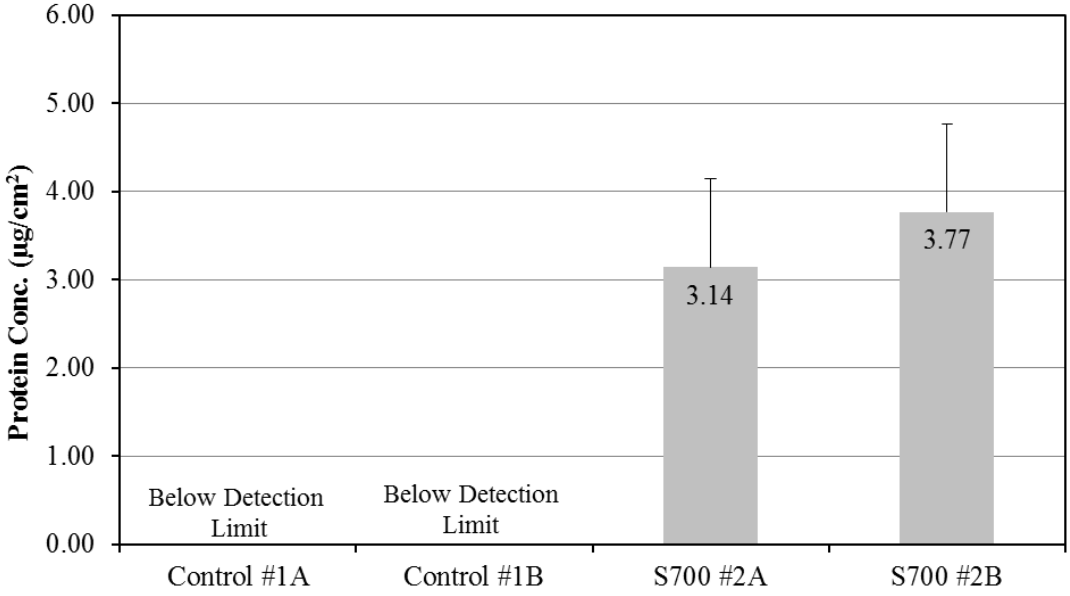

Figure 4.52. Protein analysis of third-stage RO membranes operated on 30 mg/L S700 coagulant simulating 5 mg/L coagulant breakthrough into the RO feedwater.

4.7.3. Conclusions on the Potential Effects of S700 Breakthrough and Impact on Membrane Performance

The quality of the MF effluent directly affects downstream RO performance. The results of these coagulant pretreatment studies suggest that the presence of low doses (2.5 mg/L) of S700 coagulant at the feed end of the RO do not have a significant influence on performance; however, the effect of the equivalent of 5 mg/L of coagulant breaking through to the RO feedwater will result in significant fouling in the end of the third RO stage where feedwater constituents concentrate six-fold. SEM of the feed end of the RO membranes showed a thick layer of nanoparticulates on both coagulant pretreated and untreated membranes at a simulated S700 breakthrough concentration of 2.5 mg/L in the feedwater. However, the third stage RO membrane exposed to 30 mg/L of S700 coagulant showed a thick precipitate layer covering the membrane surface and membrane spacer.

Results from this study demonstrate that MF performance can be improved by preventing nanoparticles from entering the membrane matrix, but coagulant that passes into MF effluent may have an adverse effect on downstream RO performance. Therefore, strict polymer control is needed to prevent breakthrough, which could potentially lead to severe fouling in the third RO stage in the event that MF precoagulation is employed.

4.8 Summary and Conclusions

Laboratory bench-scale experimental studies to evaluate fouling of the PP MF membranes indicated two mechanisms of MF fouling: (1) classical pore blocking via surface cake formation by particulates greater than 0.2 µm nominal pore size that are largely alleviated by backwashing and air sparging, and (2) pore plugging due to intercalation of EfOM (nanoparticulates) with dimensions less than 0.2 µm into the membrane matrix that is difficult to mitigate with regular backwashing.

The use of fluorescent nanobeads and a bench-scale reactor demonstrate that the accumulation of membrane foulants occurs from the top of the fibers (where suction is applied) and progresses toward the bottom. This observation was supported by autopsies of MF membranes recovered from the full-scale pilot unit. CHO and protein concentrations also were highest on the top portion of the membranes, suggesting that these microconstituents were deposited in a manner similar to the nanobeads.

Nanoparticulates that enter the membrane matrix and that fill the void space accounted for 80% of the flux reduction during MF operation. These nanoparticulates have a higher potential to foul the membrane than the microparticles and are most likely responsible for irreversible fouling that necessitates a chemical CIP. The size of the nanoparticles in the clarified secondary effluent responsible for MF fouling was determined by differential filtration using a graded series of microfilters and ultrafilters (down to 10 kDa MWCO). These results suggested that the fouling particle size start between 2.5 nm and 3.5 nm and range up to the effective MF cut off size of 0.2 µm.

Much of the material responsible for MF fouling appears to be biological debris, carbohydrates, proteins, and lipids that were all identified on the surface of fouled membranes from the bench-scale test cell and full-scale pilot units. EDS analysis revealed evidence of biological elements not native to PP membrane, such P, S, C, and O.

Successful MF fouling mitigation strategies must reduce the accumulation of nanomaterials within the MF matrix either by removing the materials from the feedwater or by reducing their interaction with the membrane surface. Nanoparticulate preaggregation experiments with the coagulant Sumaclear 700 were performed. The S700 coagulant was shown to aggregate nanoparticles into microparticles larger than the average MF 0.2µm pore size. This prevented the microparticles from entering the membrane matrix, extended the time between cleanings, and improved membrane performance.

By increasing the CI between CIPs, the chemical costs of the MF operation and the number of chemical cleanings to which the membranes are exposed are reduced. The resulting impact on the MF process is to increase the total lifetime of the membranes (Tang et. al., 2011)

MF pretreatment with 10 mg/L of S700 coagulant increased the cleaning interval from 21 days to 82 days (291%), improved the removal of CHO and protein from the feedwater, and reduced the total CHO and protein load on the RO process. However, application of the coagulant also resulted in Al breakthrough into the MFE thereby increasing the total RO feedwater Al concentration which may increase the potential for aluminum silicate scaling in the third stage of the RO process.

MF pretreatment with 5 mg/L of S700 increased the CI from 21 days to 54 days (157%). The addition of 5 mg/L of S700 resulted in a slight increase of Al in MFE, which could potentially result in alumina scaling farther downstream in the RO process. The addition of 2.5 mg/L of S700 increased the cleaning interval from 21 days to 36 days (71%), and it did not result in an increase of Al in MFE.

In addition to increasing the CI, the S700 pretreated membranes operated at a much lower TMP at all three coagulant concentrations, resulting in lower overall energy costs while producing the same quantity of MF product water.

It is clear that the quality of the MF effluent directly affects RO performance downstream. The results of the coagulant bleedthrough studies have suggested that the presence of low doses (2.5 mg/L) of S700 at the feed end of the RO process do not have a significant impact on RO performance. SEM of the feed end RO membranes showed a layer of nanoparticulates on both coagulant pretreated and untreated membranes. However, the effect of adding the equivalent of 5 mg/L of coagulant to the RO feedwater led to heavy fouling and loss of membrane flux in the third stage where feedwater constituents are concentrated six times. SEM analysis showed a thick precipitate covering the membrane surface and membrane spacer. Results from these studies demonstrated that MF performance can be improved by preventing nanoparticles from entering the membrane matrix, but coagulant that passes through membrane into the MF effluent may have adverse effects on the RO performance downstream. Therefore, strict polymer control is needed to prevent coagulant breakthrough, which otherwise could lead to severe fouling in the third stage RO treatment process.

4.9 Recommendations

Improving water production and water quality is an ongoing process. The application of coagulants to remove nanoparticulates from solution proved effective. However, care must be taken to ensure that any MF coagulant “bleedthrough” does not compromise the performance of the RO process downstream. Further studies with MF-RO at the pilot scale with full size elements is needed to investigate the feasibility of implementing coagulant pretreatment in an operating purification facility. A detailed characterization of the mechanism of MF fouling was a critical objective before effective measures can be implemented to minimize their negative effects on performance. MF cake formation at the surface of the hollow fibers is readily removed by backwashing and not a major hindrance to long-term operations. However, as the current studies have demonstrated, fouling by means of pore plugging by wastewater EfOM is a major impediment to MF performance. Decreasing membrane hydrophobicity may lessen the absorbance of hydrophobic colloidal carbohydrates, proteins, lipids, and other nanoparticulates, most of which are presumed to be of microbial origin. Development of new polymer fibers with low affinity for organic foulants also should be investigated. Along this line of investigation, chemical surface modification of existing commercially available membranes is another area of research for further development (similar to the studies conducted by Tang et al., 2011).

Chapter 5

Microfiltration Foulant Characterization

5.0 Isolation of MF Foulants by Solvent Extraction and Characterization by Excitation-Emission Matrix (EEM) Fluorescence Spectroscopy

5.1.1 Introduction

Initial studies were conducted to better understand the general character of the organic constituents in the MFF and MFE and the foulants recovered from the hollow fibers of the MF membranes. These studies were preliminary in nature and used to formulate new procedures for the isolation and characterization of the organic MF foulants.

5.1.2 Materials and Methods

An MF module that had reached the end of its 5-year lifetime was removed from MF cell A05 on April 6, 2011, and was submerged in tap water for 2 h to remove loosely bound foulants. Hollow fibers were removed from the top, middle, and bottom areas of a fouled MF membrane. Foulants were extracted from the membrane using two different methods. In one method, methanol (MeOH) was forced through the fibers from the inside out. A 27-gauge stainless steel needle was inserted in the end of a single fiber. The other end of the fiber was pinched closed, and MeOH was forced through the pores of the membrane with a glass and Teflon Hamilton syringe. A total of 10 fibers were extracted but no significant amount of material was released. In the second method, foulants were extracted by soaking 30 fibers from each section of the membrane in 20 mL of MeOH for 18 and 60 h, followed by sonication (see Section 5.2). The extracts were concentrated using a Speedvac (Savant ThermoScientific). Liquid/liquid extraction was performed with water/dichloromethane. The dichloromethane was added to the MeOH extract to achieve a liquid/liquid extraction similar to that described by Bligh and Dyer (1959). Eluates were redissolved in MeOH then diluted 1:1000 for EEM fluorescence spectroscopy (Horiba Jobin Yvon, FluoroMax4, Edison, NJ).

5.1.3 Results and Discussion

Figure 5.1 illustrates the three-layer separation achieved by liquid/liquid extraction of the MeOH extracts. EEM fluorescence spectra from each of the three layers are shown in Figure 5.2. The dilution factors were the same for each fraction so that the quinine sulfate equivalence (QSE) fluorescence values were comparable for each layer (water layer 0–14, interface 0–80, and bottom layer 0–400 QSE). The letters A, C, and T denote the fluorescent characteristics of humic substances (A), colored organic matter CDOM (C), and protein-like or tryptophan-containing matter (T), with excitation/emission (Ex/Em) wavelengths listed in Table 5.1 (Coble et al., 1998). Peaks in the range of Ex 225 nm and Em 609–621 nm have been assigned to hydrophilic neutral matter (Marhaba et al., 2000) but also can be an instrument artifact. Five Ex/Em wavelengths of relevant compounds are summarized in Table 5.2. Two unidentified peaks were detected with one at Ex/Em 240/352 nm and another in the aqueous phase at Ex/Em 338/438 nm.

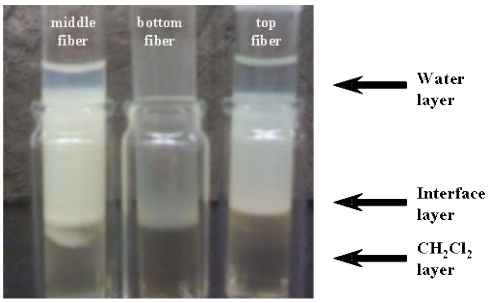

Figure 5.1. Methanol extracts (60 h) from fouled MF hollow fibers fractionated by dichloromethane.

Table 5.1. Major Fluorescence Components in Source Waters and Foulants

Peak	Ex/Em (nm)	Chemical Classification
A	260/400–460	Humic acid-like (UV)
C	320–360/420–460	Humic acid-like (visible)
T	275/305	Tryptophan-like, protein-like
M	290–310/370–410	Marine humic-like (visible)

Source: Coble, et al. (1998).

Table 5.2. Major Exication/Emission (nm) Peaks Associated with the Three Extraction Layers

Protein-Like (Peak T)	Humic-Like (Peak A)	Humic-Like (Peak C)	Unknown Peak No. 1	Unknown Peak No. 2
276/334 nm	242/436 nm	340/440 nm	338/438 nm	240/352 nm

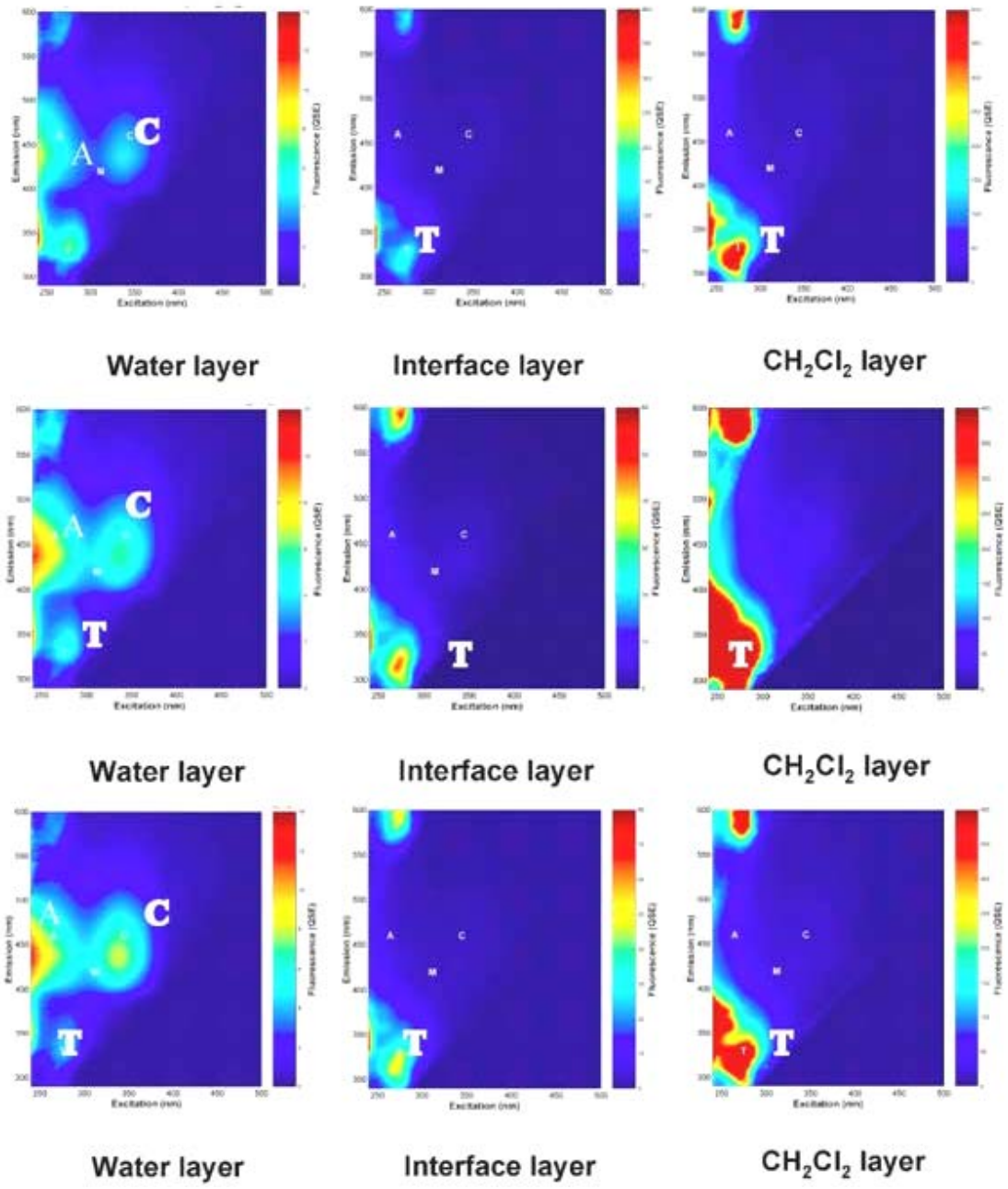

Figure 5.2. EEM fluorescence spectra of the water and dichloromethane extracts of the methanol extraction of the MF foulants recovered from hollow fibers removed from the top, middle, and bottom areas of the MF element (top to bottom of page, respectively).

5.1.4 Conclusions

Of these two foulant recovery methods, soaking the fibers in MeOH for 60 h was the most effective for removing protein and organic matter that remained on the fibers. The syringe elution, followed by the 18 h soaking, was less effective. The bulk of the material (60 h soak) consisted of hydrophobic protein-like matter with a smaller fraction of water soluble protein, natural organic matter (i.e., humic-like substances), and an unknown compound in the

aqueous phase characterized by Ex/Em 338/438 nm. The interface and dichloromethane layers contain an additional unknown compound with Ex/Em 240/352 nm. The fibers recovered from the middle section of the element retained most of the extractable protein. The organic fractions undoubtedly contain lipids whose fluorescence peaks have not been identified if, in fact, they contain fluorescent molecular features or are directly associated with constituents that fluoresce. Additional characterization was performed using sequential extraction techniques (Section 5.2).

5.2 Recovery of MF Foulants by Sequential Solvent Extraction and Characterization by EEM Fluorescence Spectroscopy

5.2.1 Introduction

The purpose of this series of experiments was to perform sequential extraction of the fouled MF hollow fibers by varying the polarity of the solvents and to improve the extraction process by applying sonication. Previous studies revealed that all the foulants were not removed from the surface of the hollow fibers by MeOH extraction. Therefore, additional measures were taken to increase the recovery of foulants. Extraction with different solvents including MeOH, acetonitrile (ACN), hexane, and 10% formic acid (protein extraction) were performed to release different classes of compounds. Sonication facilitated the release of denatured and particulate matter from the membrane surface and inner pores. Characterization was performed using EEM fluorescence spectroscopy.

5.2.2 Materials and Methods

Fouled MF fibers (15–30 cm) recovered from the mid-section of an autopsied membrane in April 2011 were extracted for 60 h at room temperature in 20 mL of four different solvents: MeOH, ACN, hexane, and 10% formic acid. The fibers were sonicated in each solvent for 10 min. The solvent was decanted into separate vials and removed under vacuum with a Speedvac. The extracts were redissolved in deionized water (1:1000), centrifuged to remove insoluble precipitates, and EEM spectra obtained. The analytical scheme is summarized in Figure 5.3. Subsequent studies showed that presoaking was not necessary to facilitate the sonication process.

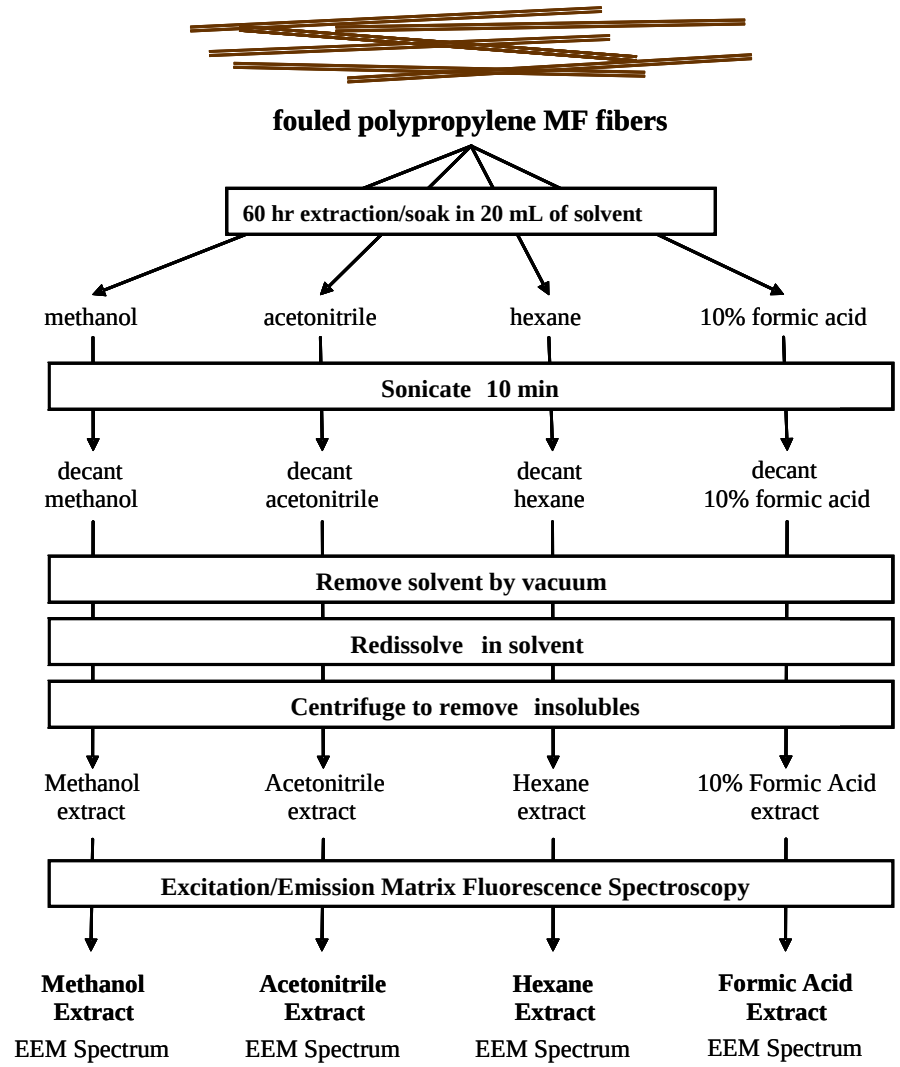

Figure 5.3. Solvent extraction and recovery protocol for fouled MF hollow fibers.

5.2.3 Results and Discussion

Sonication of the MeOH- and ACN-soaked fibers released accumulated material. The bulk of the material was removed from the fouled MF fibers with MeOH or ACN. The yield of the hexane extractable material, soluble in dichloromethane, was not improved by sonication. The EEM fluorescence spectra (Figure 5.4) of the MeOH, ACN, and hexane extracts looked similar with Ex/Em wavelengths of 250/300 nm, indicative of aromatic proteins (Chen et al., 2003). However, the hexane extracts also contained a significant amount of tryptophan protein-like matter (Ex/Em 275/330 nm) and a different class of aromatic proteins (Ex/Em ~240/350 nm). Smaller amounts of tryptophan protein were present in the MeOH, ACN, and formic acid extracts. The formic acid-extract EEM spectrum was different from that of the organic solvent extracts with Ex/Em wavelength maxima at 276/452 nm and 302/452 nm, which appear to be fulvic acid-like compounds. The formic acid extraction targets acidic/hydrophilic constituents that remain adsorbed on the membrane surface. Fluorescence band maxima are primarily red shifted in increasingly polar solvents (Homocianu et al. 2011).

The foulant extracts were diluted 1:1000 in deionized water and were mostly aqueous in composition. Thus, the EEM fluorescence spectra should not have been affected by residual solvent interactions. Park et al. (2013) recently discussed the impact of methanol and acetonitrile on fluorescence properties.

The MF fibers were air dried after extraction with the MeOH and hexane. The dried fibers were then extracted with aqueous 10% formic acid, known to solubilize proteins, releasing material that remained on the membrane surface during the organic extraction (Figure 5.5). Ex/Em wavelengths of 254/457, 275/456, and 300/456 nm were observed, which appear to be fulvic acid-like compounds. The Ex/Em peak at 275/330 nm is indicative of tryptophan protein and the peak at 350/456 nm suggests the presence of humic acid-like substances (Chen et al., 2003).

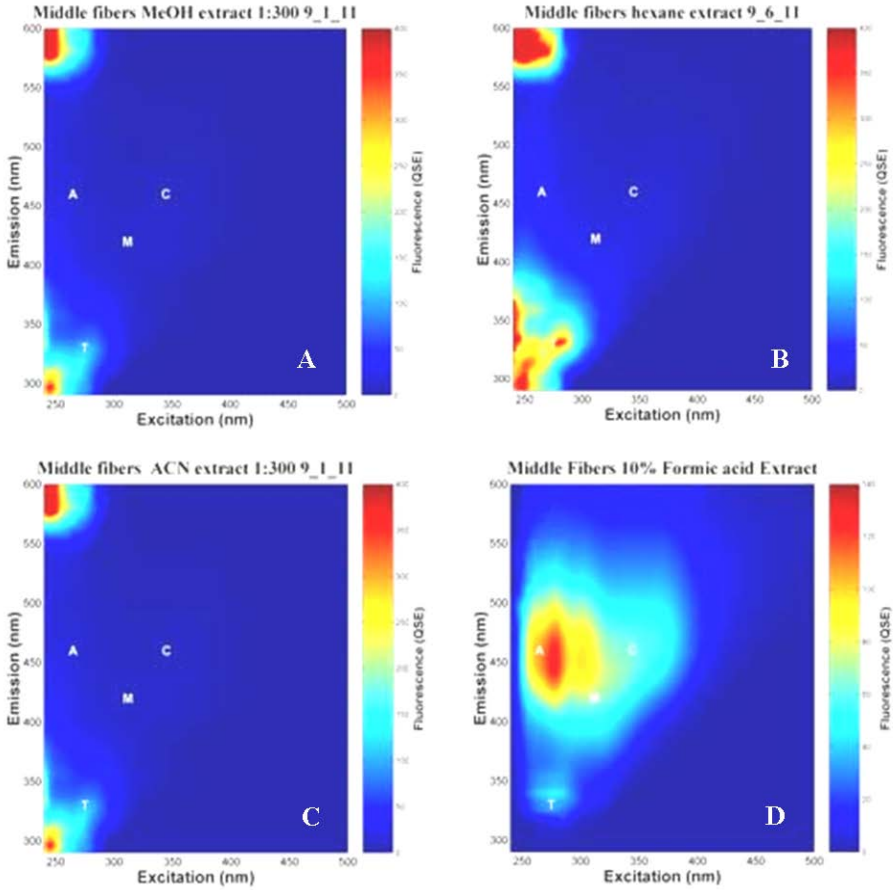

Figure 5.4. EEM fluorescence spectra of (A) methanol, (B) hexane, (C) acetonitrile, and (D) formic acid extracts from fouled MF hollow fibers.

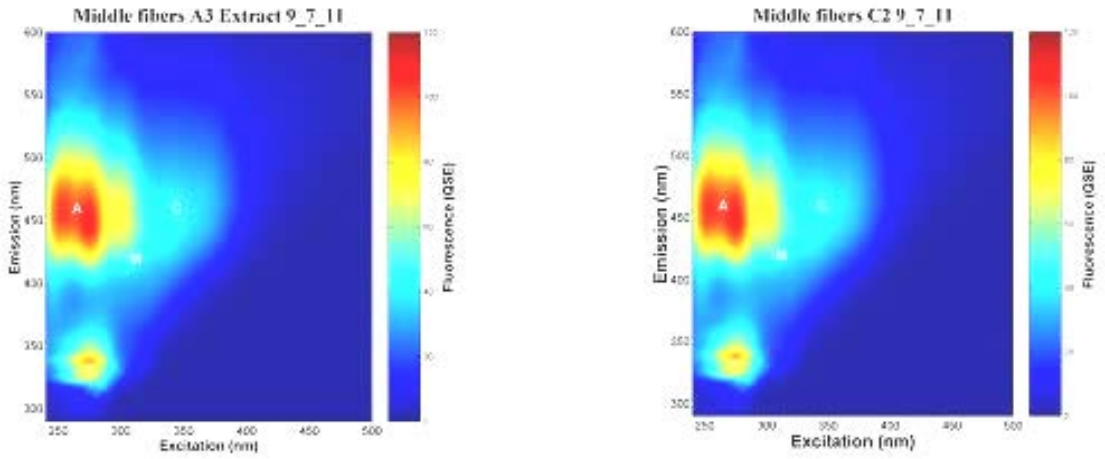

Figure 5.5. EEM fluorescence spectra of 10% formic acid extracts of methanol-extracted (left) and hexane-extracted (right) MF hollow fibers operated on a blend of 30% TFE and 70% ASE.

5.2.4 Conclusions

Sonication and sequential extraction of the MF foulants from the hollow fibers was performed with solvents of varying polarities to improve on the recovery the MF foulants. EEM fluorescence spectroscopy studies of these extracts revealed the presence of (1) three different protein-like peaks, (2) three different visible fulvic acid-like peaks, and (3) one UV humic acid-like peak associated with foulants extracted from the fouled MF membrane. The foulants consisted of both hydrophobic proteins extracted by organic solvents (MeOH and ACN) and hydrophilic proteins extracted by formic acid. A significant amount of the fulvic acid-like material was recovered by extraction with formic acid that was not effectively removed by the organic solvents.

5.3 Solid-Phase Extraction and Characterization of MF Feedwater and MF Effluent by IMA Chromatography and EEM Fluorescence Spectroscopy

5.3.1 Introduction

Immobilized metal affinity chromatography (IMAC) has been used to isolate metal-binding compounds and has been used to characterize a select subset of compounds from fresh and marine water (Cottrell et al., 2013). MFF and MFE were analyzed by IMAC to determine the differences in the elution profiles. Any decrease in the concentration of constituents between MFF and MFE would be due to a loss of material from the feedwater that adsorbed onto the surface of the polypropylene hollow fibers.

5.3.2 Materials and Methods

Chromatographic separation was performed on an iminodiacetic acid-derivatized Sepharose (GE Life Sciences). The affinity column contained a covalently bonded half-molecule of ethylenediaminetetraacetic acid (EDTA). The EDTA can bind a metal cation, in this case Cu^{2+}. Diols, heterocyclic compounds, and some fatty acids are known to chelate to metal

ions. The material bound to the virgin column packing material was eluted with a buffer at pH > 8 or pH < 2. The column resin was charged with metal ions and then washed extensively to remove unbound metal. Samples were applied to the column at a flow rate of 1 mL/min. Bound material was eluted in two steps. Weakly bound material was removed by washing the column with water. Three 5-mL fractions were collected. Tightly bound material was removed with 0.1N NH_4OH followed by 0.1N NaOH. The EEM fluorescence spectra of each eluate were measured to determine recovery. EEM fluorescence spectra of the IMAC eluates were compared to the spectra of the EfOM in the raw MFF and MFE water samples. The IMAC eluates were freeze-dried for additional analysis.

5.3.3 Results and Discussion

5.3.3.1 Characterization of MF Feedwater and MF Effluent by EEM Fluorescence Spectroscopy

EEM fluorescence spectra of the raw MFF and MFE were collected and are displayed in Figure 5.6. The differences between the spectra were determined by integrating the area under the A, C, M, and T peaks (Coble et al., 1998) and are summarized in Figure 5.7. The MFF was enriched in Peak A (Ex/Em 240/460 nm) humic acid-like matter, and the Peak C (Ex/Em 352/460 nm) chromophoric humic acid-like matter and was consistent with the ^{1}H NMR spectroscopic data (see Section 5.4). The MFE was enriched in Peak T (Ex/Em 275/330 nm) protein-like matter indicating that a significant amount of protein passes through the nominal 0.2 μm pores into the MF effluent or the MF membrane removes compounds from the feedwater that quench the tryptophan protein fluorescence.

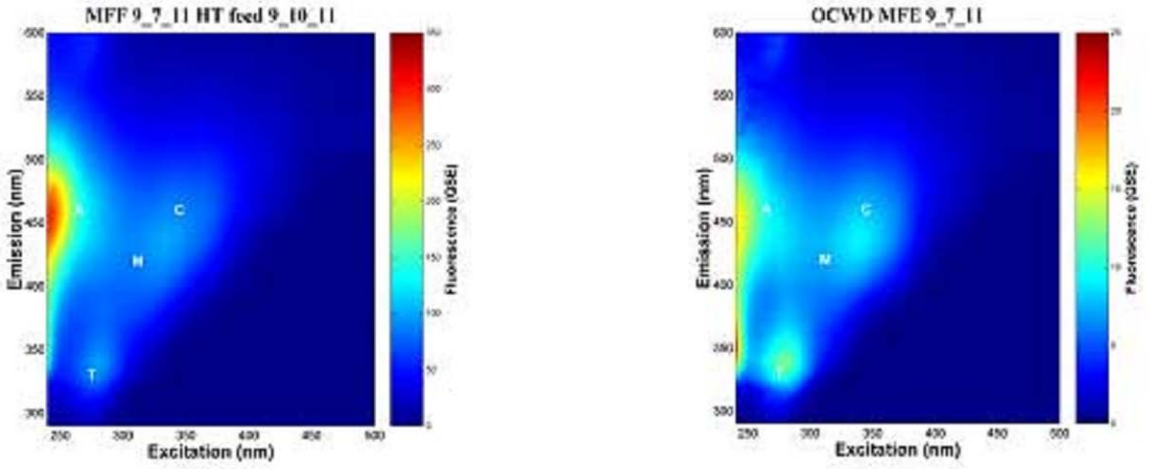

Figure 5.6. EEM fluorescence spectra of raw source water samples: MFF (left) and MFE (right).

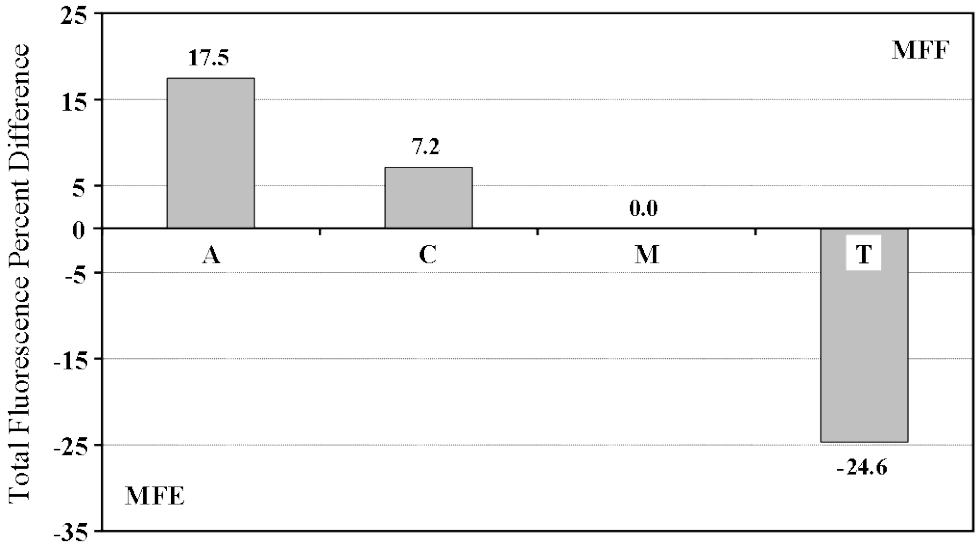

Figure 5.7. Difference in fluorescence intensities between EfOM recovered from MFF and MFE represented by (A) UV humic acid-like matter, (C) visible humic acid-like, (M) marine humic acid-like, and (T) tryptophan-or protein-like matter.

5.3.1.2 Immobilized Metal Affinity Chromatography (IMAC) and EEM Spectroscopy

IMAC was used as a fractionation technique to compare the metal-binding affinities of the constituents in MFF and MFE source waters. The fluorescence spectra of these compounds were of two types. The first type was weakly bound, perhaps because of salt interactions, and was easily eluted with water and appeared similar to the formic acid extractable material from the fouled membranes (see Figures 5.4D, and 5.8). These spectra were dominated by fulvic acid-like material (Ex/Em 250/450 nm) with lesser amounts of humic acid-like substances (Ex/Em 340/430 nm) and typtophan-like protein (Ex/Em 275/340 nm). The amount of these compounds appears to be much higher in the MFE than MFF, suggesting that the acidic/hydrophilic constituents are poorly retained on the copper-chelated Sepharose column and, more importantly, this particular group or class of compounds do not readily adsorb to the polypropylene membrane and pass through into the MF effluent (Figure 5.9). The amount of material eluted with the water washes decreased as the salt concentration decreased.

The second type of organic matter was bound strongly to the Cu^{2+} and was extracted with ammonium hydroxide followed by 0.1 NaOH. This material was protein-like in nature with Ex/Em peaks near 250/350 nm, aromatic proteins near 250/300 nm, and tryptophan protein near 275/340 nm (Figure 5.8). The EEM spectra from the MFF and MFE extracts looked similar. However, significantly more protein-like matter was bound to the MFE IMAC column and required 0.1 N NaOH for elution, which indicates that this protein-like organic matter did not readily adsorb to the surface of the polypropylene membrane, passed through into the effluent, and adsorbed firmly to the Sepharose-Cu^{2+} column support (Figure 5.10).

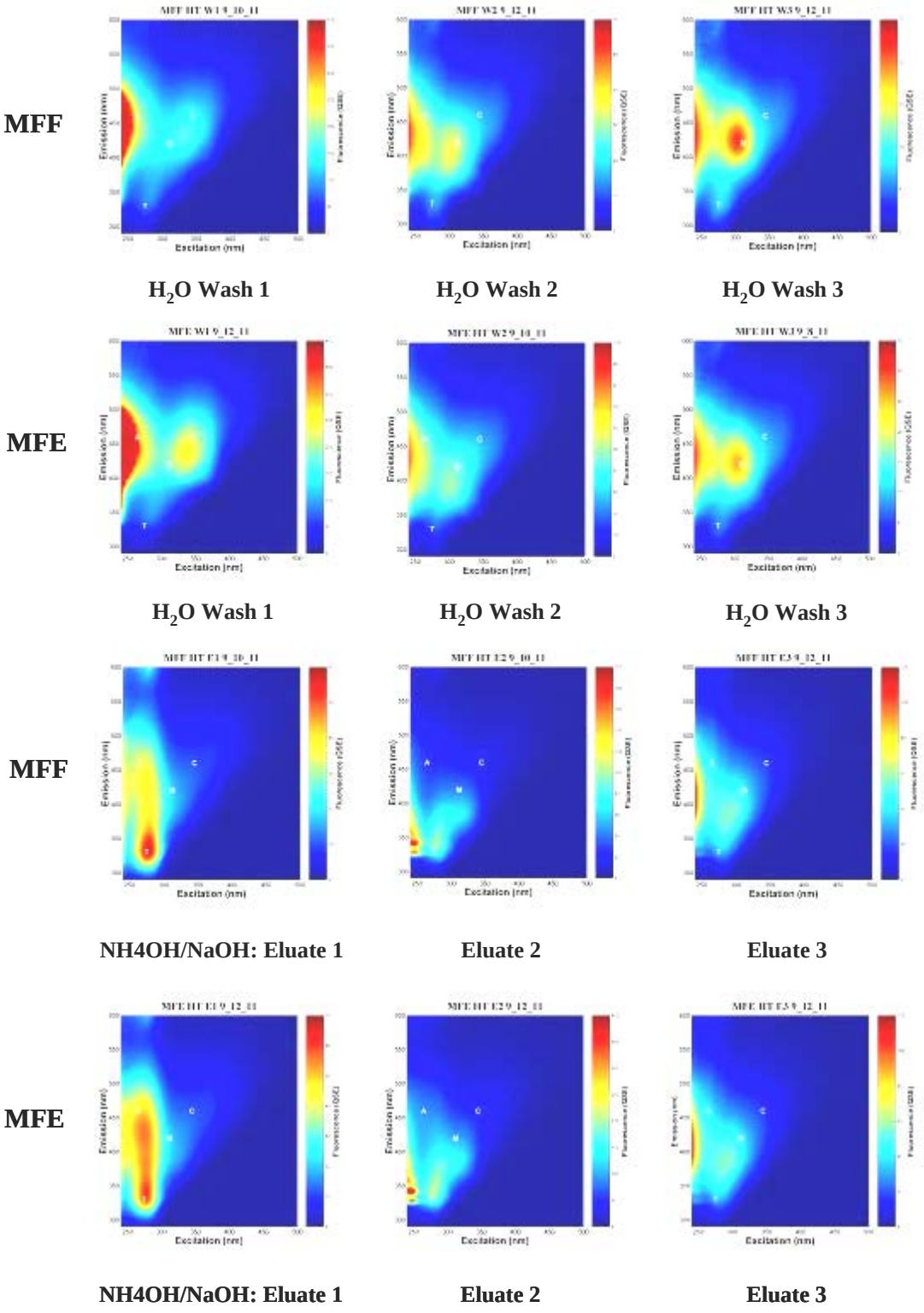

Figure 5.8. EEM fluorescence spectra of eluate extracted from the IMAC column with water followed by extraction with NH_4OH/NaOH.

Note: The fluoresence intensity scales are not the same.

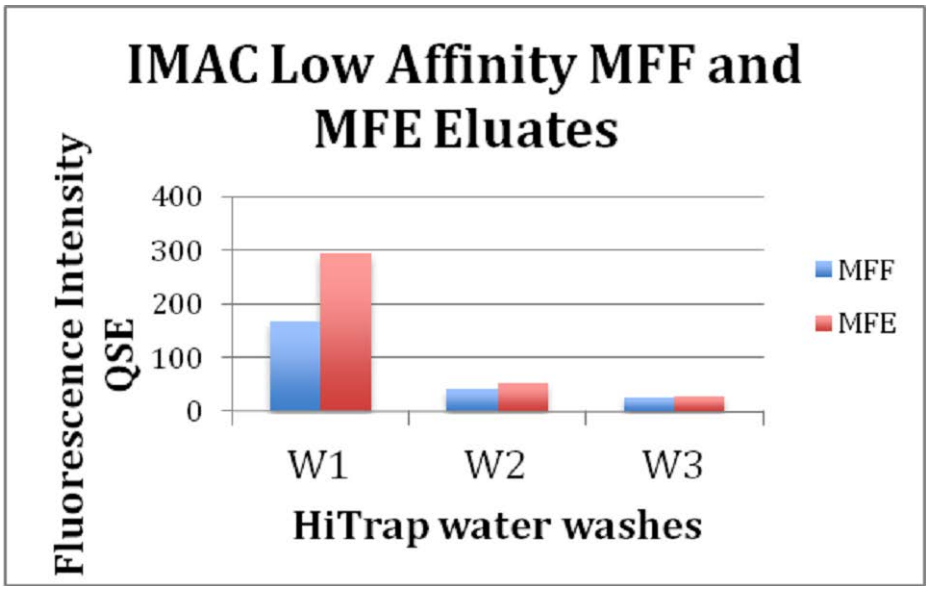

Figure 5.9. Fluorescence intensities of MFF and MFE eluates from three separate water extractions.

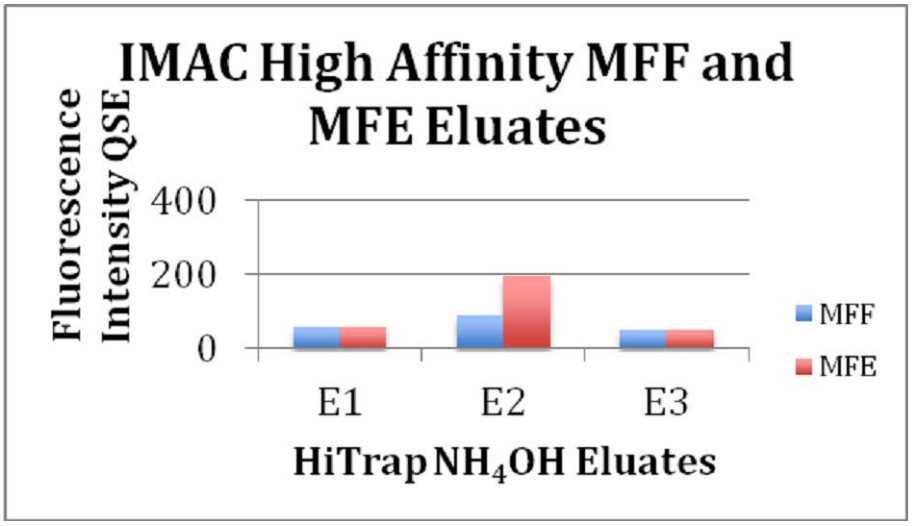

Figure 5.10. Fluorescence intensities of MFF and MFE eluates from three separate NH_4OH/NaOH extractions.

5.3.4 Conclusions

The results of the IMAC analysis of the MFF and MFE source waters indicate that significant amounts of EfOM passes through the polypropylene MF membrane into the effluent. These compounds can be broken down into two classes with different affinities for the Sepharose-Cu^{2+} column packing material: (1) an acidic/hydrophilic fraction of tryptophan-like protein and humic and fulvic acid-like compounds, and (2) aromatic and tryptophan-like proteins with a strong affinity for the column support material. These classes of compounds appeared to have a lesser tendency to adsorb on the surface of the polypropylene MF membrane as they

were detected in higher concentrations in the MFE eluate than the MFF eluate from the immobilized metal affinity column.

5.4 Isolation of MF EfOM by SPE and Characterization of Extracts and MF Membrane Foulants by ^{1}H NMR Spectroscopy

5.4.1 Introduction

The purpose of this series of experiments was to characterize MFF and MFE extracts from the PPL solid-phase extraction cartridges by ^{1}H NMR spectroscopy. Foulants also were recovered directly from a fouled MF membrane by organic solvent extraction and analyzed by ^{1}H NMR spectroscopy.

5.4.2 Materials and Methods

EfOM was isolated from MFF and MFE by SPE using Bond Elut PPL cartridges (Agilent) by the method described by Gonsior et al. (2011). MFF and MFE were acidified to pH 2 with acetic acid and prefiltered at 0.22 μm (Millipore GV PVDF, Durapore) to remove bacterial cells. The prefiltered MFF or MFE was loaded onto the SPE cartridge and the adsorbed EfOM was eluted using a three-step elution: 50% MeOH, 50:50 ACN:MeOH, and finally 100% MeOH (Figure 5.11). The ^{1}H NMR spectra (in D_2O) of each fraction were obtained at University of Toronto. The spectra were compared to the spectrum of Suwannee River NOM.

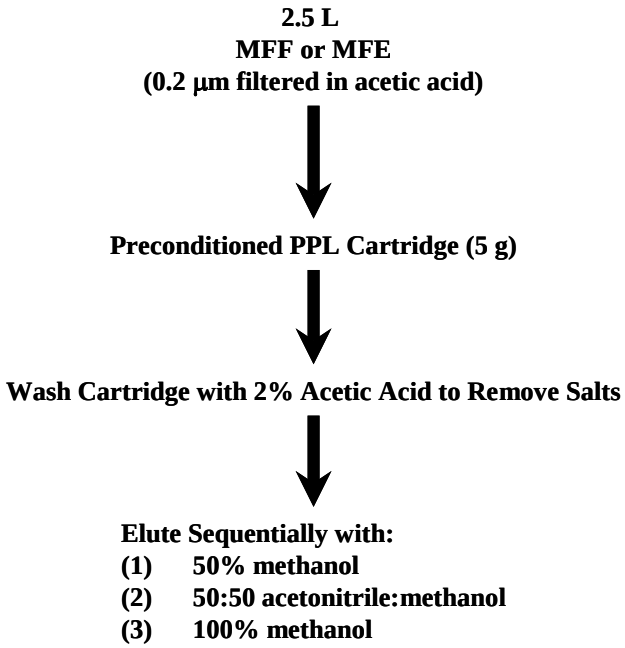

Figure 5.11. Schematic diagram of EfOM isolation procedure by solid-phase extraction.

In a separate experiment, 30 fouled hollow fibers were extracted with a series of organic solvents: dichloromethane, MeOH, and hexane. The extracts were reduced to dryness and then redissolved in deuterated MeOH for ^{1}H NMR spectroscopy.

5.4.3 Results and Discussion

The ^{1}H NMR spectrum of Suwannee River NOM is displayed in Figure 5.12. The ^{1}H NMR spectra of the MFF and MFE PPL extracts revealed that they were similar in chemical composition and contained protein-peptides/carbohydrate, carboxylate-rich alicyclic molecules (CRAM), aliphatic, and small amounts of aromatic functionality (Woods et al., 2010) (Figure 5.13). The ^{1}H NMR spectra of the 50% MeOH and 50:50 ACN:MeOH eluates also looked similar (Figures 5.14 and 5.15). However, integration of the peak areas associated with the 50:50 ACN:MeOH extracts indicated that the MFF contained more material derived from linear terpenoids (MDLT) (i.e., lipids, fatty acids, and aromatic constituents), which were presumably associated with bacterial cell wall components released into the wastewater effluent (Figure 5.16). The 100% MeOH extract of the MFF reveals an eluate that was more enriched with hydrophobic and aromatic components compared to the MeOH eluate from the MFE (Figure 5.17). These results indicate that a portion of these hydrophobic and aromatic components are removed by the MF process. The chemical shift axes of the NMR spectra are expanded and displayed in Figures 5.18 and 5.19 to highlight the differences in composition between MFF and the MFE source waters.

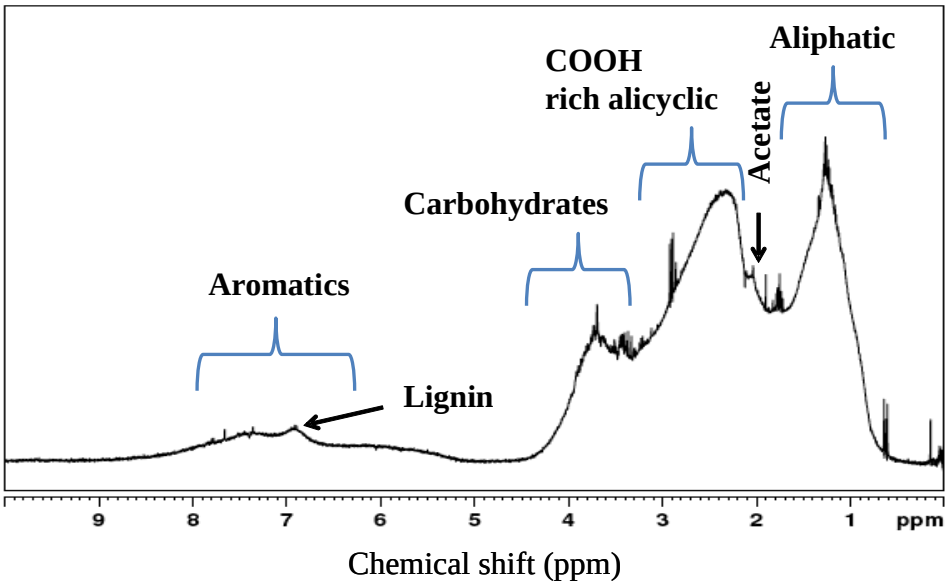

Figure 5.12. ^{1}H NMR spectrum of Suwannee River NOM.

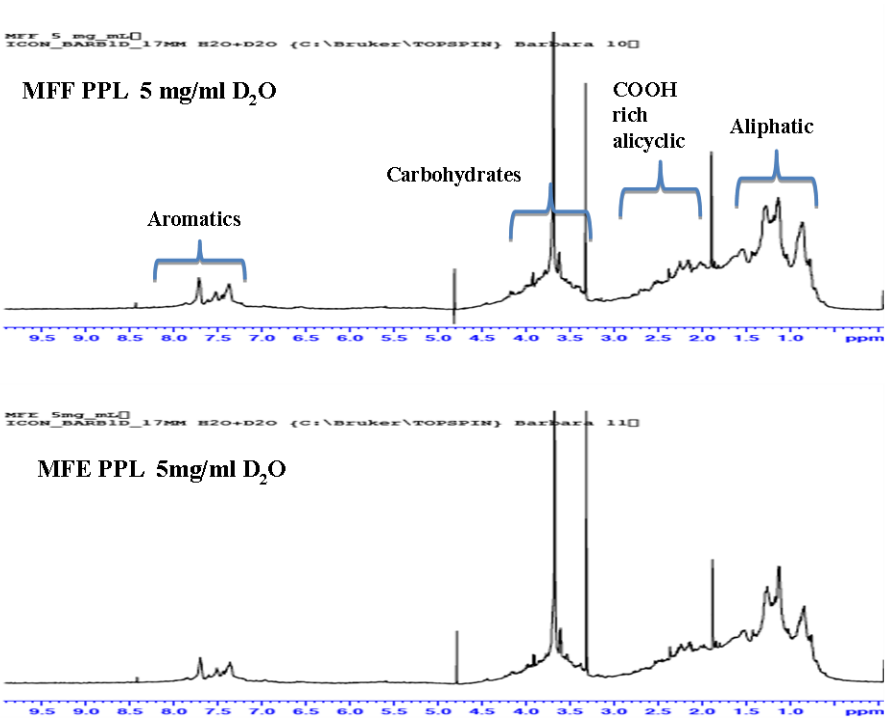

Figure 5.13. ^{1}H NMR spectra of 0.22 μm prefiltered MFF (top) and MFE (bottom) source waters prior to SPE fractionation.

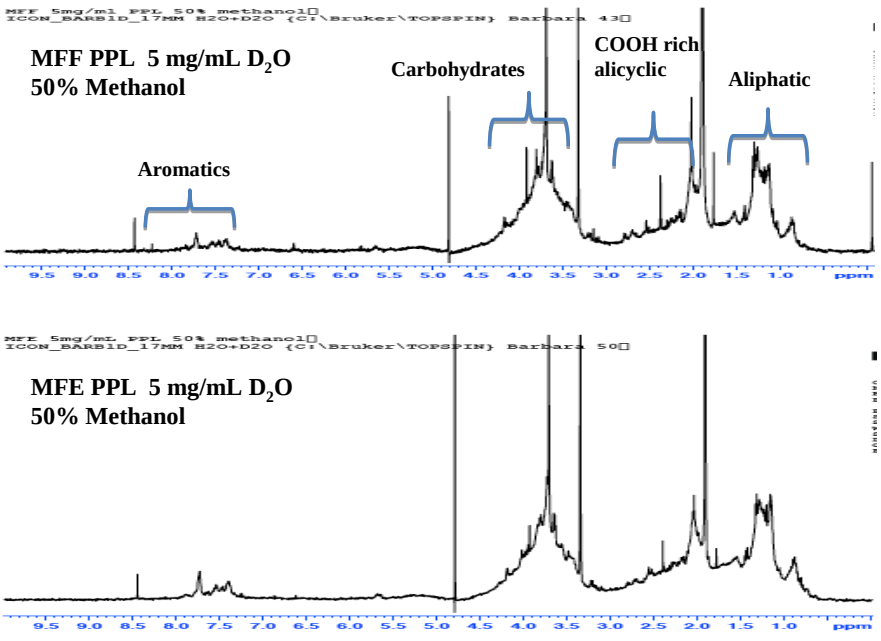

Figure 5.14. ^{1}H NMR spectra of MFF (top) and MFE (bottom) source waters extracted with 50% MeOH from PPL SPE cartridge.

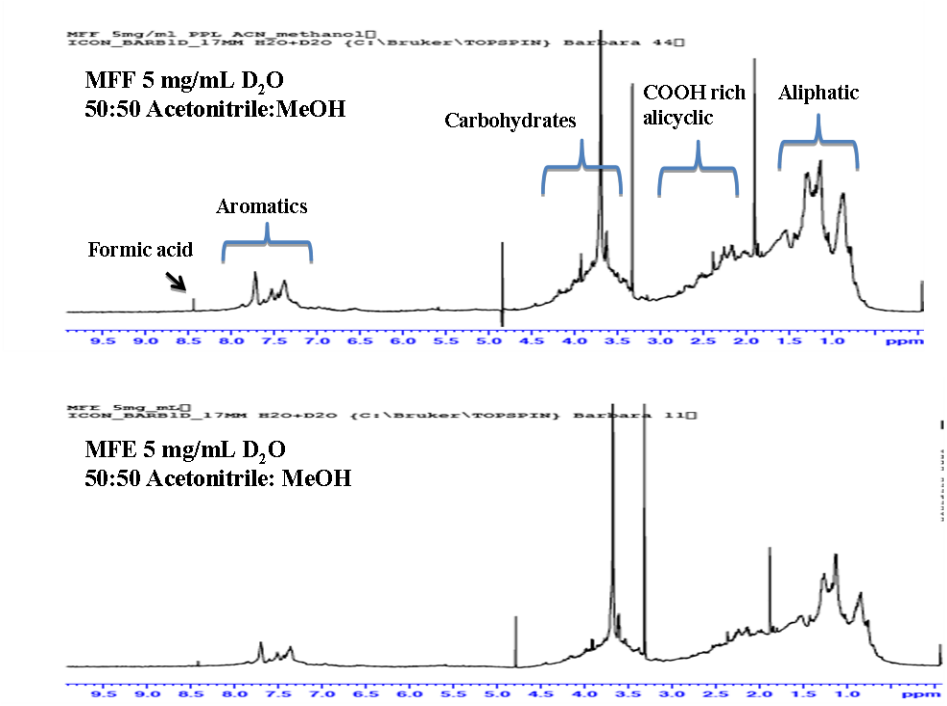

Figure 5.15. ^{1}H NMR spectra of MFF (top) and MFE (bottom) source waters extracted with 50:50 ACN:MeOH from PPL SPE cartridge.

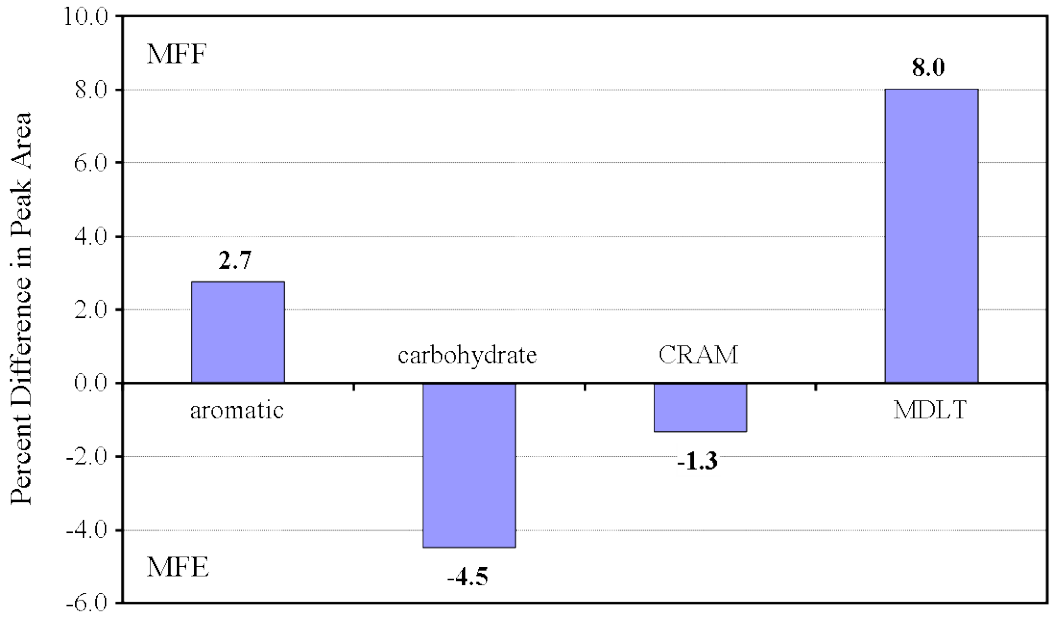

Figure 5.16. Difference in ^{1}H NMR peak areas associated with the four main functional groups (aromatic, carbohydrate, CRAM, and MDLT) between MFF and MFE eluates associated with the 50:50 ACN:MeOH extractions.

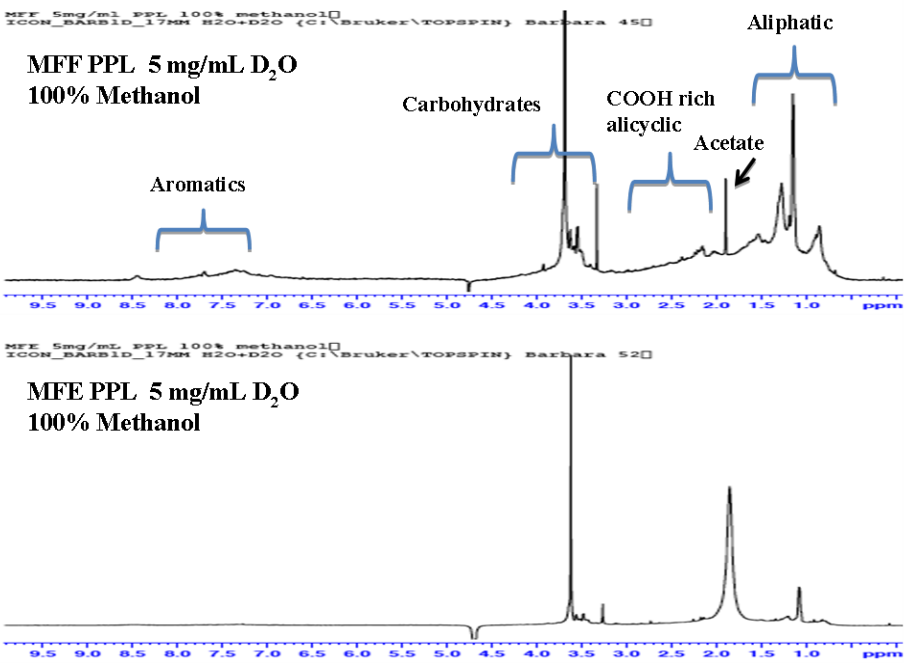

Figure 5.17. ^{1}H NMR spectra of the eluates of the MF feedwater (top) and MF effluent (bottom) extracted with 100% MeOH from PPL SPE cartridge.

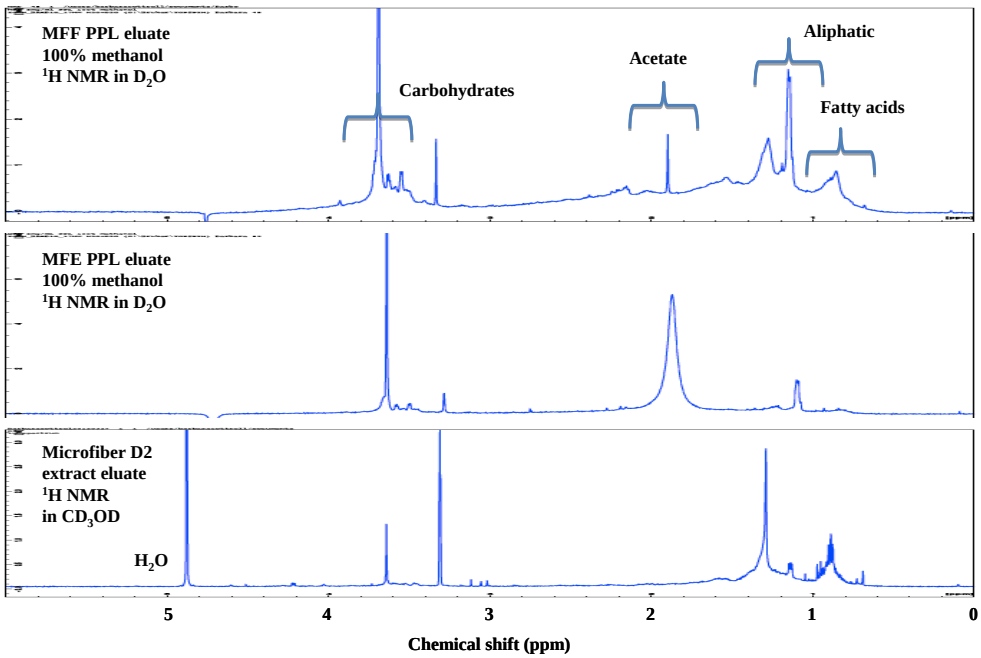

Figure 5.18. ^{1}H NMR spectra of MFF PPL SPE eluate (top), MFE PPL SPE eluate (middle), and fouled MF hollow fiber eluate (bottom).

Note: All extracted with 100% MeOH. Chemical shift range 0–6 ppm.

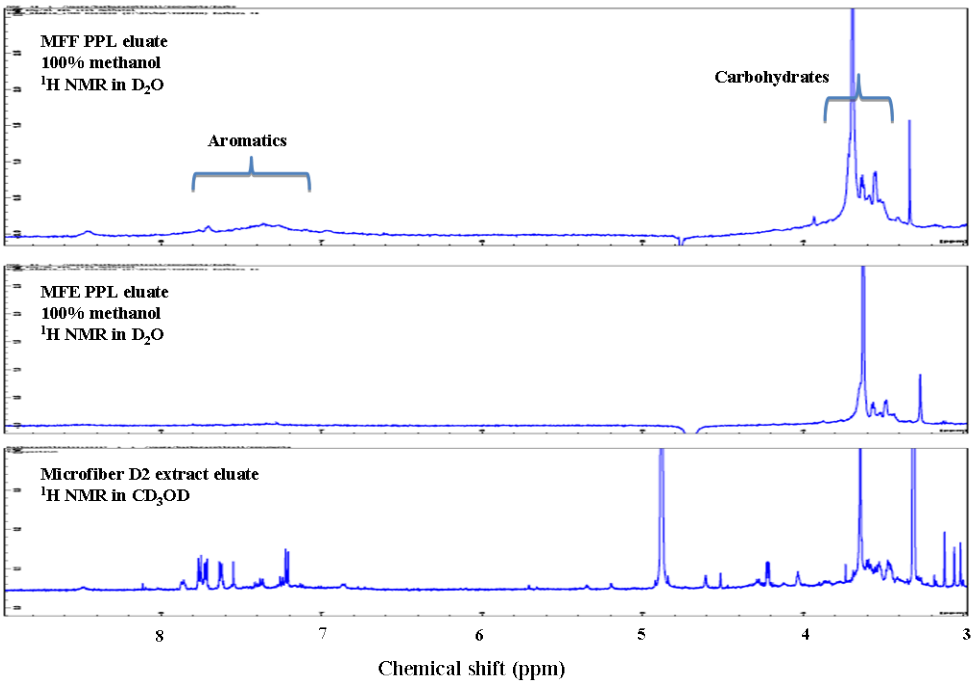

Figure 5.19. ^{1}H NMR spectra of MFF PPL SPE eluate (top), MFE PPL SPE eluate (middle), and fouled hollow fiber eluate (bottom).

Note: All extracted with 100% MeOH. Chemical shift range 3–9 ppm.

5.4.4 Conclusions

The ^{1}H NMR spectra of the raw MFF and MFE samples showed the presence of (1) carbohydrate, (2) carbohydrate-rich alicyclic, (3) aliphatic, and (4) aromatic compounds in both source waters. This revealed that these compounds present in the MF feedwater are small enough to pass through the 0.2 μm pores of the polypropylene membrane into the product water or effluent and, thus, the MF is not a complete barrier to the EfOM of the wastewater. Fractionation of the EfOM by SPE with different solvent elutions of the MFF and MFE showed small variations in the type or class of compounds that are rejected or adsorb to the membrane surface. The MFF extracts contained more hydrophobic lipids, fatty acids, and aromatic compound, which means that these constituents were removed or rejected by the MF process with material undoubtedly adsorbed on the surface of the hollow fibers and the inner surfaces of the pores. This would be expected for wastewaters treated with a hydrophobic membrane material like polypropylene. The results from the NMR spectroscopic analysis were consistent with the results obtained by EEM fluorescence spectroscopic analysis of MFF and MFE. Although this class of EfOM appeared to foul the membrane surface to a greater extent, these compounds were not completely removed, were small enough to pass through the membrane, and could potentially foul cartridge filters and RO membranes downstream.

5.5 Characterization of MF Foulant Extracts by Gas Chromatography × Gas Chromatography–Time of Flight Mass Spectrometry (GC×GC-TOFMS)

5.5.1 Introduction

The purpose of this series of experiments was to extract foulants from the surface of an MF membrane and characterize the underivatized components by comprehensive 2-D gas chromatography and time of flight mass spectrometry (GC×GC-TOFMS). Foulants were extracted with an organic solvent from hollow fibers of an MF membrane removed from service. The list of compounds identified in the foulant extract by mass spectrometry was compared to those of an unused control membrane.

5.5.2 Materials and Methods

Fouled polypropylene hollow MF fibers were soaked for 18 h in 20 mL of 10% formic acid. The fibers were rinsed with LC-MS water and the extract air dried. There was no significant amount of material extracted by formic acid. The fibers were then extracted with MeOH for 48 h. The MeOH was decanted and the volume reduced by vacuum. The sample was redissolved in dichloromethane and analyzed on a Pegasus 4D GC×GC-TOFMS (LECO Corp., St. Joseph, MO). The lead column consisted of a low-polarity Restek Rtx-5Sil-MS (35 m, 0.25 μm film), and the second column was a mid-polarity Rxi-17Sil-MS (1 m, 0.1 μm film) column.

Twenty-five fibers from an unused MF membrane were placed in 20 mL of MeOH, sonicated, the volume reduced under vacuum, and redissolved in dichloromethane before analysis by GC×GC-TOFMS. Other extraction methods did not yield results.

5.5.3 Results and Discussion

The total ion chromatograph from the MeOH extract of the fouled hollow fibers is displayed in Figure 5.20. The 14 most abundant compounds are identified on the chromatograph. Compounds with a similarity to a NIST database with a score greater than 800 are listed in Table 5.3. A total of 218 compounds were identified, and the majority are known contaminants of wastewater. Table 5.3 lists the compounds by functional group, and Figure 5.21 shows a graphical display of the functional group distribution of the MF foulants. Nitrogen-containing and chlorinated compounds contributed to 21% and 12%, respectively, of the identified compounds. Silicon contributed to 4% of the compounds, sugars 2%, and amino acids 1%.

The MeOH extract of the control fiber contained significantly fewer compounds (53 total) (Table 5.4). A plot of the distribution of the compounds identified from the foulant and surface of the control membrane are displayed in Figure 5.22. A number of the compounds identified in the extract of the control membrane were associated with industrial solvents and surfactants. Of the 53 compounds that were associated with the control, 21 also were found in the extract from the fouled membrane (Table 5.4, italic font).

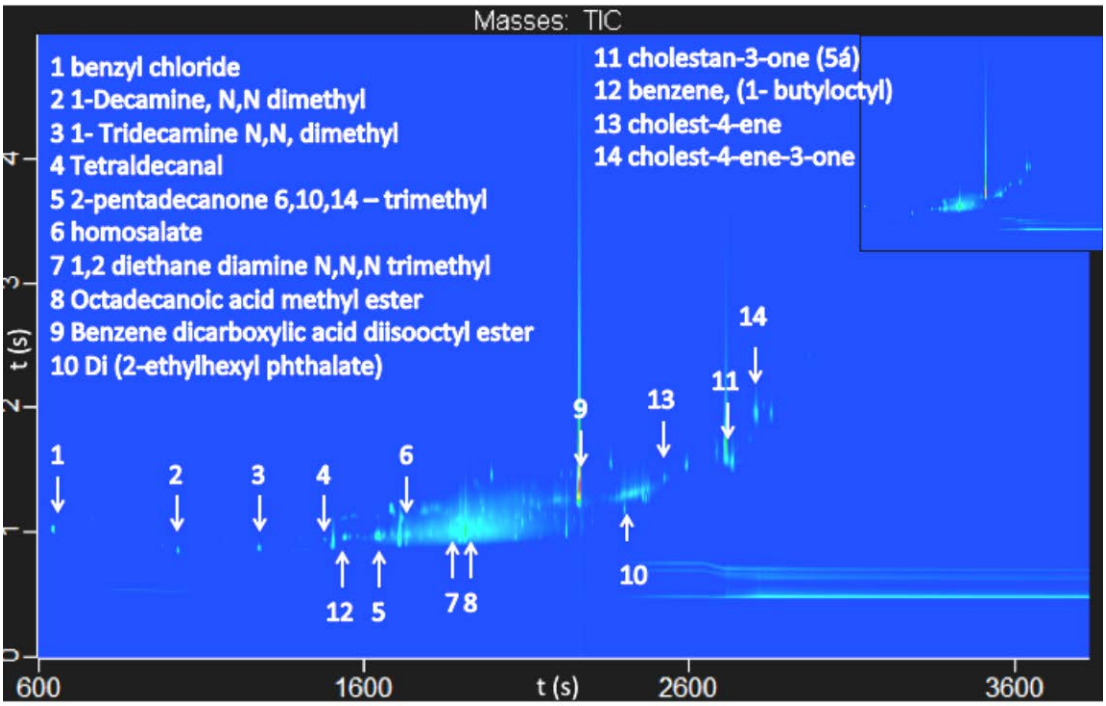

Figure 5.20. Screen capture of the total ion chromatograph of the methanol extract (after pre-extraction with formic acid) with the 14 most abundant compounds labeled with arrows.

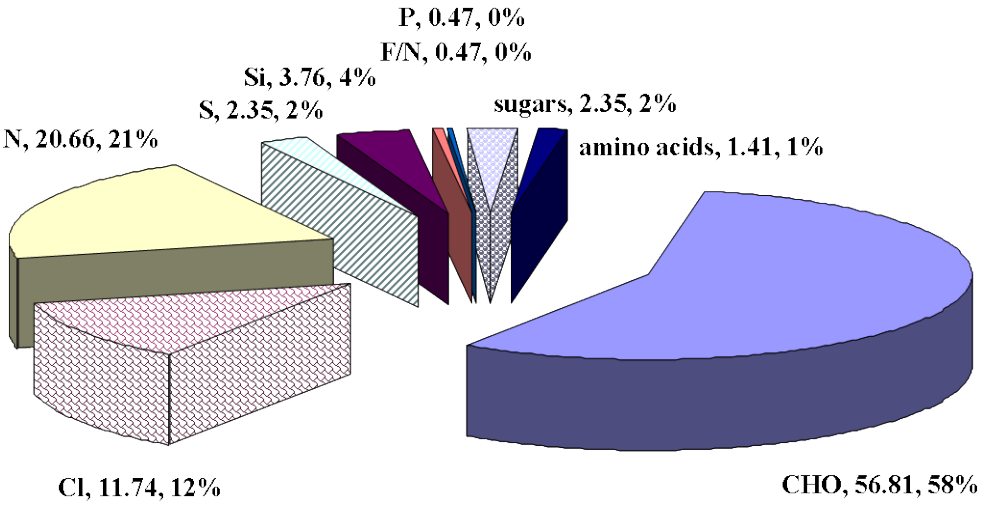

Figure 5.21. MF foulant extract elemental distributions.

No information on the quantity of each compound was obtained from this preliminary analysis. It would be necessary to run standards of each compound to determine their quantity. It is not known how these compounds contribute to the irreversible fouling of polypropylene hollow fibers, but it could be significant given the fact that sonication is required to remove the bound material. It would be necessary to determine the pressure drop across the fibers using this cleaning protocol. It may be that sonication with current cleaning

protocols would be advantageous. The protein, carbohydrate, and lipid nanoparticulate fraction of the MF foulants are believed to be the major contributor to fouling and reduction in water flux. However, the trace organic contaminants present in the secondary-treated wastewater undoubtedly are associated with the nanoparticles and membrane surface.

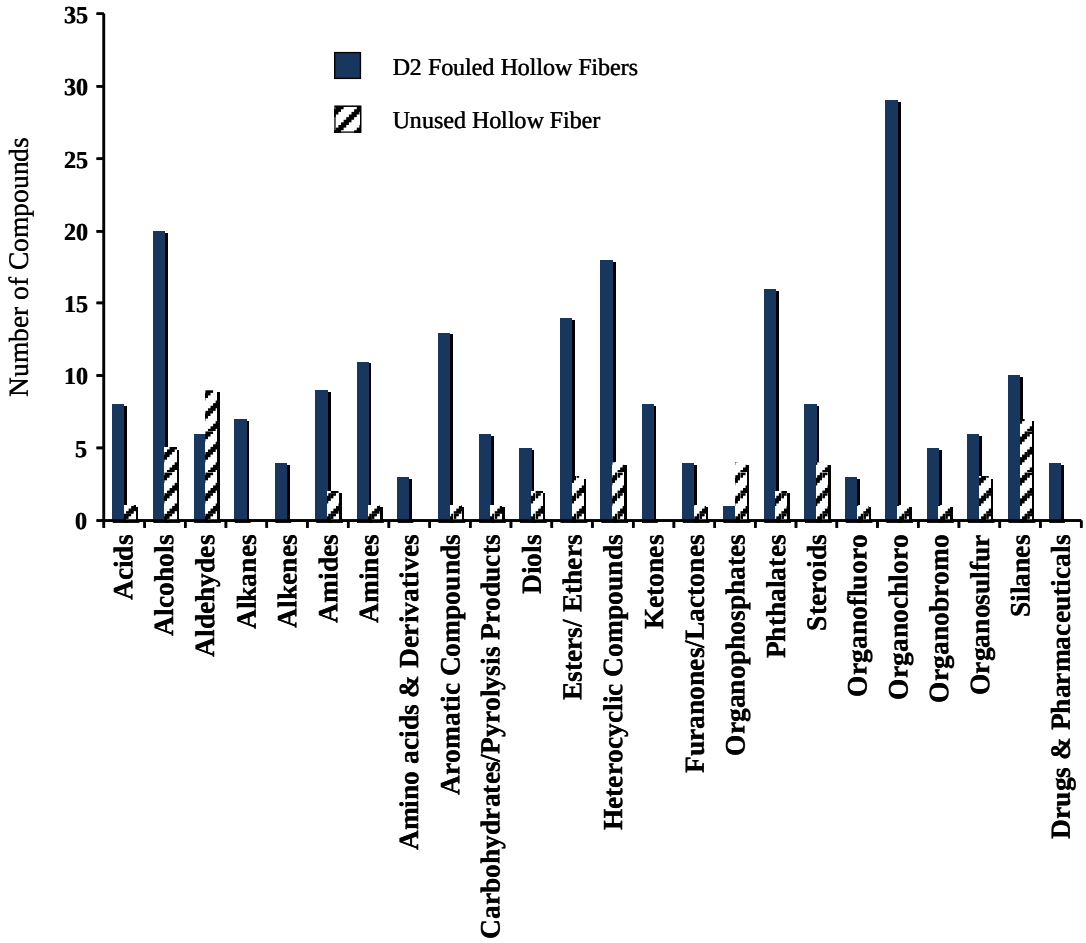

Figure 5.22. MF foulant extract functional group distribution.

Table 5.3. Compounds (218 total) Identified in Formic Acid and Methanol Extracts of Fouled Hollow Fiber MF Membranes, Grouped by Class

	Compound Name	Comment	R.T. (sec)	Similarity
8	**Acids**			
	Butanedioic acid, 2,3-bis(benzoyloxy)-, [S-(R*,R*)]-		2233.76 , 1.465	993
	Hexadecenoic acid, Z-11-	pheremone	2893.26 , 0.713	894
	Z-8-Methyl-9-tetradecenoic acid		1983.95 , 1.003	858
	17-Octadecynoic acid	enzyme inhibitor	1993.94 , 0.997	838
	n-Hexadecanoic acid (palmitic acid)	ubiquitous fatty acid	2048.9 , 0.825	872
	Oleic Acid	omega-9 fatty acid	3527.77 , 0.713	899
	2-Propenoic acid, 2-(dimethylamino)ethyl ester		2033.91 , 1.036	879
	2-Propenoic acid, 3-(4-methoxyphenyl)-, 2-ethylhexyl ester		2088.87 , 1.254	881
20	**Alcohols**			
	1-Decanol	plasticizer/surfactant	989.704 , 0.931	959
	1-Dodecen-1-ol, acetate		1624.22 , 0.970	818
	1-Hexanol, 2-ethyl-	plasticizer	649.962 , 0.878	942
	1-Octanol	water treatment	709.916 , 0.898	943
	1-Octanol, 2-butyl-	cosmetics	1644.21 , 0.950	933
	1-Propanol, 2,2'-oxybis-		669.947 , 1.016	939
	2-Dodecanol	fragrance/flavor	1379.41 , 0.871	906
	2-Hepten-3-ol, 4,5-dimethyl-		2283.72 , 1.162	920
	2-Hexadecanol	insect control	1654.2 , 0.950	912
	2-Methyl-Z,Z-3,13-octadecadienol	terpenoid	3108.09 , 0.719	866
	2-Pentadecanol	de-inking	1624.22 , 0.964	901
	2-Propanol, 1-[1-methyl-2-(2-propenyloxy)ethoxy]-		1064.65 , 1.069	930
	2-Tridecen-1-ol, (E)-	fragrances	1244.51 , 0.944	913
	E-2-Tetradecen-1-ol	pheremone	1479.33 , 0.950	912
	Propanol, [(butoxymethylethoxy)methylethoxy]-		1404.39 , 1.109	881
	Benzenemethanol, 4-ethyl-		944.738 , 1.129	814
	Benzyl alcohol	solvent,insecticide	669.947 , 1.089	935
	Ethanol, 2-[2-(4-nonylphenoxy)ethoxy]-	TSCA	1784.1 , 1.175	807
	Ethanol, 2-[4-(1,1-dimethylpropyl)phenoxy]-		1824.07 , 1.195	914
	2-Furanol, tetrahydro-2-methyl-		2128.84 , 1.129	952
	Methylazoxymethanol acetate	carcinogen	2698.4 , 0.535	936
6	**Aldehydes**			
	11-Hexadecynal	pheremone	3063.13 , 3.029	830
	Dodecanal	fragrance	1164.57 , 0.944	945
	Lilial	cosmetics	1319.45 , 1.122	925
	Nonanal	fragrances	754.882 , 0.917	890
	Octadecanal	pheremone	1514.3 , 0.964	954
	Undecanal, 2-methyl-	fragrances	1699.16 , 0.937	843
	Octadecane, 1,1-dimethoxy-		1769.11 , 0.950	809
7	**Alkanes**			
	Dodecane, 2-methyl-	fragrance	2073.88 , 0.937	886
	Eicosane, 2-methyl-	fragrance	2003.93 , 0.911	872
	Heptadecane, 2,6,10,14-tetramethyl-		1149.58 , 0.832	941
	Hexadecane	diesel fuel	1958.97 , 0.911	913
	Pentadecane		1953.97 , 0.904	880
	Tetradecane		1943.98 , 0.898	863
	Tridecane	pheromone, solvent	884.783 , 0.812	967
4	**Alkenes**			
	1-Undecene, 5-methyl-		1529.29 , 0.865	870
	1,E-11,Z-13-Octadecatriene		2523.54 , 0.766	832
	3-Tetradecene, (Z)-		1139.59 , 0.851	951
	4-Tetradecene, (Z)-		1714.15 , 0.964	884
9	**Amides**			
	[+]-2,4-Dihydroxy-3,3-dimethyl-N-[3,3-dimethylaminopropyl]butyramide		2598.48 , 1.676	916
	Acetamide, 2-(benzyl)methylamino-N-(2-dimethylamino-4-quinolinyl)-		1909 , 1.069	968
	Acetamide, N-(3-dimethylaminopropyl)-2-(1,3-dimethyl-2,6-dioxo-1,2,3,6-tetrahydropurin-7-yl)-		1993.94 , 1.175	911
	Acetamide, N-hexyl-		1884.02 , 1.102	843
	Dodecanamide		2133.83 , 1.201	901
	Formamide, N-[3-(dimethylamino)propyl]-		2458.59 , 1.247	925
	Nonanamide		2018.92 , 1.175	813
	Decanamide, N-(2-hydroxyethyl)-	surfactant	2098.86 , 1.096	894
	N-Methyldodecanamide		2158.81 , 1.168	879
11	**Amines**			
	1,2-Ethanediamine, N,N'-dimethyl-		1419.38 , 0.878	976
	2-Heptanamine, 2-methyl-		1309.46 , 0.865	815
	2-Penten-1-amine, N,N,2-trimethyl-, (E)-		1569.26 , 0.884	938
	2-Propanamine, 2-methyl-		1539.29 , 0.871	957
	Hydrazine, (2-methylpropyl)-		1983.95 , 1.254	831
	Hydrazine, 1,2-dimethyl-	pesticide	2353.67 , 0.535	835
	4,9-Decadien-2-amine, N-butyl-		1349.43 , 1.386	914
	Decane,-1,10-diamino,-N,N,N',N'-tetramethyl		1604.24 , 0.891	999
	Benzenamine, 3,4-dichloro-		1219.53 , 1.360	960
	Hydroxylamine, O-(phenylmethyl)-		2203.78 , 1.485	816
	Benzedrex	decongestant	1894.02 , 0.964	940
	2,3-Diamino-2,3-Dimethylbutane		1489.32 , 0.911	953
	Diazene, dimethyl-	rubber	1804.08 , 0.917	900
	Methyl á-dimethylaminoisobutyrate		2758.36 , 1.663	961

Table 5.3. (Continued). Compounds (218 total) Identified in Formic Acid and Methanol Extracts of Fouled Hollow Fiber MF Membranes, Grouped by Class

	Compound Name	Comment	R.T. (sec)	Similarity
3	**Amino acids and derivatives**			
	d-Tyrosine	bacterial, prevents biofilm	1739.13 , 1.102	857
	N-à,N-ê-Di-cbz-L-arginine		699.924 , 1.056	829
	l-Alanine, N-(p-toluoyl)-, hexyl ester		2218.77 , 1.115	951
13	**Aromatic compounds**			
	1,2-Diphenylcyclopropane		1559.27 , 1.267	927
	4-tert-Butyltoluene	fragrance	749.886 , 0.931	906
	Benzene, (1-butylnonyl)-		1539.29 , 0.970	873
	Benzene, (1-pentylheptyl)-		1639.21 , 0.970	876
	Benzene, (1-propyldecyl)-		1554.27 , 0.970	927
	Benzene, 1,2,3-trimethyl-		614.989 , 0.904	938
	Benzene, propoxy-		654.958 , 0.957	871
	Butylated Hydroxytoluene	food additive	1299.47 , 1.049	918
	Diphenylmethane		1214.53 , 1.214	875
	Benzene, 1,1'-(1,3-propanediyl)bis-		1469.34 , 1.201	956
	Benzenemethanethiol	wine	739.894 , 1.122	954
	o-Cymene	mono-terpene (oil constituent)	654.958 , 0.904	948
	Carbonic acid, phenyl tetradecyl ester		2203.78 , 1.221	874
	Methanamine, 1-(dicyclohexylphosphino)-N,N-dimethyl-		1879.03 , 0.957	845
	Ethylamine, 2-diethylboryloxy-		2223.77 , 1.076	904
	Benzenemethanamine, N,N-dimethyl-	TSCA	674.943 , 0.957	948
	Carbonic acid, phenyl tetradecyl ester		2203.78 , 1.221	874
	1-Propanol, dl-2-benzylamino-,		2083.87 , 1.082	961
	Methanamine, 1-(dicyclohexylphosphino)-N,N-dimethyl-		1879.03 , 0.957	845
6	**Carbohydrates/ pyrolysis products**			
	1,4:3,6-Dianhydro-à-d-glucopyranose	cellolose pyrolysis	914.761 , 1.340	847
	á-D-Glucopyranose, 1,6-anhydro-	cellulose pyrolysis	1279.48 , 1.544	934
	D-Fucose	cell surface glycan	884.783 , 1.267	809
	Levoglucosenone	cellulose pyrolisis	779.863 , 1.294	885
	Methyl-2-O-methylàd-glucopyranoside		1159.57 , 1.386	826
	Phenol, 2,6-dimethoxy- (syringol)	lignin pyrolisis	1104.62 , 1.267	806
5	**Diols**			
	(2R,4R)-(-)-Pentanediol		1604.24 , 0.970	871
	1,2-Octadecanediol	hair products	1604.24 , 0.957	900
	1,2-Propanediol, 3-benzyloxy-1,2-diacetyl-		2168.81 , 1.353	983
	2,4,7,9-Tetramethyl-5-decyn-4,7-diol	wastewater clarification	1169.57 , 0.970	883
	3,5-di-tert-Butyl-4-hydroxybenzaldehyde (BHT)	metabolite of BHT	1589.25 , 1.175	890
14	**Esters/ Ethers**			
	Methoxyacetic acid, 3-tetradecyl ester	volatile from algae	1968.96 , 0.917	888
	Oxalic acid, allyl tridecyl ester		1704.16 , 0.983	869
	Propanoic acid, 2-methyl-, 1-(1,1-dimethylethyl)-2-methyl-1,3-propanediyl ester		1389.4 , 0.990	957
	Propanoic acid, 2-methyl-, 2,2-dimethyl-1-(2-hydroxy-1-methylethyl)propyl ester		1104.62 , 1.003	873
	Propanoic acid, 2-methyl-, 3-hydroxy-2,4,4-trimethylpentyl ester		1129.6 , 0.997	949
	Homosalate	sunscreen	1714.15 , 1.115	924
	m-Anisic acid, 4-nitrophenyl ester		1524.3 , 1.122	901
	o-Anisic acid, 4-benzyloxyphenyl ester		1554.27 , 1.142	956
	Octocrylene	sunscreen	2353.67 , 1.538	838
	p-Anisic acid, 3-methylphenyl ester		1574.26 , 1.142	907
	Benzeneacetic acid, à-oxo-, methyl ester		1644.21 , 1.445	973
	Pentadecanoic acid, 14-methyl-, methyl ester	soil FAME	1909 , 1.016	867
	Fumaric acid, ethyl 3,4,5-trichlorophenyl ester		1124.6 , 1.261	857
18	**Heterocyclic compounds**			
	2H-Oxireno[3,4]cyclopenta[1,2-c]furan-2-one, 1a,1b,4,4a,5,5a-hexahydro-4-(dimethoxymethyl)-, (1bR,1a-cis,4-trans,4a-cis,5a-cis)-		1774.11 , 0.950	843
	1,3-Dioxolane, 2-(2-propenyl)-		2688.41 , 0.535	948
	5-Isopropyl-2,4-imidazolidinedione		2363.66 , 1.221	814
	5,10-Diethoxy-2,3,7,8-tetrahydro-1H,6H-dipyrrolo[1,2-a:1',2'-d]pyrazine	anti-fungal	1769.11 , 1.815	805
	Ethanone, 1-(1-methyl-1H-pyrrol-2-yl)-		999.696 , 1.175	820
	Ethanone, 1-(3-methylphenyl)-		884.783 , 1.129	935
	Furan, 2-butyltetrahydro-		1599.24 , 0.970	879
	Indole	fragrances	1039.67 , 1.346	899
	Morpholine, 4-octadecyl-		2063.89 , 1.049	997
	Spiro[1,3-dioxolane-2,1'(4'H)-naphthalen]-4'-one, octahydro-		1839.06 , 1.089	803
	2,6-Piperazinedione, 4-benzoyl-, 2-oxime		1009.69 , 1.175	911
	Tetrahydrofurfuryl chloride		859.802 , 0.917	992
	Cyclobutane, methoxy-		1674.18 , 0.911	871
	Cyclopentaneundecanoic acid	pheremone	2183.8 , 0.871	861
	Cyclopropane, 3-chloro-1,1,2,2-tetramethyl-		2113.85 , 0.990	801
	1-Dodecanone, 2-(imidazol-1-yl)-1-(4-methoxyphenyl)-		1564.27 , 1.115	844
	Propan-1-one, 1-(4-methoxyphenyl)-3-(morpholin-4-yl)-2-phenyl-		1889.02 , 1.030	809
	Acetamide, N-(3-dimethylaminopropyl)-2-(1,3-dimethyl-2,6-dioxo-1,2,3,6-tetrahydropurin-7-yl)-		1993.94 , 1.175	911
1	**Isocyanate**			
	Isophorone diisocyanate	Siemens product	1399.39 , 1.063	882

Table 5.3. (Continued). Compounds (218) Identified in Formic Acid And Methanol Extracts of Fouled Hollow Fiber MF Membranes, Grouped by Class

	Compound Name	Comment	R.T. (sec)	Similarity
8	**Ketones**			
	2-Dodecanone	fragrance/flavor	879.787 , 0.931	872
	à-(N,N-Dimethylamino)-4'-hydroxyacetophenone		2353.67 , 1.089	999
	Acetophenone	fragrance	714.913 , 1.109	957
	1-(4-tert-Butylphenyl)propan-2-one		1224.53 , 1.142	818
	4-(t-Butyl)benzaldehyde	fragrance	1054.65 , 1.089	878
	1,4-Bis[3-(dimethylamino)propionyl]benzene		1554.27 , 0.878	984
	1-Dodecanone, 2-(imidazol-1-yl)-1-(4-methoxyphenyl)-		1564.27 , 1.115	844
	3,4-Hexanedione, 2,2,5-trimethyl-	essential oil	1019.68 , 0.825	921
4	**Furanones/ lactones**			
	2(3H)-Furanone, 5-acetyldihydro-	wine	794.852 , 1.360	936
	2(3H)-Furanone, dihydro-5-methyl-5-(2-methylpropyl)-		2183.8 , 1.135	853
	l-Pantoyl lactone	bacterial	669.947 , 1.148	940
	4,8,12,16-Tetramethylheptadecan-4-olide	isoprenoid ox product of Vit E	2108.85 , 1.129	937
2	**Oxiranes**			
	Oxirane, (2-bromoethyl)-		1799.09 , 0.990	956
	Oxirane, trimethyl-		1709.16 , 0.957	998
1	**Phosphates**			
	Tributyl phosphate	detergents/pesticides	1444.36 , 1.076	866
16	**Phthalates**			
	Bis(tridecyl) phthalate	plasticizer	2358.66 , 1.267	812
	Diisooctyl phthalate	plasticizer	2253.74 , 1.274	896
	Phthalic anhydride	plastics	1069.64 , 1.340	932
	Diethyl Phthalate	plasticizer	1394.4 , 1.274	946
	Phthalic acid, 2-methylpent-3-yl octadecyl ester	plasticizer	2428.61 , 1.313	838
	Phthalic acid, 4-methylhept-3-yl undecyl ester	plasticizer	2448.59 , 1.320	873
	Phthalic acid, 5-methylhex-2-yl pentadecyl ester	plasticizer	2163.81 , 1.241	850
	Phthalic acid, 5-methylhex-2-yl pentadecyl ester	plasticizer	2128.84 , 1.228	825
	Phthalic acid, 7-methyloct-3-yn-5-yl undecyl ester	plasticizer	2458.59 , 1.327	850
	Phthalic acid, decyl nonyl ester	plasticizer	2218.77 , 1.274	890
	Phthalic acid, decyl undecyl ester	plasticizer	2468.58 , 1.333	899
	Phthalic acid, dodecyl 2-(2-methoxyethyl)hexyl ester	plasticizer	2473.58 , 1.360	821
	Phthalic acid, hex-2-yn-4-yl isobutyl ester	plasticizer	1679.18 , 1.214	833
	Phthalic acid, hex-3-yl undecyl ester	plasticizer	2413.62 , 1.294	851
	Phthalic acid, isobutyl 7-methyloct-3-yn-5-yl ester	plasticizer	2198.78 , 1.261	848
	Benzyl butyl phthalate	plasticizer	2118.84 , 1.518	922
8	**Steroids**			
	Cholest-4-en-3-one	Steroid-Marker for fecal matter	2798.33 , 1.907	901
	Cholest-4-en-6-one	Steroid-Marker for fecal matter	2743.37 , 1.716	803
	Cholest-5-en-3-ol (3á)-, tetradecanoate	Steroid-Marker for fecal matter	2533.53 , 1.439	858
	Cholesta-4,6-dien-3-ol, (3á)-	Steroid-Marker for fecal matter	2518.54 , 1.432	928
	Cholesta-4,6-dien-3-one	Steroid-Marker for fecal matter	2823.31 , 1.993	827
	Cholestan-3-one, (5á)-	Steroid-Marker for fecal matter	2708.4 , 1.591	836
	Cholestane, 3-(ethylthio)-, (3á,5à)-		2453.59 , 1.267	827
	Cholestane, 4,5-epoxy-, (4à,5à)-		2703.4 , 1.584	809
3	**Organofluoro**			
	5-Fluoro-8-quinolinol	fungicide	1559.27 , 1.135	808
	4-Trifluoroacetoxyhexadecane	bioactive compound from leaves	1689.17 , 0.964	925
	Carbamic acid, N-[1,1-bis(trifluoromethyl)ethyl]-, 4-(1,1,3,3-tetramethylbutyl)phenyl ester		1604.24 , 1.129	810
29	**Organochloro**			
	1,3-Dioxolane, 2-(dichloromethyl)-		2518.54 , 0.528	999
	1-Chloroundecane		979.711 , 0.904	934
	2-Ethoxy-3-chlorobutane		2593.48 , 0.528	978
	2-Heptanone, 7,7-dichloro-		1694.17 , 0.937	882
	2,3-Diamino-2,3-Dimethylbutane		1489.32 , 0.911	953
	2,5-Dimethylbenzyl chloride		929.749 , 1.089	910
	2-Ethoxy-3-chlorobutane		2593.48 , 0.528	978
	2-Heptanone, 7,7-dichloro-		1694.17 , 0.937	882
	2-Ethoxy-3-chlorobutane		2593.48 , 0.528	978
	2-Heptanone, 7,7-dichloro-		1694.17 , 0.937	882
	Benzene, 1-chloro-4-isocyanato-		814.837 , 1.043	947
	1,3-Dioxolane, 2-(dichloromethyl)-		2518.54 , 0.528	999
	2-Ethoxy-3-chlorobutane		2593.48 , 0.528	978
	2-Heptanone, 7,7-dichloro-		1694.17 , 0.937	882
	2-Ethoxy-3-chlorobutane		2593.48 , 0.528	978
	2-Heptanone, 7,7-dichloro-		1694.17 , 0.937	882
	1,3-Dioxolane, 2-(dichloromethyl)-		2518.54 , 0.528	999
	Phenol, 2-chloro-4-(1,1-dimethylpropyl)-	TSCA	1544.28 , 1.076	859
	p-Chloroaniline	textile/leather, pesticide	914.761 , 1.247	947
	N-(3-Chloro-2-methyl-phenyl)-N'-(2-piperazin-1-yl-ethyl)-oxalamide		1973.96 , 1.023	856
	Nonadecane, 1-chloro-		1879.03 , 0.977	845
	m-Anisic acid, 4-chlorophenyl ester		1414.38 , 1.129	889
	Benzyl chloride		644.966 , 1.043	962
	Bis[phenylsulfonyl]-4-trichloromethylphenyl chloromethane		1759.12 , 1.690	840
	1,3-Dioxolane, 2-(3-bromo-5,5,5-trichloro-2,2-dimethylpentyl)-	antimicrobial	2858.28 , 0.528	981
	Benzyl 2-chloroethyl sulfone		764.875 , 1.122	970
	Fumaric acid, ethyl 3,4,5-trichlorophenyl ester		1124.6 , 1.261	857
	Benzenamine, 3,4-dichloro-		1219.53 , 1.360	960
	Tetrahydrofurfuryl chloride		859.802 , 0.917	992

Table 5.3. (Continued). Compounds (218 total) Identified in Formic Acid And Methanol Extracts of Fouled Hollow Fiber MF Membranes, Grouped by Class

	Compound Name	Comment	R.T. (sec)	Similarity
5	**Organobromo**			
	2-Bromomethyl-1,3-dioxolane		2738.37 , 0.528	926
	Pentadec-7-ene, 7-bromomethyl-		1914 , 0.944	830
	Decane, 1-bromo-		1094.62 , 0.931	967
	1,3,4-Oxadiazole-2(3H)-thione, 5-(2-bromophenyl)-3-benzyl(methyl)aminomethyl-		2243.75 , 1.102	942
	Oxirane, (2-bromoethyl)-		1799.09 , 0.990	956
5	**Organothiols**			
	2-Aminodiphenylsulfone		1978.95 , 1.914	827
	3-(N,N-Dimethyllaurylammonio)propanesulfonate	detergent	1299.47 , 0.858	802
	3,4-Hexanedione, 2,2,5-trimethyl-	essential oil	1019.68 , 0.825	921
	Benzothiazole	rubber	949.734 , 1.287	903
	Ethanethiol, 2-dimethylamino-S-trimethylsilyl-		2323.69 , 1.201	975
4	**Drugs & pharmaceuticals**			
	Benzeneethanamine, 2-fluoro-á,3,4-trihydroxy-N-isopropyl-	amphetamine	2048.9 , 1.188	931
	Methamphetamine	drug	1224.53 , 1.175	974
	4-tert-butyl-ethylamphetamine	pharmaceutical	1489.32 , 0.898	878
	Hexestrol, O-heptafluorobutyryl-	estrogen	1624.22 , 1.135	913
10	**Silanes**			
	Silane, tetramethyl-	oil industry	2723.39 , 0.535	972
	Silane, trichlorodocosyl-		2113.85 , 0.911	803
	Silane, trimethyl(1-phenylethyl)-		2438.6 , 0.528	933
	Spiro[2.4]hept-5-ene, 5-trimethylsilylmethyl-1-trimethylsilyl-		2603.48 , 0.528	918
	Trimethyl(3,3-difluoro-2-propenyl)silane		2718.39 , 0.521	904
	Ethanamine, N,N-dimethyl-2-[(trimethylsilyl)oxy]-		2613.47 , 1.492	968
	Cyclotetrasiloxane, octamethyl- (D4)	indistrial and personal care	2338.68 , 0.508	890
	4-Methyl-2,4-bis(4'-trimethylsilyloxyphenyl)pentene-1		3018.16 , 0.488	852
	Benzeneethanamine, N,à-dimethyl-á-[(trimethylsilyl)oxy]-		644.966 , 0.792	994
	nonamethylcyclopentasiloxane		1754.12 , 0.785	931

Table 5.4. Compounds (53 total) Identified in Methanol Extract of Unused Hollow Fiber MF Membranes[a]

Compound Name	R.T. (sec)	Similarity
Acids		
n-Hexadecanoic acid	2328.69 , 0.799	828
Alcohols		
2-Butanol, 3-methoxy-	1948.97 , 1.155	821
Farnesol isomer a	2448.59 , 1.142	906
2-Butanol	1409.38 , 1.102	881
1-Propanol, 3-(dimethylamino)-, acetate	1284.48 , 0.865	992
Alkanes		
Tetradecane, 2,2-dimethyl-	1714.15 , 0.871	975
Eicosane, 2-methyl-	*2208.78 , 0.937*	*950*
Hexadecane	*2053.89 , 0.911*	*931*
Docosane, 11-butyl-	2283.72 , 0.950	946
Dodecane, 2,7,10-trimethyl-	1609.23 , 0.851	929
Pentadecane	1789.1 , 0.878	949
Nonadecane, 2-methyl-	1884.02 , 0.891	948
Heptadecane, 2,6,10,15-tetramethyl-	1739.13 , 0.871	932
Dodecane, 2-methyl-	2133.83 , 0.924	884
Amides/Amines		
9-Octadecenamide, (Z)-	2113.85 , 1.234	808
Dodecanamide	1574.26 , 1.148	943
2-Penten-1-amine, N,N,2-trimethyl-, (E)-	1709.16 , 0.904	997
Aromatic		
Benzene, (1-methyldecyl)-	1719.15 , 0.997	952
Azo		
Methylazoxymethanol acetate	2563.51 , 0.528	907
Carbohydrate		
cis-Inositol	2453.59 , 0.528	845
Diols		
2,4,7,9-Tetramethyl-5-decyn-4,7-diol	1169.57 , 0.964	906
1,2-Benzenediol, O-(4-methoxybenzoyl)-O'-(2-furoyl)-	1554.27 , 1.142	934
Esters		
2-Propenoic acid, 3-(4-methoxyphenyl)-, 2-ethylhexyl ester	1958.97 , 1.241	874
Carbamic acid, N-[1,1-bis(trifluoromethyl)ethyl]-, 4-(1,1,3,3-tetramethylbutyl)phenyl ester	1574.26 , 1.135	859
2-Propenoic acid, 3-(4-methoxyphenyl)-, 2-ethylhexyl ester	2088.87 , 1.247	895
Heterocyclic compounds		
s-Trioxane, 2,4,6-triethyl-	2173.8 , 1.201	804
1-Dodecanone, 2-(imidazol-1-yl)-1-(4-methoxyphenyl)-	1524.3 , 1.109	874
3,5-Diamino-1,2,4-triazole	1289.48 , 1.023	846
5-Isopropyl-2,4-imidazolidinedione	1694.17 , 0.997	885
Isocyanate		
Isophorone diisocyanate	1399.39 , 1.063	877
Ketones		
2-Hexanone, 3-hydroxy-3,5-dimethyl-	2043.9 , 1.148	805
9,19-Cyclolanostan-24-one, 3-acetoxy-25-methoxy-	2553.51 , 0.528	905
Acetophenone	719.909 , 1.096	985
7,9-Di-tert-butyl-1-oxaspiro(4,5)deca-6,9-diene-2,8-dione	719.909 , 1.096	985
Oxime		
2,6-Piperazinedione, 4-benzoyl-, 2-oxime	1009.69 , 1.168	906
Phthalates		
Phthalic acid, di(2-propylpentyl) ester	2253.74 , 1.241	836
Diethyl Phthalate	1394.4 , 1.267	950
Phthalic anhydride	1074.64 , 1.320	935
Benzyl butyl phthalate	2118.84 , 1.511	948

Table 5.4. (Continued). Compounds (53 total) Identified in Methanol Extract of Unused Hollow Fiber MF Membranes.[a]

Compound Name	R.T. (sec)	Similarity
Halogens, phosphates, sulfides, sulfones,silanes		
Cyclotetrasiloxane, octamethyl-	2313.7 , 0.515	876
Tributyl phosphate	1444.36 , 1.069	865
Spiro[2.4]hept-5-ene, 5-trimethylsilylmethyl-1-trimethylsilyl-	2533.53 , 0.528	976
Silane, trimethyl(1-phenylethyl)-	2683.42 , 0.535	930
Silane, tetramethyl-	2593.48 , 0.528	992
Benzene, 1,1'-[sulfinylbis(methylene)]bis-	2203.78 , 1.465	853
Cyclotrisiloxane, hexamethyl-	1919 , 0.508	912
1,3-Dioxolane, 2-(3-bromo-5,5,5-trichloro-2,2-dimethylpentyl)-	2468.58 , 0.528	894
1-Propene-1-thiol	2603.48 , 0.528	955
2-(2',4',4',6',6',8',8'-Heptamethyltetrasiloxan-2'-yloxy)-2,4,4,6,6,8,8,10,10-nonamethylcyclopentasiloxane	2013.92 , 0.785	848
Sulfurous acid, butyl dodecyl ester	2558.51 , 1.089	944
Methanamine, 1-(dicyclohexylphosphino)-N,N-dimethyl-	2218.77 , 0.964	966
2-Ethoxy-3-chlorobutane	2398.63 , 0.528	920

Note: [a]Compounds in italic were identified in the foulant extract from MF membrane.

5.5.4 Conclusions

An 18 h soak in 10% formic acid did not yield sufficient MF foulant material for analysis. However, material was recovered from these same fibers after a 48 h extraction in MeOH that was analyzed by GC×GC-TOFMS. A large number of compounds (218) were identified in the MF foulant extract, 53 of which were identified in the extract of the unused control membrane. These compounds undoubtedly became trapped in the foulant later and adsorbed on the membrane surface. The nontargeted method was useful in identifying these organic contaminants and demonstrated the potential of this relatively new technology for use in the identification of bulk and fractionated RO permeate and UV/AOP product water.

Chapter 6

Cartridge Filter Autopsy

6.1 Introduction

The purpose of this study was to autopsy and characterize the foulants on the surface of the melt-bonded polypropylene cartridge filters that are used to remove particulates from the MF effluent prior to treatment by RO. The MFE of the AWPF is delivered to a 2 million gallon break tank that provides a buffer for the operation of the RO treatment process. A number of 5 mgd RO trains go through a startup and shutdown process during the 24 h day as a result of the diurnal flow pattern of OCSD, and an adequate supply of MFE must be available at the time of the startup. The cartridge filters prevent any particulate debris from the MFE break tank from impinging on the end of the lead RO elements and blocking water transport. Under severe conditions, blockage of flow through the lead elements can lead to telescoping of the membrane sleeves (Byrne, 2002). The AWPF was originally set up with 20 μm, and later (February 2010–July 2011) 10 μm string-wound polypropylene cartridge filters. These filters were eventually (July 2011) replaced with 10 μm melt-bonded polypropylene cartridge filters. The cartridge filters are replaced when the differential pressure reaches ~8 psi, which occurs approximately every 9 months. A new and used cartridge filter was autopsied and the polypropylene surface characterized by a number of different analytical techniques.

6.2 Materials and Methods

The 50 × 2.5 in. cylindrical polypropylene cartridge filters are composed of an inner core element and outer filter element. The two elements have distinctly different polymer fiber weaves or polymer fiber densities. Swatches of material were cut from the outer and inner surfaces of the filter and analyzed by SEM and EDX spectroscopy. Swatches of element were placed in a plastic petri dish and dried in a glove box purged with compressed air passed through a Balston dryer (Parker Hannifin, Mayfield Heights, OH). The surface of the filter material was pressed against the a single-reflection germanium internal reflection element (ThunderDome, Thermo Scientific, Madison, WI) installed in the sample compartment of a Nicolet 6700 FT-IR spectrometer (Thermo Scientific). A total of 128 coadded, single-beam spectra collected at 4 cm^{-1} resolution with a DTGS detector, truncated at 670 cm^{-1}, ATR-corrected for the wavelength dependence of IR light, and baseline-corrected to zero absorbance. The spectra were "zapped" between 2390 and 2270 cm^{-1} to remove the residual carbon dioxide absorption band in the spectrum for visual clarity. An ATR-FTIR spectrum of the new cartridge filter was digitally subtracted from the spectrum of the used filter revealing the fouling material on the surface of the filter fibers. Digital images of the filters also were obtained. No R2A agar medium plating of the bacteria or microscopy was done on these samples.

6.3 Results and Discussion

Scanning electron microscopy images of the outer and inner surface of the polypropylene cartridge filter are shown in Figure 6.1. SEM images and a matching EDX spectrum of the inner and outer surface revealed carbon (C) associated with the surface (Figure 6.1). Small amounts of oxygen (O), palladium (Pd) and gold (Au) were detected on both surfaces (data

not shown). The Pd and Au are associated with the preparative coating for the SEM analysis. Digital and SEM images of the inner and outer surface of a new and used cartridge filter are shown in Figures 6.2 and 6.3. The new cartridge filters were bright white, whereas the outer membrane material of the element had a distinct yellow color. The inner core showed significantly less yellow coloration (see Figures 6.2e and 6.2f). A heavy biofilm is visible between the polypropylene fibers in Figure 3d. An SEM image of the outer surface of a used filter and the accompanying 2-D elemental data associated with the area of the surface in the image are displayed in Figures 6.4 and 6.5 and the elemental intensity spectrum in Figure 6.6, and calculated weight percentage and atom percentage distribution in Table 6.1. A similar analysis was done on a small area of the inner surface of the used filter and the results are displayed in Figures 6.7 through 6.9 and Table 6.2. EDX spectroscopic analysis indicated primarily carbon and oxygen, and nitrogen, sodium, and chloride (see Table 6.1). The EDX spectrum of the new cartridge filter was composed entirely of carbon (data not shown). The EDX C:N (wt%) ratio was much lower for the inner surface of the filter and the outer surface. This suggests that there was a heavy biofilm in the area sampled for the inside of the filter. The presence of a small amount of sulfur detected on the inside sample area also supports this conclusion. No sulfur was detected in the EDX spectrum of the outside fibers presumably because the area that was sampled was not as heavily fouled.

ATR-FTIR spectra revealing the foulants on the outer surface of the cartridge filter are displayed in Figure 6.10 and the inner surface in Figure 6.11. ATR-FTIR spectrometry revealed the presence of amide I (~1653 cm^{-1}) carbonyl stretch and amide II (~1553 cm^{-1}) N-H bend of protein and a 1083 cm^{-1} associated with the C–O–C, C–O stretch of carbohydrate material and PO_2^- symmetric stretch.

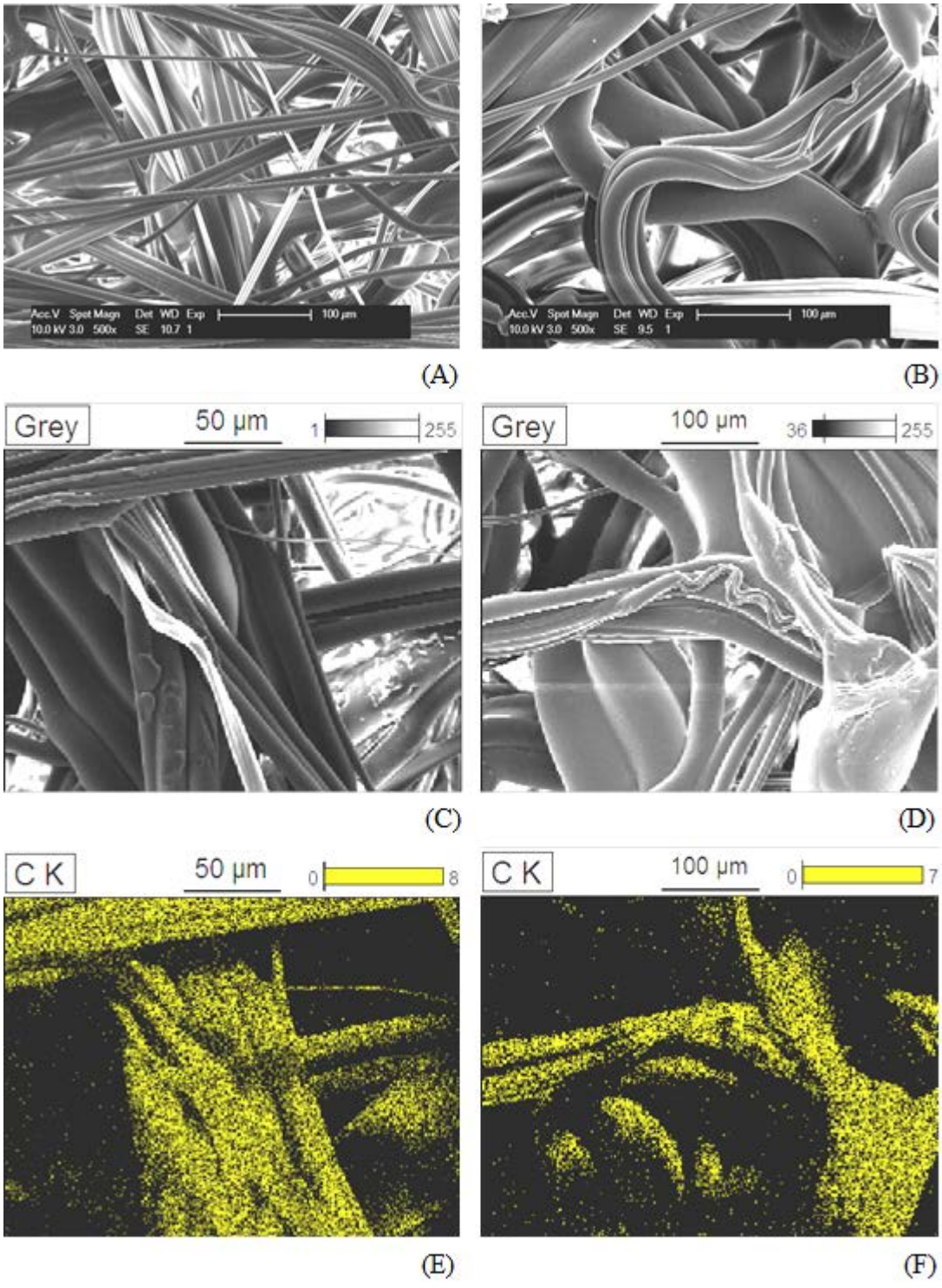

Figure 6.1. SEM images of inner surface (A, C), outer surface (B, D), EDX spectral images of inner surface (E), and outer surface (F) of a new 10 µm melt-bonded polypropylene cartridge filter.

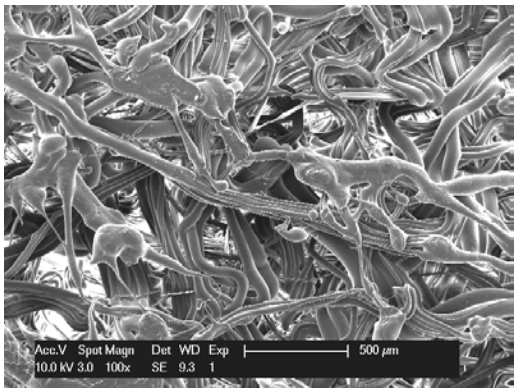

(A)

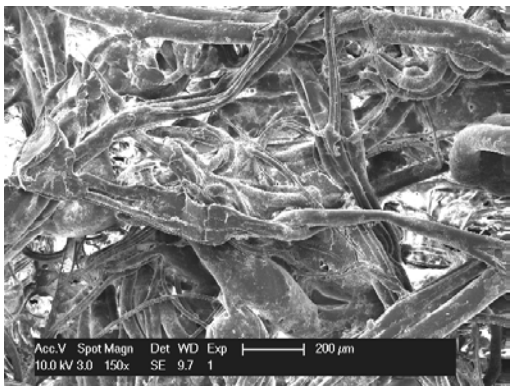

(B)

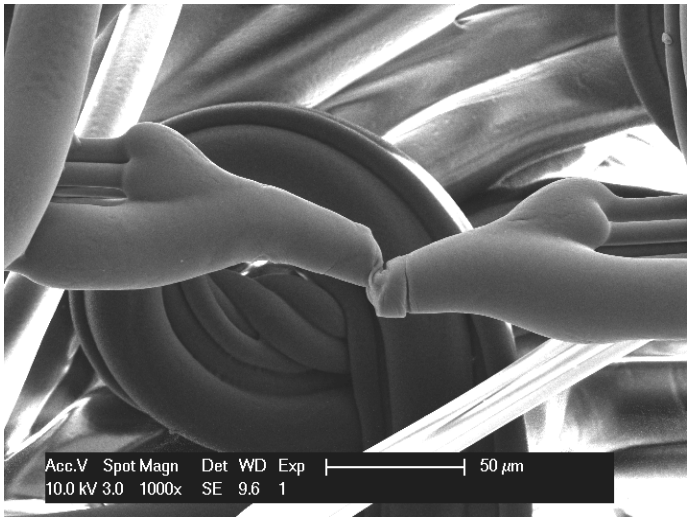

(C)

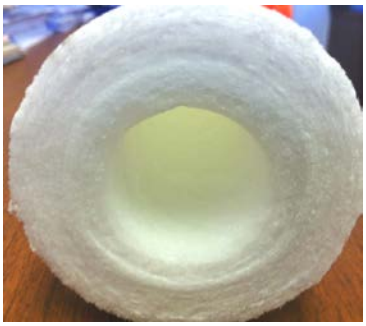

(E)

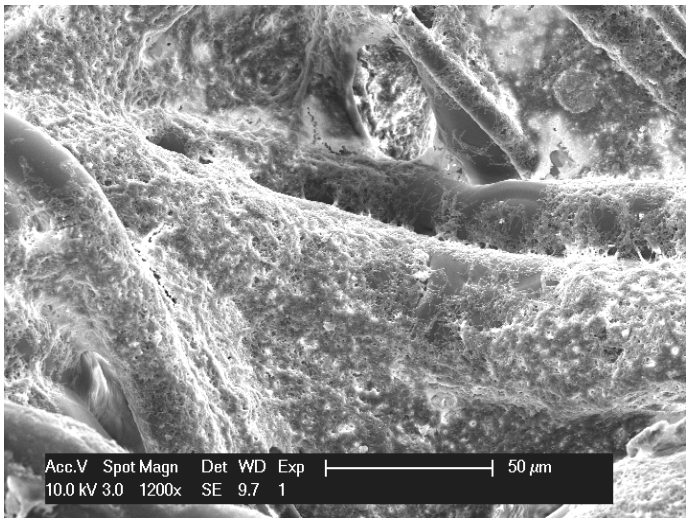

(D)

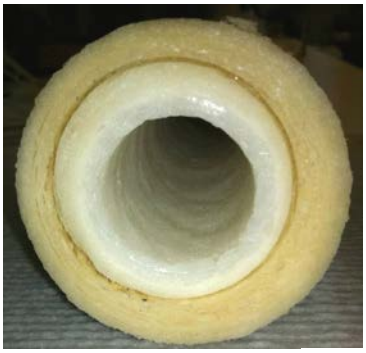

(F)

Figure 6.2. SEM images of fiber material from the outside of a new (A, C) and used (B, D), and digital images of the new (E) and used (F) 10 µm melt-bonded polypropylene cartridge filter.

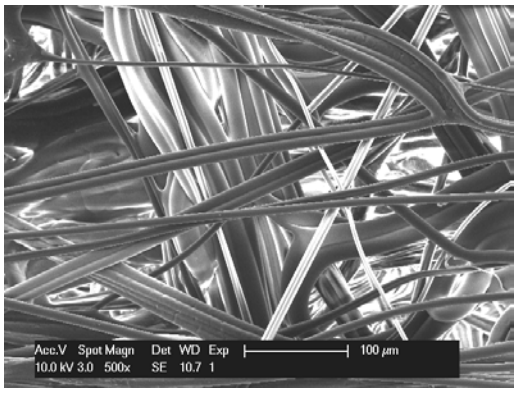

(A)

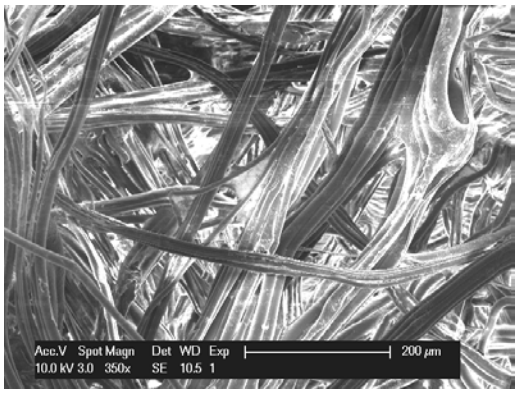

(B)

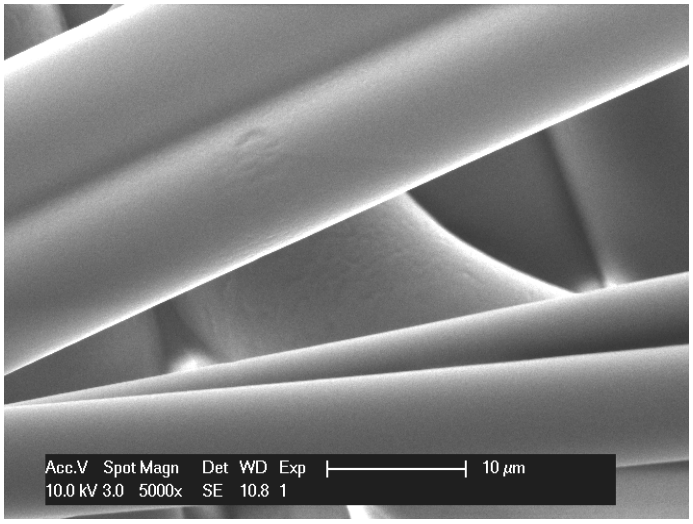

(C)

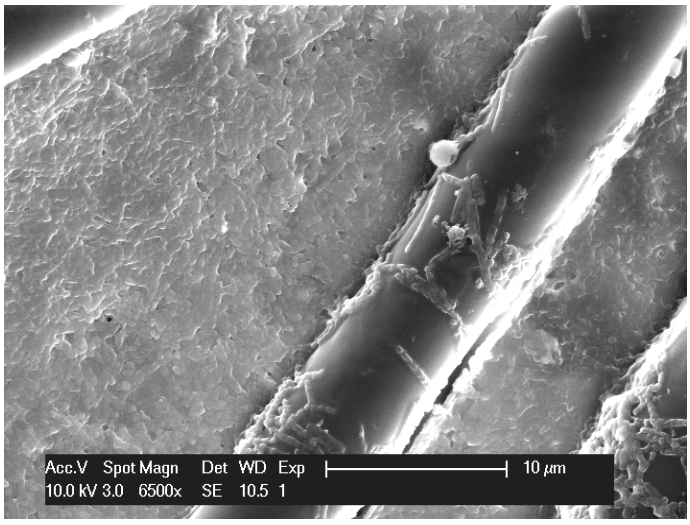

(D)

Figure 6.3. SEM images of fiber material from the inside of a new (A, C) and used (B, D) 10 µm melt-bonded polypropylene cartridge filter.

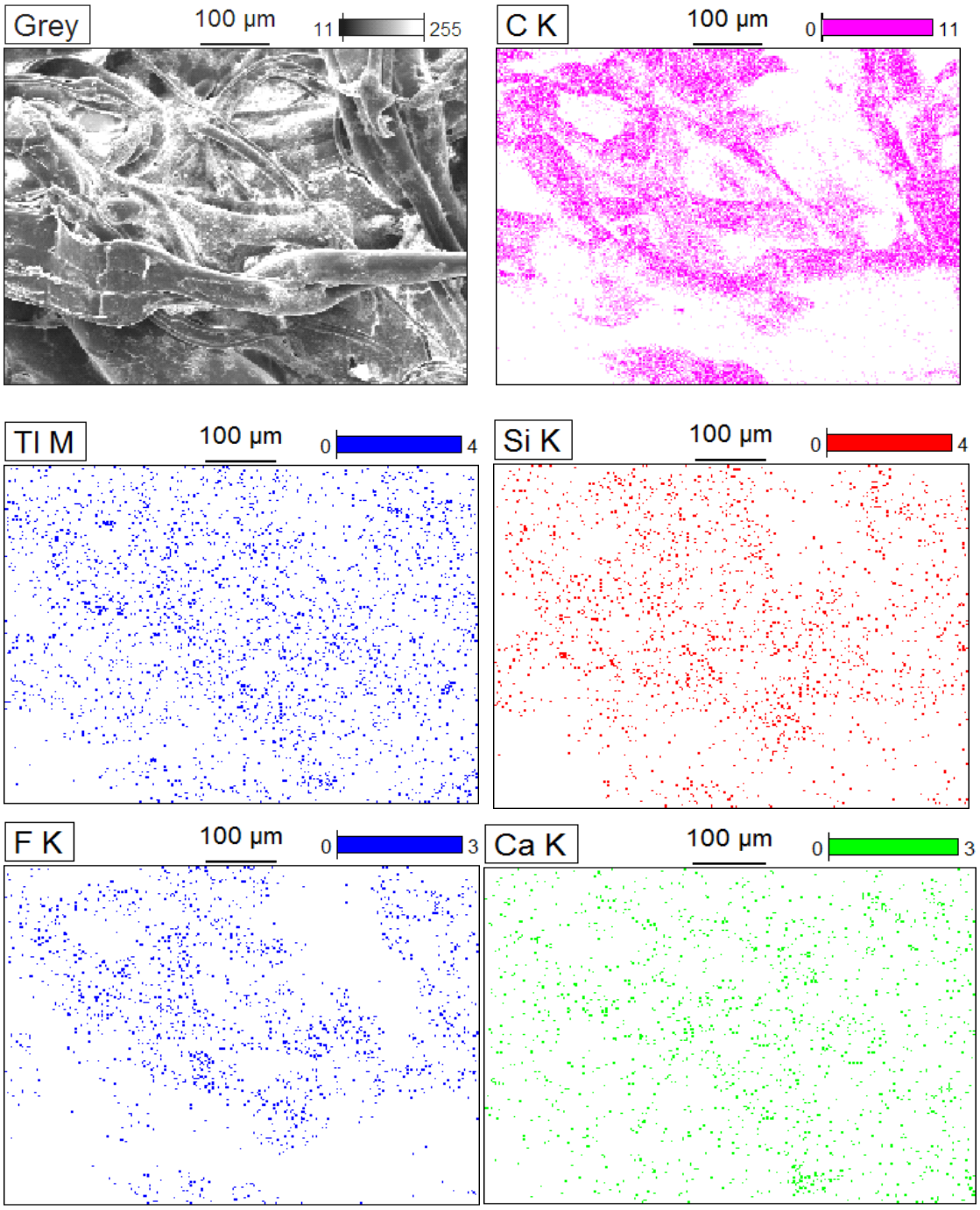

Figure 6.4. EDX elemental images of outer surface of a used 10 µm polypropylene cartridge filter.

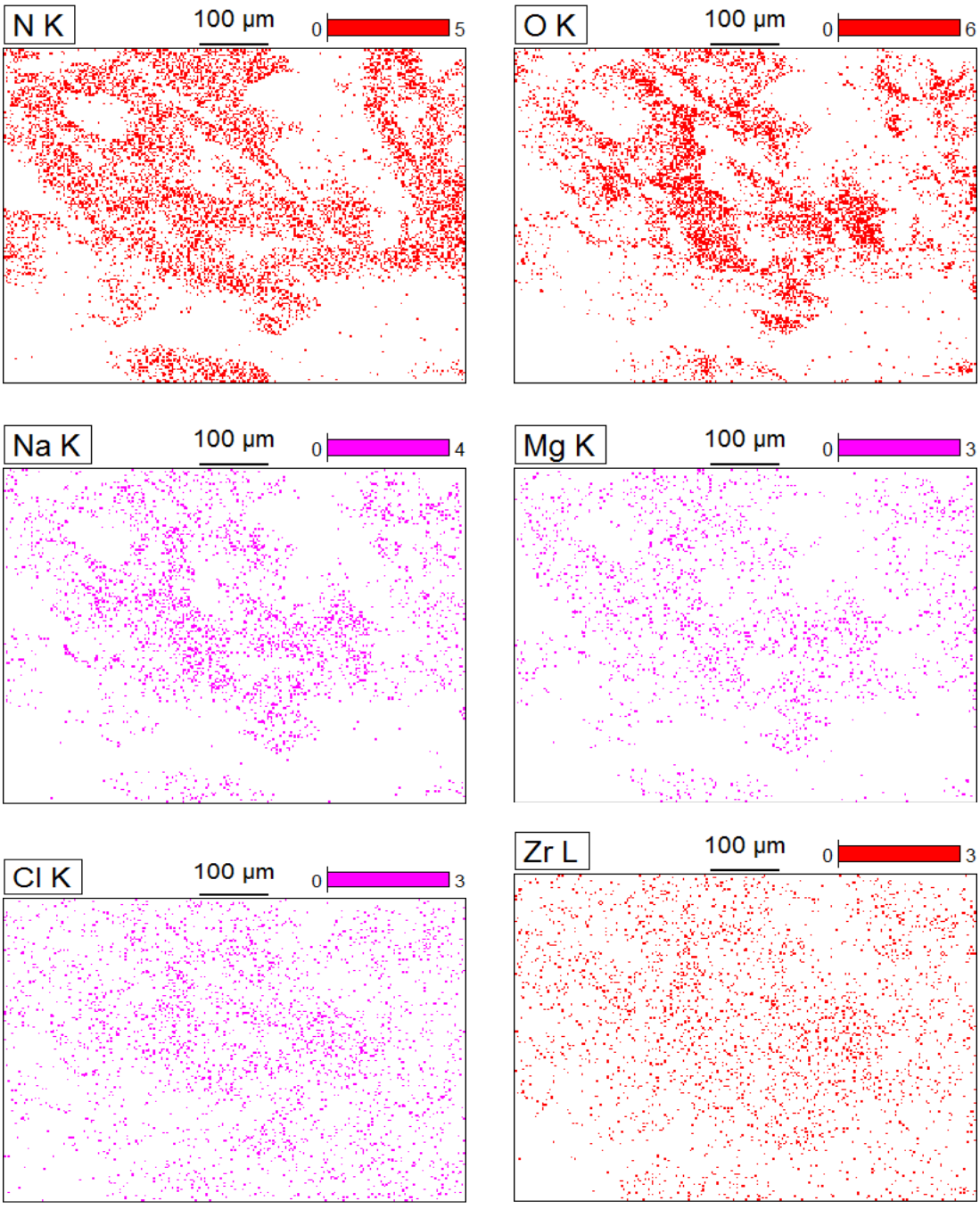

Figure 6.5. EDX elemental images of outer surface of a used 10 µm polypropylene cartridge filter.

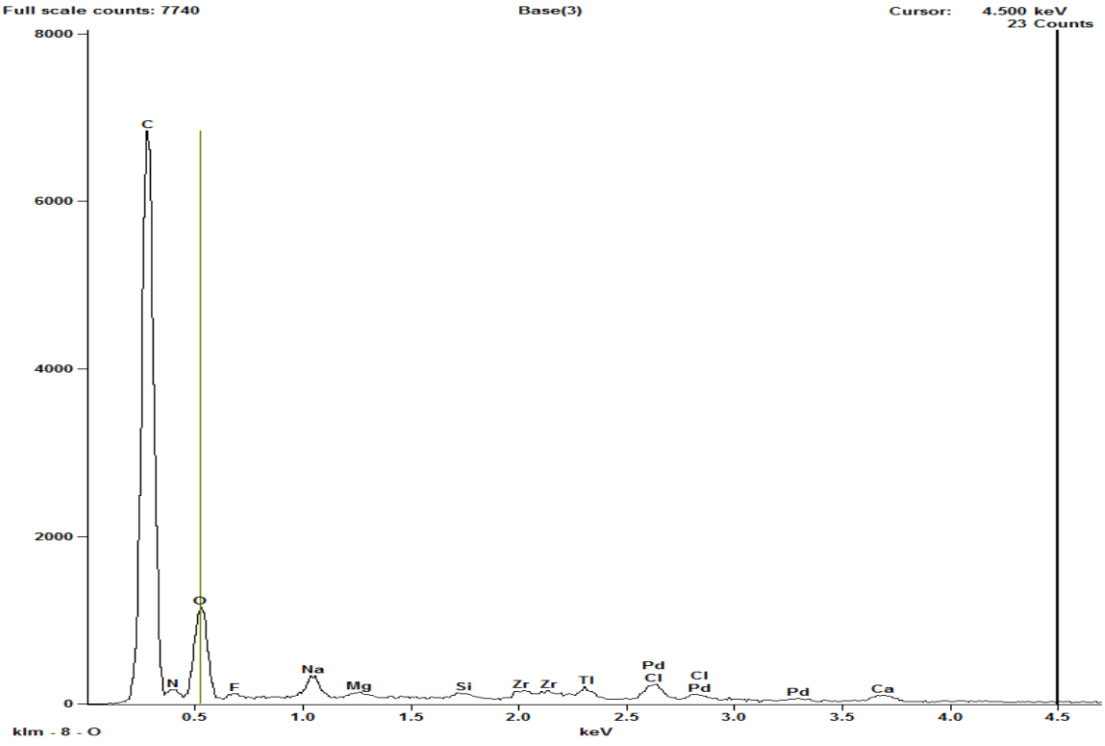

Figure 6.6. EDX elemental spectrum of the outer surface of the used 10 μm polypropylene cartridge filter.

Table 6.1 EDX Elemental Analysis of Outer Surface of a Used Cartridge Filter

Element Line	Element Wt%	Wt% Error	Atom %	Atom % Error
C K	67.21	+/-0.31	82.98	+/- 0.39
N K	2.54	+/-1.24	2.69	+/- 1.32
O K	8.84	+/-0.45	8.20	+/- 0.42
F K	0.38	+/-0.15	0.30	+/- 0.11
Na K	1.84	+/-0.10	1.19	+/- 0.06
Mg K	0.44	+/-0.04	0.27	+/- 0.02
Si K	0.68	+/-0.09	0.36	+/- 0.05
Si L	—	—	—	—
Cl K	3.88	+/-0.25	1.62	+/- 0.11
Cl L	—	—	—	—
Ca L	—	—	—	—
Ca K	2.69	+/-0.14	1.00	+/- 0.05
Zr M	—	—	—	—
Zr L	3.87	+/-0.34	0.63	+/- 0.05
Pd L	3.37	+/-0.43	0.47	+/- 0.06
Pd M	—	—	—	—
Tl M	4.24	+/-0.44	0.31	+/- 0.03
Total	100.00		100.00	

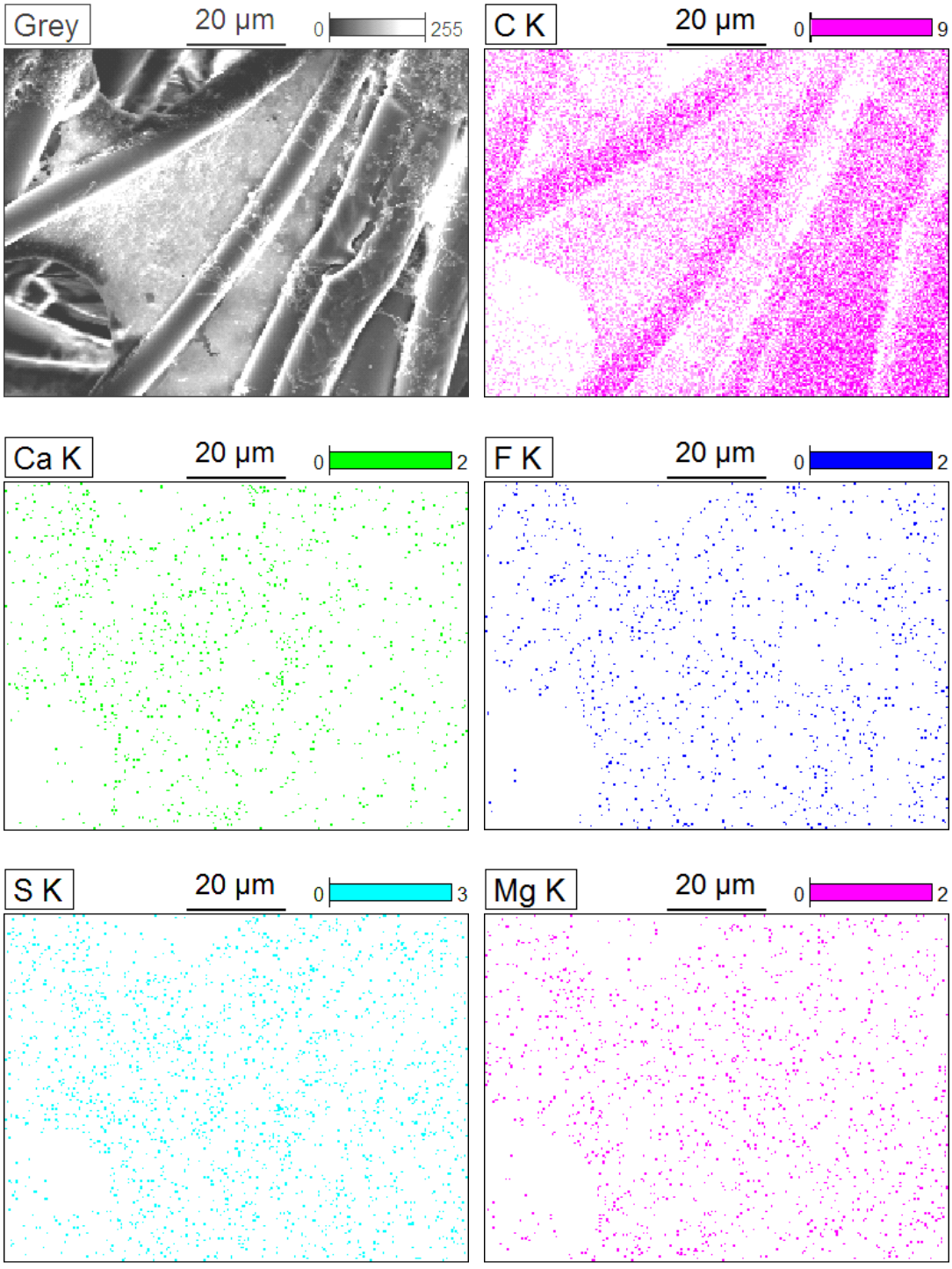

Figure 6.7. EDX elemental images of inner surface of a used 10 µm polypropylene cartridge filter.

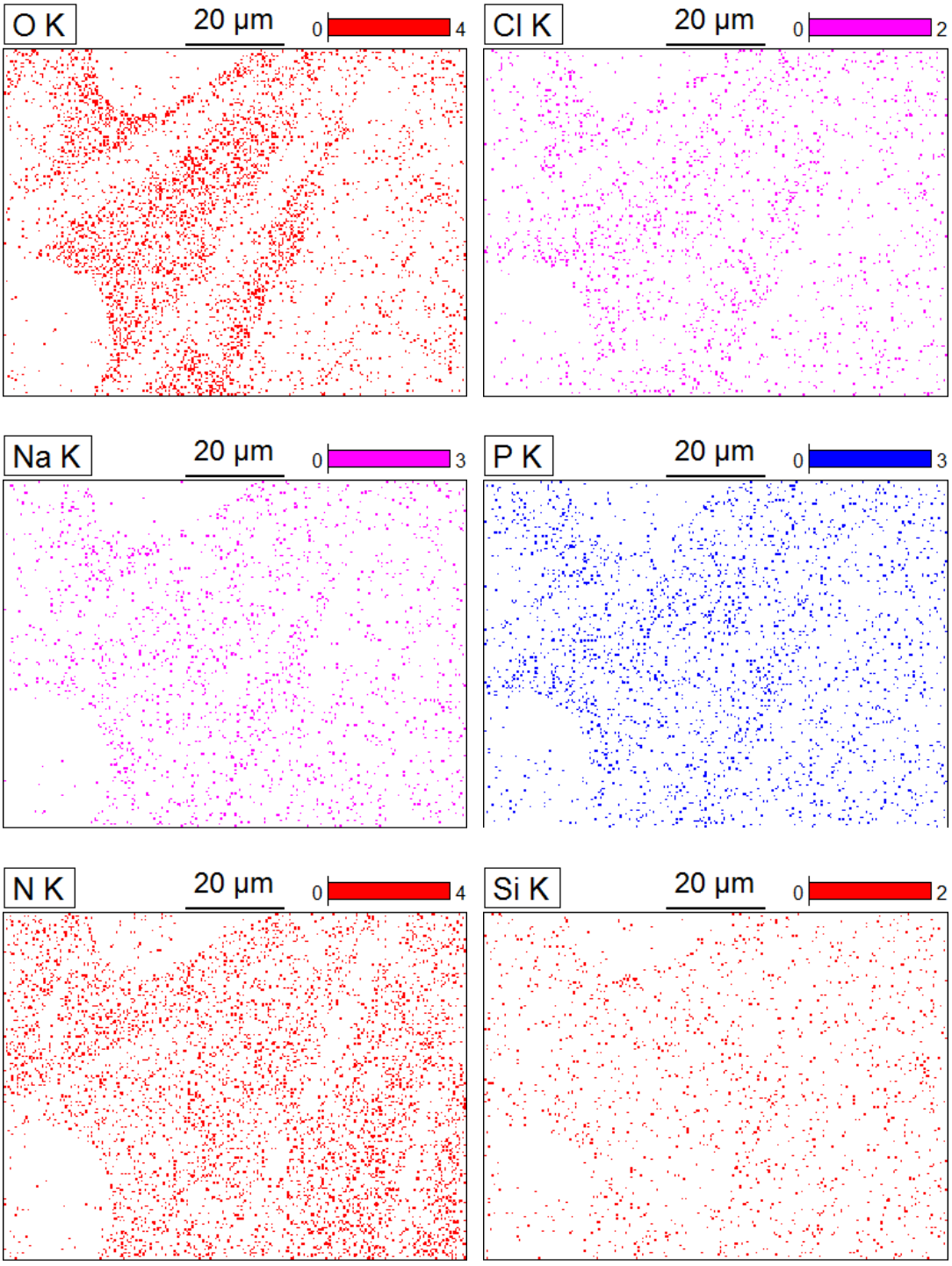

Figure 6.8. EDX elemental images of inner surface of a used 10 µm polypropylene cartridge filter.

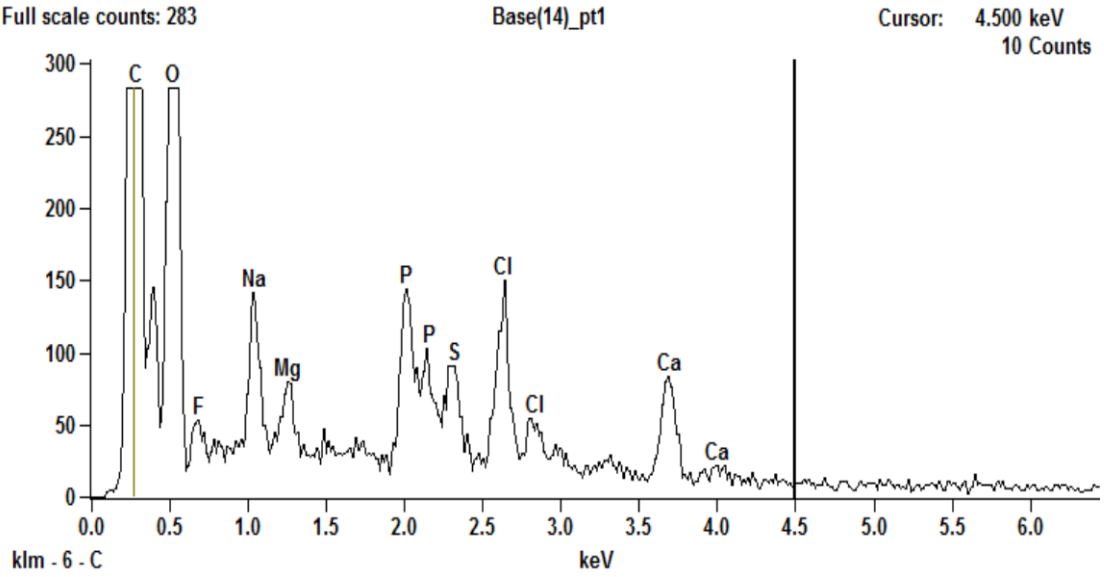

Figure 6.9. EDX elemental spectrum of the inner surface of the used 10 μm polypropylene cartridge filter.

Table 6.2. EDX Elemental Analysis of Inner Surface of a Used Cartridge Filter

Element Line	Element Wt%	Wt% Error	Atom %	Atom % Error
C K	76.42	+/-0.71	83.43	+/- 0.77
N K	5.74	+/-1.78	5.38	+/- 1.66
O K	9.05	+/-0.62	7.42	+/- 0.51
F K	0.70	+/-0.19	0.49	+/- 0.13
Na K	1.18	+/-0.07	0.67	+/- 0.04
Mg K	0.41	+/-0.05	0.22	+/- 0.03
Si K	0.62	+/-0.07	0.29	+/- 0.03
Si L	—	—	—	—
P K	0.55	+/-0.12	0.23	+/- 0.05
P L	—	—	—	—
S L	—	—	—	—
S K	0.13	+/-0.13	0.05	+/- 0.05
Cl K	2.95	+/-0.14	1.09	+/- 0.05
Cl L	—	—	—	—
Ca K	2.25	+/-0.37	0.74	+/- 0.12
Ca L	—	—	—	—
Total	100.00		100.00	

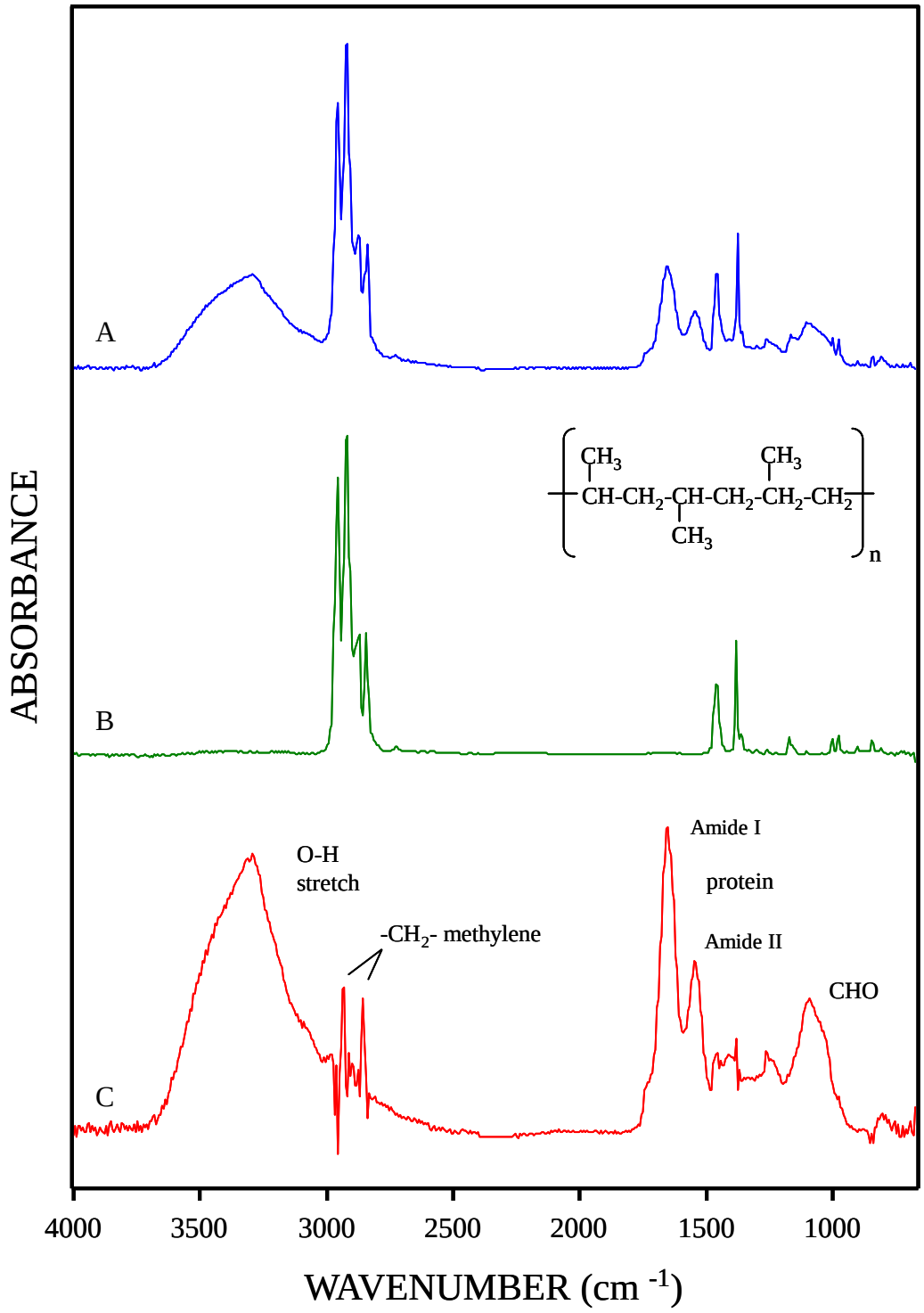

Figure 6.10. ATR-FTIR spectra of fibers from a 10 μm melt-bonded polypropylene cartridge filter taken from (A) the outside of filter that operated on MF effluent, (B) a new filter, and (C) the difference spectrum revealing the presence of protein and carbohydrate (CHO) on the surface.

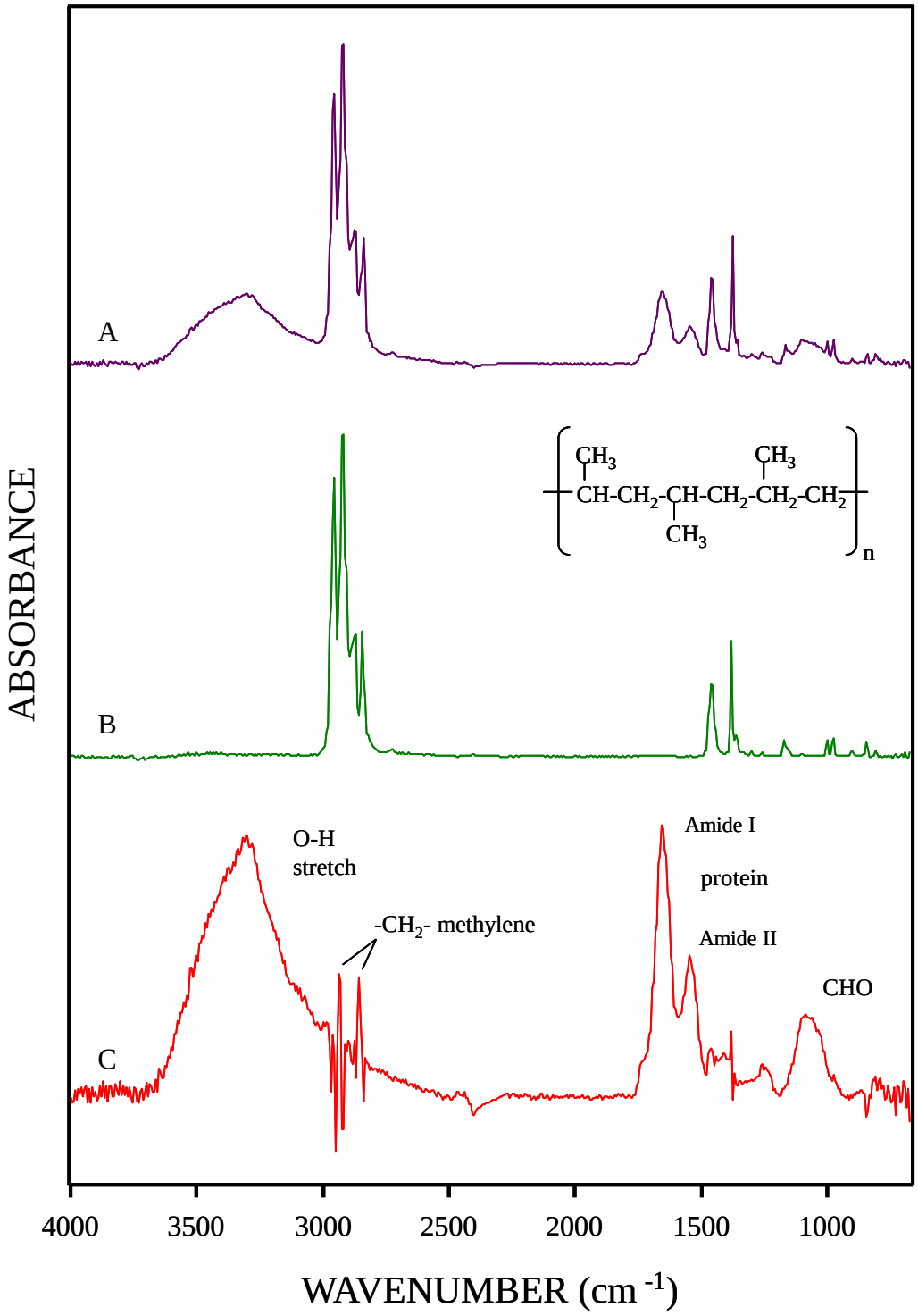

Figure 6.11. ATR-FTIR spectra of fibers from a 10 μm melt-bonded polypropylene cartridge filter taken from (A) the inside of the filter that operated on MF effluent, (B) a new filter and (C) the difference spectrum revealing the presence of protein and carbohydrate (CHO) on the surface.

6.4 Conclusions

Planktonic bacterial cells in the MF effluent can readily pass through the 10 μm pores of the cartridge filters. However, bacterial cells that attached formed a biofilm filling void spaces between the fibers in some areas of the filter. These biofilms further add to the source of bacteria that foul the RO membranes downstream, as cells "slough off" and pass through the filter. As the biofilm matures, microbial cells lyse presumably adding to the EfOM and AOC of the RO feedwater, and thus, whereas the intent of the cartridge filters is to remove large particulate debris, they also serve as a source of bacteria, EfOM, and AOC.

Chapter 7

Reverse Osmosis Fouling: Full-Scale RO Membrane Autopsy

7.1 Introduction

At the end of 2009 the RO trains exhibited an upward trend in first-stage differential pressure (delta-P) and a decrease in third-stage permeability. Increases in the first-stage delta-P are often attributed to the presence of biological fouling at the membrane surface, whereas the decrease in the permeability of the third stage is often related to aluminosilicate scale (Patel, 2010). As a result, OCWD's Water Production Department initiated cleaning regimes that targeted both issues. However, even with regular cleaning targeting organic and biological fouling on the lead RO elements and scaling in the third-stage, tail-end elements, a reduction in membrane performance continued to be observed.

Changes in water quality upstream of the RO process that occurred at the end of 2009 and through the first part of 2010 were thought to possibly be linked to the continued increase in delta-P and decrease in permeability of the RO process. Major events associated with the operations of the RO process were documented that included (1) storm events in December 2009, (2) a switch to nitrification of secondary effluent by OCSD, which resulted in spikes of high turbidity, (3) a trickling filter blend ratio that was allowed to increase from 20% to 30%, (4) a switch from 20 µm spiral wound cartridge filters to 10 µm spiral wound cartridge filters (water production staff indicated that the cartridge filters and housings were loaded with a thick foulant, which may have been the source of foulant deposition on the lead elements in the first stage), and (5) a number of changes in the total residual chlorine (chloramines) in the RO feedwater were made that included a decreased from 3 mg/L to 2.5 mg/L for approximately 5 months followed by 35 days at 4 mg/L, 9 days at 5 mg/L, 22 days at 3.5 mg/L, 4 days at 1.5 mg/L, and finally 9 days at 2 mg/L before the lead element was removed for autopsy.

An autopsy of the fouled RO membranes performed by the Water Production Department in early January 2010 showed evidence of biological fouling of the lead element. On the basis of this study, Water Production and Research and Development (R&D) staff determined that a more extensive analysis of the fouling layer on the membrane surface and a thorough examination of the feed spacer were needed to better understand the fouling material and foulant distribution. An autopsy was performed on a lead element from RO Unit C03, Vessel No. 70 (Serial No. A1240790) that was removed from service on May 12, 2010. This element was selected because it had experienced an increase in delta-P.

7.2 Materials and Methods

A known mass of each sample was scraped from the surface of the feed, middle, and brine end of the membrane with a sterile single-edge razor blade and placed into glass scintillation vials containing sterile phosphate buffered saline. Sonication (10 min) was applied to break up the biofilm and separate the microbial cells from the EPS. Analysis of the foulant material included a number of visual, microscopic, microbial, biochemical, and spectroscopic assays that are listed in Table 7.1.

Table 7.1. Analytical Techniques Used to Characterize Fouled RO Membrane

Digital images	Preliminary bacterial identification
Light microscopy	Scanning electron microscopy (SEM)
Heterotrophic plate counts (HPCs)	Energy dispersive X-ray (EDX) spectroscopy
Total bacterial (EPI) counts	Elemental mapping
Carbohydrate (CHO) analysis –unfiltered and filtered (0.2 μm)	Protein analysis –unfiltered and filtered (0.2 μm)
Attenuated total reflection Fourier transform infrared (ATR-FTIR) spectrometry	

7.2.1 Light Microscopy

Direct examination of membrane swatches and spacers from the feed, middle, and brine areas were performed using the AX70 Olympus microscope. In addition, each membrane swatch was Gram stained to better visualize any bacteria present on the membrane surface. A clean Hydranautics ESPA2 membrane and a clean feed spacer were used as controls for comparison.

7.2.2 Heterotrophic Plate Count (HPC)

The sonication step was necessary to break up the foulant material to ensure even distribution and accurate serial dilutions and plating for microbial growth. Even with the sonication step, small chunks of foulant were still visible. Plating of the sample material was done on R2A agar medium. The spread plates were incubated at 28 °C, examined, and colonies counted over a 2-week period. The number of bacteria/cm^2 was determined for each sample.

7.2.3 Total Bacterial Count/EPI Count

A total bacterial count or epifluorescent (EPI) count was done to enumerate all bacteria (live and dead) in the sample. The bacteria were stained with a fluorescent dye, 4',6-diamido-2-phenylindole (DAPI), which is incorporated into bacterial DNA. The bacteria were exposed to UV light and the individual fluorescing cells counted to determine the total bacterial/cm^2. The same sonicated preparation used for the HPC analysis was used for the total bacterial count. Epifluorescent counting with Molecular Probes LIVE/DEAD BacLight Bacterial Viability Kit (Life Technologies, Grand Island, NY) also was done.

7.2.4 Carbohydrate and Protein Assay

Total carbohydrate was determined by the Folin's reagent method of Lowrey et al. (1951), total carbohydrate by the phenol, hydrazine sulfate, sulfuric acid method of Dubois et al. (1956) using the sonicated membrane foulant preparation from the HPC analysis. The amount of CHO and protein per cm^2 were determined.

7.2.5 Scanning Electron Microscopy (SEM) / Energy Dispersive X-ray (EDX) Spectroscopy

Small pieces of fouled membrane or feed spacer were fixed to a sample mount using conductive carbon tape. Samples were coated with a layer of gold using a VG/Polaron SC 7620 sputter coater to increase sample conductivity. A Philips XL-30 FEG SEM with energy dispersive X-ray (EDX) spectrometer was used to examine the membrane and spacer surface and determine the elemental composition of the foulant layers.

7.2.6 Environmental Scanning Electron Microscopy (ESEM) and EDX

Elemental mapping was performed with a Zeiss EVO LS-15 environmental scanning electron microscope equipped with a Thermo Scientific EDX system to identify and map the inorganic and organic content on the membrane surface. The instrument has the ability to generate and overlap chemical signatures across the surface of a sample.

7.2.7 ATR-FTIR Spectrometry

Thin strips (0.5 × 3 cm) of membrane were cut from the fouled RO element and placed in a plastic petri dish. The membrane swatches were dried in a glove box purged with compressed air passed through a Balston dryer (Parker Hannifin, Mayfield Heights, OH). The surface of the fouled membrane was pressed against the a single-reflection germanium internal reflection element (ThunderDome, Thermo Scientific, Madison, WI) installed in the sample compartment of a Nicolet 6700 FT-IR spectrometer (Thermo Scientific). A total of 128 coadded, single-beam spectra collected at 4 cm^{-1} resolution with a DTGS detector, truncated at 670 cm^{-1}, ATR-corrected for the wavelength dependence of IR light, and baseline-corrected to zero absorbance. The spectra were "zapped" between 2390 and 2270 cm^{-1} to remove the residual carbon dioxide absorption band in the spectrum for visual clarity.

7.3 Results and Discussion

7.3.1 Visual Inspection of Pressure Vessel and RO Membrane

The membrane vessel was inspected upon removal the RO element from the pressure vessel. The outer membrane shell was clean and no defects were observed. The brine seal and both ends of the permeate tube appeared in good condition. Some debris was lodged in the end caps and underneath the end caps directly against the edge of the rolled membrane. The ends were removed, and the outer shell was cut open but not removed. The membrane with its shell still in place was transported to the R&D laboratory for inspection and analysis using sterile techniques, taking care not to disturb or contaminate the fouling layer on membrane surface.

7.3.2 Foulant Inspection and Removal

Each membrane sheet or sleeve of the element had a layer of brown foulant. Fouling was heavier at the feed end of the membrane and lighter at the brine end (Figure 7.1). The foulant material was easily scraped and recovered from the membrane surface for chemical analysis. Three areas of the membrane sleeve were sampled due to the differences in foulant deposition across the surface: the feed end, middle, and brine end. Swatches of the membrane and spacer also were cut and removed from the sleeve for additional testing (Figure 7.2).

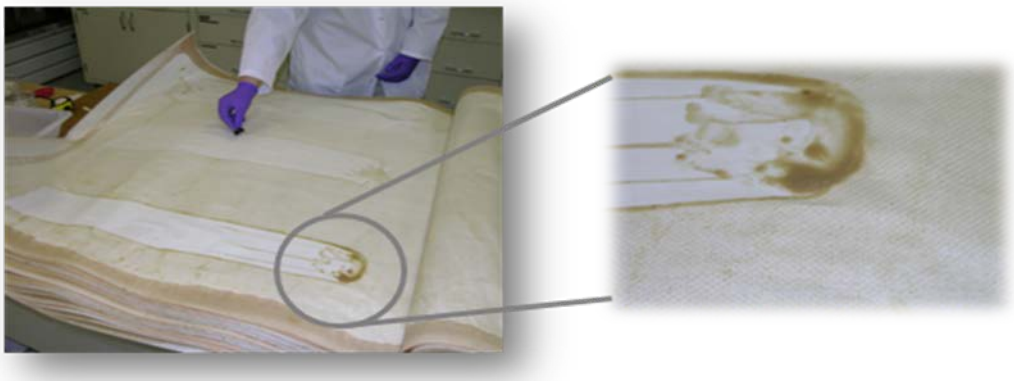

Figure 7.1. Brownish fouling layer on membrane surface was easily scraped and removed. The feed, middle, and brine areas of the membrane were scraped for analysis.

Figure 7.2. Piece of fouled membrane and the spacer material were cut from a sleeve of the Hydranautics ESPA 2 RO element.

7.3.3 Light Microscopy

Direct examination of membrane swatches and spacers from the feed, middle, and brine areas were performed using the AX70 Olympus microscope. Images of an unused Hydranautics ESPA2 membrane and feed spacer are displayed in Figure 7.3. Light microscopy of the unstained fouled membranes was difficult. No discernable structures were observed. The surface looked fuzzy and brown at all magnifications (Figures 7.4A and 7.4B). Gram staining the fouling layer resulted in sharper images that showed the presence of a thick, mostly Gram positive bacteria that covered much of the membrane surface (Figure 7.4C). Many layers of bacteria were revealed on the membrane surface by focusing up and down on the stained biofilm. Open spaces between the layers and bacteria were visible. The presence of these open spaces allow for nutrient transport into the biofilm structure (Christensen and Characklis, 1990; Costerton et al., 1995; Stewart, 2003). The morphology of the biofilm was consistent across the membrane. The biofilm appeared to be heavier at the feed than at the brine (Figures 7.4, 7.5, and 7.6). The fouled feed spacer also was difficult to visualize with the light microscope because of the translucent nature of the material.

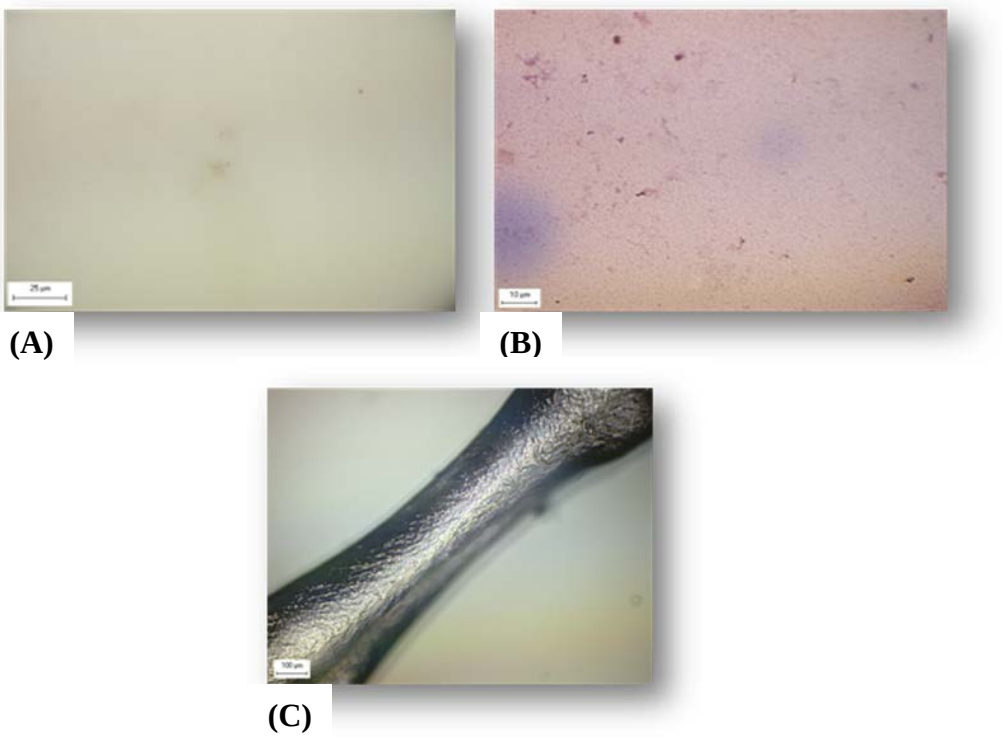

Figure 7.3. Microscopic images of a (A) clean Hydranautics ESPA2 RO membrane, (B) Gram stained clean membrane, and (C) clean feed spacer.

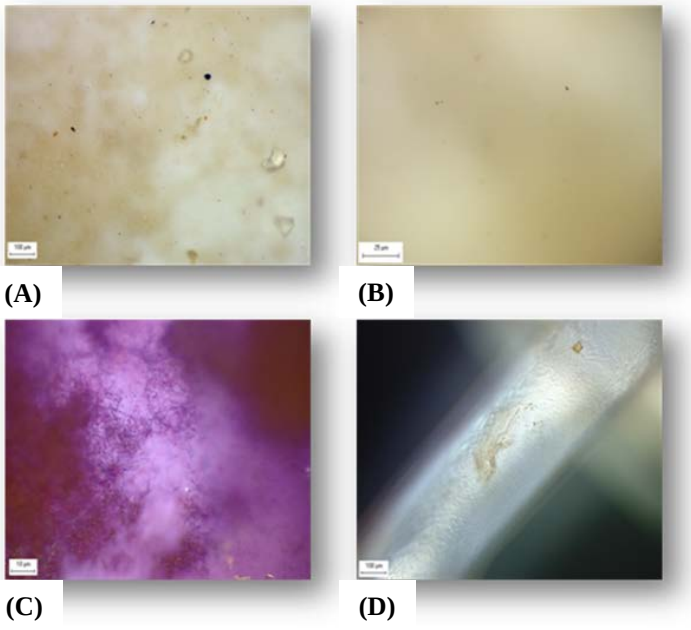

Figure 7.4. Microscopic image of feed end of Hydranautics ESPA2 membrane: (A) fouling layer at 10 times magnification, (B) fouling layer at 60 times magnification, (C) Gram stained biofilm at 100 times magnification, and (D) fouled feed spacer at 10 times magnification.

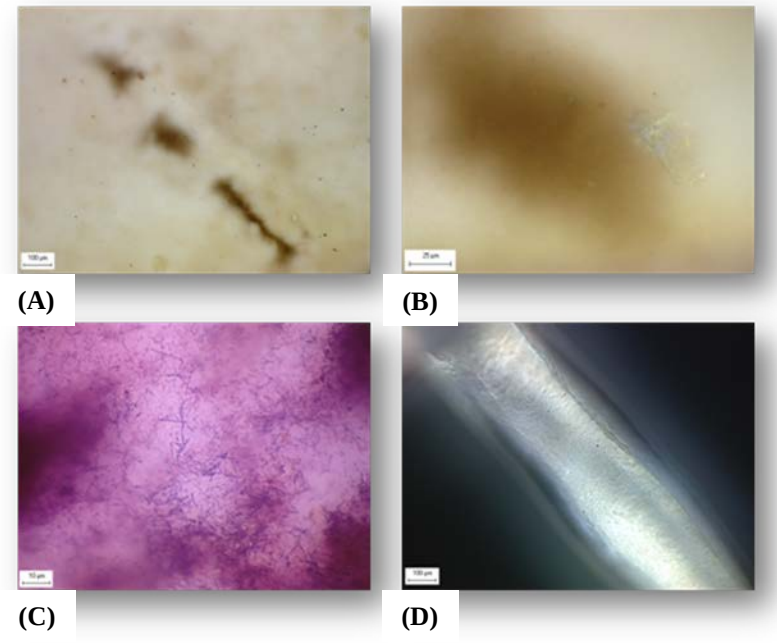

Figure 7.5. Microscopic images of the middle section of a Hydranautics ESPA2 membrane: (A) fouling layer at 10 times magnification, (B) fouling layer at 60 times magnification, (C) Gram stain of biofilm at 100 times magnification, and (D) fouled feed spacer at 10 times magnification.

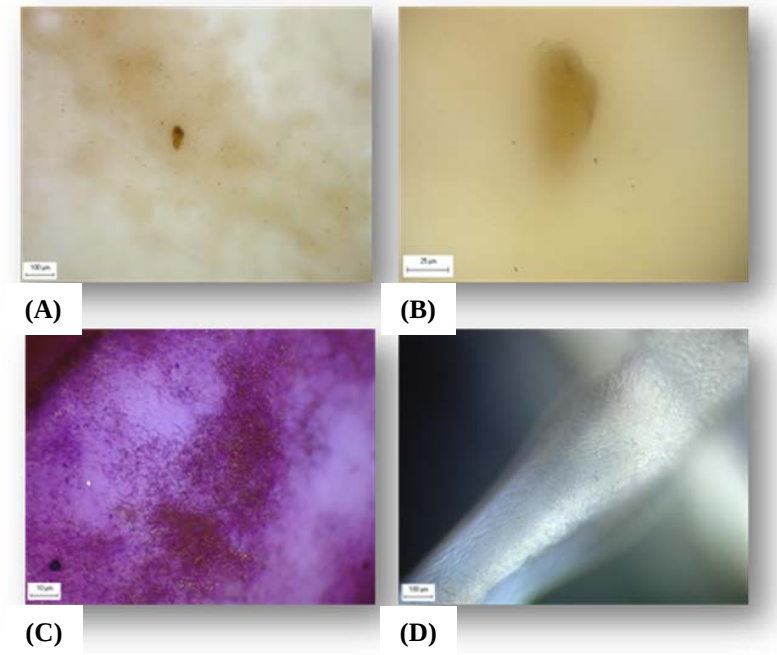

Figure 7.6. Microscopic images of brine end of Hydranautics ESPA2 membrane: (A) fouling layer at 10 times magnification, (B) fouling layer at 60 times magnification, (C) Gram stain of biofilm at 100 times magnification, and (D) fouled feed spacer at 10 times magnification.

7.3.4 Viable Bacterial/Heterotrophic Plate Counts (HPC)

The foulant matter on the membrane surface was thick and gelatinous in appearance. A known mass of foulant collected from the feed, middle, and brine sections of the membrane were placed into sterile buffer and sonicated for 10 min. The sonication step was necessary to break up the material and evenly suspend it for accurate serial dilutions and plating R2A agar medium. Small "chunks" of foulant were still visible even after sonication. The R2A plates were incubated and visually inspected and colonies counted over a 2-week period. The feed portion had the highest viable bacteria per cm^2 of membrane, and the brine end had the lowest (Figure 7.7). The number of bacteria per cm^2 also correlated to the visual macroscopic appearance of the fouled membrane (digital images not shown).

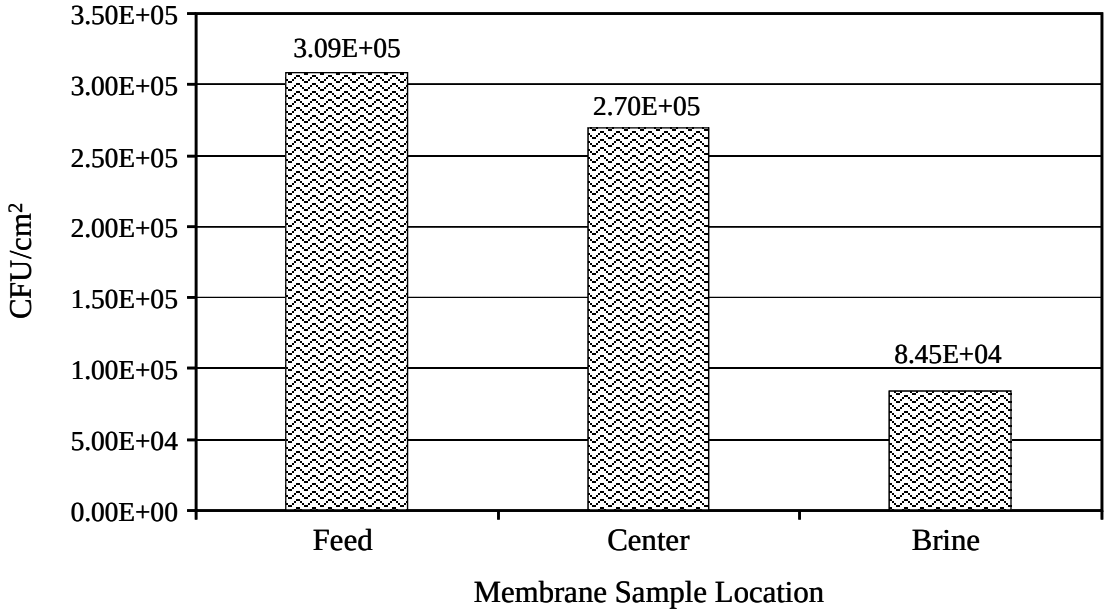

Figure 7.7. Viable bacteria on the feed, middle, and brine ends of the membrane surface based on heterotrophic plate counts on R2A agar medium.

The colonies that formed on the R2A plates looked very similar. After 2 days of incubation, the colonies were white opaque in color. After 5 days, the colonies turned brown. The majority of the colonies on the HPC plates were of the same morphology. Preliminary microbial differential tests that included Gram stain positive, catalase positive, mannitol positive, arabinose positive, and endospore, acid fast stain positive, identified the bacteria as genus *Bacillus*. Bacteria from the genus *Bacillus* are found in soil and water and are rod-shaped, straight, and approximately 0.5–2.5 × 1.2–10 µm in size. The bacillus cells form endospores that can be round, oval, or cylindrical and are very resistant to adverse conditions, in other words, chloramines, pH, salinity, and heat (Zinsser Microbiology, 1980). Treating the biofilm with chemicals may kill and remove most of the cells but because no cleaning regime is perfect endospores can be left behind. The endospores that remain dormant enable the bacterium to survive the harsh environmental conditions. When the conditions become favorable, the endospores reactivate into a vegetative state and full bacterial colonies begin to grow.

7.3.5 Total Bacteria Counts/EPI Fluorescence Counts

The same sonicated preparation used for the HPC analysis was used for the total bacterial count or EPI count analysis. Unfortunately, the cells were so clumped they could not be enumerated (Figure 7.8). The bacteria were imbedded in EPS so tightly that even sonication was not effective in breaking them apart. Because the cells from the biofilm were not completely dissociated, the HPC numbers reported are likely underestimated.

Figure 7.8. DAPI-stained mass of bacterial cells from the middle section of the fouled RO membrane.

7.3.6 Carbohydrate and Protein Analysis

The presence of carbohydrate (CHO) or protein on the membrane surface is an indication of biological activity. CHO and protein analysis were performed on an unfiltered and filtered aqueous suspension of the foulant matter. The unfiltered analysis includes microparticulate and nanoparticulate components (everything scraped from the membrane surface). The filtered effluent only measures the nanoparticulate CHO and protein components of the sample. Microparticles larger than 0.2 µm were removed by filtration through a 0.22 µm cellulose acetate filter (Costar, Cambridge, MA).

Similar to the HPC results, the unfiltered and filtered CHO concentrations varied across the membrane with the highest concentration at the feed end and lowest concentration at the brine end (Figure 7.9). The nanoparticulate portions comprised 19% of the total CHO in the feed and 15% of the total CHO for both middle and brine.

The unfiltered protein concentrations also varied across the membrane with the highest concentration at the feed end and lowest concentration at the brine end (Figure 7.10). The nanoparticulate protein portion was below the assay's detection limit.

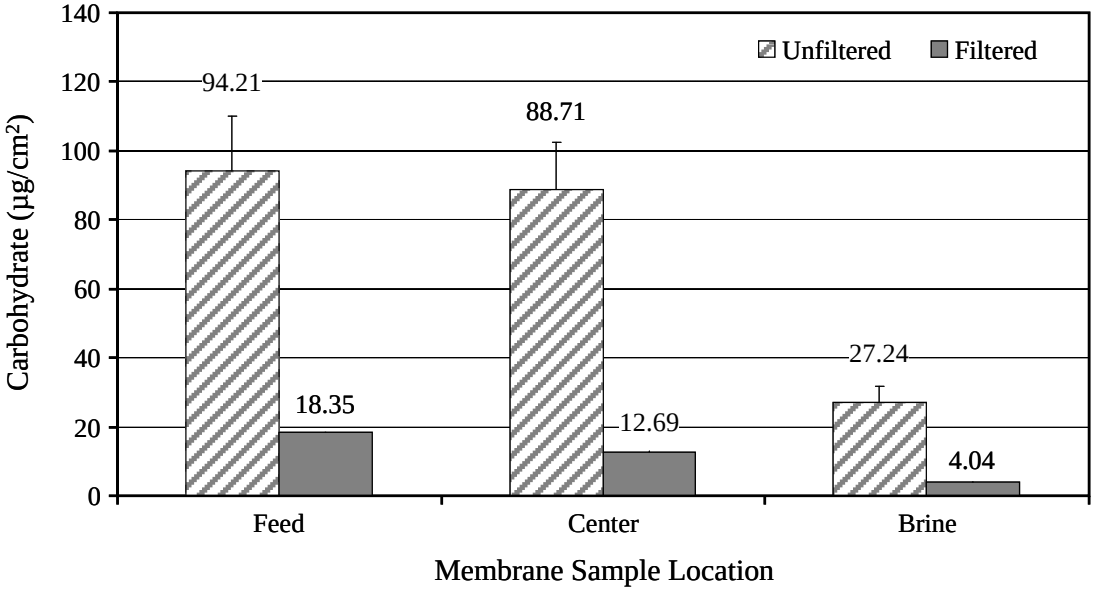

Figure 7.9. Unfiltered and filtered carbohydrate analysis of membrane foulants.

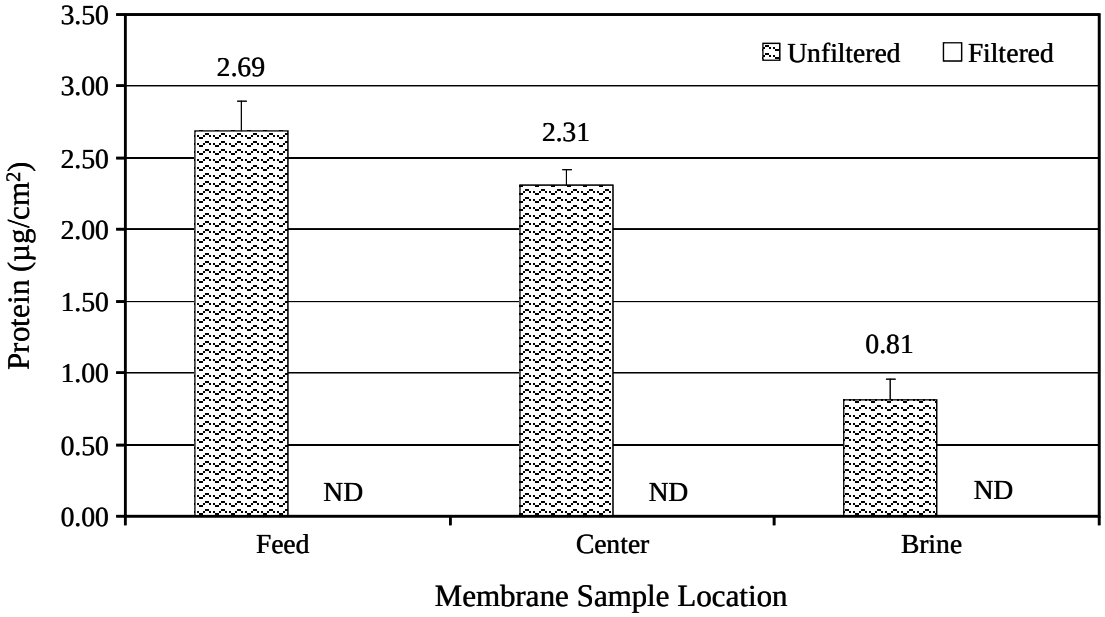

Figure 7.10. Unfiltered and filtered protein analysis of membrane foulants (ND – nondetect).

7.3.7 SEM/EDX Analysis

7.3.7.1 Fouled RO Membrane

Scanning electron microscopy images of the fouled membrane at lower magnification (i.e., 12,500 times) revealed areas with and without bacteria (Figure 7.11). At higher magnification (i.e., 200,000 times), the images showed evidence of nanoparticulate fouling (Figure 7.12). These images reveal two distinct fouling layers. The top fouling layer is made up of bacteria, and the layer below is composed of nanoparticles. The bacteria may not even be in contact with the membrane polymer itself but are adhering to the nanoparticles coating the membrane surface.

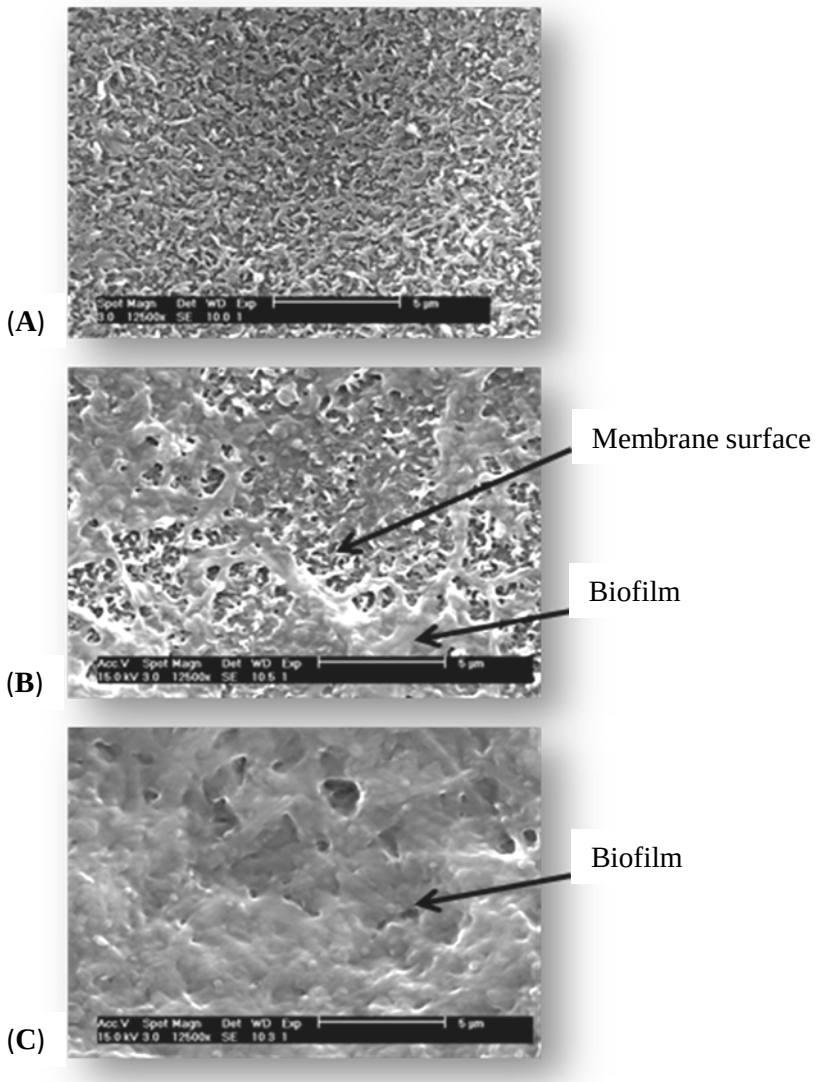

Figure 7.11. SEM images (12,500 times magnification) of a (A) clean RO membrane, (B) fouled RO membrane with visible membrane surface, and (C) membrane surface completely covered with a bacterial biofilm.

Note: The length of the bar is 5 μm.

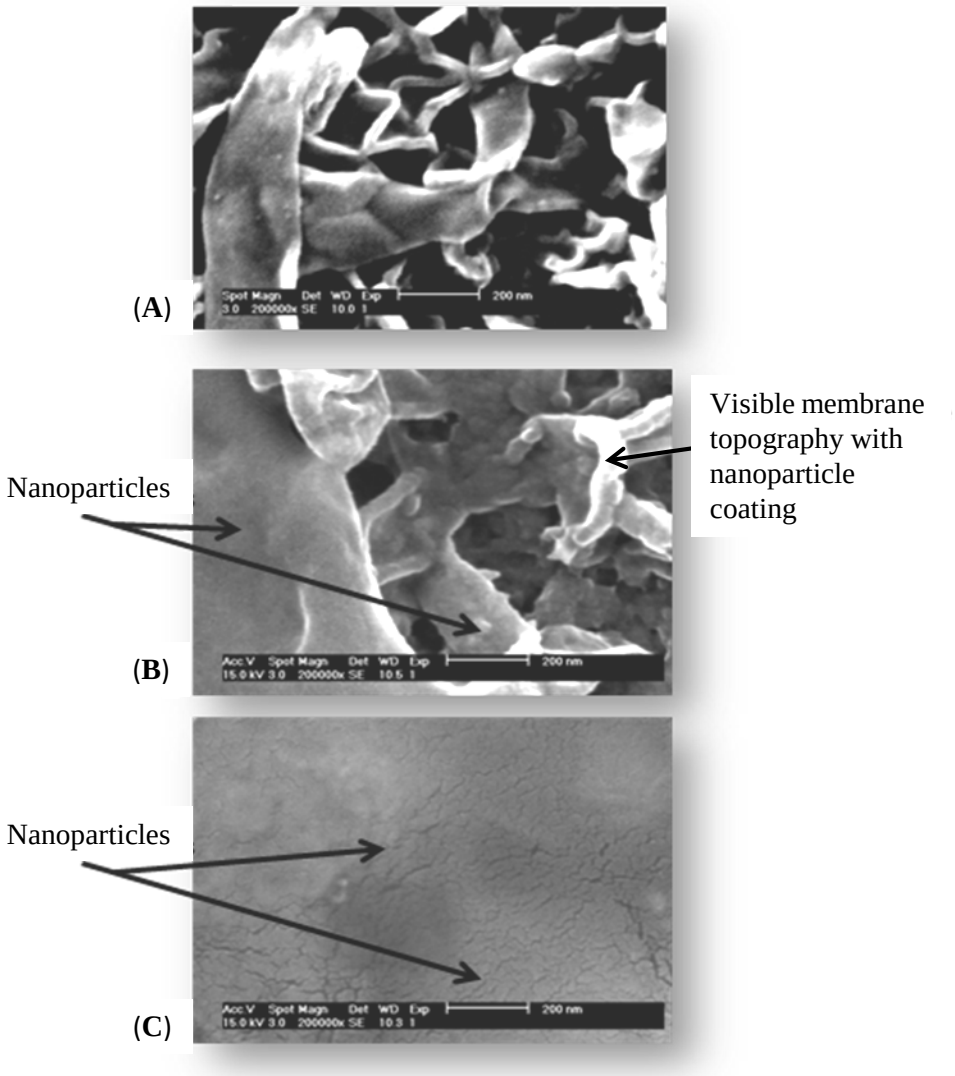

Figure 7.12. SEM images (200,000 times magnification) of a (A) a clean RO membrane, (B) nanoparticle-coated surface (right side) and heavily coated and obscured membrane surface (left side), and (C) area of membrane with no microbial biofilm but a heavy nanoparticulate covering the surface.

Note: The length of the bar is 200 nm.

SEM/EDX analysis was performed to determine the inorganic and organic content of the material coating the membrane surface. Several areas of the membrane were analyzed (Figure 7.13). The type of elements identified did not vary much across the membrane. Elements identified were carbon, oxygen, sulfur, phosphorus, calcium, chloride, sodium, magnesium, aluminum, and silicon. There were traces of aluminum and silicon that are associated with mineral scaling, but quantities were minimal. The majority of the elements identified may be associated with biological debris. The largest component was carbon, which was expected as the membrane is carbon based.

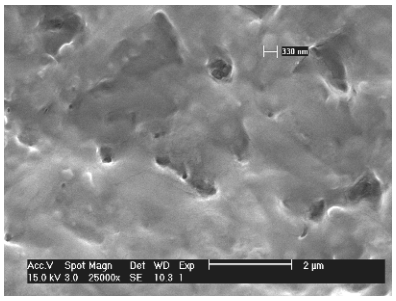

25,000X, 2 µm bar (A)

Element	Atom%
C K	81.56
N K	9.34
O K	7.55
P K	0.07
S K	1.28
Cl K	0.11
Ca K	0.09
Total	100.00

Element	Atom%
C K	73.68
N K	8.78
O K	16.24
Na K	0.13
Mg K	0.10
Al K	0.03
Si K	0.03
P K	0.24
S K	0.27
Cl K	0.27
Ca K	0.20
Total	100.00

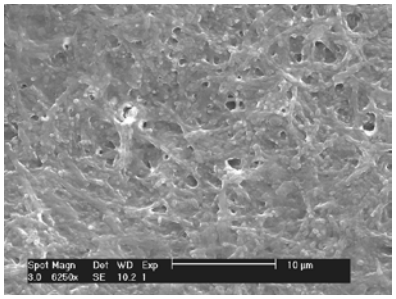

(B) 6250X, 10 µm bar

125,000X, 5 µm bar (C)

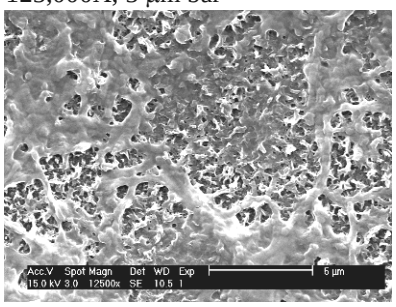

Element	Atom%
C K	83.81
N K	6.58
O K	7.55
P K	0.04
S K	1.66
Cl K	0.06
Ca K	0.01
Total	100.00

Figure 7.13. EDX spectra of fouled membrane: (A) covered with biofilm with mostly carbon and sulfur, (B) larger area covered with biofilm with traces of aluminum and silicon, and (C) biofilm with some membrane surface visible and with carbon and sulfur as the most abundant components.

7.3.7.2 Fouled Feed Spacer Analysis

The feed spacer is sandwiched between membrane sheets or sleeves and comes in contact with the membrane surface. With time, fouling occurs on the membrane surface at the junctions of the feed spacer and membrane and on the feed spacer itself. Previous autopsies did not specifically look at feed spacer fouling. A new feed spacer was imaged as a control (Figure 7.14). The clean feed spacer was very smooth with very little surface topography.

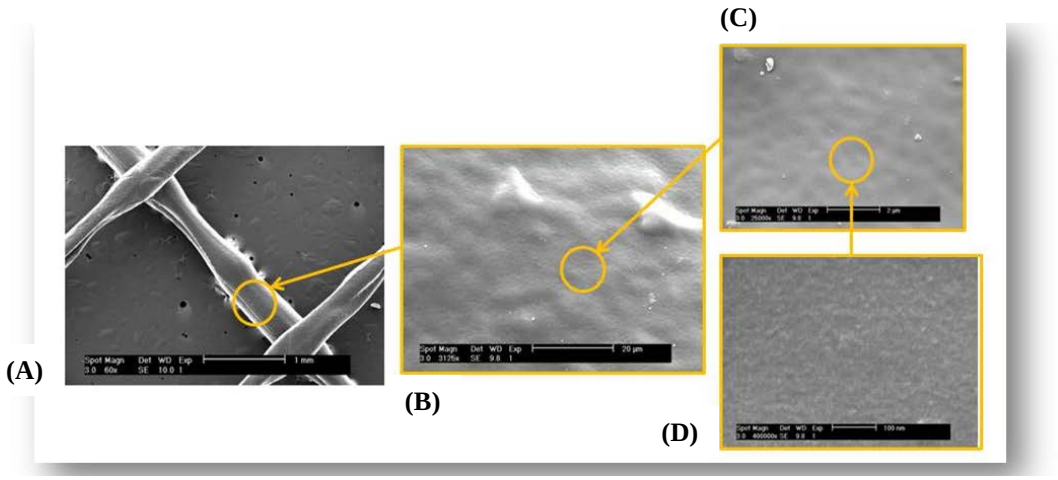

Figure 7.14. New RO membrane feed spacer: (A) low magnification (60 times) image with 1 mm bar, (B) higher magnification (3215 times) image with 20 μm, (C) medium high magnification (25,000 times) image with 2 μm, and (D) very high magnification (400,000 times) image with 100 nm bar.

Similar to the images of the fouled membrane, the images of the feed spacer showed evidence of two distinct fouling layers: a top layer of bacteria and a layer of nanoparticles below (Figure 7.15). The biofilm accumulation on the feed spacer may influence the flow pattern in the feed channel and may influence biofilm formation at the membrane surface.

EDX spectroscopic analysis also was performed on the fouled spacer material. Crystalline material on the surface of the spacer was targeted and revealed high concentrations of aluminum and silicon, suggesting the presence of aluminum silicate scale (Figure 7.16). The fouling layer on the feed spacer was analyzed and the results indicated that it was mostly composed of carbon, oxygen, and nitrogen.

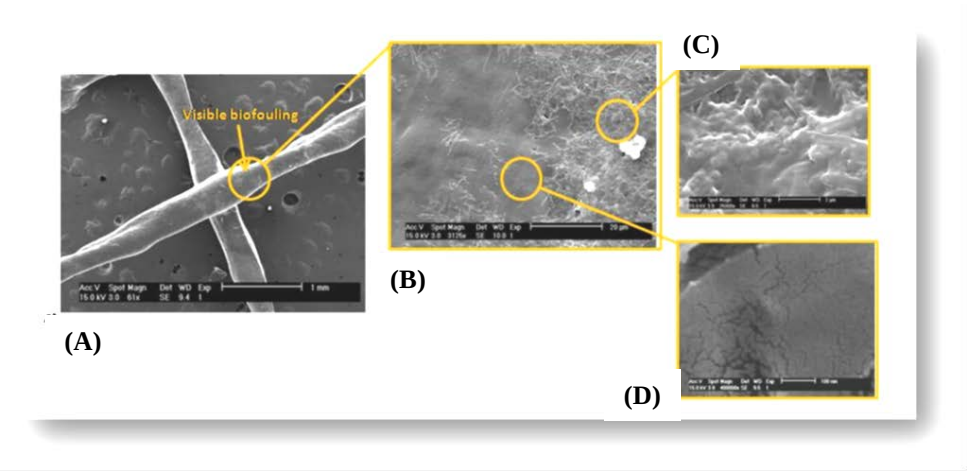

Figure 7.15. Fouled feed spacer: (A) low magnification (65 times) image with visible bacteria on the spacer surface, (B) at higher magnification (3125 times) resolution of bacteria on the spacer surface begins to occur, (C) at 25,000 times,a thick layer of bacteria is clearly visible, and (D) at very high magnification (400,000 times) nanoparticles are resolved and completely cover the surface of the spacer under the bacterial layer.

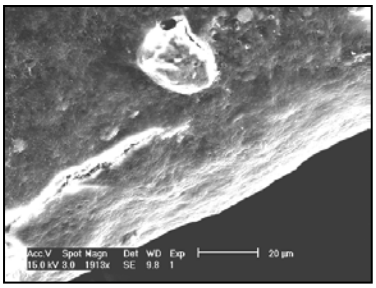

1913X, 20 μm bar (A)

Element	Atom%
C K	71.16
N K	11.03
O K	16.76
Fe L	0.00
Na K	0.15
Mg K	0.06
Al K	0.03
Si K	0.08
P K	0.16
S K	0.18
Cl K	0.17
K K	0.03
Ca K	0.15
Fe K	0.04
Total	100.00

Element	Atom%
C K	54.68
N K	4.83
O K	31.07
Fe L	0.00
Na K	1.52
Mg K	0.05
Al K	1.94
Si K	5.47
P K	0.02
S K	0.02
Cl K	0.06
K K	0.09
Ca K	0.15
Fe K	0.09
Total	100.00

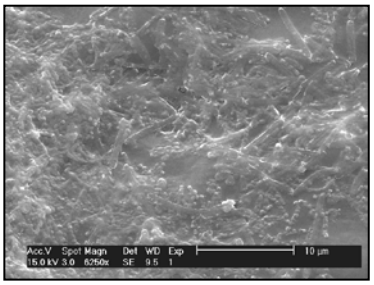

(B) 6250X, 10 μm bar

Element	Atom%
C K	84.77
N K	9.28
O K	5.88
Na K	0.01
Si K	0.01
P K	0.00
S K	0.01
Cl K	0.03
Ca K	0.02
Total	100.00

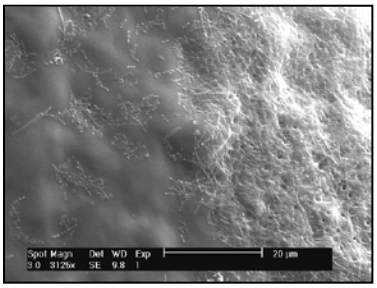

3125X, 20 μm bar (C)

Figure 7.16. EDX analysis of fouled feed spacer: (A) crystal on the spacer surface with high concentration of aluminum and silicon, (B) area covered with biofilm with a majority of elements related to biological debris, and (C) analysis that indicates the foulant is mostly carbon, oxygen, and nitrogen.

7.3.8 Environmental SEM/EDX Analysis of RO Membrane Surface

Environmental SEM/EDX spectroscopic imaging technique was performed to determine the inorganic and organic content on the membrane surface like the traditional EDX analysis as described except this instrument can map the entire area selected pixel by pixel. It has the ability to generate and overlap chemical signatures across the membrane surface.

The same elements as listed previously were identified in the mapping process. The elements were evenly distributed across the surface. Several silicon hot spots were observed, but only two silicon spots were associated with an aluminum spot (Figure 7.17). Because the two elements overlap this may be an indication of aluminosilicate scale.

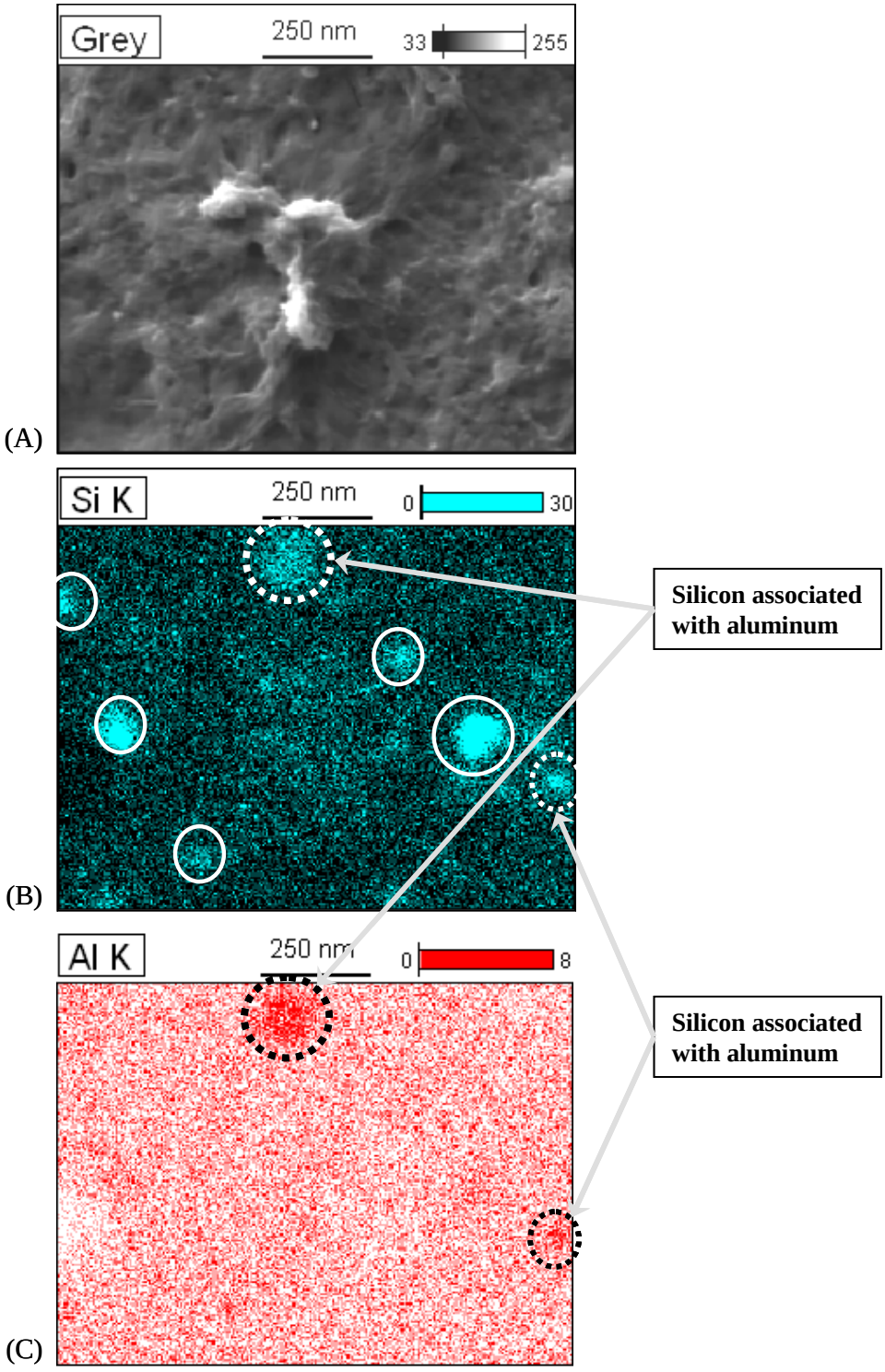

Figure 7.17. SEM images of (A) fouled RO membrane, (B) silicon map with silicon hot spots, and (C) aluminum map with aluminum hot spots.

7.3.9 Attenuated Total Reflection (ATR) Fourier Transform Infrared (FTIR) Spectrometry

Swatch samples from nine areas on a single membrane sleeve were collected and analyzed by ATR-FTIR spectrometry (Harrick, 1979; Ridgway et al., 1999). The results indicated the presence of protein and carbohydrate material on the membrane surface (Figure 7.18). The amide I (~1650 cm^{-1}) and the amide II (~1550 cm^{-1}) absorption bands are associated with protein, and the ~1040 cm^{-1} absorption band associated with carbohydrate material. Intense O-H and N-H stretching bands also are present along with aliphatic methyl ($-CH_3$) and methylene ($-CH_2-$) stretching bands that do not contribute significantly to the spectrum of the reference spectrum of a thin-film composite polyamide RO membrane (Naumann et al., 1996; Naumann, 2000; Mayo et al., 2004).

IR light from the ATR technique penetrates the foulant layer first, passing through, before it enters the underlying membrane and reflects back (Harrick, 1979; Ridgway et al., 1999). As the fouling later gets thicker and thicker less and less IR light reaches the RO membrane surface. The greater the amount of material deposited on the membrane surface the less visible are the absorption bands of the polyamide and polysulfone layers of the membrane. Therefore, conclusions can be drawn as to the relative thickness of the foulant later based on the relative ratio of the foulant absorption bands compared to the vibrational bands associated with the polyamide membrane spectrum. The greater the ratio of the foulant absorption bands to those of the RO membrane, the more extensive is the fouling. When the fouling layer is very heavy, no vibrational bands associated with the membrane may appear in the ATR-FTIR spectrum as the IR light is prevented from reaching the surface of the membrane.

Analysis of the ATR-FTIR spectra of the fouled RO membrane indicates that the biological fouling occurred to a greater extent on the feed and center areas of the membrane compared to the brine end of the membrane. Much of the polyamide spectrum of the RO membrane is obscured by the protein and carbohydrate absorption bands. This is especially evident in the spectra from the feed—inside, middle, and outside spectra and the center—inside, middle, and outside spectra (see Figure 7.18). The IR spectra in Figure 7.18 reveal no discernible signs of inorganic scale. However, this does not mean that no inorganic foulants are present on the membrane surface.

The results of the IR spectroscopic analysis correlate with HPC, carbohydrate, and protein analysis discussed earlier that indicate that there is more biofouling on the feed end of the membrane compared to the brine end of the membrane.

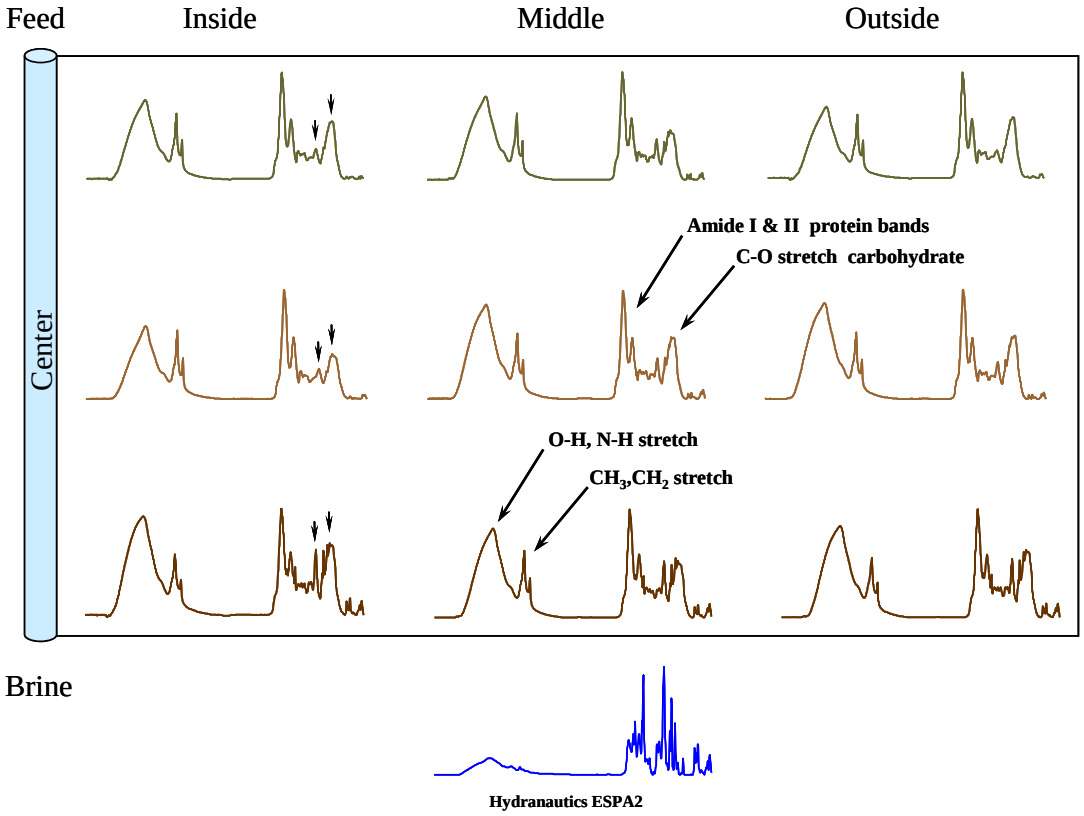

Figure 7.18. ATR-FTIR spectra of fouled Hydranautics ESPA2 membrane with a spectrum on an unused membrane at the bottom of the figure.

7.4 Conclusions

The foulant on the surface of the RO membrane was mostly biomass and nanoparticulate in composition. Much of the material consisted of whole bacterial cells and organic EPS (i.e. carbohydrates, proteins, and other bacterial debris). The biofilm appeared to be the heaviest at the feed end of the membrane and lightest on the brine end. The biofilm was a network of cells imbedded in a thick coat of EPS. The cells were "glued" together by EPS making a total bacterial count impossible.

Visualization of the Gram-stained biofilm through a series of focal planes revealed a network of bacteria in layers upon layers. Open spaces between the layers and bacteria were visible. The presence of these void spaces allow for nutrient transport into the biofilm structure. The biofilm did not appear to be very diverse in bacterial species. The majority of the bacteria present may be an endospore forming bacterium of the genus *Bacillus*, which allow a bacterium to survive harsh environmental conditions. These endospores may be left behind after membrane cleaning and remain on the membrane surface and when conditions become favorable may be reactivated, restarting the biofouling process.

The foulant material appeared to be multilayered with a top layer taking the form of a biofilm, and the bottom layer composed of nanoparticulates. A portion of the nanoparticles are of biological origin, which was evidenced by the presence of carbohydrates smaller than 0.2 µm. The hypothesis is that nanoparticulate fouling is the primary fouling layer and the

bacteria are the secondary fouling layer. Nanoparticles are the first component the membrane comes in contact with when the formation begins. Biofilm development occurs over time as conditions at the membrane surface become favorable.

Elemental mapping of the membrane surface by environmental SEM revealed a small presence of aluminum and silicon, which was attributed to aluminum silicate scaling. An EDX spectroscopic analysis of the fouled membrane revealed the presence of C, O, S, Si, Al, P, N, Na, Mg, Cl, and Ca. Analysis of the fouled feed spacer revealed the presence of similar elements.

Fouling of the feed spacer may have an impact on biofouling and membrane performance. The feed spacer had the same double layer of foulants as observed on the membrane surface. Nanoparticles that were in direct contact with the spacer and bacteria appeared to be in contact with the nanoparticles. Biofilm accumulation on and around the feed spacer may result in an increase in membrane fouling and redirect the flow of the feedwater through the membrane module.

Chapter 8

Reverse Osmosis Fouling: Artificial Neural Network (ANN) Model for Prediction of Membrane Fouling

8.1 Introduction

Recently, artificial neural networks (ANNs) and genetic algorithms (GAs) have increasingly been used to model membrane performance and fouling. Hwang et al. (2009) used input parameters from operating conditions (flow rate and filtration time), feedwater quality (turbidity, temperature, algae, and pH), and genetic programming to build a model that predicted increased membrane resistance or MF fouling. Al-Abri and Hilal (2008) used a backpropagation ANN to predict membrane fouling by humic substances. Similar work was done by Sahoo and Ray (2006) to model permeate flux decline in cross-flow membrane filtration by various sized silica suspensions in conjunction with pH, ionic strength, and transmembrane pressure. Most recently, Liu et al. (2009) built an ANN model to predict the performance of an MF system for water treatment.

The RO membranes utilized in the GWRS AWPF are subject to fouling over time by mineral and biological material so that the pressure required to produce a given water flux (delta-P) gradually increases. After about a 35% increase in delta-P, the membranes are removed from service and chemically cleaned in place (CIP) to restore performance. The effect of this cleaning is a recovery of initial membrane performance.

Materials identified on the surface of the fouled membrane include bacterial biofilms (Ridgway and Fleming, 1996; Vrouwenverlder, 1998) and mineral precipitates consisting of sulfate, phosphate, and silicate mineral materials (Cohen and Probstein, 1986; Tran et al., 2007; Bartman et al., 2011). The accumulation of these fouling materials on the membrane is thought to be governed by a combination of factors, including the surface properties of the membrane and the feedwater quality (Elimelech et al., 1997; Vrijenhoek et al., 2001; Li et al., 2007). Of the various feedwater quality parameters, those most likely to influence microbiological deposition and growth, and those most likely to influence mineral precipitation, are especially suspect. These parameters include feedwater pH, levels of species of nitrogen, phosphorous, and sulfur; levels of organic carbon and surfactants; levels of divalent cations and anions capable of forming mineral precipitates; and levels of silica. In addition, concentration of disinfectant (total chlorine) also is expected to be of importance.

To investigate the potential relationship between RO feedwater quality and membrane fouling, a quantifiable membrane fouling criterion was required to act as a dependent variable in modeling studies. The elapsed time between chemical cleanings, defined in this study as the membrane "lifetime," was chosen for this criterion. This criterion is a long-term factor that integrates membrane exposure to feedwater over a relatively long period (typically several months) and is most likely best related to the long-term accumulation of membrane fouling materials.

Reverse osmosis feedwater (ROF) water quality parameters monitored in the interval between each of the observed membrane cleaning operations were used to define potential input variables for the model construction. Both the mean value, as well as the excursion within the time frame (the minimum and maximum value), were calculated for each membrane lifetime to create exemplars for model construction.

8.1.1 Creation of the First Stage RO Membrane Lifetime Model

The study focused on the first stage of the RO, because this is the easiest to characterize as it directly receives feedwater whose chemistry is routinely monitored. Start dates, stop dates, and operation lifetimes between cleanings of first stage membranes were determined for all 15 of the 5 mgd RO units in the AWPF from April 2008 through February 2010 from a copy of the log of membrane cleaning activity for the AWPF. During the majority of this period the AWPF treated a secondary wastewater effluent processed by carbonaceous biochemical oxygen demand (CBOD). On November 9, 2009, the OCSD switched to an NDN treatment process that took approximately 2 months to stabilize. Therefore, the AWPF operated on a secondary wastewater effluent that was treated primarily by the CBOD method. In total, 49 first stage RO membrane lifetime exemplars were identified for model construction (see Table 8.1). The "start date" corresponds to the day the membrane was cleaned and put back in service, the "end date" is the date the membrane was taken out of service and cleaned again. The days between these dates were enumerated as the days the membrane was operated. Average, minimum, and maximum values of various water quality parameters were then determined for the periods corresponding to each membrane lifetime from water quality data.

8.1.2 Selection of Model Inputs Using a Genetic Algorithm

Model inputs were selected from a pool of potential input parameters (Table 8.2) chosen to best represent the factors that might be most expected to affect accumulation of chemical and biological materials on the surface of first stage RO membranes. A genetic algorithm (GA; NeuralWorks Predict v3, Neuralware, Carnegie, PA) was used to test combinations of these potential input variables and to select the best input variable set capable of describing observed RO membrane lifetime. GAs use principals of biological genetics to "evolve" the "fittest" set of input parameters that best describes a dependent variable. They are capable of dealing with cross-correlated variables that tend to confound other statistical methods, consider synergistic interactions between input variables, and may be used with linear, nonlinear and logistic transformation functions, which can greatly enhance input set fitness. GAs often yield the most descriptive input data set compared with traditional statistical methods.

Because of the relatively small number of exemplars for this analysis, 10 independent combinations of input variables were determined with the GA. The frequency with which each potential variable was included by the GA was calculated, and only those variables that were chosen by the GA greater than or equal to 50% of the time were selected to use for construction of neural models (Table 8.3). The numbers shown in the Table 8.3 are sensitivity indices for each parameter. If the sensitivity index was greater than 0, then the input was considered potentially influential (identified as a "hit"). The fraction indicates the frequency of hits for each potential input variable. Water quality parameters included with a frequency greater than or equal to 0.5 were subsequently used for ANN construction.

Table 8.1. List of First Stage RO Membrane Lifetimes Between Cleaning Determined from Water Quality Operation Log Data

Actual RO Lifetime Between Cleanings				
Start Date	**End Date**	**Train**	**Unit**	**Days Operated**
4/9/2008	10/13/2008	E	E03	187
4/15/2008	12/23/2008	D	D02	252
4/16/2008	10/8/2008	C	C03	175
8/26/2008	11/22/2008	A	A02	88
9/26/2008	12/30/2008	D	D03	95
10/8/2008	1/16/2009	C	C03	100
10/13/2008	12/25/2008	E	E03	73
11/22/2008	2/4/2009	A	A02	74
11/25/2008	4/30/2009	A	A01	156
11/26/2008	2/1/2010	A	A03	432
12/1/2008	12/5/2009	B	B01	369
12/15/2008	4/4/2009	E	E02	110
12/17/2008	3/12/2009	E	E01	85
12/23/2008	1/9/2009	D	D02	17
12/25/2008	3/18/2009	E	E03	83
12/30/2008	3/12/2009	D	D03	72
1/2/2009	1/10/2010	D	D01	373
1/8/2009	7/9/2009	C	C02	182
1/9/2009	7/18/2009	D	D02	190
1/16/2009	4/7/2009	C	C03	81
1/22/2009	12/22/2009	B	B02	334
1/29/2009	2/5/2010	B	B03	372
2/4/2009	1/29/2010	A	A02	359
3/12/2009	12/30/2009	D	D03	293
3/12/2009	12/23/2009	E	E01	286
3/18/2009	1/5/2010	E	E03	293
4/4/2009	12/26/2009	E	E02	266
4/7/2009	7/13/2009	C	C03	97
4/30/2009	1/27/2010	A	A01	272
5/27/2009	12/8/2009	C	C01	195
7/9/2009	12/2/2009	C	C02	146
7/13/2009	1/3/2010	C	C03	174
7/18/2009	1/14/2010	D	D02	180
12/2/2009	5/13/2010	C	C02	162
12/5/2009	5/15/2010	B	B01	161
12/8/2009	5/11/2010	C	C01	154
12/22/2009	2/7/2010	B	B02	47
12/23/2009	5/8/2010	E	E01	136
12/26/2009	3/31/2010	E	E02	95
12/30/2009	5/7/2010	D	D03	128
1/3/2010	5/14/2010	C	C03	131
1/5/2010	5/9/2010	E	E03	124
1/10/2010	5/5/2010	D	D01	115
1/14/2010	5/16/2010	D	D02	122
1/27/2010	5/23/2010	A	A01	116
1/29/2010	5/24/2010	A	A02	115
2/3/2010	5/25/2010	A	A03	111
2/5/2010	5/22/2010	B	B03	106
2/7/2010	5/20/2010	B	B02	102

Table 8.2. ROF Water Quality Parameters Chosen as Potential Input Parameters for the ANN Model

Ammonia Nitrogen (NH3-N)	Aggressivity Index (AI)	Total Nitrogen (TOT-N)
Calcium (2+) ion (Ca)	Silica (SiO2)	Total Dissolved Solids (TDS)
Magnesium (2+) ion (Mg)	Surfactant (MBAS)	Total Organic Carbon (TOC)
Sulfate (2-) ion (SO4)	Field pH (F-pH)	Total Amperometric Chlorine (TOTCLA)
		Total Titrimetric Chlorine (TOTCL2)

Table 8.3. GA Inclusion Frequency of Potential ANN Input Parameters Surviving in the Final ANN Model

GA Trials	NH3-N Max	NH3-N Avg.	Ca Max	Ca Avg.	SO4 Avg.	TOTCLA Max
1	0	0.004774	0.3705	0	−0.1378	0.5251
2	0.4905	−0.4362	0.5797	−0.8223	0	0.4014
3	0	−0.4286	0.4714	−0.4748	−0.2609	0.4333
4	0	0	0.5895	−0.4652	−0.6590	0.4107
5	0.2775	−0.7176	0.3532	0	0	0.4399
6	1.4058	−1.1434	0	0.07671	0	0.4762
7	0	0	0.4019	−0.7765	−0.2412	0.2987
8	0.6046	−0.2907	0.3129	0	−0.3105	0.5179
9	0	0	0.4711	−0.6946	−0.6284	0.5151
10	0.6177	0	0	0.2249	−0.1539	0.5512
Total Hits	5	6	8	7	7	10
Fraction	0.5	0.6	0.8	0.7	0.7	1.0

8.2 Construction of the Artificial Neural Network (ANN) Model

8.2.1 Definition of a Neural Network Model

ANN models represent an empirical modeling approach like multiple linear regression (MLR) to explain or to predict the output behavior of a system using one or more input parameters. As with other empirical modeling approaches, the ANN is constructed from the observed behavior of the system, and once built, is capable of mimicking the system behavior. This allows the experimenter to perform virtual experimental manipulation of the model system in ways not easily managed with the real system in order to reveal hidden properties, or to predict system behavior in often a far more accurate way than can be achieved with more traditional multiple linear or nonlinear regression modeling techniques.

The fundamental structure of a neural network consists of three (or more) layers of computational elements (perceptrons) that mimic the action of biological neurons. Inputs to these perceptrons are processed by an internal summing function with weighting factors assigned during construction of the network, and the output switched by a threshold function. The inputs and outputs of the perceptrons are then connected in the layers to form the

network. In the design used for this study, a three-layer network was constructed consisting of an "input layer" that received input data to the system via transformation functions that normalized the data to a -1 to +1 range read by the ANN, a "hidden layer," and an "output layer," where the ANN output was delivered to a transformation function that converted it back to a real world output value (in this case, to days of membrane lifetime).

8.2.2 ANN Model Construction

ANN models were constructed using a software package (NeuralWorks Predict v3, Neuralware, Carnegie, PA). Prior to network construction, exemplary data were randomly ordered, then divided into a "training" set used to construct the ANN model and a "test" set not used in construction but used to evaluate the predictive ability of the model. The internal weighting factors in the network were established using the exemplary data in the training set. In other words, the network was "trained," and the degree of success determined using Pearson's r correlation coefficient (the closer the value is to 1.0000, the better the behavior of the network). The success of the network's ability to predict the behavior of the system under study was evaluated using the "test" set data. The network was first used to predict the test set output values, and a correlation value determined as with the training set. The closer the training and test set correlation values match, the better the ANN is capable of predicting system behavior. The greater both correlation values become, the better the input variables chosen with which to construct the ANN model can explain the system behavior. Thus, it is desirable to obtain high correlation values for the training and test set data and have both match as closely as possible for a good model. As with any empirical model, ability to predict system behavior is limited to the range of the data used in the training and test sets—unless the model is keying into major behavioral principals that extend beyond this limit. Typically, extrapolation is not desirable, and often with ANNs, can lead to erroneous conclusions. so it is to be avoided.

Normally, about 25% of the exemplars are withheld as test exemplars. In this case, of the 49 exemplars available, 29 exemplars were used to train the model, and 20 exemplars were used to test the model (41% test), a highly conservative evaluation. Three ANN models were constructed at a time and the best of the three chosen using the overall Pearson's r correlation coefficient for the model and similarity between the Pearson's r value for the training and test sets.

Following construction, a sensitivity analysis was performed to determine the degree of participation of each of the input parameters in the ANN model. If any input parameters were observed to exhibit overall zero sensitivity, that parameter was dropped from the input list, and another ANN model constructed. This was done until all of the inputs were seen to have nonzero sensitivity index values. This resulted in a more robust model and also had the added advantage of reducing the input data set.

Exemplars used for final model construction, along with the model output for each exemplar are presented in Table 8.4. A statistical description of the final model behavior is shown in Table 8.5. The final model had a 6:4:1 architecture. Statistical parameters evaluated include (1) the Pearson's r value for real world data values, (2) the r value for the internal (untransformed) values, (3) the average of the absolute difference between model and real world outputs, (4) the maximum difference between model and real world outputs, (5) the RMS difference between model and real world outputs, (6) the accuracy (the fraction of the time the prediction was within 20% of the actual value), (7) the 95% confidence limits (real world values), and (8) how many records (exemplars) were used in training and testing the

model. The input parameters are shown with their corresponding sensitivity index values in the model. Increasing longevity of the first-stage RO membrane lifetime was, in general, positively related to (1) maximum total ammonia (NH3-N) levels, (2) maximum calcium levels, (3) average total amperometric chlorine levels, and negatively related to (4) average ammonia (NH3-N), (5) average calcium, and (6) average sulfate levels in the RO feedwater.

Table 8.4. Exemplars (49) Used for Final ANN Model Construction: Input Water Quality Data, Measured Membrane Lifetime Data, and Membrane Lifetime Predicted by the Model

NH3-N Max	NH3-N Avg	Ca Max	Ca Avg	SO4 Avg	TOTCLA Max	Start Date	End Date	Train	Unit	Measured Days Operated	Predicted Days Operated
31.2	23.6	81.2	78.5	249.3	2.3	4/9/2008	10/13/2008	E	E03	187	179.5
31.2	23.4	82.4	79.6	275.1	2.3	4/15/2008	12/23/2008	D	D02	252	174.7
31.2	23.1	81.2	78.6	256.6	2.3	4/16/2008	10/8/2008	C	C03	175	186.8
26.8	20.9	82.4	79.6	298.3	1.9	8/26/2008	11/22/2008	A	A02	88	140.9
27.2	22.3	82.4	81.4	306.0	1.9	9/26/2008	12/30/2008	D	D03	95	74.6
27.5	24.2	82.4	80.7	316.3	1.9	10/8/2008	1/16/2009	C	C03	100	71.4
27.2	23.7	82.4	81.4	306.0	1.9	10/13/2008	12/25/2008	E	E03	73	63.6
27.5	26.0	79.7	79.1	316.0	1.6	11/22/2008	2/4/2009	A	A02	74	49.3
27.5	24.2	94.0	85.4	298.4	2.0	11/25/2008	4/30/2009	A	A01	156	132.2
27.5	20.7	94.0	80.8	287.8	3.2	11/26/2008	2/1/2010	A	A03	432	347.8
27.5	22.9	94.0	80.5	289.6	3.2	12/1/2008	12/5/2009	B	B01	369	333.5
27.5	24.6	94.0	85.3	304.3	2.0	12/15/2008	4/4/2009	E	E02	110	121.1
27.5	25.4	94.0	87.2	310.7	2.0	12/17/2008	3/12/2009	E	E01	85	87.2
27.5	25.8	78.5	78.5	347.0	1.5	12/23/2008	1/9/2009	D	D02	17	45.3
27.5	25.3	94.0	87.2	310.7	2.0	12/25/2008	3/18/2009	E	E03	83	88.9
27.5	25.3	94.0	87.2	310.7	2.0	12/30/2008	3/12/2009	D	D03	72	88.9
27.4	20.9	94.0	80.8	285.9	3.2	1/2/2009	1/10/2010	D	D01	373	348.8
27.4	23.0	94.0	85.3	285.0	2.0	1/8/2009	7/9/2009	C	C02	182	169.9
27.4	23.0	94.0	83.5	282.7	2.0	1/9/2009	7/18/2009	D	D02	190	222.0
27.4	24.0	94.0	91.6	292.5	2.0	1/16/2009	4/7/2009	C	C03	81	107.6
27.4	21.2	94.0	81.0	280.4	3.2	1/22/2009	12/22/2009	B	B02	334	347.2
27.4	19.3	94.0	81.1	283.1	3.2	1/29/2009	2/5/2010	B	B03	372	355.0

Table 8.4. (Continued). Exemplars (49) Used for Final ANN Model Construction: Input Water Quality Data, Measured Membrane Lifetime Data, and Membrane Lifetime Predicted by the Model

NH3-N Max	NH3-N Avg	Ca Max	Ca Avg	SO4 Avg	TOTCLA Max	Start Date	End Date	Train	Unit	Measured Days Operated	Predicted Days Operated
27.4	19.6	94.0	81.1	283.1	3.2	2/4/2009	1/29/2010	A	A02	359	353.6
25.6	20.1	85.7	78.6	277.7	3.2	3/12/2009	12/30/2009	D	D03	293	283.6
25.6	20.5	85.7	78.6	277.7	3.2	3/12/2009	12/23/2009	E	E01	286	279.5
25.6	20.1	85.7	78.6	277.7	3.2	3/18/2009	1/5/2010	E	E03	293	283.6
25.6	20.0	85.7	78.6	277.7	3.2	4/4/2009	12/26/2009	E	E02	266	284.1
25.6	22.0	85.7	83.3	259.3	2.0	4/7/2009	7/13/2009	C	C03	97	92.6
25.6	18.7	83.9	78.2	281.9	3.2	4/30/2009	1/27/2010	A	A01	272	267.4
25.6	22.1	80.4	75.9	283.0	3.2	5/27/2009	12/8/2009	C	C01	195	191.1
24.6	22.3	77.8	75.0	296.0	3.2	7/9/2009	12/2/2009	C	C02	146	121.4
24.6	18.9	82.7	76.3	286.8	2.7	7/13/2009	1/3/2010	C	C03	174	247.8
24.6	17.4	82.7	77.8	294.2	3.2	7/18/2009	1/14/2010	D	D02	180	235.9
8.6	4.4	84.0	82.9	281.7	2.6	12/2/2009	5/13/2010	C	C02	162	147.7
6.8	4.1	84.0	82.9	281.7	2.6	12/5/2009	5/15/2010	B	B01	161	146.3
6.8	4.1	84.0	82.9	281.7	2.6	12/8/2009	5/11/2010	C	C01	154	146.3
6.8	4.5	82.0	82.0	313.0	1.3	12/22/2009	2/7/2010	B	B02	47	88.5
6.8	4.2	84.0	83.0	302.0	2.6	12/23/2009	5/8/2010	E	E01	136	121.4
6.8	4.5	84.0	83.0	302.0	2.6	12/26/2009	3/31/2010	E	E02	95	120.2
6.8	4.5	84.0	83.0	302.0	2.6	12/30/2009	5/7/2010	D	D03	128	120.2
6.8	4.5	84.0	83.0	302.0	2.6	1/3/2010	5/14/2010	C	C03	131	120.2
6.8	4.5	84.0	83.0	302.0	2.6	1/5/2010	5/9/2010	E	E03	124	120.2
6.8	4.5	84.0	83.0	302.0	2.6	1/10/2010	5/5/2010	D	D01	115	120.2
6.8	4.8	84.0	84.0	291.0	2.6	1/14/2010	5/16/2010	D	D02	122	104.6

Table 8.4. (Continued). Exemplars (49) Used for Final ANN Model Construction: Input Water Quality Data, Measured Membrane Lifetime Data and Membrane Lifetime Predicted by the Model

NH3-N Max	NH3-N Avg	Ca Max	Ca Avg	SO4 Avg	TOTCLA Max	Start Date	End Date	Train	Unit	Measured Days Operated	Predicted Days Operated
6.8	4.8	84.0	84.0	291.0	2.6	1/27/2010	5/23/2010	A	A01	116	104.5
6.8	4.4	84.0	84.0	291.0	2.6	1/29/2010	5/24/2010	A	A02	115	105.9
6.8	4.4	84.0	84.0	291.0	2.6	2/3/2010	5/25/2010	A	A03	111	105.9
5.4	3.8	84.0	84.0	291.0	2.6	2/5/2010	5/22/2010	B	B03	106	106.3
5.4	3.8	84.0	84.0	291.0	2.6	2/7/2010	5/20/2010	B	B02	102	106.3

Table 8.5. Statistical Description of the Best ANN Model

Days Operated	R	Net-R	Avg. Abs.	Max. Abs.	RMS	Accuracy (20%)	Conf. Interval (95%)	Records
All	0.96071	−0.94740	19.8966	84.1905	27.7137	0.97959	55.51712	49
Train	0.97243	−0.95822	17.1757	84.1905	24.1698	0.96552	49.44523	29
Test	0.94051	−0.92933	23.8420	77.2936	32.1662	1	67.36721	20

Average	NH3-N Max	NH3-N Avg	Ca Max	Ca Avg	SO4 Avg	TOTCLA Max		
Net Output 1	0.22583	−0.46238	0.59559	−0.80738	−0.19681	0.079991		

8.2.3 Statistical Analysis of the ANN Model's Performance

The overall ability of the ANN model to explain RO membrane lifetimes in the original training/test data sets was evaluated using Statgraphics Centurion XV (StatPoint, Inc., Herndon, VA). Comparison of the model's prediction to the observed membrane lifetime data are shown in Figure 8.1. The central line is the model fit (perfect fit = 1.0 slope), the first boundary lines represent the 95% confidence limits and the second boundary lines represent prediction limits. Data obtained from all RO units are represented in the model, which explained membrane lifetime between cleanings very well. Five data points were identified as outliers by this analysis. They lie on or outside the prediction limit boundary lines. A Box-Cox diagram displaying the spread of the residuals (the difference between the predicted and observed values) is shown in Figure 8.2. In this analysis, the small cross (+) within the box is the mean value (0), the line through the box is the median value, the box ends represent first and fourth quartile, and the bars represent the largest and smallest data values in the population. Points/square symbols indicate outliers (data more than 1.5 times the interquartile distance). The five outliers detected in the original model construction appear here as points outside the bars. The interquartile distance, representing 50% of the data, is quite narrow (gray box), and in this region model predictions were ±15 days of observation. Five exemplars included in the original model construction were identified as statistical outliers in this analysis. Figure 8.3 shows the results of the removal of these outliers, which slightly improved the fitness of the ANN model. Figure 8.4 shows a Box-Cox diagram of the resultant spread of the residuals. They did not seriously harm the predictive ability or change the interquartile range of the residuals, meaning that their presence did not significantly damage the model's ability to predict membrane lifetime. Tables 8.6 and 8.7 summarizes a statistical evaluation of the ability of the ANN model to describe first stage RO membrane lifetime (evaluated on the basis of the deviation of the predicted-to-actual scatterplot from a slope 1.0000 line) using exemplar data obtained from April 2008 through February 2010. More than 99% of the variance in the observed membrane operation lifetime between cleanings was explained by the ANN model. Because the p-value was less than 0.01, the ANN model was significant at greater than 99% confidence level.

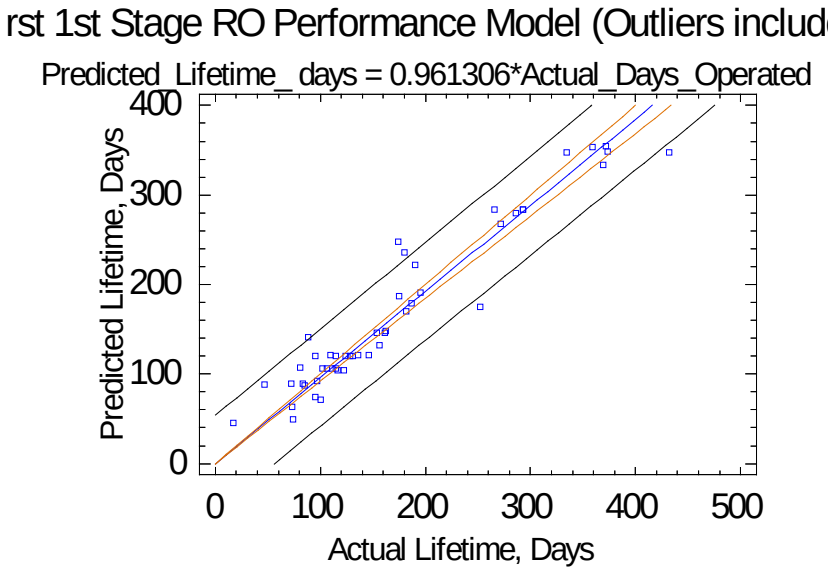

Figure 8.1. Graphical comparison of ANN model prediction with observed membrane lifetime.

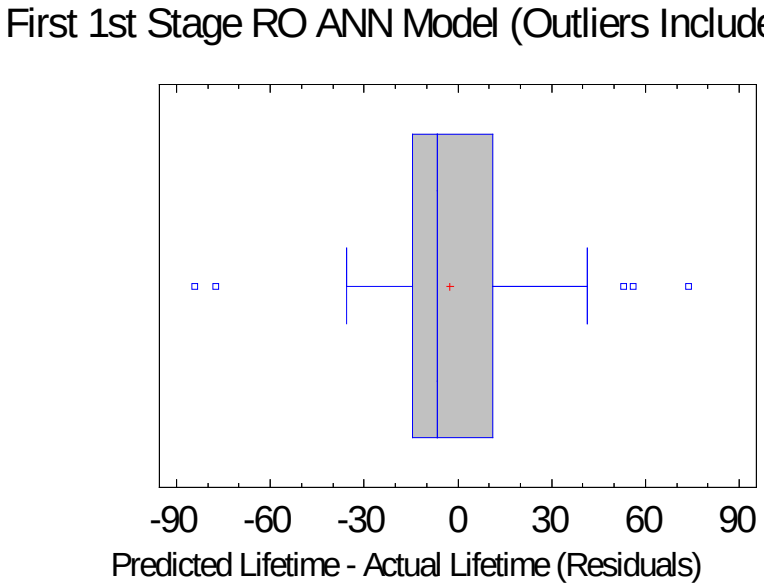

Figure 8.2. Box-Cox diagram showing the spread of the ANN model residuals.

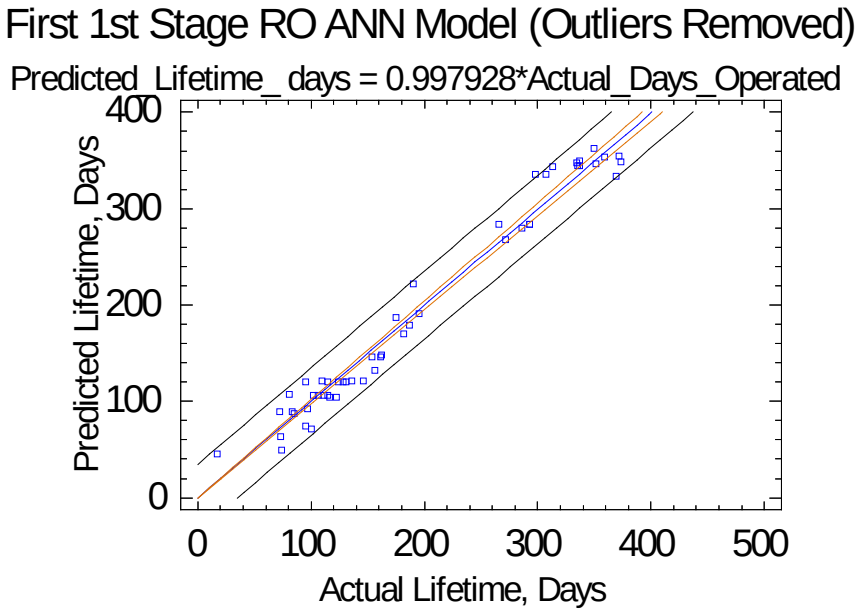

Figure 8.3. ANN model with the five outliers were removed.

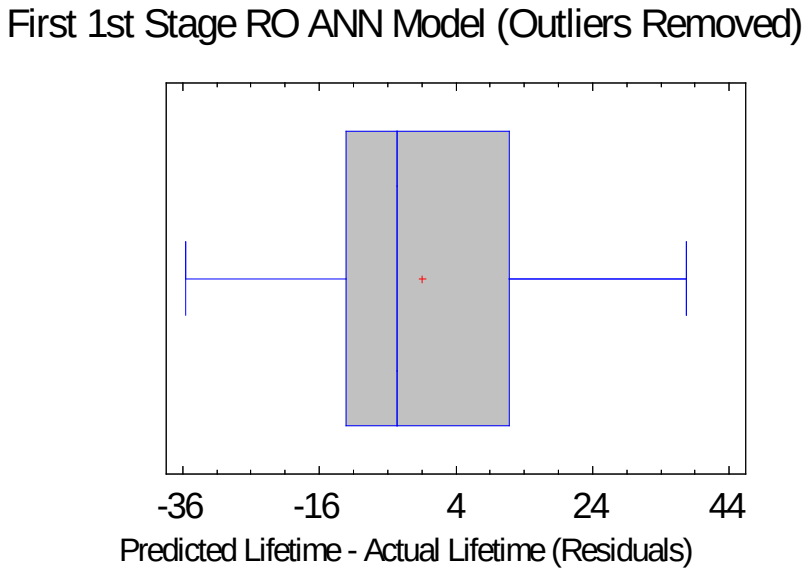

Figure 8.4. Box-Cox diagram showing the spread of the ANN model residuals with the five outliers removed from this analysis.

Table 8.6. Statistical Evaluation of ANN Model for the Description of First Stage RO Lifetime

Parameter	Least Squares Estimate	Standard Error	T Statistic	p-Value
Slope	0.997928	0.0111011	89.8943	0.0000

Notes: Y (measured)=Predicted lifetime days; X (actual)=Actual days operated; Selection variable include <1Linear model: Y = b*X

Table 8.7. Analysis of Variance of ANN Model for Description of First Stage RO Lifetime

Source	Sum of Squares	Df	Mean Square	F-Ratio	p-Value
Model	2.44532E6	1	2.44532E6	8080.99	0.0000
Residual	15130.1	50	302.602		
Lack-of-Fit	13975.7	46	303.818	1.05	0.5561
Pure Error	1154.42	4	288.606		
Total	2.46045E6	51			

Notes: Correlation Coefficient = 0.996921; % R^2 = 99.3851%; % R^2 (adjusted for d.f.) = 99.3851%; Standard Error of Est. = 17.3954; Mean absolute error = 14.3104; Durbin-Watson statistic = 1.16936; Lag 1 residual autocorrelation = 0.381793

8.2.4 Summary of ANN Model for the Prediction of First Stage RO Membrane Lifetimes

Overall, the ANN model explained more than 99% of the variation of observed first stage RO membrane lifetimes using six inputs observed during each membrane's lifetime between cleanings. The six input variables were:

1. maximum observed ammonia (NH3-N Max)
2. average ammonia (NH3-N Avg)
3. maximum calcium ion (Ca Max)
4. average calcium ion (Ca Avg)
5. average sulfate ion (SO4 Avg)
6. maximum total amperometric chlorine (TOTCLA Max)

The p-value for the model was 0.0000 and the lack-of-fit was 0.5561, suggesting that this was a highly descriptive model. The standard error of the estimate was 17.4 days.

8.3 Validation of the ANN Model with Recent First Stage RO Membrane Lifetime Data

8.3.1 ANN Model Validation Exemplars

The overall fitness of an ANN model is determined using a "validation set." This represents data gathered from the system under study independent of those used in the construction of the model and may be obtained simultaneously with training/test data or represent data acquired later in time. In this case, the validation data presented here represent a total of 19 new membrane lifetime exemplars and corresponding RO feedwater water chemistry data obtained from first stage RO cleaning events that occurred from March 31, 2010, through December 15, 2010 (Table 8.8).

8.3.2 ANN Model Validation Results

The water chemistry data from the validation set were input into the ANN model and membrane lifetime predictions obtained, which were then compared with the observed membrane lifetime data. The model was able to predict eight of 19 lifetimes of first stage RO membranes in Units A01, A03, B01, B02, B03, D01, D02, and D03 fairly well but not the other units, where membrane lifetime was often significantly less than model predictions.

Although the ANN model originally was able to predict well (or explain) the observed variances in lifetimes across each of the 5 mgd RO units observed prior to March 2010, when challenged with the validation data acquired after that time, the ability of the ANN model to predict the validation values varied considerably from one RO unit to another. In some cases a good-to-excellent fit was observed, but in other cases it was not. Figures 8.5 through 8.9 show the results of these validation test results for each of the three RO units (01–03) and for each of the five RO Trains (A–E).

For Train A (Figure 8.5) the model predicted performance of Units A01 and A03 well, but Unit A02 underperformed the model prediction (following the December 6, 2010, cleaning). The model predicted performance of Units B01, B02, and B03 quite well (Figure 8.7). Although the ANN model agreed well with historical performance (cleaning pre-May 2010) used in model construction, all three of the RO units in Train C significantly underperformed model predictions (C01: following May 11 and December 9, 2010, cleaning; C02: following May 13 and December 10, 2010, cleaning; C03: following May 14 and December 15, 2010, cleaning). As with Train B, the model predicted performance of Units D01, D02, and D03 quite well (Figure 8.8). Although the ANN model agreed well with historical performance (cleaning pre-May 2010) used in model construction, all three of the RO units in Train E underperformed model predictions (E01: following May 8, 2010, cleaning; E02: following March 31, 2010, and May 26, 2010, cleaning; E03: following May 9, 2010, cleaning) (Figure 8.9).

Table 8.8. Validation Data for First Stage RO Lifetime ANN Model

	NH3-N Avg	Ca Max	Ca Avg	SO4 Avg	TOTCLA Max	Start Date	End Date	Train	Unit	Observed Days Operated	Predicted Days Operated
4.8	2.1	86.3	84.2	283.5	4.5	3/31/2010	5/26/2010	E	E02	56	162.0
5.0	2.5	87.0	71.8	254.2	2.3	5/23/2010	5/8/2011	A	A01	350	362.9
5.0	3.5	87.0	79.0	260.8	2.3	12/6/2010	5/6/2011	A	A02	151	331.2
5.0	2.5	87.0	78.1	254.2	2.5	5/25/2010	5/11/2011	A	A03	351	346.6
5.0	2.5	87.0	77.6	255.9	2.3	5/15/2010	4/17/2011	B	B01	337	349.6
5.0	2.5	87.0	78.1	254.2	2.3	5/20/2010	4/20/2011	B	B02	335	344.6
5.0	2.5	87.0	78.1	254.2	2.3	5/22/2010	4/24/2011	B	B03	337	344.6
4.3	1.8	83.6	78.0	253.2	2.0	5/11/2010	12/9/2010	C	C01	212	292.7
5.0	3.5	87.0	77.8	267.5	2.3	12/9/2010	4/3/2011	C	C01	115	345.9
4.3	1.8	83.6	77.5	250.1	2.0	5/13/2010	12/10/2010	C	C02	211	299.7
5.0	3.5	87.0	77.8	267.5	2.3	12/10/2010	3/30/2011	C	C02	110	345.9
4.3	1.9	83.6	77.5	253.9	2.0	5/14/2010	12/15/2010	C	C03	215	299.5
5.0	3.5	87.0	78.0	262.0	2.3	12/15/2010	4/6/2011	C	C03	112	344.9
5.0	2.3	87.0	78.5	260.3	2.0	5/5/2010	2/27/2011	D	D01	298	335.7
5.0	2.3	87.0	78.5	260.3	2.0	5/6/2010	3/9/2011	D	D02	307	335.7
5.0	2.4	87.0	77.9	257.6	2.0	5/7/2010	3/16/2011	D	D03	313	343.4
5.0	2.2	87.0	78.7	261.8	2.0	5/8/2010	2/5/2011	E	E01	273	332.4
5.0	2.2	87.0	78.4	260.2	2.0	5/26/2010	2/9/2011	E	E02	259	337.1
5.0	2.2	87.0	78.7	261.8	2.0	5/9/2010	2/11/2011	E	E03	278	332.4

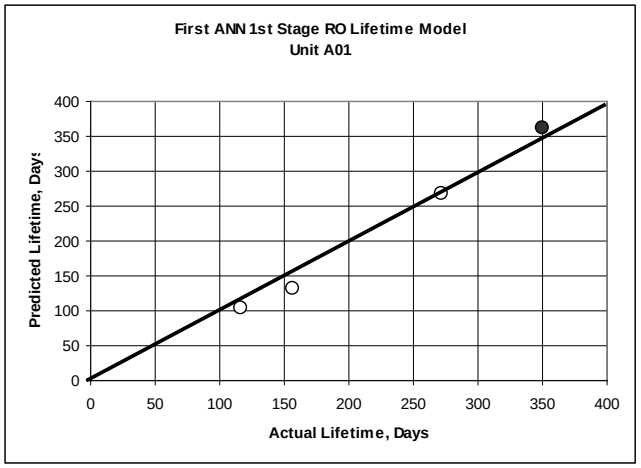

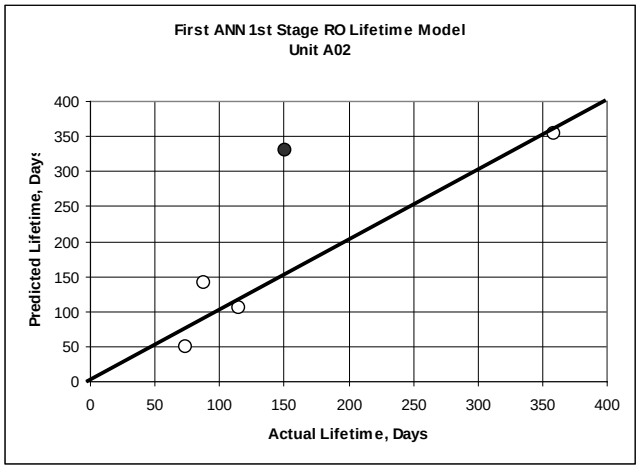

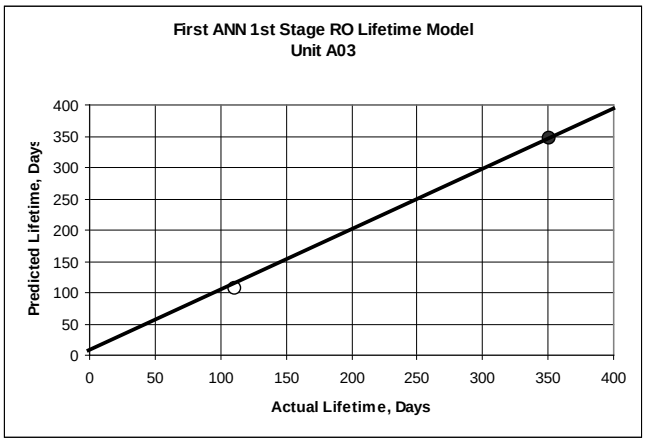

Figure 8.5. Actual membrane lifetime versus lifetime predicted by the ANN model for AWPF Train A RO Units.

Notes: Open circles = exemplars used in model construction. Closed circles = validation exemplars (model prediction of performance). Horizontal line = perfect prediction by model.

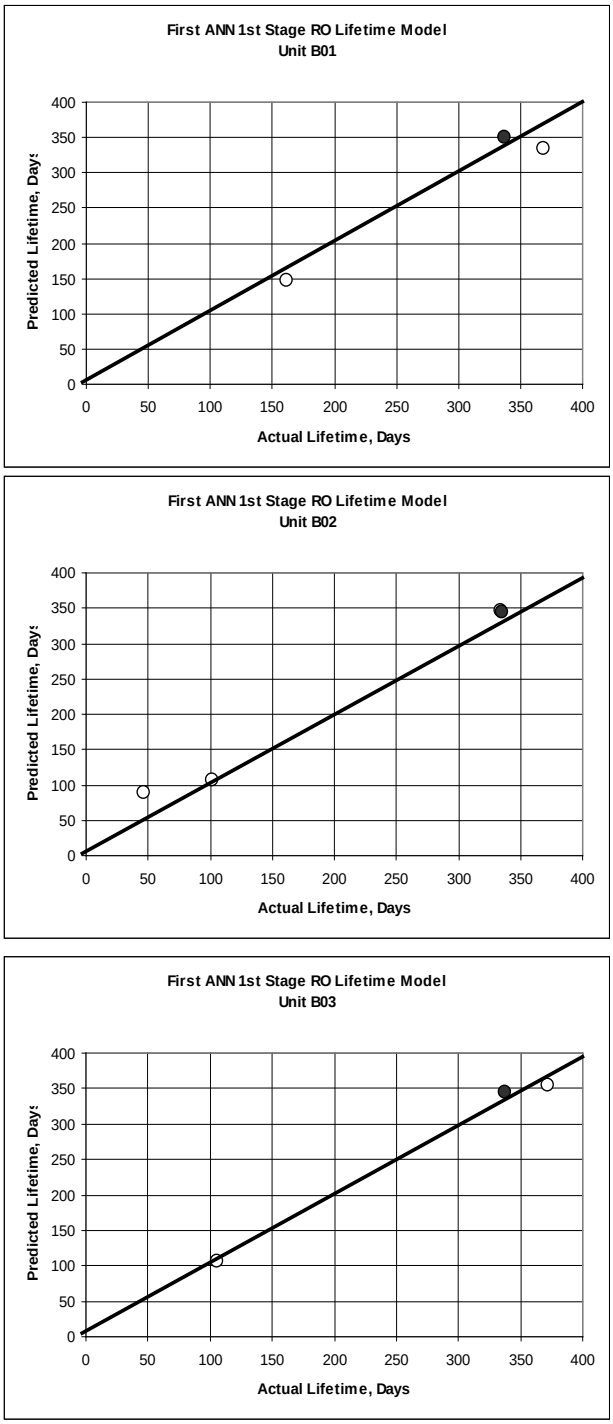

Figure 8.6. Actual membrane lifetime versus lifetime predicted by the ANN model for AWPF Train B RO Units.

Notes: Open circles = exemplars used in model construction. Closed circles = validation exemplars (model prediction of performance). Horizontal line = perfect prediction by model.

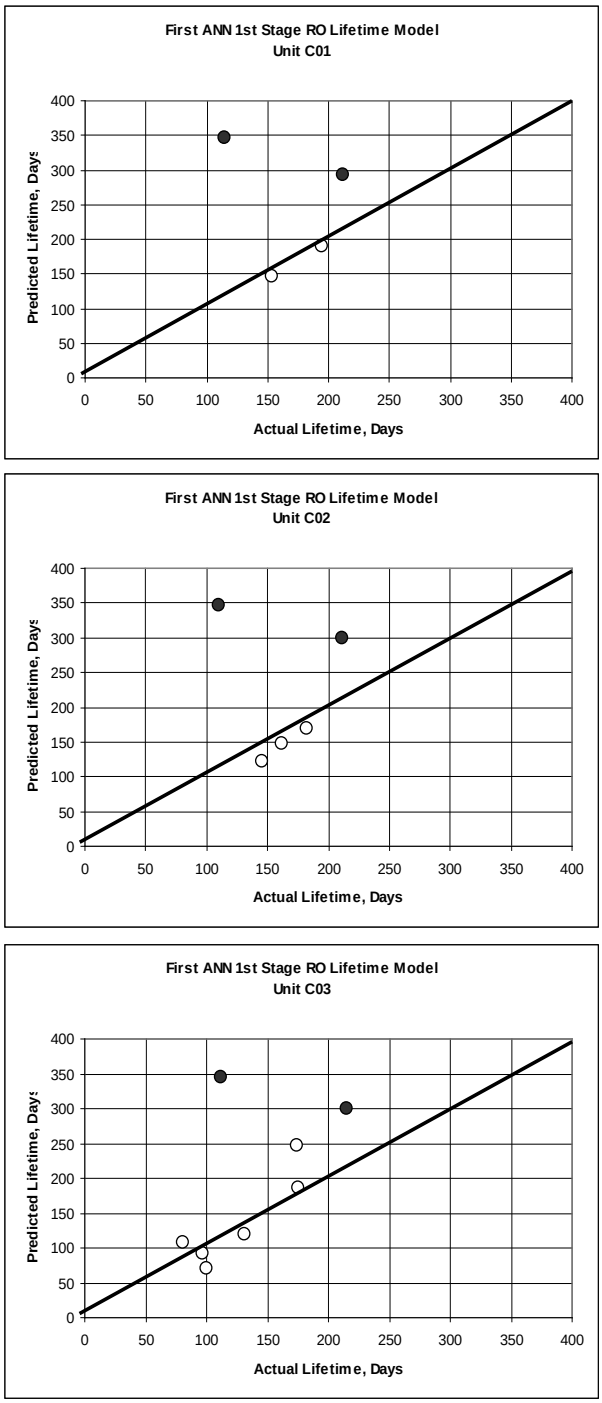

Figure 8.7. Actual membrane lifetime versus lifetime predicted by the ANN model for AWPF Train C RO Units.

Notes: Open circles = exemplars used in model construction. Closed circles = validation exemplars (model prediction of performance). Horizontal line = perfect prediction by model.

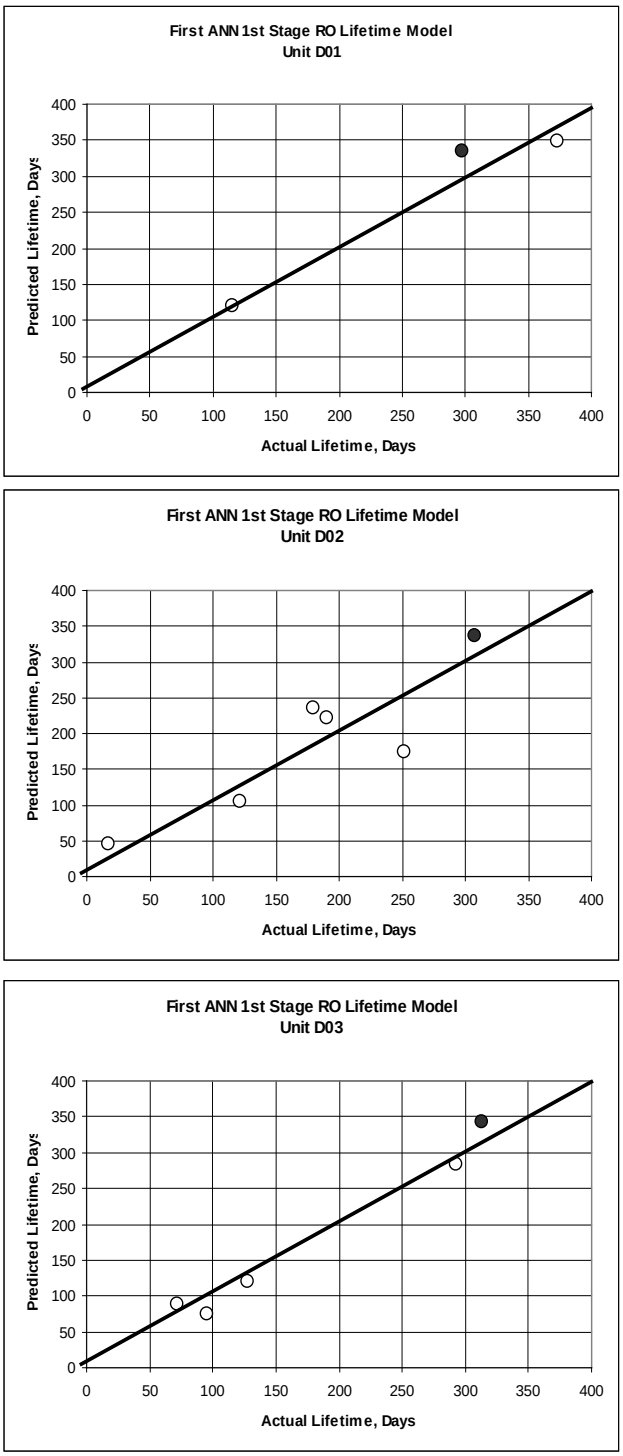

Figure 8.8. Actual membrane lifetime versus lifetime predicted by the ANN model for AWPF Train D RO Units.

Notes: Open circles = exemplars used in model construction. Closed circles = validation exemplars (model prediction of performance). Horizontal line = perfect prediction by model.

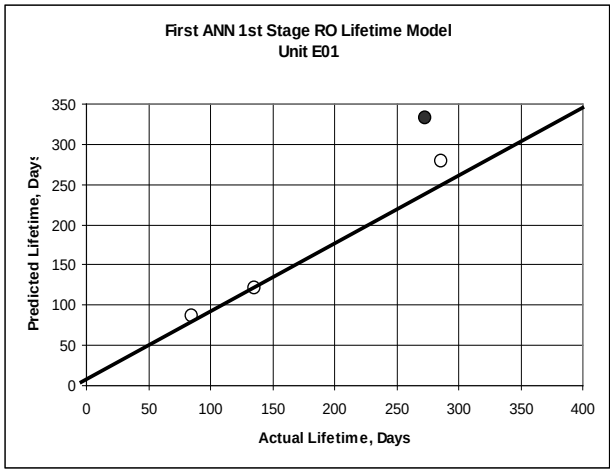

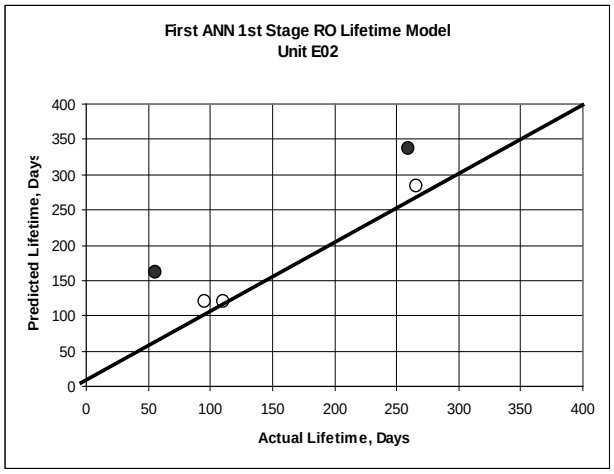

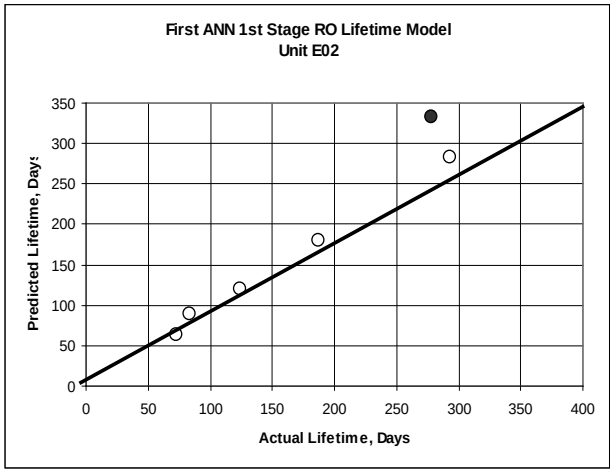

Figure 8.9. Actual membrane lifetime versus lifetime predicted by the ANN model for AWPF Train E RO Units.

Notes: Open circles = exemplars used in model construction. Closed circles = validation exemplars (model prediction of performance). Horizontal line = perfect prediction by model.

8.3.3 Summary of the Validation of ANN Model for First Stage RO Membrane Fouling

All the data from the RO units that were used in the model construction (membranes cleaned before May 2010) showed a good fit with behavior predicted by the ANN model, indicating that the RO feedwater water quality parameters used in the model (1) maximum observed NH_3-N, (2) the average NH_3-N, (3) the maximum Ca, (4) the average Ca, (5) the average SO_4, and (6) the maximum total amperometric chlorine were strongly correlated with the observed time between first stage chemical cleaning (lifetime). These water quality parameters were capable of explaining in excess of 94% (from the ANN statistics using all of the data) to 99% (outliers removed) of the observed variance in the first stage RO membrane lifetime measured from April 2008 to February 2010.

The input parameters make sense as membrane fouling predictors from a chemical and biological standpoint. Calcium and sulfate levels in the RO feedwater are involved in gypsum ($CaSO_4 \cdot H_2O$) mineralization, which has been implicated to form in the presence of membrane biofilms. Ammonia nitrogen (NH_3-N) and total amperometric chlorine (TOTCLA) are related to the level of chloramines, the primary disinfection agents for the AWPF RO purification process. The fact that the maximum, as well as the average levels of NH_3-N and of Ca are important, suggests that the magnitude of excursions of these parameters within the lifetime of the RO membrane are as influential as their overall concentration present in RO feedwater. Certainly variation in ammonia nitrogen could affect disinfection speciation, with higher levels favoring formation of monochloramine over di- and trichloramine. Some of the parameters indicated in the model can be easily manipulated (e.g., total chlorine), whereas others could be manipulated with greater difficulty (ammonia levels and perhaps calcium and sulfate load) using this model as a guide to maximize first stage RO membrane lifetime.

New (validation) data for first stage RO membrane lifetime acquired after the ANN model was constructed (March 2010 to December 2010) was well predicted by the ANN model for RO Units A01, A03, B01, B02, B03, D01, D02, and D03, and for these units the model appeared to be valid. However, for RO Units A02, C01, C02, C03, E01, E02, and E03, the fit to the validation data was relatively poor, that is, for these units the model was unable to predict the newly observed membrane lifetime based on the selected water quality parameters. In each of these cases, the actual membrane lifetime was consistently less than that predicted by the model. Because behavior of all of the units was explainable pre-March 2010, and more than half of the units were highly predictable post March 2010, it seems that around March 2010 the remaining RO units (A02, C01, C02, C03, E01, E02, and E03) may have undergone changes that altered their relationship with the water quality parameters identified in the model, with the result that their first stage membrane lifetimes between cleanings appear to have become significantly less than predicted.

8.4 Conclusions

Overall, it was possible, based on historic data from the AWPF from April 2008 through February 2010, to explain first stage RO membrane lifetime (defined as the time between chemical cleaning in place) using only six inputs involving four ROF water quality parameters by employing an ANN-based multivariate model. The predictive ability of this model was further tested using 8 months of data obtained from the AWPF from March 2010 through December 2010 with mixed success.

Input parameters identified as predictive of first stage RO membrane lifetime included (1) the maximum observed NH_3-N value, (2) the average NH_3-N, (3) the maximum Ca, (4) the average Ca, (5) the average SO_4, and (6) the maximum total chlorine (amperometric) observed during each membrane's lifetime between cleanings (all in mg/L).

Although the original ANN model performance suggested a highly explanatory and predictive model, the validation study yielded mixed results. Eight of the 15 RO units exhibited a close fit with the model, which accurately predicted their membrane lifetime performance, whereas with the other seven RO units from the validation set, the model failed to predict membrane lifetimes (A02, C01, C02, C03, E01, E02 and E03). In these cases, the observed membrane lifetimes were significantly less that that predicted by the model.

Because the ANN model was quite capable in more than half of the cases of predicting the validation exemplar responses of the membranes, it does appear to be generally valid. One hypothesis as to why it failed to predict the behavior of the other units' membranes may lie in changes specific to those units that occurred between when the ANN model was constructed and when the validation lifetime data were obtained. It is hoped that further historical data can be obtained on the particular RO units where the model failed, and if those units now have a history disparate from the others, it may be possible to identify a quantifiable factor or factors that will allow inclusion of their behavior in a new membrane lifetime model.

8.5 Future Studies

In the next phases this modeling effort will be expanded to include second and third stage RO membrane lifetime analysis. It is anticipated that the second stage membranes will behave materially as did the first stage membranes, because they were often cleaned in concert. The third stage membranes, however, are expected to exhibit completely different dependencies on RO feedwater water quality parameters, which only indirectly influence the feedwater chemistry in the third stage feed channel.

Chapter 9

Reverse Osmosis Fouling: Quantification of RO Membrane Fouling Factors

9.1 Introduction

Upon exposure to environmental water sources, RO membranes become coated with inorganic, organic, and biological materials that can reduce RO efficiency by both impeding water transport to the membrane surface and increasing the polarization layer by impeding transport of solutes away from the membrane surface (Sabiani et al., 2001; Hoek and Elimelech, 2003). Adsorption of these materials at the membrane surface is dictated by the feedwater matrix, which varies continuously along the length of the RO feed channel as water is extracted and solutes become more concentrated. In a multistage RO system, the feedwater solute concentration increases significantly from stage to stage. In the three-stage RO system of the AWPF, which operates at 85% recovery, a greater than six-fold increase in solute concentration occurs at the end of the RO feed channel of the final stage.

RO membrane performance is described by the ability of the membrane to reject solutes and is most often cited as a percent rejection or log removal. The efficiency of the membranes in producing product water is expressed as the product water flux as a function of applied hydraulic pressure. The latter measurement, specific product water flux, is strongly related to the cost of water production and is affected heavily by the accumulation of fouling materials on the membrane surface, which makes the measurement a sensitive indicator of RO membrane fouling.

Although many observations have been made regarding the accumulation of materials on RO membranes as a function of time and in some instances as a function of membrane performance (water flux, rejection), there is a paucity of studies comparing the relationship between accumulation of materials on RO membranes and loss of specific water flux (Herzberg and Elimelech, 2007; Lee et al., 2010; Schneider et al., 2005). Moreover, fewer have looked at this as a function of position along the feed channel in a full-scale RO system (Chen et al., 2004). It is hypothesized that as position changes along the RO feed channel and the water matrix is altered, the nature of the dominant foulant material also will shift. Understanding the nature of this shift and the identity of the principal fouling mechanisms that affect the production of water at each stage of a multistage RO system are important in optimizing the process in order to minimize the cost of water production by reverse osmosis.

This study was implemented to determine the relationship between observed RO fouling and accumulation of materials on the membrane surface in an RO train at full scale. To achieve this, a test system was devised that was capable of assessing RO membrane performance by receiving feedwater matrices from each of four critical locations in the three-stage RO train, the beginning of the first, second, and third stages and the end of the third stage. This system employed multiple large-scale membrane coupons or swatches that were sacrificed at determined performance milestones, and then subjected to autopsy in order to obtain qualitative and quantitative information regarding accumulated materials on the membrane surface and feed spacer with each feedwater matrix. During the study, levels of biocide (mono- and dichloramine), dissolved solids, monovalent and divalent ions, metals, pH,

temperature, suspended solids, and so on in the RO feedwater were presumed to remain at nominal levels. All membrane swatches were treated in a similar fashion during the exposure tests to help reduce the potential for biases in their water production responses. Statistical methods were employed to relate this accumulation to measured membrane performance, and identify the materials most related to RO fouling in the full-scale system of each stage.

9.2 Materials and Methods

9.2.1 Experimental Apparatus

AWPF full-scale 5 mgd RO Unit E01 of the 15 mgd Train E was equipped with a feedwater tap at the beginning of the first, second, and third RO stages, and at the end of the third RO stage. Feedwater from each of these taps under pressure determined by the RO unit was conveyed to a manifold supporting five stainless steel 4 × 6 in. RO membrane test cells, design modified from the Osmonics test cell configuration (GE Osmonics, Trevose, PA). Each test cell was equipped with a thin-film composite polyamide Hydranautics ESPA2 (Oceanside, CA) RO membrane swatch obtained from a freshly dissected RO element. The polypropylene Vexar spacer was included in each cell so that the hydrodynamics in the cell mimicked as closely as possible that of a spiral wound element. A total of 20 RO test cells were thus employed in the study, providing the ability to monitor the four key water matrices in RO Unit E01 and provide up to five sample points for regression analysis (Figure 9.1).

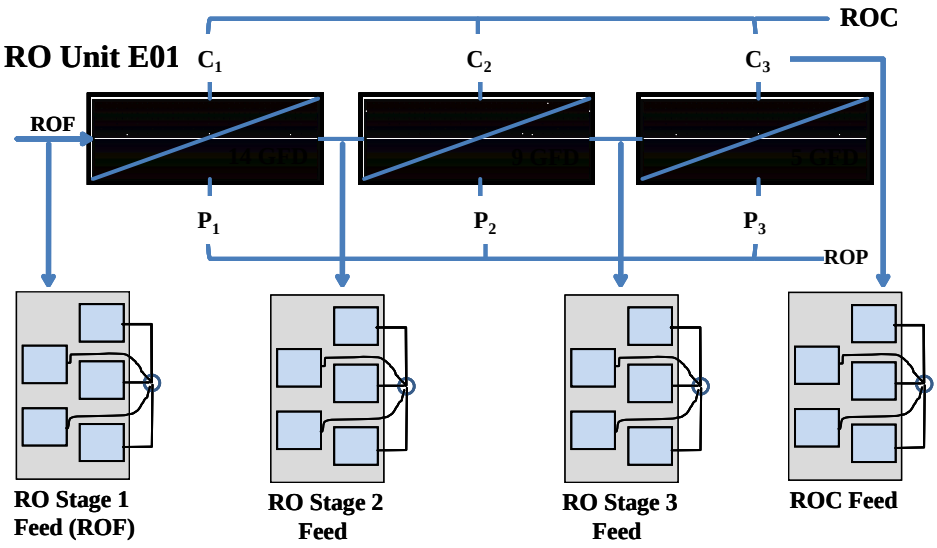

Figure 9.1. Schematic of RO test cell array connected to AWPF 5 mgd RO Unit E01.

9.2.2 Water Quality and Membrane Performance Monitoring−Determination of Dependent Experimental Factors

The RO test cells for Stages 1, 2, and 3 were operated near constant water flux consistent with that of the full-scale RO system at the point where the feedwater was recovered to supply to the test beds, whereas the final set of test cells were operated off the brine (ROC) at the feed pressure supplied unrestricted or unregulated. Membrane product water flux was calculated in gallons per square foot per day (gfd). The normalized water flux was determined by correcting the measured water flux to a temperature of 25 °C. This was then divided by the

transmembrane pressure (TMP) in pounds per square inch (psi) to yield the normalized specific water flux (gfd/psi @ 25 °C). The normalized specific water flux, which is relatively independent of the small local fluctuations in pressure and flow, was used as the dependent experimental parameter for the regression analyses.

9.2.3 Milestones for Test Membrane Recovery

Membrane performance milestones were derived from current RO management practices of the AWPF. In RO Stages 1 and 2, membranes are considered fouled enough to warrant chemical cleaning when their TMP increases 35% over their initial TMP. In Stage 3, the membranes are chemically cleaned when the membrane product water flux has declined to 50% of its initial value.

In this study, 100% fouling refers to these operational milestones. For each source water, the milestone determining the time of sacrifice was based on 10%, 20%, 50%, and 100% of fouling as described. The indicator points are summarized in Table 9.1.

Table 9.1. Performance Milestones for Termination of Test Cells and Swatch Recovery

Swatch Name	Stage 1 Feed (ROF)		Stage 2 Feed		Stage 3 Feed		Stage 3 Brine (ROC)	
	% Fouled	TMP Inc.	% Fouled	TMP Inc.	% Fouled	TMP Inc.	% Fouled	% Flux Loss
A	10	3.5%	10	3.5%	10	5.0%	10	5.0%
B	20	7.0%	20	7.0%	20	10.0%	20	10.0%
C	50	17.5%	50	17.5%	50	25.0%	50	25.0%
D	70	24.5%	70	24.5%	70	35.0%	70	35.0%
E	100	35.0%	100	35.0%	100	50.0%	100	50.0%

9.2.4 Determination of Independent Experimental Parameters for Regression Analysis Based on Membrane Autopsy

9.2.4.1 Biochemical and Microbial Characterization Parameters

When the membrane swatch reached the performance milestone, it was recovered along with the spacer, and an autopsy was performed. The feed, middle, and brine ends along the flow path across each swatch were analyzed to determine six independent biochemical and microbial characterizing properties (Table 9.2). Total protein was determined by Lowrey et al. (1951), total carbohydrate by Dubois et al. (1956), total bacteria by enumeration of organisms recovered from the membrane surface using membrane filtration and epifluorescent counting with DAPI staining, viable aerobic heterotrophic organisms by enumeration of organisms recovered from the membrane surface using R2A agar medium plate counting, “viable” and “dead” bacteria by enumeration of organisms recovered from the membrane surface using membrane filtration and epifluorescent counting with Molecular Probes LIVE/DEAD BacLight bacterial viability kit (Life Technologies, Grand Island, NY).

Table 9.2. Membrane Surface Fouling Parameters

Biochemical and Microbial Constituents
total protein ($\mu g/cm^2$)
total carbohydrate ($\mu g/cm^2$)
total bacteria by epifluorescent counting (bacteria/cm^2)
total viable aerobic heterotrophic bacteria (bacteria/cm^2)
total "live" epifluorescent bacteria (bacteria/cm^2)
total "dead" epifluorescent bacteria (bacteria/cm^2)
Elemental Atom/Carbon Atom Ratio Determined by SEM-EDX Spectroscopy
oxygen/carbon (O/C ratio)
nitrogen/carbon (N/C ratio)
fluorine/carbon (F/C ratio)
sodium/carbon (Na/C ratio)
magnesium/carbon (Mg/C ratio)
aluminum/carbon (Al/C ratio)
silicon/carbon (Si/C ratio)
phosphorus/carbon (P/C ratio)
sulfur/carbon (S/C ratio)
chlorine/carbon (Cl/C ratio)
calcium/carbon (Ca/C ratio)
potassium/carbon (K/C ratio)
iron/carbon (Fe/C ratio)
copper/carbon (Cu/C ratio)

9.2.4.2 Atomic Characterization Parameters

The accumulation of materials on membrane flat sheets was investigated by SEM and EDX spectroscopy. EDX spectroscopy utilizes a probe electron beam that impinges on the specimen. The electrons induce emission of X-rays from atoms under the beam, the wavelength of which are characteristic of the elements each atom represents. Thus, from the pattern of the emergent EDX spectrum, the atomic composition of the material on the surface of the specimen can be deduced. The contribution of each of the elements in the spectrum is normally expressed as a fraction of the total emergent X-ray energy (as an atom-percent). The penetration of the electron beam is typically on the order of a few micrometers so that the EDX signal from an RO membrane represents the composition of the surface material (foulant), the permselective polyamide layer, and a small quantity of the polysulfone support layer.

Although the percentage of atomic composition provides a means of confirming the presence of elements on and in the specimen and provides a semiquantitative assessment of their concentration relative to all the elements detected, it does not allow determination of absolute

concentration. And although the intensity of X-ray emission is proportional to the concentration of atoms in the path of the electron beam, the absolute value of the area counts obtained is a function of the beam energy, geometry, and specimen topography. Thus, the value alone cannot be used to determine concentration of individual elements but requires a normalization factor in order to account for differences in the detection sensitivity from specimen to specimen. Moreover, in determining atom percentages, different background levels are used for each specimen, as frequently different numbers of elements are detected on different specimens. Therefore, if the amount of a single element is to be quantified, a normalization strategy is needed, one capable of accounting for all of these difficulties.

Although the RO membrane and spacer samples are primarily carbonaceous, the carbon X-ray signal is expected to be ubiquitous among membrane specimens, and because the density of carbon atoms is not likely to vary widely, the carbon signal may serve as a common basis for normalization of the other elemental EDX signals. Thus, by taking the ratio of a particular element's raw EDX signal to that of carbon, a quantitative representation of the concentration of that element on the membrane or spacer should result that would be comparable from specimen to specimen. A total of 14 independent elemental atom-to-carbon atom ratios were determined, combined with the six biochemical and microbial parameters, for a total of 20 independent parameters for the entire study (see Table 9.2)

9.2.5 Linear Regression Analysis

The autopsy data from the membrane surface and from the surface of the Vexar polypropylene spacer were analyzed. Simple linear regression analyses for the study were performed using Statgraphics Centurion XV (Statpoint, Herndon, VA). Insufficient data were obtained to attempt multiple regression analyses. Transformation functions were chosen for each analysis (i.e., biochemical, microbial, and elemental) to achieve the largest possible percent % R-squared (% R^2) values. The 95% confidence level was chosen as the criterion with which to assess statistical significance for all regression models, but models where % R^2 values were greater or equal to 50% also were noted.

For each element/carbon ratio and for each feed condition (Stages 1, 2, 3, and RO brine), linear regression analysis was used to determine the relationship between the element's deposition relative to the carbon content and the observed membrane normalized specific water flux (gfd/psi @ 25 °C). The degree to which variations in the element/carbon atom ratios were able to describe variations in the specific water flux was determined using the percent R-squared (% R^2) value. Fitness of the models were assessed by examination of the p-values ($p \leq 0.05$ indicating statistical significance at or greater than the 95% confidence level). The direction of the overall influence also was noted, as it would be expected that the deposition of elements comprising compounds contributing to membrane surface fouling should be inversely proportional to the observed membrane normalized specific water flux.

The same type of linear regression analyses also were performed for spacer element/carbon ratios. In this case, if the deposition of material on the spacers led to a reduction of cross-flow at the membrane surface, then it is likely that membrane normalized specific water flux should appear to be negatively related to the element/carbon ratios of elements comprising these spacer foulants.

9.3 Results and Discussion

The fouling characterization study was prematurely terminated when RO Unit E01 was cleaned, and test cells were inadvertently exposed to the cleaning solutions. The adulterated membrane swatches were not included in the study.

9.3.1 Temporally Resolved Membrane Performance: Swatch-to-Swatch Reproducibility

Performance of the experimental membrane swatches in terms of the normalized specific water flux (gfd/psi @ 25 °C) plotted as a function of time is summarized in Figures 9.2 through 9.5. The four sets of RO test cells were started at the same time on January 5, 2012.

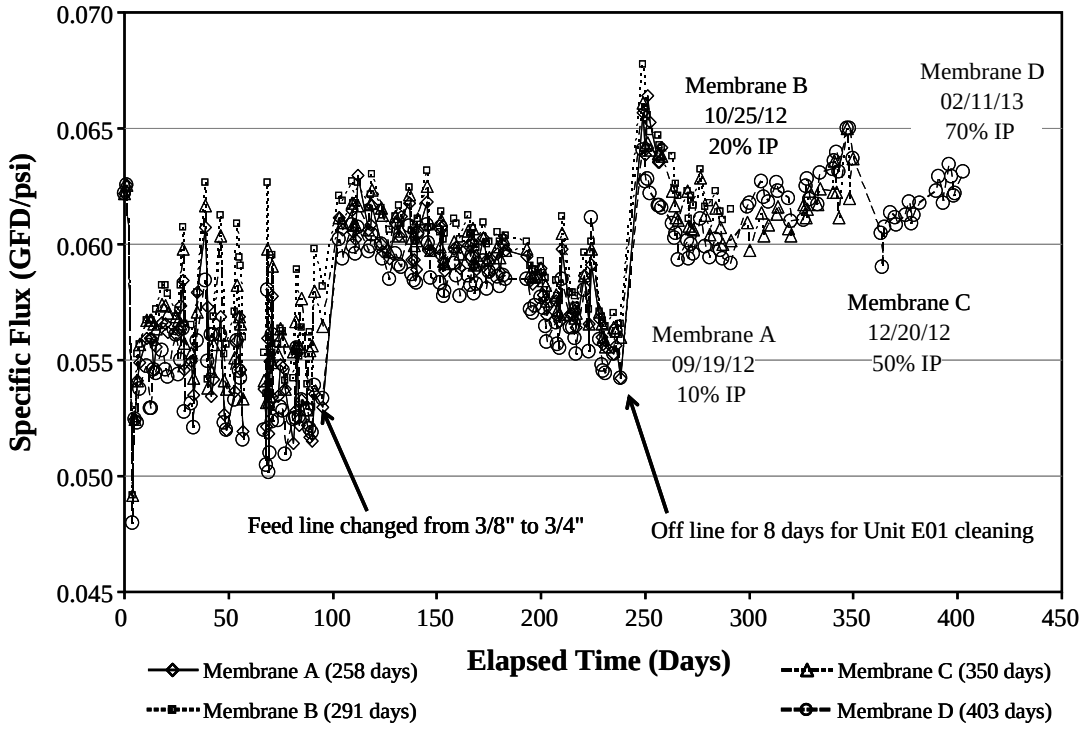

Figure 9.2. Normalized specific water flux plotted as a function of time for all RO membrane swatches receiving water from Unit E01 Stage 1 feed (ROF).

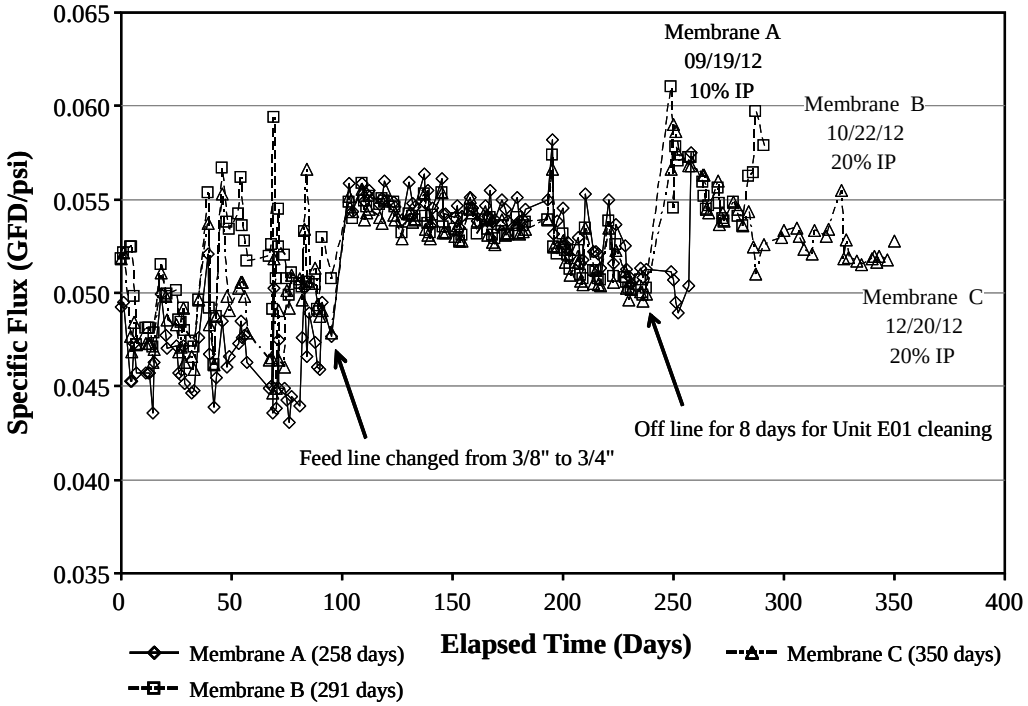

Figure 9.3. Normalized specific water flux plotted as function of time for all RO membrane swatches receiving water from Unit E01 Stage 2 feed.

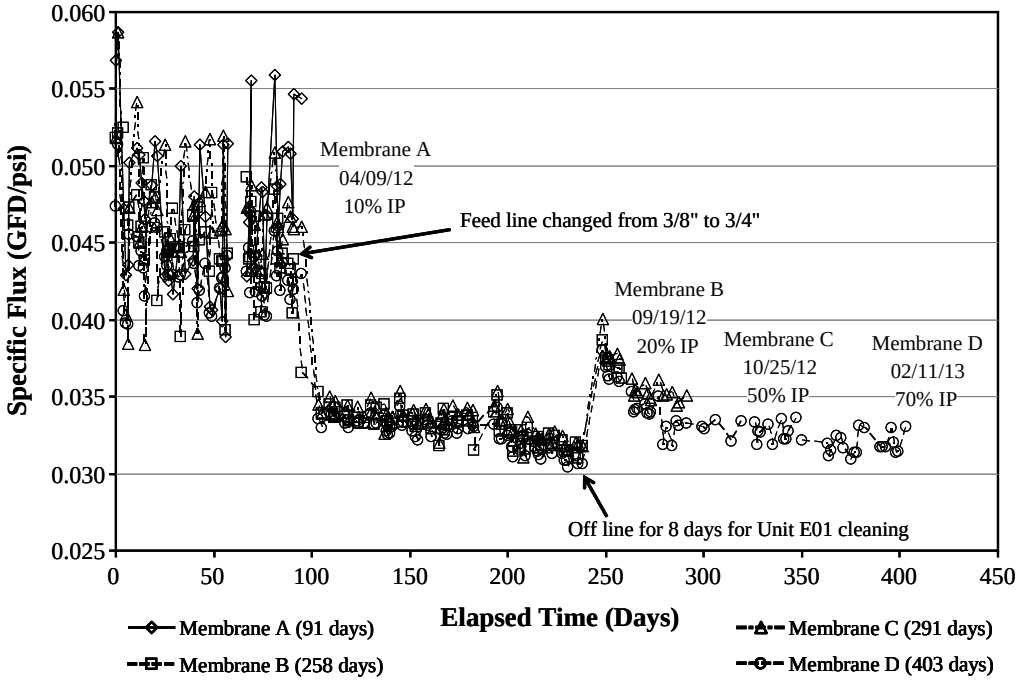

Figure 9.4. Normalized specific water flux plotted as a function of time for all RO membrane swatches receiving water from Unit E01 Stage 3 feed.

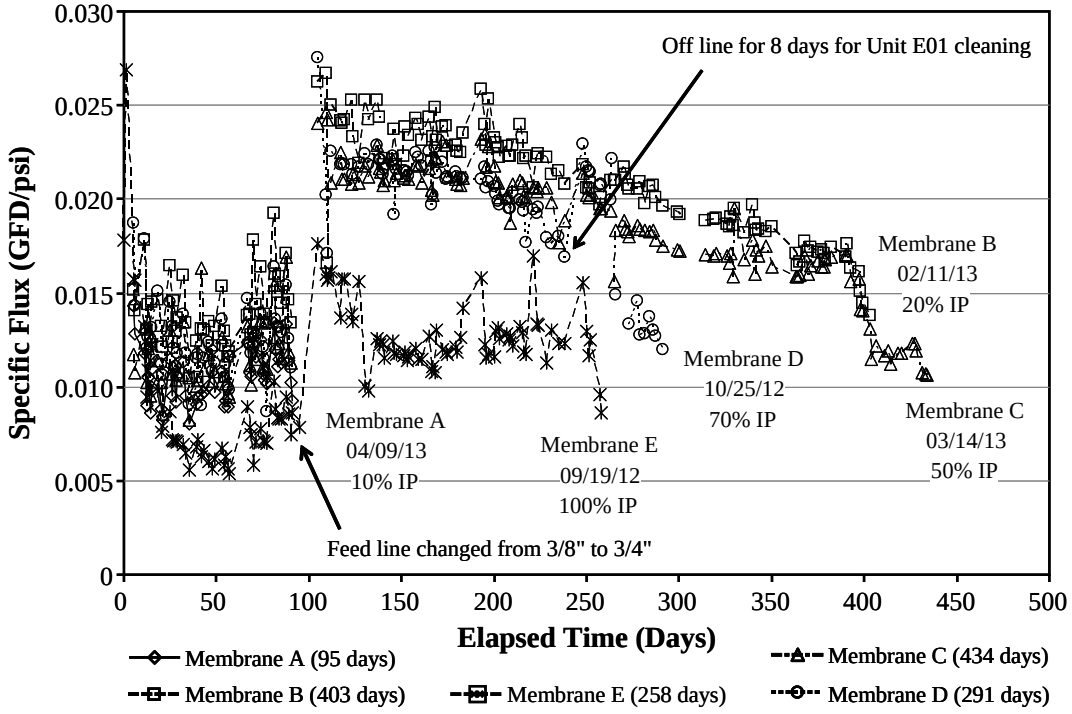

Figure 9.5. Normalized specific water flux plotted as a function of time for all RO membrane swatches receiving water from Unit E01 Stage 3 brine (ROC).

At the start of the study, there were four test beds each containing five test cells loaded with Hydranautics ESPA2 membrane swatches, and in theory, each of the five swatches should have produced the same specific product water flux. Overall, the swatch-to-swatch variability within a given test bed was very small, which was an important observation, as there were no replicates available for each of the performance milestones. Therefore, the behavior of any single swatch was considered representative of the five membrane swatches as a group.

Initially the undersized 3/8 in. feed tubing to the four test beds limited the feed pressure and resulted in imbalances between the test cells, which were characterized by noisier specific water flux measurements. However, once the feed tubing was properly sized (to 3/4 in.) so as to not limit flow to the units, all of the cells behaved similarly on each feed source. Because the normalized specific water fluxes were highly perturbed during this initial feedwater-limited period, for the purpose of analyses, no cells that reached their milestones during the initial period of flow limitation were used in the regression analysis.

9.3.2 Membrane Swatch Performance and Feed Spacer Characterization Data

The results of the membrane autopsy for recovered swatches and the normalized specific water flux data are shown for the biochemical and microbial constituents in Table 9.3. In this table, the percent of the milestone indicator point (% IP) represents the percent of fouling, defined by an increase in TMP for Stages 1, 2, and 3 from feedwater exposure or the loss of water flux for the Stage 3 brine-exposed swatches that would occur in the full-scale plant to be considered sufficiently fouled to warrant membrane cleaning. Not all of the milestone points could be recovered for all feedwater exposures because of the premature termination of the study caused by accidental exposure of the 4 × 6 in. swatches to cleaning solutions from the full-scale cleaning of RO membranes in Unit E01. Autopsy data obtained from the feed,

middle, and brine ends of each of the test swatches were averaged to represent the whole swatch. These averaged data are expressed in the tables following and were used in the subsequent linear correlation analyses.

The raw elemental EDX spectroscopic data from the membrane surface and the feed spacer are displayed in Tables B.1 through B.5 in Appendix B. Averages of raw EDX signal data, (i.e., element area counts) from SEM studies were obtained for all the fouled RO swatches and their associated spacer elements. For each element detected, the element-to-carbon raw signal ratio was determined. These results were tabulated for each of the feed conditions that each swatch was exposed to during the given experiment (Tables 9.4–9.7).

Table 9.3. Membrane Performance and Autopsy Data for Membrane Swatches Exposed to AWPF RO Unit E01 Source Waters

Sample Date	% IP	HPC (cells/cm^2)	EPI Count (cells/cm^2)	"Dead" (Red) (cells /cm^2)	"Live" (Green) (cells/cm^2)	Total Protein±S.D. (ug/cm^2)	Total Carbohydrate ±S.D. ug/cm^2	Product Flux (gfd)	Temperature (°C)	Temperature Correction Factor	Normalized Product Flux (gfd)	TMP (psi)	Normalized Specific Product Flux (gfd/psi @25°C)
E01 Stage 1 Feed (ROF)													
19-Sep-12	10	1.28E+05	2.03E+06	5.08E+05	1.56E+05	6.17±1.75	4.51±0.11	12.0	29.2	0.88	10.58	165	0.0641
25-Oct-12	20	4.80E+04	3.17E+06	7.56E+05	4.83E+05	3.43±0.14	4.61±0.15	12.0	27.8	0.92	11.03	180	0.0613
20-Dec-12	50	1.32E+03	9.12E+06	3.80E+06	2.57E+06	9.49±1.05	1.89±0.28	12.0	24.7	1.01	12.11	190	0.0637
11-Feb-13	70	2.89E+05	1.15E+06	ND	ND	9.84±3.29	6.14±0.43	12.0	23.3	1.05	12.64	200	0.0632
E01 Stage 2 Feed													
19-Sep-12	10	1.25E+03	1.24E+06	2.72E+05	1.13E+05	1.92±0.34	4.52±1.00	9.0	29.2	0.88	7.94	136	0.0583
25-Oct-12	20	2.83E+03	5.63E+07	7.35E+05	2.51E+05	6.99±0.72	2.13±0.16	9.0	27.8	0.92	8.27	149	0.0555
20-Dec-12	50	8.59E+02	9.15E+06	2.14E+05	5.16E+04	10.52±0.90	1.60±0.25	9.0	24.7	1.01	9.08	170	0.0534
E01 Stage 3 Feed													
5-Apr-12	10	4.16E+03	1.91E+05	8.37E+04	2.74E+04	3.84±0.68	3.52±0.49	5.0	24.8	1.01	5.03	93	0.0541
19-Sep-12	20	3.84E+02	1.03E+06	2.49E+05	3.46E+04	6.99±0.72	2.13±1.50	5.0	29.2	0.88	4.41	122	0.0361
25-Oct-12	50	1.43E+03	3.89E+05	6.74E+04	3.61E+05	3.20±1.58	4.94±0.82	5.0	27.8	0.92	4.60	132	0.0348
11-Feb-13	70	3.44E+03	6.94E+05	NA	NA	8.68±0.65	5.72±1.89	5.0	23.3	1.05	5.27	161	0.0327
E01 Stage 3 Brine (ROC)													
5-Apr-12	10	7.24E+02	2.06E+05	1.04E+05	2.03E+04	4.60±0.93	2.99±0.73	0.6	24.8	1.01	0.57	62	0.0092
11-Feb-13	20	4.55E+02	2.33E+05	NA	NA	8.99±0.26	5.90±1.52	1.8	23.3	1.05	1.90	138	0.0137
14-Mar-13	50	8.78E+03	1.38E+05	NA	NA	1.11±0.37	5.84±0.95	1.5	24.4	1.02	1.53	144	0.0106
25-Oct-12	70	4.54E+02	8.57E+05	421428.6	35250	3.28±0.09	3.20±0.45	1.3	27.8	0.92	1.19	100	0.0119
19-Sep-13	100	6.50E+03	6.56E+05	4.21E+05	6.81E+04	10.26±1.65	2.92±1.01	1.0	29.2	0.88	0.88	103	0.0086

Table 9.4. Element/Carbon Ratios Determined from EDX Raw Signal Intensity Detected on Membrane Swatches and Spacers Exposed to RO Unit E01 Stage 1 Feedwater (ROF) and Associated Normalized Specific Product Water Flux

Membrane	O to C	N to C	F to C	Na to C	Mg to C	Al to C	Si to C	P to C	S to C	Cl to C	Ca to C	K to C	Fe to C	Cu to C	Spc. Flux gfd/psi @ 25°C
10% ESPA2	0.0131								0.0198		0.0003				0.0641
20% ESPA2	0.0613		0.0022	0.0018		0.0014	0.0053	0.0008	0.2438	0.0062	0.0025		0.0005	0.0011	0.0613
50% ESPA2	0.1785			0.0098	0.0049	0.0066	0.0190	0.0124	2.8791	0.0459	0.0186				0.0637
70% ESPA2		0.1188	0.0061	0.0083	0.0047	0.0078	0.0344	0.0111	1.1698	0.0283	0.0216				0.0632
Spacer	**O to C**	**N to C**	**F to C**	**Na to C**	**Mg to C**	**Al to C**	**Si to C**	**P to C**	**S to C**	**Cl to C**	**Ca to C**	**K to C**	**Fe to C**	**Cu to C**	**Spc. Flux gfd/psi @ 25°C**
10% Spacer	0.0057		0.0003	0.0063	0.0017	0.0009		0.0058		0.0021	0.0019	0.00015			0.0641
20% Spacer	0.2968	0.0806	0.0410	0.0659	0.0211	0.0019	0.0045			0.0540	0.0382	0.0129		0.0013	0.0613
50% Spacer	0.0977	0.0327	0.0043	0.0124	0.0059			0.0076	0.0029	0.0106	0.0069	0.0018			0.0637
70% Spacer		0.0227		0.0103	0.0036	0.0016	0.0025	0.0047	0.0037	0.0110		0.0014	0.0065		0.0632

Table 9.5. Element/Carbon Ratios Determined from EDX Raw Signal Intensity Detected on Membrane Swatches and Spacers Exposed to RO Unit E01 Stage 2 Feedwater (ROF) and Associated Normalized Specific Product Water Flux

Membrane	O to C	N to C	F to C	Na to C	Mg to C	Al to C	Si to C	P to C	S to C	Cl to C	Ca to C	K to C	Fe to C	Cu to C	Spc. Flux gfd/psi @ 25°C
10% ESPA2	0.1375		0.0065	0.0102	0.0045		0.0061		0.1907	0.0126	0.0079				0.0583
20% ESPA2	0.1038		0.0061	0.0054			0.0101		0.1580	0.0074	0.0056				0.0555
50% ESPA2	0.2606			0.0493	0.0123	0.0131	0.0523	0.0271	3.3568	0.1548	0.0640	0.0132	0.0115		0.0534
Feed Spacer	**O to C**	**N to C**	**F to C**	**Na to C**	**Mg to C**	**Al to C**	**Si to C**	**P to C**	**S to C**	**Cl to C**	**Ca to C**	**K to C**	**Fe to C**	**Cu to C**	**Spc. Flux gfd/psi @ 25°C**
10% Spacer	0.0043		0.0048	0.0190	0.0035	0.0020	0.0052			0.0151	0.0049	0.0025	0.0030	0.0029	0.0583
20% Spacer	0.0091		0.0050	0.0042	0.0035	0.0028	0.0071			0.0031	0.0063	0.0014	0.0036		0.0555
50% Spacer				0.0010	0.0012					0.0014	0.0008				0.0534

Table 9.6. Element/Carbon Ratios Determined from EDX Raw Signal Intensity Detected on Membrane Swatches and Spacers Exposed to RO Unit E01 Stage 3 Feedwater (ROF) and Associated Normalized Specific Product Water Flux

Membrane	O to C	N to C	F to C	Na to C	Mg to C	Al to C	Si to C	P to C	S to C	Cl to C	Ca to C	K to C	Fe to C	Cu to C	Spc. Flux gfd/psi @ 25°C
10% ESPA	0.0929			0.0175	0.0063		0.0000		0.1881	0.0228	0.0091				0.0541
20% ESPA	0.1738			0.0244	0.0056	0.0045	0.1614		1.3350	0.0260	0.0173			0.0048	0.0361
50% ESPA	0.2020		0.0149	0.0342	0.0103	0.0174	0.0240		3.1763	0.0914	0.0437	0.0091	0.0089	0.0161	0.0348
70% ESPA	0.1615		0.0080	0.0144	0.0036	0.0060	0.0241		0.7361	0.0145	0.0122	0.0000	0.0047		0.0327
Feed Spacer	**O to C**	**N to C**	**F to C**	**Na to C**	**Mg to C**	**Al to C**	**Si to C**	**P to C**	**S to C**	**Cl to C**	**Ca to C**	**K to C**	**Fe to C**	**Cu to C**	**Spc. Flux gfd/psi @ 25°C**
10% Spacer				0.0062			0.0026			0.0066	0.0031				0.0541
20% Spacer	0.0339		0.0044	0.0490	0.0061	0.0057	0.0292	0.0037	0.0182	0.0510	0.0192	0.0042	0.0036	0.0014	0.0361
50% Spacer			0.0134			0.0021	0.0031			0.0023	0.0018			0.0017	0.0348
70% Spacer			0.0090	0.0034	0.0015	0.0016	0.0053			0.0037	0.0021				0.0327

Table 9.7. Element/Carbon Ratios Determined from EDX Raw Signal Intensity Detected on Membrane Coupons and Spacers Exposed to RO Unit E01 Stage 3 Brine (ROC) and Associated RO Membrane Normalized Specific Product Flux

Membrane	O to C	N to C	F to C	Na to C	Mg to C	Al to C	Si to C	P to C	S to C	Cl to C	Ca to C	K to C	Fe to C	Cu to C	Spc. Flux gfd/psi @ 25°C
10% ESPA	0.4844		0.0195	0.0654	0.0210		0.2628	0.0000	0.2885	0.0560	0.0416	0.0074			0.0092
20% ESPA	1.7977		0.0949	0.0908	0.0273	0.2576	1.5202		0.2708	0.0653	0.0502	0.0268			0.0137
50% ESPA	2.4682		0.1259	0.1915	0.0427	0.3181	3.2134		0.4175	0.0614	0.0768	0.0433			0.0106
70% ESPA	0.4225		0.0556	0.0459		0.0376	0.2272		1.8144	0.0907	0.0220				0.0119
100% ESPA	0.4653		0.0739	0.0603	0.0191	0.0796	0.3722	0.0374	2.5339	0.0826	0.0861	0.0238	0.0175	0.0193	0.0086
Feed Spacer	**O to C**	**N to C**	**F to C**	**Na to C**	**Mg to C**	**Al to C**	**Si to C**	**P to C**	**S to C**	**Cl to C**	**Ca to C**	**K to C**	**Fe to C**	**Cu to C**	**Spc. Flux gfd/psi @ 25°C**
10% Spacer	2.0133	0.0883		1.7523	0.2797	0.1497	1.1283		0.6055	0.9962	0.1616	0.0507			0.0092
20% Spacer	0.1445		0.0113	0.0136	0.0032	0.0434	0.1590	0.0005		0.0042	0.0089	0.0057	0.0017		0.0137
50% Spacer	1.0018		0.0656	0.1084	0.0271	0.2127	0.9539			0.0295	0.0365	0.0275			0.0106
70% Spacer	0.0650		0.0130	0.0080	0.0031	0.0271	0.1082			0.0077	0.0088	0.0057		0.0037	0.0119
100% Spacer	0.0404		0.0120	0.0215	0.0040	0.0161	0.0695		0.0000	0.0107	0.0081	0.0036		0.0050	0.0086

9.3.3 Correlation Between Membrane Performance and Biochemical and Microbial Autopsy Data from Membrane Surface—Linear Regression Analysis

9.3.3.1 RO Unit E01 Stage 1 (ROF) Feedwater Membranes

Under nominal conditions in the AWPF, it appeared that at the beginning of the RO process (Table 9.8), the loss of normalized specific water flux was not strongly related to biofouling in the form of either accumulation of whole (viable or nonviable) microorganisms or to the deposition of protein or carbohydrate materials as previously anticipated.

Results of linear regression analyses for membrane swatches exposed to Unit E01 Stage 1 feedwater associated with protein, carbohydrate, total bacteria, and (viable and nonviable) bacteria are shown in Figures B.1 through B.6 in Appendix B.

Table 9.8. Summary of Linear Regression Modeling Results for Membrane Swatches Exposed to Feedwater from Unit E01 Stage 1 (ROF)

	Membrane Surface					
Parameter	**Total Protein ($\mu g/cm^2$)**	**Total Carbohydrate ($\mu g/cm^2$)**	**Total Bacteria /EPI Count ($cells/cm^2$)**	**Total Heterotrophic Bacteria ($cells/cm^2$)**	**Total "Live" Bacteria ($cells/cm^2$)**	**Total "Dead" Bacteria ($cells/cm^2$)**
# Swatches	4	4	4	4	3	3
Model Type	Double Reciprocal	Sq. Y Recip. X	Recip. Y Sq. X	Double-reciprocal	Sq. Y Recip. X	Recip. Y Sq. X
p-Value	0.167	0.6876	0.7344	0.6782	0.7551	0.7599
F-ratio	4.53	0.22	0.15	0.23	0.16	0.16
% R^2	69.39	9.76	7.05	10.36	14.09	13.56
Sig @ 95% CL?	No	No	No	No	No	No

9.3.3.2 RO Unit E01 Stage 2 Feedwater Membranes

Results of linear regression analyses for membrane swatches exposed to Unit E01 Stage 2 feedwater are shown in Figures 9.6 and 9.7 and Figures B.7 through B.10 in Appendix B. The inner lines next to the regression line represent the 95% confidence limit, and the outer lines represent the prediction limit when displayed.

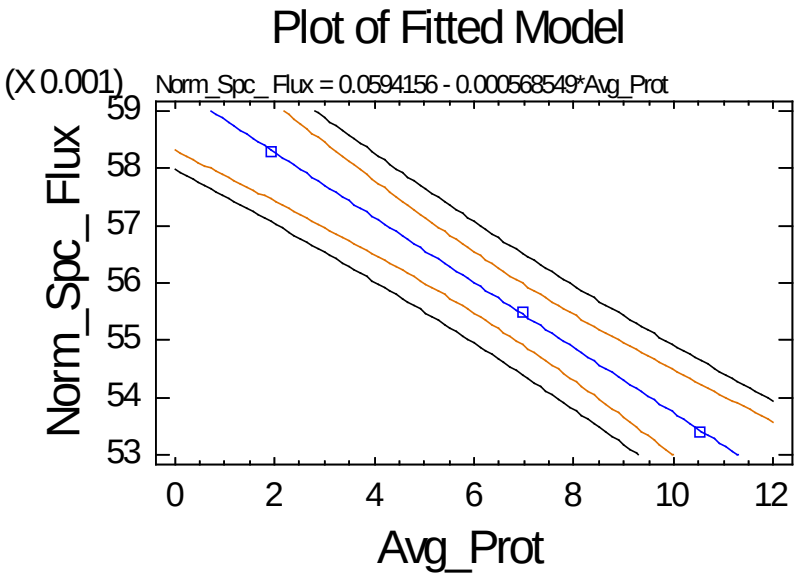

Figure 9.6. Membranes receiving Unit E01 Stage 2 feedwater. Normalized specific water flux (gfd/psi @ 25 °C) as a function of average total protein (µg/cm^2) accumulated on the membrane surface.

At the transition between the first and second RO stage unlike at the beginning of the first stage, there was one significant relationship between the deposition of foulants and the reduction of the normalized specific water flux (Table 9.9). Accumulation of total protein (% R^2 = 99.96%, p = 0.0132) on the membrane surface was the biochemical parameter most closely linked to RO fouling of all the biochemical and microbial parameters that were tested. As with the beginning of the first RO stage, this parameter was very strongly linked to the reduction in membrane water flux (% R^2 = 69.39). Moreover, because a very high % R^2 value was observed, it is highly unlikely that fouling in this region of the RO unit is related to another unexplored variable. The relationship between membrane fouling and carbohydrate deposition was more puzzling (Figure 9.7), as it appeared that membrane performance was actually enhanced with increasing carbohydrate deposition (% R^2 = 0.086, p = 0.0237).

Proliferation of whole bacteria on the membrane surface was once again not a significant factor in membrane fouling at the end of the first stage and beginning of the second stage. No strong relationships were related to total bacteria/cm^2 or to viable aerobic heterotrophic

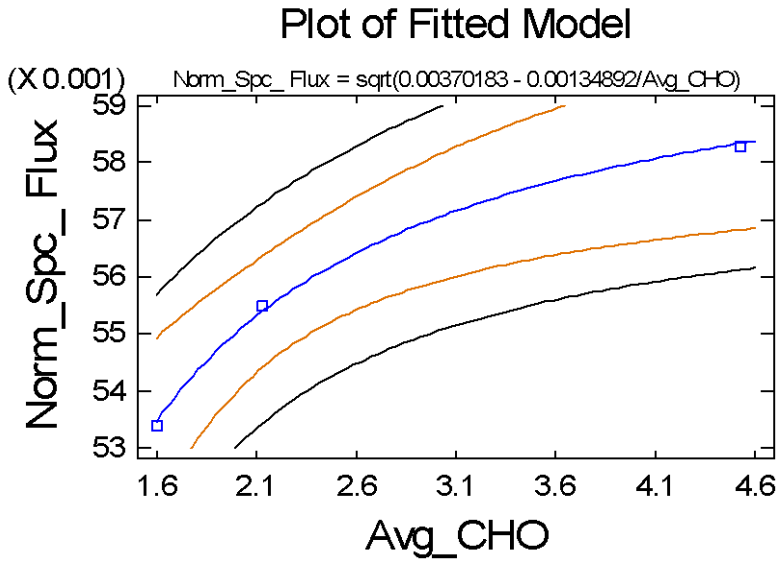

Figure 9.7. Membranes receiving Unit E01 Stage 2 feedwater. Normalized specific water flux (gfd/psi @ 25 °C) as a function of average carbohydrate (µg/cm^2) accumulated on the membrane surface.

bacteria/cm^2, contrary to the current hypotheses regarding first and second stage RO fouling. However, total protein deposition could be related to biological activity upstream in the feed channel or at points upstream of the RO process and might thus respond to the periodic variations in the loading of biocides (chloramines) in the feedwater. Protein molecules are nanoscopic colloids and can pass through the pores of the MF hollow fibers (see Chapter 4), so the source of the material could be anywhere along the purification process. As the concentration of the constituents in the feedwater increase (i.e., two-fold increase) as it passes through the first stage, the solubility of the proteins may decrease causing them to more readily accumulate on the membrane surface.

Table 9.9. Summary of Linear Regression Models Results for Membrane Swatches Exposed to Feedwater from Unit E01 Stage 2

	Membrane Surface					
Parameter	**Total Protein/cm^2**	**Total Carbohydrate/cm^2**	**Total Bacteria /cm^2**	**Total Heterotrophic Bacteria/cm^2**	**Total "Live" Bacteria /cm^2**	**Total "Dead" Bacteria/cm^2**
# Swatches	**3**	**3**	3	3	3	3
Model Type	**Linear**	**Sq. Y Recip. X**	Sq. Y Recip. X	Double-reciprocal	Double-reciprocal	Double-reciprocal
p-Value	**0.0132**	**0.0237**	0.3408	0.7406	0.57	0.8472
F-Ratio	**2326.89**	**720.97**	2.84	0.19	0.64	0.06
% R^2	**99.96**	**99.86**	73.98	15.70	39.10	5.65
Sig @ 95% CL?	**Yes**	**Yes**	No	No	No	No

Note: NA=Not available.

9.3.3.3 RO Unit E01 Stage 3 Feedwater Membranes

Results of linear regression analyses for membrane swatches exposed to RO Unit E01 Stage 3 feedwater are shown in Figure 9.8 and Figures B.11 through B.15 in Appendix B. The results of the statistical analysis for membranes exposed to RO Unit E01 Stage 3 feedwater are summarized in Table 9.10.

At the transition between the second and third RO stages, the accumulation of total aerobic heterotrophic bacteria on the membrane surface was the sole factor observed to be strongly negatively related to normalized specific product flux (% R^2 = 99.96%, p = 0.0121) (see Table 9.10). This was a highly statistically significant relationship, making it very likely that surface concentration of these bacteria are directly related to membrane fouling in this region of the three-stage RO unit and highly unlikely that any other unexamined factors influence fouling in this region.

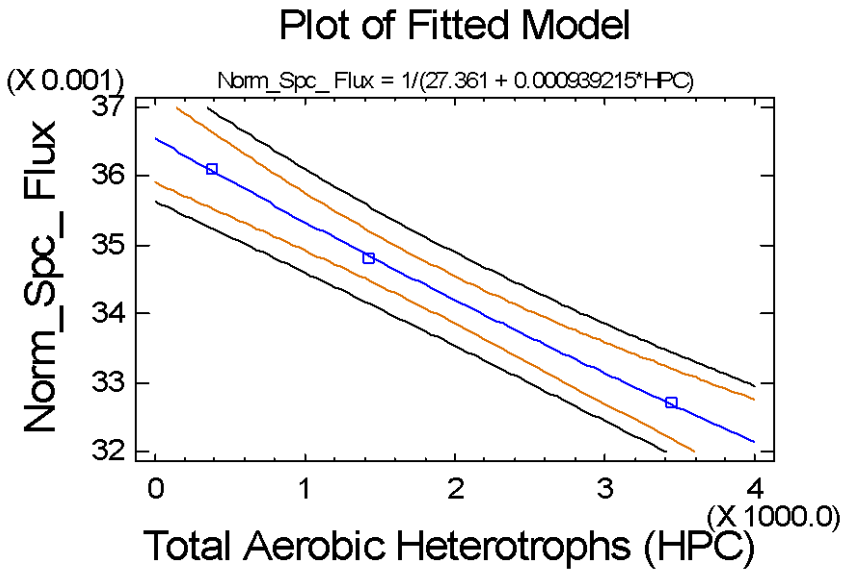

Figure 9.8. Membranes receiving Unit E01 Stage 3 feedwater. Normalized specific water flux (gfd/psi @ 25 °C) plotted as function of total aerobic heterotrophic bacteria (cells/cm^2) accumulated on the membrane surface.

This relationship resembles what would be expected in a classical membrane biofouling scenario. The total viable aerobic heterotrophs are the subset of viable bacteria that could be recovered from the RO membrane surface and could grow under aerobic conditions on R2A environmental agar plates. They typically represent a fraction of the total bacteria recoverable from the surface measured by epifluorescent counting. The R2A media is of higher salinity—and thus higher osmotic pressure—than wastewater (~5000 mg/L TDS compared to 900–1000 mg/L) and may select for more osmotically tolerant organisms. However, it is also a "complete" medium with multiple complex carbon sources and can recover injured organisms as well.

The fact that total bacteria on the membrane surface was not significantly related to fouling (i.e., the loss of water flux) is notable and suggests that a property unique to living organisms is the cause of the reduction of membrane specific water flux and not merely surface coverage by biomass. Apparently, neither carbohydrate nor protein deposition (i.e., EPS deposition is the mechanism) as neither total membrane carbohydrate nor protein were strongly related to the loss of membrane water flux in the transition between the second and third RO stages.

Variations in the biocide loading should have a profound effect on RO performance at the end of the second RO stage and beginning of the third RO stage, as the organisms are proliferating in equilibrium with the background load of mono- and dichloramines present in the RO feedwater. Reducing the concentration of biocide should result in a rapid increase in microbial growth rates and thus a rapid loss of membrane performance.

Table 9.10. Summary of Linear Regression Models for Membrane Swatches Exposed to Feedwater from RO Unit E01 Stage 3

Parameter	Membrane Surface					
	Total Protein/cm^2	**Total Carbohydrate/cm^2**	**Total Bacteria /cm^2**	**Total Heterotrophic Bacteria/cm^2**	**Total "Live" Bacteria /cm^2**	**Total "Dead" Bacteria /cm^2**
# Swatches	3	3	3	**3**	2	2
Model Type	Sq. Y Recip. X	Double Squared	Double Squared	**Reciprocal Y**	Linear	Linear
p-Value	0.8392	0.2255	0.6444	**0.0121**	NA	NA
F-ratio	0.07	7.31	0.39	**2750.24**	NA	NA
Pearson r	0.2499	-0.9379	0.5300	**0.9998**	NA	NA
% R^2	6.24	87.97	28.09	**99.96**	NA	NA
Sig @ 95% CL?	No	No	No	**Yes**	NA	NA

Note: NA=Not assessable because of lack of data.

9.3.3.4 RO Unit E01 Stage 3 Brine (ROC) Membranes

Results of linear regression analyses for membrane swatches exposed to RO Unit E01 Stage 3 brine (ROC) are shown in Figures B.16 through B.19 in Appendix B. The results of the statistical analysis for membranes exposed to RO Unit E01 Stage 3 brine (ROC) are summarized in Table 9.11. At the end of the third RO stage, no strong relationship (% R^2 >90%) was observed between any of the biochemical or microbial material accumulated on the membrane surface and the normalized specific product flux, similar to that seen in the other regions of the three-stage RO process.

Accumulation of total aerobic heterotrophic bacteria was correlated with the loss of specific water flux (% R^2 = 73.07, p = 0.1452). In this instance, insufficient data were available to assess whether the “live” or “dead” bacterial fractions were descriptive of RO normalized flux decline. Of those parameters where data were available, there were no statistically significant relationships ($p \leq 0.05$) noted among any of the input parameters.

Finally, unlike with the beginning of the first RO stage, the transition between the first and second RO stages and the transition between the second and third RO stages, there is a significant amount of variation (~22%) in the observed normalized RO membrane product flux decay, which is not explained by any of the measured experimental biochemical or microbial parameters associated with the RO brine (ROC). This suggests that either a missing parameter exists or an interaction between the measured parameters occurs. Because multivariate analysis was not possible with this sparse data set, it was not possible to probe biochemical and microbial parameter interactions during this study. It is hoped that with data from all five coupons from the next planned fouling study that multiple regression analysis will be possible, and fouling at the tail end of the third RO stage can be better elucidated.

Table 9.11. Summary of Linear Regression Models Results for Membrane Swatches Exposed to Brine from Unit E01 Stage 3 (ROC)

Parameter	Membrane Surface					
	Total Protein/cm^2	Total Carbohydrate/cm^2	Total Bacteria/cm^2	Total Heterotrophic Bacteria/cm^2	Total "Live" Bacteria/cm^2	Total "Dead" Bacteria/cm^2
# Swatches	4	4	4	4	2	1
Model Type	Recip. Y Sq. X	Double Reciprocal	Recip. Y Sq. Root X	Sq. Y Recip. X	Linear	NA
p-Value	0.6642	0.3891	0.7101	0.1452	NA	NA
F-ratio	0.25	1.19	0.18	5.43	NA	NA
% R^2	11.28	37.32	8.41	73.07	NA	NA
Sig @ 95% CL?	No	No	No	No	NA	NA

Note: NA=Not assessable because of lack of data.

9.3.4 Comparison of Fouling Characteristics of the First, Second, and Third Stages of the RO Unit E01

Because the test cells were fed with source waters derived from the front and back of each of the three RO stages in Unit E01 of Train E, the factors affecting overall fouling of membranes within each RO stage can be deduced by an examination of the test cell behavior bracketing them. Thus, the behavior of membranes in the vessels of the first stage can be expected to be bracketed by that of the membranes swatches in the test cells receiving feedwater from the feed to the first stage and those swatches receiving water from the feed to the second stage. The second stage full-scale RO membranes can be expected to be bracketed by membrane swatches in the test cells receiving feedwater from the second stage of Unit E01 and those receiving feedwater from third stage. And finally this applies also for the third stage RO membranes, by membrane swatches in the test cells receiving feedwater from the third stage and those test cells receiving RO brine from the third stage.

Principal foulants on the RO membrane surface were hypothesized to be primarily bioorganic matter comprised of (1) protein and carbohydrate materials, both as nanoparticulate colloidal extracellular polymeric substances (EPS) derived from organisms upstream of the RO unit and from microorganisms growing on the RO membranes, (2) biofilm bacteria, both living and dead, and (3) mineral colloids or crystalline precipitates. Of these constituents, the bioorganics were expected to be the principal foulants encountered in the first two stages of the RO unit, whereas mineral foulants would be found mainly in the third stage. Only bioorganic foulants were quantified and discussed in this section of the study results. Where these constituents were dominant, a strong correlation with membrane fouling was anticipated, and where mineral fouling was dominant, a poorer correlation was anticipated.

9.3.5 Fouling Factors Best Related to Loss of Normalized Specific Water Flux in RO Stage 1

Stage 1 RO fouling in the AWPF was best characterized by the surface deposition of protein and carbohydrate, as opposed to the buildup of whole bacteria (either culturable or not). Toward the front end of the stage, where ROF first interacts with the membranes, protein accumulation on the membrane surface accounted for nearly 70% of the variation in RO normalized specific product flux. This was consistent with IR results of RO membrane autopsy (see Chapter 6, Section 6.3.9). An unusual observation was made in that the relationship was positive (i.e., better water flux was seen at higher membrane surface protein levels). Although unexpected, there was one datum point (3.43 mg/L protein, 0.0613 gfd/psi) in the set that may have skewed this relationship as the normalized specific product flux was abnormally low. When that datum point was omitted from the analysis, the best model % R^2 increases to greater than 78%, and the relationship changed such that membrane fouling was correlated with the buildup of protein (Figure 9.9).

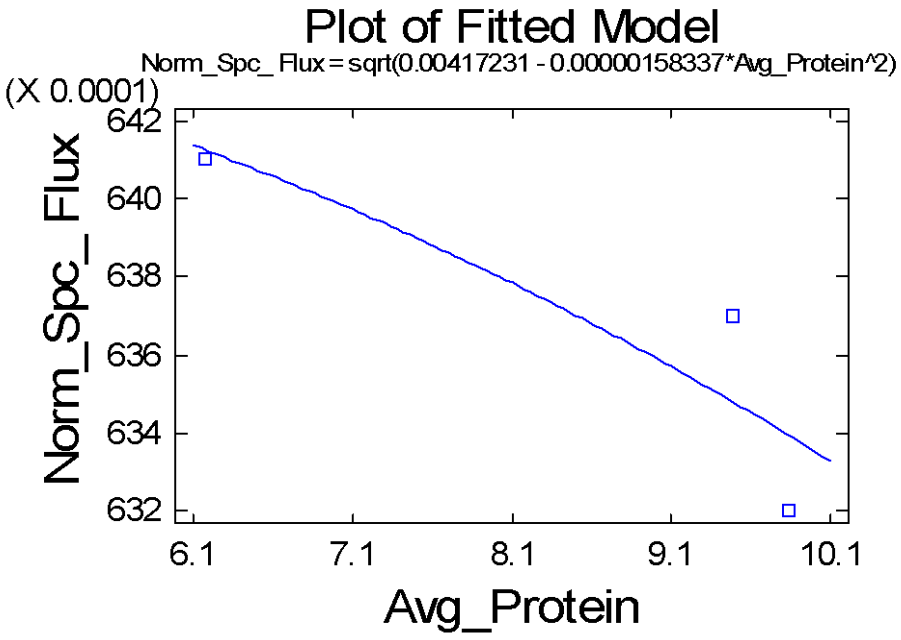

Figure 9.9. Relationship between protein on the membrane surface and the normalized specific product flux at the front of RO Stage 1, omitting the 20% fouling indicator point from the data set (see Figure B.1).

At the end of the first RO stage, membrane fouling is dominated mainly by protein and carbohydrate buildup on the membrane surface. Each factor accounts for greater than 99% of the observed variance in the normalized specific product flux at this point. To a lesser extent the total bacteria found on the surface accounted for nearly 74% of the observed variance in normalized specific product flux. The stronger relationship was with protein. This was linearly negative with respect to normalized specific water flux, which is what would be expected if protein buildup interferes with membrane performance. The carbohydrate results did not behave similarly. The relationship with membrane fouling was very strong, but there was a positive trend and not a negative one that would have been expected. Superficially, it appeared that the membrane performed better with increased carbohydrate on the surface.

Examination of the cross-correlated relationship between average protein levels and average carbohydrate levels on the membrane surface revealed a powerful negative relationship (Figure 9.10). As a consequence, variance in membrane fouling related to carbohydrate levels will appear to move in exactly the opposite direction as they do with protein and making the apparent decrease in fouling observed with increase in membrane surface carbohydrate wholly artifactual. Because the protein relationship with membrane fouling had the slightly greater % R^2 and behaved in a more or less anticipated fashion, it seems reasonable to reject the carbohydrate relationship in favor of the protein relationship.

Total bacteria load on the membrane surface (see Figure B.7) did show a mildly strong negative relationship with normalized specific water flux in the last part of Stage 1 and first part of Stage 2; however, the relationship was not statistically significant at the 95% confidence level (see Table 9.9). The data are sparse, but the implication is that initially the small amount of organisms on the surface had little effect on fouling; however, once the load exceeded 2×10^6 cells/cm^2, there was a significant loss of flux.

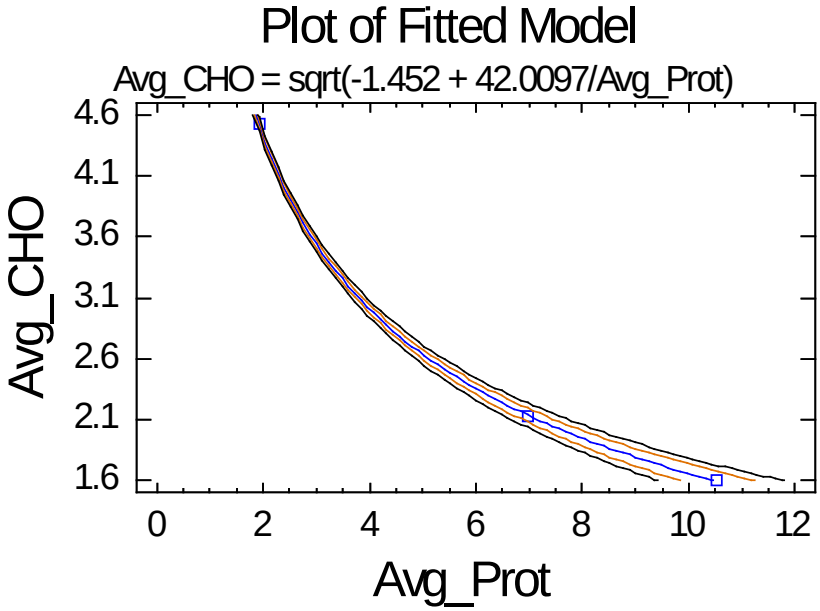

Figure 9.10. Relationship between average protein and average carbohydrate on RO membrane surfaces exposed to Unit E01 Stage 2 feedwater.

Previous studies have indicated that the whole bacteria on the membrane surface account for only a small fraction of the observed protein measured on the surface (Safarik and Phipps, 2013). Thus, the conclusion is that colloidal protein is likely the principal foulant throughout the first RO stage, followed by the total bacterial load greater than 10^6 cells/cm^2. A calculation of how many 0.5×3.0 μm microorganisms it takes to produce a monolayer comes to approximately 7×10^7 cells/cm^2.

9.3.6 Fouling Factors Best Related to Loss of Normalized Specific Water Flux in RO Stage 2

Examination of biochemical and microbial factors best correlated with the decline in the normalized specific membrane water flux in the second RO stage, characterized by the

behavior of test units fed with Unit E01 Stage 2 feedwater and Unit E01 Stage 3 feedwater suggested significant differences in primary fouling factors from the feed end to the brine end of the stage. Protein deposition dominated fouling at the front end of the stage (% R^2 = 99.86%), whereas primarily total heterotrophic bacterial accumulation (% R^2 = 99.96%) and secondarily total carbohydrate deposition (% R^2 = 87.97%) dominated fouling at the brine end of the second RO stage. Neither protein accumulation nor total bacteria correlated well with membrane performance at the brine end. At the brine end of the stage, total aerobic heterotrophic bacterial coverage was nearly linearly inversely proportional to specific water flux; there was no plateau or breaking point in the relationship. Over the time range analyzed, the coverage of aerobic heterotrophic bacteria from the membrane autopsy indicated a nearly 10-fold increase from 3.84×10^2 to 3.44×10^3 cells/cm^2 over which the normalized specific product water flux was seen to decline from 0.0361 to 0.0327 gfd/psi @ 25 °C, a decrease of a little more than 9%.

9.3.7 Fouling Factors Best Related to Loss of Normalized Specific Water Flux in RO Stage 3

The fouling behavior of the third RO stage membranes was characterized based on observations made at the feed end taken from fouling characteristics of Stage 3 feedwater and at the brine end taken from fouling characteristics of Stage 3 brine (ROC). As with the second RO stage, the third RO stage appeared to exhibit a transition in its fouling behavior. At the feed end that received third stage feedwater, the increase in total heterotrophic bacterial coverage and carbohydrate accumulation appeared to be best related to the decline in specific water flux. At the brine end of the third stage, no "statistically significant" relationship with fouling by the biochemical and microbial constituents was observed (see Table 9.11). The total heterotrophic bacterial accumulation correlation exhibited a % R^2 value of 73.07%, which may be considered an indicator of a "strong" relationship. However, unlike the nearly linear negative relationship seen at the beginning of the stage, by the end of the third stage the relationship was sharply logarithmic in appearance (see Figure B.19). An increase in the aerobic heterotrophic organism load in excess of 5×10^2 cells/cm^2 correlated with a dramatic reduction in the normalized specific product flux. Total bacteria also were correlated negatively, but the regression fit was fairly poor, as was the fit for the other experimental factors. Thus, as with the second RO stage, it appears that in the third RO stage the accumulation of viable heterotrophic organisms generally best correlated with loss of membrane water flux, in other words, membrane fouling.

Traditionally, it would be expected that a significant loss of membrane water flux in the third stage of an 85% recovery RO system treating a secondary wastewater effluent would be brought about by precipitation of mineral material (silicates, sulfates, and phosphates) as opposed to accumulation of biological organisms. However, these data suggest that in the AWPF this might not be the case, as the majority of the fouling appeared to correlate with an increase in surface viable organisms. It is certainly anticipated that the remaining approximately 30% of the variance observed in fouling is due to mineral accumulation, although this study was unable to quantify mineral deposition. Data from SEM images (data not shown) and the EDX spectroscopic analysis may be able to provide a semiquantitative approach to determine the role mineral fouling plays in loss of water flux (see Chapter 9, section 9.3.8).

The results of linear regression analyses on the impact of the deposition of elements on the membrane surface and normalized specific membrane product flux are shown in Table 9.12. In this table, bolded data represent models of interest including those with (1) high % R^2

values indicating that the model described the majority of the observed variations in the membrane normalized specific water flux, (2) low p-values indicating the models are statistically significant, and (3) high fouling potential, in other words, an increase in the element/carbon ratio negatively related to normalized specific water flux.

Table 9.12. Comparison of Linear Regression Models Derived from Membrane EDX Element/Carbon Ratios for Membrane Swatches Receiving Different Feedwater Sources from RO Unit E01

	E01 Stage 1 (ROF) Feed			E01 Stage 2 Feed			E01 Stage 3 Feed			E01 Stage 3 Brine Feed		
Element/C Ratio	**+/- Prop.**	**Best % R^2**	**p-value**	**+/- Prop.**	**Best % R^2**	**p-value**	**+/- Prop.**	**Best % R^2**	**p-value**	**+/- Prop.**	**Best % R^2**	**p-value**
O/C	+/-	5.57	0.7641	-	57.22	0.4539	+	24.39	0.6712	+	12.96	0.5762
N/C	+/-	0.58	0.9241	NC	NC	NC	NC	NC	NC	NC	NC	NC
F/C	-	27.05	0.4799	+	78.34	0.3082	-	38.02	0.5770	+/-	0.58	0.9240
Na/C	+	12.69	0.6437	-	67.33	0.3874	+	63.33	0.4141	-	1.60	0.8736
Mg/C	+	13.16	0.6372	-	58.04	0.4486	+	45.59	0.5281	-	2.25	0.8499
Al/C	+	7.96	0.7179	-	69.87	0.3699	+/-	4.59	0.8625	+	10.72	0.6726
Si/C	+	2.81	0.8325	**-**	**98.64**	**0.0745**	+	63.81	0.4110	+	6.65	0.7421
P/C	+	13.83	0.6283	-	69.87	0.3705	NC	NC	NC	**-**	**77.65**	**0.1188**
S/C	+	24.73	0.5027	-	69.79	0.3723	+	49.59	0.5026	**-**	**60.31**	**0.2234**
Cl/C	+	13.93	0.6267	-	69.52	0.3741	+	42.92	0.5452	-	9.12	0.6981
Ca/C	+	21.89	0.5321	-	69.26	0.3699	+	30.03	0.6308	**-**	**67.79**	**0.1766**
K/C	NC	NC	NC	-	69.87	0.3699	+/-	2.57	0.8975	-	5.41	0.7674
Fe/C	**-**	**91.74**	**0.0422**	NC	NC	NC	-	37.38	0.5812	**-**	**77.65**	**0.1188**
Cu/C	**-**	**91.74**	**0.0422**	NC	NC	NC	+	45.24	0.5303	**-**	**77.65**	**0.1188**

Notes: +/- Prop. = whether the normalized specific product flux (GFD/psi @ 25 °C) was negatively or positively proportional to the element/carbon ratio.

Best % R^2 = the best regression model's % R^2 value. p-value = the p-value for the best model. Statistical significance of the model at the 95% confidence level required $p \leq 0.05$. Bolded models represent ones with high % R^2 and low p = values thought to be of interest.

9.3.8 Correlation of Membrane Performance and Element/Carbon Ratios from Membrane and Feed Spacer Surface—Linear Regression Analysis

9.3.8.1 Element/Carbon Ratios Associated with Membrane Surface Best Related to the Loss of Normalized Specific Water Flux: Beginning of the First Stage RO

At the lead end of the first stage of the RO process, only iron (Fe) and copper (Cu) on the membrane swatches appeared to be significantly related to membrane fouling.

Fe/C Ratio

The iron-to-carbon (Fe/C) ratio on the membrane surface was strongly negatively related to the loss of membrane specific water flux (Figure 9.11). This relationship represented 91.74% of the observed variation in the normalized water flux and was statically significant at greater than 95% confidence level (p = 0.0422).

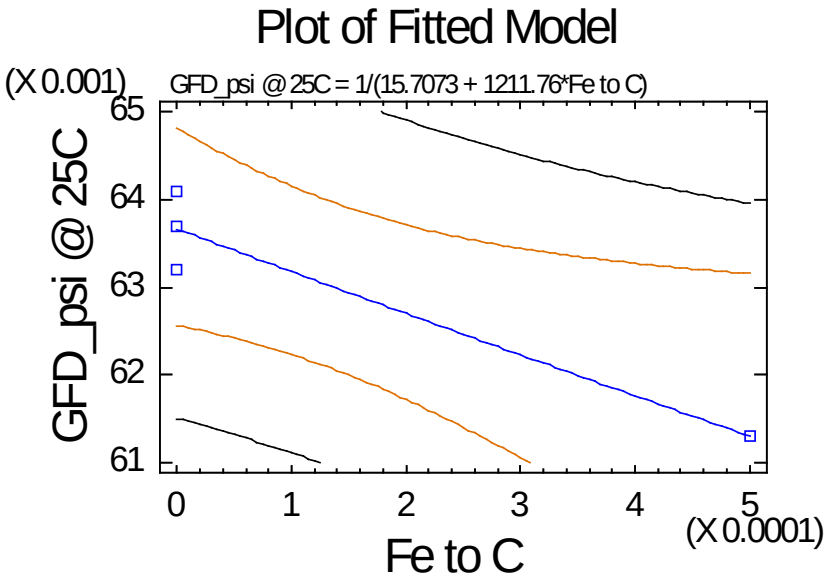

Figure 9.11. Best linear regression model describing loss of normalized specific water flux of membranes at the beginning of RO Stage 1 plotted as a function of the Fe/C EDX signal.

Notes: % R^2 = 91.74%, p = 0.0422

The presence of iron on the membrane appears to be strongly linked to membrane fouling; however, as iron was only detected on the most fouled membranes, the relationship needs to be further investigated with more samples.

Cu/C Ratio

The copper-to-carbon (Cu/C) ratio on the membrane swatch was strongly negatively related to loss of membrane specific water flux (Figure 9.12). This relationship represented 91.74% of the observed variation in normalized water flux and was statically significant at greater than 95% confidence level (p = 0.0422).

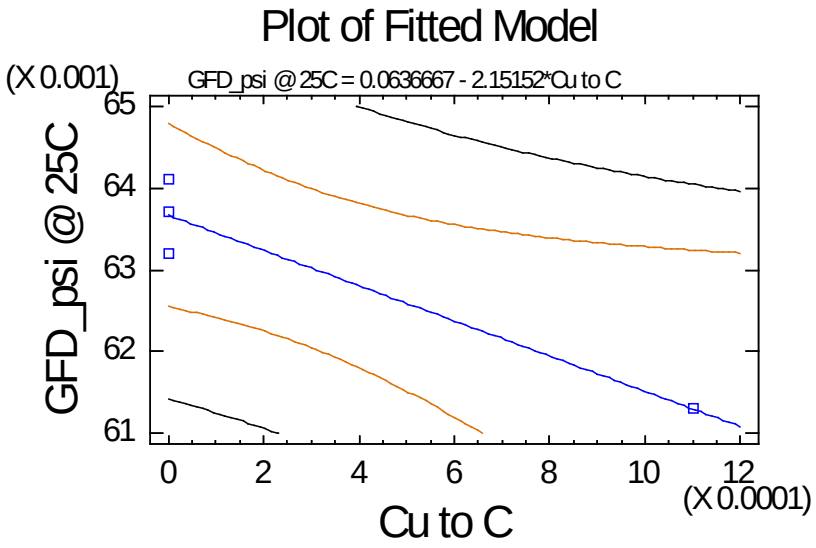

Figure 9.12. Best linear regression model describing loss of normalized specific water flux of membranes at the beginning of RO Stage 1 plotted as a function of the Cu/C EDX signal.

Notes: % R^2 = 91.74%, p = 0.0422

As with iron, the presence of copper on the membrane appears to be strongly linked to fouling; however, as copper was only detected on the most fouled swatch, the relationship needs to be further investigated with more samples.

9.3.8.2 Element/Carbon Ratio Associated with the Membrane Surface Best Related to Loss of Normalized Specific Water Flux: Beginning of the Second RO Stage

Loss of membrane normalized specific water flux on membrane swatches representing the end of the first RO stage and beginning of the second RO stage were only statistically significantly related to the Si/C signal ratio.

Si/C Ratio

The presence of silicon on the membrane appears to be strongly linked to membrane fouling (Figure 9.13). The Si/C ratio on the membrane surface could explain 98.64% of the observed variability in the normalized specific water flux, and this may be strongly linked with a majority of the fouling occurring at the end of the first RO stage and beginning of the second RO stage.

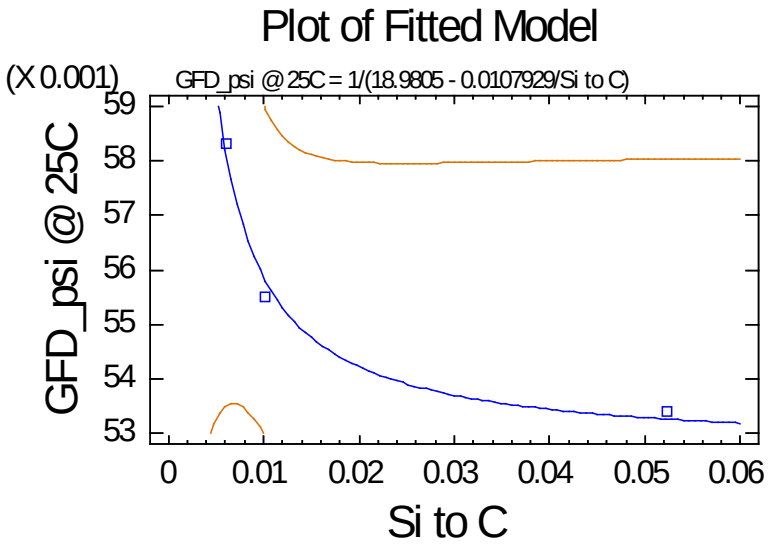

Figure 9.13. Best linear regression model describing loss of normalized specific water flux of membranes at the end of RO Stage 1/beginning of RO Stage 2 as a function of the Si/C EDX signal.

Notes: % R^2 **= 98.64%, p = 0.074.**

The relationship was statistically significant at less than 90% confidence level but not the 95% confidence interval (p = 0.0745). Because silicon is known to foul RO membranes in the form of silicates, it is not particularly surprising to see this relationship. What is surprising is that it does not appear to be seen further down the RO feed channel in the third membrane stage. Possibly the use of antiscalants (which are added to the RO feed) help prevent accumulation of silicon-containing materials on the membrane surfaces.

9.3.8.3 Element/Carbon Ratio Associated with the Membrane Surface Best Related to Loss of Normalized Specific Water Flux: Beginning of the Third RO Stage

There were no statistically significant relationships (>90% confidence level) observed between the EDX derived element/C ratios on the membrane coupons representing the end of the second RO stage and the beginning of the third RO stage and loss of normalized specific water flux.

9.3.8.4 Element/Carbon Ratio Associated with the Membrane Surface Best Related to Loss of Normalized Specific Water Flux: End of the Third RO Stage

There were no relationships between the EDX derived element/C ratios and RO membrane fouling statistically significant at the 95% confidence level, although four relationships were of interest because they (1) represented anticipated fouling materials in the third RO stage, (2) were negatively related to RO membrane normalized specific water flux, and (3) their p-values were small compared to most other relationships observed. These included the P/C ratio, the Fe/C ratio, the Cu/C ratio, and the Ca/C ratio.

P/C Ratio

The relationship between the phosphorus/carbon (P/C) ratio and the normalized specific water flux for the membrane coupon representing the tail end of the RO third stage is shown in Figure B.20 in Appendix B.

The relationship is not as strong as others that have been observed (only 77.65% of the observed variance in the normalized specific water flux can be explained), and the statistical significance is limited to slightly less than 90% confidence level. However, phosphorus is known to participate in the formation of membrane foulants (as polyphosphate precipitates), and so it is not unexpected that where the feedwater dissolved solids become most concentrated, precipitated phosphorous compounds are contributing to membrane fouling.

One difficulty is the lack of data available with which to examine this relationship, and it will be of great interest to see if it holds up when more data points become available as this study is repeated.

Fe/C Ratio

The relationship between the iron/carbon (Fe/C) ratio and the normalized specific water flux for the membrane coupon representing the tail end of the RO third stage is shown in Figure B.21.

The relationship is essentially the same as the phosphorus/carbon ratio relationship and also represents 77.65% of the observed variance in the normalized specific water flux with a statistical significance limited to slightly less than 90% confidence level. There is a strong covariance between the P/C and the Fe/C ratios on this membrane coupon (% R^2 = 100%, data not shown), suggesting that the foulant compound or compounds on the membrane surface might contain both iron and phosphorus. Candidate compounds could include iron phosphate. Iron phosphates are poorly soluble in water, and iron is often used to remove phosphorus during wastewater treatment.

Because the pH at the membrane surface in the polarization layer might vary considerably from that of the bulk phase in the feed channel at the end of the third stage, it is not beyond reason that iron phosphates might be significant membrane foulants.

Cu/C Ratio

The relationship between the copper/carbon (Cu/C) ratio and the normalized specific product flux for the membrane coupon representing the tail end of the RO third stage is shown in Figure B.22.

The relationship is essentially the same as the phosphorus/carbon ratio relationship and also represents 77.65% of the observed variance in the normalized specific water flux with a statistical significance limited to slightly less than 90% confidence level. There is a strong covariance between the P/C and the Cu/C ratios on this membrane coupon (% R^2 = 100%; data not shown), suggesting that the foulant compound or compounds on the membrane surface might contain both copper and phosphorus. Candidate compounds could include copper phosphate, which is insoluble in water. As with the Fe/C ratio, the small number of

experimental samples weakens the relationship, which otherwise might appear much more statistically significant with more data.

Ca/C Ratio

As with iron and copper, the calcium/carbon (Ca/C) ratio is relatively strongly linked to loss of membrane performance at the end of the third RO stage (Figure B.23). Calcium phosphate could form as a precipitate. However, the % R^2 value is less and the indication is that, unlike with iron and copper, this calcium relationship is probably not linked through phosphorus. Also, there is a fairly poor relationship between the Ca/C and P/C ratios (% R^2 <50%; data not shown), suggesting that calcium may participate in other chemistries on the membrane surface besides merely making phosphates. Another candidate could be calcium sulfate; however, the S/C ratio was noted to be negatively related to loss of specific water flux, the relationship was only moderately strong (% R^2 = 60.31%) and not very significant ($p = 0.2234$).

9.3.9 Correlation of the Membrane EDX Element Data with Membrane Performance—Linear Regression Analysis

Unlike with the traditional chemical and biological assays used to probe membrane fouling, use of EDX requires such a small a sample area that it can be equally applied to the membrane spacer material as to the membrane surface. The following sections relate the element/C ratios observed on the membrane spacer to performance loss of the membranes exposed to feedwater corresponding to the beginning of the first, second, and third RO stages and the end of the third RO stage of AWPF 5-MGD RO Unit E01.

As with the membrane surface data, best fitted linear correlation models were constructed from the EDX element/carbon ratios from the feed spacer and observed membrane performance data. The results of these linear regression analyses of membrane deposition of various elements against normalized specific membrane product flux are shown in Table 9.13. In this table, bolded data represent models of interest with (1) high % R^2 values, in other words, models that described the majority of the observed variations in the membrane normalized specific product flux, (2) low p-values, in other words models that are statistically significant, and (3) models that indicate fouling potential, in other words an increase in element/carbon ratio that was negatively related to normalized specific water flux.

Table 9.13. Comparison of Linear Regression Models Derived from Feed Spacer EDX Element/Carbon Ratios for Membrane Spacers Receiving Different Feedwater Sources from RO Unit E01

Element/C Ratio	E01 Stage 1 (ROF) Feed			E01 Stage 2 Feed			E01 Stage 3 Feed			E01 Stage 3 Brine (ROC) Feed		
	+/- Prop.	Best % R^2	p-value	+/- Prop.	Best % R^2	p-value	+/- Prop.	Best % R^2	p-value	+/- Prop.	Best % R^2	p-value
O/C	**-**	**90.31**	**0.0497**	+	39.47	0.5676	+	63.82	0.4109	-	31.18	0.3821
N/C	**-**	**93.17**	**0.0348**	NC	NC	NC	NC	NC	NC	NC	NC	NC
F/C	**-**	**91.69**	**0.0425**	+	68.24	0.3812	-	40.96	0.5705	-	7.52	0.7529
Na/C	**-**	**94.92**	**0.0257**	**+**	**99.82**	**0.0273**	+	63.42	0.4135	-	21.28	0.5387
Mg/C	**-**	**92.42**	**0.0386**	+	69.87	0.3699	+	58.57	0.4452	-	17.99	0.5758
Al/C	**-**	**74.56**	**0.1365**	+	55.99	0.4618	**+**	**90.43**	**0.2002**	+	35.60	0.4033
Si/C	**-**	**98.15**	**0.0093**	+	57.03	0.4551	+	61.97	0.4231	+	27.36	0.4769
P/C	**+**	**93.25**	**0.0343**	NC	NC	NC	+	63.82	0.4109	**+**	**66.68**	**0.1834**
S/C	+	11.77	0.6569	NC	NC	NC	+	63.82	0.4109	NC	NC	NC
Cl/C	**-**	**97.20**	**0.0141**	**+**	**99.11**	**0.0602**	+	63.55	0.4126	**-**	**64.83**	**0.1948**
Ca/C	**-**	**91.43**	**0.0438**	+	66.45	0.3933	+	63.55	0.4126	-	4.88	0.7791
K/C	**-**	**95.38**	**0.0234**	**+**	**98.63**	**0.0747**	+	63.82	0.4109	+	15.47	0.6067
Fe/C	+	0.58	0.9241	+	62.43	0.4200	+	63.82	0.4109	**+**	**66.68**	**0.1834**
Cu/C	**-**	**91.74**	**0.0422**	+	82.70	0.2731	+	81.37	0.2841	-	56.26	0.2500

Notes: +/- Prop. = whether the normalized specific water flux (GFD/psi @ 25 °C) was negatively or positively proportional to the element/carbon ratio. Best % R^2 = the best regression model's % R^2 value. p-value = the p-value for the best model. Statistical significance of the model at the 95% confidence level required $p \leq 0.05$. Bolded models represent ones with high % R^2 and low p-values thought to be of interest.

9.3.9.1 Element/Carbon Ratio of the Feed Spacer Best Related to Loss of Normalized Specific Water Flux: Beginning of the First RO Stage

The spacer material recovered from the membrane swatches exposed to Unit E01 first stage feedwater (ROF) presented the most interesting relationships with membrane performance of any of the feedwaters tested. Greater than 90% of the loss of membrane water flux was statistically significantly (>95% confidence level) described by the accumulation of the EDX element/C ratios of Si, Cl, K, Na, P, N, Mg, Cu, F, Ca, O, and Al (listed in order of the strength of the observed relationships). Because these elements can all hypothetically participate in the deposition of potential organic and mineral precipitants, it would appear that the buildup of material on the feed spacer at the start of the first RO stage (but apparently not so much at other areas in the RO train) was a significant factor in RO performance degradation. The most probable mechanism of interference with RO performance in this case was disruption of the cross flow over the membrane surface by the buildup of material on the spacer.

Si/C Ratio

Figure 9.14 shows the relationship between the EDX silicon/carbon ratio (Si/C) on the membrane spacer and the RO membrane performance (normalized product flux, gfd/psi @ 25 °C).

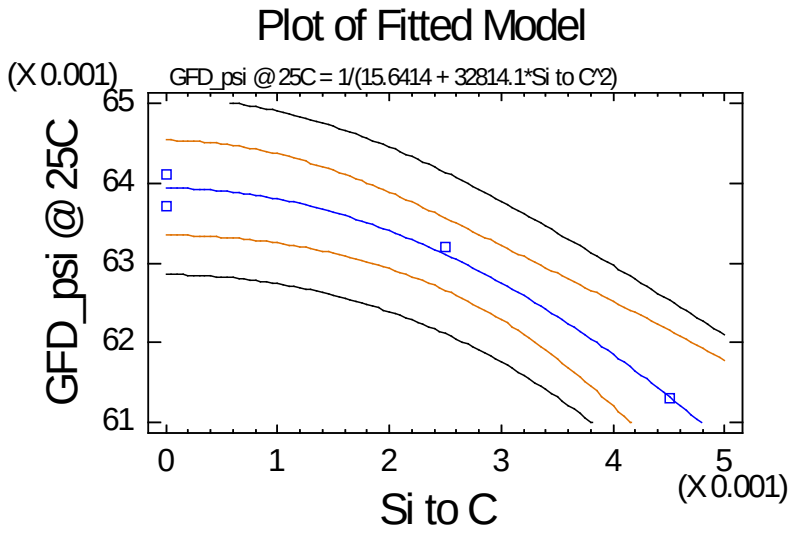

Figure 9.14. Best linear regression model describing loss of normalized specific water flux of membranes at the beginning of RO Stage 1 as a function of the Si/C EDX signal on the membrane spacer.

Notes: % R^2 = 98.15%, p = 0.0093.

This is the strongest of the noted relationships, with the model describing 98.15% of the observed variance in membrane normalized specific water production. Additionally, it is statistically significant at greater than 99% confidence level (p = 0.0093). Silicates are known foulants on the membrane surface but also can accumulate on the polypropylene Vexar spacer material. Silicates contain oxygen and can compound many cations, such as Al, Ca, Na, K, and Mg.

Cl/C Ratio

Figure 9.15 shows the relationship between the EDX chlorine/carbon ratio (Cl/C) on the membrane spacer and the RO membrane performance (normalized water flux, gfd/psi @ 25 °C).

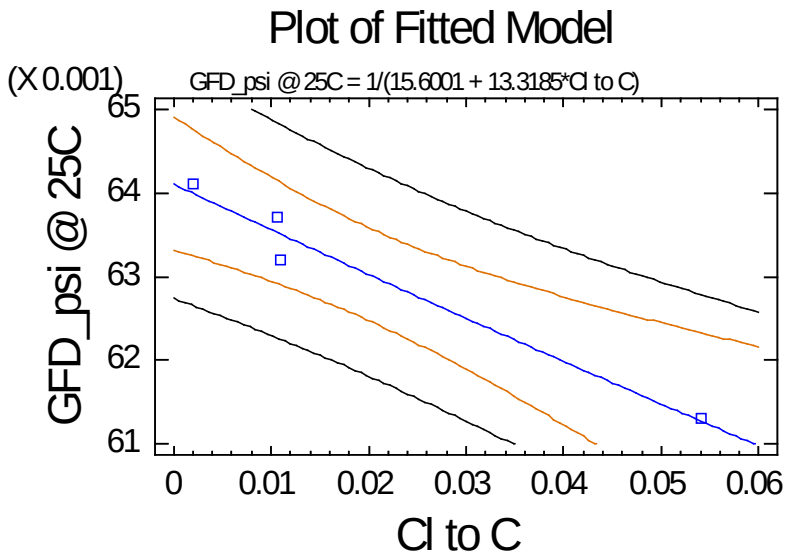

Figure 9.15. Best linear regression model describing loss of normalized specific water flux of membranes at the beginning of RO Stage 1 as a function of the Cl/C EDX signal on the membrane spacer.

Notes: % R^2 = 97.20%, p = 0.0141.

This is the second strongest of the noted relationships, with the model describing 97.20% of the observed variance in membrane normalized specific water production. In addition, it is statistically significant at nearly the 99% confidence level (p = 0.0141). Although chlorine as a chloride ion does not participate in the formation of insoluble compounds, it can be present in organic and mineral halides. Because the specimen for SEM analysis was dehydrated from its wetted state, chlorine may have been bound up in the mineral salts that formed from precipitation of organic and mineral cations.

K/C Ratio

The relationship between the EDX potassium/carbon (K/C) ratio on the spacer at the beginning of the first RO stage and the membrane performance in terms of normalized specific water flux is shown in Figure 9.16. A total of 95.38% of the variance in membrane normalized specific water flux was described, with the model statistically significant at nearly 98% confidence level (p = 0.0234). Although as with chlorine, potassium salts are usually soluble. When the specimen was dehydrated for SEM analysis, potassium may have become bound up in mineral salts that formed from precipitated organic and mineral anions, such as silicates.

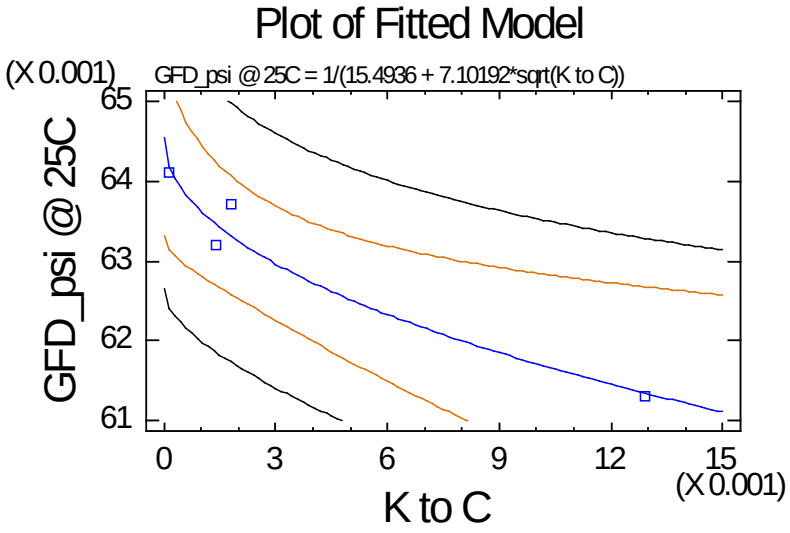

Figure 9.16. Best linear regression model describing loss of normalized specific water flux of membranes at the beginning of RO Stage 1 as a function of the K/C EDX signal on the membrane spacer.

Notes: % R^2 = 95.38%, p = 0.0234.

Na/C Ratio

The relationship between the EDX sodium/carbon (Na/C) ratio on the spacer at the beginning of the first RO stage and the membrane performance in terms of normalized specific water flux is shown in Figure 9.17. A total of 94.92% of the variance in membrane normalized specific water flux is described, with the model statistically significant at nearly 97% confidence level (p = 0.0257).

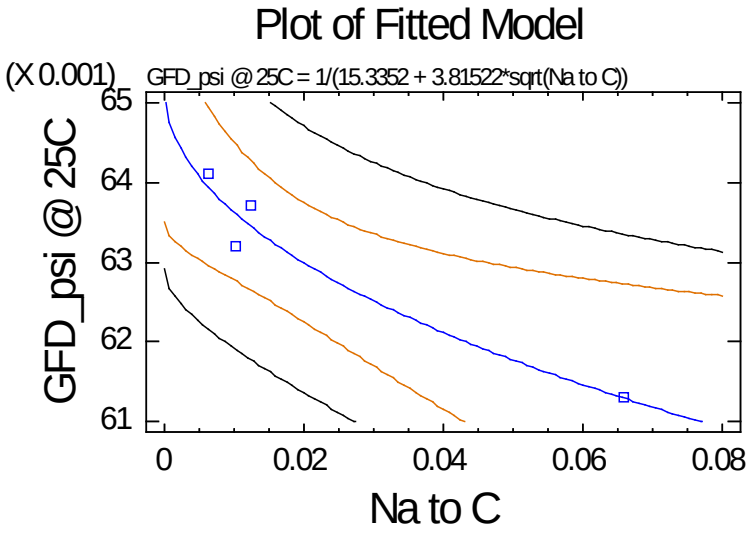

Figure 9.17. Best linear regression model describing loss of normalized specific water flux of membranes at the beginning of RO Stage 1 as a function of the Na/C EDX signal on the membrane spacer.

Notes: (% R^2 = 94.92%, p = 0.0257).

As with potassium, sodium salts are usually soluble. When the specimen was dehydrated for SEM analysis, sodium may have become bound up in mineral salts that formed from precipitated organic and mineral anions, such as silicates.

N/C Ratio

The relationship between the EDX nitrogen/carbon (N/C) ratio on the spacer at the beginning of the first RO stage and the membrane performance in terms of normalized specific water production is shown in Figure 9.18. A total of 93.17% of the variance in membrane normalized specific water flux was described, with the model statistically significant at nearly 96% confidence level (p = 0.0348).

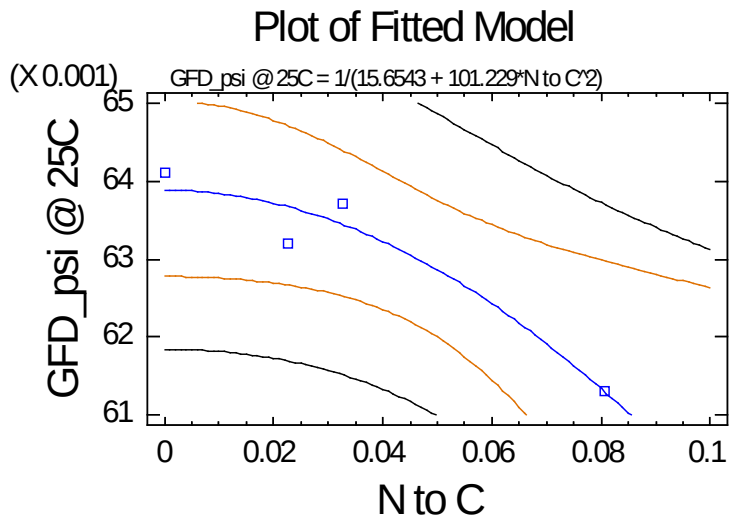

Figure 9.18. Best linear regression model describing loss of normalized specific water flux of membranes at the beginning of RO Stage 1 as a function of the N/C EDX signal on the membrane spacer.

Notes: % R^2 = 93.17%, p = 0.0348.

Nitrogen is a common component of many organic and biological molecules (proteins), as well as whole organisms that could be expected to adhere to the Vexar polypropylene surface of the spacer.

Mg/C Ratio

The relationship between the EDX magnesium/carbon (Mg/C) ratio on the spacer at the beginning of the first RO stage and the membrane performance in terms of normalized specific water flux is shown in Figure 9.19. A total of 92.42% of the variance in membrane normalized specific water flux was described, with the model statistically significant at nearly 96% confidence level (p = 0.0386).

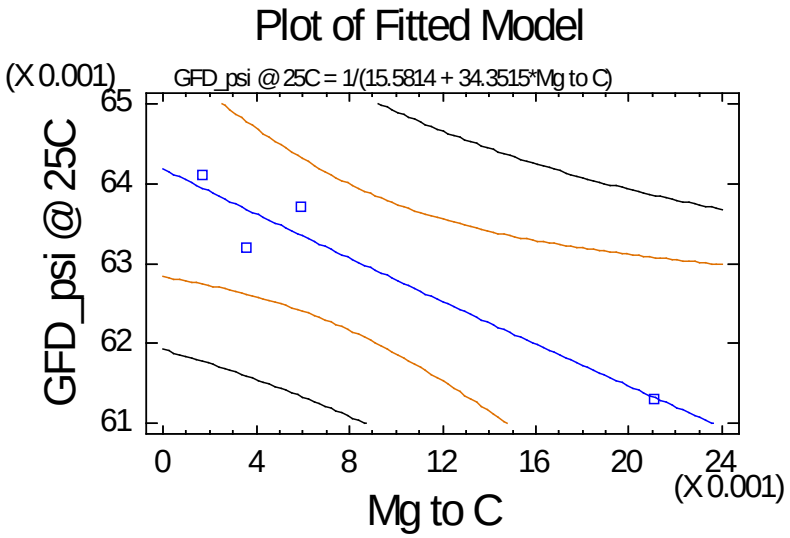

Figure 9.19. Best linear regression model describing loss of normalized specific water flux of membranes at the beginning of RO Stage 1 as a function of the Mg/C EDX signal on the membrane spacer.

Notes: % R^2 = 92.42%, p = 0.0386.

Magnesium could be associated with silicates or phosphates fouling the spacer surfaces.

Cu/C Ratio

The relationship between the EDX copper/carbon (Cu/C) ratio on the spacer at the beginning of the first RO stage and the membrane performance in terms of normalized specific water flux is shown in Figure 9.20. A total of 91.74% of the variance in membrane normalized specific water flux was described, with the model statistically significant at nearly 96% confidence level (p = 0.0422).

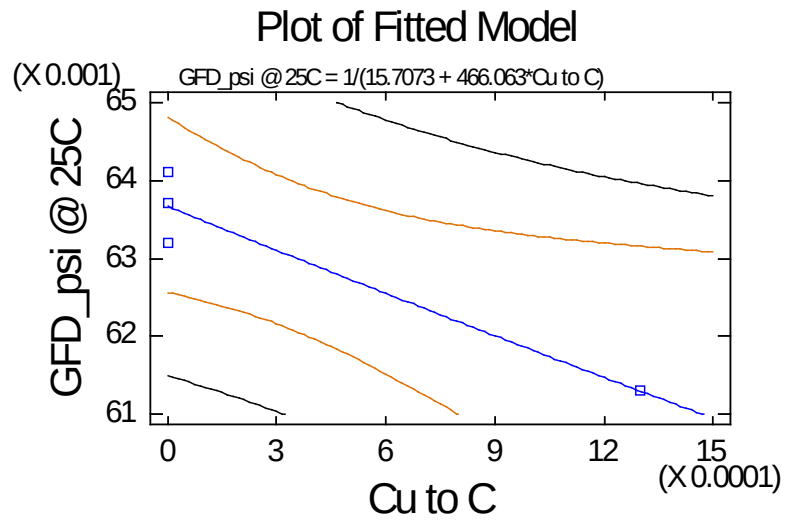

Figure 9.20. Best linear regression model describing loss of normalized specific water flux of membranes at the beginning of RO Stage 1 as a function of the Cu/C EDX signal on the membrane spacer.

Notes: % R^2 = 91.74%, p = 0.0422.

Copper could form insoluble phosphates and possibly also silicates on the spacer surfaces.

F/C Ratio

The relationship between the EDX fluorine/carbon (F/C) ratio on the spacer at the beginning of the first RO stage and the membrane performance in terms of normalized specific water flux is shown in Figure 9.21. A total of 91.69% of the variance in membrane normalized specific water flux was described, with the model statistically significant at nearly 96% confidence level (p = 0.0422).

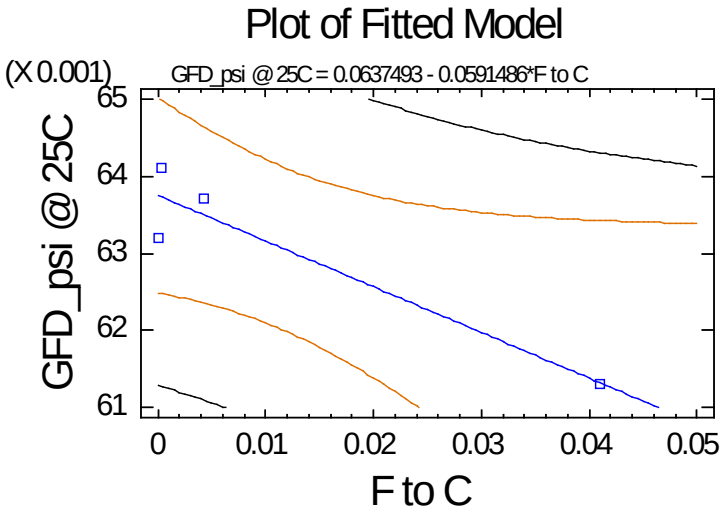

Figure 9.21. Best linear regression model describing loss of normalized specific water flux of membranes at the beginning of RO Stage 1 as a function of the F/C EDX signal on the membrane spacer.

Notes: % R^2 = 91.69%, p = 0.0425.

Fluorine can form a number of insoluble mineral salts (fluorites) and also may be associated with precipitate cations on the spacer surface.

Ca/C Ratio

The relationship between the EDX calcium/carbon (Ca/C) ratio on the spacer at the beginning of the first RO stage and the membrane performance in terms of normalized specific water flux is shown in Figure 9.22. A total of 91.43% of the variance in membrane normalized specific water flux was described, with the model statistically significant at nearly 96% confidence level (p = 0.0438).

Calcium can be associated with numerous potential foulants, and as a divalent ion can bridge anionic bacterial and contribute to fouling itself. Silicates and phosphates are potential insoluble compounds that might contain calcium.

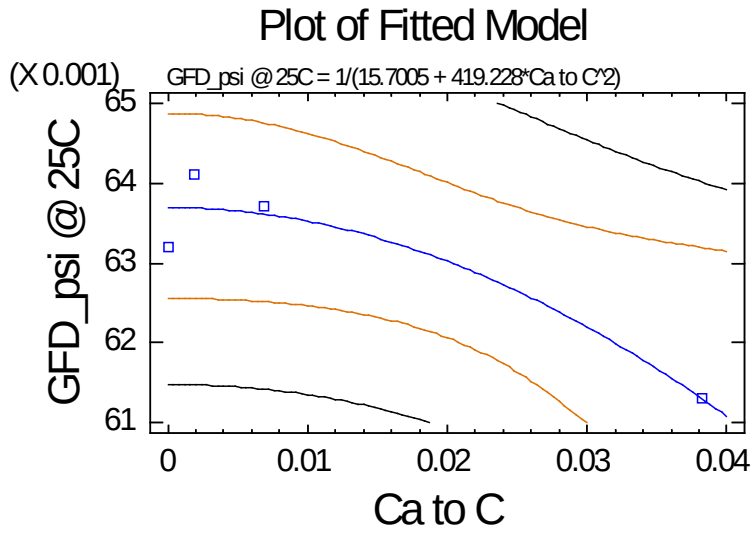

Figure 9.22. Best linear regression model describing loss of normalized specific water flux of membranes at the beginning of RO Stage 1 as a function of the Ca/C EDX signal on the membrane spacer.

Notes: % R^2 = 91.43%, p = 0.0438.

O/C Ratio

The relationship between the EDX oxygen/carbon (O/C) ratio on the spacer at the beginning of the first RO stage and the membrane performance in terms of normalized specific water flux is shown in Figure 9.23. A total of 90.31% of the variance in membrane normalized specific water flux was described, with the model statistically significant at nearly 95% confidence level (p = 0.0497).

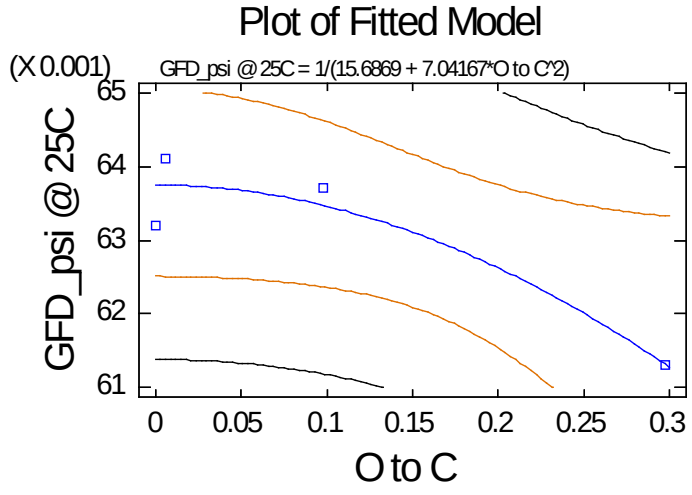

Figure 9.23. Best linear regression model describing loss of normalized specific water flux of membranes at the beginning of RO Stage 1 as a function of the O/C EDX signal on the membrane spacer.

Notes: % R^2 = 90.31%, p = 0.0497.

Oxygen was not found in polypropylene but is ubiquitous in biological materials, biopolymers, silicates, and phosphates—all of which could adhere to the Vexar spacer.

Al/C Ratio

The relationship between the EDX aluminum/carbon (Al/C) ratio on the spacer at the beginning of the first RO stage and the membrane performance in terms of normalized specific water flux is shown in Figure B.24 in Appendix B. A total of 74.56% of the variance in membrane normalized specific water flux was described, however, the model was only statistically significant at less than 90% confidence level (p = 0.1365).

Aluminum can form aluminum silicate, a potent foulant material. However, the lower % R^2 value suggests that the relationship between whatever foulant it formed on the spacer was not as nearly as influential as that formed by the other elements as discussed and indicates that aluminum may act through a completely different mechanism. Because the influences of Si, Cl, K, Na, P, N, Mg, Cu, F, Ca, and O are so very similar, it is tempting to hypothesize that that they are all related to the same fouling mechanism on the Vexar spacer.

P/C Ratio

The relationship between the EDX phosphorus/carbon (P/C) ratio on the spacer at the beginning of the first RO stage and the membrane performance in terms of normalized specific water flux is shown in Figure 9.24. A total of 93.25% of the variance in membrane normalized specific water flux was described, and the model was statistically significant at greater than 96% confidence level (p = 0.0343).

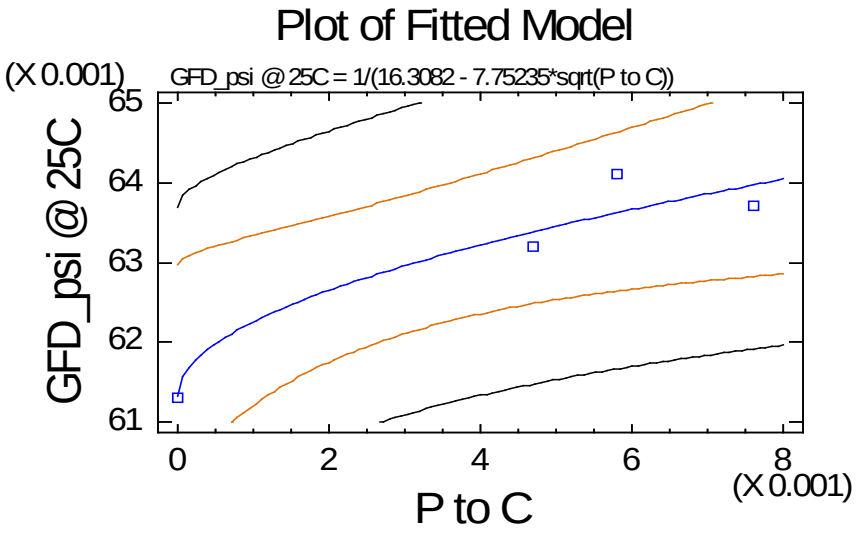

Figure 9.24. Best linear regression model describing loss of normalized specific water flux of membranes at the beginning of RO Stage 1 as a function of the P/C EDX signal on the membrane spacer.

Notes: % R^2 = 93.25%, p = 0.0343.

Although the first stage element can participate in fouling (as phosphates); here its accumulation on the spacer appeared to relate positively to normalized specific water flux but the reason is unclear as to why this should be so or in what form the phosphorus appears to have a positive effect on normalized specific water flux. Its presence may possibly be due to some sort of detergent residue (e.g., sodium tripolyphosphate) that induces detachment of material from the spacer.

Table 9.14 shows a Pearson's r intercorrelation analysis of all of the statistically significant element/C EDX ratios from this part of the study. The analysis illustrates the unusually strong intercorrelations between the O, N, F, Na, Mg, Ca, K, Cl, and Cu ratios ($r > 0.9$), suggesting that they are likely all bound up in the same mass of material on the spacer surface, whereas the higher Si and Al ratio correlations much of those elements may exist as aluminum silicate. These results are consistent with the hypothesis that mineral and biomolecular deposition on the polypropylene Vexar spacer result in a loss of normalized specific water flux. The most likely explanation is that such deposition retards or blocks the flow of water through the membrane feed channel. This results in reduced cross flow over the RO membrane surface and an increase in the polarization layer on the membrane surface that increases the osmotic backpressure. The overall effect is to reduce the net driving pressure available for the RO process. This effect could be partially reversed by dislodging matter from the spacer as a consequence of flow rate shifting, which occurs when the RO units are shut down. This also suggests that mechanical cleaning strategies (e.g. air sparging) that dislodge foulants on the spacer that block the feed channel may have the potential to recover early loss of membrane productivity in the first RO stage.

Table 9.14. Pearson's Intercorrelation (r) Analyses of All Statistically Significant EDX Ratios

	O to C	N to C	F to C	Na to C	Mg to C	Al to C	Si to C	Ca to C	K to C	Cl to C	K to C	Cu to C	P to C
O to C		0.9572	0.9737	0.9637	0.9828	0.3669	0.7010	0.9851	0.9645	0.9554	0.9645	0.9464	-0.7674
N to C			0.9383	0.9476	0.9730	0.4634	0.8175	0.9377	0.9564	0.9676	0.9564	0.9152	-0.7874
F to C				0.9975	0.9927	0.5575	0.8075	0.9976	0.9956	0.9868	0.9956	0.9951	-0.8906
Na to C					0.9940	0.6007	0.8464	0.9909	0.9995	0.9951	0.9995	0.9960	-0.9106
Mg to C						0.5284	0.8194	0.9913	0.9957	0.9935	0.9957	0.9810	-0.8650
Al to C							0.8783	0.4989	0.5993	0.6173	0.5993	0.6315	-0.8721
Si to C								0.7672	0.8535	0.8788	0.8535	0.8412	-0.9391
Ca to C									0.9888	0.9774	0.9888	0.9867	-0.8577
K to C										0.9976	1.0000	0.9330	-0.9072
Cl to C											0.9976	0.9485	-0.9089
K to C												0.9930	-0.9072
Cu to C													-0.9297
P to C													

Note: Notice strong positive correlations between O, N, Na, F, Mg, Si, Ca, K, Cl, and Cu (r >0.9) and strong negative correlation between P and all of these. Al correlated best with Si, suggesting formation of aluminum silicate.

9.3.9.2 Element/Carbon Ratio of the Feed Spacer that Best Related to Loss of Normalized Specific Water Flux: Beginning of the Second RO Stage

Unlike with the beginning of the first RO stage, at the transition between the first RO stage and the second RO stage (represented by test membranes fed with AWPF RO Unit E01 second stage RO feedwater) there were no elements detected on the Vexar spacer whose element/C ratios exhibited a strong negative relationship with membrane normalized water flux. There were several elements whose element/C ratios exhibited a relatively strong positive relationship (% R^2 >50%) indicating that as the ratio increased, the normalized specific water flux also increased, and the membranes tended to perform better. These elements included Na, Cl, K, Cu, Mg, F, Ca, Fe, Si, and Al. Of these, only the Na, K, and Cl ratios were statistically significantly related to the normalized membrane water flux at greater than 90% confidence level ($p < 0.10$). Na was related at greater than 95% confidence level ($p < 0.05$).

It is unclear why the relationships are positive. One interpretation is that because what is being examined is the ratio of the element to carbon, if the carbon signal should become lower by deposition of a low carbon-containing/high element-containing foulant at the surface of the Vexar spacer, then even though the mass of material fouling the spacer is increasing, the element/C ratios would be observed to increase. Absolute quantification of the mass of carbon (or any other element) from the foulant independent of the membrane or spacer by EDX spectroscopy cannot be done.

Na/C Ratio

The relationship between the EDX sodium/carbon (Na/C) ratio on the spacer at the end of the first RO stage and beginning of the second RO stage and the membrane performance in terms of normalized specific water flux is shown in Figure 9.25. A total of 99.82% of the variance in membrane normalized specific water flux was described, and the model was statistically significant at greater than 97% confidence level ($p = 0.0273$).

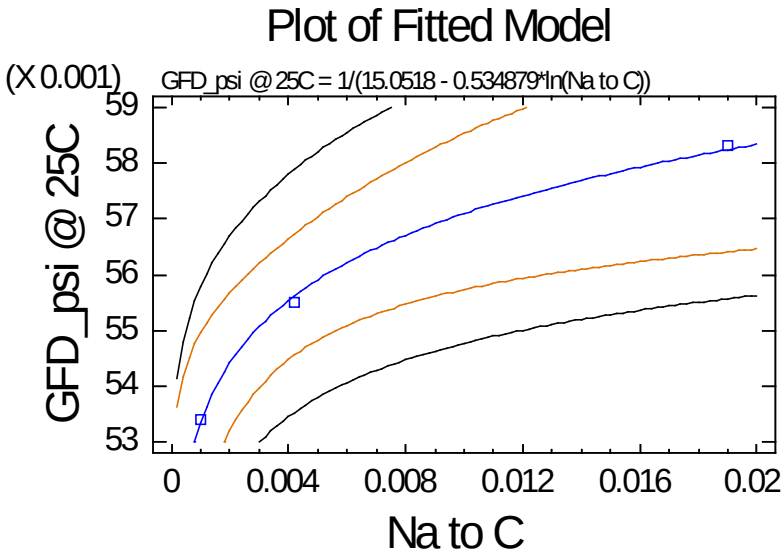

Figure 9.25. Best linear regression model describing loss of normalized specific water flux of membranes at the end of RO Stage 1 and beginning of RO Stage 2 as a function of the Na/C EDX signal on the membrane spacer.

Notes: % R^2 = 99.82%, p = 0.0273.

In this instance, the suggestion is that as the Na/C ratio increases (as sodium levels increase on the Vexar spacer with respect to carbon), membrane performance tends to improve. There are not many data points; however, they are spaced well, thus the trend appears fairly significant.

K/C Ratio

The relationship between the EDX potassium/carbon (K/C) ratio on the spacer at the end of the first RO stage and beginning of the second RO stage and the membrane performance in terms of normalized specific water flux is shown in Figure 9.26. A total of 98.63% of the variance in membrane normalized specific water flux was described, and the model is statistically significant at greater than 90% confidence level (p = 0.0747).

As with sodium, as the ratio of potassium to carbon increased on the spacer, the observation was that the membrane normalized water flux tended to improve.

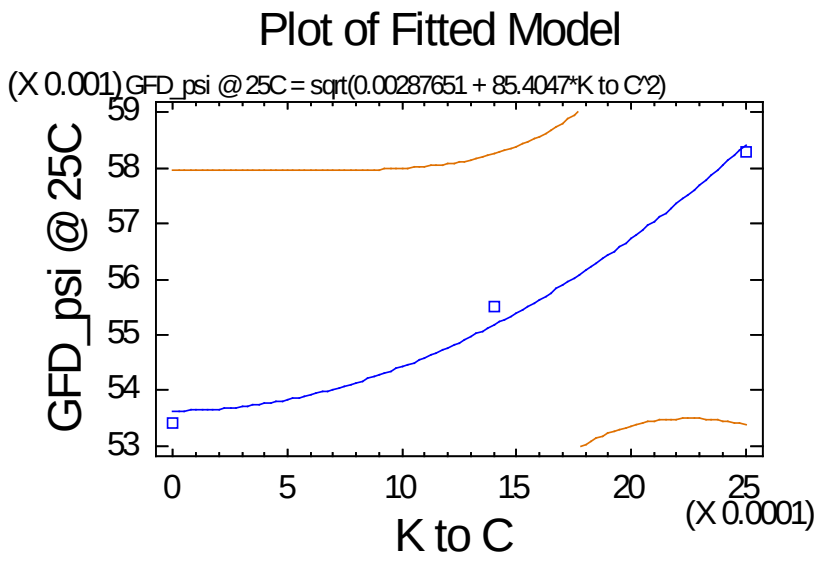

Figure 9.26. Best linear regression model describing loss of normalized specific water flux of membranes at the end of RO Stage 1 and beginning of RO Stage 2 as a function of the K/C EDX signal on the membrane spacer.

Notes: % R^2 = 98.63%, p = 0.0747.

Cl/C Ratio

The relationship between the EDX chlorine/carbon (Cl/C) ratio on the spacer at the end of the first RO stage and beginning of the second RO stage and the membrane performance in terms of normalized specific water flux is shown in Figure 9.27. A total of 99.11% of the variance in membrane normalized specific water flux was described, and the model was statistically significant at greater than 90% confidence level (p = 0.0602).

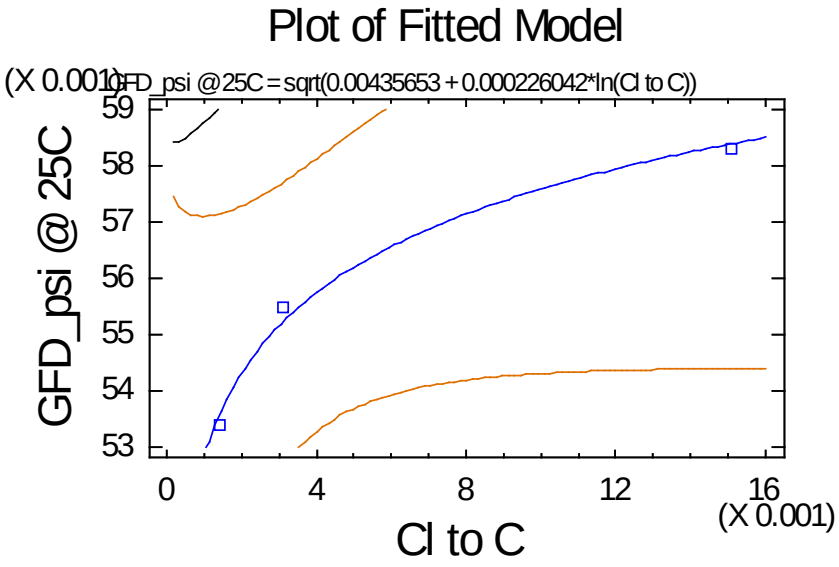

Figure 9.27. Best linear regression model describing loss of normalized specific water flux of membranes at the end of RO Stage 1 and beginning of RO Stage 2 as a function of the Cl/C EDX signal on the membrane spacer.

Notes: % R^2 = 99.11%, p = 0.0602.

As with sodium and potassium, as the Cl/C ratio of chlorine to carbon increased on the spacer the observation was that the membrane normalized water flux tended to improve. Also, as with sodium and potassium, chlorine (as chloride ion) tends to form soluble compounds, so it is unclear how any of these elements as ions associated with the Vexar spacer could be directly related to changes in the RO membrane normalized specific water flux.

Material that adheres to the Vexar spacer may change its hydrophobicity, and that, in turn, influences the water flow over the spacer material and over the RO membrane surface. The Vexar spacer is composed of polypropylene, which is a hydrophobic aliphatic hydrocarbon polymer that resists wetting. However, after exposure to colloidal organic matter in the feedwater matrix, accumulation of charged organics on the Vexar surface may tend to decrease its hydrophobicity, in which case the water flux beyond the spacer material might improve. Increasing the surface charge of the Vexar material also could increase the association of the common soluble monovalent cations (Na, K) and anions (Cl), which could have become fixed to the surface of the Vexar specimen when it was dehydrated for SEM-EDX analysis. Thus, the more hydrophilic the Vexar surface becomes, the greater is the monovalent element/C ratio that is seen there, so there is a better tendency for water to flow over the surface and a better cross flow across the membrane, which would result in an observation of improved normalized specific water flux.

9.3.9.3 Element/Carbon Ratio of the Feed Spacer that Best Related to Loss of Normalized Specific Water Flux: Beginning of the Third RO Stage

At the transition between the second and third RO stage (represented by test coupons fed with AWPF Unit E01 third stage feedwater), only one element was found on the Vexar spacer—aluminum—whose element/carbon ratio was able to explain greater than 90% of the observed variance in the normalized specific membrane water flux, although Cu, Fe, K, S, P, O, Ca, Cl, Si, and Mg ratios all exhibited % R^2 values greater than 50% when regressed against

normalized specific water flux. However, as with the transition from the first RO stage to the second stage, the Al/C relationship was positive (i.e., where the ratios increased). The membrane performance also increased, which is just the opposite of what would be expected if the increasing element to carbon ratios are an indication of simple spacer fouling with partial occlusion of the RO feed channel.

Al/C Ratio

The relationship between the EDX aluminum/carbon (Al/C) ratio on the spacer at the end of the second RO stage and beginning of the third RO stage and the membrane performance in terms of normalized specific water flux is shown in Figure 9.28. A total of 90.43% of the variance in membrane normalized specific water flux was described; however, the model was not statistically significant (p = 0.2002).

As with the end of the first RO stage/beginning of the second RO stage, this relationship was not simple to explain. Aluminum compounds (especially aluminum silicate) are significant membrane surface foulants and can certainly be expected to accumulate on the feed spacer as the concentration increases progressively down the length of the feed channel.

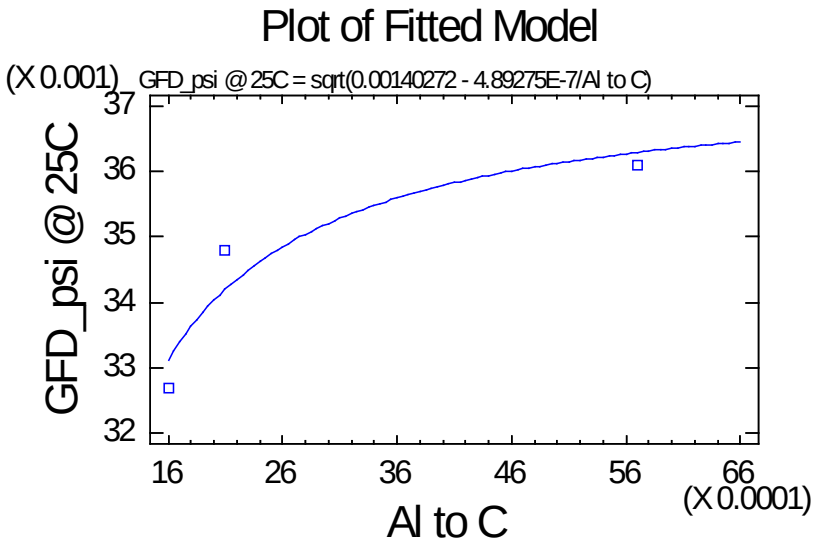

Figure 9.28. Best linear regression model describing loss of normalized specific water flux of membranes at the end of RO Stage 2 and beginning of RO Stage 3 as a function of the Al/C EDX signal on the membrane spacer.

Notes: % R^2 = 90.43%, p = 0.2002.

In this case, the data suggest that an increase in the ratio of aluminum to carbon on the Vexar spacer in the end of the second RO stage and beginning of the third RO stage was actually related to an improvement in the observed normalized specific water flux.

Although many of the same element/C ratios on the Vexar spacer in this part of the RO train were positively related to the normalized specific water flux as they were observed to be in the transition between the first and second RO stages (see Section 9.3.4.5), here, those relationships have become less clear (% R^2 values greatly reduced in comparison). However, the relationship with aluminum improved here with % R^2 increasing from 55.99% to 90.43%.

The positive relationship between the Al/C ratio and membrane normalized specific water flux does not appear to be linked through another element/C ratio relationship, as the only negative relationship observed was that between Vexar spacer F/C ratio and water flux. In this case, the % R^2 was merely 40.95% and the p–value equal to 0.5705, which is not a strong relationship and not statistically significant. The Pearson's r value for Al and F was +0.1111.

9.3.9.4 Element/Carbon Ratio of the Feed Spacer that Best Related to Loss of Normalized Specific Product Flux: End of the Third RO Stage (ROC)

By the end of the third RO stage (ROC), the element/C ratios for elements on the Vexar feed spacer were reduced until only Fe, P, Cl, and Cu showed a % R^2 >50%. Ratios of P and Fe on the spacer showed a positive relationship with respect to the observed normalized specific water flux on the membrane representative of the very end of the treatment train. The only element showing a negative relationship was chlorine (Cl).

Fe/C Ratio

The relationship between the EDX iron/carbon (Fe/C) ratio on the spacer at the end of the third RO stage and the membrane performance in terms of normalized specific water production is shown in Figure B.25 in Appendix B. A total of 66.68% of the variance in membrane normalized specific water flux was described; however, the model was not statistically significant (p = 0.1834).

At the end of the third RO stage the feedwater concentration of solutes has reached a maximum level, and the tendency for precipitation to occur should be high. Iron is an element that can participate in precipitation events. However, in this case, the greater Fe/C ratio on the Vexar spacer was associated with an increase, not a decrease in RO membrane normalized specific water flux. The Fe/C ratio of the Vexar spacer also was seen to be related to water flux in the second stage and beginning of the third RO stages (% R^2, p-values of 62.43%, 0.4200 and 63.82%, 0.4109 respectively), but these values were not statistically significant here at the end of the third RO stage.

P/C Ratio

The relationship between the EDX phosphorus/carbon (P/C) ratio on the spacer at the end of the third RO stage and the membrane performance in terms of normalized specific water flux is shown in Figure B.26 in Appendix B. A total of 66.68% of the variance in membrane normalized specific water flux was described; however, the model was not statistically significant (p = 0.1834).

As with iron, an increase in the P/C ratio on the Vexar spacer at the end of the third RO stage was related to improvement in the membrane water flux. It is not clear what mechanisms are at work here, and the relationship was fairly weak compared to others observed with Vexar spacer EDX data.

Cl/C Ratio

The relationship between the EDX chlorine/carbon (Cl/C) ratio on the spacer at the end of the third RO stage and the membrane performance in terms of normalized specific water flux is shown in Figure B.27 in Appendix B. A total of 64.83% of the variance in membrane water flux was described; however, the model was not statistically significant (p = 0.1948).

In this instance, the relationship between the Cl/C ratio on the Vexar spacer and the normalized specific product flux observed on the RO membrane at the end of the third RO stage was negative, suggesting that as the chlorine signal proportionally increased on the spacer, membrane performance declined. This is consistent with the accumulation of a foulant material on the Vexar spacer that interferes with water transport through the feed channel. Chlorine, as the ion chloride, does not form insoluble salts, but as a chlorine atom, it can be incorporated into numerous organic and mineral compounds that could act as foulants.

The formation of mineral scale is undoubtedly expected as a primary fouling mechanism on the spacer in the tail end of the third RO stage; however, the data for the element/C ratios of many of the elements anticipated to form mineral foulants on the spacer (such as Si, Al, Ca, Mg, Fe, Cu, and S) appear not to be strongly negatively related to the decline in membrane specific water flux.

9.3.10 Summary of the Impact of Biochemical, Microbial, and Elemental Parameters on RO Membrane Performance

The relationship between the accumulation of biological and organic and inorganic matter on the RO membrane surface and the feed spacer and loss of normalized specific membrane product water flux (i.e., membrane and spacer fouling) were investigated using linear correlation analysis for each stage of a three-stage AWPF RO unit. RO stage performance was characterized by the behavior of membranes at the leading end (feed end) of the stage and at the tail end (brine end) of each stage using sets of five 4 × 6 in. flat sheet test cells fed with water collected at both ends of the stage.

Correlation was ranked based on the statistical significance of the observed relationship using the 95% confidence level, $p \leq 0.05$, as the criterion, as well as on the percentage of the observed variability in fouling or flux decline that could be explained by the observed variability in the accumulation of material on the membrane surface (% R^2). Based on this approach, the results of the study suggest that factors related to membrane fouling change significantly along the RO feed channel from stage to stage.

9.3.10.1 Biochemical and Microbial Parameters

In the first AWPF RO stage, fouling was best related to the accumulation of protein material on the membrane surfaces. In the second RO stage, this relationship transitioned from accumulation of protein to accumulation of viable aerobic heterotrophic bacteria. And finally in the third AWPF RO stage, fouling was initially influenced by the presence of viable bacteria at the beginning of the stage but transitioned toward an “uncharacterized factor” that influenced fouling at the end of the stage. This uncharacterized factor may possibly be associated with mineral scaling. The biochemical and microbial data are summarized in Figure 9.29.

9.3.10.2 Element/Carbon Ratio Parameter

SEM-EDX provides a means of identifying the presence of atomic elements on the surface of the RO membrane and feed spacer. The relationship between the element/C ratios determined for RO membrane swatches exposed to feedwaters from RO Unit E01 corresponding to those at the beginning of the first RO stage, the second RO stage, the third RO stage, and the end of the third RO stage were regressed against the observed normalized specific membrane product water flux. Elemental analysis of the membrane surface and the Vexar spacer

material were determined by EDX spectroscopy. Elements incorporated into fouling matter were anticipated to show a negative relationship between their element/C ratios and membrane normalized specific water flux. The strength of the relationships was determined using the linear regression % R^2 (the percent of the variance in the normalized specific water flux that could be explained by variations in the element/C ratio) and the statistical significance of the relationships evaluated using the regression model p-values, where $p \leq 0.05$ corresponds to significance at the 95% confidence level. The EDX spectroscopic data are summarized in Figure 9.29.

Membrane Surface

Examination of elements on the RO membrane surface representative of the front end of the RO train (i.e., the lead end of the first element) revealed more than 90% of the observed decline in normalized specific water flux could be explained by the increase in iron/C and copper/C ratios alone. The element/C ratios of the other elements measured at the membrane surface were insignificantly related to the normalized specific water flux.

At the end of the first RO stage and beginning of the second RO stage, the increase in silicon/C ratio on the membrane surface could explain the greater than 98% observed decline in the normalized specific water flux. Observed variances in element/C ratios of O, Na, F, Mg, Al, P, S, Cl, Ca, and K each corresponded to half or more of the variations in the normalized specific water flux (see Table 9.12). This suggests that each of these elements also played a role in the composition of surface fouling material on the membrane in this region of the RO train.

At the end of the second RO stage and beginning of the third RO stage, an increase in no element/C ratio accounted for the greater than 38% observed decline in the normalized specific product flux, suggesting that another factor was primarily responsible for membrane fouling in this region of the RO train.

At the end of the third RO stage, several element/C ratios were fairly strongly negatively related to the observed decline in the normalized specific water flux, although not to the degree seen in other regions of the RO train. These elements included

iron (% R^2 = 77.65%, p = 0.1188)
copper (% R^2 = 77.65%, p = 0.1188)
phosphorus (% R^2 = 77.65%, p = 0.1188)

All of these elements can combine to form potentially insoluble mineral compounds, so higher ratios of them to carbon on the membrane surface should be linked to loss of membrane water flux.

Feedwater Spacer

Accumulation of material on the Vexar spacer was hypothesized to have the potential to partially or completely occlude the feed channel and cause a loss of normalized specific membrane water flux. This would cause a disruption in the cross flow over the RO membrane surface. The resulting increase in the polarization layer would result in an increase in the membrane surface osmotic pressure resulting in a decrease of the net hydraulic pressure available for solute separation.

Examination of element/C ratios on the Vexar spacer revealed that at the front end of the RO train (corresponding to the lead end of the first RO element in the first RO stage), several element ratios were strongly significantly negatively related (at the 95% confidence level, $p \leq 0.05$) to the membrane normalized specific water flux. These included the following (in order of the strength of the relationship):

silicon	(% R^2 = 98.15%, p = 0.0093)
chlorine	(% R^2 = 97.20%, p = 0.0141)
potassium	(% R^2 = 95.38%, p = 0.0234)
sodium	(% R^2 = 94.92%, p = 0.0257)
nitrogen	(% R^2 = 93.17%, p = 0.0348)
magnesium	(% R^2 = 92.42%, p = 0.0386)
copper	(% R^2 = 91.74%, p = 0.0422)
fluorine	(% R^2 = 91.69%, p = 0.0425)
calcium	(% R^2 = 91.43%, p = 0.0438)
oxygen	(% R^2 = 90.31%, p = 0.0497)

In addition, aluminum (% R^2 = 74.56%, p = 0.1365) also was strongly negatively related to the membrane normalized specific water flux. In addition, all of these element/C ratios were strongly cross correlated with each other, suggesting that they all may have been incorporated into the same suite of foulant material. Aluminum and silicon also were strongly interrelated, which suggests that aluminum silicate may have formed on the Vexar spacer. Taken together, these data strongly suggest the possibility that fouling of the Vexar spacer may have even more influence on the loss of RO membrane water flux at the front end of the first RO stage than foulants deposited on the membrane surface.

In the tail part of the third RO stage, the chlorine/C ratio on the Vexar spacer was the only spacer element/C ratio observed to be fairly strongly negatively associated with the normalized specific membrane water flux (% R^2 = 64.83%, p = 0.1948). The copper/C ratio also appeared to exhibit a weak negative relationship (% R^2 = 56.26%, p = 0.2500).

No other strong (% R^2 >90%), statistically significant ($p \leq 0.05$) negative relationships were observed among any of the Vexar spacer element/C ratios and the normalized specific water flux at any of the other points examined (end of the first and beginning of the second, end of the second and beginning of the third, or end of the third RO stages) in the RO train.

However, strong positive relationships were observed between ratios for

sodium	(% R^2 = 99.82%, p = 0.0273)
chlorine	(% R^2 = 99.11%, p = 0.0602)
potassium	(% R^2 = 98.63%, p = 0.0747)

at the end of the first RO stage and beginning of the second RO stage; for

aluminum	(% R^2 = 90.43%, p = 0.2002)

at the end of the second RO stage and beginning of the third RO stage, and for

iron	(% R^2 = 66.68%, p = 0.1834)
phosphorus	(% R^2 = 66.68%, p = 0.1834)

at the end of the end of the third RO stage (ROC). The positive relationships between element/C ratios on the Vexar spacers and normalized specific water flux were much more difficult to explain but may have to do with an increase in Vexar surface charge that improved hydrodynamic flow over the spacer by decreasing the hydrophobicity of the polypropylene spacer. Dehydration of the spacer in preparation for analysis would then result in counter ions associating with the adsorbed charged surface molecules and detection by the EDX spectroscopy

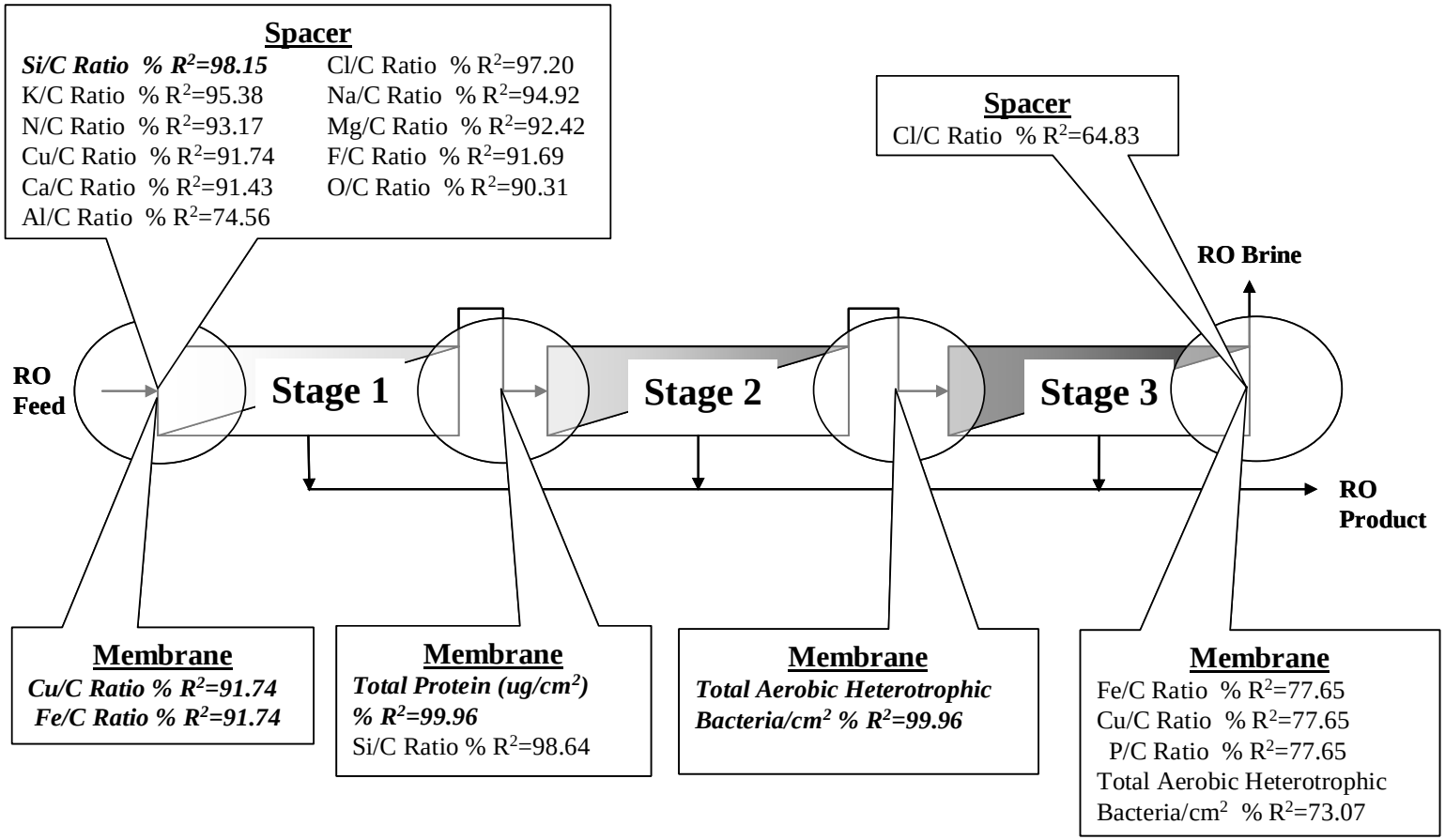

Figure 9.29. Accumulated material most significantly related by linear regression models to fouling at each location on the RO membrane.

Note: Parameters in bold italic indicate the strongest relationships that were statistically significant at the ≥95% confidence level.

9.4 Conclusions

In many cases, the element/C ratios calculated from SEM-EDX data on the membrane surfaces and on the Vexar spacer were found to be negatively related to membrane performance, which was consistent with their correlation with the accumulation of foulant material directly on the RO membranes or on the Vexar spacer in a fashion that disrupted operation of the membrane swatches.

One difficulty encountered in the study was the lack of experimental samples or exemplars with which to define the linear regression models. Although five membrane swatches were exposed to each RO feed type, experimental difficulties associated with the operation of the RO facility limited the study to only four exemplars, and in many cases this became reduced to only three, which made establishing statistically significant relationships very challenging. In addition, in a number of cases, clustering of the data was seen, with a lack of exemplars in mid-points of the model relationships. In many cases, conclusions were based on the behavior of a single data point, which greatly weakened the statistical significance of many of the models.

SEM-EDX data are relatively simple to obtain for both RO membranes and the Vexar spacers. Therefore, it is intended that this study will be repeated with another set of membranes with the hope that all five swatches can be harvested for analysis.

Chapter 10

UV/H_2O_2 Advanced Oxidation Process

10.1 Introduction

Advanced oxidation processes (AOPs) utilize oxidizing free radical intermediates to transform recalcitrant organic and inorganic contaminants of environmental and public health concern. A number of different methods exist to generate hydroxyl radicals that can be broken down into two general categories: photochemical and nonphotochemical methods. Some of the more common methods of generating hydroxyl radicals are listed in Table 10.1 (USEPA, 1998, 2001; Munter, 2001; von Sonntag, 2008).

Table 10.1. Methods for Generating Hydroxyl ($^{\bullet}OH$) Radicals

Photochemical	Non-Photochemical
UV / Ozone	Ozone at high pH
UV / H_2O_2	Ozone / H_2O_2
Fe^{3+} / UV / H_2O_2	Fe^{2+} / H_2O_2 (Fenton)
Ozone / UV / H_2O_2	
UV / TiO_2 catalytic	
E-Beam	

The hydroxyl radical has one of the highest electrochemical oxidation potentials (Table 10.2). In the presence of UV light at wavelengths less than 280 nm, a molecule of H_2O_2 can undergo photolysis to form two hydroxyl radicals with a quantum yield of one (von Sonntag, 2008; Legrini et al., 1993). At the 254 nm wavelength emitted by low-pressure mercury amalgam lamps, the molar absorptivity of H_2O_2 is only 19.6 $M^{-1}cm^{-1}$ (Glazer et al., 1987; Baxendale and Wilson, 1957). Therefore, the quantity of hydroxyl radicals formed is quite low. In order to be an effective oxidant, a high concentration of hydroxyl radicals must be generated under steady state conditions. The yield of hydroxyl radicals can be increased with the application of more energy (i.e. more photons at 254 nm, or by increasing the concentration of H_2O_2 in solution). However, increasing the H_2O_2 concentration will lead to more self-adsorption of light and beyond a certain point also will lead to more hydroxyl radical scavenging by peroxide itself.

The hydroxyl radical is highly reactive and will readily oxidize organic (and inorganic) contaminants upon contact (Haag and Yao, 1992; von Gunten, 2003; Cooper et al., 2010; Rosario-Ortiz et al., 2011; Gerrity et al., 2012). The reaction between the hydroxyl radical and the target compound (Eq. 10.1) is second-order with the overall rate of the reaction determined by the hydroxyl radical rate constant ($k_{cpd\text{-}OH}$), the concentration of the hydroxyl radicals, and the concentration of the target compound (Eq. 10.2). Therefore, the rate of removal of a given compound is determined by more than the magnitude of its

Table 10.2. Absolute Oxidation Potential of Common Oxidants[a]

Oxidant	Electrochemical Oxidation Potential E^0 (volts)
Fluorine (F_2)	3.06
Hydroxyl Radical ($^{\bullet}OH$)	**2.80, 2.38[b], 2.7[c]**
Singlet Oxygen ($^1O_2$)	2.42
Ozone (O_3)	2.07
Hydrogen Peroxide (H_2O_2)	1.77
Permanganate ion (MnO_4^-)	1.51
Chlorine (Cl_2)	1.36
Oxygen (O_2)	1.23

Sources: [a]Summers (1975); [b]Hoare (1985); [c]Bielski and Cabelli (1995).

hydroxyl radical rate constant ($k_{cpd\text{-}OH}$), and several studies have indicated that hydroxyl radical reaction efficiency with organic compounds can vary (e.g., Peller et al., 2009; Jeong, et al., 2010).

$$\text{Chemical compound (cpd)} + {}^{\bullet}OH \rightarrow \text{oxidation products} \quad (10.1)$$

$$R_{cpd\text{-}OH} = k_{cpd\text{-}OH} \times C_{OH} \times C_{cpd} \quad (10.2)$$

The transformation process is typically initiated by the abstraction of a hydrogen atom from the reacting target compound by hydroxyl radicals with rate constants for the organic compounds that typically varying from 10^6 to 10^{10} $M^{-1}s^{-1}$. A list of some of the major contributing photochemical and chemical reactions associated with the UV/H_2O_2 AOP and reactions with common constituents in reverse osmosis permeate are shown in Table 10.3 (Buxton et al., 1988; Crittenden et al., 1999; Johnson et al., 2002).

When studying the AOP, the focus should not be solely directed toward the hydroxyl radical rate constants. Compounds with a small rate constant that are present at high concentrations in the source water can have a significant effect on the rate at which target contaminants are removed because of competitive reactions; in other words. hydroxyl radical scavenging (see Table 10.3). For example, bicarbonate (Eq. 10.10; pH ≤ 8), although having a relatively low hydroxyl radical rate constant (8.5×10^6 $M^{-1}s^{-1}$), can affect the removal efficiency of trace contaminants if present at a much higher concentration than the targeted compounds. The bicarbonate could become a factor to consider, because the bicarbonate radical does not play an important role in contaminant remediation as it rapidly undergoes deprotonation (Czapski, 1999).

Other constituents, such as the combined chlorine (chloramines) present in an RO permeate source water, for example, would appear to have a significant negative effect on the AOP as the chloramines screen or absorb 254 nm light reducing the extent to which hydroxyl radicals are generated from the photolysis of H_2O_2 (Yiin and Margerum, 1990; Li and Blatchley, 2009). The chloramines also can scavenge hydroxyl radicals once formed. Monochloramine has a reported hydroxyl radical rate constant between 5.2×10^8 $M^{-1}s^{-1}$

(Poskrebyshev et al., 2003) and (2.8 ±0.2) ×10^9 $M^{-1}s^{-1}$ (Johnson et al., 2002), thus can have a significant impact on the AOP. Johnson et al. (2002) proposed reactions in Eqs. 10.12 through 10.15, although the mechanisms associated with the three chloramines are not clear. Other constituents in the source water including ammonia, nitrite, nitrate, organic nitrogen, and the uncharacterized total organic carbon can have an effect on the efficiency of the AOP. Thus, although the reaction of hydroxyl radicals with trace contaminants seems straightforward, the details of the chemical dynamics are quite complex and not well understood.

Table 10.3. Reactions of the UV/H_2O_2 Advanced Oxidation Process

Reactions	Rate Constant ($M^{-1}s^{-1}$)	Equation
$H_2O_2 + h\nu \rightarrow 2\ ^{\bullet}OH$		(10.3)
$^{\bullet}OH + {}^{\bullet}OH \rightarrow H_2O_2$	$k = 5.5 \times 10^9\ M^{-1}s^{-1}$	(10.4)
$H_2O_2 + {}^{\bullet}OH \rightarrow H_2O_2 + HO_2^{\bullet}$	$k = 2.7 \times 10^7\ M^{-1}s^{-}$	(10.5)
$H_2O_2 + HO_2^{\bullet} \rightarrow {}^{\bullet}OH + H_2O + O_2$		(10.6)
$^{\bullet}OH + HO_2^{-} \rightarrow HO_2^{\bullet} + OH^{-}$	$k = 7.5 \times 10^9\ M^{-1}s^{-1}$	(10.7)
$R_{cpd}H + {}^{\bullet}OH \rightarrow H2O + {}^{\bullet}R_{cpd}$	$k = 10^6 - 10^{10}\ M^{-1}s^{-1}$	(10.8)
$^{\bullet}OH + O_2 \rightarrow$		(10.9)
$^{\bullet}OH + HCO_3^{-} \rightarrow H_2O + CO_3^{\bullet-}$	$k = 8.5 \times 10^6\ M^{-1}s^{-1}$	(10.10)
$^{\bullet}OH + CO_3^{2-} \rightarrow OH^{-} + CO_3^{\bullet-}$	$k = 3.9 \times 10^8\ M^{-1}s^{-1}$	(10.11)
$^{\bullet}OH + NH_2Cl \rightarrow {}^{\bullet}NHCl + H_2O$	$k = (2.8 \pm 0.2) \times 10^9\ M^{-1}s^{-1}$[a] $k = 5.2 \times 10^8\ M^{-1}s^{-1}$ [b]	(10.12)
$^{\bullet}OH + NH_2Cl \rightarrow {}^{\bullet}NH_2 + HOCl$		(10.13)
$^{\bullet}OH + NHCl_2 \rightarrow NHCl + {}^{\bullet}Cl$		(10.14)
$^{\bullet}OH + NCl_3 \rightarrow NCl^{2-}, NCl_2^{-}$		(10.15)
$^{\bullet}OH + NH_3 \rightarrow NO_3^{-}$	$k = 9.7 \times 10^7\ M^{-1}s^{-1}$[c,d]	(10.16)
$^{\bullet}OH + NO_2^{-} \rightarrow$	$k = 6 \times 10^9\ M^{-1}s^{-1}$ [e]	(10.17)
$^{\bullet}OH + NO_3^{-} \rightarrow$		(10.18)

Sources: [a] Johnson et al., 2002; [b] Poskrebyshev et al., 2003; [c] Hickel and Sehested, 1992; [d] Hoigne and Bader, 1978; [e] Løgager and Sehested, 1993.

10.2 Background on the UV/AOP Facility of the OCWD AWPF

The UV treatment process of the AWPF was designed to achieve greater than 4-log inactivation of MS-2 coliphage at greater than 50 mJ/cm^2 and greater than 1.2-log reduction of N-nitrosodimethylamine (NDMA) based on the 2003 NWRI/AWWARF UV Guidelines (NWRI/AWWARF, 2003). The CDPH gave sufficient credits for removal of microorganisms

by the UV irradiation such that chlorine disinfection could possibly have been removed from the treatment process, which would have reduced the potential for NDMA formation. However, a combined chlorine residual (chloramines) in the feedwater is needed to control biological fouling on the surface of the RO membranes. Later the CDPH requested the addition of hydrogen peroxide for destruction of trace organic contaminants in the RO permeate (e.g. 1,4-dioxane, by advanced oxidation). A UV/H_2O_2-based AOP was not specifically mandated. UV/H_2O_2 was chosen because the UV process was already implemented for disinfection and removal of NDMA from the RO permeate.

During the time this study was completed, the UV/AOP facility of the AWPF was equipped with eight Trojan Technologies UVPhox (London, ON, Canada) reactor trains with a ninth three-chamber train operated in parallel as three independent two-reactor, single-chamber trains. The UVPhox train consists of three vertically stacked chambers. Each chamber contains two reactors. Each reactor contains 72 low-pressure high-output (LPHO) mercury amalgam lamps. The ballast power level (BPL) can be operated between 60% and 100% of their nominal input power of 257 watts. A detailed analysis of the performance of the ballast is discussed in Appendix C. Each reactor consumes 18.5 kW of electricity running at 100% power. The Trojan system logic controls the flow to each train, adjusts the BPL and the number of reactors turned on based on five operational parameters: water temperature, flow rate, UVT at 254 nm, lamp age, and a UV fouling index. Cleaning of the quartz sleeves is not required as the RO permeate has a low fouling potential.

The AWPF operated between 50 and 70 mgd with the flow through each UVPhox train typically between 6.5 mgd (4500 gpm) and 7.9 mgd (5500 gpm) at an electrical energy dose (EED) between 0.25 and 0.35 kWh/kgal. At the designed AWPF maximum flow of 70 mgd, each of the eight UVPhox reactor trains would have to operate at the maximum flow rate of 8.75 mgd (6076 gpm) with a maximum possible EED of 0.304 kWh/kgal. However, the system logic was designed to make use of the ninth backup parallel train, thereby reducing the load on the eight main reactor trains to 5100 to 5500 gpm during operation of the plant at 70 mgd.

The conditional approval permit to operate granted to OCWD by the CDPH stated that the equivalent of four reactors running at 100% BPL at a flow rate of 8.75 mgd (6076 gpm) must be maintained at all times. These conditions correspond to a minimum EED of 0.203 kWh/kgal. This CDPH-mandated level of operation provides the district with the minimum 4-log reduction of MS-2 coliphage plus more than two-fold redundancy in the event of a reactor failure (Pacifico, 2008). The flow rate, number of reactors in service, and BPL can be adjusted in different combinations to achieve the minimum 0.203 kWh/kgal EED. Note that this minimum operating EED was adjusted upward to 0.230 kWh/kgal to ensure 0.5-log removal of 1,4-dioxane from the RO permeate by the UV/H_2O_2 AOP (see discussion following).

In December 2007 a study was conducted to measure the removal efficiency of 1,4-dioxane by the UVPhox reactor prior to the January 2008 commissioning of the AWPF. The RO permeate was spiked with 1,4-Dioxane with the targeted H_2O_2 residual in the feedwater to the UV/AOP facility set at 3 mg/L (Ishida et al., 2010). A spiked concentration of 25 µg/L (ppb) of 1,4-dioxane was attenuated by 0.48 to 0.61 logs at a measured H_2O_2 concentration of ~1.5 mg/L and an EED between 0.23 and 0.29 kWh/kgal, which met the 0.5-log goal requested by the CDPH. The effluent from the experiment was discharged to OCSD and the 5-mile ocean outfall. On the basis of the results of this study, it was determined that the minimum operational EED of the UVPhox was to be 0.230 kWh/kgal in the presence of H_2O_2

at a measured residual of 3 mg/L (Pacifico, 2009). Whereas a 0.5-log reduction of 1,4-dioxane was achieved with 1.5 mg/L of H_2O_2 through the single demonstration experiment, a 3 mg/L (minimum 2.6 mg/L rounded up to one significant figure of 3 mg/L for compliance) measured residual of hydrogen peroxide in the feedwater to the UV/AOP was still requested by the CDPH (Bernados, 2009). The UV/AOP facility of the AWPF currently operates in a manner to achieve an EED greater than or equal to 0.230 kWh/kgal and a measured H_2O_2 concentration greater than or equal to 2.6 mg/L.

The fact that 0.5-log reduction of 1,4-dioxane was achieved with such a low concentration of peroxide during the December 2007 study warranted further investigation into the feasibility of operating the UV/H_2O_2 AOP at a lower residual peroxide feedwater dose. Any reduction in the peroxide dose would lead to savings in chemical costs. A reduction in the feedwater H_2O_2 concentration also would reduce the residual in the FPW, lessen the impact of peroxide on applications or processes downstream, and lessen the demand for peroxide removal if necessary for environmental or public health reasons. The permit to operate the AWPF does not require quenching of the residual chlorine or hydrogen peroxide in the FPW.

The focus of this section of the research project was to characterize the UV/H_2O_2 AOP of the AWPF through a combination of full-scale and pilot UV reactor studies and to analyze historical data from the operation of the UV/AOP facility. The pilot UV reactor studies were conducted at various H_2O_2 concentrations, 1,4-dioxane concentrations, and flow rates (i.e. EEDs) to mimic the performance of the full-scale system, model the UV/H_2O_2 process, and determine the optimum concentration of peroxide for removal of the 1,4-dioxane in the AWPF. An analysis of the volatile organic compounds (VOCs) in the RO permeate and UV/AOP feed and product waters were conducted to begin the process of characterizing and measuring the impact of the UV/AOP on the organic constituents on the RO permeate (see Chapter 11). And finally, the removal efficiency of pharmaceuticals and personal care products (PPCPs) from the RO concentrate were measured, and the development of a potential surrogate for monitoring AOP was investigated (see Chaper 12).

10.3 Characterization of the UV/H_2O_2 AOP of the AWPF

10.3.1 Stability of Hydrogen Peroxide Feedstock

A 50% (w/w) feedstock of hydrogen peroxide for the AOP is maintained onsite at the AWPF. The concentrated H_2O_2 is added to a carrier stream of decarbonated RO product water (DPW) before it is added to the RO permeate prior to exposure to UV light. A study was conducted to determine the stability of the 50% H_2O_2 over a 3-month period. Following the delivery of a new load of peroxide, samples were grabbed from the storage tank on a weekly basis and the peroxide concentration measured by titration with a 0.1 M $KMnO_4$ standard solution. At the start of the study the storage tank contained 9638 gal of 50% hydrogen peroxide. Over the 3-month period, peroxide was drawn from the tank for use in the operation of the UV/AOP of the AWPF. The peroxide concentrations, storage tank volume, and temperature of the peroxide when grabbed are displayed in Table 10.4.

The temperature of the feedstock ranged from 14.4 to 17.8 °C at the time the samples were grabbed in the mornings between 7:30 a.m. and 8:30 a.m. On February 11, 2009, the 250-mL peroxide grab sample was inadvertently mistaken for a TOC sample and contaminated with 0.3 mL of phosphoric acid, which is used as a preservative. The addition of the acid did not appear to affect the results of the analysis as the sample reported out as 49.75% H_2O_2. On March 4, 2009, no sample was obtained from the storage tank. After 76 days the study was

terminated and a new load of peroxide was delivered and added to the storage tank. Results from this study indicated that the 50% H_2O_2 did not undergo a significant amount of decomposition over the 2½ month period of time. Commercially supplied hydrogen peroxide is usually stabilized with phosphates and tin (IV) materials (Jones, 1999). Furthermore, 50% hydrogen peroxide has been reported to decompose very slowly at a rate of less than 1% per year (Schumb et al., 1955).

Table 10.4. Stability of 50% (w/w) Hydrogen Peroxide Feedstock

Tank A03 Storage Time (days)	Sample Date	H_2O_2 Concentration (w/w%)	Tank Volume (gal)	Temperature of H_2O_2 in Tank (°C)
0	21-Jan-09	49.8	9638	17.5
7	28-Jan-09	49.7	7740	16.9
14	4-Feb-09	48.2	5817	17.5
21	11-Feb-09	49.75[a]	5452	15.8
28	18-Feb-09	48.9	5083	14.4
35	25-Feb-09	50.2	3651	15.4
42	4-Mar-09	No Sample*	3607	16.6
48	11-Mar-09	43.4	3559	16.2
55	18-Mar-09	49.4	3518	16.3
62	25-Mar-09	49.9	3448	16.6
69	1-Apr-09	48.2	3394	17.4
76	8-Apr-09	49.5	3344	17.8

Note: *Laboratory personnel inadvertently contaminated sample with phosphoric acid.

10.3.2 Performance of Low-Pressure High-Output Mercury Amalgam UV Lamps

The 257-watt low-pressure high-output (LPHO) mercury (Hg) amalgam lamps used in Trojan Technologies' UVPhox reactor trains have an advertised end-of-lamp-life (EOLL) of 12,000 h, at which time they are to be replaced. The LPHO Hg lamp is reported to emit 82% of the intensity of a new lamp at the EOLL. A small study was conducted to verify the lamp performance out to the EOLL and beyond.

A number of lamps with run times between 500 and 11,000 h and lamps that had reached their 12,000-h EOLL were removed from reactor trains. The UV output of these lamps was measured using a single-lamp reactor that was manufactured with quartz windows in the sidewalls such that the output of the lamp could be measured with a radiometer. This allowed for accurate measurement of UV intensity along the length of the lamp and the determination of the reduction in UV output at various lengths of run time.

10.3.2.1 Experimental Method

Measurements of UV lamp output were made using a manufactured copy of Trojan Technologies' single-lamp reactor. The LPHO lamp was powered by the same ballast used in the full-scale UVPhox. The BPL was set at 100%. Three UV-transparent 25 × 2 mm quartz windows (Edmund Optics, Barrington, NJ) were manufactured into the sidewall of the reactor so that the UV intensity from the middle of the lamp, two-thirds the distance down from the

electrical connection, and the end of the lamp could be measured (Figure 10.1). RO permeate was pumped through the UV reactor at a flow rate of 3.3 to 3.6 gpm. The lamps were allowed to stabilize for 10 min and then UV output in units of mW/cm^2 was measured with an IL1400A radiometer (International Light Technologies, Peabody, MA) equipped with a SEL240 detector and QNDS2 neutral-density filter. The TD integrating filter was not attached to the detector for these measurements. The meter was zeroed with the black plastic protective cap installed before collecting UV measurements at the three lamp positions. The lamp measurements were made over several days. The water temperature of the reactor effluent was measured with a thermocouple and varied from 20.1 to 25.5 °C over the period in which the measurements were made. The UVT at 254 nm of the RO permeate obtain from the MF/RO pilot unit or tap water at the OCWD Research Center varied from 96.9 to 98.0 %T. Total chlorine was measured in the feedwater and effluent to the single-lamp reactor by the DPD colorimetric method using a DR4000U spectrophotometer (HACH Company, Program 1485). The total chlorine in the source waters varied from 0.1 to 2.4 mg/L.

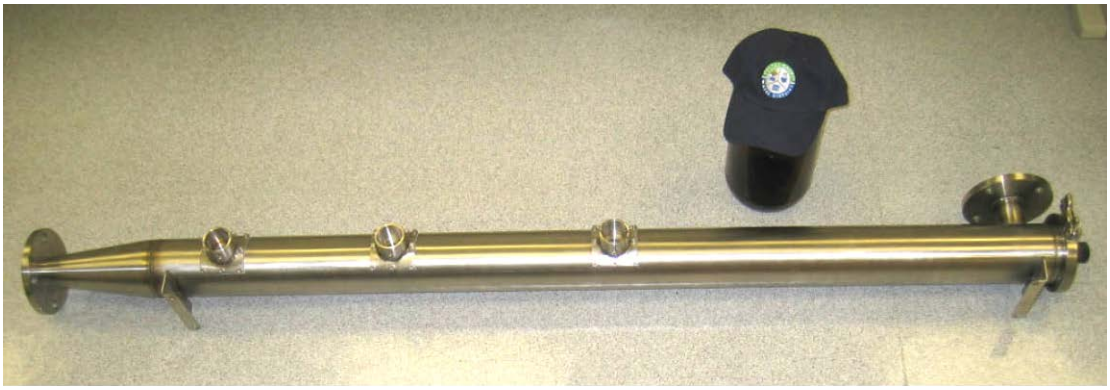

Figure 10.1. Single-lamp reactor with quartz windows for measuring UV intensity of 257-watt LPHO Hg amalgam lamp.

Three "groups" of lamps were tested. The first group of 28 lamps had accumulated 500 to 6500 h of run time, the second group of four lamps had 11,999 h of run time and the final group of three had 13,515 h of run time. The lamps with 13,515 h of run time were saved from Train A during the operation of OCWD's Interim Water Factory, which operated from March 2004 to August 2006 as an MF/RO/UV/H_2O_2 AOP purification process. These lamps were removed from the UVPhox train on September 25, 2006, and stored in the laboratory.

The LPHO UV lamps (Model No. 302509) are 0.746 in. (1.895 cm) in diameter, the quartz sleeves are 1.108 in. (2.814 cm) in diameter and the internal diameter of the 316 stainless steel UV reactor is 3.79 in. (9.627 cm). Therefore, the surface of the quartz sleeve is 1.341 in. (3.406 cm) from the inner wall of the reactor that has a 4 in. outer diameter, where the quartz window is located. The total length of the lamp is 60.75 in., and the distance between the ionizing electrodes is 58 in.

10.3.2.2 Results and Discussion

A chart displaying the UV intensity as a function of lamp run time hours is displayed in Figure 10.2. There was a small amount of UV variation across the length of each lamp. The average UV output and standard deviation are displayed in Table 10.5 for the three groups of lamps. The middle of the lamp did not always exhibit the most intense emission. At 3.4 cm

from the surface of the quartz sleeve the average of all three measurements across the lamp or the 500 to 10,727 h group of lamps was 7.21 ± 1.00 mW/cm^2 (n = 66), the average for the 11,799 h group of lamps was 5.55 ± 0.69 mW/cm^2 (n = 4), and the average for the 13,515 h group was 5.45 ± 1.05 mW/cm^2 (n = 3).

On average the 11,799 h lamps emitted 77% of the UV intensity of a 500 to 10,727 h lamp. However, if one excluded the measurements made near the end of the lamp, the lamps did maintain a UV output near 82% at the 12,000 h EOLL, as reported by Trojan Technologies. Individually, the measured output at 11,799 h from the middle, two-thirds, and end positions on the lamps were 82%, 80%, and 70% respectively.

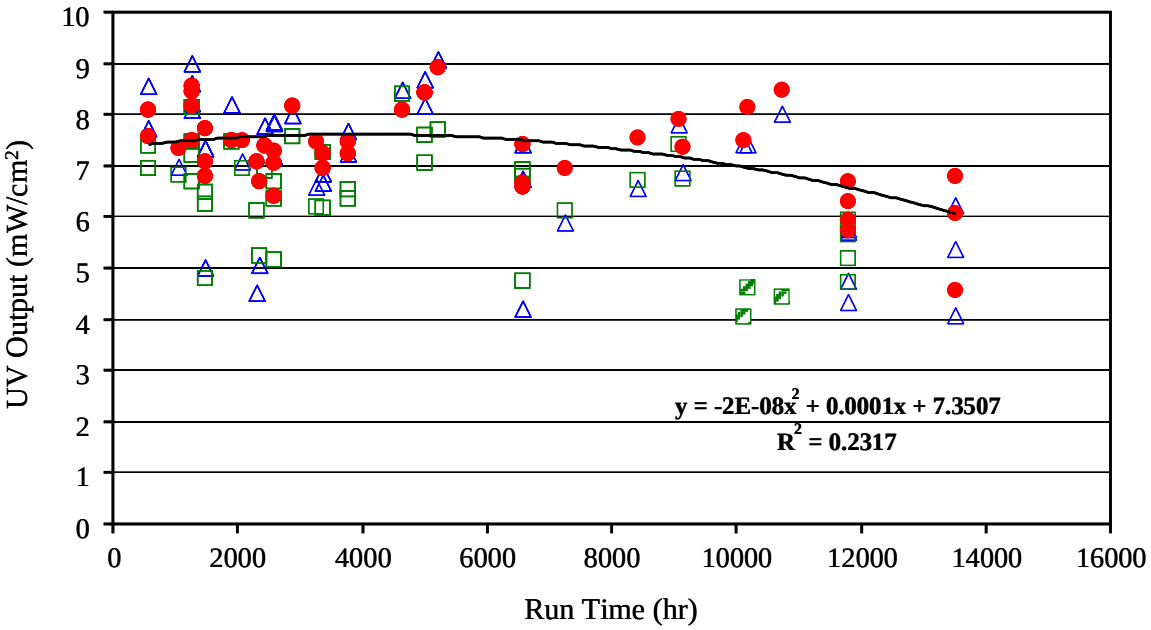

Figure 10.2. Plot of the UV intensity (mW/cm^2) as a function of run time (h) at locations at the end (open triangle), two-thirds down the length (open square), and middle (solid circle) of the lamp.

Note: Dashed squares near 10,000 h indicate measurements made at two-thirds position on lamp when path of light was obscured by unknown material.

Table 10.5. UV Output of 257-Watt LPHO Mercury Amalgam Lamps

Lamp Life (hr)	End (mW/cm^2)	Two-thirds Down (mW/cm^2)	Middle (mW/cm^2)	All (mW/cm^2)	Percentage of UV Output at EOLL[a]
500–10,727 h (66 lamps)	7.35 ± 1.21	6.72 ± 0.87	7.54 ± 0.64	7.21 ± 1.00	—
11,799 h (4 lamps)	5.13 ± 0.71	5.37 ± 0.54	6.16 ± 0.42	5.55 ± 0.69	77%
13,515 h (3 lamps)	5.22 ± 0.84	5.34 ± 1.30	5.80 ± 1.14	5.45 ± 1.05	76%

Note: [a]Percentage of 254-nm output relative to lamps with 500 to 10,727 hr run time based on the average of all three measurement positions along the lamp.

In another small study, three lamps were driven out to 15,000 h. One of the lamps burned out before a measurement could be made at 13,000 h. The UV output of the other two lamps were between 70% and 80% of capacity at 14,950 h relative to a 1050 h UV lamp, on the basis of average UV intensity (mW/cm^2) at the three lamp positions. A more extensive study was not conducted beyond these three lamps because of operational constraints associated with the AWPF. Lamp performance at 12,000 h and beyond was known to be unpredictable (data not shown). The threshold for servicing a 72-lamp reactor is eight lamps out of service.

10.3.2.3 Summary and Conclusions

The UV output (mW/cm^2) of the 257-watt LPHO mercury amalgam lamps was measured using a radiometer and single-lamp reactor with quartz windows. A total of 73 lamps with run times in the range of 500 to 10,727 h (66), 11,799 h (4), and 13,515 h (3) were tested. On average, the UV intensity at the 12,000 h EOLL dropped to 77% of the average intensity of a 500 to 10,727 h lamp. However, if the UV measurements for the EOLL lamps collected at the end of the lamp were removed from the data set, the average output intensity (80%–82%) was equal to that stated by Trojan Technologies for a 12,000 h lamp.

10.3.3 Estimation of UV Dose Associated with UVPhox Reactor Train

There is no way to directly measure the fluence inside the UVPhox reactor; therefore, an estimate of the fluence or UV dose (mJ/cm^2) was made based on a combination of published collimated beam data and full-scale reactor data specifically related to the removal of NDMA. Prior to the commissioning of the AWPF in January 2008, a number of benchtop and full-scale UV reactor studies were performed to characterize and validate the operation of the UV/AOP facility of the AWPF. One-log reduction of NDMA from RO permeate containing 2.1 mg/L of combined chlorine, no hydrogen peroxide, and a UVT at 254 nm of 97 %T was achieved with a collimated beam of 254 nm light at a UV dose of 550 mJ/cm^2 (Soroushian et al., 2001). In a full-scale validation test conducted by Trojan Technologies on October 7, 2008, NDMA removal was measured at the maximum reactor flow rate of 8.75 mgd (6076 gpm) with the reactor BPL set at 100% (Brown, 2008). There was 3 mg/L of combined chlorine and 2.8 to 3.5 mg/L of hydrogen peroxide in the RO permeate (i.e. UVF, with a UVT of 97–98 %T). Samples were grabbed with 1, 2, 4, and 6 reactors turned on. A linear regression line fit to the data indicated that 1-log reduction of NDMA was achieved at an EED of 0.168 kWh/kgal. The EED was simply calculated by tabulating the number of lamps turned on and multiplying by the power of the 257-watt LPHO lamp (without accounting for the age of the lamps, quartz sleeve, or water quality factors) and then dividing by the 8.75 mgd flow rate in units of kgal/h.

Because 1-log reduction of NDMA at an EED of 0.168 kWh/kgal by the UVPhox corresponds to 1-log reduction of NDMA achieved with a UV dose of 550 mJ/cm^2 with a collimated beam of UV light in the absence of hydrogen peroxide, it was estimated that a UVPhox with 72 lamps per reactor operating at an EED of 0.168 kWh/kgal was approximately equivalent to delivering a UV dose of 550 mJ/cm^2. The actual equivalent UV dose delivered by the UVPhox to achieve 1-log reduction of NDMA is slightly higher than 550 mJ/cm^2 at the EED of 0.168 kWh/kgal, because there was ~3 mg/L of H_2O_2 present in the UV feedwater when the full-scale study was conducted and an undetermined amount of NDMA was presumably removed by hydroxyl radical-mediated advanced oxidation (Landsman, et al., 2007). NDMA has a hydroxyl radical rate constant reported at $3.3 \times 10^8\ M^{-1}s^{-1}$ by Wink et al. (1991) and $(4.30 \pm 0.12) \times 10^8\ M^{-1}s^{-1}$ by Mezyk et al. (2004). Sharpless and Linden (2003) reported a 30% increase in the fluence-based rate of degradation in the presence of 100 mg/L H_2O_2 in the range of 200 to 1600 mJ/cm^2. However, Soroushian

et al. (2001) did not report a significant difference in NDMA remove in the presence of 5 mg/L of peroxide in the range of 1000 to 2500 mJ/cm^2 based on collimated beam studies. The amount of NDMA removal solely by the hydroxyl radical-mediated AOP was not determined during this study.

Previous full-scale UVPhox validation studies at OCWD indicated that the effect of each individual reactor is additive (Trojan Technologies, 2004). Therefore, the combined EED associated with the reactors in service was used to estimate the UV dose that is delivered to the feedwater. The apparent UV dose of the 72-lamp UVPhox of the AWPF is estimated at 3274 mJ/cm^2 per kWh/kgal. Currently with the AWPF operating at 70 mgd at an EED of 0.26 kWh/kgal with ~2.6 mg/L of combined chlorine (measured by online amperometric analyzer), ~2.6 mg/L of hydrogen peroxide, and a UVT ~97 %T, the UVPhox reactor train has an apparent UV dose of ~850 mJ/cm^2.

10.3.4 Photolysis of Hydrogen Peroxide and Combined Chlorine

For the UV/AOP of the AWPF, hydrogen peroxide (50% w/w) is added to a carrier stream of decarbonated UV product water (DPW) by a diaphragm pump. The diluted peroxide solution is injected into the RO permeate through a diffuser that spans a 78 in. pipeline that carries feedwater to the UV/AOP facility. The contact time of peroxide with the RO permeate prior to reaching the UV reactor trains at a flow of 70 mgd varies from an estimated 28 s to Train A (the closest) to 34 s to Train L (the farthest) (Figure 10.3). The actual contact time with UV light inside the reactor train varies from 10 to 14 s depending on the flow rate and the number of reactors in service.

The H_2O_2 concentration in the UVF, UVP, and the FPW are measured on a weekly basis by OCWD's AWQA laboratory. Independent studies of H_2O_2 photolysis also were conducted in an effort to characterize the performance of the UVPhox reactor train. Hydrogen peroxide concentrations above and below the CDPH-requested 3-mg/L measured residual were investigated.

A combined chlorine (chloramines) residual is maintained in the feedwater to the RO process to control biofouling on the membrane surface. A major portion of the chloramines passes through the membrane into the permeate. The chloramines in the feedwater to the AOP can have a measurable effect on H_2O_2 photolysis and hydroxyl radical generation as mono-, di-, and trichloramine all absorb at 254 nm and are readily photolyzed (Li and Blatchley, 2009; Örmeci et al., 2005). They effectively screen UV light from reaching peroxide molecules reducing the production of hydroxyl radicals, and the chloramines also can scavenge hydroxyl radicals after they are formed (Eqs. 10.12–10.15). The hydroxyl radical rate constant for monochloramine has been reported at 2.8×10^9 M^{-1}s^{-1} by Johnson et al. (2002) and at 5.2×10^8 M^{-1}s^{-1} by Poskrebyshev et al. (2003). The hydroxyl radical rate constants for the reaction with dichloramine and trichloramine have not been reported in the literature.

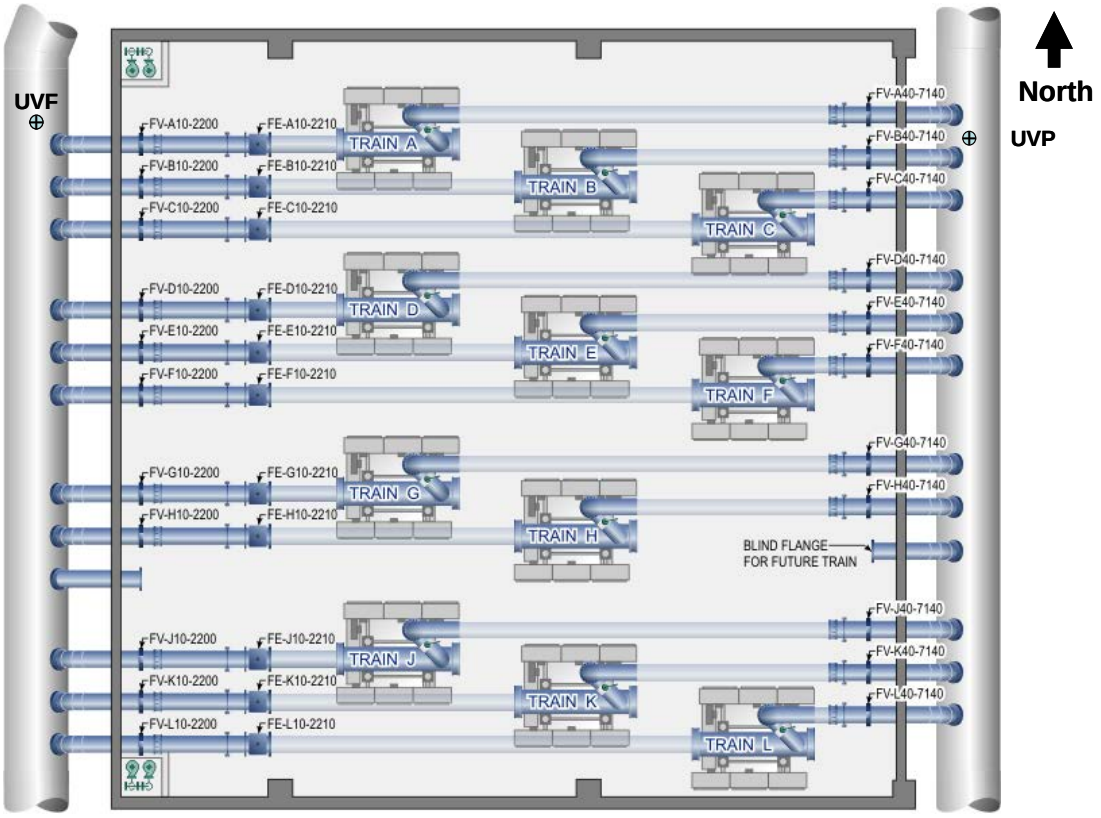

Figure 10.3. Diagram of the layout of UVPhox reactor trains of the UV/AOP facility of the Advanced Water Purification Facility at OCWD with UV feedwater (UVF) and UV product water (UVP) sample stations.

Source: Diagram courtesy of Trojan Technologies.

10.3.4.1 Experimental Methods

Weekly grab samples (1 gal) are collected at the UVF, UVP, and FPW sample stations on Wednesday mornings and delivered to the AWQA laboratory for analysis. The H_2O_2 concentration is determined by the titanium oxalate method (U.S. Peroxide; www.h2o2.com) without any modifications to the protocol posted on the Web site. This method of peroxide analysis works without any interference from combined chlorine (chloramines) up to a concentration of 5 mg/L Cl_2 (Brandhuber and Korshin, 2008).

For independent studies, grab samples were collected across a single UVPhox train in order to acquire a more accurate measure of reactor performance. Initially grab samples were limited from 300 to 700 mL. Later the sample size was increased from 8 to 10 L to smooth out the fluctuations in the H_2O_2 concentration associated with the delivery system. The EED was calculated based on the recorded flow (gpm) and the actual power (kW) consumed by the reactor train. These readings were obtained from the Delta V history files associated with the SCADA system and converted to units of kWh/kgal.

Total residual chlorine was measured with a HACH DR/4000U spectrophotometer (HACH Company, Program 1485) and a 5 mL sample volume. Ten percent of the measured H_2O_2 reported out as total chlorine when measured by the HACH Program 1485 colorimetric method.

Two full-scale studies were conducted in which the targeted residual H_2O_2 concentration in the RO permeate feedwater (UVF) to the UV/AOP facility was adjusted to 5 mg/L and then down to 1.5 mg/L. The flow of 50% H_2O_2 into the DPW carrier stream was set via the SCADA system to achieve these concentrations in the UVF.

Historical H_2O_2 consumption data from the AWPF were tabulated and plotted over periods when the targeted peroxide residual was set at different concentrations. These data were compared to the hydrogen peroxide consumption data gathered from independent experiments with a single six-reactor UVPhox train.

10.3.4.2 Results and Discussion

The initial grab sample studies of H_2O_2 photolysis across a full-scale UV reactor train revealed large fluctuations in the measured concentration of H_2O_2. Samples from these studies were limited from 300 to 700 mL, which represented a small sampling from one turnover volume of the six-reactor train. Although the average of 20 successive grab samples reported out at 3.0 ± 0.3 mg/L H_2O_2, large variations between back-to-back samples as high as 0.9 mg/L and 1.2 mg/L were reported. These large fluctuations often led to the reporting of a negative consumption or formation of H_2O_2 across the reactor train when UVF and UVP water samples were compared. Based on these results, the grab sample volume was increased from 700 mL to 8 to 10 L to minimize the impact of fluctuations in H_2O_2 concentration associated with the peroxide delivery system.

The amount of photolysis or consumption that occurred from 1.5, 3, and 5 mg/L H_2O_2 in the UVF feedwater was studied. To complete each experiment, a total of nine samples were grabbed in the following order: one UVF/UVP pair representative of the entire UV/AOP facility, three pairs of UVF-D/UVP-D samples from Train D, a pair of UVF/UVP samples, three pairs of UVF-D/UVP-D, and a final pair of UVF/UVP samples. A volume of 8 L of

water was grabbed at UVF/UVP from a total volume of 142,797 gal that passed through the pipeline, and 9.6 L grabbed at UVF-D/UVP-D across Train D from a total of 20,560 gal that passed through the UV reactor train. The average run time for the 72 lamps in each of the six reactors that was turned on varied between 4861 and 8888 h for the 1.5 mg/L H_2O_2 experiment, between 3000 and 6000 h for the 3-mg/L H_2O_2 experiment, and between 4196 and 8245 h for the 5 mg/L H_2O_2 experiment associated with Train D. The UVT at 254 nm for the 1.5, 3, and 5 mg/L H_2O_2 experiments were 99.6, 95.1, and 98.7 %T, respectively. The pH of the UVF feedwater to the UV/AOP facility was 5.4 for all three experiments.

The H_2O_2 concentration measured in the larger sample grabs showed greater consistency. At the lowest H_2O_2 targeted residual of 1.5 mg/L, a concentration of 1.4 ± 0.1 mg/L H_2O_2 was measured in UVF-D, and a 1.3 ± 0.1 mg/L H_2O_2 concentration measured in UVP-D, indicating 10% consumption of H_2O_2 at an EED of 0.26 kWh/kgal or ~850 mJ/cm^2 (Figure 10.4). The average total chlorine concentration in UVF-D was 1.7 ± 0.3 mg/L and 0.4 ± 0.05 mg/L in UVP-D, representing a 76% reduction of total chlorine across reactor Train D (Figure 10.5).

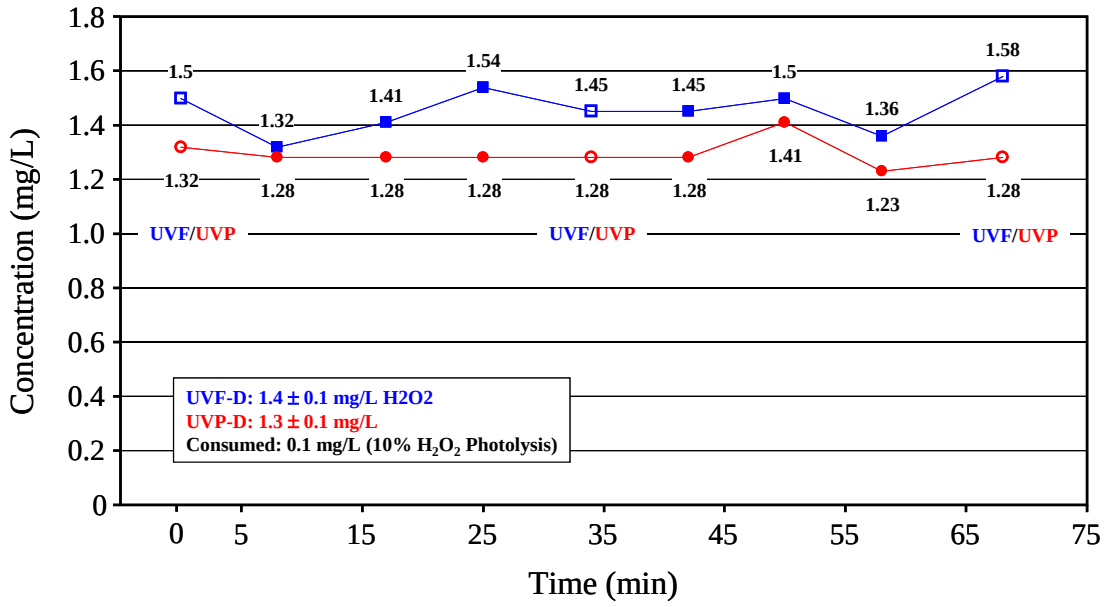

Figure 10.4. UVF (open square), UVP (open circle), UVF-D (filled square) and UVP-D (filled circle) representing hydrogen peroxide concentrations (mg/L) in grab samples separated. by time (min).

Note: Train D was operated at an EED of 0.26 kWh/kgal.

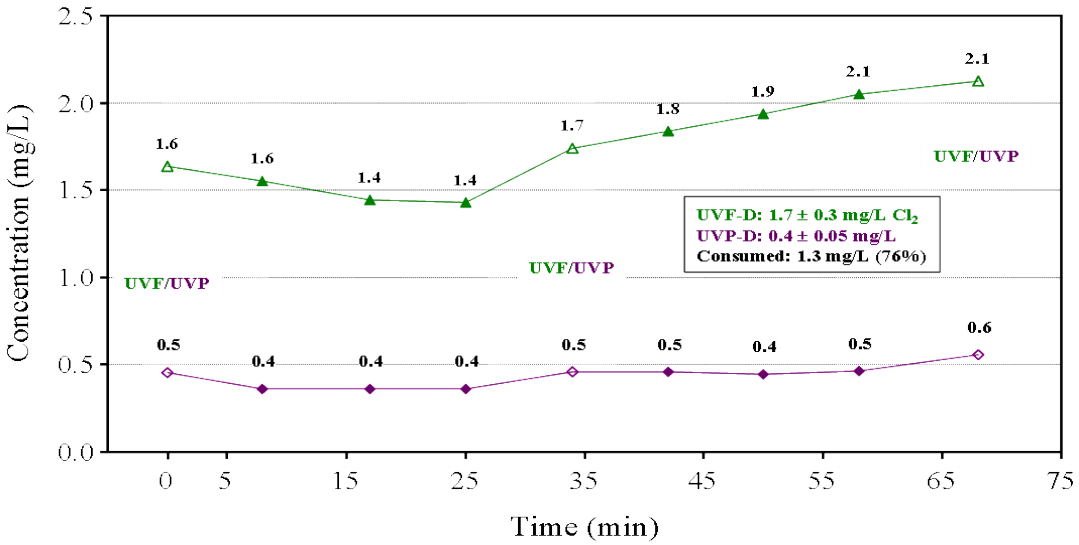

Figure 10.5. UVF (open triangle), UVP (open diamond), UVF-D (filled triangle), and UVP-D (filled diamond) representing the total chlorine concentrations (mg/L) in grab samples separated by time (min).

Note: Train D was operated at an EED of 0.26 kWh/kgal.

At the targeted 3 mg/L residual in the UVF, the average measured UVF-D H_2O_2 concentration to Train D was 3.3 ± 0.1 mg/L (Figure 10.6). The UVP-D product concentration was 2.9 ± 0.2 mg/L. The H_2O_2 concentration dropped by 0.4 mg/L across the single UVPhox train representing 12% consumption at an EED of 0.295 kWh/kgal. The total residual chlorine concentration in the UVF feedwater was measured at 5.0 ± 0.1 mg/L (Figure 10.7). The total chlorine dropped to 2.0 ± 0.1 mg/L Cl_2 across Train D, which represented a 60% reduction in the total chlorine concentration across the reactor train.

In the final experiment, a 5 mg/L H_2O_2 residual was targeted in the UVF. The average measured UVF-D H_2O_2 concentration to Train D was 5.3 ± 0.1 mg/L (Figure 10.8). The UVF concentration for the UV/AOP facility was not as stable, averaging 5.4 mg/L with a standard deviation of ±0.8 mg/L. There was only a 0.2 mg/L drop in H_2O_2 concentration between the first UVF-D sample and the last UVF-D sample that were separated by 45 min as compared to a 1.54 mg/L increase in concentration between the first and last UVF samples collected across the UV/AOP facility 59 min apart (see Figure 10.8). An independent hold-time study indicated no decomposition of H_2O_2 in the UVF samples after 2 h and a 4.8% drop in concentration after 24 h (data not shown). The H_2O_2 concentration in the Train D grab samples dropped to 4.6 ± 0.8 mg/L, representing 0.7 mg/L of consumption or 14% at an EED of 0.26 kWh/kgal (at an estimated UV dose of ~850 mJ/cm^2).

A plot of the H_2O_2 consumption data from the 1.5, 3, and 5mg/L H_2O_2 feedwater experiments associated with Train D is displayed in Figure 10.9. The data were fit to a linear regression line y = 0.1331x (forced through zero) with an R^2 = 0.9731, indicating 13% consumption of the H_2O_2 from a feedwater with a UVT of 98.7 to 99.6 %T, total chlorine ~1.8 mg/L at an average EED of 0.26 kWh/kgal for Train D. The seemingly high amount of H_2O_2 photolysis at such a low EED (0.260 kWh/kgal compared to 0.295 kWh/kgal) may be related to the lower concentration of total chlorine (i.e., 1.8 mg/L Cl_2 compared to 2.6 mg/L Cl_2; see discussion of historical AWPF data in the following) present in the RO product water during the time the 1.5 mg/L and 5 mg/L H_2O_2 experiments were conducted. The presence of

chloramines has a direct impact on the UVT. The lower concentrations of chloramines in the UVF and resulting increase in the transmittance of 254 nm light (i.e. 99.6 %T for the 1.5 mg/L H_2O_2 experiment and 97.8 %T for the 5 mg/L H_2O_2 experiment) undoubtedly led to improved photolysis of H_2O_2 across the reactor train. The 5 mg/L H_2O_2 experiment was run at a higher EED 0.295 kWh/kgal but at a much lower UVT of 95.1 %T. These H_2O_2 photolysis results were much closer to the recent February 2009 to May 2010 historical H_2O_2 consumption data (Figure 10.9).

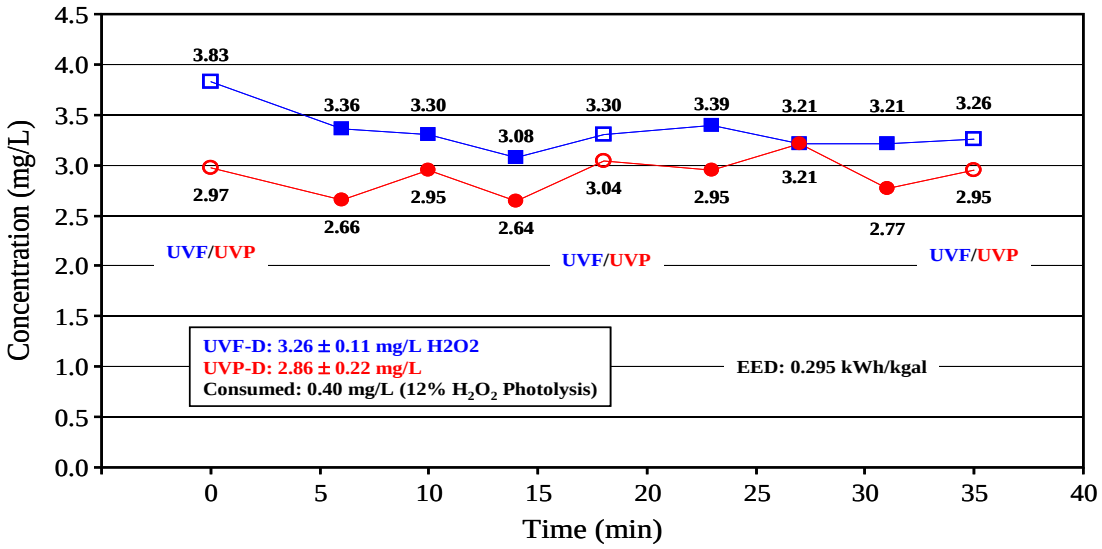

Figure 10.6. UVF (open square), UVP (open circle), UVF-D (filled square) and UVP-D (filled circle) representing hydrogen peroxide concentrations (mg/L) in grab samples separated by time (min).

Note: Train D was operated at an EED of 0.295 kWh/kgal.

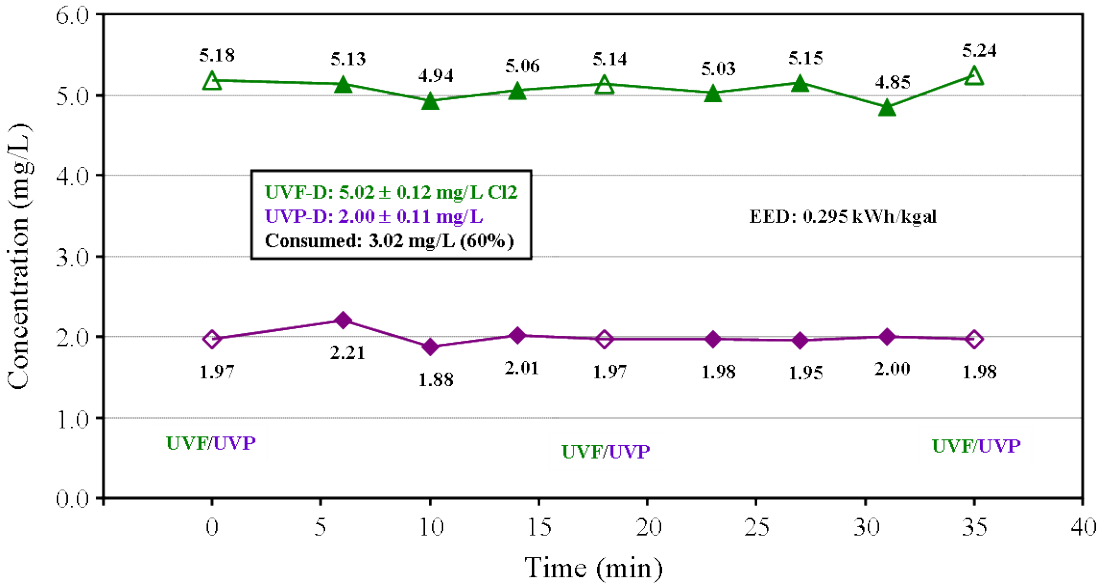

Figure 10.7. UVF (open triangle), UVP (open diamond), UVF-D (filled triangle) and UVP-D (filled diamond) representing the total chlorine concentrations (mg/L) in grab samples separated by time (min).

Note: Train D was operated at an EED of 0.295 kWh/kgal.

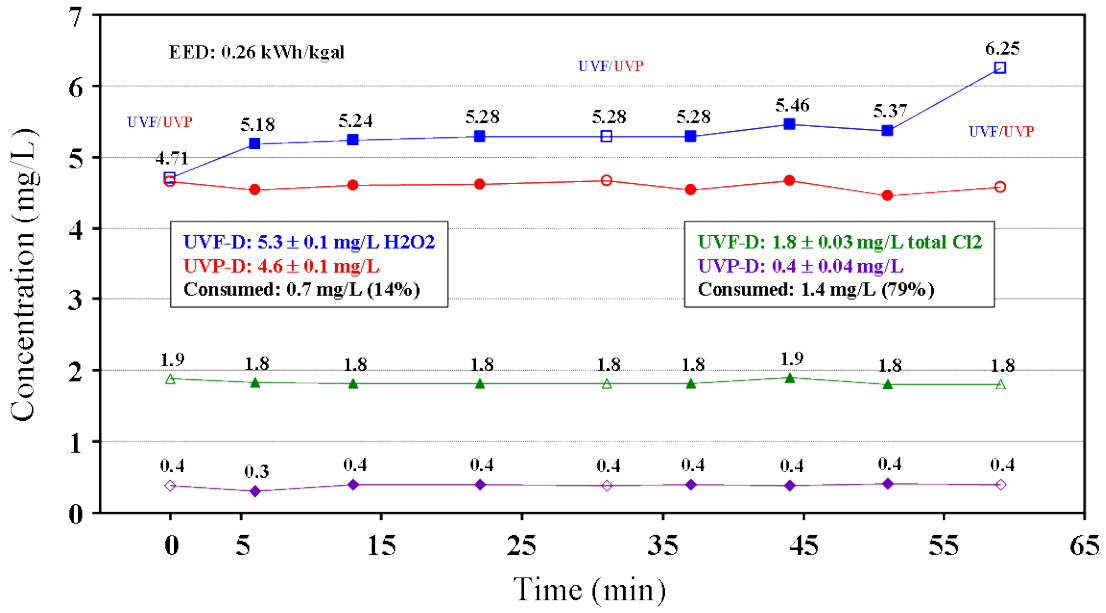

Figure 10.8. UVF (open squares), UVP (open circles), UVF-D (filled squares) and UVP-D (filled circles) representing hydrogen peroxide and UVF (open triangles), UVP (open diamonds), UVF-D (filled triangles) and UVP-D (filled diamonds) representing total chlorine concentrations (mg/L) in grab samples separated by time (min).

Note: Train D was operated at an EED of 0.26 kWh/kgal.

The H_2O_2 consumption data tabulated from the weekly Wednesday grab samples for the AWPF also are displayed in the plot in Figure 10.9. These data were not included in the fit of the regression line. The weekly Wednesday H_2O_2 grab sample data from the AWPF are represented by three independent data sets for (1) the initial January 2008 UVF SCADA set point of 3.0 mg/L, (2) an increase in the set point to 3.3 mg/L in February 2009, and (3) a reduction in the set point back to 3.0 mg/L H_2O_2 in May 2010. Between January 16, 2008, and February 12, 2009, when the H_2O_2 concentration in UVF was set at 3.0 mg/L (Table 10.6), the average measured H_2O_2 residual was 2.8 mg/L, and 0.6 mg/L was consumed at an average EED of 0.321 kWh/kgal (n = 77). On February 12, 2009, the H_2O_2 feed set point was increased to 3.3 mg/L in an effort to increase the measured residual in the feedwater to the UV/AOP facility to the CDPH-requested 3 mg/L.

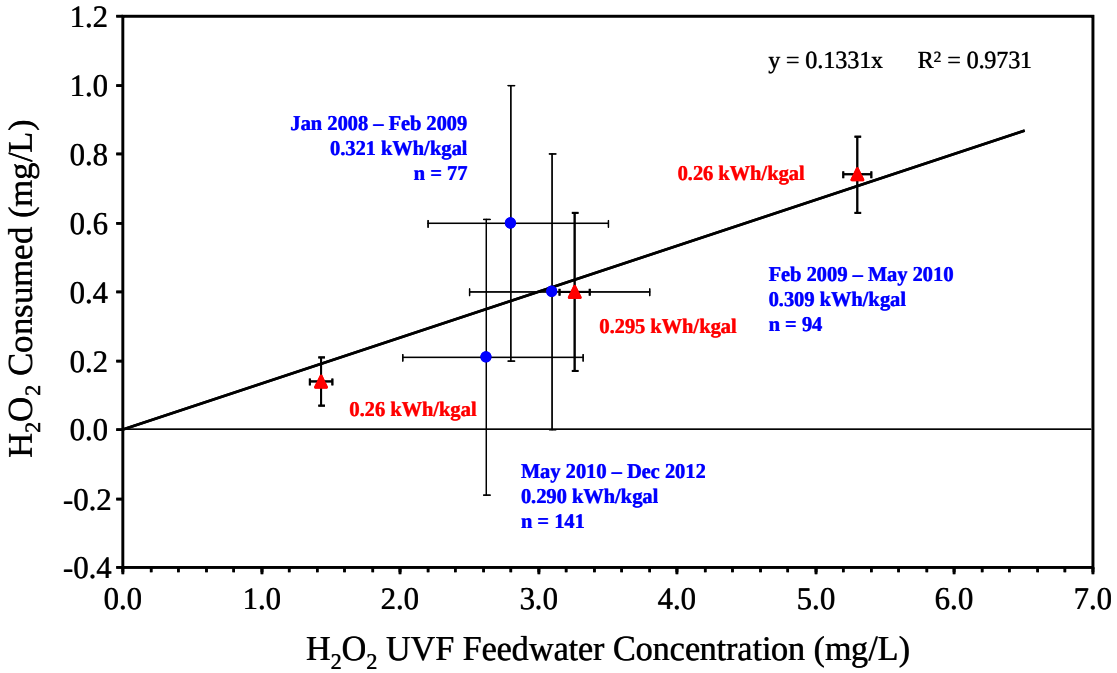

Figure 10.9. Average H_2O_2 consumption across Train D (triangles) and H_2O_2 consumption data during various periods of operation of the UV/AOP facility between January 2008 and December 2012 (circles).

Between February 17, 2009, and May 5, 2010, an average of 3.0 mg/L of H_2O_2 was measured in the UVF and 0.4 mg/L was consumed at an average EED of 0.309 kWh/kgal (n = 94). On May 12, 2010, the peroxide set point was reduced back to 3.0 mg/L, as the CDPH approved a measured residual as low as 2.6 mg/L H_2O_2 to be rounded up to one significant figure and acceptable for the requested 3 mg/L H_2O_2 concentration in the feedwater to the UV/AOP facility (Table 10.6). In the recent data set, there appeared to be a much higher H_2O_2 demand from the DPW and RO permeate that reduced the measured residual to an average 2.6 mg/L (n = 151), down 0.2 mg/L from what was measured at the 3 mg/L SCADA set point. A "drawdown" measurement associated with the H_2O_2 delivery system and the associated AWPF plant flow are made twice a day to confirm that 3 mg/L of H_2O_2 is delivered into the RO permeate.

Table 10.6. Hydrogen Peroxide Consumption Across the UV/AOP Facility of the AWPF

Period of Operation	UVF (mg/L)	UVP (mg/L)	EED (kWh/kgal)	Percent (%) Consumed	Mass (mg/L) Consumed	FPW (mg/L)
Jan 16, 2008 – Feb 12, 2009 3 mg/L set pt. (n = 77)	2.8 ± 0.7	2.2 ± 0.6	0.321 ± 0.038	21	0.6 ± 0.4	2.3 ± 0.4
Feb 17, 2009 – May 5, 2010 3.3 mg/L set pt. (n = 94)	3.0 ± 0.6	2.7 ± 0.5	0.308 ± 0.037	13	0.4 ± 0.4	2.5 ± 0.3
May 12, 2010 – Dec 26, 2012 3 mg/L set pt. (n = 151)	2.6 ± 0.5	2.4 ± 0.3	0.290 ± 0.027	7.7	0.2 ± 0.3	2.3 ± 0.3

Note: Average ± one standard deviation.

Hydrogen peroxide is not consumed by quenching reactions with the chloramines that are present in the RO permeate as the rate constants are small, on the order of 10^{-2} $M^{-1}s^{-1}$ for monochloramine and 10^{-5} $M^{-1}s^{-1}$ for dichloramine (McKay et al., 2013), and hold time studies indicate no significant decomposition of H_2O_2 within the time frame (4–6 h) of the analysis. However, the 0.4 mg/L difference in the calculated delivered dose based on the twice daily H_2O_2 calibrating drawdown measurements and the measured UVF peroxide residual may be associated with reactions with uncharacterized RO constituents. For example, catalase produced by bacteria in the biofilm on the walls of the pipeline may contribute to a small portion of the peroxide demand.

Other areas of the facility where high doses of H_2O_2 are introduced to the source waters could be points of high demand. Concentrated 50% H_2O_2 is added to the DPW carrier water, which contains ~1 mg/L of combined chlorine and bacteria shed from the walls and surfaces of the decarbonators that may exert catalase activity. At a plant flow of 70 mgd, the decarbonated carrier water contains a high concentration of H_2O_2 (~8 g/L), which is injected into the RO permeate by a diffuser that spans the RO pipeline. Insufficient mixing within the pipe and sampling off the sidewall of a large pipeline also can contribute to the variations in the measured UVF H_2O_2 concentrations.

Careful analysis of the historical UVF and UVP H_2O_2 data over a period from July through November 2012 indicated that there were a number of cases where the measured concentration of the H_2O_2 in the UVP was greater than the concentration in the UVF (data not shown). This had the effect of reducing the reported amount of peroxide consumed across the UV/AOP facility. These results revealed that the frequent fluctuations in the H_2O_2 concentration in the RO permeate (UVF) were captured by the small 1 gal grab samples analyzed by the AWQA laboratory. The H_2O_2 concentrations in the UVP samples showed greater consistency, presumably because of sufficient mixing within the reactor train. Further investigation is needed to resolve this issue between the SCADA peroxide set point and the actual measured residual of H_2O_2 in the UVF.

Much of the difference in H_2O_2 consumption over the three different periods of operation of the UV/AOP facility was attributed to the difference in EED (see Table 10.6 and Figure 10.9). Photolysis of hydrogen peroxide is directly proportional to the applied EED (kWh/kgal) or UV dose (mJ/cm^2) (Li and Blatchley, 2009; Sharpless and Linden, 2003; Watts and Linden, 2007). During the first year of the operation of the AWPF (January 2008–February 2009), the average EED of the UV/AOP facility was significantly higher, running at 0.32 kWh/kgal compared to the current average near 0.29 kWh/kgal. This drop in EED was due to the increase in total flow through the plant and the way the SCADA system is programmed to turn reactor trains on and adjust flow to each train. Thus, over the years, as the total AWPF flow has increased, the average EED has gradually dropped, and the amount of H_2O_2 photolyzed has decreased. Presumably with the decrease in H_2O_2 consumption, the production of hydroxyl radicals has dropped, resulting in less advanced oxidation across the UV/AOP facility. However, it should be noted that the UV/AOP facility was operated (and will continue to be operated) above the 0.23 kWh/kgal threshold established by the CDPH (Pacifico, 2009).

A significant improvement in H_2O_2 photolysis could theoretically be achieved if the UVT were increased by the removal of chloramines from the RO permeate. Speciation of the chloramines by membrane introduction mass spectrometry (MIMS) indicated approximately equal mass quantities (mg/L) of mono- and dichloramine in the RO permeate of the AWPF (Afifi and Blatchley, 2012; Kotiaho et al, 1991a, 1991b; Wong et al., 1995). Calculations of UVT at 254 nm based on molar absorptivities support this finding. Recent analysis of RO permeate indicate 2.6 mg/L of total residual chlorine (HACH colorimetric assay) and a UVT of 97 %T. Using molar absorptivities for monochloramine (ε = 344 $M^{-1}cm^{-1}$) and dichloramine (ε = 142 $M^{-1}cm^{-1}$) at 254 nm (Li and Blatchley, 2009), a sample containing equal 1.3 mg/L concentrations of mono- and dichloramine would theoretically have a UVT of 97 %T. The contributions from trichloramine were considered to be negligible in source water with a chlorine-to-nitrogen ratio approximately 2:1 and pH 5.4 that favors dichloramine. If the residual chlorine (chloramines) were removed from the RO permeate, the UVT of the feedwater to the UV/AOP facility would approach 100 %T. However, complete removal of chloramines is not feasible at this time, as a chloramine residual in the RO feedwater is needed to control biological fouling on the surface of the membranes.

For the opposite reason, complete removal of chloramines may not be warranted as the combined chlorine appears to contribute to the AOP process. A significant amount (~25%) of 1,4-Dioxane was removed in the presence of 2.3 to 2.6 mg/L of total residual chlorine and in the absence of any H_2O_2 (see discussion in Section 10.3.5). It is not known if the theoretical improvement in H_2O_2 photolysis through an increase in UVT at 254 nm from the removal of chloramines would outweigh the loss of AOP achieved with the chloramines present in the feedwater to the UV/AOP. Also, it is not known if the AOP associated with chloramines is simply additive or if there is a synergetic relationship between H_2O_2 and chloramines that provides more advanced oxidation than the sum from these two sources of advanced oxidants. Further studies need to be done to resolve these issues.

10.3.4.3 Summary, Conclusions, and Recommendations

Photolysis of hydrogen peroxide and the generation of hydroxyl radicals with 254-nm light is not the most efficient process as the molar absorption coefficient is only 19.6 M^{-1} cm^{-1}. Under controlled experimental conditions (i.e., performance-based studies with a single UVPhox train) at an EED of 0.26 kWh/kgal, UVT at 254 nm between 98.7 and 99.6 %T, and 1.8 mg/L of total residual chlorine, 13% of the H_2O_2 in the RO permeate feedwater was photolyzed

across a six-reactor UVPhox train. At the CDPH requested 3 mg/L H_2O_2 feedwater residual, this would amount to 0.4 mg/L of H_2O_2 consumed and 2.6 mg/L, or 87% of the feedwater H_2O_2 left in the FPW of the AWPF. Currently there are no requirements to remove the residual peroxide (or the residual chloramines) from the FPW from the AWPF of OCWD's GWR System.

Analysis of the historical hydrogen peroxide consumption data from the UV/AOP facility over three extended periods of operation indicated a gradual reduction of the amount of H_2O_2 consumed from an initial 21% to a current ~8% consumption. This drop in H_2O_2 photolysis was attributed to the reduction in the EED from an average of 0.321 kWh/kgal down to an average of 0.290 kWh/kgal. However, irregularities in the measured concentration of H_2O_2 in the source waters may contribute to the lower reported consumption measurements. A more thorough sampling of the UVF and UVP may be needed to obtain a more accurate accounting of the H_2O_2 consumption. This would entail capturing a larger volume of grab sample from the UVF and UVP sample stations on a regular basis in order to average out the fluctuations in the H_2O_2 concentration in the pipelines, which was most apparent in the UVF water samples.

The AOP will undoubtedly improve if more hydroxyl radicals are generated. There are two options to increase the amount of H_2O_2 that is photolyzed or consumed that could be implemented immediately: (1) increase the concentration of the H_2O_2 in the feedwater and (2) increase the applied UV, in other words,, the electrical energy dose (EED). The UV/AOP reactors typically operate at 70% of full electrical capacity (~80 kW of 111 kW maximum), thus a small amount of capacity still exists. Increasing the EED by reducing the flow rate through the reactors is less of an option, as this will reduce the FPW production rate. Increasing the concentration of the H_2O_2 is the more open-ended solution; however, it is not without consequence, as this can lead to self-quenching of hydroxyl radicals and greater quantities of residual peroxide in the FPW. The chlorine data from this study indicated that a reduction of combined chlorine (chloramines) resulted in an increase in the UVT at 254 nm, which led to a significant increase in the H_2O_2 photolysis. However, a chloramine residual in the RO feedwater must be maintained to control membrane biofouling. The overall impact on the AOP because of the loss of chloramine-based AOP (i.e. the loss of oxidizing chorine radicals from photolyzed chloramines) is not known at this time, and more studies are needed (see Section 10.3.5). Finally, development of lamps that emit UV light of shorter wavelength (<254 nm) where the absorptivity of H_2O_2 is much greater would improve peroxide photolysis and hydroxyl radical generation of the AOP.

10.3.5 Removal of 1,4-Dioxane by the Full-Scale UV/H_2O_2 AOP

10.3.5.1 Introduction

Commonly 1,4-dioxane is used as an industrial solvent and chemical stabilizer (USEPA, 2013). Personal care products including shampoos, liquid soaps, sunscreens, and lotions contain 1,4-dioxane ranging from 3 to 100 mg/L (ppm). Its water solubility renders it a potential contaminant in recycled wastewater applications and a potential threat to public health. In 1998 the CDPH established a drinking water notification level (NL) of 3 μg/L (ppb) for 1,4-dioxane (CDPH, 2011). However, in November 2010, the CDPH reduced the NL to 1 μg/L due to increased concern over its cancer risk (CDPH, 2011). This decision was based in part on an August 2010 USEPA IRIS toxicological review (USEPA, 2010).

Often 1,4-dioxane appears at very low (ppb) concentrations in the secondary-treated wastewater effluent from the OCSD. Historically, the levels of 1,4-dioxane in the Q1 secondary effluent have been on the order of 2 to 4 μg/L. Although 1,4-dioxane can pass through the pores of the MF hollow fibers, 0.8 to 1 logs of removal are achieved by the three-stage RO process, which utilize thin-film composite polyamide membranes. Therefore, 1,4-dioxane is rarely detected in the RO permeate of the AWPF. (Note, however, that the 1,4-dioxane removal efficiency by RO membranes varies from manufacturer to manufacturer.)

Although 1,4-dioxane has not been observed in the RO permeate on a regular basis, it has served as a benchmark indicator for measuring the efficacy of the UV/H_2O_2 AOP of the AWPF. It is not directly photolyzed at 254 nm and requires an AOP to undergo transformation or degradation. Its presence in source waters throughout the AWPF is monitored on a weekly basis through grab samples and laboratory analysis. Historical 1,4-dioxane data were tabulated, and the removal efficiency was determined. A summary of the monitoring data over a 5-year period from January 2008 to December 2012 is discussed following.

10.3.5.2 Materials and Methods

OCWD's AWQA laboratory utilizes a purge-and-trap GC/MS/MS technique for the trace-level determination of 1,4-dioxane in water (Yoo, et al., 2002, 2003). Most laboratories use the isotope dilution method (USEPA Method 8270c) over the purge-and-trap method because of better sensitivity (RDL = 1 μg/L) and reproducibility. However, the isotope dilution method involves labor intensive liquid-liquid extraction and 100 to 200 mL of methylene chloride for each sample.

The OCWD AWQA laboratory implemented a series of modifications to the purge-and-trap extraction instrumentation for EPA Method 524.2 to improve the sensitivity and reproducibility for the determination of 1,4-dioxane in water. To improve the purging efficiency, the purge time was increased from 11 min to 20 min and the sample temperature was increased to 60 °C. A different type of trap that contains more Carbopack was utilized, which improved the response and 1,4-dioxane peak shape. The RDL of 1,4-Dioxane by this modified purge-and-trap method is 1 μg/L.

At a number of locations 1,4-dioxane is monitored on a weekly basis throughout the AWPF including the secondary effluent (Q1) entering the purification plant, UVF, UVP, and the FPW. Historical data from the UV/AOP facility were tabulated and the removal efficiency by the full-scale UV/H_2O_2 AOP assessed.

10.3.5.3 Results and Discussion

Over the 5-year period from January 2008 to December 2012, only 18 UVF samples of 279 collected contained a detectable amount (≥1 μg/L) of 1,4-dioxane. Of these 18 samples, only one UVP sample reported out above the RDL and NL of 1 μg/L (ppb) at 1.2 μg/L. The raw data for the 17 UVP 1,4-dioxane samples that were below the RDL were recovered from OCWD's LIMS database. A plot of the mass concentration (μg/L) of the 1,4-dioxane removed from the UVF as a function of the initial UVF concentration is displayed in Figure 10.10. The data were fit to a linear regression line equal to $y = 0.7032x + 0.1209$ with an $R^2 = 0.89$. This regression line represents a reduction of 0.52-logs of 1,4-dioxane from the feedwater. The data represent by the 18 UVF/UVP sample pairs originated from grab samples

from the full-scale UV/AOP facility operated with an applied EED that varied between 0.24 and 0.32 kWh/kgal, UVT between 97 and 98 %T, an H_2O_2 concentration in the feedwater that varied from 2.6 to 3.3 mg/L, and a total residual chlorine concentration that varied from 1.5 to 5 mg/L. The majority of the data were collected when the targeted total residual chlorine concentration in the RO feedwater was 3 or 4 mg/L with 2.6 or 3.6 mg/L total chlorine measured in the RO permeate. Two of the three major factors that are believed to have the most impact on the UV/H_2O_2 AOP, the H_2O_2 concentration and the total chorine concentration, are not routinely analyzed in conjunction with the weekly UVF/UVP grab sample pairs for 1,4-dioxane analysis. Therefore, the impact of changes in the concentration of these two constituents on 1,4-dioxane removal could not be accurately assessed. The third factor, EED, was recovered from the Delta V history files and matched with the time of the grab samples for 1,4-dioxane analysis. However, a significant relationship ($R^2 = 0.02$) between EED and the removal of 1,4-dioxane was not readily apparent (data not shown).

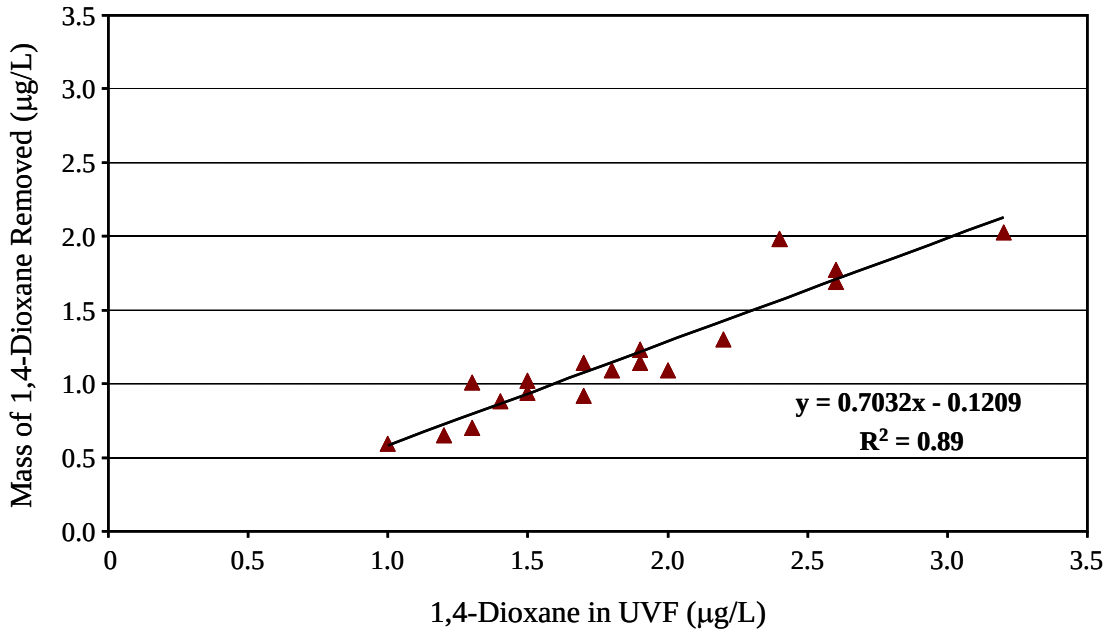

Figure 10.10. 1,4-Dioxane (µg/L) removed from the UVF feedwater to the UV/H_2O_2 AOP facility of the AWPF from January 2008 through December 2012. Purge-and-trap GC/MS/MS method of analysis.

Note: RDL = 1 µg/L

A plot of the electrical energy dose per log order of reduction (EE/O) in units of kWh/kgal/log is displayed in Figure 10.11 for the 18 samples that had a measurable amount of 1,4-dioxane at or above the 1 µg/L RDL in the UVF. The average EE/O for 1,4-dioxane was 0.658 ± 0.132 kWh/kgal/log (n = 18). The single UVF/UVP sample pair that had a reportable UVF and UVP concentration had an EE/O of 0.604 kWh/kgal/log. Note again that the other 17 UVP samples contained 1,4-dioxane concentrations below the RDL.

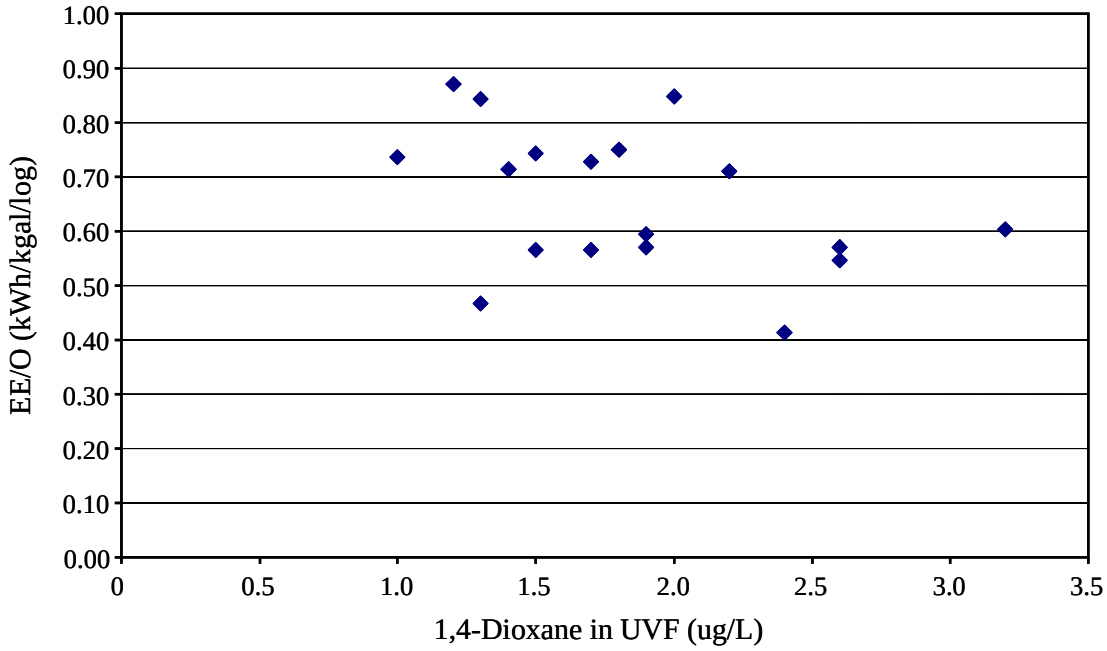

Figure 10.11. EE/O (kWh/kgal/log) of 1,4-dioxane removed from the UVF feedwater to the UV/H_2O_2 AOP facility of the AWPF from January 2008 through December 2012.

10.3.5.4 Conclusions

The limited availability of reportable 1,4-dioxane data from the UVF and UVP source waters of the AWPF UV/AOP facility made accurate assessment of the performance of the AOP difficult. Eighteen samples (of 279 total) with a UVF 1,4-dioxane concentration above the RDL of 1 μg/L were used to determine the removal efficiency by the hydroxyl radical-based AOP. Seventeen of these sample pairs had an UVP concentration below the RDL. A linear regression line fit to the data (R^2 = 0.89) indicate 70% or 0.52-logs reduction of 1,4-dioxane was achieved under the operating conditions of an applied EED that varied between 0.24 and 0.32 kWh/kgal, an H_2O_2 concentration in the feedwater that varied from 2.6 to 3.3 mg/L, a total chlorine (chloramines) concentration that varied from 2.6 to 3.6 mg/L, and a UVT of 97 to 98 %T. The average EE/O was 0.658 ± 0.132 kWh/kgal/log (n = 18). The single UVF/UVP sample pair that had a reportable UVF and UVP 1,4-dioxane concentration above 1 μg/L had an EE/O of 0.604 kWh/kgal/log.

10.4 Linear and Multiple Linear Regression Models of the Advanced Oxidation of 1,4-Dioxane from Pilot UV Reactor Studies

10.4.1 Introduction

Over a 5-year period of operation of OCWD's AWPF, the vast majority of the RO permeate feedwater samples to the UV/AOP did not contain a reportable concentration of 1,4-dioxane. Only 18 of 279 UVF feedwater samples contained a concentration of 1,4-dioxane at a reportable level. As there was no way to predict when a measurable quantity of 1,4-dioxane was present in RO permeate, the full-scale UV/AOP facility could not be reliably used to study the advanced oxidation process. Instead, a series of pilot reactor experiments were

conducted to mimic the performance of the full-scale UVPhox reactor train. This allowed for the study of the hydroxyl radical-based AOP under varying operating conditions that included UV contact time or EED, the H_2O_2 dose, and the 1,4-Dioxane concentration in the feedwater. 1,4-dioxane served as a good benchmark indicator for the AOP study because it has a large hydroxyl radical rate constant at 2.8×10^9 $M^{-1}s^{-1}$ (Thomas, 1965) and the automated GC/MS/MS method renders the analysis straightforward. Data from these experiments were used to generate statistical models associated with the pilot reactor to predict the removal of 1,4-dioxane from the RO permeate and further characterize and optimize the UV/H_2O_2 AOP of the AWPF.

10.4.2 Experimental Methods

10.4.2.1 Experimental Design

The experimental design and subsequent data analysis were performed using StatGraphics Centurion version XV (Statpoint Technologies, Inc., Herndon, VA). Experimental factors (independent variables) chosen for the pilot study included the concentration of hydrogen peroxide (mg/L) in the feedwater, concentration of 1,4-dioxane (μg/L) in the feedwater, and the reactor flow rate (gpm). The reactor flow rate was inversely proportional to the UV exposure, as the lower flows resulted in longer residence times and, hence, a greater EED (kWh/kgal) or UV dose (mJ/cm^2). The minimum and maximum ranges chosen for the independent variables were based on levels observed in the full-scale reactor trains.

In designing the experimental matrix, the minimum, maximum, and middle levels of the experimental factors were considered. A fully factorial design explicitly covering all of the combinations of these conditions would have required 27 experimental runs. To reduce the requirements for laboratory analyses, a Box-Behnken experimental design was employed. This design tested the three experimental factors in one block with a single response parameter (e.g., log reduction of 1,4-dioxane) using 15 experimental runs that provided three centerpoints and five degrees of freedom. The order of the experiments were randomized in order to provide some protection against the effects of the influence of "lurking" variables, such as trends in the data as a function of time. In addition, three additional experiments were performed in order to investigate removal of 1,4-dioxane in the absence of hydrogen peroxide.

10.4.2.2 Data Acquisition and Analysis

A replica of Trojan Technologies' (London, ON, Canada) single-lamp reactor was manufactured with quartz windows to measure the UV output of the lamp (see Section 10.3.2.1; Figure 11.1).

A 350-gal polyethylene tank (U.S. Plastic Corp., Lima, OH) was filled with 137 gal of RO permeate from the AWPF on the day the experiments were run. Hydrogen peroxide (29–32% w/w, Alfa Aesar) was added to the break tank followed by manual mixing with a PVC pipe and flange plunger device. 1,4-dioxane (ACS grade, Fisher Scientific) was added and the contents of the break tank remixed. The RO permeate that contained H_2O_2 (with and without 1,4-dioxane) was identified as UV feedwater (UVF). The UV lamp was turned on and the flow of UVF through the reactor turned on 3 min later. After a minimum 6 min warmup time, the UV output was measured at three locations along the length of the lamp (end, two-thirds. and middle) with a Model IL1400A radiometer and SEL240 detector equipped with a TD filter, and QNDS2 neutral density filter (International Light Technologies, Peabody, MA).

The outer surface of the quartz sleeve was 3.4 cm from the wall of the reactor where the UV intensity was measured. The lamp had approximately 250 h of run time at the beginning of the planned studies, and the lamp was on for approximately 40 min for each experiment.

Four UVF and four UVP paired samples were collected for each experiment. A volume of 2.5 L of each sample was collected. At the end of the experiment, the lamp was turned off and the reactor allowed to flush clear of the irradiated feedwater (~10 min) before a UVF and a "no-light pass-through" UVP sample were collected. Samples were immediately returned to the lab for analysis of total chlorine by colorimetric assay (HACH DR/4000U, Program 1485), pH, and hydrogen peroxide by the titanium oxalate method (U.S. Peroxide; www.h2o2.com). The RDL for the H_2O_2 assay is 0.1 mg/L. The total chlorine concentration was corrected to account for the contribution of peroxide to the assay; ten percent of the H_2O_2 concentration reported out as total chorine. A UV spectrum between 200 and 400 nm (Spectral Instruments-Photonics 440, Tucson, AZ) and UVT at 254 nm also were measured for one pair of UVF/UVP samples. Fluorescence emission was measured at 415 nm following excitation at 260 nm with a spectrofluorometer (Shimadzu RF5000U) equipped with a 1 cm quartz cuvette and a 300 nm low-pass filter on the emission side. Samples were submitted to the OCWD's AWQA laboratory for analysis of total organic carbon (TOC), bicarbonate (HCO3), total alkalinity (TOTALK, $CaCO_3$), nitrate-N (NO3-N), nitrite-N (NO2-N), and ammonia-N (NH3-N) by standard methods. The 1,4-dioxane concentration was measured by the OCWD AWQA laboratory's modified purge-and-trap GC/MS/MS method (RDL = 1 μg/L).

Chemical actinometry associated with the consumption of hydrogen peroxide was used to match the performance of the single-lamp pilot reactor with the full-scale six-reactor, 432-lamp UVPhox. The flow rate of the pilot reactor was adjusted to achieve the same mass (mg/L) consumption from a 3 mg/L H_2O_2 feedwater. It was assumed under these conditions that the two product waters (pilot and full-scale) were irradiated by the same total number of photons or equivalent UV dose (mJ/cm^2). A total of three different H_2O_2 concentrations (1, 3, and 5 mg/L) and three different flow rates (3, 4, and 5 gpm) were initially investigated. Later during the study, a fourth flow rate, 6 gpm, was investigated to more closely model the current operational conditions of the full-scale UV/AOP facility. Data from these experiments were used to build descriptive models of 1,4-dioxane removal, hydrogen peroxide consumption, chlorine consumption, and fluorescence signal reduction across the pilot reactor.

The relationship between experimental parameters and removal of 1,4-dioxane was investigated using multiple linear regression. Parameters which were significant at 95% confidence level ($p \leq 0.05$) were included in the models. The best models were evaluated based on the highest adjusted R-squared values, lowest Mallow's CP index, and lowest p-value. Inclusion of variables was determined using both forward selection (all variables initially absent, then variables added stepwise and retained based on lowest p-values) and backward selection (all variables initially present, then variables removed from model in order of highest p-values) to eliminate the order of inclusion as a factor. In most cases, these two selection processes converged on a common experimental variable set.

Because of the initial experimental design, there was not a significant amount of cross correlation between the experimental factors. In addition, other water quality parameters that were not specifically manipulated, but naturally varied in the course of the pilot experiments, also were tested as potentially influential variables in models.

10.4.3 Results and Discussion

10.4.3.1 RO Permeate Water Quality

The general water quality of the RO permeate is displayed in Table 10.7. The pH of the ROP feedwater to the reactor varied between 5.50 and 5.86. The bicarbonate (HCO3) concentration varied between 7.3 and 12.4 mg/L, and the TOC varied between 0.09 and 0.17 mg/L. The online TOC readings (GE Sievers 900) were typically on the order of 0.050 to 0.075 mg/L or half the concentration reported by the AWQA laboratory. Samples submitted to the laboratory were open-air grab samples analyzed with a GE Sievers 5310C. There was no measurable nitrite (NO_2 N) in the RO permeate (RDL = 0.002 mg/L).

Table 10.7. UV Pilot Reactor RO Permeate Water Quality

	Total Cl_2 (mg/L)	HCO3 (mg/L)	TOTALK (mg/L)	NH3-N (mg/L)	NO3-N (mg/L)	TOC (mg/L)	pH	UVT (%)
Average[a]	2.44	10.3	8.4	0.5	1.1	0.15	5.74	96.8
Std. Dev.	±0.44	±1.6	±1.4	±0.1	±0.2	±0.03	±0.10	±0.7

Note: [a] n = 22 samples

10.4.3.2 UV Lamp Performance

The UV output of the 257-watt LPHO lamp is displayed in Figure 10.12 for each of the 22 pilot experiments. There was approximately a 3.5% to 5% variation in UV intensity of the radiometer readings taken at the end and middle positions of the lamp. The UV intensity two-thirds down the length of the lamp dropped significantly, as much 44%, compared to the initial output readings. However, the lamp was not replaced when the measurements at two-thirds distance started to drop because the lamp was not believed to have malfunctioned, as the readings at the end and middle of the lamp were unaffected. Also, the peroxide photolysis data and AOP data collected following the drop in the measured UV intensity at the two-thirds distance did not appear to have a measurable effect on the H_2O_2 or 1,4-Dioxane removal, the decision was made to complete all the experiments with the same lamp in place (see the following discussion). Quartz sleeves from the full-scale AOP facility have experienced “clouding” that is believed to scatter but not absorb the UV light (see Appendix D).

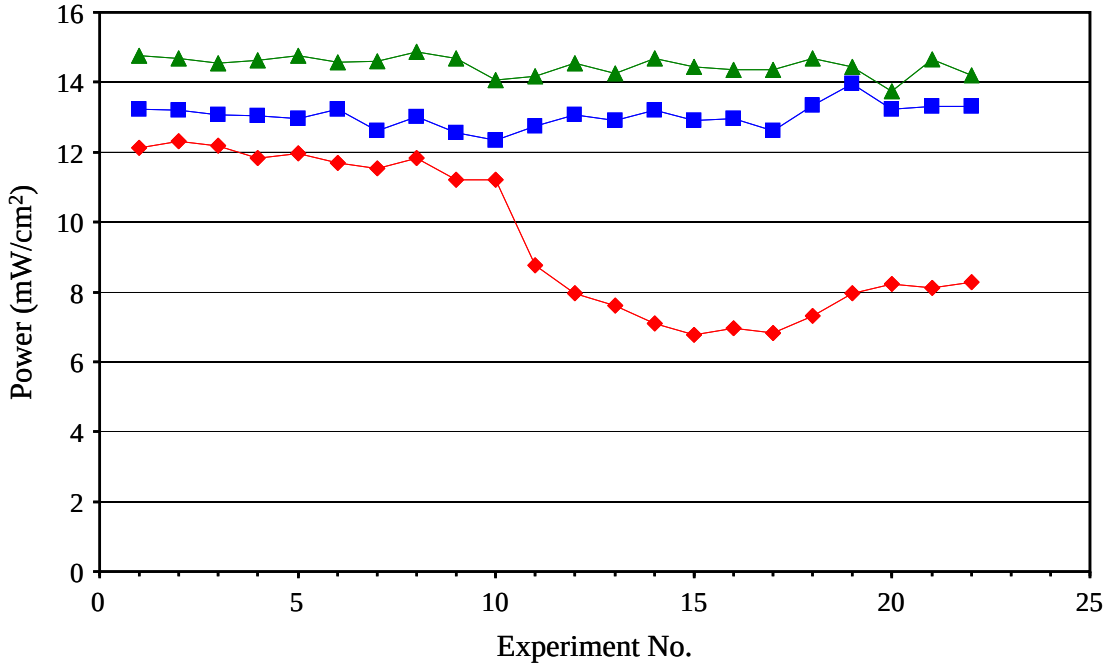

Figure 10.12. UV output (mW/cm^2) of 257 nm LPHO Hg amalgam lamp measured at end (triangle), two-thirds from the end (diamond), and middle (square) of the lamp.

10.4.3.3 Hydrogen Peroxide Consumption

Three different concentrations (1, 3, and 5 mg/L) of H_2O_2 were studied at four different flow rates (3, 4, 5, and 6 gpm). A plot of the H_2O_2 consumption as a function of H_2O_2 concentration in the feedwater is displayed in Figure 10.13. The standard deviation for the four sample measurements was typically less than 0.1 mg/L and is not displayed for clarity. The 5 and 6 gpm flow rates most closely mimicked the operational conditions of the full-scale UV/AOP reactors with respect to consumption of H_2O_2. The linear regression line for the pilot reactor operated at a flow rate of 5 gpm indicated that 13% of the peroxide in the feedwater was consumed (Figure 10.13), which was equivalent to the UV/AOP facility historical data dating back from February 17, 2009, to May 5, 2010, when 0.4 mg/L of H_2O_2 was consumed from an 3.0 mg/L average feed at an EED of 0.308 kWh/kgal, an ~3 mg/L total chlorine concentration, and a UVT of 97 to 98 %T (see Table 10.6). At 6 gpm the peroxide consumption dropped to 9%, which closely matched the full-scale UV/AOP facility operating at 0.290 kWh/kgal, where 0.2 mg/L of H_2O_2 was consumed from an average 2.6 mg/L H_2O_2 in the feedwater with 3 to 4 mg/L of total residual chlorine and a UVT of 97 to 98 %T (Table 10.6).

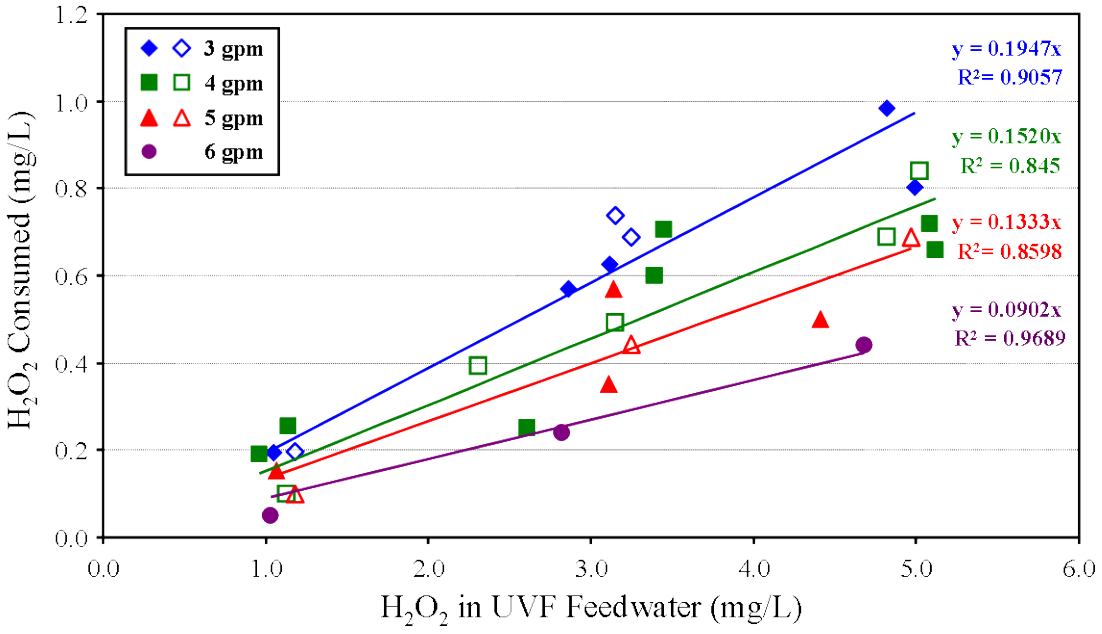

Figure 10.13. Hydrogen peroxide consumption (mg/L) across the pilot UV reactor at flow rates of 3 (diamonds), 4 (squares), 5 (triangles), and 6 (circles) gpm.

Note: Open symbols represent data points from the initial calibration of the pilot reactor with no 1,4-dioxane in the feedwater.

10.4.3.4 Total Residual Chlorine Consumption

A large portion of the UV absorbance at 254 nm can be attributed to the combined chlorine in the RO permeate, because all three chloramines absorb at 254 nm. The UVT at 254 nm increased in varying amounts across the reactor, as a result of photodegradation of the chloramines (mono-, di-, and tri-) in the feedwater (Li and Blatchley, 2009) and oxidation of chloramines by reaction with hydroxyl radicals when peroxide was present (Johnson et al., 2002; Poskrebyshev et al., 2003). There was no correlation between the increase in UVT and the contact time or H_2O_2 concentration (data not shown). However, the fraction of total chlorine removed from the feedwater across the reactor did increase with increasing contact time (slower flow rates) and varied from 60% to 90% (Figure 10.14). Removal of the chloramines from the RO permeate could significantly increase the UVT of the feedwater to the UV/AOP, improve the efficiency of H_2O_2 photolysis, increase the formation of hydroxyl radicals, and reduce the amount of hydroxyl radicals lost to scavenging by chloramines. However, there is evidence that photolysis of chloramines leads to free radical generation that aids in the AOP (see the following discussion).

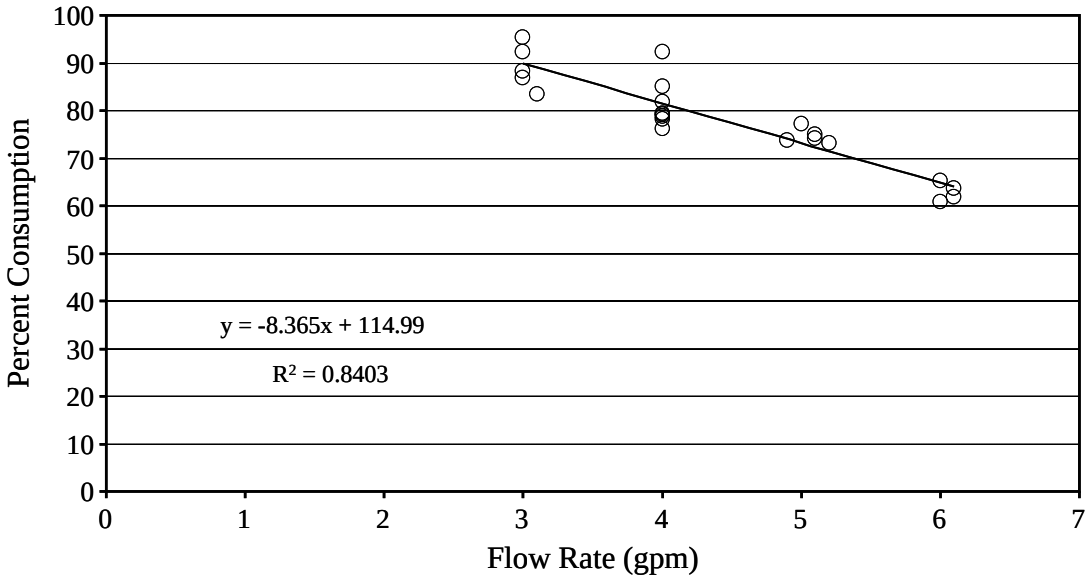

Figure 10.14. Percentage of total residual chlorine consumed across the pilot UV reactor plotted as a function of flow rate (gpm).

10.4.3.5 1,4-Dioxane Removal from RO Permeate

The 1,4-dioxane data from the 22 experiments were plotted as a function of the H_2O_2 concentration in the feedwater at each flow rate and displayed in Figure 10.15. Removal of 1,4-doxane from the UVF feedwater followed expected trends; greater quantities were removed at higher peroxide concentrations and more was removed at lower flow rates, (i.e., greater UV contact time or greater UV dose). However, the 1,4-dioxane removal efficiency unexpectedly dropped off at a flow rate of 4 gpm in the presences of 5 mg/L H_2O_2. This caused the 4 gpm regression line to drop below the model for the data from the flow rate at 5 gpm. Closer analysis of the H_2O_2 consumption data helped to explain this trend.

At a reactor flow rate of 4 gpm and a concentration of 5 mg/L, there was a significant drop-off in H_2O_2 consumption (Figure 10.16). The UVT of the feedwaters were similar, thus transmission and exposure to UV light were similar. The drop in H_2O_2 consumption and hydroxyl radical production was unexplained but could be related to the fluid dynamics of the reactor or possibly be associated with competing reactions with other feedwater constituents. The trend appeared to be real, as duplicate experiments run at markedly different 1,4-dioxane concentrations (18.5 and 4.1 μg/L) two months apart produced similar results.

Another unexpected trend was observed at a flow rate of 6 gpm. Only 0.04 mg/L H_2O_2 (3.9%) was consumed from the feedwater to the reactor. The peroxide concentration in the UVF was 1.03 ± 0.03 mg/L and 0.98 ± 0.02 mg/L (n = 4) in the UVP. Technically the RDL for the colorimetric assay is only 0.1 mg/L. However, despite the small amount of H_2O_2 consumed, 11.8 μg/L (0.39-logs or 59%) of 1,4-dioxane was removed from the feedwater that contained 20.0 μg/L of 1,4-dioxane (Figure 10.15). The total chlorine (2.2 mg/L) and bicarbonate (9.8 mg/L) were not unusually high, nor was the UVT (97.4 %T) unusually low.

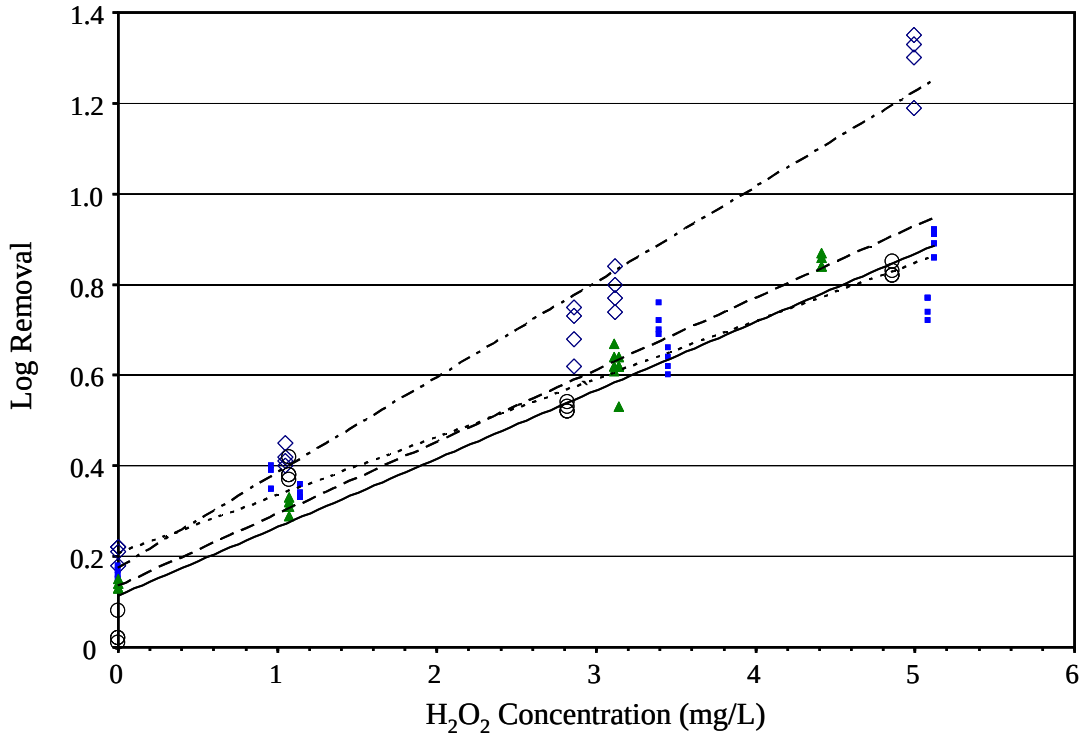

Figure 10.15. 1,4-Dioxane log removal data plotted as a function of the concentration of the H_2O_2 in the feedwater for the 22 pilot UV experiments representing flow rates of 3 (open diamond), 4 (square), 5 (triangle), and 6 (open circle) gpm.

The linear regression line for the 1,4-dioxane removal data collected at a flow rate of 5 gpm (under conditions of 13% H_2O_2 photolysis) indicates that for every 1 mg/L of H_2O_2 added to the feedwater an additional 0.16-logs reduction of 1,4-dioxane will be achieved beyond what is achieved in the absence of peroxide and presence of ~2.4 mg/L of total chlorine and independent of the 1,4-dioxane concentration in the feedwater to the UV reactor at constant EED (Table 10.8). Operation of the UV pilot reactor at 5 gpm is the equivalent to the full-scale 72-lamp UVPhox reactor operating at 0.308 kWh/kgal. The regression line for 1,4-dioxane removal data at 6 gpm (under conditions of 9% H_2O_2 photolysis) predicts 0.15-logs reduction for every 1 mg/L H_2O_2 in the RO permeate feedwater to the reactor beyond what is achieved in the absence any H_2O_2 and presence of ~2.4 mg/L of total chlorine in the feedwater. Operation of the UV pilot reactor at 6 gpm is the equivalent of the full-scale reactor operating at 0.290 kWh/kgal. These two pilot reactor models most closely represent the operation of the full-scale UV/AOP facility based solely on matching the measured consumption of H_2O_2 across the UVPhox trains under normal operating conditions of the AWPF.

A significant amount of 1,4-dioxane was removed from the RO permeate in the absence of added H_2O_2. A total of 0.14 to 0.21-logs (28–38%) reduction of 1,4-dioxane was achieved in the presence of combined chlorine in the range of 2 to 3 mg/L. Munakata (2011) also reported a significant amount of 1,4-dioxane removal (0.1–0.3-logs or 20–50%) from the RO permeate of ultrafiltration-pretreated and membrane bioreactor-pretreated wastewaters in the presence of 3 to 4 mg/L of total chlorine (Munakata, 2012). Watts et al. (2007) and Feng et al. (2007) have reported on advanced oxidation with UV light and free chlorine (HOCl), Plewa et al. (2012) and Sichel et al. (2011) have performed pilot testing, and recently,

Pisarenko et al. (2013) described the oxidation of NOM with chlorine-based AOP. However, there is no free chlorine in the source waters of the AWPF as there is residual ammonia (2.4 mg/L-N) in the secondary-treated wastewater (Q1) effluent. Sodium hypochlorite (NaOCl) is added to the secondary effluent prior to the MF process leading to the formation of chloramines. Measures are taken to avoid free chlorine breakthrough to prevent oxidation of the thin-film composite polyamide RO membranes. Analysis of RO permeate by membrane introduction mass spectrometry indicated an approximate 50:50 (wt/vol) distribution of mono- and dichloramine, and trace amounts of trichloramine (Afifi and Blatchley, 2012). Theoretical calculations of UVT based on molar absorptivities at 254 nm supported these findings. The ROP, with 2.6 mg/L of total chlorine, had a UVT of 97 %T, which equates to 50:50 mass (mg/L) distribution of mono- and dichloramine.

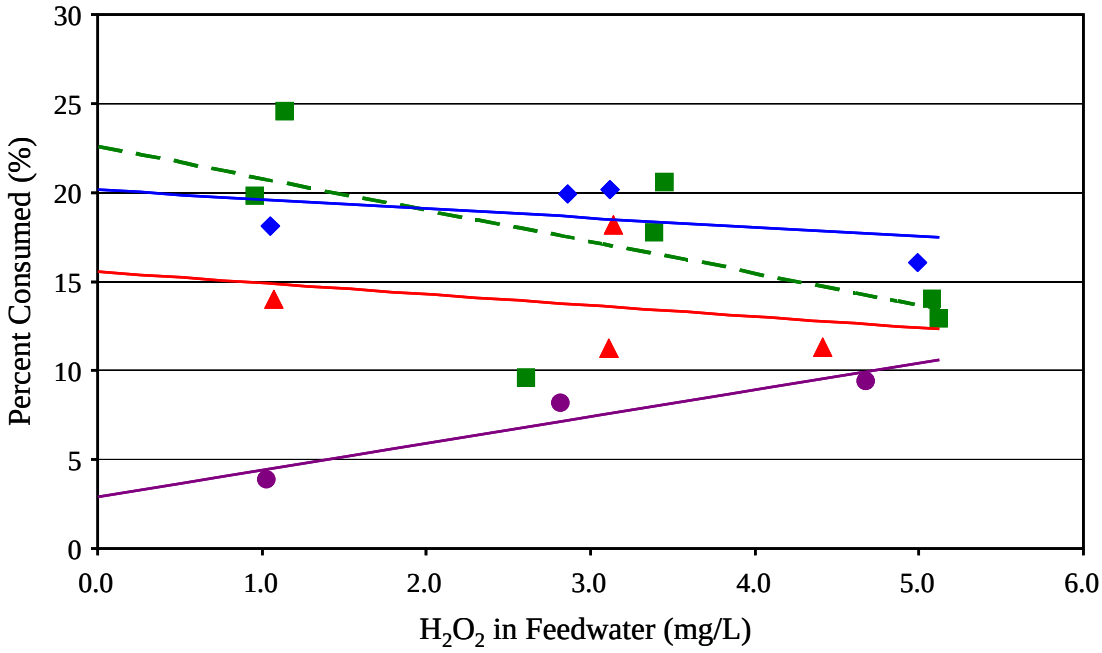

Figure 10.16. Percentage of hydrogen peroxide consumption plotted as function of concentration in feedwater for flow rates at 3 (diamonds), 4 (squares), 5 (triangle), and 6 (circles) gpm.

Table 10.8. Linear Regression Pilot Reactor Models for 1,4-Dioxane Log Removal from RO Permeate by UV/H_2O_2 AOP

Flow Rate (gpm)	Linear Regression Model Pilot UV Reactor	Predicted Logs Removed per mg/L H_2O_2	EED (kWh/kgal)	EE/O[a] (kWh/kgal/log)
3	y = 0.2101x + 0.1754	0.21	1.43	1.82 ± 0.10
4	y = 0.1280x + 0.2075	0.13	1.07	1.60 ± 0.13
5	y = 0.1588x + 0.1355	0.16	0.857	1.35 ± 0.06
6	y = 0.1508x + 0.1144	0.15	0.714	1.35 ± 0.02

Note: [a] EE/O associated with 2.8 to 3.4 mg/L H_2O_2, 2.4–2.6 mg/L of total chlorine (chloramines) in the UV feedwater with a UVT of ~97 %T.

If chorine radicals are formed in the UV reactor, they most likely originate from the combined chlorine. However, a detailed understanding of chlorine radical ($Cl^{\bullet}$) generation from mono- and dichloramine is currently lacking.

10.4.3.6 Matching Pilot-Scale and Full-Scale Reactor AOP Performance

Reactor geometry and fluid dynamics have a significant impact on the performance of the pilot UV reactor and the full-scale UVPhox. Hydrogen peroxide photolysis was used to actinometrically match the performance of the single-lamp pilot reactor to the performance of the full-scale UV/AOP facility. Two different operating conditions of the facility were specifically targeted. For a period during the research project, the UV/AOP facility was operated at a nominal 0.308 kWh/kgal EED with a 3.0 mg/L H_2O_2 residual and a 3 to 4 mg/L total chlorine (chloramine) concentration in the UVF feedwater. Under these conditions 0.4 mg/L or 13% of the H_2O_2 in the feedwater was consumed (Table 10.6). The equivalent amount of H_2O_2 was consumed when the pilot reactor was operated at an EED of 0.857 kWh/kgal, which was achieved with the lamp running at 100% BPL, a flow rate of 5 gpm with ~2.6 mg/L of total chlorine in the feedwater, and a UVT of ~97 %T (Table 10.9). This means that the UVPhox was 2.8 times more efficient at photolyzing H_2O_2 than the single-lamp reactor operating at a flow rate of 5 gpm.

In May 2010, the targeted H_2O_2 residual in the feedwater to the UV/AOP facility was reduced to 2.6 mg/L and was accompanied by an unplanned drop in the EED from 0.308 to 0.290 kWh/kgal. As a result of these changes, the H_2O_2 consumption dropped from 0.4 mg/L (13%) to 0.2 mg/L or 8% in the presence of ~2.6 mg/L of total residual chlorine at a UVT of ~97 %T (Table 10.9). A flow rate of 6 gpm through the pilot reactor closely matched these conditions with 8.8% projected to be removed from a 2.6 mg/L concentration of H_2O_2 and 2.6 mg/L of total chlorine in the feedwater.

Table 10.9. Comparison of Pilot UV Reactor and Full-Scale Reactor Performance

Pilot Reactor Flow Rate (gpm)	Projected Pilot H_2O_2 Consumed/Feed mg/L/mg/L (%)	Single-Lamp Pilot Reactor EED (kWh/kgal)	UVPhox H_2O_2 Consumed/Feed mg/L/mg/L (%)	72 Lamp UVPhox Average EED (kWh/kgal)
5	0.40/3.0 (13%)	0.857	0.4/3.0 (13%)	0.308
6	0.23/2.6 (8.8%)	0.714	0.2/2.6 (7.7%)	0.290

Operation of the pilot reactor under these conditions in conjunction with spike studies allows for future projections of contaminant removal by the full-scale reactors without having to spike the RO permeate feedwater to the UV/AOP facility of the AWPF, which is prohibited.

10.8.4 Multiple Linear Regression Pilot Models for 1,4-Dioxane Removal from RO Permeate by UV/H_2O_2 AOP

The relationship between the experimental parameters and removal of 1,4-dioxane was investigated using multiple linear regression. Twenty-six water quality parameters also were used to characterize the AOP (Table 10.10).

Table 10.10. Parameters Used to Characterize and Model the AOP

Parameter	Abbreviation	Parameter	Abbreviation
H_2O_2 Feed	[H2O2]	NH_3-N Feed	[NH3-N]
H_2O_2 Consumed	[H2O2 Used]	NO_3-N Feed	[NO3-N]
Percent H2O2 Used	[PCT H2O2 Used]	HCO_3 Feed	[HCO3]
1,4-dioxane Feed	[F 14D]	Total Alkalinity Feed	[TOTALK]
1,4-dioxane Product	[P 14D]	pH Feed	[F pH]
Total Cl2 Feed	[F Cl2]	pH Product	[P pH]
Total Cl2 Product	[P Cl2]	UVT Feed	[F UVT]
Total Cl2 Removed	[Mass Cl2]	UVT Product	[P UVT]
1,4-dioxane Logs Removed	[Log 14D]	UV Fluorescence Feed Control	[CF Fluor]
Total Cl2 Logs Removed	[Log Cl2]	UV Fluorescence Product Control	[CP Fluor]
TOC Feed	[TOC]	UV Fluorescence Feed	[F Fluor]
Flow Rate	[F Fluor]	UV Fluorescence Product	[P Fluor]
		Fraction of Fluorescence Removed	[Red Fluor]

The raw data are displayed in Table E.1 in Appendix E. A number of models were generated from the data set (Eqs. 10.19–10.25). These models of the pilot UV reactor produced the best fit:

- Mass of 1,4-dioxane removed
- Log 1,4-dioxane removed
- Mass of hydrogen peroxide used
- Percent hydrogen peroxide used
- Mass total chlorine removed
- Log total chlorine removed
- Fluorescence signal reduction

Mass of 1,4-Dioxane Removed

$$\textbf{Mass 14DIOX} = -3.047 + 2.408 \times \textbf{[H2O2]} + 0.621 \times \textbf{[F 14DIOX]} + 2.464 \times \textbf{[F Cl2]} - 0.0142 \times \textbf{[F Fluor]} \quad (10.19)$$

Log 1,4-Dioxane Removed

$$\textbf{Log 14D} = 0.435 + 0.155 \times \textbf{[H2O2]} - 0.0580 \times \textbf{[Flow]} \quad (10.20)$$

Mass of Hydrogen Peroxide Used

$$\textbf{H2O2 Used} = 0.0236 + 0.136 \times \textbf{[H2O2]} \quad (10.21)$$

Percentage of Hydrogen Peroxide Used

$$\textbf{PCT H2O2 Used} = 31.881 - 3.791 \times \textbf{[Flow]} \quad (10.22)$$

Mass Total Chlorine Removed

$$\textbf{Mass Cl2} = 3.526 - 0.2190 \times \textbf{[Flow]} - 0.00722 \times \textbf{[F 14D]} + 0.6737 \times \textbf{[F Cl2]} - 0.3798 \times \textbf{[F pH]} \quad (10.23)$$

Log Total Chlorine Removed

$$\textbf{Log Cl2} = -2.596 - 0.2035 \times \textbf{[Flow]} + 0.1895 \times \textbf{[F Cl2]} - 0.04743 \times \textbf{[TOTALK]} - 0.007478 \times \textbf{[F 14D]} \quad (10.24)$$

Fluorescence Signal Reduction

$$\textbf{Red Fluor} = 0.2403 + 0.01596 \times \textbf{[F Fluor]} \quad (10.25)$$

10.8.5 Conclusions

A pilot reactor that housed the same LPHO Hg UV lamp used in the UVPhox was used to mimic the performance of the full-scale AOP. A series of experiments were conducted at various H_2O_2 concentrations and flow rates (i.e., varying the EED) through the reactor. A number of linear regression models were generated from the pilot data that mimicked the performance of the full-scale reactor at different flow rates. A model of H_2O_2 photolysis was generated that indicated that 0.2 mg/L H_2O_2 is consumed from an RO permeate feedwater with a UVT of ~97 %T, containing 2.6 mg/L H_2O_2 in the presence of ~2.6 mg/L of total residual chlorine (that consists of 50% (w/v) monochloramine and 50% dichloramine) at a flow rate of 6 gpm. The consumption of 0.2 mg/L of H_2O_2 across the pilot reactor running at a flow rate of 6 gpm and a lamp powered at a BPL of 100% was consistent with the operation of the full-scale UV/AOP facility of the AWPF that consumed 0.2 mg/L of H_2O_2 from an RO permeate feedwater that containing ~2.6 mg/L of H_2O_2, ~2.6 mg/L of total chorine, and a UVT of ~97% operating at an average EED of 0.290 kWh/kgal. A linear regression model from data generated from the pilot studies predicted 0.5-log reduction of 1,4-dioxane from RO permeate with 2.6 mg/L of total chlorine (chloramines), a UVT of ~97 %T, and 2.6 mg/L of H_2O_2 operated at 6 gpm (equivalent to operating the full-scale EED of 0.290 kWh/kgal).

The full-scale 1,4-dioxane removal data, collected over a 5-year period under varying operating conditions, indicated 0.5 logs of reduction (one significant figure). However, the determination of the log removal required the use of UV product water data that did not meet the standards of the AWQA laboratory at a reportable level. Seventeen of the 18 UVP samples for 1,4-dioxane were recorded below the 1 μg/L RDL of the method. A median removal of 0.43 logs and an average of 0.45 logs removal of 1,4-Dioxane was measured (n = 18).[6] The corresponding EE/O for this small set of data was 0.658 ± 0.132 kWh/kgal/log.

[6] CDPH (Pacifico, 2009) approved 0.45-logs reduction of 1,4-dioxane to be rounded off to one significant figure representing 0.5-logs reduction of 1,4-dioxane for the conditional permit to operate the UV/H_2O_2 AOP facility of

The single UVF/UVP sample pair that had a reportable concentrations of 1,4-dioxane had an EE/O of 0.604 kWh/kgal/log.

The effective UV dose delivered by a 72-lamp UVPhox reactor of the AWPF was estimated to be 3274 mJ/cm^2 per kWh/kgal based on a combination of published collimated beam data (Souroushian et al., 2001) and historical full-scale UVPhox NDMA removal data (Brown, 2008). On the basis of the estimated UV dose per EED, a UV Phox reactor train operating at an EED of 0.26 kWh/kgal on the RO permeate with ~2.6 mg/L of combined chlorine (measured by online amperometric analyzer), an average 2.6 mg/L of H_2O_2, and a UVT ~97 to 98 %T at 254 nm, would deliver an estimated effective UV dose of 850 mJ/cm^2.

Application of a measured 2.6 mg/L residual of H_2O_2 in the feedwater to the full-scale UVPhox operating at an EED of 0.290 kWh/kgal, containing ~2.6 mg/L total residual chlorine with a UVT of ~97 %T would result in a measured 0.51-logs reduction of 1,4-dioxane based on the predictive model of the pilot UV reactor. An additional 0.15 logs 1,4-dioxane removal could be achieved per each additional 1 mg/L of H_2O_2 added to the feedwater to the full-scale UVPhox reactor operating at an EED of 0.290 kWh/kgal.

---

the AWPF at a minimum 0.23 kWh/kgal and minimum 2.6 mg/L of H_2O_2 in the feedwater rounded to one significant figure of 3 mg/L (Bernados, 2009).

Chapter 11

Analysis of Volatile Organic Compounds Associated with the UV/H_2O_2 AOP

11.1 Introduction

UV/H_2O_2 AOP is applied to the ROP as a final polishing step of the purification process of the AWPF. The purpose of this non-targeted study was to begin the difficult process of characterizing the TOC (50–75 μg/L) in the RO permeate, potentially identifying new disinfection byproducts, and determine the possibility of identifying of a new class (or group) of reaction by-products through the UV/H_2O_2 AOP process. UV product water was collected and analyzed by a modified purge-and-trap GC/MS method for volatile organic compounds (VOCs). Samples were collected before and immediately after the RO and after the UV/H_2O_2 process. Preliminary studies indicated that indeed, a new class of reaction by-products, alkyl (methyl, ethyl, and isopropyl) nitrates, were formed, and then further studies were conducted to verify their existence and to estimate the concentration in solution. Currently no human or environmental health water quality standards have been established for these alkyl nitrates.

11.2 Materials and Methods

11.2.1 Sample Collection

Water samples were collected from three sites, ROF, ROP, and UVP (Table 11.1) in 40 mL amber glass Teflon-lined screw cap vials with and without quencher (~10 mg sodium thiosulfate) and no head space. Two or four replicates were collected together with one travel blank at each of the three sample stations. Travel blanks consisted of E-pure deionized water (Barnstead, ThermoScientific) collected in 40 mL amber vials in advance and transferred into new vials at each site. These experiments were conducted on three different dates: Set 1: October 24, 2012, Set 2: December 19, 2012, and Set 3: December 26, 2012.

Table 11.1. Survey of VOCs Across RO and UV/AOP

	AWPF Sample Station		
Sample Treatment	**ROF**	**ROP**	**UVP**
With $Na_2S_2O_3$ quencher	Travel blank × 1 ROF × 2	Travel blank × 1 ROP × 2	Travel blank × 1 UVP × 2
No quencher	Travel blank × 1 ROF × 2	Travel blank × 1 ROP × 2	Travel blank × 1 UVP × 2

11.2.2 Sample Preparation

The analytical system that was used for this portion of the project was designed for gas samples (Colman et al., 2001; Sive, 1998). Therefore, a system was designed to transfer volatile organic compounds in water samples to a 1.9 L stainless steel canister (Figure 11.1). The glass vessel for purging or degassing was flushed with ultra pure helium (UPH) for

10 min at a flow rate of 80 mL/min. The glass vessel was then pressurized with UPH to 760 torr that took ~24 min to fill. Nine mL of water sample was injected into the glass vessel and then flushed with UPH at 80 mL/min until 760 torr of degassed sample was collected in the stainless steel canister at room temperature.

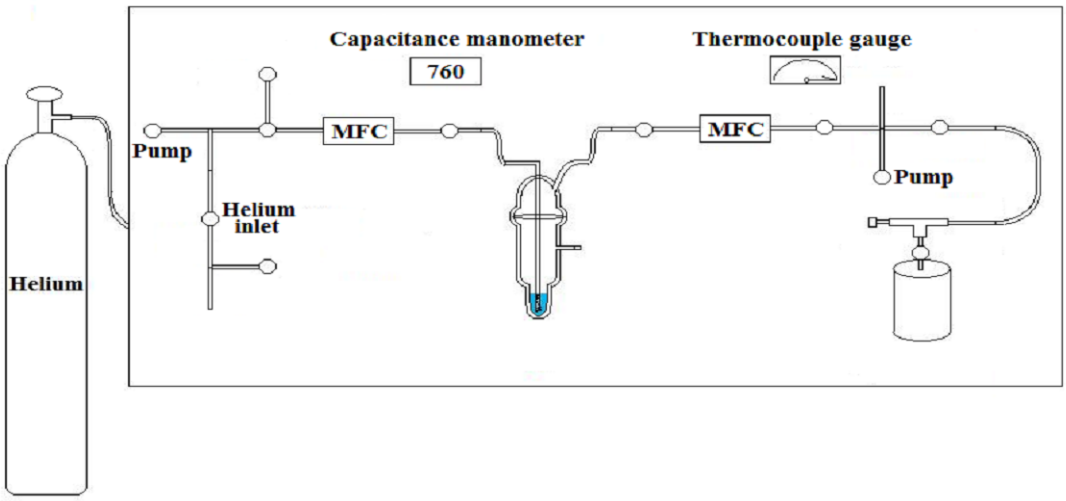

Figure 11.1. Purging/degassing system used to capture volatile organic compounds in water samples for GC/MS analysis.

The analysis was completed by transferring 500 torr of the sample from the 1.9 L canister into a gas chromatograph equipped with a mass selective detector. This system was a modified version of the full analytical system for measuring atmospheric VOCs.

11.2.3 Calculation of VOC Concentration from Purged Sample Mixing Ratio

A total of 760 torr of degas sample was collected at STP from a 9 mL water sample.

$$\text{Alkyl Nitrate (moles)} = \frac{\text{mixing ratio (L/L)} \times P_t\ \text{(atm)} \times V_t\ \text{(L)}}{R\ (\text{L} \cdot \text{atm} \cdot \text{mole}^{-1} \cdot \text{K}^{-1}) \times T\ \text{(K)}}$$

$$\text{Alkyl Nitrate (ng/L)} = \frac{\text{alkyl nitrate (mole)} \times \text{M.W.(g/mole)} \times 10^9\ \text{(g/ng)}}{\text{volume (L)}}$$

An example calculation is displayed below for methyl nitrate from a sample from Set 3. The average methyl nitrate measured in unquenched UVP, purged samples was 740 ± 30 ng/L (ppt),

The moles of methyl nitrate in the degassed sample,

$$\frac{740(\text{L})/10^{12}(\text{L}) \times 1\,(\text{atm}) \times 1.9(L)}{0.08206\,(\text{L} \cdot \text{atm} \cdot \text{K}^{-1} \cdot \text{mol}^{-1}) \times 298.15(\text{K})} = 5.8 \times 10^{-11} \text{ mole methyl nitrate}$$

Concentration of methyl nitrate in water,

$$\frac{5.8 \times 10^{11}\ (\text{mole}) \times 77.04\ (\text{g/mole}) \times 10^9\ (\text{g/ng})}{0.009\,(\text{L})} = 490 \pm 20 \text{ ng/L methyl nitrate}$$

Concentration in water sample corrected with purging efficiency of 90 ± 8% for methyl nitrate,

$$(490 \pm 20 \text{ ng/L}) / (90 \pm 8) \times 100 = 540 \pm 60 \text{ ng/L methyl nitrate}$$

11.3 Results and Discussion

11.3.1 RO Permeate Water Quality Data

A small amount of RO permeate water quality data were recorded from the online analyzers at the time the source waters were grabbed. The data are displayed in Table 11.2. Historical ROP water quality data is presented in Chapter 3. The average H_2O_2 concentration in the UVF feedwater (ROP containing H_2O_2) to the UV/AOP facility was 2.6 mg/L.

Table 11.2. RO Permeate Water Quality Data

Sample Date	EED (kWh/kgal)	pH	UVT (%)	TOC (mg/L)	Total Cl_2 (mg/L)
Set 1 10/24/12	0.284	5.60	97.8	54.1	3.10
Set 2 12/19/12	0.266	5.56	97.8	29.7	2.75
Set 3 12/26/12	0.264	5.54	98.1	30.0	2.97

11.3.2 Methyl Nitrate

The quantitation of methyl nitrate from the purged samples are summarized in Table 11.3 and plotted in Figures 11.2 and 11.3. The concentration of methyl nitrate in the all three of the travel blanks (ROF, ROP, and UVP) were below the MDL of 1 ppt.

Table 11.3. Methyl Nitrate Concentration in ROF, ROP, and UVP Source Waters from the AWPF

Sample Date	Quenching Agent	Travel Blank[a] (ng/L)	ROF (ng/L)	ROP (ng/L)	UVP (ng/L)
Set 1	Yes	<1	18 ± 2	15 ± 1	640 ± 60
10/24/12	No	<1	40 ± 4	16 ± 1	620 ± 60
Set 2	Yes	<1	12 ± 1	10 ± 1	470 ± 40
12/19/12	No	<1	18 ± 2	11 ± 1	450 ± 50
Set 3	Yes	<1	11 ± 1	18 ± 2	590 ± 60
12/26/12	No	<1	20 ± 2	16 ± 2	550 ± 6

Notes: Average ± standard deviation (n = 2).

[a] Travel blanks for ROF, ROP, and UVP.

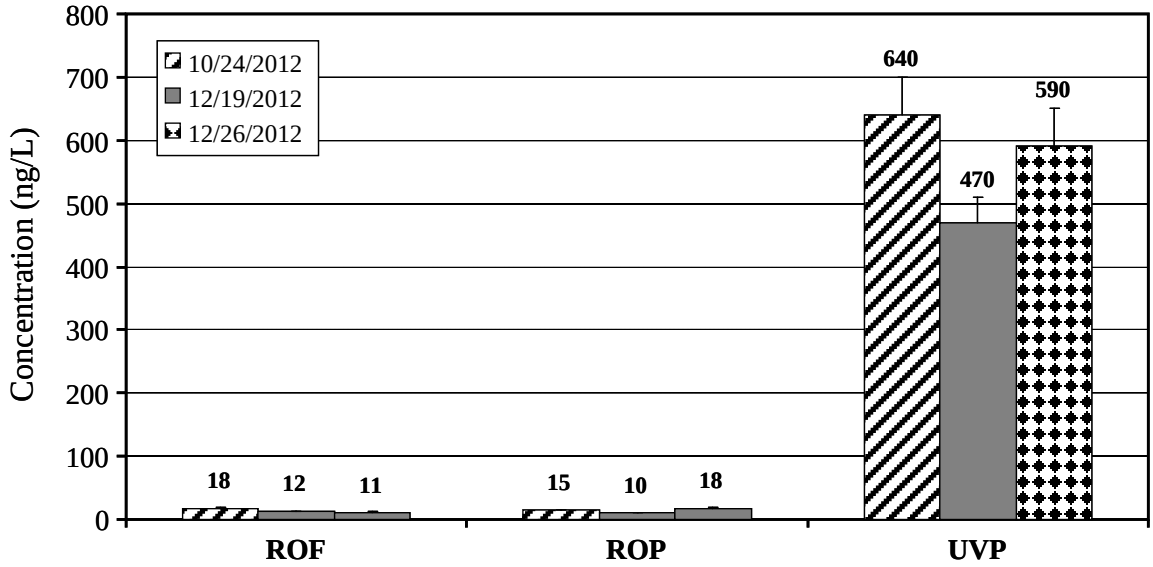

Figure 11.2. Plot of the methyl nitrate concentration (ng/L) recovered from in ROF, ROP, and UVP water samples that were quenched with ~10 mg sodium thiosulfate.

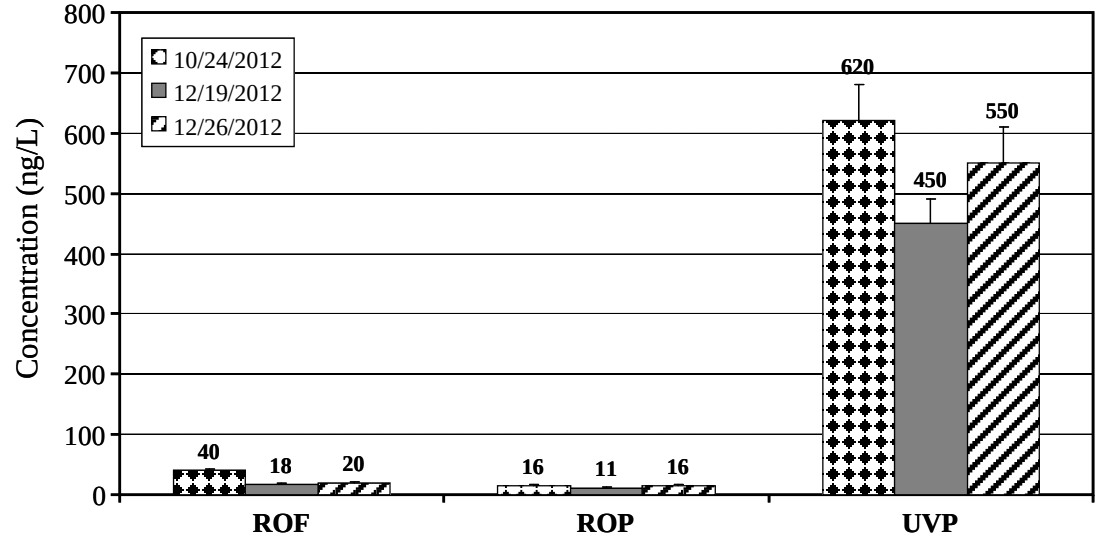

Figure 11.3. Plot of the methyl nitrate concentration (ng/L) recovered from in ROF, ROP, and UVP samples that were *not* quenched.

Small quantities (10–40 ng/L) of methyl nitrate were present in the feed and product water of the RO process. The sodium thiosulfate used to quench the combined chlorine appeared to have an effect on the methyl nitrate recovered from the ROF. Significantly less methyl nitrate was recovered from ROF samples that were quenched. Between 0.1 and 0.4 logs (20–60%) removal of methyl nitrate was achieved across the RO process. Similar quantities of methyl nitrate were recovered in the RO permeate for both quenched and unquenched samples that further indicated that the sodium thiosulfate has an impact on the recovery of methyl nitrate from the RO feedwater. The pH of the MF effluent is adjusted with sulfuric acid to 6.8, and a proprietary antiscalant is added at a concentration of 3.5 mg/L. At this time, it is not known why the thiosulfate inhibits the recovery of methyl nitrate from the RO feedwater.

The methyl nitrate concentration in the UV product water (UVP) increased significantly over the concentration recovered from the ROP (see Table 11.3 and Figures 11.2 and 11.3). The methyl nitrate concentration in the quenched UVP increased 33 to 47 times over the concentration recovered from the quenched ROP sample and increased by a factor of 34 to 41 times in the unquenched UVP sample. This data indicate that it is a disinfection byproduct that has heretofore not been reported.

11.3.3 Ethyl Nitrate

The data for the analysis of ethyl nitrate are summarized in Table 11.4 and Figures 11.4 and 11.5. All of the travel blanks report out at a concentration less than 1 ng/L (i.e. below the MDL). Except for one sample, the sodium thiosulfate quenching did not have an impact on the ethyl nitrate recovered from the RO permeate. The data indicated that 0.10 to 0.27 logs (20– 45%) of ethyl nitrate were removed from the RO feedwater by the RO process in the nonquenched samples. The data from the quenched ROF and ROP samples is less clear with two ROF/ROP pair showing a decrease and one pair unchanged. There appeared to be an increase in ethyl nitrate formed across the UV/AOP process, although the concentration was far less than that of methyl nitrate. The concentration of the ethyl nitrate increased by 100% to 128% across the UV/AOP in the samples collected in October. The increase was not as great for the two December samples, increasing 17% to 75% for the quenched samples and 50% to 60% for the nonquenched samples. The ROP water quality data on the three sample dates were similar except for the TOC concentration on October 24, which was ~24 μg/L higher than the December ROP samples. The ROP grab on the October day may have contained a larger concentration ethyl nitrate precursors or possibly a greater quantity of oxidants were present or formed inside the UV/AOP reactors.

Table 11.4. Ethyl Nitrate Concentration in ROF, ROP, and UVP Source Waters from the AWPF

Sample Date	Quenching Agent	Travel Blank[a] (ng/L)	ROF (ng/L)	ROP (ng/L)	UVP (ng/L)
Set 1	Yes	<1	9 ± 1	7 ± 1	16 ± 1
10/24/12	No	<1	13 ± 1	7 ± 1	14 ± 1
Set 2	Yes	<1	6 ± 1	6 ± 1	7 ± 1
12/19/12	No	<1	7 ± 2	5 ± 0.4	8 ± 1
Set 3	Yes	<1	5 ± 0.4	4 ± 0.3	7 ± 1
12/26/12	No	<1	5 ± 0.4	4 ± 0.5	6 ± 0.5

Notes: Average ± standard deviation (n = 2).

[a] Travel blanks for ROF, ROP, and UVP.

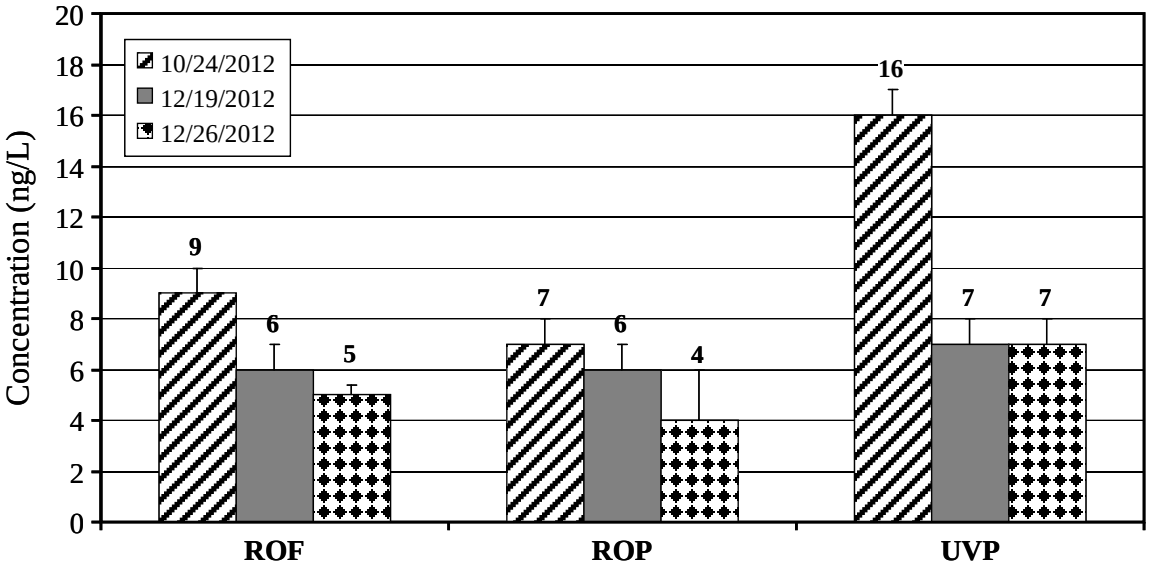

Figure 11.4. Plot of the ethyl nitrate concentration (ng/L) recovered from in ROF, ROP, and UVP samples that were quenched with ~10 mg sodium thiosulfate.

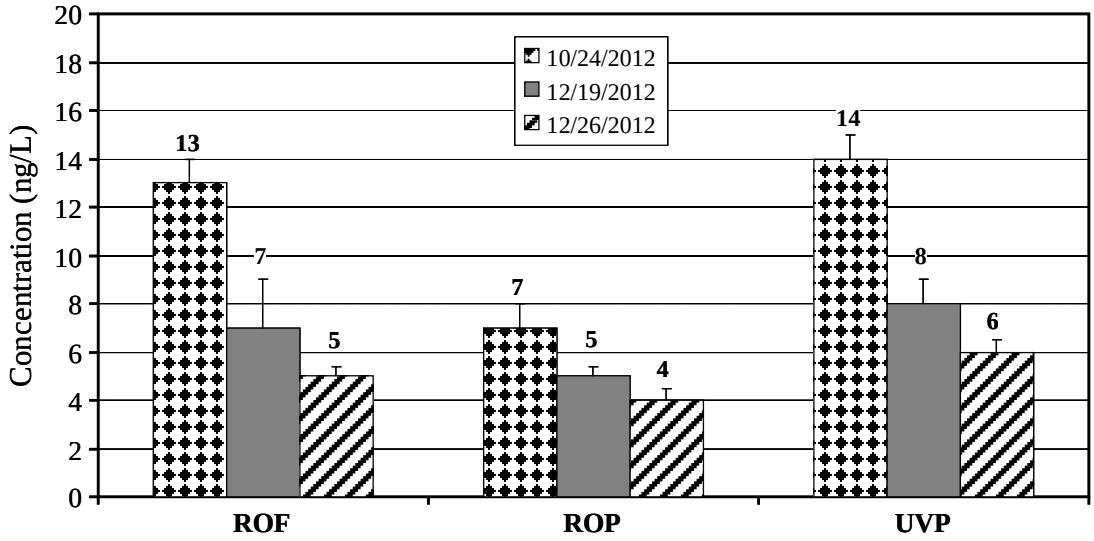

Figure 11.5. Plot of the ethyl nitrate concentration (ng/L) recovered from in ROF, ROP, and UVP samples that were *not* quenched.

11.3.4 Isopropyl Nitrate

The data for the analysis of isopropyl nitrate are summarized in Table 11.5 and the data are plotted in Figures 11.6 and 11.7. The concentrations of isopropyl nitrate in the travel blanks were less than the 1 ng/L MDL.

Table 11.5. Isopropyl Nitrate Concentration in ROF, ROP, and UVP Source Waters from the AWPF

Sample Date	Quenching Agent	Travel Blank[a] (ng/L)	ROF (ng/L)	ROP (ng/L)	UVP (ng/L)
Set 1	Yes	<1	6 ± 1	2 ± 0.3	8 ± 1
10/14/12	No	<1	11 ± 2	2 ± 0.3	7 ± 1
Set 2	Yes	<1	4 ± 1	1 ± 0.2	5 ± 1
12/19/12	No	<1	6 ± 1	1 ± 0.2	5 ± 1
Set 3	Yes	<1	3 ± 0.4	1 ± 0.2	5 ± 1
12/26/12	No	<1	5 ± 0.7	1 ± 0.2	5 ± 0.7

Notes: Average ± standard deviation (n = 2).

[a] Travel blanks for ROF, ROP, and UVP.

The data indicated that there is a small amount of isopropyl nitrate removal across the RO process with 0.5–0.6 logs (68–75%) removal from the quenched samples and 0.70–0.78-logs (80–83%) removal from the unquenched RO feedwater samples. The concentration, which was very low in the ROF (near the MDL) did appear to increase after the application of UV/H_2O_2 AOP. There was approximately a four-fold increase in the isopropyl nitrate concentration in both quenched and nonquenched UVP water samples with slightly more formed in the October 24 samples as observed with ethyl nitrate.

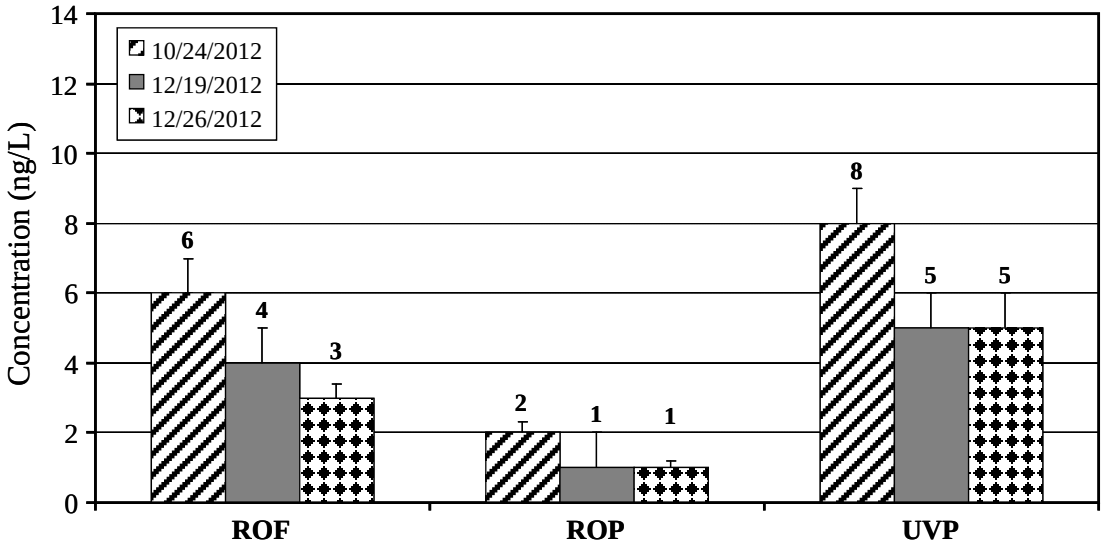

Figure 11.6. Plot of the isopropyl nitrate concentration (ng/L) recovered from in ROF, ROP, and UVP samples that were quenched with ~10 mg sodium thiosulfate.

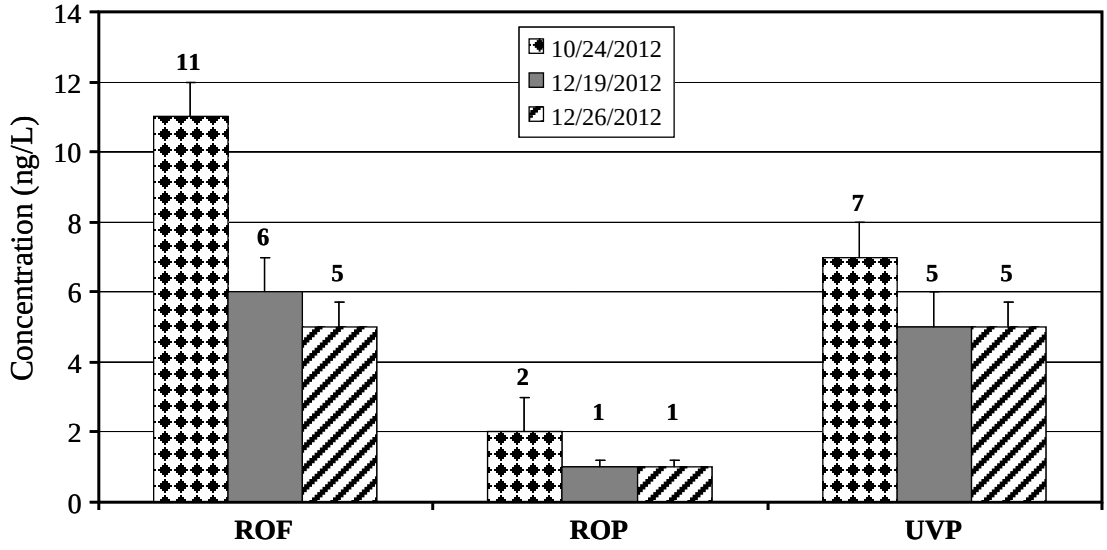

Figure 11.7. Plot of the isopropyl nitrate concentration (ng/L) recovered from in ROF, ROP, and UVP samples that were *not* quenched.

11.3.5 Formation of Alkyl Nitrates

Alkyl nitrates have been observed in natural waters, such as seawater (Ballschmiter, 2002; Dahl et al., 2007; Moore and Blough, 2002), snow (Hauff et al., 1998), and air (Blake et al., 2003; Simpson et al., 2002). In the atmosphere, one of the pathways of the reaction of alkyl peroxyl radicals ($ROO^{\bullet}$) with nitric oxide ($NO^{\bullet}$) radicals generates alkyl nitrates (Eqs. 11.1 and 11.2)

$$ROO^{\bullet} + NO^{\bullet} \rightarrow RO + NO_2 \qquad k_{1a} \qquad (11.1)$$

$$ROO^{\bullet} + NO^{\bullet} \rightarrow RONO_2 \qquad k_{1b} \qquad (11.2)$$

$$\alpha = k_{1b} / (k_{1a}+k_{1b}) \qquad (11.3)$$

Chuck et al. (2002) measured methyl nitrate and ethyl nitrate levels in seawater and air samples. The mixing ratio for both methyl and ethyl nitrates were elevated in marine air samples compared to the continental air samples. The concentrations for methyl and ethyl nitrates in seawater were significantly higher than the values calculated from Henry's Law constant, which implied that there was a source of alkyl nitrate in the seawater. Based on the relationship of methyl and ethyl nitrates and their correlation with algae, Chuck et al. (2002) proposed that the mechanism of formation of methyl and ethyl nitrates were similar and likely to result from biogenic processes.

Moore and Blough (2002) proposed a radical reaction mechanism for the formation of marine alkyl nitrates. Nitric oxide (NO) radicals were generated from the photolysis of nitrite (NO_2^-). Zafiriou and McFarland, (1981) and Moore and Blough (2002) also proposed that chromophoric dissolved organic matter (CDOM) were the primary source of alkyl radicals, which then reacted with oxygen to generate alkyl peroxyl radicals. The reaction of alkyl peroxyl radicals and NO radicals produced alkyl nitrates in the seawater. Dahl et al. (2012)

studied how the content of dissolved organics matter (DOM) may affect the ratios of alkyl nitrates (methyl, ethyl, isopropyl nitrates) in seawater. The observed effect may be a result of the change in ratios of alkyl peroxyl radicals with changes in the DOM (Johnson et al., 1996; Kieber and Blough, 1990).

The radical reaction mechanism for alkyl nitrates involving aqueous nitrite, alkane, oxygen, and irradiation is the only one that has been confirmed. Dahl et al. (2007) examined the radical mechanism in both natural waters and Milli-Q water with UV irradiation (see eqs. 11.4 through11.9 below). Methyl, ethyl, and isopropyl nitrates were successfully generated, thus confirming the feasibility of the alkyl peroxy radical and nitric oxide radical mechanism. The results from the work of Dahl et al. (2007) also demonstrated that the branching ratios are higher in the aqueous solution than in the atmosphere.

$$H_2O_2/HO_2^- + h\nu \rightarrow 2\ HO^\bullet \quad (11.4)$$

$$NO_2^- + H_2O \rightarrow NO^\bullet + HO + OH^- \quad (11.5)$$

$$R\text{-}H + HO^\bullet \rightarrow R^\bullet + H_2O \quad (11.6)$$

$$R^\bullet + O_2 \rightarrow RO_2^\bullet \quad (11.7)$$

$$RO_2^\bullet + NO^\bullet \rightarrow RO + NO_2 \quad (11.8)$$

$$RO_2^\bullet + NO^\bullet \rightarrow RONO_2 \quad (11.9)$$

Recently, nitrite has not been detected in the ROP and UVP of the AWPF operating at an EED near 0.290 kWh/kgal. However, nitrite (5–25 μg/L) in UVP has been detected in the past when the EED reached 0.30 kWh/kgal and above.

11.4 Summary

A purging or degassing system for the GC/MS analysis of atmospheric VOCs was modified to measure VOCs in water samples. This study showed that alkyl nitrates are present in ROF, ROP, and UVP source waters of the AWPF. The analysis of RO feedwater indicates that there are small amounts (on the order of μg/L or ppt) of methyl, ethyl, and isopropyl nitrates present in the source water. The amount recovered by the helium purge and GC/MS analysis varied from day to day. Quenching of the ROF samples with sodium thiosulfate resulted in a slight reduction in the recovery of all three alkyl nitrates from the ROF. The sodium thiosulfate quenching agent did not appear to affect the recovery of the alkyl nitrates from the ROP and UVP water samples.

The RO process removed a portion of all three alkyl nitrates from the feedwater—methyl nitrate 0.1 to 0.4-logs reduction, ethyl nitrate 0.10 to 0.27-logs reduction, and isopropyl nitrate 0.48 to 0.78-logs reduction. However, a significant increase in the methyl nitrate concentration was measured in the UV/H_2O_2 AOP product water. The methyl nitrate concentration increased by a factor of 34 to 41times in the unquenched UVP water samples and by 33 to 47 times in the quenched UVP samples. The ethyl nitrate concentration increased 17% to 75% in the quenched samples and 50% to 100% in the unquenched UVP samples. The appendix nitrate concentration increased four-fold across the UV/H_2O_2 AOP in both the quenched and unquenched samples. Although these observed changes in alkyl nitrate concentration were consistent on each sampling date, the variation in concentrations reflected

differences in the source water content on different days. Currently there are no human or environmental health water quality standards established for these alkyl nitrates, and the fate of these volatile compounds in the FPW has not been determined.

11.5 Recommendations

These results suggest that additional basic research should be conducted to determine the presence and formation mechanisms of these alkyl nitrate compounds. The extent to which the alkyl nitrates are removed by the decarbonation process downstream of the UV/H_2O_2 AOP, the quantity that remains in the FPW, and the FPW at the end of the 13-mile GWRS pipeline at the recharge basins in Anaheim are not known and should be determined.

Chapter 12

Removal of Trace Contaminants from RO Concentrate[8]

12.1 Introduction

The AWPF recycles wastewater using MF, RO, and UV/H_2O_2. The RO brine or concentrate from the AWPF is returned to OCSD for discharge to an ocean outfall. Concern over the impact of pollutants from ocean outfalls has warranted further investigation into the application of AOPs to treat wastewater effluents. Several studies on the degradation of PPCPs from RO concentrate (ROC) using ozonation have appeared in the literature (Lee et al., 2009; Westerhoff et al., 2009; Benner, et al., 2008); however, there are no detailed kinetic and/or modeling studies of $^{\bullet}OH$-mediated degradation of PPCPs in ROC.

The ROC was screened for 27 pharmaceutical and trace organic compounds using solid-phase extraction (SPE) and ultra performance liquid chromatography (UPLC)-MS/MS. Of the 27 compounds, 18 were identified from the RO brine at µg/L (ppb) concentrations, high enough that they could provide insight into the utility of AOP treatment without having to "spike" the source water. Samples of ROC were subjected to γ-irradiation at various absorbed doses under N_2O saturated solutions. The N_2O was used to isolate $^{\bullet}OH$ as the only oxidant while the absolute secondary reaction rate constants were used to estimate the initial degradation rates before reactions with breakdown products became a significant contributing factor.

The development of surrogate indicators for the assessment of the removal efficiency of PPCPs during AOP operations was a second objective of this study (Dickenson et al., 2009). Absorption in the UV at 254 nm has been correlated with the degree of removal of many endocrine disrupting compounds (Wert et al., 2009a; Wert et al., 2009b; Nanaboina and Korshin, 2010). However, excitation-emission matrix (EEM) fluorescence spectroscopy of ROC and the potential changes in the fluorescence spectra have not been explored.

12.2 Materials and Methods

The detailed analytical experimental methods have been summarized in Abdelmelek et al. (2011). Steady-state γ-irradiation of ROC was employed under N_2O saturated conditions to investigate the kinetic details of PCPPs removal by AOP. Bimolecular reaction rate constants between $^{\bullet}OH$ and PPCPs and the EfOM in ROC were determined by competition kinetics with thiocyanate (SCN^-) based on the monitoring of $(SCN)_2^{\bullet-}$ absorption at 472 nm. (Note: ROC EfOM is a simplification of the total combined organic and inorganic constituents in the ROC.) At the time this study was completed, OCSD was treating the activated sludge by CBOD and the feedwater to the AWPF consisted of a blend of 20% trickling filter effluent

[8] A major portion of this chapter was reprinted with permission from Removal of Pharmaceutical and Personal Care Products from Reverse Osmosis Retentate Using Advanced Oxidation Processes, Sihem Ben Abdelmelek, John Greaves, Kenneth P. Ishida, William J. Cooper, and Weihua Song, *Environ. Sci. Technol.* **2011**, *45*, 3665–3671. Copyright 2011. American Chemical Society.

and 80% activated sludge effluent. In November 2009, OCSD switched to a nitrification-denitrification treatment process of the activated sludge.

12.3 Results and Discussion

12.3.1 Screening of PPCPs in the RO Concentrate

The chemical characteristics of the RO concentrate used for this study are summarized in Table 12.1. A total of 27 PPCPs (Table 12.2) were screened as they are frequently detected in treated wastewater effluent (Kolpin et al., 2002). Of the 27 compounds, 18 compounds were identified in the ROC with concentrations that ranged from 0.1 to 7.9 µg/L (Table 12.2). Those detected at the highest concentrations were gemfibrozil, naproxen, erythromycin, and atenolol, in agreement with other studies suggesting that conventional biological treatment is relatively inefficient in removing these compounds (Kim et al., 2007; Westerhoff et al., 2005).

Table 12.1. Water Quality of the RO Concentrate[a]

Parameter	Value/Concentration
pH	7.59
Total dissolved solids (TDS)	5985 mg/L
Na^+	1305 mg/L
Mg^{2+}	148 mg/L
Ca^{2+}	513 mg/L
K^+	107 mg/L
SO_4^{2-}	1759 mg/L
PO_4^{3-}	4.00 mg/L
Ammonia[b]	24.5 mg/L as N
Nitrite[b]	0.45 mg/L as N
Nitrate[b]	1.68 mg/L as N
Total Hardness	1904 mg/L as CaCO3
Alkalinity	684 mg/L as CaCO3

Notes: [a]Average historical data from January 2008 to October 2009. ROC sample was collected at August 19, 2009. [b]Concentration measured in the RO feed water (not in the ROC).

Table 12.2. The Concentrations of the Targeted Compounds in RO Concentrate

Compounds	IDL[a] (µg/L)	R_0[b] (µg/L)
Atenolol	0.2	2.634
Atorvastatin	0.1	ND
Caffeine	0.1	0.708
Carbamazepine	0.01	0.134
Cimitidine	0.2	ND
5,5 Diphenylhydantoin	0.1	0.145
DEET	0.01	0.766
Enrofloxacin	0.01	ND
Erythromycin	0.1	7.984
Famotidine	0.2	2.1
Gemfibrozil	0.02	6.979
Iohexol	0.1	2.400
Iomeprol	0.1	0.386
Iopamidol	0.2	2.626
Iopromide	2	ND
Lovastatin	0.1	ND
Metoprolol	0.1	0.470
Nalidixic Acid	0.01	0.189
Naproxen	0.02	1.416
Ofloxacin	0.01	0.299
Ranitidine	2	ND
Sulfamethoxazole	0.4	0.437
Sulfamethazine	0.1	ND
Sulfamethizole	0.5	ND
Sulfamerazine	0.1	ND
Trimethoprim	0.4	1.124
Venlafaxine	0.2	0.333

Notes: [a]instrumental detection limit; [b]initial concentration; ND = not detected

Table 12.3. Selected Pharmaceutical Compounds, their Structures, Bimolecular $^{\bullet}$OH Reaction Rate Constants, and Experimental and Calculated Degradation Rates

Name	Structure	Initial Concentration (nM)	Experimental Degradation Rate (nM/min)	Calculated Degradation Rate (nM/min)	$^{\bullet}$OH Radical Reaction Rate Constant (M^{-1} s^{-1})
Atenolol	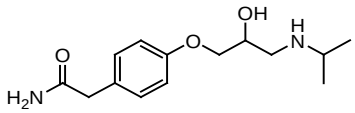	9.90	0.533	0.484	7.05×10^9 (Song et al., 2008)
Caffeine	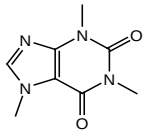	3.64	0.194	0.215	8.5×10^9 (Vinchurkar et al., 1999)
Carbamazepine	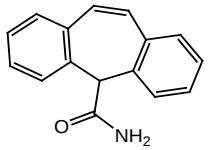	0.566	0.0344	0.0345	8.80×10^9 (Huber et al., 2003)
DEET	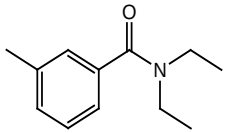	3.19	0.15	0.11	4.95×10^9 (Song et al., 2009)
Erythromycin	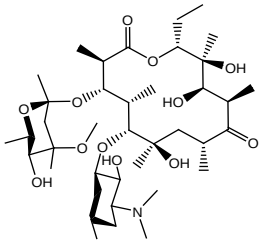	10.9	0.225	0.226	*3.00×10^9

Table 12.3. Selected Pharmaceutical Compounds, their Structures, Bimolecular $^{\bullet}$OH Reaction Rate Constants, and Experimental and Calculated Degradation Rates

Name	Structure	Initial Concentration (nM)	Experimental Degradation Rate (nM/min)	Calculated Degradation Rate (nM/min)	$^{\bullet}$OH Radical Reaction Rate Constant (M^{-1} s^{-1})
Gemfibrozil	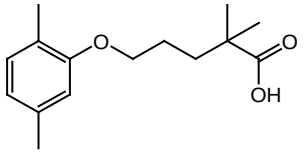	27.9	1.65	1.93	1.00×10^{10} (Razavi et al., 2009)
Metoprolol	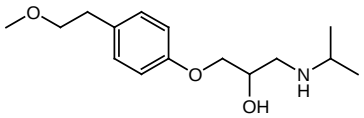	1.37	0.0736	0.0796	8.39×10^{9} (Song et al., 2008)
Naproxen	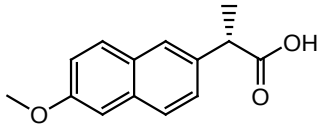	6.21	0.325	0.344	*7.99×10^{9}
Nalidixic Acid	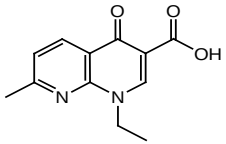	0.81	0.0379	0.0395	*6.74×10^{9}
Ofloxacin	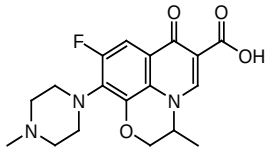	0.83	0.0426	0.0440	7.66×10^{9} (Santoke et al., 2009)

Table 12.3. Selected Pharmaceutical Compounds, their Structures, Bimolecular $^{\bullet}$OH Reaction Rate Constants, and Experimental and Calculated Degradation Rates

Name	Structure	Initial Concentration (nM)	Experimental Degradation Rate (nM/min)	Calculated Degradation Rate (nM/min)	$^{\bullet}$OH Radical Reaction Rate Constant (M^{-1} s^{-1})
Trimethoprim	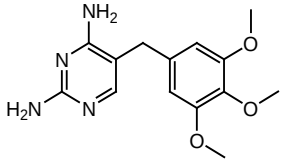	9.82	0.595	0.607	*8.92×10^9
Venlafaxine	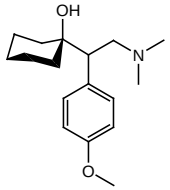	1.20	0.0418	0.056	*8.46×10^9
Iohexol	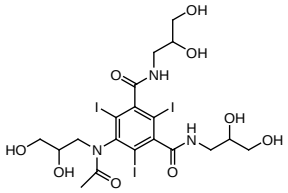	2.92	0.11	0.0647	3.21×10^9 (Jeong et al., 2010)
Sulfamethoxazole	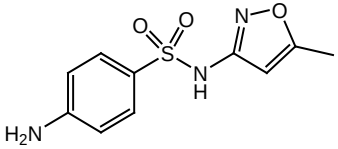	1.72	0.0902	0.101	8.5×10^9 (Mezyk et al., 2007)

Note: *reaction rate constant, see Abdelmelek et al., 2011, supporting information.

12.3.2 Kinetic Studies of ˙OH Oxidation of PPCPs

The kinetic details of AOPs were studied using steady-state γ-irradiation. The ROC, saturated with N_2O, simulated hydroxyl radical formation. In all of the samples, a decrease in PPCP concentration was observed with increasing irradiation doses (increasing hydroxyl radical concentration). Of the 18 PPCPs found, the degradation of 14 was measured, as the four remaining (famotidine, 5,5-diphenylhydantoin, iopamidol, and iomeprol) were too low in initial concentration to quantify. In all cases the data were consistent with previous reported irradiation studies for other contaminants in wastewater effluent (Peller et al., 2009; Sánchez-Polo et al., 2009). An example of the data obtained is shown in Figure 12.1 for atenolol. Table 12.3 summarized the experimentally determined degradation rate and the calculated rate based on Eq. 5.

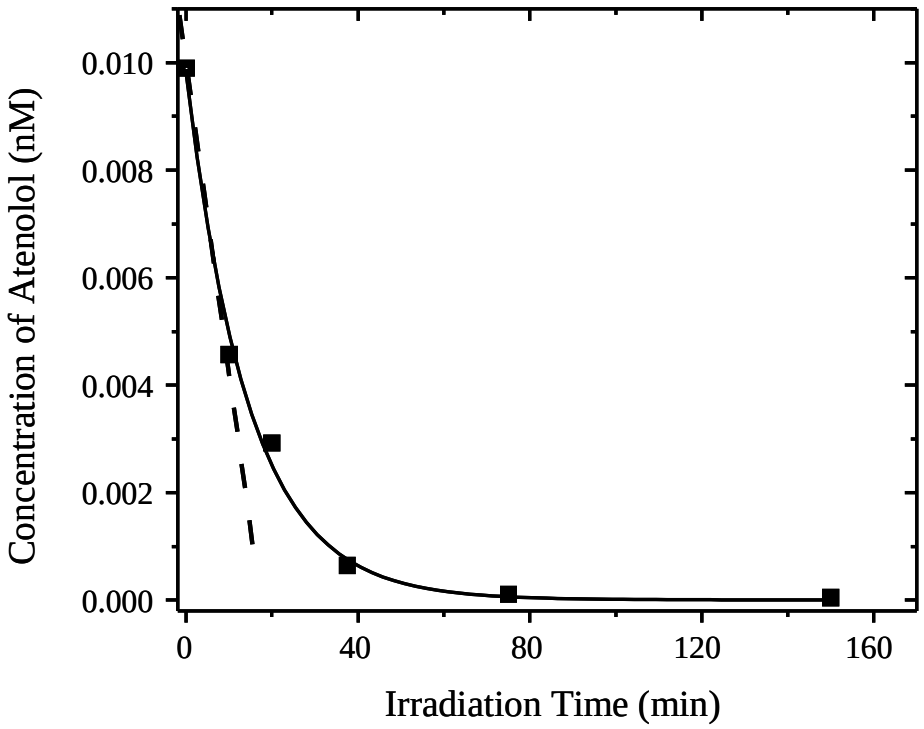

Figure 12.1. Loss of atenolol in N_2O saturated solutions of RO concentrate using ^{60}Coγ-irradiation.

Note: The curve corresponds to fitted loss (square), whereas the dashed straight line is the experimentally determined initial degradation rate of 0.533 nM/min.

12.3.3 Reaction Rate Constant for ˙OH and RO Concentrate

The bimolecular reaction rate constant of ˙OH and ROC was determined using the ROC that contains both the organic and inorganic constituents. The approach used competition kinetics with SCN^- (Eqs. 12.1 and 12.2) and was based on monitoring the $(SCN)_2^{\bullet-}$ absorption at 472 nm. EfOM nomenclature used in this section is a simplification and includes all the organic and inorganic constituents (Table 12.1), and the trace PPCPs in the ROC. The overall reaction rate constant ($k_{OH,\ EfOM}$ or k_2),in other words the "apparent rate constant" determined by competition kinetics, included all of the constituents that react with ˙OH, as opposed to

observing the growth of the transient absorption spectra of just the organic fraction of the ROC.

$$^{\bullet}OH + EfOM \xrightarrow{k_2} H_2O + Intermediate \quad (12.1)$$

$$^{\bullet}OH + SCN^{-}(+ SCN^{-}) \xrightarrow{k_3} OH^{-} + (SCN)_2^{\bullet -} \quad (12.2)$$

The following equation was solved to estimate the k_2:

$$\frac{[(SCN)_2^{\bullet -}]_0}{[(SCN)_2^{\bullet -}]} = 1 + \frac{k_2[EfOM]}{k_3[SCN^-]} \quad (12.3)$$

where $[(SCN)_2^{\bullet -}]_0$ is the absorbance of this transient at 472 nm when only SCN^- is present, and $[(SCN)_2^{\bullet -}]$ is the reduced yield of this transient when the substrate (ROC) was present.

Therefore, a plot of $[(SCN)_2^{\bullet -}]_0/[(SCN)_2^{\bullet -}]$ against the $[EfOM]/[SCN^-]$ should give a straight line of slope k_2/k_3. On the basis of the established rate constant for hydroxyl radical reaction with SCN^-, $k_3 = 1.05 \times 10^{10}\ M^{-1}s^{-1}$, the rate constant ($k_2$) for EfOM can be calculated. The rate constant of EfOM is reported as the molar concentration of DOC, assuming 12 g C per mole C.

The data obtained are summarized in Figure 12.2A and, as expected, a decrease in the maximum $(SCN)_2^{\bullet -}$ absorption intensity was observed when increasing amounts of ROC were added. The transformed plot of the data shown in Figure 12.2B gives a weighted linear fit $k_{OH,\,EfOM} = (5.18 \pm 0.13) \times 10^8\ M_C^{-1}\ s^{-1}$. This rate constant was similar to the average value of $(8.6 \pm 3.5) \times 10^8\ M_C^{-1}\ s^{-1}$, recently reported for non-isolated EfOM in wastewater (Rosario-Ortiz et al., 2008).

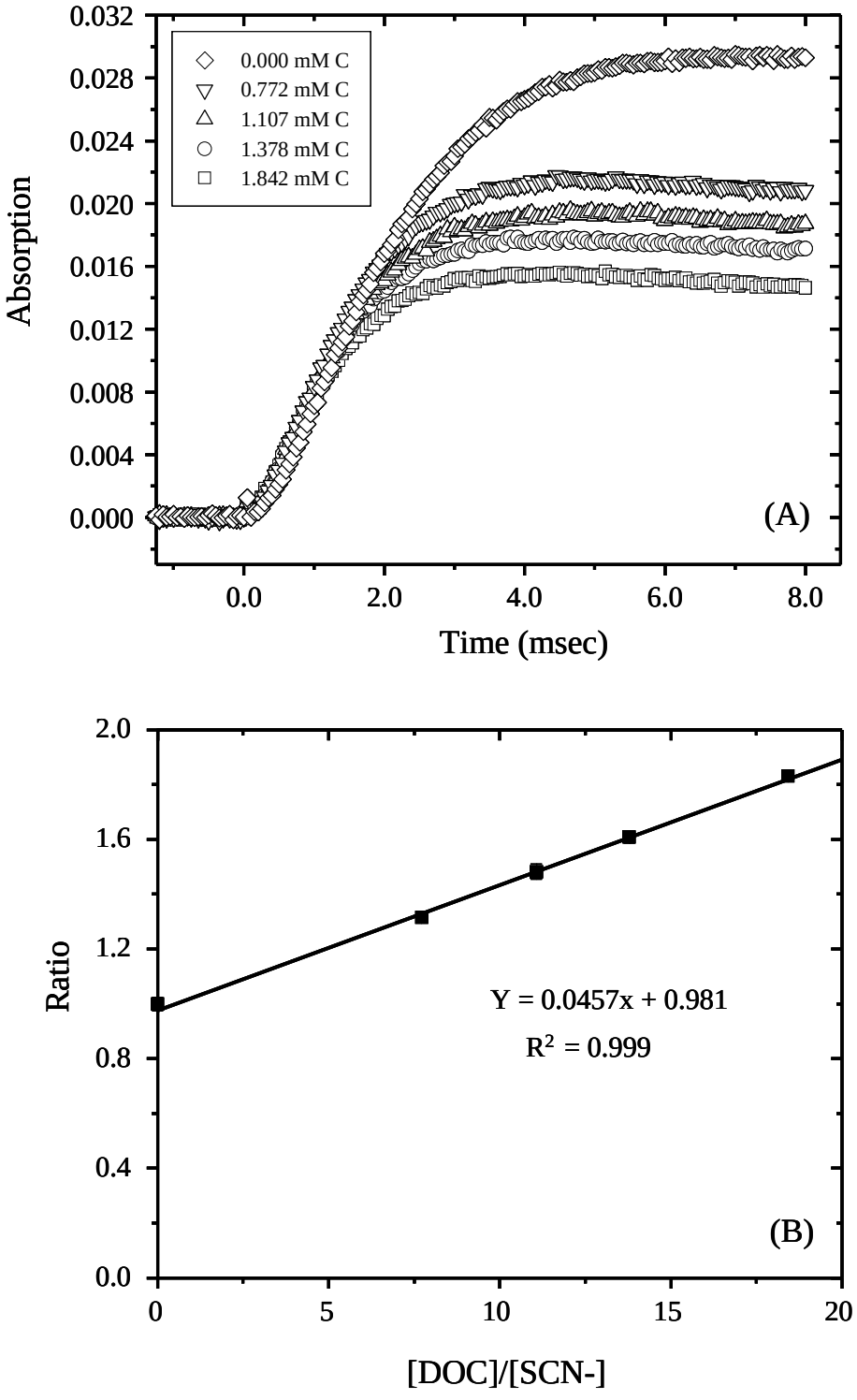

Figure 12.2. (A) Kinetics of the rate of formation of $(SCN)_2^{\bullet-}$ containing 0 (open diamond), 0.772 (∇),1.107 (Δ), 1.378 (open circle), and 1.842 (open square) mM_C RO concentrate and (B) competition kinetic plot for hydroxyl radical reaction with RO concentrate using SCN^- as a standard.

Note: Solid line is a weighted linear fit with a slope of 0.0457± 0.0011.

12.3.4 Modeling Data for ·OH Oxidation of PPCPs in the RO Concentrate

Although several studies indicated the hydroxyl radical reaction efficiency with PPCPs may vary (Peller et al., 2009; Jeong et al., 2010), we assumed that the efficiency was 100% to simplify the model. The calculated degradation slopes or reaction (loss) rate of a PPCP, can be expressed as the fraction of ·OH that reacts with the PPCPs, as in Eq. 12.5:

$$\text{Calculated slope (nM min}^{-1}\text{)} = G \times \text{dose rate} \times \frac{\text{Initial Conc.}_{[PPCPs]} \times k_{OH,\,PPCPs}}{\text{Initial Conc.}_{[EfOM]} \times k_{OH,\,EfOM}} \qquad (12.5)$$

The absorption coefficient was calculated using a *G*-value of 0.59 µmol/J for the hydroxyl radical in N_2O saturated solutions, based on the intraspur scavenging model calculations (LaVerne and Pimblott, 1993). The hydroxyl radical reaction rate constants, for the individual PPCPs, $k_{OH,\,PPCPs}$, were obtained from the literature or measured by pulse radiation.

The absolute reaction rate constants, not yet reported in the literature, for five pharmaceutical compounds, trimethoprim, naproxen, nalidixic acid, venlafaxine, and erythomycin with ·OH were determined from the compounds transient absorption spectra at the wavelength maximum. The pseudo first-order reaction rates were obtained by curve fitting the change in adsorption at different concentrations (in units of s^{-1}). Briefly, the absolute hydroxyl radical rate constants were obtained by fitting exponential curves to the pseudo first-order growth kinetics (Figure 12.3A) and plotting these values as a function of the concentrations of the individual PPCP (Figure 12.3B) to obtain the rate constants summarized in Table 12.3. An example of the data obtained for the compounds is presented in Figure 12.3 for naproxen.

The calculated degradation rates obtained from Eq. 12.5 (Figure 12.4) for the 14 PPCPs, based on the absolute ·OH reaction rate constants, showed excellent (linear) correlation with experimentally determined degradation slope from γ irradiation ($R^2 = 0.98$, n = 14). This result suggested that the combination of ·OH reaction rate constants of individual PPCPs and the bulk EfOM may be an effective tool to evaluate the likelihood of effective removal of PPCPs by AOPs.

Figure 12.4 summarized the data for the 14 compounds determined in Table 12.2.

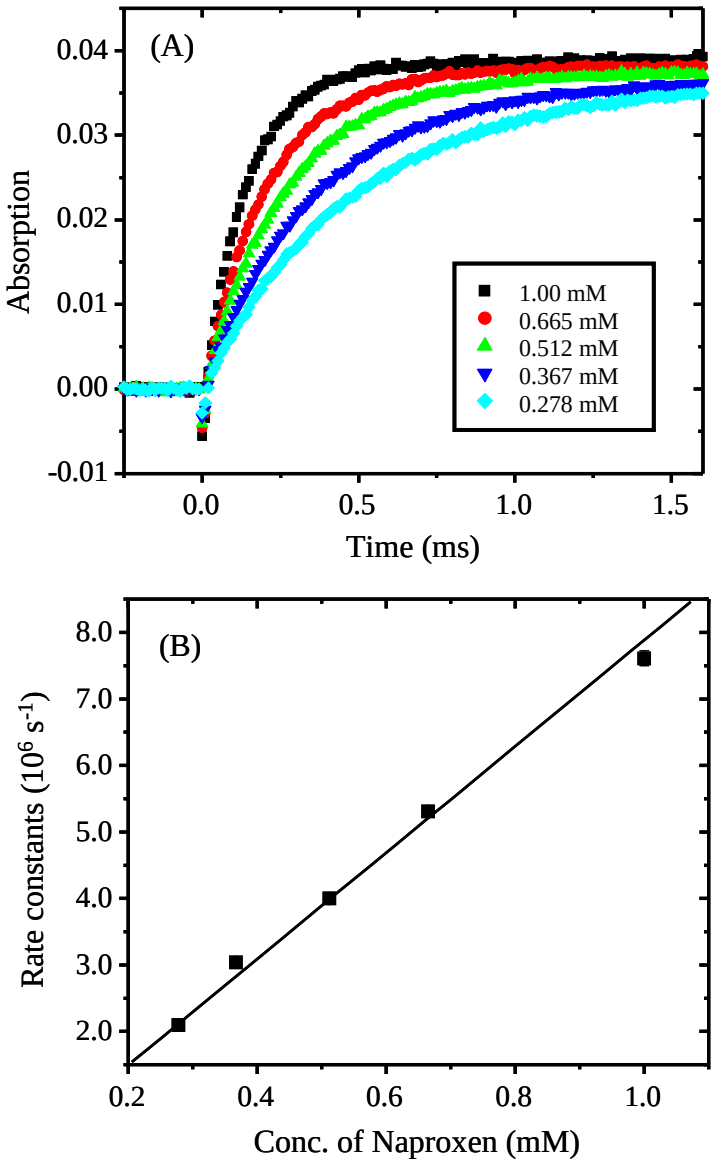

Figure 12.3. (A) Growth kinetics observed for the hydroxyl radical oxidation at 330 nm for 1.00 (open square), 0.665 (O), 0.512 (Δ), 0.367 (∇) and 0.278 (open diamond) mM naproxen at pH 7.0 and room temperature, and (B) second order rate constant determination for the reaction of hydroxyl radicals with naproxen.

Note: The straight line is the weighted linear plot, with a slope of (7.99±0.28) x 10^9 M^{-1} s^{-1}.

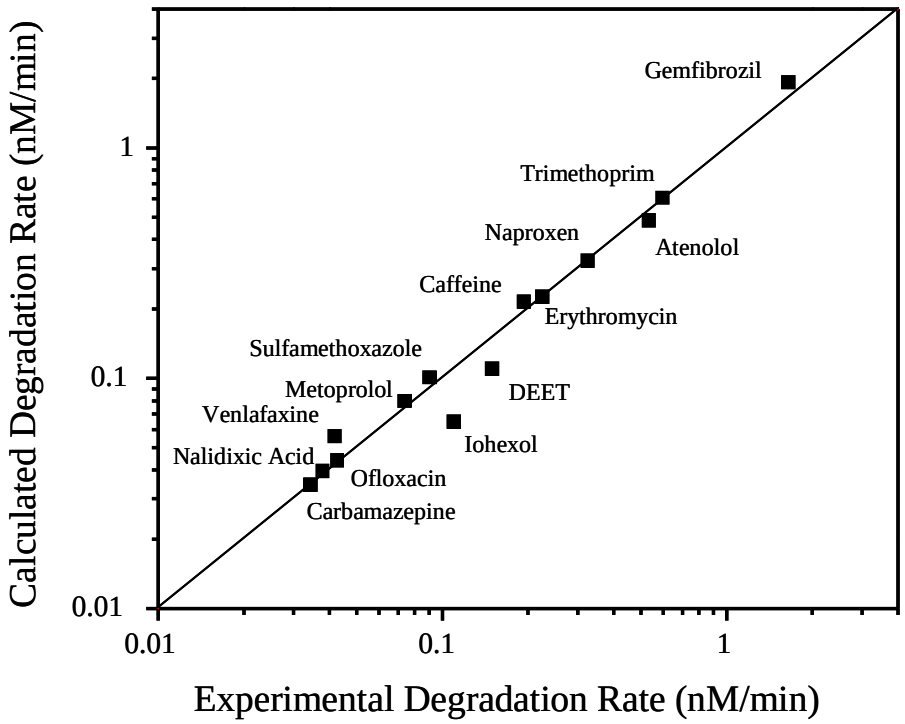

Figure 12.4. The relationship between the experimentally determined degradation rate and the calculated rate based on Eq. 12.5.

12.3.5 Correlation Between UV/Visible, EEM Spectra, and PPCPs Oxidation

UV/visible spectra of the ROC were obtained with increasing doses (Figure 12.5). The change in the overall character of the spectra was minimal, and it appeared that any correlation to removal of PPCPs would not provide an acceptable correlation.

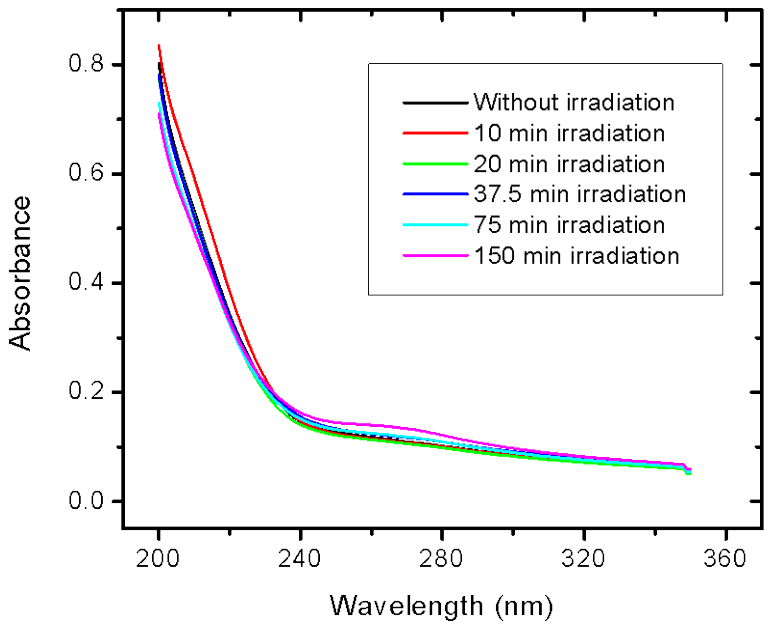

Figure 12.5. Change in the UV absorbance spectra of ˙OH oxidation of RO concentrates, diluted five times, during 150 min of irradiation, corresponding to a total dose of 1.68 kGy and a cumulative concentration of 0.991 mM ˙OH.

A relatively recent advance in fluorescence spectroscopy, excitation-emission matrix (EEM) fluorescence appears to make a better choice for an easily accessible tool for assessing PPCP removal using AOPs. An EEM spectrum of the ROC was obtained (Figure 12.6) and the progressive changes observed in EEM spectra of ROC during hydroxyl radical oxidation were investigated (Figure 12.7). Three peak integrals were identified from the original ROC as illustrated in Figure 12.6. On the basis of the classification of EEM fluorescent peaks as described in previous studies (Coble, 1996; Coble et al., 1998; Coble et al., 1990; Green and Blough, 1994; Chen et al., 2003), these peaks were assigned as: UV humic-like peak (Ex: 240–265 nm, Em: 400–500 nm), visible humic-like peak (Ex: 320–360 nm, Em: 420–460 nm), and protein-like peak (Ex: 260–290 nm, Em: 300–350 nm).

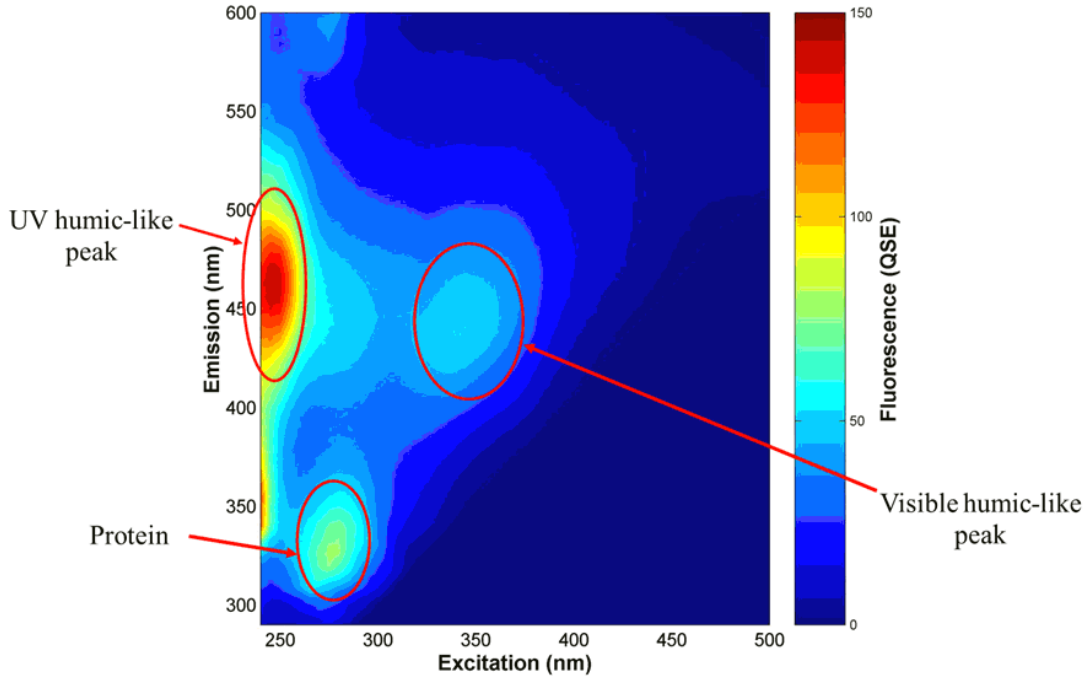

Figure 12.6. Fluorescence excitation-emission matrix spectrum of RO concentrate. Three major peaks were identified as UV humic-like, visible humic-like, and protein-like.

Steady-state irradiation of ROC, under N_2O saturated conditions, decreased the intensity of these three peaks as the dose increased (Figure 12.8). The UV humic-like peak degradation was similar to that of the visible humic-like peak; however, they were both significantly different from the protein-like peak, as shown in Figure 12.7. The loss of fluorescence of the humic-like peaks did not exhibit the simple first-order decay that was observed for the protein-like peak. This suggested that some components of humic matrixes were more resistant to $^{\bullet}OH$ oxidation than was the protein-like peak.

By integrating the area under the three different peaks and plotting the loss in area as a function of increasing dose, it was obvious that the protein-like peak decreased similar to the loss of the various PPCPs (Figure 12.9).

The association of the changes in the EEM spectra with the removal of individual PPCPs was evaluated. The results showed that the removal of PPCPs approached 80% to 100%, whereas there was a 40% to 50% reduction of UV and visible humic-like peaks (as illustrated in Figure 12.9). At the same time, the protein-like peak showed good correlation with individual PPCP removal up to 80%. This result suggests that monitoring the protein-like peak may be a suitable indicator for evaluating the hydroxyl radical loss of PPCPs in RO concentrates.

In other studies, the correlation of $^{\bullet}OH$ rate constants with nonisolated EfOM, was evaluated and an empirical equation that included terms relating to UV absorption, fluorescence index of EfOM, and polarity was obtained (Rosario-Ortiz et al., 2008). According to both results, it

is possible to estimate the effectiveness of AOPs for removing specific PPCPs based on absolute $^{\bullet}OH$ reaction rate constants and bulk EfOM physical-chemical properties.

In studies by others, several research groups have reported UV_{254} absorbance and color changes as methods for assessing the removal of PPCPs from wastewater effluent being treated by oxidation with O_3 or O_3/H_2O_2 (Wert et al., 2009b; Nanaboina and Korshin, 2010). The relative decrease of absorbance ranged from less than 30% for wavelengths less than 250 nm to >80% for wavelengths greater than 320 nm. The removal of PPCPs correlated very well with relative change in UV absorbance (Nanaboina and Korshin, 2010). In comparison, there was no significant change in the UV spectrum of ROC when $^{\bullet}OH$ was the sole oxidant under our experimental conditions (Figure 12.5). These results suggest that ozone was more selective and reacted with specific chromophores in the EfOM, which resulted in the loss of UV absorbance. Hydroxyl radical reacts nonselectively with aromatic groups resulting in the loss of fluorescence; however, no loss of UV/visible absorbance at the low $^{\bullet}OH$ exposure used in this study was observed.

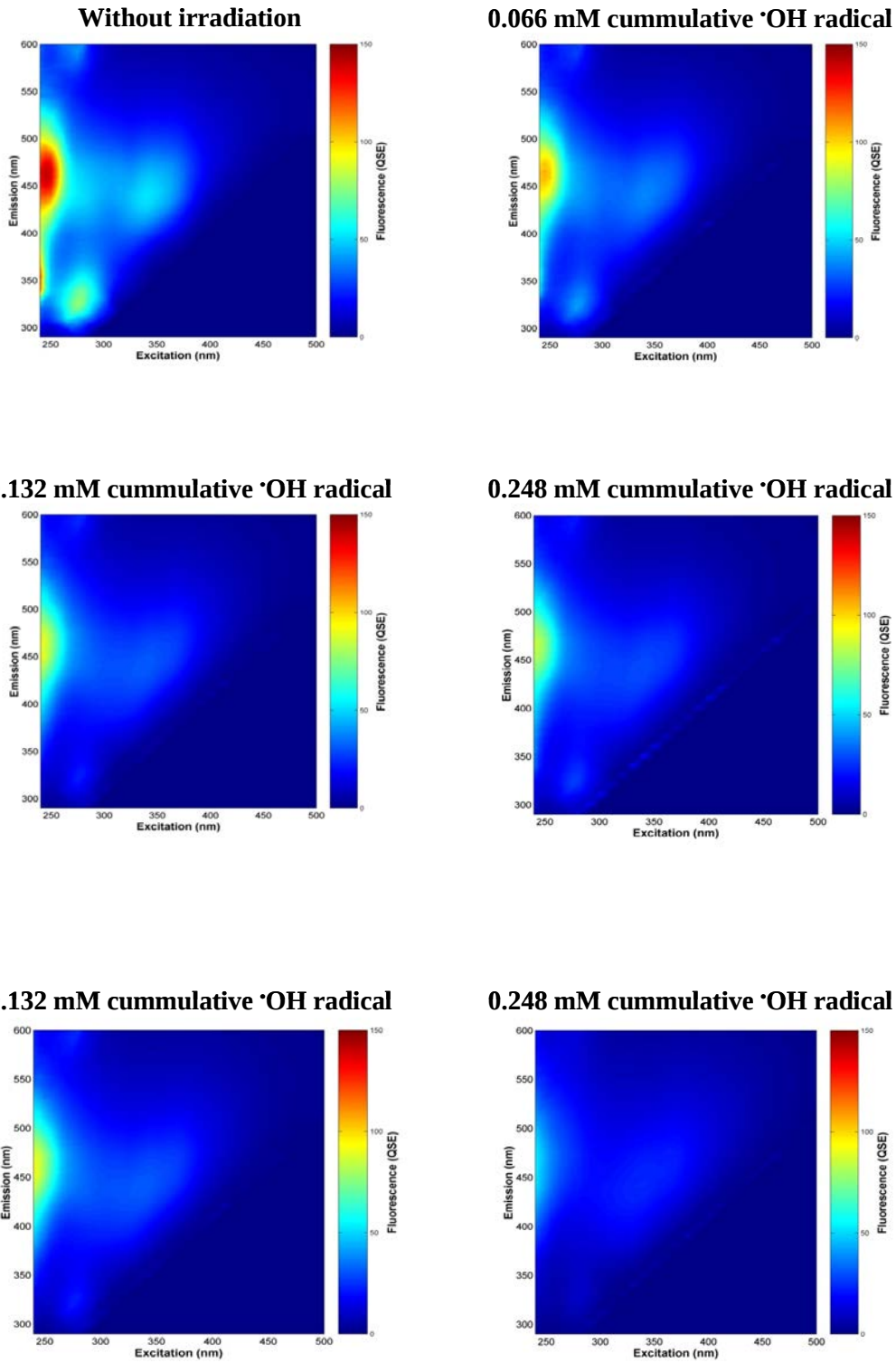

Figure 12.7. The transformation of fluorescence excitation-emission matrix spectra of RO concentrates vs hydroxyl radical oxidation.

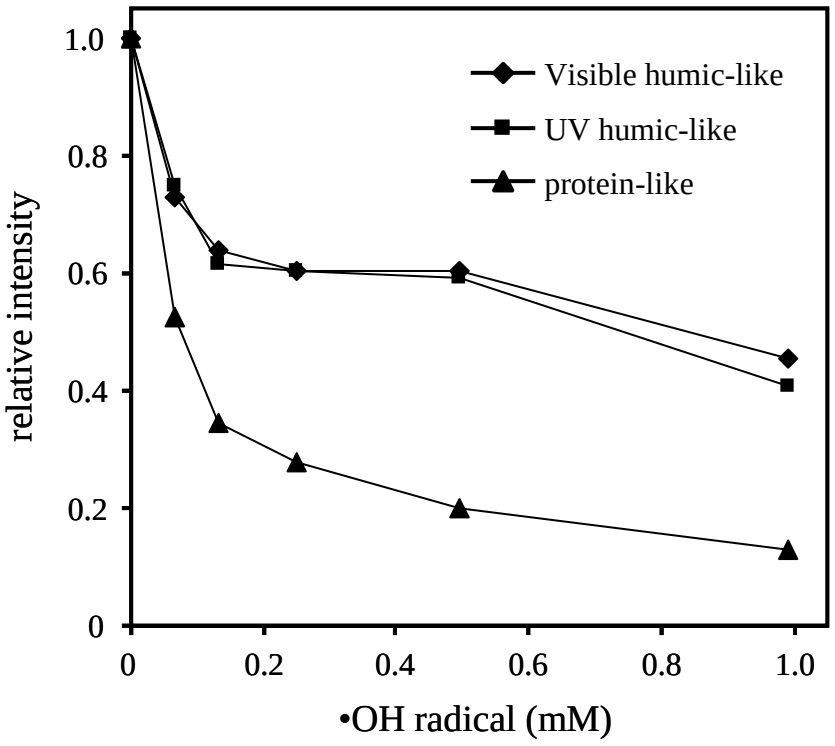

Figure 12.8. Relative intensity of the fluorescence peaks as a function of ˙OH oxidation. (square = UV humic-like peak: λ_{ex}=245 nm, λ_{em}=459 nm, diamond = visible humic-like peak: λ_{ex}=345 nm, λ_{em}=445 nm, triangle = protein-like peak: λ_{ex}=276 nm, λ_{em}=329 nm)

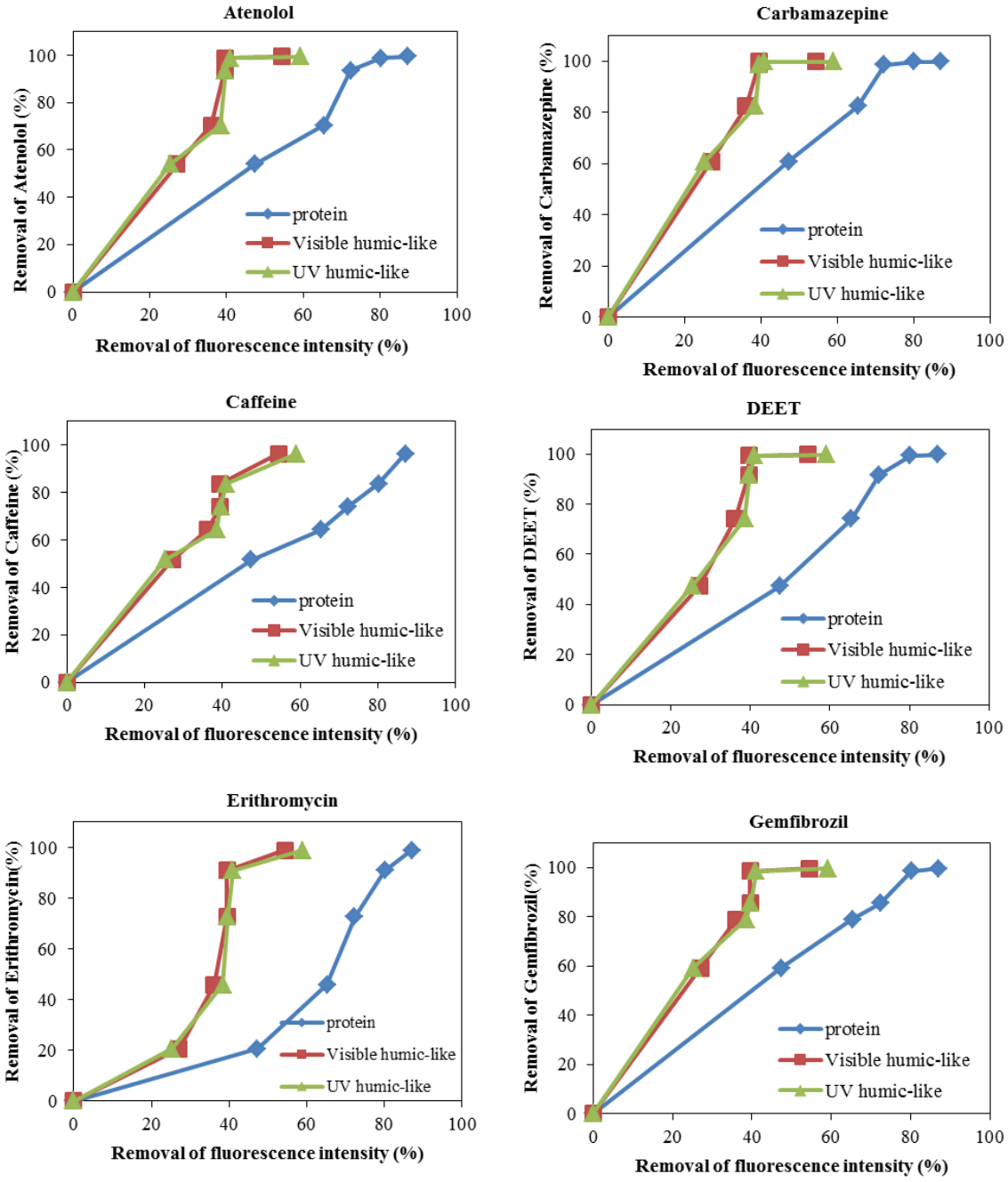

Figure 12.9. The reduction of fluorescence intensity vs. the removal of PPCPs.

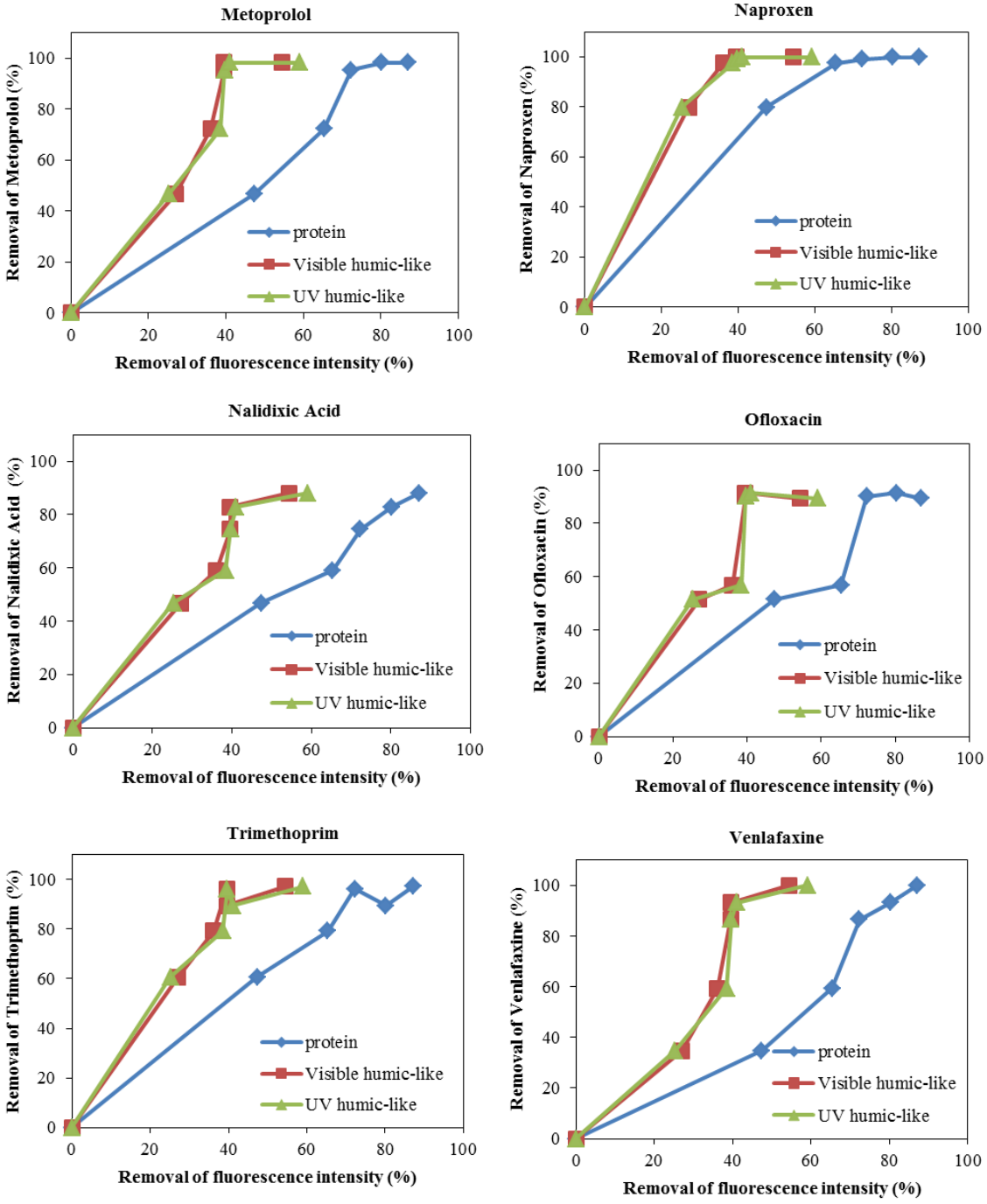

Figure 12.9. (Continued). The reduction of fluorescence intensity vs. the removal of PPCPs.

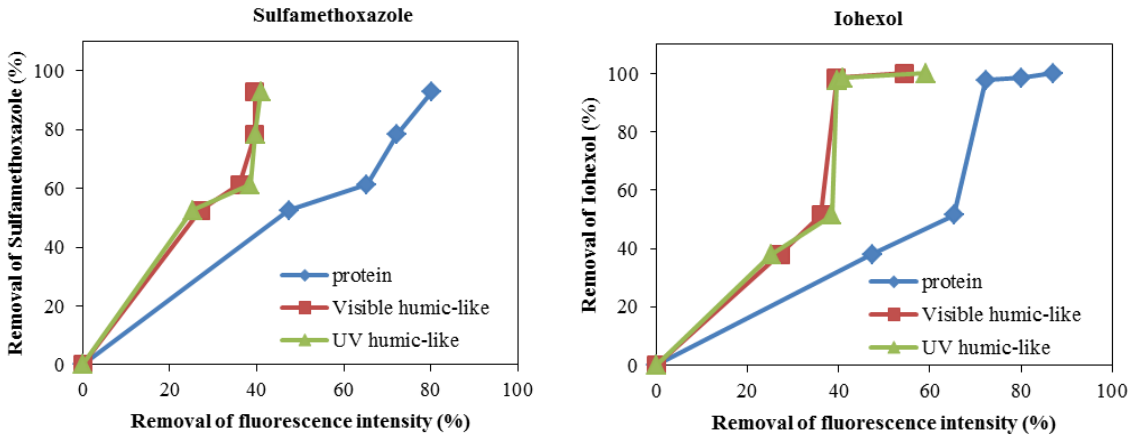

Figure 12.9. (Continued). The reduction of fluorescence intensity vs. the removal of PPCPs.

12.4 Conclusions

The results presented indicate that AOPs can effectively remove PPCPs from RO concentrates. This is the first attempt to evaluate the kinetics of $^{\bullet}OH$ oxidation of PPCPs and to model their degradation in ROC. The biomolecular reaction rate constants of individual PPCP and ROC (EfOM) were employed to predict the removal rate of PPCPs, and the calculated results are in accordance with the experimental results. In addition, the removal of PPCPs is well correlated with the reduction of protein-like fluorescence of RO concentrate, suggesting that monitoring the changes of this fluorescence peak may provide a rapid and inexpensive method for the quantitative estimation of PPCPs degradation under treatment plant conditions.

Chapter 13

Carbon and Energy Footprint Analysis of the AWPF

13.1. Introduction

This section is divided in two parts: energy footprint model development and application of the energy footprint model to OCWD's AWPF. The energy footprint model development includes the main process components MF, RO, UV/AOP, and pumping processes.

13.2. Background

13.2.1 Microfiltration

The filtration flux (J) through an MF membrane is influenced by the net transmembrane pressure (P), viscosity of the filtrate (μ), resistance provided by the membrane material (R_m), and by deposits on membrane (R_c). Thus

$$J = \frac{P}{\mu(R_m + R_c)} \tag{13.1}$$

If α_c is the specific cake resistance and the mass of cake deposited per unit area is m_c,

$$R_c = m_c \alpha_c \tag{13.2}$$

When a constant flux is set during the filtration cycle,

$$m_c = J_i t C_f \tag{13.3}$$

where J_i is the operating flux, t is the filtration time, and C_f is the concentration of the solids in the feedwater. Eq. 13.1 therefore becomes

$$P = J_i \mu R_m + J_i^2 \mu t C_b \alpha_c \tag{13.4}$$

when high-pressure backwashing is applied at the end of the cycle and $P = P_F$, the maximum TMP selected by operators/engineers. Solving for the operating cycle time t_c, we have

$$t_c = \frac{P_F - \mu J_i R_m}{\mu J_i^2 C_b \alpha_c} \tag{13.5}$$

Equation 13.5 shows that t_c is very sensitive to the operating flux J_i, and inversely proportional to the feed concentration. Although most of the deposits on the membrane are removed during the air scouring backwash, some of the deposits remain attached to the membrane, trapped within pores or held on the surface by adhesion. These deposits contribute additional resistance to the filtration process in subsequent cycles and eventually the

application of chemicals is required for cleaning.

Equations 13.4 and 13.5 were derived based on the assumption that the flux and cake resistance are constant along the membrane surface. However, in hollow fiber membranes the flux and the cake resistance have been reported to vary along the fiber length (Chang and Fane, 2001; Parameshwaran et al., 2001). Therefore, the previous equations use the average specific cake resistance along the fiber length.

13.2.2 Reverse Osmosis

Osmotic pressure is strictly a function of the dissolved solid concentration presented in the influent water, described by the van't Hoff equation for osmotic pressure:

$$\pi = CRT \tag{13.6}$$

where π is osmotic pressure (bars), C is the concentration of all solutes (moles/L), R is universal gas constant , and T is absolute temperature (K).

The driving force for water flux through RO membranes is the net pressure differential, in other words, the difference between applied (Π) and osmotic (π) pressure differentials:

$$\Delta\Pi_{NET} = \Delta\Pi - \Delta\pi = (\Pi_F - \Pi_P) - (\pi_F - \pi_P) \tag{13.7}$$

The water flux through the RO membrane is described by the following expression:

$$J_W = K_W(\Delta\Pi - \Delta\pi) \tag{13.8}$$

where K_W is determined experimentally by membrane manufacturers and water flux is dependent on the pressure gradient.

Finally, the power required for the RO process can be calculated according to the following equation (Lin, 2001):

$$P = jQ\frac{\Pi_F}{\eta\gamma_w} \tag{13.9}$$

where P is the power (kW), j is a constant (1.661 in SI units), Q is the flow (m^3/min), Π_F is the RO feed pressure (bar), η is process efficiency, and γ_w is specific gravity of water.

13.2.3 Ultraviolet Radiation

A diverse classification of constituents can be found at low concentrations in conventional secondary-treated effluent coupled with reverse osmosis treatment (Plumlee et al., 2008; Snyder et al., 2007; Al-Rifai et al., 2011; Yuksel et al., 2013) Trace constituents are of concern because of the associated known or suspected toxicity. They may need to be removed during water reclamation depending on the regional reuse requirements.

N-Nitrosodimethylamine (NDMA) is one of several N-nitrosamines classified as potential human carcinogen by the U.S. Environmental Protection Agency (USEPA, 2013) and is regulated in California with a notification level (NL) at 10 ng/L (ppt) in drinking water

(CDPH, 2011). In addition to NDMA, the EPA has listed five other nitrosamines on the Unregulated Contaminant Monitoring Rule 2 (UCMR 2) to be monitored from 2008 to 2010 (USEPA, 2006). These trace constituents may be regulated in future water reuse applications (Fine et al., 1977; USEPA, 2007).

The industrial solvent 1,4-dioxane(USEPA, 2013) and potential carcinogen (USEPA, 2013), also is regulated by the state of California and has an NL of 1 μg/L (ppb) (CDPH, 2013). Also, 1,4-dioxane is not directly photolyzed with UV light and requires an oxidant to be removed from the source water.

To target these compounds of concern, hydroxyl radicals are employed and formed by exposing H_2O_2 to UV light (200–280 nm). The electrical power requirement for photolytic reactions is significant due to the process challenges, and is represented by Eq. 13.10 for flow-through operation (Bolton et al., 1998):

$$EE/O = \frac{P(t)}{Q(t) \cdot \log_{10}\left(\frac{c_i}{c_f}\right)} = \frac{P}{Q \cdot \log_{10}\left(\frac{c_i}{c_f}\right)} \tag{13.10}$$

where EE/O is electric energy per order of magnitude removed (kWh), P is rated power (kW), Q is flow rate (m^3/h), and c_i, c_f are influent and effluent concentrations of the trace constituent to be removed (e.g., NDMA).

13.3 Energy Footprint Compartments

The energy footprint is carried out by mechanical equipment. Therefore, to study the energy consumption in a large treatment facility like AWPF, the equipment inventory employed by this facility was securitized, especially in the energy intensive processes.

The study was confined to the equipment sets of the three energy intensive AWPF processes that included the MF, RO, and UV/H_2O_2 AOP. Table 13.1 summarizes the itemized equipment that is utilized by these processes, the quantity, and the associated nominal electrical power.

Table 13.1. AWPF Summarized Equipment Inventory

Equipment List	Quantity	Nominal Power Per Unit (HP)	Nominal Power Per Unit (kW)
MF-Operating Stage			
NaOCl - Transfer Pump	2	7.5	5.6
NaOCl - Metering Pump	3	1.5	1.1
MF Filtrate Pump	26	60	44.8
Waste Sump Pump	8	5	3.7
RO Transfer Pumps	5	1250	932.5
MF-Backwash Stage			
MF Backwash Pump	5	200	149.2
MF Blowers	6	125	93.3
MF Spent Backwash	6	60	44.8
MF Compressors	4	20	14.9
MF-Clean In Place (CIP) Stage			
MF CIP Pump	2	10	7.5
MF CIP Tank Fill (Pump)	2	20	14.9
Chemical Transfer Pump (Citric Acid)	2	7.5	5.6
Chemical Transfer Pump (Caustic)	4	15	11.2
Chemical Transfer Pump	2	30	22.4
Tank Heater	24	20	14.9
Tank Heater	8	100	74.6
MF-RO Transfer			
Threshold Inhibitor Metering Pump	5	1250	932.5
RO-Pretreatment Stage			
Sulfuric Acid Metering Pump	3	2	1.5
Threshold Inhibitor Metering Pump	2	0.5	0.4
RO-Operation Stage			
RO Feed	15	1000	746.0
DPW Pumps	3	25	18.7
RO-Clean In Place (CIP) Stage			
RO CIP Pump	2	125	93.3
RO Flush Pump	3	50	37.3
Citric Acid Metering Pump	2	7.5	5.6
AOP (UV/H_2O_2)			
UV Trojan lamp	3456	111	82.8

13.3.1 MF Process

Because of the diverse operating conditions of the process, the MF mechanical operation was divided in three stages: operation, backwash, and CIP. In the operating stage, the permeate water is drawn by vacuum through 0.2 μm nominal pores into the hollow fiber membranes.

The current operating schedule is production for 22 min followed by a 165 s process interruption for backwash. During the backwash stage, the TMP is periodically inverted to lift the fouling layer from the surface of MF membranes. It takes 16 s of liquid backwash followed by a 40 s drawback of high-pressure air. During the CIP stage, which occurs approximately every 21 days, a wide range of chemicals (i.e., proprietary solutions and reactive agents, including citric acid and caustic) are used to clean off the persistent foulants.

The results for an average 70 mgd AWPF RO permeate production (Figure 13.1) indicate that the operations stage (i.e., filtrate pumps) amount to 30% of the total MF energy footprint. The results presented in Figure 13.1 were calculated based on the main components of energy consumption. The equipment sets with negligible energy consumption were neglected in this analysis.

The backwash stage accounts for 52% of the total energy footprint of the entire MF process. Within this energy component, backwash blowers are the most energy intensive part of the process, with a 38% contribution associated with the blowers for air scouring. Besides air scouring, transfer of the MF effluent from the break tank back to the MF backwash tanks accounts for 14% of the total MF energy footprint.

Finally, the transfer of the backwash waste to OCSD amounts to 18% of the total MF energy footprint. This portion accounts for the transfer of MF concentrate (MFC) from the MF basins to the adjacent wastewater treatment plant (OCSD) for retreatment by activated sludge. This portion is site-specific and could vary based on the type of wastewater treatment that is being treated and the required pumping distance to that process.

Overall, the equipment employed in the three major processes was categorized into three parts: pumps, blowers, and storage tank heaters.

The details of these equipment sets are as follows:

- **Pumps.** The pumps utilized by the MF process are responsible for 62% of the entire MF footprint and were divided into three categories:
  - *Filtrate Pumps* draw water through the hollow fibers of MF membranes. These pumps are energy intensive, due to the pressure head that they need to overcome. Deposition of solids on the membrane creating hydraulic resistance and exacerbate the energy footprint of this component. As presented in Figure 13.1, this is responsible for 30% of the MF energy footprint.
  - *Liquid Transfer Pumps* transfer the MF effluent from the MF break tank to the backwash tanks and transfer the backwash waste (MFC) to the adjacent wastewater treatment plant. This is represents 32% of the MF energy footprint.
  - *Chemical Transfer Pumps* add chemicals into the MF effluent, required for the operation of clean in place (CIP) stage. The volume of chemicals transferred is very small compared to the volume of the water used in the CIP. Thus, the energy footprint of the CIP pumps was neglected in this study.

- **Blowers.** Blowers are employed for air scouring during the backwash cycle. These are responsible for 38% of the MF energy footprint.
- **Storage Tank Heaters.** Heaters are employed for preheating chemicals for the CIP process. Although tank heating is energy intensive process, it only occurs on a monthly

basis, thus this thermal operation has a negligible contribution to the energy footprint compared to other continuous mechanical operations.

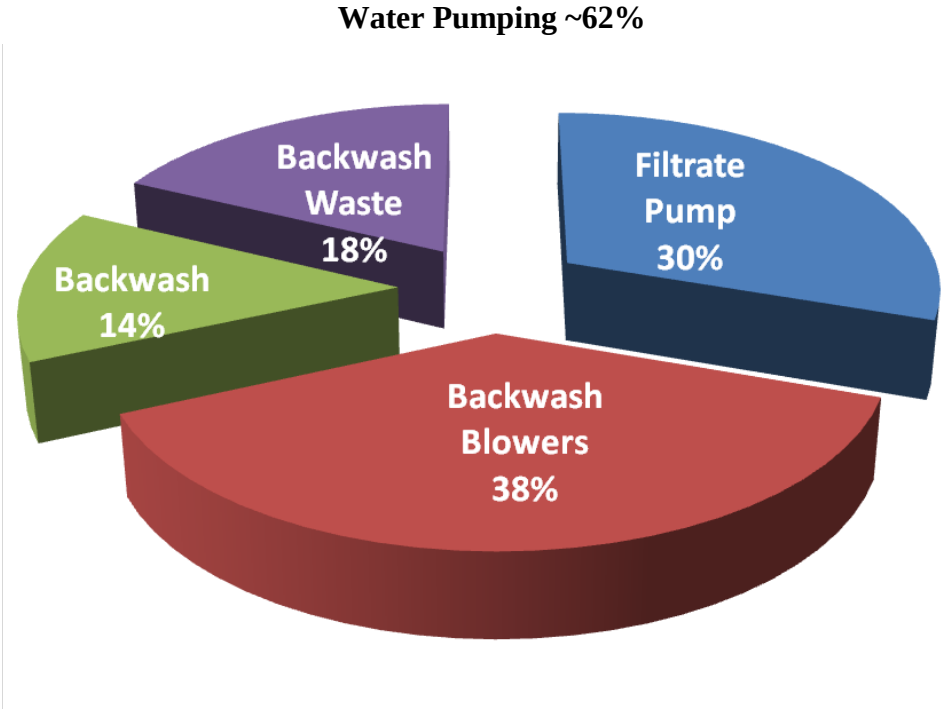

Figure 13.1. Breakdown of MF main energy compartments of the AWPF.

A breakdown of the total energy footprint of the main AWPF energy intensive processes (i.e., RO, MF, and UV/H_2O_2 AOP) is displayed in Figure 13.2. The results were based on the energy intensive equipment inventory and the parts deemed to be negligible were eliminated. Besides the aforementioned processes, this figure also represents the energy footprint required to supply the RO process with the MF effluent. The results from the analysis indicate that the MF process encompasses 14% of the total AWPF energy footprint and is the most energy intensive application after the RO process. The normalized energy footprint of the MF process was 272 kWh/MG of water production (see Figure 13.3).

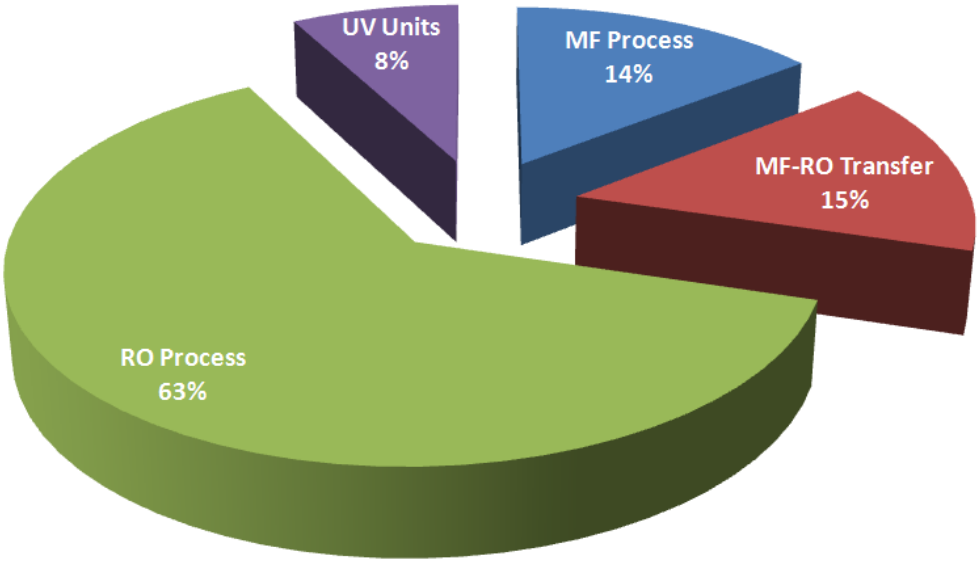

Figure 13.2. Breakdown of the total electrical energy usage by the individual processes of the AWPF, including RO, MF, and UV/H_2O_2 AOP.

Note: The energy footprint for the transfer of water from MF to RO through a 2 MG reservoir is presented separately. The results are based on the main operating equipment (i.e., small or intermittently operated equipment were neglected).

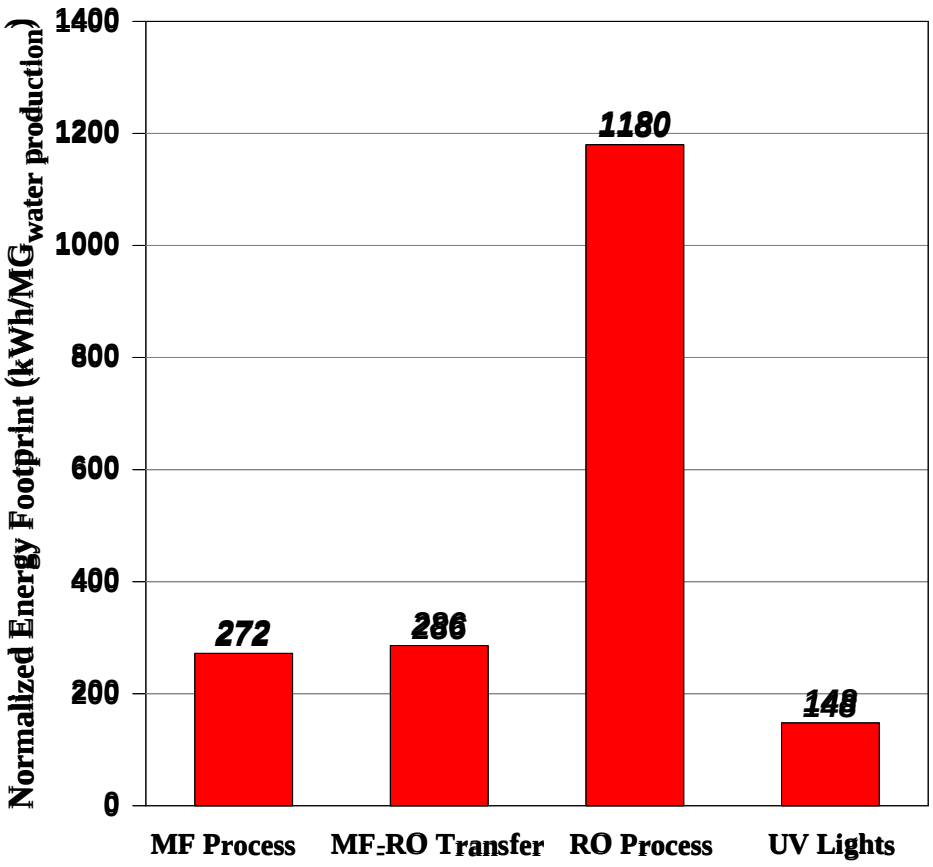

Figure 13.3. Normalized energy footprint (kWh/MG) presented on the main energy components of the AWPF.

13.3.2 MF-RO Transfer

Between the MF and RO processes there is a 2 MG partially interred reservoir that stores MF effluent. Inside the transfer pump station, there are five 1250 HP pumps that move the water from MF break tank through the cartridge filters to the RO treatment process. This reservoir allows the purification facility to feed an even flow of MF effluent to the RO membranes. The energy footprint for MF-to-RO pumping amounts to 15% of the entire AWPF energy footprint (Figure 13.2) and is the most energy intensive unit after the RO process. This transfer unit is site-specific and could vary between the treatment facilities. The normalized energy footprint of this component is 286 kWh/MG (Figure 13.3).

13.3.3 RO Process

During the RO process, water is forced through the molecular structure of the 0.2 to 0.5 μm thick polyamide layer of the RO membrane under high pressure (~150 psi). During this process, dissolved salts, minerals, organic materials, pharmaceuticals, and viruses are removed from the feedwater. The water produced is near-distilled water quality. In the RO process, feed pumps dominate the energy footprint and make the footprint of the rest of the equipment (e.g., chemical transfer pumps or the pumps employed for CIP process) negligible. The RO process accounts for 63% of the entire AWPF energy footprint (Figure 13.2). The normalized energy footprint of the RO process is 1180 kWh/MG (Figure 13.3).

13.3.4 UV/H_2O_2 AOP

The UV/AOP facility consists of eight trains, each containing three chambers stacked vertically in a series and one backup train consisting of three chambers laid down in parallel. The chambers hold two reactors with 72 low-pressure high-output (LPHO) 257 watt mercury amalgam lamps each for a total of 432 lamps per three-chamber train and a total of 3888 lamps in the entire UV/AOP facility. The energy footprint of this process is dominated by the UV lamps. The normalized energy footprint of the UV/AOP process is 148 kWh/MG (Figure 13.3).

13.3.5 Diurnal Variations

The diurnal dynamics of the upstream biological wastewater treatment processes (e.g., activated sludge process) have been addressed since the introduction of dynamic simulations (e.g., Curds, 1973; Busby and Andrews, 1975; Ekama and Marais, 1979); however, in the available literature, the process conditions of water purification have mostly been discussed and investigated under diurnal steady-state conditions.

In fact, the downstream water purification facility inherits environmental variations that occur in the upstream wastewater reclamation influent. Alhough part of these variations is attenuated through the wastewater treatment processes, abrupt or gradual variations are observed in the water purification influent during different hours of a diurnal period. The variable parameters, can include hydraulic load, pollutant loads (i.e., suspended solids and dissolved solids), and water temperature. The variations in these environmental parameters affect the process parameters and consequently create a dynamic energy footprint during the diurnal cycle.

There are other process parameters that vary with larger time-constants (e.g., decline in equipment performance because of MF and RO membrane fouling), and these are recordable on a monthly to yearly scale. However, these parameters can be considered constant when considering the time domain of the diurnal cycle.

Of all the influent water parameter characteristics, hydraulic load, turbidity, and conductivity vary considerably (Figure 13.4). Diurnal variations of the water temperature could affect membrane filtration and its associated energy footprint. However, due to Southern California's coastal climate condition, significant variations in temperature are not observed.

13.3.6 Hydraulic Load

During a typical operating day (i.e., with average of 65 to 70 MG of water production) the hydraulic load decreases between midnight and 6:00 a.m. It stayed at its minimum value between 6:00 to 9:00 a.m. and then started to rise until noon. Between 12:00 p.m. and 12:00 a.m. the influent flow was stable (Figure 13.4a). Hence, a 45% variation among the MF influent hydraulic load could be expected in a typical production day.

13.3.7 Constituent Load: Turbidity

The SCADA system of the AWPF stores the turbidity data of the influent and effluent water of purification processes. Turbidity represents the cloudiness and haziness of the water caused by suspended solids. As a result, variations in the turbidity were used to describe the variation in the total suspended solids (TSS) of the MF influent or MFF feedwater

(Figure 13.4b). During the MF process, the emphasis is mostly on TSS removal. As a consequence, the TSS variation is an indicator of variations in MF energy footprint. Overall, the results reveal lower turbidity between midnight and noon, and higher turbidity during the afternoon hours until midnight. A 30% variation among the TSS of MF influent could be expected in a typical production day.

13.3.8 Constituent Load: Conductivity

The SCADA system also monitors the electrical conductivity (EC) of the influent and effluent water of the purification processes as well. Conductivity measurements represent the ionic content in the water. Changes in the EC were used to describe the variations in the concentration of the total dissolved solids (TDS; Figure 13.4c). The emphasis of RO process is on TDS removal. As a consequence, the TDS variation affects the RO energy footprint. The results indicate that the TDS decreases between midnight and 9:00 a.m. After this, the TDS starts to rise and reaches a peak during the afternoon (e.g., 3:00 p.m.), and then declines again until midnight. A 15% variation among the TDS of MF influent water could be expected in a typical production day.

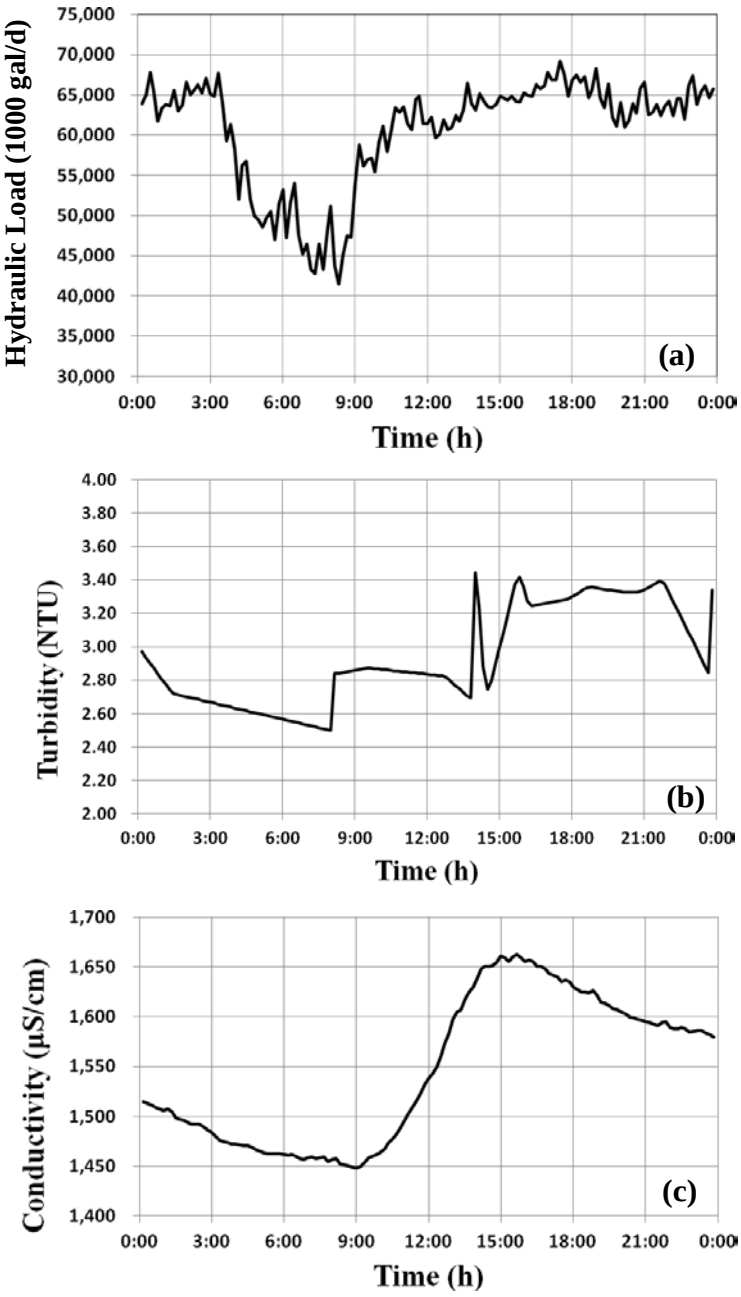

Figure 13.4. Variations of MF influent water characteristic during a typical operating day (e.g., January 17, 2012), (a) presents the hydraulic load variation, (b) presents the suspended solids variation, and (c) presents the dissolved solid variations.

Note: In this figure, turbidity and conductivity variations describe suspended solids and dissolved solids variations, respectively.

13.3.9 Dynamics of MF Operating Cycle

Equations 13.1 to 13.5 describe the water flux and the time of each operating cycle, t_c, during the MF operations. On the basis of these equations, t_c can be modified during a diurnal period because of the variations among the following dynamic parameters: flux, net transmembrane

pressure, and solids concentration (i.e., TSS for MF process). Other parameters affect the t_c value; however, they are considered either constant (e.g., membrane resistance, R_m) or vary insignificantly (e.g., water viscosity) during the diurnal period.

Water flux and the suspended solids in the feedwater vary because of variations in hydraulic and constituent load. However, the net transmembrane pressure changes due to the variation in applied pressure, which is a parameter that is monitored by the MF process control. Under normal operating conditions, pump pressure is synchronized with influent load (i.e., hydraulic and constituent load). Increased pump pressure always follows the escalation of the MF influent load and as the influent load decreases, the pressure requirement for pumping decreases.

Equation 13.5 is used to calculate the variation in the time of the operating cycle, t_c, variations (Δt_c):

$$\Delta t_c = \left[\frac{\left(1+\frac{\Delta J}{J}\right)}{\left(1+\frac{\Delta J}{J}\right)^2\left(1+\frac{\Delta C}{C}\right)} - 1 \right] t_c - \frac{\left|\frac{\Delta J}{J} - \frac{\Delta P_F}{P}\right| R_m}{\left(1+\frac{\Delta J}{J}\right)^2\left(1+\frac{\Delta C}{C}\right) J^2 C_\alpha} \tag{13.11}$$

The second part of Eq. 13.11 is negligible and the simplified equation is as follows:

$$\begin{cases} t_{c_2} = \dfrac{\left(1+\frac{\Delta P_F}{P_F}\right)}{\left(1+\frac{\Delta J}{J}\right)^2\left(1+\frac{\Delta C}{C}\right)} t_{c_1} \quad \text{for} \quad \dfrac{\Delta J}{J} \geq \dfrac{\Delta P_F}{P_F} \\ t_{c_2} = \dfrac{\left(1+\frac{\Delta J}{J}\right)}{\left(1+\frac{\Delta J}{J}\right)^2\left(1+\frac{\Delta C}{C}\right)} t_{c_1} \quad \text{for} \quad \dfrac{\Delta J}{J} < \dfrac{\Delta P_F}{P_F} \end{cases} \tag{13.12}$$

Figure 13.5 represents the flow and turbidity characteristics of the MF influent water at 10 min intervals. The data provided were collected by the AWPF SCADA system. The data pattern shows the intermittent on-off pumping cycle of the operating process. To limit the variability of the data associated with the intermittent cycles, the diurnal period was divided into 3 h intervals, and the 3 h averages were plotted. In Figure 13.5 $<Q>_{3h}$ is the 3 h average flow and $<Q>$ is the daily average flow; analogous definitions apply to the turbidity. The average values of each water parameter during those periods were used to estimate the dynamics of the theoretical cycle time t_c (i.e., time between backwash events) for each 3 h period (Figure 13.6). The results presented here are based on the considerations leading to Eq. 13.12; however, to achieve a more realistic t_c value, site-specific pilot studies would be necessary.

Comparisons between the t_c values based on dynamic estimations and on the operating parameters during 3 h periods and the t_c values based on the average-load and maximum-load operating conditions of the entire diurnal period are displayed in Figure 13.6. The results indicate that from midnight until noon (i.e., when the MF influent load is lower), t_c could be much longer compared to the maximum and average load operating condition. For example, from 6:00 to 9:00 a.m., when the hydraulic and constituent loads are at a minimum, the MF operating cycle could be 2.2 times longer compared to the operating cycle required at the maximum load and 1.5 times longer compared to the operating cycle required for the average load.

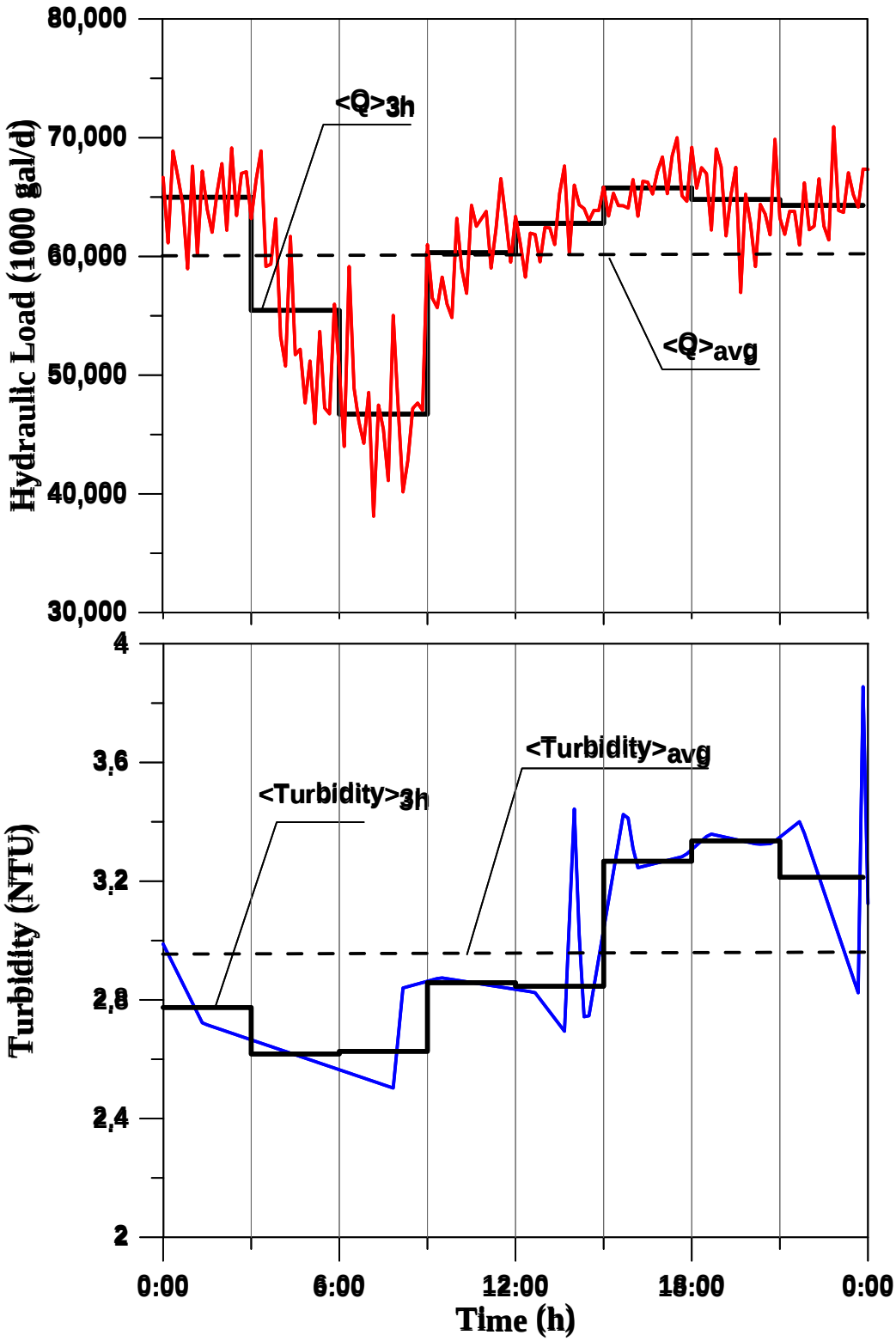

Figure 13.5. Diurnal variations of flow and turbidity in the MF process (January 17, 2012).

Notes: $<Q>_{3h}$ is the 3 h average flow; <Q> is the daily average flow. Analogous definitions apply to the turbidity.

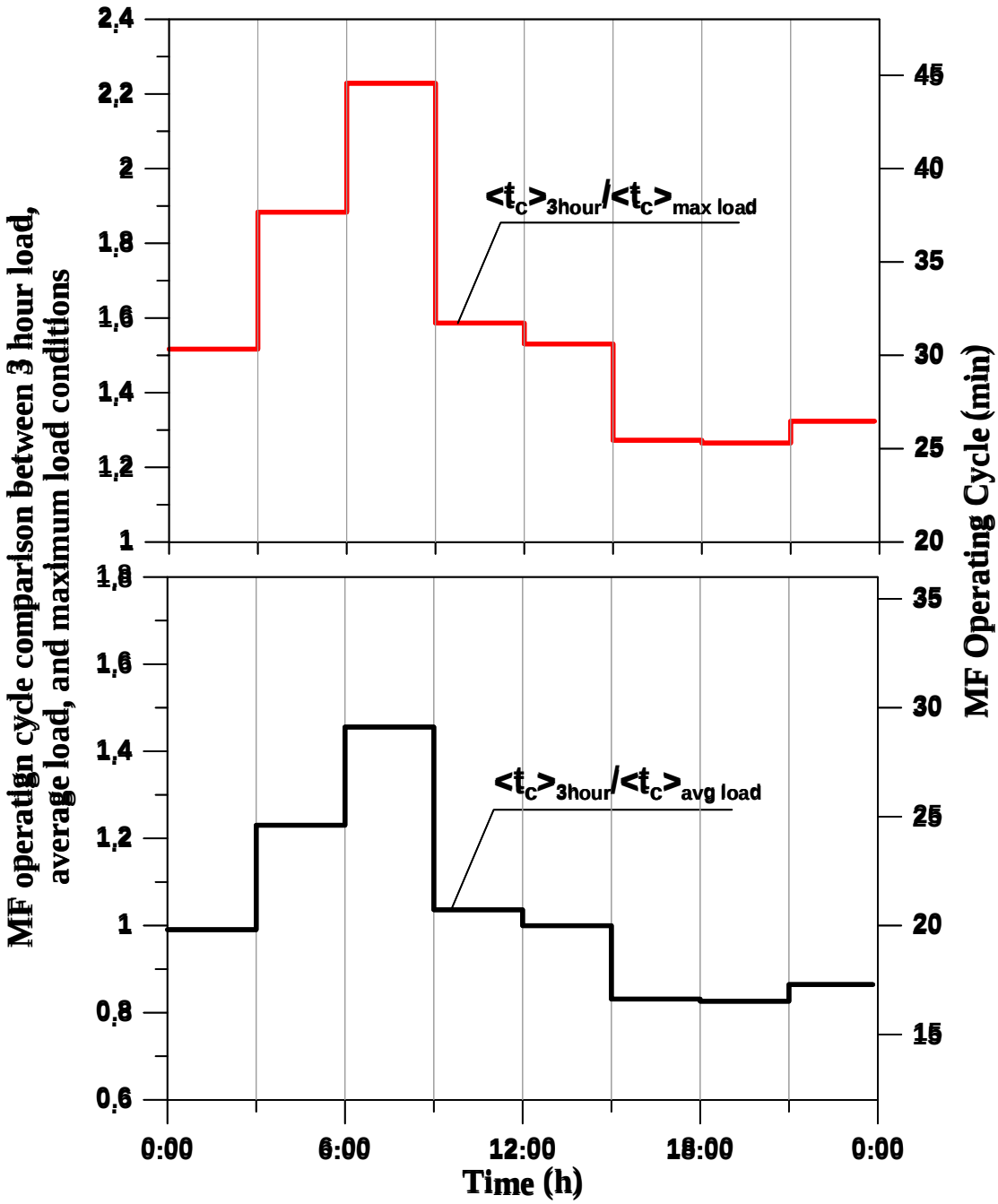

Figure 13.6. Comparison of current and dynamic-estimated MF operating cycle (i.e., time between backwash events).

Notes: $<t_c>_{3h}$ is the 3 h average cycle time; $<t_c>$ is the daily average cycle time.

Currently, the MF process operates under 21 min fixed operating cycle. After each operating cycle, the MF process is halted for backwash, which is a combination of water and air scour. The MF filtration amounts to 30% of the MF energy footprint, whereas the backwash process accounts for 70% of the energy.

Overall, it is predicted that adaptive backwash cycling, determined from the dynamic influent load, can decrease the number of backwashes in a diurnal period and decrease the energy consumption required for the MF backwash process. Any long-term effect on the permanent degradation of MF membrane performance that is due to extended periods between backwash also should be investigated.

13.3.10 Dynamics of RO Feed Pump Energy Consumption

According to Eqs. 13.6 through 13.9, fluctuations in the dissolved solid concentration result in a variation in the osmotic pressure. When RO influent contains a higher constituent load (i.e., TDS concentration), a higher applied pressure is required to keep the RO flux at a stable level. Therefore, an increase in the applied pressure requires higher power consumption by the feed pumps (see Eq. 13.9). During the off-peak hours, when the constituent load is lower, lower applied pressure and consequently lower power consumption is needed.

In addition to the constituent load, Eq. 13.9 also indicates that the power consumption of the RO feed pumps will vary because of the fluctuations in hydraulic load. Other parameters presented through Eqs. 13.6 through 13.9 (e.g., water temperature) could affect the RO power consumption as well. However, these were considered as insignificant variations with negligible effect during the diurnal period (e.g., long-term membrane fouling).

The variations of the power consumption can be simplified and calculated based on the diurnal load variations as follows (according to Eqs. 13.6 through13.9):

$$\Delta P = \Delta Q \cdot \Delta \Pi_F \tag{13.13}$$

By replacing $\Delta\Pi_F$ with the variation in TDS concentration (i.e.. represented by the conductivity differential ΔTDS), the variation of the theoretical required power among the RO feed pumps can be simplified and calculated by

$$\Delta P = \Delta Q \cdot \Delta TDS_{RO_{feed}} \tag{13.14}$$

On the basis of the plant characteristics from this study and Eq. 13.14, the diurnal power variations are mostly the result of the load fluctuations of the RO feedwater. The results presented in Figure 13.7 indicate that whereas the hydraulic and constituent loads (i.e., represented here by conductivity) fluctuate 56% and 13%, respectively, the RO power required for the feed pumps varied 74% during a typical diurnal period. Between midnight and noon, the power variation is dominated by the flow variation. From afternoon until midnight the feedwater flow is stable, thus the power variation is dominated by the variation in conductivity.

The data revealed that the required power for RO pumping decreases at midnight until 7:00 a.m. because of the simultaneous decrease of the RO feed flow and electrical conductivity. After 8:00 a.m., flow and conductivity increase, and the required power starts to rise. During the afternoon, the feed flow stabilizes; however, the conductivity increases, thus

a steady increase in required power occurs until approximately 5:00 p.m. After this, the required power decreases until midnight when the feedwater conductivity in the feed flow decreases.

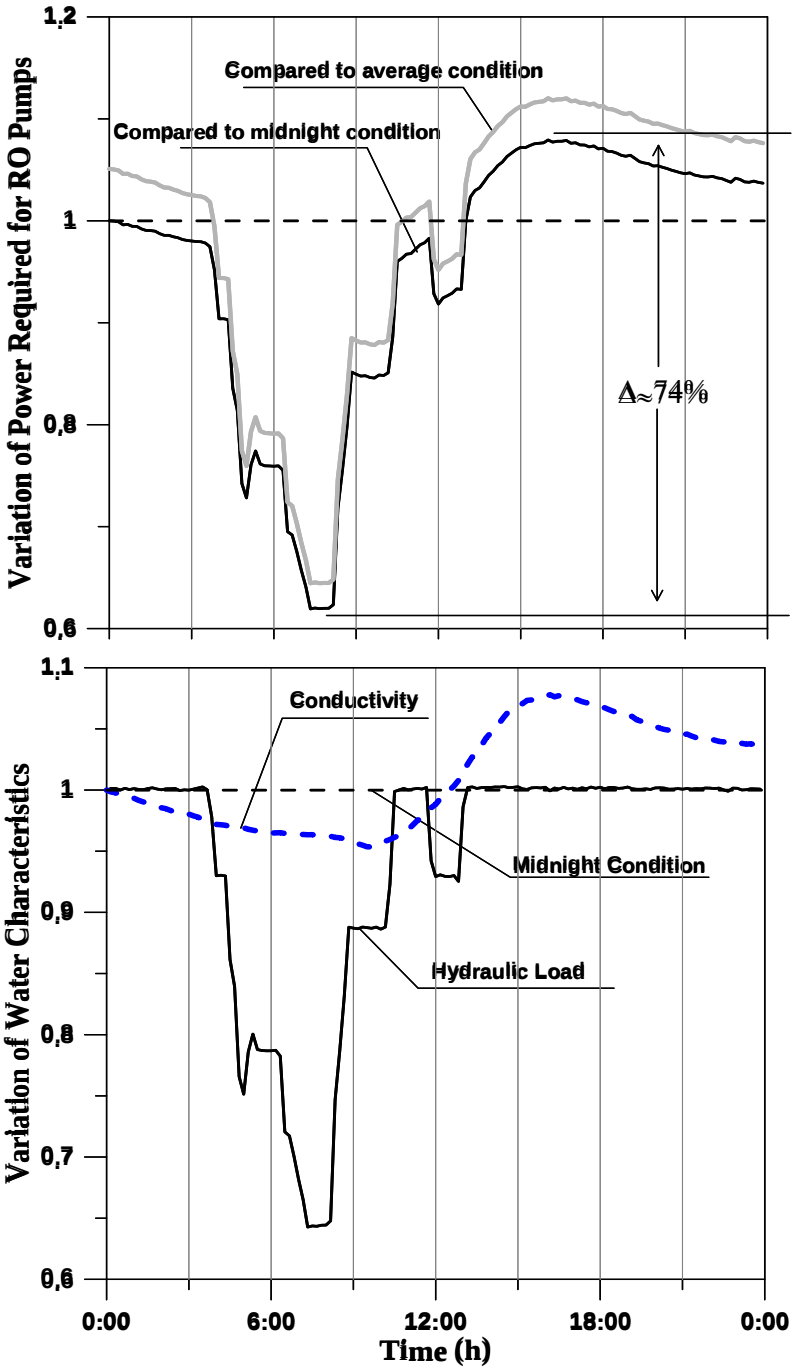

Figure 13.7. Diurnal variations of RO required power caused by fluctuations of RO hydraulic and constituent (i.e., conductivity) loading.

13.3.11 Dynamics of UV Lamp Energy Consumption

The energy footprint breakdown of the main water purification units presented in Figure 13.2 shows that UV lights account for 8% of the total energy consumption of AWPF. This contribution is sensitive to the target trace-constituent removal level (in this case, NDMA). An alternative to escalating the energy footprint is a reduction of the hydraulic throughput (i.e., Q) per unit process, shown in Figure 13.8, which would imply increased capital costs to meet the same flow production targets. Figure 13.8 shows that during the diurnal cycle the removal of the target constituent NDMA is variable. This implies that if dynamic operations were in place, the target removal could still be reached on a daily average adjusting the Q or HRT of the process for the current situation.

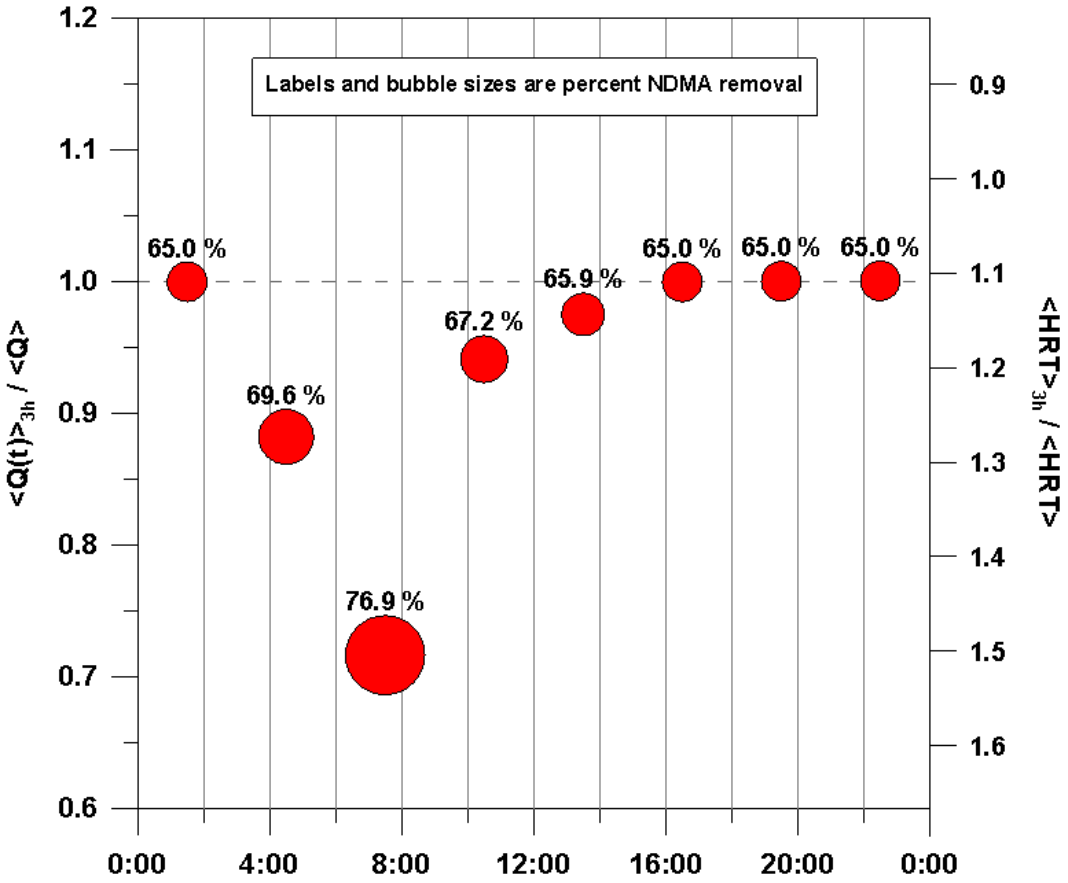

Figure 13.8. Projection of the reduction in AOP's effluent flow rate (Y axis) as a function of increasing NDMA removal (X axis).

Notes: Labels and bubble sizes show the relative increase in hydraulic retention time within the UV reactors. Constant EE/O was assumed.

13.4 AWPF Carbon Footprint

13.4.1 Background

The principal greenhouse gases (GHGs) emitting to the atmosphere are carbon dioxide (CO_2), methane (CH_4), nitrous oxide (N_2O) and chlorofluorinated gases (USEPA, 2013). Each gas has a global warming potential, which quantifies the molecular potential to accumulate heat

relative to that of carbon dioxide (IPCC, 2007). Therefore, GHGs reported in this study are in terms of the equivalent amount of carbon dioxide (CO_2eq).

Generally, during the carbon footprint analyses of an operating facility, the GHG emissions are categorize into the direct and indirect emissions. Moreover, a special category is defined for the indirect emission associated with imported electrical power. For reporting purposes (e.g., when using an accounting and reporting protocol such as the LGOP, 2010) the direct emission can be labeled as Tier I, the indirect emissions for power importation as Tier II, and all other indirect emissions as Tier III. The boundary we considered in this study includes all tiers.

Because of their small contributions, direct CO_2, CH_4, and N_2O emissions of treatment processes (i.e., MF, RO and AOP) are considered negligible. This is because the unit operations employed in the AWPF are largely relying on electrical power and do not emit directly carbon- or nitrogen-based gases. The indirect emissions are categorized as follows:

1. Tier II: GHG emissions associated to the electricity consumed by the energy intensive treatment processes. The electricity is purchased from the local power provider agencies.
2. Tier III: GHG emissions associated to the chemicals transported to the treatment facility by trucks.

More GHG emissions indirectly connected to this facility could be listed, such as the following:

1. The carbon and energy footprint associated to the manufacturers who produce the chemicals consumed by the AWPF's treatment processes
2. The GHG emissions associated to the other treatment agencies who are involved in AWPF's waste treatment (e.g., the MF backwash waste is pumped to adjacent water reclamation facility for further treatment)
3. The GHG emissions associated to the pumping that transfers the water out of the facility boundaries (e.g., the produced water is pumped many mil for both aquifer recharge and seawater intrusion purposes, or the RO concentrate is discharged to the ocean by the adjacent water reclamation facility)

Also, because any of these indirect contributions are beyond the boundary of the AWPF plant they would require a model of their own to be quantified, and this would be both impractical and potentially unattainable. For example, one could think at the carbon footprint of manufacturing a gallon of chemical used in the process. Even in the cases where the carbon footprint of the manufacturing process were quantified, unless the location of the manufacturing plant or of the raw material mines were known, the overall carbon footprint of the unit-volume of chemical would be impossible to quantify. Therefore, because we are here limiting our analysis to a carbon footprint calculation and not extending it to the life-cycle assessment, these additional indirect emissions are excluded from our analysis.

A final introductory note pertains to the difference between quantification and reporting of GHG emissions and equivalents. In this work we quantified all emission without making distinctions between emissions to be reported or not, should a regulatory framework for GHG emission reporting be in place.

13.4.2 Energy Consumption

Note: Customary units for carbon footprint are metric tons
(1 metric ton=1 tonne=1000 kg=1 t)

The treatment processes utilized by AWPF are amid the most energy intensive processes available to the water industry. However, because of the nature of the purification treatment and the concentration limits for product water, this energy consumption is inevitable. Different energy sources are utilized by power supply companies for electricity generation (CEC, 2011). Among them we can mention conventional sources (e.g., natural gas, coal, nuclear power, and hydroelectricity), as well as nontraditional renewable sources (e.g., photovoltaic, biogas, and wind power).

In the state of California during 2010, natural gas contributed for 53%, nuclear power for 16%, hydroelectricity for 15%, and renewable sources for 14.6% of the in-state power generated (CEC, 2011). Nevertheless, in 2010 29.3% of the consumed power was imported from the out-of-state power sources (i.e., 8.5% from Northwest United States, and 20.8% from Southwest United States). Among the imported power, coal-source power contributed for 22.3%, natural gas for 14.0%, and 41% had unspecified sources (CEC, 2011).

The GHG emissions of electricity generation ($gCO_{2\ eq}$/kWh) vary between the aforementioned power sources. Whereas hydroelectricity (with the average emission of 15 gCO_2/kWh) and nuclear power (with the average emission of 62 gCO_2/kWh) have low associated carbon footprint, the conventional fossil fuel sources, such as coal (with the average emission of 993 gCO_2/kWh) and natural gas (with the average of emission of 664 gCO_2/kWh), have the highest GHG emissions (Fridleifsson et al., 2008; Lenzen, 2008).

Figure 13.9 presents the energy-associated CO_{2eq} emission+ of main AWPF's treatment processes. The results are calculated based on the energy (kWh) consumed by the AWPF's treatment processes during 2011 and the published data for Southern California carbon emission of 236 gr CO_{2eq}/kWh (PG&E, 2013). The results indicate that RO has the highest monthly emission of 909 tonne/month, following by MF and AOP with monthly emissions of 439 tonne/month and 138 tonne/month, respectively.

Although a dynamic calculation of the energy-associated carbon footprint is possible within a diurnal cycle, the average daily or monthly power consumption is adequate as a basis for calculation, because the AWPF processes are operated at steady state.

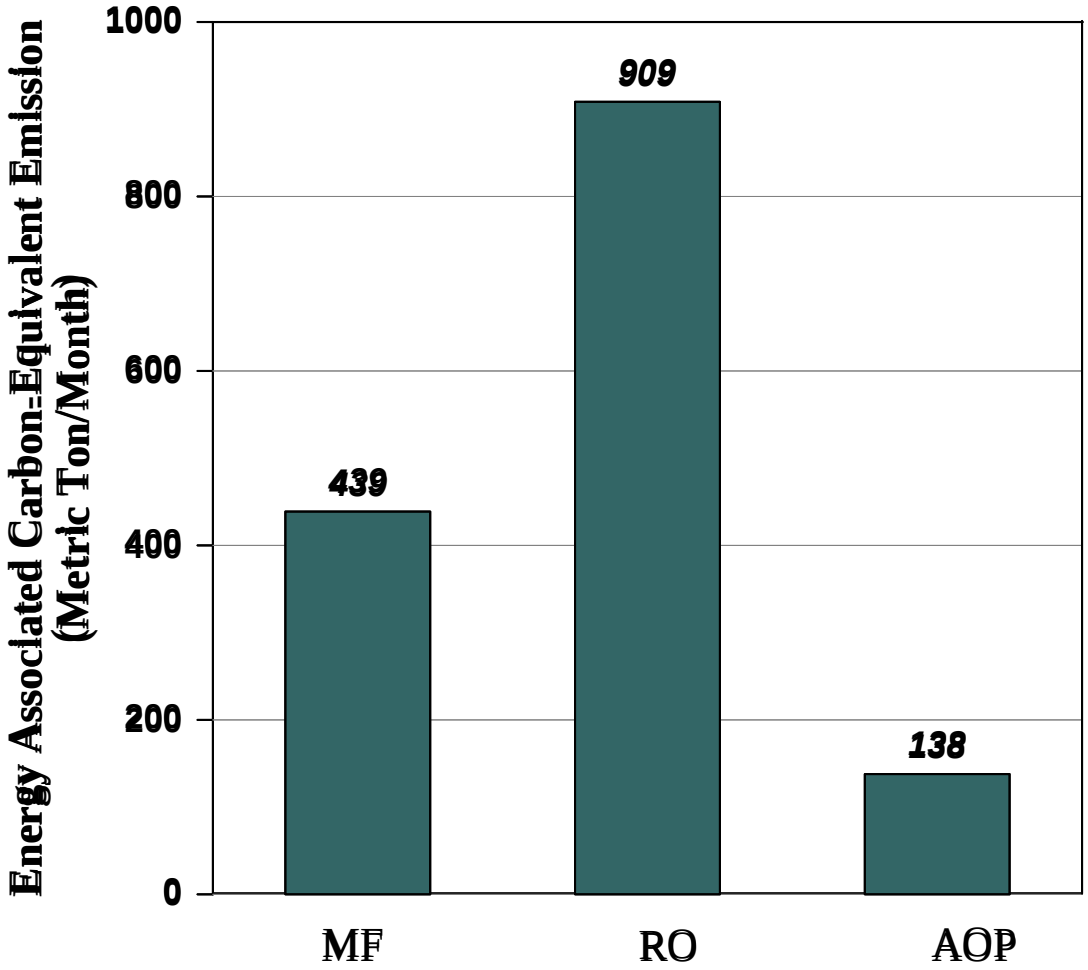

Figure 13.9. Monthly energy associated CO_{2eq} emission of the AWPF treatment processes based on the energy consumption reported during 2011.

13.4.3 Chemical Transportation

The water purification processes are chemical intensive. AWPF uses the chemicals for different treatment stages including operating and CIP stages of the MF process, operating and posttreatment stages of the RO process and operating stage of the AOP process. There is almost no chemical use for the MF backwash. The chemicals are carried to the treatment plant mostly by trucks and stored appropriately for diurnally or periodically (e.g., the chemicals required for MF CIP stage) consumption. Table 13.2 presents the main chemicals that are used for water purification processes, the number of onsite tanks available for each chemical, and the monthly average of tank loads. The last column is calculated on the basis of chemical usage reported by the treatment agency during 2011 and the truck loading capacity.

A comparison between the quantitative truckloads associated with AWPF's treatment processes is presented in Figure 13.10. As evident in this figure, the RO process has the highest associated monthly truckload count (i.e., 79.3 truckloads/month), mainly because of the lime consumption required for the RO posttreatment stage (i.e., 62.4 average monthly truck loads). The MF process accounts for an average of 39.1 monthly loads. AOP has the lowest monthly truckloads with an average of 2.2 monthly loads. Overall, of the monthly average 120 truckloads entering the AWPF, half of them are related to the lime chemical consumption.

Table 13.2. Chemical Usages by Different Stages of AWPF Treatment Processes and Their Associated Truckloads

Chemical List	Quantity of Tanks	Tank Volume (gal)	Available Volume (gal)	Monthly Consumption (ton[a]/month)	Truck Load (ton[a])	Monthly Truck Load
MF-Operating Stage						
NaClO	6	32000	192000	520.75	25	20.83
MF-Backwash Stage						
N/A	-	-	-	-	-	-
MF-Clean In Place (CIP) Stage						
Caustic (Sodium Hydroxide)	1	7500	7500	372.4	25.0	14.9
Memclean-C Bulk	1	500	500	1.1	1.0	1.1
Memclean-C Reusable Tote	1	250	250			1
Citric Acid –Bulk Tank	2	3490	6980	28.6	22.5	1.3
Citric Acid –Day Tank	1	1768	1768			
RO-Operation Stage						
Sulfuric Acid	4	32000	128000	358.9	25	14.4
Treshold Inhibitor (anti-scalant)	2	4500	9000	31.16	22.5	1.4
Ro-Post-Treatment Stage						
Lime	n/a	n/a	n/a	1497.0	24	62.4
RO-Clean In Place (CIP) Stage						
Sodium Tripolyphosphate (STPP)	n/a	n/a	n/a	3.5	14.0	0.3
Sodium Dodecylbenzene Sulfonate (SDDBS)	n/a	n/a	n/a	0.4	1.3	0.3
RO CIP[b]	n/a	n/a	n/a	1.9	3.0	0.6
AOP-Operation Stage						
Hydrogen Proxide	n/a	n/a	n/a	48.95	22.5	2.2

Notes: n/a=not available; [a] short-ton, equal to 2000 lb (907.2 kg); [b] includes: Avista P112, PWT Lavasol V, and HCl.

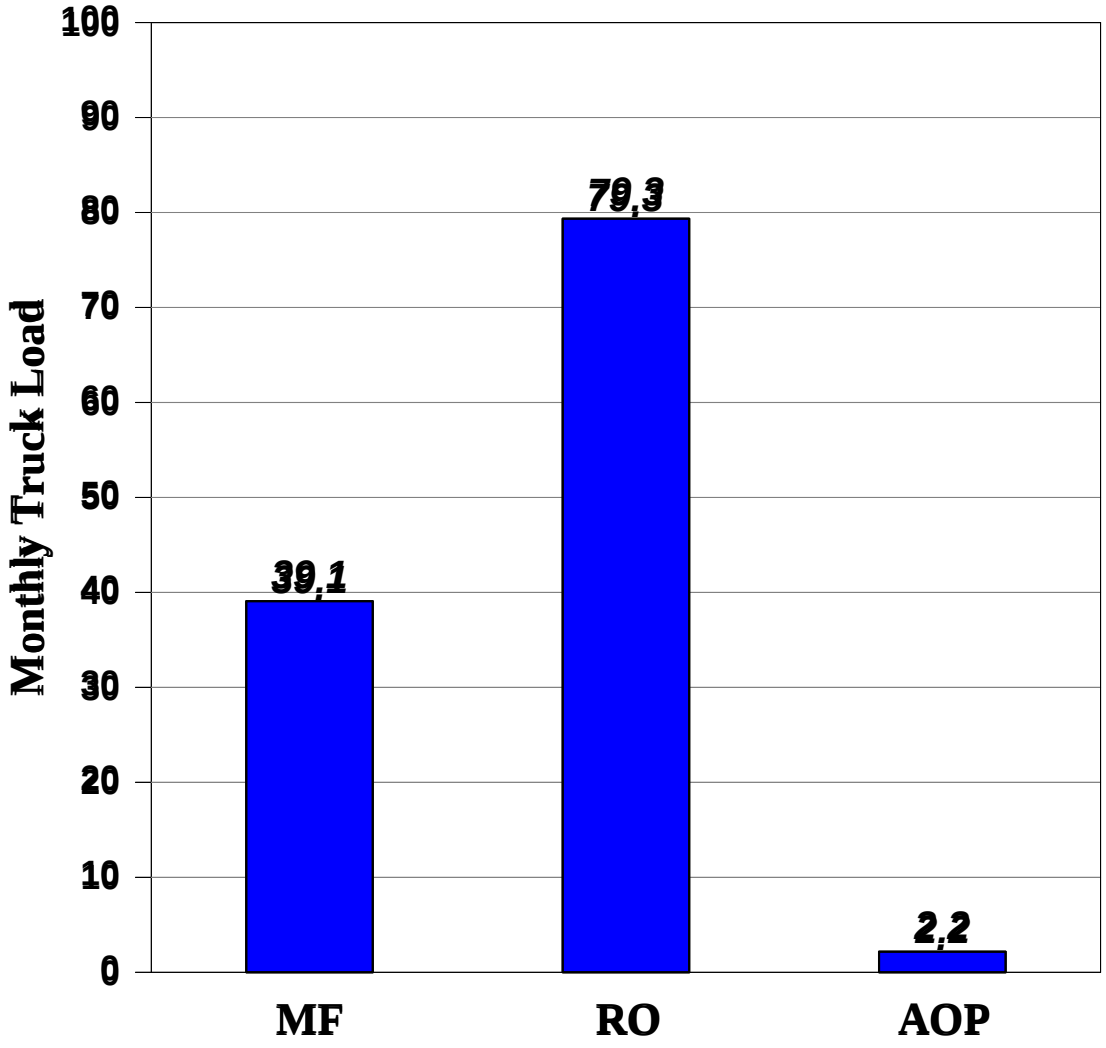

Figure 13.10. Comparison of monthly truck loads between AWPF's treatment processes. The truckloads provide chemicals required for purification processes.

Note: RO includes lime posttreatment in this figure.

In the United States, trucks are powered by diesel engines. The combustion of diesel fuel and the products of diesel exhaust release GHGs. In this study a carbon footprint analysis of chemical transportation by semi-trailer trucks was conducted. The analysis is based on the average fuel consumption of 2426 kJ t^{-1} km^{-1} for semi-trailer trucks in the United States (USDOE, 2007). This can be converted to mass of CO_2 per unit distance traveled per unit mass transported:

$$\mathrm{CO_2\,Emission} = \begin{pmatrix}\text{Fuel}\\ \text{Consumption}\end{pmatrix} \times \begin{pmatrix}\text{Energy Density}\\ \text{of Diesel Fuel}\end{pmatrix} \times \begin{pmatrix}\text{Carbon Dioxide}\\ \text{Equivalent Emission}\end{pmatrix} \qquad (13.15)$$

$$\left(\mathrm{CO_2}\right)_{\mathrm{Truck}} = \frac{2426\mathrm{kJ}}{\mathrm{t}\cdot\mathrm{km}} \times \frac{1\mathrm{L}_{\text{Diesel Fuel}}}{36.4\mathrm{MJ}} \times \frac{2.682\mathrm{kg\ CO_2}}{1\mathrm{L}_{\text{Diesel Fuel}}} = 0.179\frac{\mathrm{kgCO_2}}{\mathrm{km}\cdot\mathrm{tonne}} \qquad (13.16)$$

It is also important to consider CH_4 and N_2O emission factors that are due to the combustion of diesel fuel. Heavy diesel-powered vehicles were responsible for nearly one-half (44.1%) of highway vehicle nitrogen oxide emissions in 2005, whereas light gasoline vehicles were responsible for the rest (USDOE, 2007). The emission factors for CH_4 and N_2O are from USEPA (2008). Nitrous oxide emissions from diesel combustion trucks were included as 4.93×10^{-6} kg t^{-1} km^{-1} (1.47×10^{-3} $kg_{CO2,eq}$ t^{-1} km^{-1}). From the same source we calculated the methane emissions as 5.26×10^{-6} kg t^{-1} km^{-1} (1.31×10^{-3} $kg_{CO2,eq}$ t^{-1} km^{-1}) for trucks. The total diesel emissions as carbon dioxide equivalent for each transportation mode were determined adapting the transportation model by Rosso and Chau (2009):

$$\mathrm{GHG\ Emissions} = \mathrm{CO_2\ Emission} + \left(298 \times \mathrm{N_2O\ Emission}\right) + \left(25 \times \mathrm{CH_4\ Emission}\right) \qquad (13.17)$$

$$\begin{pmatrix}\text{Diesel}\\ \text{Emission}\end{pmatrix}_{Trucks} = \frac{1.79\cdot10^{-1}kg_{CO_2}}{tonne\cdot km} + \left(298\times\frac{4.93\cdot10^{-6}kg_{N_2O}}{tonne\cdot km}\right) + \left(25\times\frac{5.26\cdot10^{-6}kg_{CH_4}}{tonne\cdot km}\right) = \frac{1.80\cdot10^{-1}kg_{CO_2,eq}}{tonne\cdot km} \qquad (13.18)$$

To quantify the GHG emissions associated with the chemical transportation, we multiplied the average monthly chemical consumption (i.e., presented in Table 13.2) by 180 gr CO_{2eq}/tonne.km (i.e., from Eq. 13.18). The transportation distance was assumed 50 mi (80 km). This is because in general the chemical manufacturers have production overseas and subsequent shipment to a local depot is performed to maintain regional stock. After contacting all manufacturers, none were able to backtrack the origin of their product to a single location, but it was rather a blend of the same chemical coming from different points of production. Therefore, we limited our transportation distance to the local depots, which are on average approximately 50 mi from the AWPF.

Figure 13.11 provides a comparison between the GHG emissions associated to the chemical transportation for different AWPF's processes. The results indicate that the RO process has the highest GHG emissions because of the high volume of lime required for its posttreatment process. The average monthly CO_{2eq} emission associated to the truck transportation for RO process is calculated 27 metric ton/month, for MF process is 13 metric ton/month, and for AOP is calculated 0.7 metric ton/month.

Instead of 50 mi (80 km), if we consider a 100 mi (160 km) transportation distance, the transportation associated GHG emissions would be doubled (i.e., 54 ton for RO, 26 ton for MF and 1.4 ton for AOP). However, our sensitivity analysis (see Section 14.2.4) shows that because of the intensive GHG emissions associated to the intensive energy consumed by AWPF's treatment processes, the total AWPF's carbon footprint is not sensitive to the transportation distance.

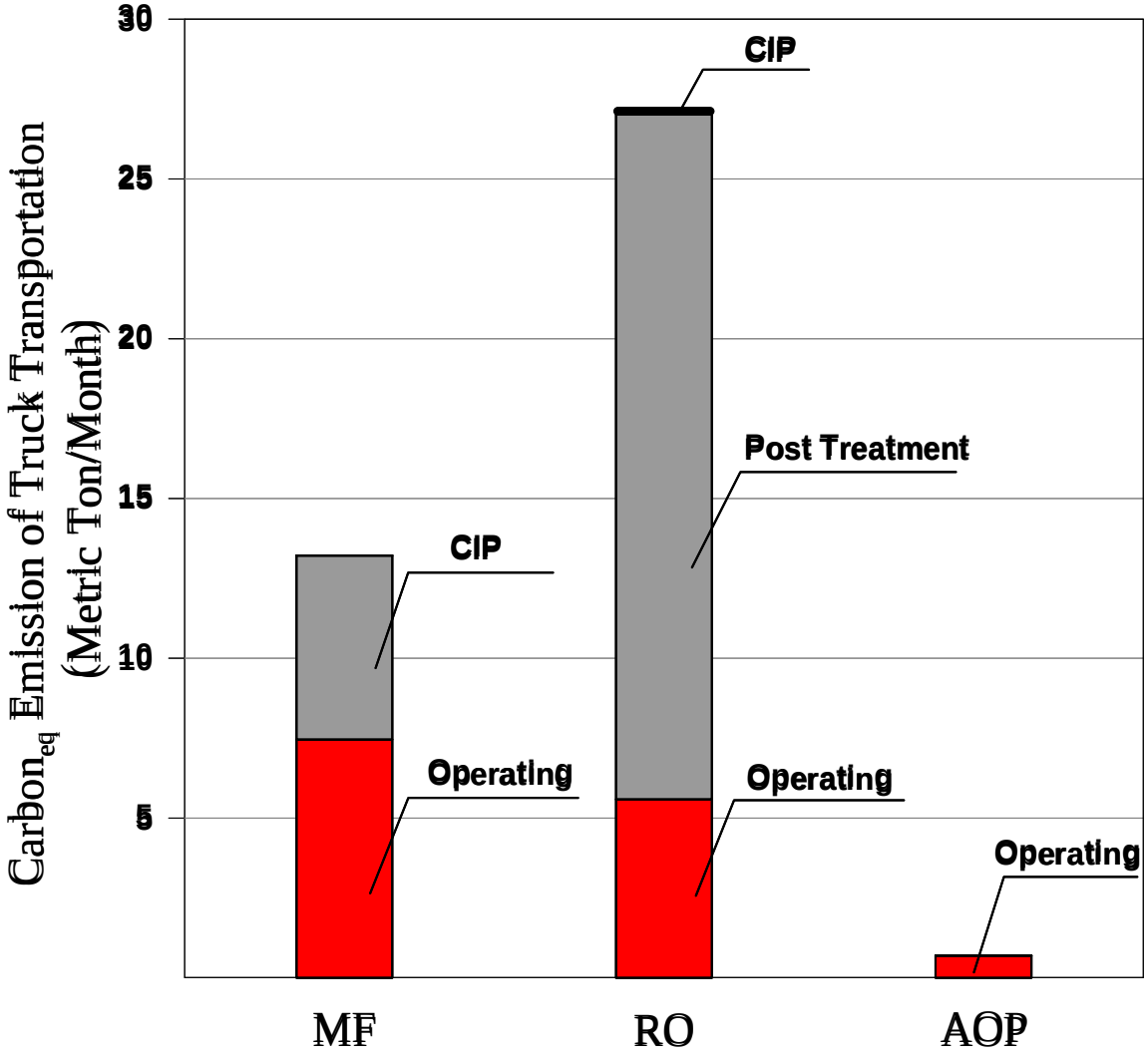

Figure 13.11. Monthly CO_{2eq} emission associated to the chemical transportation.

Note: The results are calculated based on the monthly chemical consumption (presented in Table 13.2) and an assumption of 50 mi (80 km) transportation distance.

13.4.4 Sensitivity Analysis

The energy consumption and chemical transportation are the main GHG emission components for AWPF. As discussed in background section, there are more GHG emissions that are actually (or potentially) involved with AWPF's treatment processes (see Section 13.4.1). However, these were eliminated them from the analysis because of the boundaries defined for this study. The results of GHG emission analysis (Figure 13.12) indicate that the AWPF's total carbon footprint is dominated by the energy-associated carbon emission (i.e., 97% contribution).

Meanwhile, the carbon emissions associated with chemical transportation are only responsible for a small 3% contribution among the studied components. The results are based on 50 mi of chemical transportation. If this parameter is doubled to an average 100 mi of transportation for the consumed chemicals, the contribution of this component would increase by ~2% (i.e., overall 5% contribution), which shows how low in sensitivity the total carbon footprint is for this parameter.

The energy associated carbon emissions were discussed in Section 13.4.2. The results of the calculations were based on the GHG emissions reported for the unit energy generation by local power supply agencies (236 gr CO_{2eq}/kWh). However, other studies (among others, Sobhani et al. 2012) indicated that the carbon emissions associated with the unit energy generation could vary seasonally. In the state of California, the carbon emission of unit energy generation is higher during the summer season compared to the winter. This is due to a greater contribution of fossil fuel sources in power generation to fulfill the augmented power demand during the peak hours of hot summer days. California is gradually changing its portfolio of energy sources employed for electrical power generation. A greater contribution from renewable sources with lower carbon emission compared to traditional fossil fuel power sources are expected in the future. The contribution of energy consumption is very large, thus any variation in the unit energy GHG emissions can significantly change the total carbon footprint of the AWPF and make this parameter significantly sensitive.

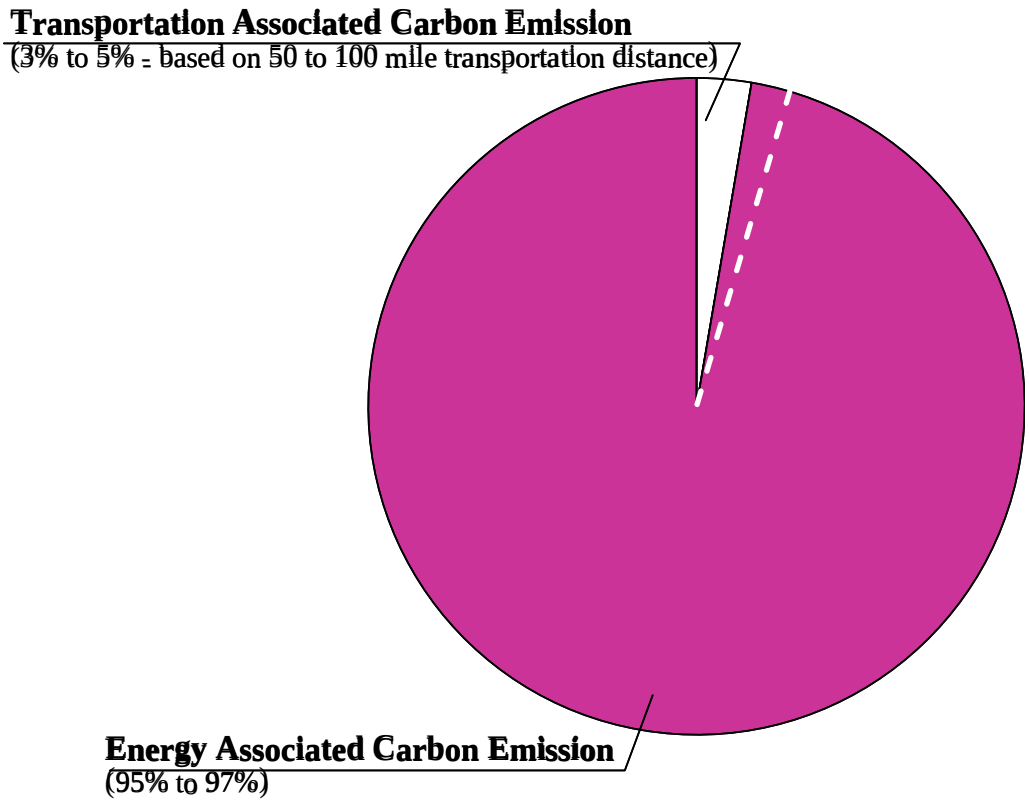

Figure 13.12. Breakdown of total CO_{2eq} emission components of the AWPF.

Note: The dashed line represents the different distribution if a distance of 100 mi for chemicals delivery is assumed.

13.4 Conclusions

A dynamic energy footprint model and its application to MF/RO/UV/AOP of OCWD's AWPF was generated. The model presents the diurnal variation of input parameters (e.g., hydraulic load and pollution concentration) and its effects on electricity consumption and its amplitude of variation. The results show the benefit of adaptive MF backwash cycling (determined from the dynamic influent load), and reveal the significant variation in required power for RO pumping in a regular diurnal period. Furthermore, this chapter analyzes the indirect greenhouse gas emission associated to AWPF process operations. The results indicate that this emission is dominated by the emission associated to electricity consumption (i.e., 95~97% contribution) compared to the emission associated to chemical transportations (i.e., 3~ 5% contribution).

References

Abdelmelek, S. B.; Greaves, J.; Ishida, K. P.; Cooper, W. J.; Song, W. Removal of Pharmaceutical and Personal Care Products from Reverse Osmosis Retentate Using Advanced Oxidation Processes. *Environ. Sci. Technol.* **2011**, *45*, 3665–3671.

Adams, C. D.; Scanlan, P. A.; Secrist, N. D. Oxidation and Biodegradability Enhancement of 1,4-Dioxane using Hydrogen Peroxide and Ozone. *Environ. Sci. Technol*. **1994**, *28*, 1812–1818.

Afifi, M. Z.; Blatchley, E. R., III. Characterization of Chloramines in Source Waters from an Advanced Water Purification Facility (AWPF) by Membrane Introduction Mass Spectrometry (MIMS) and Wet-Chemical Methods. **2012**, unpublished work.

Ahmad, S. R.; Reynolds, D. M. Monitoring of Water Quality Using Fluorescence Technique: Prospect of On-Line Process Control. *Water Res.* **1999**, *33*, 2069–2074.

Al-Abri, M.; Hilal, N. Artificial Neural Network Simulation of Combined Humic Substance Coagulation and Membrane Filtration. *Chem. Eng. J.* **2008**, *141*, 27–34.

Alegre, M. L.; Gerones, M.; Rosso, J. A.; Berolotti, S. G.; Braun, A. M.; Martire, D. O.; Gonzales, M. C. Kinetic Study of the Reactions of Chlorine Atoms and Cl_2-Radical Anions in Aqueous Solutions. 1. Reaction with Benzene. *J. Phys. Chem. A.* **2000**, *104*, 3117–3125.

Al-Rifai, J. H.; Khabbaz, H.; Schäfer, A. I. Removal of Pharmaceuticals and Endocrine Disrupting Compounds in a Water Recycling Process Using Reverse Osmosis Systems. *Sep. Purif. Technol.* **2011**, *77*, 60–67.

Andreozzi, R.; Caprio, V.; Insola, A.; Marotta, R. The Oxidation of Metol (N-methyl-P-aminophenol) in Aqueous Solution by UV/H_2O_2 Photolysis. *Water Res*. **2000a**, *34*, 463–472.

Andreozzi, R.; Caprio, V.; Insola, A.; Marotta, R.; Sanchirico, R. Advanced Oxidation Processes for the Treatment of Mineral Oil-Contaminated Wastewaters. *Water Res.* **2000b**, *34*, 620–628.

Aoki, T. Continuous Flow Method for Simultaneous Determination of Monochloramine, Dichloramine, and Free Chlorine: Application to a Water Purification Plant. *Environ. Sci. Technol*. **1989**, *23*, 46–50.

Baghoth, S. A.; Dignum, M.; Grefte, A.; Kroesbergen, J.; Amy, G. L. Characterization of NOM in a Drinking Water Treatment Process Train with No Disinfectant Residual. *Water Sci. Technol.* **2009**, *9*, 379–386.

Bai, B. R.; Leow, H. F. Modeling and Experimental Study of Microfiltration using a Composite Module. *J. Memb. Sci.* **2002**, *204*, 359–377.

Baker, J. S.; Dudley, L. Y. Biofouling in Membrane Systems–A Review. *Desalination* **1998**, *118*, 81–90.

Ballschmiter, K. A Marine Source for Alkyl Nitrates. *Science* **2002,** *297*, 1127–1128.

Bartman, A. R.; Lyster, E.; Rallo, R.; Christofides, P. D.; Mineral Scale Monitoring for Reverse Osmosis Desalination via Real-Time Membrane Surface Image Analysis. *Desalination* **2011**, *273*, 64–71.

Baxendale, J. H.; Wilson, J. A. The Photolysis of Hydrogen Peroxide at High Light Intensities. *Trans. Farad. Soc*. **1957**, *53*, 344–356.

Bazylinski, D. A; Hollocher, T.C. Evidence from the Reaction between Trioxodinitrate (II) and Nitrogen-15 Labeled Nitric Oxide that Trioxodinitrate (II) Decomposes into Nitrosyl Hydride and Nitrite in Neutral Aqueous Solution. *Inorg. Chem.* **1985**, *24*, 4285–4288.

Beltrán, F. J.; Rivas, J.; Alvarez, P. M.; Alonso, M. A.; Acedo, B. A Kinetic Model for Advanced Oxidation Processes of Aromatic Hydrocarbons in Water: Application Phenanthrene and Nitrobenzene. *Ind. Eng. Chem. Res*. **1999**, *38*, 4189–4199.

Benner, J.; Salhi, E.; Ternes, T.; von Gunten, U. Ozonation of Reverse Osmosis Concentrate: Kinetics and Efficiency of Beta Blocker Oxidation. *Water Res.* **2008**, *42*, 3003–3012.

Bereschenko, L. A.; Heilig, G. H. J.; Nederlof, M. M.; van Loosdrecht, M. C. M.; Stams, A. J. M.; Euverink, G. J. W. Molecular Characterization of the Bacterial Communities in the Different Compartments of a Full-Scale Reverse-Osmosis Water Purification Plant. *Appl. Environ. Microbiol*. **2008**, *74*, 5297–5304.

Bereschenko, L. A.; Stams, A. J. M.; Euverink, G. J. W.; van Loosdrecht, M. C. M. Biofilm Formation on Reverse Osmosis Membranes is Initiated and Dominated by Sphingomonas spp. *Appl. Environ. Microbiol*. **2010**, *76*, 2623–2632.

Bernados, B. California Department of Public Health (CDPH), Drinking Water Technical Program. Personal communication, August 2009.

Bielski, B. H. J.; Cabelli, D. E. Superoxide and Hydroxyl Radical Chemistry in Aqueous Solution. In *Active Oxygen Chemitry*; Foote, C. S.; Ed.; Chapman & Hall: Glasgow, UK, 1995, pp 66–67.

Black, E. D.; Hayon, E. Pulse Radiolysis of Phosphate Anions H2PO4-, HPO42-, PO43-, and P2O74- in Aqueous Solutions. *J. Phys. Chem.* **1970**, *74*, 3199–3203.

Blake, N. J.; Blake, D. R.; Sive, B. C.; Katzenstein, A. S.; Meinardi, S.; Wingenter, O.W.; Rowland, F. S. The Seasonal Evolution of NMHCs and Light Alkyl Nitrates at Middle to High Northern Latitudes during TOPSE. *J. Geophys. Res.: Atmos.* **2003,** *108*, 8359–8375.

Bligh, E. G.; Dyer, W. J. A Rapid Method of Total Lipid Extraction and Purification. *Can. J. Biochem. Physiol.* **1959**, *37*, 911–917.

Bolton, J. R.; Valladares, J. E.; Zanin, J. P.; Cooper, W. J.; Nickelsen, M. G.; Kajdi, D. C.; Waite, T. D.; Kurucz, C. N. Figures-of-Merit for Advanced Oxidation Technologies: A Comparison of Homogeneous UV/H_2O_2, Heterogeneous UV/TiO_2 and Electron Beam Processes. *Adv. Oxidation. Technol.* **1998**, *3*, 174–181.

Brandhuber, P. J.; Korshin, G. *Methods for the Detection of Residual Concentrations of Hydrogen Peroxide in Advanced Oxidation Processes*. WateReuse Research Foundation: Alexandria, VA, 2008; pp 1–64.

Brink, L. E. S; Elbers, S. J. G.; Robbertsen, T.; Both, B. The Anti-Fouling Action of Polymers Preadsorbed on Ultrafiltration and Microfiltration Membranes. *J. Memb. Sci*. **1993**, *76*, 281–291.

Brown, N. *Orange County Water District UV Disinfection and Oxidation System Final Performance Validation Report*; Trojan Technologies: London, ON, Canada, November 25, 2008; pp 1–12.

Brown, N. Trojan Technologies. Personal communication, 2013.

Busby, J. B.; Andrews, J. F. Dynamic Modeling and Control Strategies for the Activated Sludge Process. *J. Wat. Pollut. Control Fed.* **1975**, *47*, 1055–1080.

Buxton, G. V.; Stuart, C. R. Re-Evaluation of the Thiocyanate Dosimeter for Pulse Radiolysis. *J. Chem. Soc. Farad. Trans*. **1995**, *91*, 279.

Buxton, G. V.; Greenstock, C. L.; Helman, W. P.; Ross, A. B. Critical Review of Rate Constants for Reactions of Hydrated Electrons, Hydrogen Atom and Hydroxyl Radicals ($^{\bullet}OH/^{\bullet}O^{-}$) in Aqueous Solutions. *J. Phys. Chem. Ref. Data* **1988**, *17,* 513–886.

Byrne, W. *Reverse Osmosis: A Practical Guide for Industrial Users*, 2nd ed.; Tall Oaks Publishing: Littleton, CO, 2002, p 55.

California Department of Public Health (CDPH). 1,4-Dioxane. Certificates and Licenses, Drinking Water Systems, http://www.cdph.ca.gov (accessed December 7,, 2013)

CDPH A Brief History of NDMA Findings in DrinkingWater Supplies and Related Activities. http://www.cdph.ca.gov/certlic/drinkingwater/Pages/NDMAhistory.aspx, (accessed January 4, 2011).

California Energy Commission (CEC) Quarterly Fuel and Energy Report, California Energy Commission. Total Electricity System Power, Total System Power for 2012: Changes From 2011. http://energyalmanac.ca.gov/electricity/total_system_power.html, 201 (accessed March 2013).

Carl, I. L. Back to Basics: Particle Characterization. Malvern Instruments, Worchestershire, UK. 2012, http://www.malvern.com/malvern/kbase.nsf/allbyno/KB003555/ $file/MRK1855-01.pdf (accessed December 2010).

Chang, S.; Fane, A. G. The Effect of Fiber Diameter on Filtration and Flux Distribution Relevance to Submerged Hollow Fiber Modules. *J. Membr. Sci.* **2001**, *184*, 221–231.

Chen, C. L.; Liu, W.-T.; Chong, M. L.; Wong, W. T.; Ong, S. L.; Seah, H.; Ng, W. J. Community Structure of Microbial Biofilms Associated with Membrane-Based Water Purification Processes as Revealed Using a Polyphasic Approach. *Appl. Microbiol. Biotechnol.* **2004**, *63*, 466–473.

Chen, W.; Westerhoff, P.; Leenheer, J. A.; Booksh, K. Fluorescence Excitation-Emission Matrix Regional Integration to Quantify Spectra for Dissolved Organic Matter. *Environ. Sci. Technol.* **2003**, *37*, 5701–5710.

Chin, M.; Wine, P. H. A Temperature-Dependent Kinetics Study of the Aqueous Phase Reaction $OH + SCN^{-} \rightarrow SCNOH^{-}$ and $SCN + SCN^{-} \leftrightarrow (SCN)_2^{-}$. *J. Photochem. Photobiol. A.* **1992**, *69*, 17–25.

Chiron, S.; Fernandez-Alba, A.; Rodriguez, A.; Garcia-Calvo, E. Pesticide Chemical Oxidation: State-of-the-Art. *Water Res.* **2000**, *34*, 366–377.

Choi, J.; Valentine, R. L. Formation of N-nitrosodimethylamine (NDMA) from Reaction of Monochloramine: A New Disinfection By-Product. *Water Res*. **2002**, *36*, 817–824.

Chow, C. W. K.; Fabris, R.; Drikas, M. A Rapid Fractionation Technique to Characterize Natural Organic Matter for the Optimisation of Water Treatment Processes. *J. Water Supply: Res. Technol.–AQUA* **2004**, *53*, 85–92.

Christensen, B. E.; Characklis, W. G. Physical and Chemical Properties of Biofilms. In *Biofilms*; Characklis, W. G.; Marshall, K. C.; Ed.; Wiley: NY, 1990; pp 93–130.

Christensen, H. S.; Sehestend, K.; Corfitzan, H. Reactions of Hydroxyl Radicals with Hydrogen Peroxide at Ambient and Elevated Temperatures. *J. Phys. Chem.* **1982**, *86*, 55–68.

Chuck, A. L.; Turner, S. M.; Liss, P. S. Direct Evidence for a Marine Source of C1 and C2 Alkyl Nitrates. *Science* **2002,** *297***,** 1151–1154.

Coble, P. G. Characterization of Marine and Terrestrial DOM in Seawater Using Excitation-Emission Matrix Spectroscopy. *Mar. Chem.* **1996**, *51*, 325–346.

Coble, P. G.; Del Castillo, C. E.; Avril, B. Distribution and Optical Properties of CDOM in the Arabian Sea during the 1995 Southwest Monsoon. *Deep-Sea Res. Part II* **1998**, *45*, 2195–2223.

Coble, P. G.; Green, S. A.; Blough, N. V.; Gagosian, R. B. Characterization of Dissolved Organic Matter in the Black Sea by Fluorescence Spectroscopy. *Nature* **1990**, *348*, 432–435.

Cohen, R. D.; Probstein, R. F. Colloidal Fouling of Reverse Osmosis Membranes. *J. Colliod Interf. Sci.* **1986**, *114*, 194–207.

Colman, J. C.; Swanson, A. L.; Meinardi, S.; Sive, B. C.; Blake, D. R.; Rowland, F. S. Description of the Analysis of a Wide Range of Volatile Organic Compounds in Whole Air Samples Collected during PEM-Tropics A and B. *Anal. Chem.* **2001,** *73*, 3723–3731.

Comerton, A. M.; Andrews, R. C.; Bagley, D. M. Evaluation of an MBR–RO System to Produce High Quality Reuse Water: Microbial Control, DBP Formation and Removal. *Water Res.* **2005**, *39*, 3982–3990.

Cooper, W. J.; Jones, A. C.; Whitehead, R. F.; Zika, R. G. Sunlight-Induced Photochemical Decay of Oxidants in Natural Waters: Implications in Ballast Water Treatment. *Environ. Sci. Technol.* **2007**, *41*, 3728–3733.

Cooper, W. J.; Snyder, S. A.; Mezyk, S. P.; Peller, J. R.; Nickelsen, M. G. *Reaction Rates and Mechanisms of Advanced Oxidation Processes (AOPs) for Water Reuse*. WateReuse Research Foundation: Alexandria, VA, 2010; pp 1–52.

Corbett, R. E.; Metcalf, W. S.; Soper, F. G. Studies of N-halogeno-compounds IV: The Reaction between Ammonia and Chlorine in Aqueous Solution and the Hydrolysis Constants of Chloramines. *J. Chem. Soc*. **1953**, *395*, 1927–1929.

Costerton, J. W.; Lewandowski, Z.; Caldwell, D. E.; Korber, D. R.; Lappen-Scott, H. M. Microbial Biofilms. *Annu. Rev. Microbiol.* **1995**, *49*, 711–745.

Cottrell, B. A.; Gonsior, M.; Timko, S. A.; Simpson, A. J.; Cooper, W. J. Photochemistry of Marine and Fresh Waters: A Role for Copper-Dissolved Organic Matter Ligands. *Mar. Chem.* **2014,** *62***,** 77–88**.**

Crescenzi, C.; Di Corcia, A.; Marchiori, E.; Saamperi, R.; Marcomini, A. Simultaneous Determination of Alkylbenzenesulfonates and Dialkyltetralinsulfonates in Water by Liquid Chromatography. *Water Res*. **1996**, *30*, 722–730.

Crittenden, J. C.; Hu, S.; Hand, D. W.; Green, S. A. A Kinetic Model for H_20_2/UV Process in a Completely Mixed Batch Reactor. *Water Res*. **1999**, *33*, 2315–2328.

Curds, C. R. A Theoretical Study of Factors Influencing the Microbial Population Dynamics of the Activated-Sludge Process—II. A Computer Simulation Study to Compare Two Methods of Plant Operation. *Water Res.* **1973**, *7*, 1439–1452.

Czapski, G.; Lymar, S. V.; Schwarz, H. A. Acidity of the Carbonate Radical. *J. Phys. Chem. A.* **1999**, *103*, 3447–3450.

Dahl, E. E.; Yvon-Lewis, S. A.; Saltzman, E. S. Alkyl Nitrate (C1-C3) Depth Profiles in the Tropical Pacific Ocean. *J. Geophys. Res.: Oceans.* **1999,** *112*, C01012.

De Henau, H.; Mathijs, E.; Hopping, W. D. Linear Alkylbenzenesulfonates (LAS) in Sewage Sludges, Soils, and Sediments: Analytical Determination and Environmental Safety Considerations. *Int. J. Environ. Anal. Chem.* **1986**, *26*, 279–293.

Derrigan, J.; Lin, L.; Jensen, J. N. Comparison of Free and Total Chlorine Measurement Methods in Municipal Wastewaters. *Water Environ. Res*. **1993**, *65*, 205–212.

Dialynas, E.; Mantzavinos, D.; Diamadopoulos, E. Advanced Treatment of the Reverse Osmosis Concentrate Produced during Reclamation of Municipal Wastewater. *Water Res*. **2008**, *42*, 4603–4608.

Dickenson, E. R. V.; Drewes, J. E.; Sedlak, D. L.; Wert, E. C.; Snyder, S. A. Applying Surrogates and Indicators to Assess Removal Efficiency of Trace Organic Chemicals during Chemical Oxidation of Wastewaters. *Environ. Sci. Technol*. **2009**, *43*, 6242–6247.

Di Corcia, A.; Capuani, L.; Casassa, F.; Marcomini, A.; Samperi, R. Fate of Linear Alkyl Benzenesulfonates, Coproducts, and Their Metabolites in Sewage Treatment Plants and in Receiving River Waters. *Environ. Sci. Technol.* **1999a**, *33*, 4119–4125.

Di Corcia, A.; Casassa, F.; Crescenzi, C.; Marcomini, A.; Samperi, R. Investigation of the Fate of Linear Alkyl Benzenesulfonates and Coproducts in a Laboratory Biodegradation Test by Using Liquid Chromatography/Mass Spectrometry. *Environ. Sci. Technol.* **1999b**, *33*, 4112–4118.

Ding, W.-H.; Fujita, Y.; Aeschimann, R.; Reinhard, M. Identification of Organic Residues in Tertiary Effluents by GC/EI-MS, GC/CI-MS and GC/TSQ-MS. *Fresenius J. Anal. Chem*. **1996**, *354*, 48–55.

Dittmar, T.; Koch, B.; Hertkorn, N.; Kattner, G. A Simple and Efficient Method for the Solid-Phase Extraction of Dissolved Organic Matter (SPE-DOM) from Seawater. *Limnol. Oceanogr.: Methods* **2008**, *6*, 230–235.

Drewes, J. E.; Croue, J. P. New Approaches for Structural Characterization of Organic Matter in Drinking Water and Wastewater Effluents. *Water Sci. Tech.: Water Supply* **2002**, *2*, 1–10.

Drewes, J. E. *Development of Indicators and Surrogates for Chemical Contaminant Removal during Wastewater Treatment and Reclamation*. WateReuse Research Foundation: Alexandria, VA. 2008, pp 1–169.

Drouiche, M.; Lounici, H.; Mameri, N.; Piron, D.L.; Kharroune, M. Utilisation of Factorial Experiments for the UV/H_2O_2 Process in a Batch Reactor. *Water SA* **2001**, *27*, 551–557.

Dubois, M.; Gilles, K. A.; Hamilton, J. K.; Rebers, P. A.; Smith, F. Colorimetric Method for Determination of Sugars and Related Substances. *Anal. Chem.* **1956**, *28*, 350–356.

Ekama, G. A.; Marais, R. Dynamic Behavior of the Activated Sludge Process. *J. Wat. Pollut. Control Fed.* **1979**, *51*, 534–556.

Elimelech, M.; Zhu, X.; Childress, A. E.; Hong, S. Role of Membrane Surface Morphology in Colloidal Fouling of Cellulose Acetate and Composite Aromatic Polyamide Reverse Osmosis Membranes. *J. Membrane Sci.* **1997**, *127*, 101–109.

Ellis, D.A.; Mabury, S.A.; Martin, J.W.; Muir, D.C. Thermolysis of Fluoropolymers as a Potential Source of Halogenated Organic Acids in the Environment. *Nature* **2001**, *412*, 321–324.

Encyclopedia of Membrane Science and Technology; Hoek, E. M. V.; Tarabara, V. V., Eds.; Wiley: New York, NY, 2013; Vol. 1., pp 1–798.

Farahbaksh, K.; Smith, D. W. Performance Comparison and Treatment Evaluation of Three Water Treatment Membrane Pilot Plants Treating Low Turbidity Water. *J. Envi. Eng. Sci.* **2002**, *1*, 113–122.

Farre, M. J.; Radjenovic, J.; Gernjak, W. Assessment of Degradation Byproducts and NDMA Formation Potential during UV and UV/H_2O_2 Treatment of Doxylamine in the Presence of Monochloramine. *Environ. Sci. Technol*. **2012**, *46*, 12904–12912.

Feng, Y.; Smith, D. W.; Bolton, J. R. Photolysis of Aqueous Free Chlorine Species (HOCl and OCl^-) with 254 nm Ultraviolet Light. *J. Environ. Eng. Sci.* **2007**, *6*, 277–284.

Ferlita, R. R.; Phipps, D., Jr.; Safarik, J.; Yeh, D. H. Cryo-Snap: A Simple Modified Freeze-Fracture Method for SEM Imaging of Membrane Cross-Sections. *Env. Progress.* **2008**, *27*, 204–209.

Fine, D. H.; Rounbehler, D. P.; Fan, T.; Ross, R. Human Exposure to N-Nitroso Compounds in the Environment. In *Origins of Human Cancer;* Hiatt, H. H.;Watson, J. D.; Winsten, J. A., Eds.; Cold Spring Harbor Laboratory: Cold Spring Harbor, NY, 1977; pp 293–308.

Flemming, H.-C.; Schaule, G. Biofouling on Membranes–A Microbiological Approach. *Desalination* **1988**, *70*, 95–119.

Fridleifsson, I. B.; Bertani, R.; Huenges, E.; Lund, J. W.; Ragnarsson, A.; Rybach, L. The Possible Role and Contribution of Geothermal Energy to the Mitigation of Climate Change. In *IPCC Scoping Meeting on Renewable Energy Sources–Proceedings*, Lubeck, Germany, January 20–25, 2008; Hohmeyer, O.; Trittin, T., eds.; Intergovernmental Panel on Climate Change (IPCC), 2008, pp 59–80.

Frimmel, F. H.; Abbt-Braun, G. Basic Characterization of Reference NOM from Central Europe. Similarities and Differences. *Environ. Int.* **1999**, *25*, 191–207.

Gerrity, D.; Gamage, S.; Jones, D.; Korshin, G. V. ; Lee, Y.; Pisarenko, A.; Trenholm, R. A.; von Gunten, U.; Wert, E. C.; Snyder, S. A. Development of Surrogate Correlation Models to Predict Trace Organic Contaminant Oxidation and Microbial Inactivation During Ozonation. *Water Res.* **2012**, *19*, 6257–6272.

Glazer, W. H.; Kang, J.-W.; Chapin, D. H. The Chemistry of Water Treatment Processes Involving Ozone, Hydrogen Peroxide and Ultraviolet Radiation. *Ozone-Sci. Eng.* **1987**, *9*, 335–352.

Gonsior, M.; Peake, B. M.; Cooper, W. J.; Cooper, W. T.; Podgorski, D.; D'Andrilli, J. Photochemically-Induced Changes in Dissolved Organic Matter Identified by Ultrahigh Resolution Fourier Transform Ion Cyclotron Resonance Mass Spectrometry. *Environ. Sci. Technol*. **2009**, *43*, 698–703.

Gonsior, M.; Zwartjes, M.; Cooper, W. J.; Song, W.; Ishida, K. P.; Tseng, L. Y.; Jeung, M. K.; Rosso, D.; Hertkom, N.; Schmitt-Kopplin, P. Molecular Characterization of Effluent Organic Matter Identified by Ultrahigh Resolution Mass Spectrometry. *Water Res.* **2011**, *45*, 2943–2953.

Gonzalez-Mazo, E.; Honing, M.; Barcelo, D.; Gomez-Parra, A. Monitoring Long-Chain Intermediate Products from the Degradation of Linear Alkylbenzene Sulfonates in the Marine Environment by Solid-Phase Extraction Followed by Liquid Chromatography/Ionspray Mass Spectrometry. *Environ. Sci. Technol.* **1997**, *31*, 504–510.

Gonzalez-Mazo, E.; Pajares, J. M. F.; Gomez-Parra, A. Fate and Distribution of Linear Alkylbenzene Sulfonates in the Littoral Environment. *Environ. Sci. Technol*. **1998**, *32*, 1636–1641.

Gordon, G.; Cooper, W. J.; Rice, R. G.; Pacey, G. E. *Disinfectant Residual Measurement Methods. Water Quality and Analysis.* 2nd ed.; AWWA Research Foundation, American Water Works Association: Denver, CO, 1992.

Gray, N. F. *The Biology of Wastewater Treatment*, 2nd ed.; Imperial College Press: London, 2004; Vol. 4, pp 1–1421.

Green, S. A.; Blough, N. V. Optical Absorption and Fluorescence Properties of Chromophoric Dissolved Organic Matter in Natural Waters. *Limnol. Oceanogr*. **1994**, *39*, 1903–1916.

Greenberg, G.; Hasson, D.; Semiat, R. Limits of Reverse Osmosis Recovery Imposed by Calcium Phosphate Precipitation. *Desalination* **2005**, *183*, 789–804.

Gros, M.; Petrovic, M.; Barcelo, D. Development of Multi-Residue Analytical Methodology Based on Liquid Chromatography–Tandem Mass Spectrometry (LC-MS/MS) for Screening and Trace Level Determination of Pharmaceuticals in Surface and Wastewaters. *Talanta* **2006**, *70*, 678–690.

Gros, M.; Petrovic, M.; Barcelo, D., Tracing Pharmaceutical Residues of Different Therapeutic Classes in Environmental Waters by Using Liquid Chromatography/Quadrupole-Linear Ion Trap Mass Spectrometry and Automated Library Searching. *Anal. Chem*. **2009**, *81*, 898–912.

Grunheid, S.; Amy, G.; Jekel, M. Removal of Bulk Dissolved Organic Matter Carbon (DOC) and Trace Organic Compounds by Bank Filtration and Artifical Recharge. *Water Res*. **2005**, *39*, 3219–3228.

Gur-Reznik, S.; Katz, I.; Dosoretz, C. G. Removal of Dissolved Organic Matter by Granular-Activated Carbon Adsorption as a Pretreatment to Reverse Osmosis of Membrane Bioreactor Effluents. *Water Res*. **2008**, *42*, 1595–1605.

Haag, W.; Yao, C. Rate Constants for Reaction of Hydroxyl Radicals with Several Drinking Water Contaminants. *Environ. Sci. Technol*. **1992**, *26*, 1005–1013.

Haarhoff, J.; Kubare, M.; Mamba, B.; Krause, R.; Nkambule, T.; Matsebula, B.; Menge, J. NOM Characterization and Removal at Six Southern African Water Treatment Plants. *Drinking Water Eng. Sci.* **2010**, *3*, 53–61.

Han, S. K.; Nam, S. N.; Kang, J. W. OH Radical Monitoring Technologies for AOP Advanced Oxidation Process. *Water Sci. Technol*. **2002**, *46*, 7–12.

Hauff, K.; Kischer, R. G.; Ballschmiter, K. Determination of C1-C5 Alkyl Nitrates in Rain, Snow, White Frost, Lake, and Tap Water by a Combined Codistillation Head-Space Gas Chromatography Technique. Determination of Henry's Law Constants by Head-Space GC. *Chemosphere* **1998,** *37*, 2599–2615.

Harrick, N. J. Applications of Internal Reflection Spectroscopy. In *Internal Reflection Spectroscopy*; Harrick Scientific Corporation: Ossining, NY, 1979; pp 217–295.

Hawkins, C. L.; Davies, M. J. Hypochlorite–Induced Damage to Nucleosides: Formation of Chloramines and Nitrogen-Centered Radicals. *Chem. Res. Toxicol*. **2001**, *14*, 1071–1081.

Heffner, C.; Silwal, I.; Peckenham, J. M.; Solouki, T. Emerging Technologies for Identification of Disinfection Byproducts: GC/FT−ICR MS Characterization of Solvent Artifacts. *Environ. Sci. Technol.* **2007**, *41*, 5419–5425.

Hertkorn, N.; Benner, R.; Frommberger, M.; Schmitt-Kopplin, P.; Witt, M.; Kaiser, K.; Kettrup, A.; Hedges, J. I. Characterization of a Major Refractory Component of Marine Dissolved Organic Matter. *Geochim. Cosmochim. Acta* **2006**, *70*, 2990–3010.

Hertkorn, N.; Frommberger, M.; Witt, M.; Koch, B.; Schmitt-Kopplin, P.; Perdue, E. M. Natural Organic Matter and the Event Horizon of Mass Spectrometry. *Anal. Chem.* **2008**, *80*, 8908–8919.

Hertkorn, N.; Ruecker, C.; Meringer, M.; Gugisch, R.; Frommberger, M.; Perdue, E. M.; Witt, M.; Schmitt-Kopplin, P. High-Precision Frequency Measurements: Indispensable Tools at the Core of the Molecular-Level Analysis of Complex Systems. *Anal. Bioanal. Chem.* **2007**, *389*, 1311–1327.

Herzberg, M.; Elimelech, M. Biofouling of Reverse Osmosis Membranes: Role of Biofilm-Enhanced Osmotic Pressure. *J. Membr. Sci.* **2007**, *295*, 11–20.

Hickel, B.; Sehested, K. Reaction of Hydroxyl Radicals with Ammonia in Liquid Water at Elevated Temperatures. *Radiat. Phys. Chem.*,**1992**, *39*, 355–357.

Ho, T. L.; Bolton, J. R. Toxicity Changes During the UV Treatment of Pentachlorophenol in Dilute Aqueous Solution. *Water Res*. **1998**, *32*, 489–497.

Hoare, J. P. Oxygen. In *Standard Potentials in Aqueous Solution*; Bard, A. J.; Parsons, R.; Jordon, J.; Eds.; Marcel Dekker: New York, NY, 1985; p 63.

Hoek, E. M. V.; Elimelech, M. Cake-Enhanced Concentration Polarization: A New Fouling Mechanism for Salt-Rejecting Membranes. *Environ. Sci. Technol*. **2003**, *37*, 5581–5588.

Hoigné, J.; Bader, H. Rate Constants of Reactions of Ozone with Organic and Inorganic Compounds in Water—II Dissociating Organic Compounds. *Water Res.* **1983**, *17*, 185–194.

Homocianu, M.; Airinei, A.; Ortansa Dorohoi, D. Solvent Effects on the Electronic Absorption and Fluorescence Spectra. *J. Adv. Res Phys*. **2011**, *2*, 1–9.

Huang, L.; Morrisey, M. T. Fouling of Membranes during Microfiltration of Surini Wash Water: Roles of Pore Blocking and Surface Cake Formation. *J. Membr. Sci*. **1998**, *144*, 113–123.

Huber, M. M.; Canonica, S.; Park, G.-Y.; von Gunten, U. Oxidation of Pharmaceuticals during Ozonation and Advanced Oxidation Processes. *Environ. Sci. Technol*. **2003**, *37*, 1016–1024.

Hug, G. L; Wang, Y.; Schoneick, C.; Jiang, P.-Y.; Fessenden, R. W. Multiple Time Scales in Pulse Radiolysis. Application to Bromide Solutions and Dipeptides. *Radiat. Phys. Chem.* **1999**, *54*, 559–566.

Huston, P. L.; Pignatello, J. Degradation of Selected Pesticide Active Ingredients and Commercial Formulations in Water by the Photo-Assisted Fenton Reaction. *Water Res*. **1999**, *33*, 1238–1246.

Hwang, T.-M.; Oh, H.; Choung, Y.-K.; Oh, S.; Jeon, M.; Kim, J. H.; Nam, S. H.; Lee, S. Prediction of Membrane Fouling in the Pilot-Scale Microfiltration System Using Genetic Programing. *Desalination* **2009**, *247*, 285–294.

Ignarro, L. J.; Fukuto, J.M.; Griscavage, J. M.; Rogers, N. E.; Byrns, R. E. Oxidation of Nitric Oxide in Aqueous Solution to Nitrite but Not Nitrate: Comparison with Anzymatically Formed Nitric Oxide from L-Arginine. *Proc. Natl. Acad. Sci*. **1993**, *90*, 8103–8107.

Ikehata, K.; Naghashkar, N. J.; Gamal El-Din, M. Degradation of Aqueous Pharmaceuticals by Ozonation and Advanced Oxidation Processes: A Review. *Ozone: Sci. Eng*. **2006**, *28*, 353–414.

Imai, A.; Fukushima, T.; Matsushige, K.; Kim, Y. H.; Choi, K. Characterization of Dissolved Organic Matter in Effluents from Wastewater Treatment Plants. *Water Res.* **2002**, *36*, 859–870.

Intergovermental Panel on Climate Change (IPCC). *Climate Change 2007: Mitigation. Contribution of Working Group III to the Fourth Assessment Report of the Intergovermental Panel on Climate Change*, Metz, B.; Davidson, O. R.; Bosch, P. R.; Dave, R.; Meyer, L. A., Eds.; Cambridge University Press: New York, 2007.

Iritani, E. A Review on Modeling of Pore-Blocking Behaviors of Membranes during Pressurized Membrane Filtration. *Dry Technol*. **2013**, *31*, 146–162.

Ishida, K.; Fitzsimmons, S.; Phipps, D., Jr. Characterization of NDMA Photolysis and 1,4-Dioxane Oxidation of the UV Facility at the AWPF. Poster Session. WateReuse California Annual Conference, San Diego, CA, March 7–9, 2010.

Jafvert, C. T.; Valentine, R. L. Dichloramine Decomposition in the Presence of Excess Ammonia. *Water Res*. **1987**, *21*, 967–973.

Jafvert, C. T.; Valentine, R. L. Reaction Scheme for the Chlorination of Ammoniacal Water. *Environ. Sci. Technol*. **1992**, *26*, 577–578.

Jansen, H. P.; Stenstrom, M. K.; de Koning, J. Development of Indirect Potable Reuse in Impacted Areas of the United States. *Water Sci. Technol*. **2007**, *55*, 357–366.

Jarusutthirak, C.; Amy, G. Understanding Soluble Microbial Products (SMP) as a Component of Effluent Organic Matter (EfOM). *Water Res.* **2007**, *41*, 2787–2793.

Jarusutthirak, C.; Amy, G.; Croue, J. P. Fouling Characteristics of Wastewater Effluent Organic Matter (EfOM) Isolates on NF and UF Membranes. *Desalination* **2002**, *145*, 247–255.

Jensen, J. N.; Johnson, J. D. Interferences by Monochloramine and Organic Chloramines in Free Available Chlorine Methods. *Environ. Sci. Technol*. **1990**, *24*, 985–990.

Jeong, J.; Jung, J.; Cooper, W. J.; Song, W. Degradation Mechanisms and Kinetic Studies for the Treatment of X-Ray Contrast Media Compounds by Advanced Oxidation/ Reduction Processes. *Water Res*. **2010**, *44*, 4391–4398.

Johnson, H. D.; Cooper, W. J.; Mezyk, S. P.; Bartels, D. M. Free Radical Reactions of Monochloramine and Hydroxylamine in Aqueous Solution. *Radiat. Phys. Chem.* **2002**, *65*, 317–326.

Johnson, C. G.; Caron, S.; Blough, N.V. Combined Liquid Chromatography/Mass Spectrometry of the Radical Adducts of a Fluorescamine-Derivatized Nitroxide. *Anal. Chem.* **1996**, *68*, 867–872.

Jones, C. W. Activation of Hydrogen Peroxide Using Inorganic and Organic Species. In *Applications of Hydrogen Peroxide and Derivatives*; RSC Clean Technology Monographs, J. H. Clark, Ed.; RSC Publishing: Cambridge, UK, 1999, pp 37–47.

Kieber, D. J.; Blough, N. V. Determination of Carbon-Centered Radicals in Aqueous Solution by Liquid Chromatography with Fluorescence Detection. *Anal. Chem.* **1990,** *62*, 2275–2283.

Kieber, D. J.; Blough, N. V. Flourescence Detection of Carbon-Centered Radicals in Aqueous Solution. *Free Radical Res. Comm.* **1990,** *10*, 109–117.

Kim, S.; Kramer, R. W.; Hatcher, P. G. Graphical Method for Analysis of Ultrahigh-Resolution Broadband Mass Spectra of Natural Organic Matter, the Van Krevelen Diagram. *Anal. Chem*. **2003**, *75*, 5336–5344.

Kim, S. D.; Cho, J.; Kim, I. S.; Vanderford, B. J.; Snyder, S. A. Occurrence and Removal of Pharmaceuticals and Endocrine Disruptors in South Korean Surface, Drinking, and Waste Waters. *Water Res*. **2007**, *41*, 1013–1021.

Kimura, K.; Iwase, T.; Kita, S.; Watanabe, Y. Influence of Residual Organic Macromolecules Produced in Biological Wastewater Treatment Processes on Removal of Pharmaceuticals by NF/RO Membranes. *Water Res*. **2009**, *43*, 3751–3758.

Knepper, T. P.; de Voogt, P.; Barcelo, D. *Analysis and Fate of Surfactants in the Aquatic Environment*, Elsevier Science: Amsterdam, NL, 2003, Vol. XL, pp 1–994.

Knepper, T. P.; Barcelo, D.; Lindner, K.; Seel, P.; Reemtsma, T.; Ventura, F.; de Wever, H.; van der Voet, E.; Gehringer, P.; Schoenerklee, M. Removal of Persistent Polar Pollutants through Improved Treatment of Wastewater Effluents (P-THREE). *Water Sci. Technol.* **2004**, *50*, 195–202.

Koch, B. P.; Witt, M.; Engbrodt, R.; Dittmar, T.; Kattner, G. Molecular Formulae of Marine and Terrigenous Dissolved Organic Matter Detected by Electrospray Ionization Fourier Transform Ion Cyclotron Resonance Mass Spectrometry. *Geochim. Cosmochim. Acta* **2005**, *69*, 3299–3308.

Kolpin, D. W.; Furlong, E. T.; Meyer, M. T.; Thurman, E. M.; Zaugg, S. D.; Barber, L. B.; Buxton, H. T. Pharmaceuticals, Hormones, and Other Organic Wastewater

Contaminants in U.S. Streams, 1999–2000: A National Reconnaissance. *Environ. Sci. Technol*. **2002**, *36*, 1202–1211.

Korshin, G. V.; Li, C.-W.; Benjamin, M. M. Monitoring the Properties of Natural Organic Matter through UV Spectroscopy: A Consistent Theory. *Water Res*. **1997a**, *31*, 1787–1795.

Korshin, G. V.; Li, C.-W.; Benjamin, M. M. The Decrease of UV Absorbance as an Indicator of TOX Formation. *Water Res*. **1997b**, *31*, 946–949.

Kotiaho, T.; Lauritsen, F. R.; Choudhury, T. K.; Cooks, R. G. Membrane Introduction Mass Spectrometry. *Anal. Chem*. **1991a**, *63*, 875A–883A.

Kotiaho, T.; Hayward, M. J.; Cooks, R. G. Direct Determination of Chlorination Products of Organic Amines Using Membrane Introduction Mass Spectrometry. *Anal. Chem*. **1991b**, *63*, 1794–1801.

Kujawinski, E. B.; Del Vecchio, R.; Blough, N. V.; Klein, G. C.; Marshall, A. G. Probing Molecular-Level Transformations of Dissolved Organic Matter: Insights on Photochemical Degradation and Protozoan Modification of DOM from Electrospray Ionization Fourier Transform Ion Cyclotron Resonance Mass Spectrometry. *Mar. Chem.* **2004**, *92*, 23–37.

Landsman, N. A.; Swancutt, K. L.; Bradford, C. N.; Cox, C. R.; Kiddle, J. J.; Mezyk, S. P. Free Radical Chemistry of Advanced Oxidation Process Removal of Nitrosamines in Water. *Environ. Sci. Technol*. **2007**, *41*, 5818–5823.

Laszlo, B.; Alfassi, Z. B.; Neta, P.; Huie, R. E. Kinetics and Mexhanism of the Reaction of NH_2 with O_2 in Aqueous Solutions. *J. Phys. Chem. A* **1998**, *102*, 8498–8504.

LaVerne, J. A.; Pimblott, S. M. Yields of Hydroxyl Radical and Hydrated Electron Scavenging Reactions in Aqueous Solutions of Biological Interest. *Radiat. Res*. **1993**, *135*, 16–23.

Lee, H. J. Breath Analysis on End-Stage Renal Disease Patients during Hemodialysis Treatment. Ph.D. Dissertation. University of California, Irvine, CA, 2011.

Lee, L.; Ng, H.; Ong, S.; Hu, J.; Tao, G.; Kekre, K.; Viswannath, B.; Lay, W.; Seah, H. Ozone-Biological Activated Carbon as a Pretreatment Process for Reverse Osmosis Brine Treatment and Recovery. *Water Res.* **2009**, *43*, 3948–3955.

Legrini, O.; Oliverose, E.; Braun, A. M. Photochemical Processes for Water Treatment. *Chem. Rev*. **1993**, *93*, 671–698.

Leon, V. M.; Saez, M.; Gonzalez-Mazo, E.; Gomez-Parra, A. Occurrence and Distribution of Linear Alkylbenzene Sulfonates and Sulfophenylcarboxylic Acids in Several Iberian Littoral Ecosystems. *Sci. Total Environ.* **2002**, *288*, 215–226.

Lenzen, M. Life Cycle Energy and Greenhouse Gas Emissions of Nuclear Energy: A Review. *Energ. Convers. Manage.* **2008**, *49*, 2178–2199.

Leow, H. F.; Bai, R. B. Nylon Screen Incorporated into Hollow Fiber Microfiltration System for Wastewater Treatment. *Water Sci. Technol.* **2001**, *1*, 131–139.

Li, J. and Blatchley, E. R., III; UV Photodegradation of Inorganic Chloramines. *Environ. Sci. Technol.* **2009**, *43*, 60–65.

Li, Q.; Xu, Z.; Pinnau, I. Fouling of Reverse Osmosis Membranes by Biopolymers in Wastewater Secondary Effluent: Role of Membrane Surface Properties and Initial Permeate Flux. *J. Membr. Sci.* **2007**, *290*, 17–181.

Lin, S. *Water and Wastewater Calculations Manual*. Lee, C. C., Ed.; McGraw Hill Professional: NY, 2001; pp 1–854.

Liu, Q.-F.; Kim, S.-H.; Lee, S. Prediction of Microfiltration Membrane Fouling Using Artificial Neural Network Models. *Sep. Purif.. Technol.* **2009**, *70*, 96–102.

Liu, W.; Andrews, S. A.; Stefan, M. I.; Bolton, J. R. Optimal Methods for Quenching H_2O_2 Residuals Prior to UFC Testing. *Water Res.* **2003**, *37*, 3697–3703.

Local Government Operations Protocol (LGOP). CARB-CCAR-ICLEI-TCR, 2010. http://www.theclimateregistry.org/resources/protocols/local-government-operations-protocol/ (accessed March 2013).

Løgager, T.; Sehested, K. Formation and Decay of Peroxynitrous Acid: A Pulse Radiolysis Study. *J. Phys. Chem.* **1993**, *97*, 6664–6669.

Lowery, O. H.; Rosenbrough, N. J.; Farr, A. L.; Randall, R. J. Protein Measurement with Folin Phenol Reagent. *J. Biol. Chem*. **1951**, *193*, 265–275.

Lukasewycz, M. T.; Bleringer, C. M.; Llukkonen, R. J.; Fitzsimmons, M. E.; Corcoran, S. L.; Carlson, R. M. Analysis of Inorganic and Organic Chloramines: Derivatization with 2-Mercaptobenzothiazole. *Environ. Sci. Technol*. **1989**, *23*, 196–199.

Ma, J.; Ibekwe, M.; Leddy, M.; Yang, C.-H.; Crowley, D. E. Assimilable Organic Carbon (AOC) in Soil Water Extracts Using *Vibrio harveyi* BB721 and Its Implications for Microbial Biomass. *PLoS One* **2012**, *7*, e28519.

Mack, J.; Bolton, J. R. Photochemistry of Nitrite and Nitrate in Aqueous Solution: A Review. *J. Photochem. Photobiol. A: Chem*. **1999**, *128*, 1–13.

Mark, G.; Korth, H.-G.; Schuchmann, H.-P.; von Sonntag, C. The Photochemistry of Aqueous Nitrate Ion Revisited. *J. Photoch. Photobio. A* **1996**, *101*, 89–103.

Margerum, D. W.; Schurter, L. M.; Hobson, J.; Moore, E. E. Water Chlorination Chemistry: Nonmetal Redox Kinetics of Chloramine and Nitrite Ion. *Environ. Sci. Technol*. **1994**, *28*, 331–337.

Marhaba, T. F.; Van, D.; Lippincott, R. L. Rapid Identification of Disolved Organic Matter Factions in Water by Spectral Fluorescent Signatures. *Water Res.* **2000**, *34*, 3543–3550.

Matthijs, E.; Holt, M. S.; Kiewiet, A.; Rijs, G. B. J. Environmental Monitoring for Linear Alkylbenzene Aulfonate, Alcohol Ethoxylate, Alcohol Ethoxy Sulfate, Alcohol Sulfate, and Soap. *Environ. Toxicol. Chem*. **1999**, *18*, 2634–2644.

Maurino, V.; Calza, P.; Minero, C.; Pelizzetti, E.; Vincenti, M. Light-Assisted 1,4-Dioxane Degradation. *Chemosphere* **1997**, *35*, 2675–2688.

Mayo, D. W.; Miller, F. A.; Hannah, R. W. *Course Notes on the Interpretation of Infrared and Raman Spectra*. John Wiley & Sons: Hoboken, NJ, 2004; pp 1–567.

McAvoy, D. C.; Dyer, S. D.; Fendinger, N. J.; Eckhoff, W. S.; Lawrence, D. L.; Begley, W. M. Removal of Alcohol Ethoxylates, Alkyl Ethoxylate Sulfates, and Linear Alkylbenzene Sulfonates in Wastewater Treatment. *Environ. Toxicol. Chem*. **1998**, *17*, 1705–1711.

McAvoy, D. C.; Eckhoff, W. S.; Rapaport, R. A. Fate of Linear Alkylbenzene Sulfonate in the Environment. *Environ. Toxicol. Chem.* **1993**, *12*, 977–987.

McElroy, W. J. A Laser Photolysis Study of the Reaction of SO_4^- with Cl^- and the Subsequent Decay of Cl_2^- in Aqueous Solution. *J. Phys. Chem.* **1990**, *94*, 2435–2441.

McKay, G.; Sjelin, B.; Chagnon, M.; Ishida, K. P.; Mezyk, S. P. Kinetic Study of the Reactions Between Chloramine Disinfectants and Hydrogen Peroxide: Temperature Dependence and Reaction Mechanism. *Chemosphere* **2013**, *92*, 1417–1422.

Mezyk, S. P.; Cooper, W.J.; Madden, K.P.; Bartels, D.M. Free Radical Destruction of N-Nitrosodimethylamine in Water. *Environ. Sci. Technol*. **2004**, *38*, 3161–3167.

Mezyk, S. P.; Neubauer, T. J.; Cooper, W. J.; Peller, J. R. Free-Radical-Induced Oxidative and Reductive Degradation of Sulfa Drugs in Water: Absolute Kinetics and Efficiencies of Hydroxyl Radical and Hydrated Electron Reactions. *J. Phys. Chem. A* **2007**, *111*, 9019–9024.

Mitch, W. A.; Sedlak, D. L. Formation of N-nitrosodimethylamine (NDMA) from Dimethylamine during Chlorination. *Environ. Sci. Technol*. **2002**, *36*, 588–595.

Moore, R. M.; Blough, N. V. A Marine Source of Methyl Nitrate. *Geophys. Res. Lett.* **2002,** *29*, 271–274.

Munakata, N. Pilot Demonstration of UV/AOP for Treatment of Microconstituents in Recycled Water. Water Reuse and Desalination Research Conference, Las Vegas, NV, May 16–17, 2011.

Munakata, N. Los Angeles County Sanitation District, Whittier, CA, Personal communication, 2012.

Munter, R. Advanced Oxidation Processes-Current Status and Prospects. *Proc. Estonian Acad. Sci. Chem.* **2001**, *50*, 59–80.

Nam, S.-N.; Amy, G. Differentiation of Wastewater Effluent Organic Matter (EfOM) from Natural Organic Matter (NOM) Using Multiple Analytical Techniques. *Water Sci. Technol.* **2008**, *57*, 1009–1015.

Nanaboina, V.; Korshin, G. V. Evolution of Absorbance Spectra of Ozonated Wastewater and Its Relationship with the Degradation of Trace-Level Organic Species. *Environ. Sci. Technol*. **2010**, *44*, 6130–6137.

National Water Research Institute (NWRI) and American Water Works Association Research Foundation (AWWARF), *Ultraviolet Disinfection–Guidelines for Drinking Water and Water Reuse*, 2nd ed.; NWRI: Fountain Valley, CA, 2003; pp 1–64.

Naumann D.; Schultz, C.; Helm, D. What Can Infrared Spectroscopy Tell Us about the Structure and Composition of Intact Bacterial Cells. In *Infrared Spectroscopy of Biomolecules;* Mantsch, H. H.; Chapman, D.; Eds.; Wiley-Liss: New York, NY, 1996; pp 279–310.

Naumann, D. Infrared Spectroscopy in Microbiology. In *Encyclopedia of Analytical Chemistry*; Meyers, R. A., Ed.; Wiley & Sons Ltd: Chichester, UK, 2000; pp 102–131.

Novak, B. J. Non-invasive Monitoring of Metabolism, Diabetes, and Oxidative Stress using Exhaled Human Breath. Ph.D. Dissertation. University of California, Irvine, CA, 2007.

Nguyen, M.-L.; Westerhoff, P.; Baker, L.; Hu, Q.; Esparza-Soto, M.; Sommerfeld, M. Characteristics and Reactivity of Algae-Produced Dissolved Organic Carbon. *J. Environ. Eng.* **2005**, *131*, 1574–1582.

Nguyen, T.; Roddick, F. A.; Fan, L. Biofouling of Water Treatment Membranes: A Review of the Underlying Causes, Monitoring Techniques and Control Measures. *Membranes* **2012**, *2*, 804–840.

Oliveri, V. P.; Willingham, G. A.; Vickers, J. C.; McGahey, C. *Continuous Microfiltration of Secondary Wastewater Effluent*, AWWA Membrane Technology Conference Proceedings, Orlando, FL, 1991.

Oppelt, E.T. *Handbook on Advanced Photochemical Oxidation Processes*. USEPA: Washington, DC, 1998.

Örmeci, B.; Ducoste, J. J.; Linden, K. G. UV Disinfection of Chlorinated Water: Impact of Chlorine Concentration and UV Dose Delivery. *J. Water Supply Res. Tech–AQUA* **2005**, *54*, 189–199.

Pacific Gas and Electric Company (PG&E). Carbon Footprint Calculator Assumptions. http://www.pge.com/myhome/environment/calculator/assumptions.shtml (accessed March 2013).

Pacifico, O. C. System No. 309001–Conditional Approval of the Trojan UVPhox™ UV System as the Disinfection Unit Process for the Advanced Water Purification Facility (AWPF). California Department of Public Health (CDPH), Southern California Drinking Water Field Operations Branch, Santa Ana District, Correspondence letter, dated January 3, 2008.

Pacifico, O. C. System No. 309001–Characterization of NDMA and 1,4-Dioxane Oxidation at the Full Scale Advanced Water Purification Facility. California Department of Public Health (CDPH), Southern California Drinking Water Field Operations Branch, Santa Ana District, Correspondence letter, dated August 28, 2009.

Painter, H. A.; Zabel, T. The Behavior of LAS in Sewage Treatment. *Tenside Surfact. Det*. **1989**, *26*, 108–115.

Parameshwaran K.; Fane A. G.; Cho B. D.; Kim K. J. Analysis of Microfiltration Performance with Constant Flux Processing of Secondary Effluent. *Water Res.* **2001**, *35*, 4349–4358.

Park, H.-R.; Daun, Y.; Park, J. K.; Bark, K.-M. Spectroscopic Properties of Flavonoids in Various Aqueous-Organic Solvent Mixtures. *Bull. Korean Chem. Soc*. **2013**, *34*, 211–220.

Patel, M. Orange County Water District, Fountain Valley, CA. Personal communication, June 2010.

Peller, J.; Ciadella, R. L., Turpin, R.; Cooper, W. J.; Mezyk, S. P. Advanced Oxidation Processes (AOP)-Based Remediation of Bisphenol A in Treated Wastewaters, *J. Water Supply Res.Tech.–AQUA* **2011**, *60*, 69–78.

Peller, J.; Wiest, O.; Kamat, P. V. Mechanism of Hydroxyl Radical-Induced Breakdown of the Herbicide 2,4-Dichlorophenoxyacetic Acid (2,4-d). *Chem-Eur. J*. **2003**, *9*, 5379–5387.

Peller, J. R.; Mezyk, S. P.; Cooper, W. J. Bisphenol A Reactions with Hydroxyl Radicals: Diverse Pathways Determined between Deionized Water and Tertiary Treated Wastewater Solutions. *Res. Chem. Intermed.* **2009**, *35*, 21–34.

Pernet-Coudrier, B.; Clouzot, L.; Varrault, G.; Tusseau-Vuillemin, M.-H.; Verger, A.; Mouchel, J.-M. Dissolved Organic Matter from Treated Effluent of a Major Wastewater Treatment Plant: Characterization and Influence on Copper Toxicity. *Chemosphere* **2008**, *73*, 593–599.

Pisarenko, A. N.; Stanford, B. D.; Snyder, S. A.; Rivers, S. B.; Boal, A. K. Investigation of the Use of Chlorine Based Advanced Oxidation in Surface Water: Oxidation of Natural Organic Matter Formation of Disinfection Byproducts. *J. Adv. Oxid. Technol.* **2013**, *16*, 137–150.

Plewa, M. J.; Wagner, E. D.; Metz, D. H.; Kashinkunti, R.; Jamriska, K. J.; Meyer, M. Toxicity of Drinking Water Disinfected with Combinations of Ultraviolet Radiation and Chlorine. *Environ. Sci. Technol.* **2012**, *46*, 7811–7817.

Plumlee, M. H.; Lopez-Mesas, M.; Heidlberger, A.; Ishida, K. P.; Reinhard M. N-nitrosodimethylamine (NDMA) Removal by Reverse Osmosis and UV Treatment and Analysis via LC–MS/MS. *Water Res.* **2008,** *42*, 347–355.

Poskrebyshev, G. A.; Huie, R. E.; Neta, P. Radiolytic Reaction of Monochloramine in Aqueous Solution. *J. Phys. Chem. A* **2003**, *107*, 7423–7428.

Pressley, T. A.; Bishop, D. F.; Roan, S. G. Ammonia-Nitrogen Removal by Breakpoint Chlorination. *Environ. Sci. Technol*. **1972**, *6*, 622–628.

Radjenovic, J.; Petrovic, M.; Ventura, F.; Barcelo, D. Rejection of Pharmaceuticals in Nanofiltration and Reverse Osmosis Membrane Drinking Water Treatment. *Water Res*. **2008**, *42*, 3601–3610.

Rahn, R. O. Potassium Iodide as a Chemical Actinometer for 254 nm Radiation: Use of Iodate as an Electron Scavenger. *J. Photochem. Photobiol*. **1997**, *66*, 450–455.

Ramon-Azcon, J.; Galve, R.; Sanchez-Baeza, F.; Marco, M. P. Development of an Enzyme-Linked Immunosorbent Assay for the Determination of the Linear Alkylbenzene Sulfonates and Long-Chain Sulfophenyl Carboxylates Using Antibodies Generated by Pseudoheterologous Immunization. *Anal. Chem.* **2005**, *78*, 71–81.

Rapaport, R. A.; Eckhoff, W. S. Monitoring Linear Alkyl Benzene Sulfonate in the Environment: 1973–1986. *Environ. Toxicol. Chem*. **1990**, *9*, 1245–1257.

Razavi, B.; Song, W.; Cooper, W. J.; Greaves, J.; Jeong, J. Free-Radical-Induced Oxidative and Reductive Degradation of Fibrate Pharmaceuticals: Kinetic Studies and Degradation Mechanisms. *J. Phys. Chem. A* **2009**, *113*, 1287–1294.

Ridgway, H. F. Microbial Fouling of Reverse Osmosis Membranes: Genesis and Control. In *Biological Fouling of Industrial Water Systems: A Problem Solving Approach*; Mittelman, M.W.; Geesey, G. G., Eds.; Water Micro Associates, San Diego, CA, 1987; pp 138–193.

Ridgway, H.; Ishida, K.; Rodriguez, G.; Safarik, J.; Knoell, T.; Bold, R. Biofouling of Membranes: Membrane Preparation, Characterization, and Analysis of Bacterial Adhesion. In *Methods in Enzymology;Doyle, R. J.*, Ed.; Academic Press: NY, 1999; Vol. 310, pp 463–494.

Ridgway, H. R.; Flemming, H.-C. Membrane Biofouling. In *Water Treatment Membrane Processes;* Mallevialle, J.; Odendaal, P. E.; Wiesner, M. R., Eds.; McGraw-Hill: NY, 1996; pp 6.1–6.62.

Riu, J.; Gonzalez-Mazo, E.; Gomez-Parra, A.; Barcelo, D. Determination of Parts per Trillion Level of Carboxylic Degradation Products of Linear Alkylbenzenesulfonates in Coastal Water by Solid-Phase Extraction Followed by Liquid Chromatography/ Ionspray/Mass Spectrometry Using Negative Ion Detection. *Chromatographia* **1999**, *50*, 275–281.

Rosario-Ortiz, F. L.; Wert, E. C.; Snyder, S. A.; Mezyk, S. P. *Optimization of Advanced Oxidation Processes for Water Reuse.* WateReuse Research Foundation: Alexandria, VA, 2011; p 1–102.

Rosario-Ortiz, F. L.; Mezyk, S. P.; Doud, D. F. R.; Snyder, S. A. Quantitative Correlation of Absolute Hydroxyl Radical Rate Constants with Non-Isolated Effluent Organic Matter Bulk Properties in Water. *Environ. Sci. Technol*. **2008**, *42*, 5924–5930.

Rosenfeldt, E. J.; Linden, K. G.; Canonica, S.; von Gunten, U. Comparison of the Efficiency of OH Radical Formation During Ozonation and the Advanced Oxidation Processes O_3/H_2O_2 and UV/H_2O_2. *Water Res.* **2006**, *40*, 3695–3704.

Rosenfeldt, K. J.; Linden, K. G. Degradation of Endocrine Disrupting Chemicals Bisphenol A, Ethinyl Estradiol, and Estradiol During UV Photolysis and Advanced Oxidation Processes. *Environ. Sci. Technol*. **2004**, *38*, 5476–5483.

Rosso, D.; Stenstrom, M. K. Carbon-Sequestration Potential of Municipal Wastewater Treatment. *Chemosphere* **2008**, *70*, 1468 – 1475.

Rosso, D.; Huo, D. L.; Stenstrom, M. K. Effects of Interfacial Surfactant Contamination on Bubble Gas Transfer. *Chem. Eng. Sci*. **2006**, *61*, 5500–5514.

Rosso, D., Chau, A. M. *Carbon Footprint of Biosolids Disposal to Landfills and Land Farms in the United States.* WEF Residuals and Biosolids Specialty Conference–Sustainable Biosolids Management Proceedings. May 3–6, 2009, Portland, OR.

Sabiani, S. S.; Goosen, M. F. A.; Al-Belushi, R.; Wilf, M. Concentration Polarization in Ultrafiltration and Reverse Osmosis: A Critical Review. *Desalination* **2001**, *141*, 269–289.

Sadr Ghayeni, S. B.; Beatson, P. J.; Schneider, R. P.; Fane, A. G. Adhesion of Waste Water Bacteria to Reverse Osmosis Membranes. *J. Membrane Sci.* **1998**, *138*, 29–42.

Safarik, J.; Phipps, D., Jr. *Role of Microfiltration (MF) Cake Layer Composition and Stability in Desalination Efficiency*; Final Report DWRP13, Contract No. 41818, 2005.

Safarik, J.; Phipps, D., Jr. *Microbial Diversity in a Three Stage Reverse Osmosis System;* 17th Annual Water Reuse and Desalination Research Conference, May 6–7, 2013, Phoenix, AZ.

Sahoo, G. B.; Ray, C. Predicting Flux Decline in Crossflow Membranes Using Artificial Neural Networks and Genetic Algorithms. *J. Membr. Sci.* **2006**, *283*, 147–157.

Sánchez-Polo, M.; López-Peñalver, J.; Prados-Joya, G.; Ferro-García, M. A.; Rivera-Utrilla, J. Gamma Irradiation of Pharmaceutical Compounds, Nitroimidazoles, as a New Alternative for Water Treatment. *Water Res*. **2009**, *43*, 4028–4036.

Santoke, H.; Song, W.; Cooper, W. J.; Greaves, J.; Miller, G. E. Free-Radical-Induced Oxidative and Reductive Degradation of Fluoroquinolone Pharmaceuticals: Kinetic Studies and Degradation Mechanism. *J. Phys. Chem. A* **2009**, *113*, 7846–7851.

Schmidt, F.; Elvert, M.; Koch, B. P.; Witt, M.; Hinrichs, K.-U. Molecular Characterization of Dissolved Organic Matter in Pore Water of Continental Shelf Sediments. *Geochim. Cosmochim. Acta* **2009**, *73*, 3337–3358.

Schneider, R. P.; Ferreira, L. M.; Binder, P.; Ramos, J. R. Analysis of Foulant Layer in Elements of an RO Train. *J. Membr. Sci.* **2005**, *261*, 152–162.

Schreiber, I. M.; Mitch, W. A. Enhanced Nitrogenous Disinfection Byproduct Formation Near the Breakpoint: Implications for Nitrification Control. *Environ. Sci. Technol.* **2007**, *41*, 7039–7046.

Schuler, R. H.; Hartzell, A. L.; Behar, B. Track Effects in Radiation Chemistry. Concentration Dependence for the Scavenging of Hydroxyl by Ferrocyanide in Nitous Oxide-Saturated Aqueous Solutions. *J. Phys. Chem.* **1981**, *85*, 192–199.

Schumb, W. C.; Satterfield, C. N.; Wentworth, R. L. *Hydrogen Peroxide, ACS Monograph No. 128*, Reinhold Publishing: New York, 1955; p 526.

Schurter, L. M.; Bachelo, P. P.; Margerum, D. W. Nonmetal Redox Kinetics: Mono-, Di-, and Trichloramine Reactions with Cyanide Ion. *Environ. Sci. Technol*. **1995**, *29*, 1127–1134.

Seckler, D.; Barker, R.; Amarasinghe, U. Water Scarcity in the Twenty-First Century. *Int. J. Water Resour. D* **1999,** *15*, 29–42.

Sedlak, D.; Kavanaugh, M. *Removal and Destruction of NDMA and NDMA Precursors during Wastewater Treatment.* WateReuse Research Foundation: Alexandria, VA, 2006.

Seidel, W.C.; Scherer, K.V. Jr.; Cline, D.Jr.; Olson, A.H.; Bonesteel, J.K. Chemical, Physical and Toxicological Characterization of Fumes Produced by Heating Tetrafluoroethene Homopolymer and Its copolymers with Hexafluoropropene and Perfluoro(propyl vinyl ether). *Chem. Res. Toxicol.* **1991**, *4*, 229–236.

Sharp, J. O.; Wood, T. K.; Alvarez-Cohen, L. Aerobic Biodegradation of N-nitrosodimethyl-amine (NDMA) by Axenic Bacterial Strains. *Biotechnol. Bioeng*. **2005**, *89*, 608–618.

Sharpless, C. M.; Linden, K. G. Environmental and Model Comparisons of Low- and Medium-Pressure Hg Lamps for the Direct and H_2O_2 Assisted UV Photodegradation of N-Nitrosodimethylamine in Simulated Drinking Water. *Environ. Sci. Technol.* **2003**, *37*, 1933–1940.

Sharpless, C. M.; Page, M. A.; Linden, K. G. Impact of Hydrogen Peroxide on Nitrate Formation during UV Disinfection. *Water Res.* **2003**, *37*, 4730–4736.

Shiraishi, Y.; Hara, H.; Hirai, T.; Komasawa, I. A Deep Desulfurization Process for Light Oil Photosensitized Oxidation Using a Triplet Photosensitizer and Hydrogen Peroxide in an Oil/Water Two-Phase Liquid-Liquid Extraction System. *Ind. Eng. Chem. Res*. **1999**, *38*, 1589–1595.

Shon, H. K.; Vigneswaran, S.; Snyder, S. A. Effluent Organic Matter (EfOM) in Wastewater: Constituents, Effects, and Treatment. *Crit. Rev. Env. Sci. Tec*. **2006**, *36*, 327–374.

Sichel, C.; Garcia, C. Andre, K. Feasibility Studies: UV/Chlorine Advanced Oxidation Treatment for the Removal of Emerging Contaminants. *Water Res.* **2011**, *45*, 6371–6380.

Simpson, I. J.; Meinardi, S.; Blake, D. R.; Blake, N. J., Rowland, F. S.; Atlas, E.; Flocke, F. A Biomass Burning Source of C1-C4 Alkyl Nitrates. *Geophys. Res. Lett.* **2002,** *29*, 2168, doi:10.1029/2002GL016290.

Sirivedhin, T.; Gray, K. A. Part I. Identifying Anthropogenic Markers in Surface Waters Influenced by Treated Effluents: A Tool in Potable Water Reuse. *Water Res.* **2005**, *39*, 1154–1164.

Sive, B. C. Ph.D. Dissertation, University of California, Irvine, CA, 1998.

Sirtori, C.; Zapata, A.; Oller, I.; Gernjak, W.; Aguera, A.; Malato, S. Solar Photo-Fenton as Finishing Step for Biological Treatment of a Pharmaceutical Wastewater. *Environ. Sci. Technol.* **2009,** *43*, 1185–1191.

Sleighter, R. L.; Hatcher, P. G. Molecular Characterization of Dissolved Organic Matter (DOM) Along a River to Ocean Transect of the Lower Chesapeake Bay by Ultrahigh Resolution Electrospray Ionization Fourier Transform Ion Cyclotron Resonance Mass Spectrometry. *Mar. Chem.* **2008**, *110*, 140–152.

Smulders, E.; von Rybinski, W.; Sung, E.; Rähse, W.; Steber, J.; Wiebel, F.; Nordskog, A. *Ullmann's Encyclopedia of Industrial Chemistry*, Wiley-VCH Verlag GmbH, 2007; p 113.

Snyder, S. A. Occurrence, Treatment, and Toxicological Relevance of EDCs and Pharmaceuticals in Water. *Ozone: Sci. Eng*. **2008**, *30*, 65–69.

Snyder, S. A.; Adham, S.; Redding, A. M.; Cannon, F. S.; DeCarolis, J.; Oppenheimer, J.; Wert, E. C.; Yoon, Y. Role of Membranes and Activated Carbon in the Removal of Endocrine Disruptors and Pharmaceuticals. *Desalination* **2007**, *202*, 156–181.

Snyder, S. A.; Westerhoff, P.; Yoon, Y.; Sedlack, D. L. Pharmaceuticals, Personal Care Products, and Endocrine Disruptors in Water: Implications for the Water Industry. *Environ. Eng. Sci*. **2003**, *20*, 449–469.

Sobhani, R.; Larson, L. E.; Rosso, D. *Energy Footprint Dynamics of Water Reclamation and Purification Processes During The Short-Term Periods.* Proceedings, WefTec: 85th Annual Water Environment Federation Conference, New Orleans, IL. September 29–October 3, 2012.

Sondhi, R.; Bhave, R. Role of Backpulsing in Fouling Minimization in Crossflow Filtration with Ceramin Membranes. *J. Membr. Sci.* **2001**, *186*, 41–52.

Song, W.; Cooper, W. J.; Mezyk, S. P.; Greaves, J.; Peake, B. M. Free Radical Destruction of β-Blockers in Aqueous Solution. *Environ. Sci. Technol.* **2008**, *42*, 1256–1261.

Song, W.; Cooper, W. J.; Peake, B. M.; Mezyk, S. P.; Nickelsen, M. G.; O'Shea, K. E. Free-Radical-Induced Oxidative and Reductive Degradation of N,N′-diethyl-m-toluamide (DEET): Kinetic Studies and Degradation Pathway. *Water Res*. **2009**, *43*, 635–642.

Soroushian, F.; Shen, Y.; Patel, M.; Wehner, M. *Evaluation and Pilot Testing of Advanced Processes for NDMA Removal and Reformation Prevention*. Proceedings, American Water Works Association Annual Conference, Washington, DC, 2001.

Spinks, J. W. T.; Woods, R. J. *An Introduction to Radiation Chemistry;* Wiley: NY, 1990.

Stefan, M. I.; Bolton, J. R. Mechanism of the Degradation of 1,4-Dioxane in Dilute Aqueous Solution Using the UV/Hydrogen Peroxide Process. *Environ. Sci. Technol*. **1998**, *32*, 1588–1595.

Stenson, A. C.; Marshall, A. G.; Cooper, W. T. Exact Masses and Chemical Formulas of Individual Suwannee River Fulvic Acids from Ultrahigh Resolution Electrospray Ionization Fourier Transform Ion Cyclotron Resonance Mass Spectra. *Anal. Chem.* **2003**, *75*, 1275–1284.

Stewart, P. S. Diffusion in Biofilms. *J. Bacteriol.* **2003**, *185*, 1485–1491.

Sultan, J.; Gabryelski, W. Structural Identification of Highly Polar Nontarget Contaminants in Drinking Water by ESI-FAIMS-Q-TOF-MS. *Anal. Chem*. **2006**, *78*, 2905–2917.

Summers, D. B. *Chemistry Handbook*. 2nd ed.; Willard Grant Press: Boston, MA, 1975.

Swanson, A. L.; Blake, N. J.; Dibb, J. E.; Albert, M. R.; Blake, D. R.; Sherwood Rowland, F. Photochemically Induced Production of CH_3Br, CH_3I, C_2H_5I, Ethane, and Propene within Surface Snow at Summit Greenland. *Atomos. Environ.* **2002**, *36*, 2671–2682.

Takada, H.; Ishiwatari, R. Linear Alkylbenzenes in Urban Riverine Environments in Tokyo: Distribution, Source, and Behavior. *Environ. Sci. Technol*. **1987**, *21*, 875–883.

Tang, Y. C.; Chang, T. H.; Fane, A. G. Colloidal Interactions and Fouling of NF and RO Membranes: A Review. *Adv. Colloid Interfac.* **2011**, *164*, 126–143.

Thomas, J. K. Rates of Reaction of the Hydroxyl Radical. *Trans. Faraday Soc.* **1965**, *61*, 702–707.

Tobien, T.; Cooper, W. J.; Nickelson, M. G.; Pernas, E.; O'Shea, K. E.; Asmus, K.-D. Odor Control in Wastewater Treatment: The Removal of Thioanisol from Water–A Model Case Study by Pulse Radiolysis and Electron Beam Treatment. *Environ. Sci. Technol.* **2000**, *34*, 1286–1291.

Tran, T.; Bolto, B.; Gray, S.; Hoang, M.; Ostarcevic, E. An Autopsy Study of a Fouled Reverse Osmosis Membrane Element Used in Brackish Water Treatment Plant. *Water Res.* **2007**, *41*, 3915–3923.

Trehy, M. L.; Gledhill, W. E.; Mieure, J. P.; Adamove, J. E.; Nielsen, A. M.; Perkins, H. O.; Sckhoff, W. S. Environmental Monitoring for Linear Alkylbenzene Sulfonates, Dialkyltetralin Sulfonates and their Biodegradation Intermediates. *Environ. Toxicol. Chem.* **1996**, *15*, 233–240.

Trojan Technologies. Orange County Groundwater Replenishment System—Demonstration UV Disinfection and Oxidation System Performance Validation Report. July 30, 2004.

Tsuneda, S.; Ishihara, Y.; Hamachi, M.; Hirata, A. Inhibition Effect of Chlorine Ion on Hydroxyl Radical Generation in UV-H_20_2 Process. *Water Sci. Technol*. **2002**, *46*, 33–38.

Türetgen, I. Comparision of the Efficacy of Free Residual Chlorine and Monochloramine Against Biofilms in Model and Full Scale Cooling Towers. *Biofouling* **2004**, *20*, 81–85.

U. S. Department of Energy (DOE). *Transportation Energy Data Book: Edition 26*; ORNL-6978; USDOE Center for Transportation Analysis Engineering Science and Technology Division; Oak Ridge National Laboratory: Oak Ridge, TN, 2007. http://stuff.mit.edu:8001/afs/athena/dept/cron/Backup/project/urban_

metabolism/TGOFF/readings%20and%20websites/Edition26_Full_Doc.pdf (accessed August 2013)

U.S. Environmental Protection Agency (USEPA). *Low-Pressure Membrane Filtration for Pathogen Removal: Application, Implementation, and Regulatory Issues*; EPA 815-C-01-001; Office of Water, U. S. Government Printing Office: Washington, DC, 2001.

USEPA. *Inventory of U.S. Greenhouse Gas Emissions and Sinks: 1990–2006*; EPA 430-R-08-005; Government Printing Office: Washington DC, 2008.

USEPA. *Inventory of U.S. Greenhouse Gas Emissions Sinks: 1990–2011*; EPA 430-R-13-001; Government Printing Office: Washington, DC, 2013.

USEPA. Handbook on Advanced Nonphotochemical Oxidation Processes, EPA/625/R-01/004; U. S. Environmental Protection Agency: Cincinnati, OH, 2001; p 132.

USEPA. Handbook on Advanced Photochemical Oxidation Processes, EPA/625/R-98/004; U. S. Environmental Protection Agency: Cincinnati, OH, 1998; p 97.

USEPA. Technical Fact Sheet–1,4-Dioxane, EPA 505-F-13-001; Office of Solid Waste and Emergency Response, Washington, DC, January 2013.

USEPA. 1,4-Dioxane (CASRN 123-91-1); Research, Environmental Assessment, Integrated Risk Information System (IRIS); Washington, DC; http://www.epa.gov/iris/subst/0326.htm (accessed September 20, 2013).

USEPA. Unregulated Contaminant Monitoring Rule 2 (UCMR 2); Water, Laws and Regulations, Regulatory Information, Safe Drinking Water Act, Washington, DC, 2006. http://water.epa.gov/lawsregs/rulesregs/sdwa/ucmr/ucmr2/index.cfm (accessed September 20, 2013)

USEPA. A-Z Substance List; Research, Environmental Assessment, Integrated Risk Information System (IRIS); Washington, DC, 2007. http://cfpub.epa.gov/ncea/iris/ index .cfm? fuseaction=iris.showSubstanceList (accessed September 20, 2013)

USEPA. N-Nitrosodimethylamine (CASRN 62-75-9); Research, Environmental Assessment, Integrated Risk Information System (IRIS), Washington, DC; http://www.epa.gov/iris/subst/0045.htm (accessed August 2013).

Vairavamurthy, A.; Mopper, K. Geochemical Formation of Organosulfur Compounds (Thiols) by Addition of Hydrogen Sulfide to Sedimentary Organic Matter. *Nature* **1987**, *329*, 623–625.

Valentine, R. L.; Jafvert, C. T. General Acid Catalysis of Monochloramine Disproportionation. *Environ. Sci. Technol*. **1988**, *22*, 691–696.

Vikesland, P. J.; Ozekin, K.; Valentine, R. L. Effect of Natural Organic Matter on Monochloramine Decomposition: Pathway Elucidation Through the use of Mass and Redox Balances. *Environ. Sci. Technol*. **1998**, *32*, 1409–1416.

Vikesland, P. J.; Ozekin, K.; Valentine, R. L. Monochlororamine Decay in Model and Distribution System Waters. *Water Res*. **2001**, *35*, 1766–1776.

Vinchurkar, M. S.; Rao, B. S. M.; Mohan, H.; Mittal, J. P. Kinetics, Spectral and Redox Behavior of OH Adducts of Methylxanthines: A Radiation Chemical Study. *J. Chem. Soc. Perk T. 2* **1999**, *3*, 609–617.

von Gunten, U. Ozonation of Drinking Water: Part I. Oxidation Kinetics and Product Formation. *Water Res.* **2003**, *37*, 1443–1467.

von Sonntag, C. Advanced oxidation processes: mechanistic aspects. *Water Sci. Technol.* **2008**, *58*, 1015–1021.

Vrijenhoek, E. M.; Hong, S.; Elimelech, M. Influence of Membrane Surface Properties on Initial Rate of Colloidal Fouling of Reverse Osmosis and Nanofiltration Membranes. *J. Membr. Sci.* **2001**, *188*, 115–128.

Vrouwenverlder, H. S.; van Paassen, J. A. M.; Folmer, H. C.; Hofmann, J. A. M. H.; Nederlof, M. M.; van der Kooij, D. Biofouling of Membranes for Drinking Water Production. *Desalination* **1998**, *118*, 157–166.

Vrouwenvelder, J.S.; Beyer, F.; Dahmani, K.; Hasan, N.; Galjaard, G.; Kruithof, J.C.; Van Loosdrecht, M. C. M. Phosphate Limitation to Control Biofouling. *Water Res.* **2010**, *44*, 3454–3466.

Wade, R. Orange County Sanitation District, Fountain Valley, CA, Personal communication 2010.

Wang, P.; Tan, K. L.; Kang, T. E.; Neoh, K. G. Plasma-Induced Immobilization of Poly(ethylene glycol) onto Poly(vinylidenefluoride) Microporous Membrane. *J. Membrane Sci.* **2002**, *195*, 103–114.

Waters, J.; Feijtel, T. C. J. AIS/CESIO Environmental Surfactant Monitoring Program: Outcome of Five National Pilot Studies on Linear Alkylbenzene Sulfonate (LAS). *Chemosphere* **1995**, *30*, 1939–1956.

Watts, M. J.; Linden, K. G. Chlorine Photolysis and Subsequent OH Radical Production During UV Treatment of Chlorinated Water. *Water Res*. **2007**, *41*, 2871–2878.

Weeks, J. L.; Rabani, J. The Pulse Radiolysis of Deaerated Aqueous Carbonate Solutions. I. Transient Optical Spectrum and Mechanism. II. pK for OH Radicals. *J. Phys. Chem.* **1966**, *70*, 2100–2106.

Wert, E. C.; Rosario-Ortiz, F. L.; Snyder, S. A. Effect of Ozone Exposure on the Oxidation of Trace Organic Contaminants in Wastewater. *Water Res*. **2009a**, *43*, 1005–1014.

Wert, E. C.; Rosario-Ortiz, F. L.; Snyder, S. A. Using Ultraviolet Absorbance and Color to Assess Pharmaceutical Oxidation During Ozonation of Wastewater. *Environ. Sci. Technol*. **2009b**, *43*, 4858–4863.

Westerhoff, P.; Moon, H.; Minakata, D.; Crittenden, J. Oxidation of Organics in Retentates from Reverse Osmosis Wastewater Reuse Facilities *Water Res*. **2009**, *43*, 3992–3998.

Westerhoff, P.; Yoon, Y.; Snyder, S. A.; Wert, E. C. Fate of Endocrine-Disruptor, Pharmaceutical, and Personal Care Product Chemicals During Simulated Drinking Water Treatment Processes. *Environ. Sci. Technol*. **2005**, *39*, 6649–6663.

Whitham, K.; Lyons, S.; Miller, R.; Nett, D.; Treas, P.; Zante, A.; Fessenden, R.W.; Thomas, M.D.; Wang, Y. Linear Accelerator for Radiation Chemistry Research at Notre Dame 1995, In *IEEE Proceedings Particle Accelerator Conference and International Conference on High Energy Accelerators*, Dallas, Texas, 1995.

Willingham, G. A.; Vickers, J. C.; McGahey, C. *Microfiltration as Tertiary Treatment – Eighteen Month Trial*, AWWA Membrane Technology Conference Proceedings, Baltimore, MD. 1993.

Wink, D. A.; Nims, R. W.; Desrosiers, M. F.; Ford, R. C.; Keefer, L. K. A Kinetic Investigation of Intermediates Formed During the Fenton Reagent Mediated Degradation of N-Nitrosdimethylamine: Evidence for an Oxidative Pathway Not Involving Hydroxyl Radical. *Chem. Res. Toxicol.* **1991**, *4*, 510–512.

Wintgens, T.; Melin, T.; Schafer, A.; Khan, S.; Muston, M.; Bixio, D.; Thoeye, C. The Role of Membrane Processes in Municipal Wastewater Reclamation and Reuse. *Desalination* **2006**, *187*, 271–282.

Woltering, E. A. General Surgery: Fine-Needle Aspiration of Thyroid Nodules. *Western J. Med*. **1987**, *146*, 737–738.

Wong, P. S. H.; Cooks, R. G.; Cisper, M. E.; Hemberger, P. H. On-Line, In Situ Analysis with Membrane Introduction MS. *Environ. Sci. Technol*. **1995**, *29*, 215A–218A.

Woods, G. C.; Simpson, M. J.; Kelleher, B. P.; McCaul, M.; Kingery, W. L.; Simpson, A. J. Online High-Performance Size Exclusion Chromatography–Nuclear Magnetic Resonance for the Characterization of Dissolved Organic Matter. *Environ. Sci. Technol.* **2010**, *44*, 624–630.

Yiin, B. S.; Margerum, D. W., 1990. Non-Metal Redox Kinetics: Reactions of Trichloramine with Ammonia and with Dichloramine. *Inorg. Chem.* **1990**, *29*, 2135–2141.

Yoo, L.; Fitzsimmons, S.; Shen, Y.; Wehner, M. Improved Purge-Trap and GC/MS/MS Techniques for the Trace-Level Determination of 1,4-Dioxane in Water. Water Quality Technology Conference, Seattle, WA, November 10–14, 2002.

Yoo, L.; Fitzsimmons, S.; Shen, Y.; Wehner, M. Simultaneous Determination of 1,2,3-Trichloropropane and 1,4-Dioxane in Drinking Water by GC/MS/MS Using Purge and Trap Techniques. Water Quality Technology Conference, Philadelphia, PA, November 2–6, 2003.

Yoon, J.; Jensen, J.N. Chlorine Transfer from Inorganic Monochloramine in Chlorinated Wastewater. *Water Environ. Res*. **1995**, *67*, 842–847.

Yüksel, S.; Kabay, N.; Yüksel, M. Removal of Bisphenol A (BPA) from Water by Various Nanofiltration (NF) and Reverse Osmosis (RO) Membranes. *J. Hazard Mater*. **2013**, *263*, 307–310.

Zafirinu, O.C.; Joussot-Dubien, J.; Zepp, R.G.; Zika, R.G. Photochemistry of Natural Waters. *Environ. Sci. Technol*. **1984**, 18, 358A–371A.

Zafiriou, O. C.; McFarland, M. Nitric Oxide from Nitrate Photolysis in the Central Equatorial Pacific. *J. Geophys. Res.-Oceans.* **1981,** *86*, 3173–3182.

Zenker, M. J.; Borden, R. C.; Barlaz, M. A. Occurrence and Treatment of 1,4-Dioxane in Aqueous Environments. *Environ. Eng. Sci*. **2003**, *20*, 423–432.

Zepp, R. G.; Sheldon, M. W.; Moran, M. A. Dissolved Organic Fluorophores in Southeastern U.S. Coastal Waters: Correction Method for Eliminating Rayleigh and Raman Scattering Peaks in Excitation-Emission Matrices. *Mar. Chem.* **2004**, *89*, 15–36.

Zhao, Y. Fouling and Regeneration of Ceramic Microfiltration Membranes in Processing acid Wastewater Containing Fine TiO_2 Particles. *J. Membrane Sci.* **2002**, *208*, 331–334.

Zinsser Microbiology; 17th ed.,W. K. Joklik; Willett, H. P.; Amos, D. B., Eds. Appleton-Century-Crofts: NY, 1980; pp 805–810.

Appendix A

Total Chlorine Analysis: Online Chlorine Analyzers and Standard Methods

Chlorine is added to the AWPF influent before microfiltration in the form of sodium hypochlorite (bleach) but is quickly converted into chloramine species (mono-, di- and tri-) and organic chloramines due to the presence of an excess of free ammonia (2.4 mg/L NH_3-N) and organic nitrogen (0.7 mg/L Org-N) in the secondary-treated sewage effluent. The AWPF employs numerous online amperometric total chlorine analyzers, which are used to monitor total chlorine that is present at key points in the plant, including the MFF, ROF, and ROP source waters. These automated analyzers operate based on an iodine-sensitive electrode driven by the conversion of a buffered iodide reagent to iodine by the free and combined chlorine present in the source water. The AWQA laboratory routinely (Monday and Wednesday) measures total chlorine in grab samples by amperometric titration and DPD-FAS titration standard methods. The R&D department uses a DPD colorimetric method (HACH Company, Program 1485).

The online chlorine analyzers are calibrated by zeroing the internal iodine sensitive electrode against deionized water to correct for background. This is followed by a single-point slope-adjustment based on the results of a DPD-FAS titration of a grab sample from the analyzer location.

The chlorine level in ROF is a critical control point in the AWPF. Plant operators visually monitor the online chlorine analyzer and make adjustments to the 12.5% NaOCl dosing pump in order to maintain the desired level of residual chlorine in the ROF. The SCADA system does not adjust the flow of the bleach to maintain the targeted ROF total chlorine set point.

Three different water matrices can be identified between the feed side of the MF process and the product side of the RO process and are defined by major changes in the water quality. These are (1) pre-RO before acid/antiscalant addition: MFF/MFE, (2) pre-RO after acid/antiscalant addition: ROF, and (3) post-RO: ROP (without hydrogen peroxide).

Results derived from the different methods of total chlorine analysis do not entirely agree and, depending on the water matrix, may differ by as much as 2 mg/L (see Figure A.1). In these box-and-whisker plots, the waist line or notch represents the median of the data, the upper box line the third quartile, the lower box line the first quartile, the upper whisker the maximum value, and the lower whisker the minimum value. Historically, the online chlorine analyzers tend to report higher concentrations than the laboratory standard methods for total chlorine. Data in Figure A.1 are from matched sample times collected from May to August, 2011 when the ROF target was 4 mg/L total chlorine (n=30).

In general, for all sample points (MFF, ROF, and ROP), there was better agreement between the laboratory DPD-FAS and the amperometric titration methods than there was with the online total chlorine analyzers, which appeared to overestimate the total chlorine concentration. Reasons for differences in the total chlorine measurements may be related to differences in the water matrix, with the simpler water matrix (ROP) showing the smallest differences in signal response between the methods.

All of these total chlorine methods are based on chemistry, and thus, all are potentially susceptible to matrix effects that can alter their chemical reactions so as to read higher or lower than true total chlorine levels. As no independent total chlorine standards are used for any of the methods, no means exist of probing the matrix effects through an internal standard technique. This makes it difficult to determine which total chlorine method is the most reliable (i.e., the "gold standard"). One possible solution is to examine the extent to which the total chlorine methods are altered by the three major water matrices: follow the transition from complex matrix (MFF, MFE, ROF) to a simple matrix (ROP), and determine how the different total chlorine methods behave against each other.

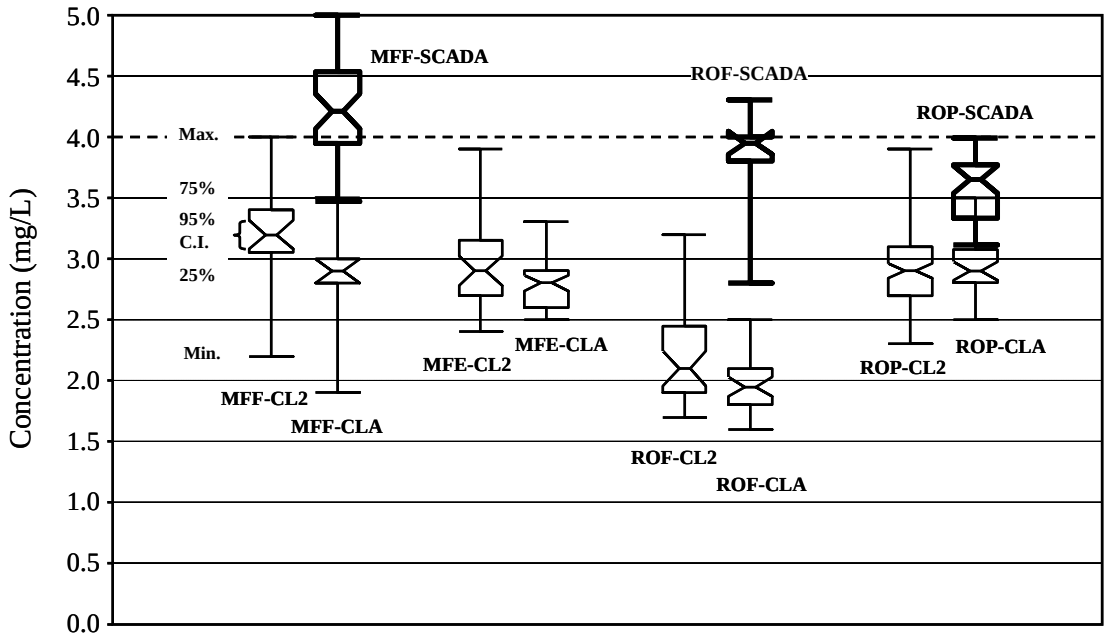

Figure A.1. Box-and-whiskers plot of the total chlorine reported by the online amperometric total chlorine analyzers (SCADA), the laboratory DPD-FAS standard method titration (CL2), and the standard method amperometric titration (CLA).

A strong total chlorine demand between MFF and ROP was not apparent as indicated by the laboratory amperometric titration data (Figure A.2). In this case, the level of total chlorine observed between MFF, MFE, and ROP appeared nearly the same, suggesting that a significant difference associated with this method does not exist. Overall, a large total chlorine demand across the AWPF (dotted line) was not observed. However, the concentrations observed in ROF appeared significantly lower. Because ROP was not depressed along with ROF, this suggests that rather than a demand, there is a matrix inhibition of the amperometric titration method. This inhibition may be due to the presence of the antiscalant or acid, which is present at ROF but not at MFF, MFE, or ROP.

The chlorine analyzers associated with the SCADA system were 50% higher than the concentration measured by the AWQA laboratory by DPD-FAS and amperometric titrations. If the online chlorine analyzers are calibrated based on the results of the DPD-FAS titration, the total chlorine concentrations reported by these online analyzers and the AWQA laboratory's amperometric titration results should not differ by this great amount. Assuming an average 3 h hold time, the AWQA laboratory readings should only be 3% to 7% lower.

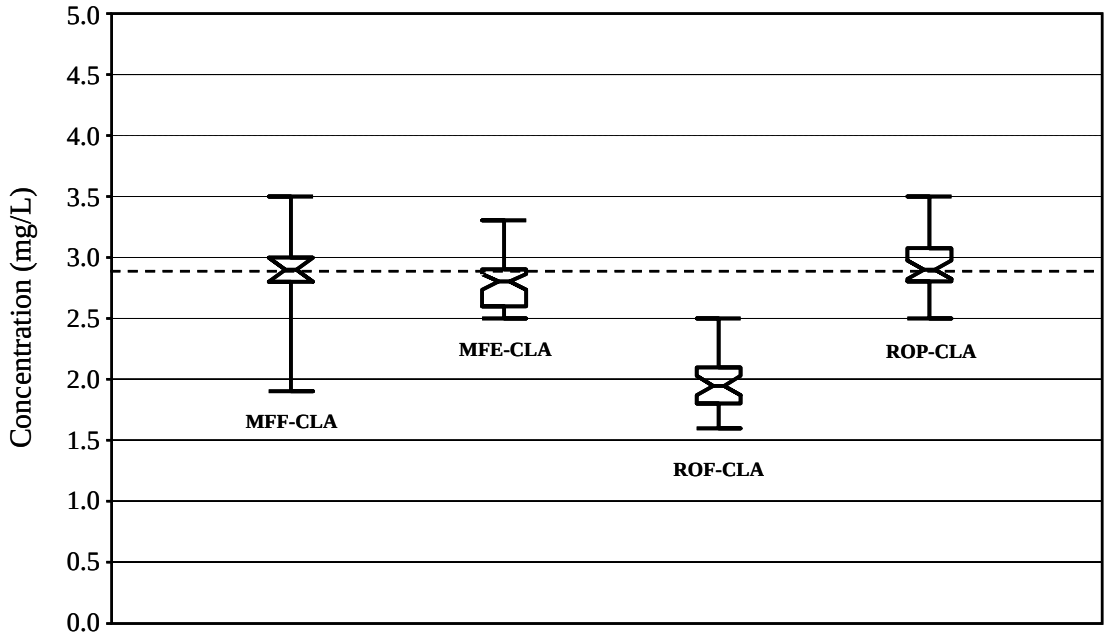

Figure A.2. Box-and-whiskers plot of the laboratory measured total chlorine concentration of MFF, MFE, ROF, and ROP source waters by standard method amperometric titration (n=30).

Comparison of the laboratory DPD-FAS titration method with the laboratory amperometric titration method (Figure A.3) showed a similar overall response, although there was a slight overestimation (0.1–0.2 mg/L) of total chlorine with the DPD-FAS titration method in the more complex water matrices (MFF, MFE, and ROF). However, this difference disappeared with the simpler water matrix of ROP. As with the amperometric total chlorine assay, the DPD-FAS method showed a significantly lower value for ROF, suggesting that, as with the former, the presence of the antiscalant and acid may have inhibited the total chlorine signal in this matrix.

When the online amperometric analyzers were considered and compared to the results obtained by standard methods, the deviations appeared to be much more extreme (Figure A.4). Even when data were temporally matched such that the online data represented the point in time when the samples were grabbed for laboratory analysis, in all cases the online analyzers over reported the total chlorine compared to the laboratory results.

Sample hold time experiments performed by the AWQA laboratory staff showed that handling of the samples does not account for the discrepancy (see Figure A.5). Sample hold time resulted in only 3% to 7% loss in total chlorine concentration after 3 h (as determined by amperometric titration). However, differences as much as 50% were observed with the online amperometric analyzer (ROF) at times matching the grab samples for laboratory analysis. Whereas these online amperometric analyzers are “calibrated” by matching their performance with the DPD-FAS titration method, and this study showed a reasonably good correlation between the historical data from the DPD-FAS and amperometric methods (see Figure A.3), this was not observed with the historical online analyzer total chlorine data. Again, the online total chlorine concentration recorded by the SCADA system were 50% higher than the concentration measured by the AWQA laboratory by DPD-FAS and amperometric titrations.

If the online chlorine analyzers are calibrated on the basis of the results of the DPD-FAS titration, the total chlorine concentrations reported by these online analyzers and the AWQA laboratory's amperometric titration results should not differ by this great amount. Assuming an average 3 h hold time, the AWQA laboratory readings should be only 3% to 7% lower.

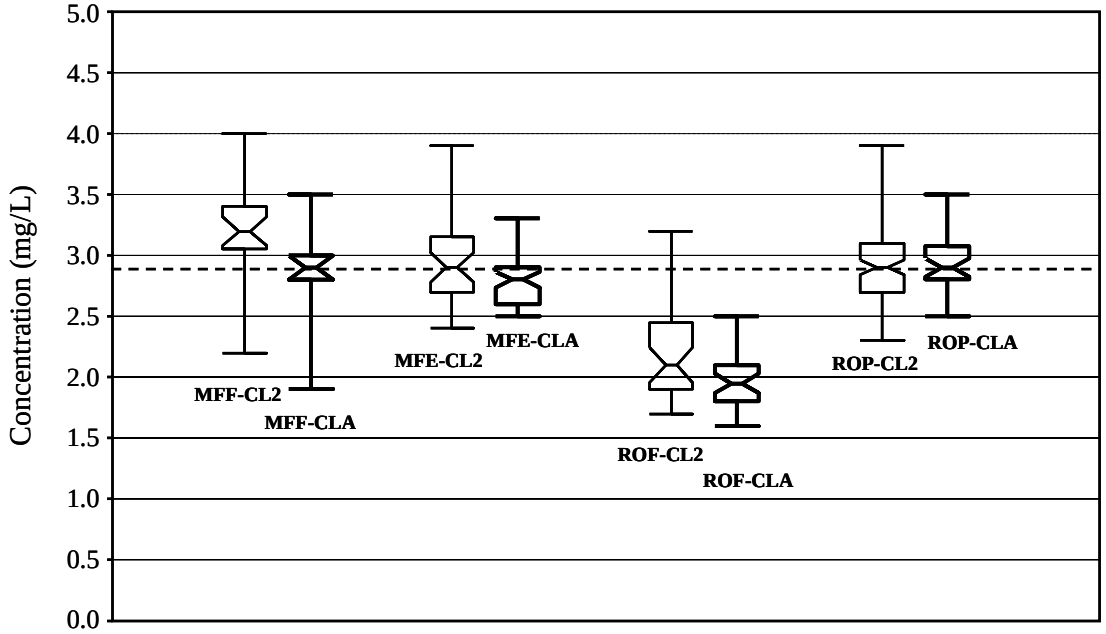

Figure A.3. Comparison of the laboratory DPD-FAS titration method (CL2) with the amperometric titration method (CLA) for total chlorine for MFF, MFE, ROF, and ROP source waters.

An additional difficulty was the apparent lack of depression of response observed with the online analyzer data for ROF to match that observed with the amperometric and DPD-FAS methods. This suggests that the response of the online analyzers to the ROF water matrix is very different from the laboratory methods, and if so, it is not possible to compare the responses of the two methods (online vs. laboratory) in this water matrix.

The R&D laboratory uses the HACH total chlorine method (Program 1485), which is a DPD-based colorimetric assay that gives results similar to the DPD-FAS and amperometric titration methods (see Figure A.6). This method will underestimate the amperometric online chlorine analyzer results for this reason.

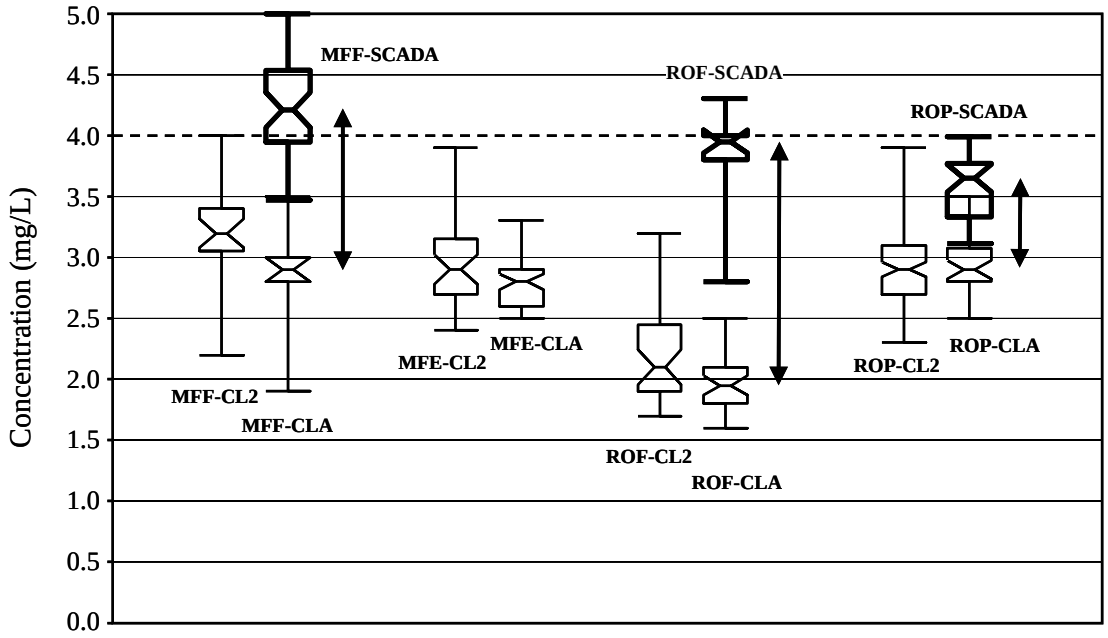

Figure A.4. Comparison of the online total chlorine analyzer data (SCADA) for the same sample times as the grab samples for laboratory DPD-FAS (CL2) titration and amperometric titration (CLA) of total chlorine for MFF, MFE, ROF, and ROP.

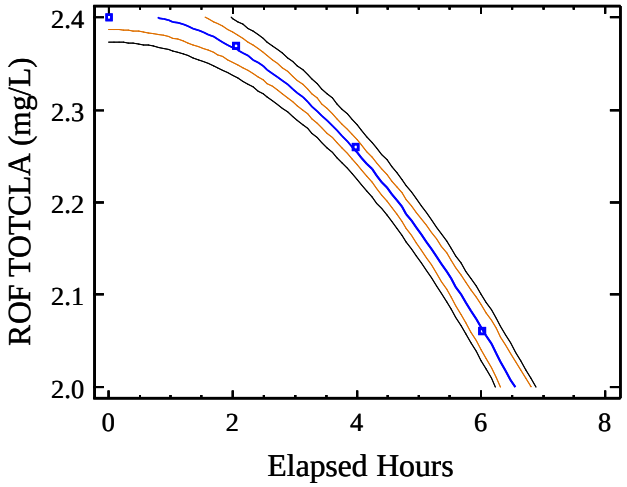

Model Statistics:
Correlation Coefficient = -0.9995
R^2 = 99.8959
Adjusted R2 = 99.8438
p = 0.0005
T_0 Value = 2.4 mg/L
Predicted value at T = 3 h = 2.32 mg/L
Loss = 0.08 mg/L (3.3%)

Figure A.5. Results of the AWQA laboratory holding time experiment for ROF. Average hold times for total chlorine samples is 3 h (4 °C).

The results from these studies suggest that a closer look at the performance of the AWPF online total chlorine analyzers is needed as they appear to respond differently compared with the three other methods for determining total chlorine. Of especial concern is the apparent lack of agreement between the laboratory DPD-FAS titration results for MFF, ROF, and ROP samples and the online analyzer data obtained in the same time frame as the sample grabs, as this was ostensibly the method used to calibrate the online analyzers. In addition, the apparent depression of total chlorine signal following addition of sulfuric acid and antiscalant (i.e., ROF total chlorine) and lack of this with the online analyzer total chlorine signal for ROF

suggests that the actual total chlorine dose to the AWPF is not being accurately reported, perhaps by either methods. One possible solution would be to consider relocation of the sample point for total chlorine dosage control before the acid/antiscalant addition to avoid potential inhibition of the total chlorine signal.

Comparison of the statistical variability of the box-and-whisker plots in Figures A.1–A.4 suggest that the measurement precision of the online analyzers is on par with that of the laboratory methods for determining total chlorine; however, accuracy is another matter. The online analyzers give a good representation of the drift in total chlorine dosage and can be used to keep the targeted chlorine residual constant (a role served by the ROF analyzer), but without better absolute calibration they apparently are overestimating the true total chlorine dosage in the AWPF. In the case of the data presented here, an average ROF chorine residual of 4 mg/L by the online analyzer, reported out by the laboratory (both DPD-FAS and amperometric) on the order of ~2 mg/L total chlorine. Corrected for the apparent depression to the ROF water matrix, this probably would be actually ~2.8 mg/L.

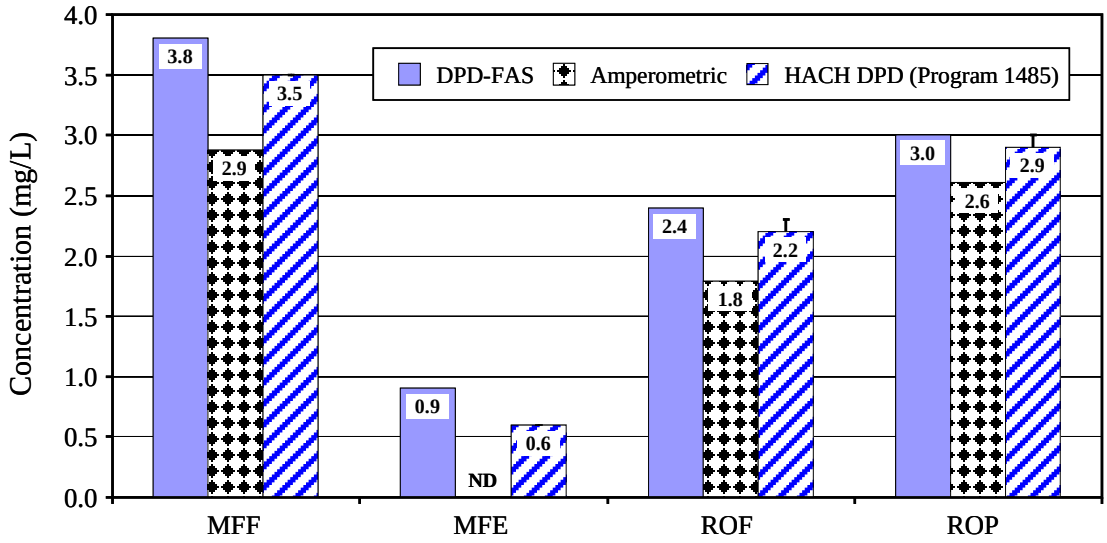

Figure A.6. Comparison of response of the HACH Program 1485 method for total chlorine (DPD-colorimetric) to that of the DPD-FAS and amperometric standard methods for MFF, MFE, ROF, and ROP water matrices.

Another possible solution is to calibrate the online total chlorine analyzers with a chloramine standard in a simple water matrix (e.g., DI water). It should be possible to produce such a standard in the AWQA laboratory in the morning, which then can be used for the day to calibrate all of the online analyzers. ROP held in the dark at 4 °C has exhibited stable total chlorine levels for up to 4 days; ROP could be collected in the morning, analyzed (by either DPD-FAS or amperometric titration methods) then used to calibrate all of the total chlorine analyzers free of bias from the water matrix.

If it is just important to operate the AWPF at a stable concentration at ROF, it is not necessary to worry about the actual real-time chlorine dosage used as long as it is controlled and provides the desired RO performance. However, if it is necessary to duplicate total chlorine dosage in a pilot system or accurately report the biostatic total chlorine load that is being dosed in the AWPF to others, closer attention should be paid to these data, and an attempt to understand actual total chlorine dosage, demand, and water matrix influences on

our various methods of total chlorine analysis in order to understand why the methods disagree should be sought.

Appendix B

EDX Spectroscopic Data and Plots of Linear Regression Analysis Associated with Membrane and Feed Spacer Fouling

Raw EDX elemental spectroscopic data from the membrane surface and the surface of the feed spacer are displayed in Tables B.1 through B.5.

Plots of linear regression analysis for membrane swatches exposed to Unit E01 Stage 1, 2, and 3 feedwater, and Stage 3 RO brine Figures B.1 through B.27. No strong relationships ($\%R^2$ >90%) were observed between material accumulated on the membrane surface or the Vexar spacer and the normalized specific flux in the plots displayed as follows.

Table B.1. EDX Spectroscopic Data from Control RO Membrane

	CONTROL (CLEAN)	
Element	**Surface**	**Feed Spacer**
C	209,390	557,409
O	35,461	
Na	11,344	
S	45,952	
Cl	3197	

Table B.2. EDX Spectroscopic Data from Membrane Swatches and Feed Spacers Exposed to Stage 1 RO Feedwater

	COUNTS 10%			COUNTS 20%				COUNTS 50%			COUNTS 70%		
Element	**ESPA 2 (1)**	**Spacer (1)**	**Spacer (2)**	**ESPA 2 (1)**	**ESPA 2 (2)**	**Spacer (1)**	**Spacer (2)**	**ESPA 2 (1)**	**ESPA 2 (2)**	**Spacer (1)**	**ESPA 2 (1)**	**ESPA 2 (2)**	**Spacer (1)**
C	642,661	3,416,451	399,926	2,148,024	182,620	31,937	789,890	240,089	190,589	119,692	361,611	102,491	1,138,468
O	8408	5213	3925	35,264	19,373	18,410	13,621	37,927	37,921	11,691			
N						4829	7836			3918	46,738	11,111	25,821
F		914		2134	615	1310				515		628	
Na		6133	4353	937	593	3935	6819	2402	1827	1482	2487	989	11,734
Mg		1155	1220			1230	2852	1368	798	710		482	4113
Al		3204		2961			1492	1593	1247		1992	1041	1840
Si				5416	1489		3519	4686	3539		10211	4163	2803
P			2331	1707				2971		914		1139	5345
S	12736			592,785	38,660			616,644	607,944	349	376,509	133,081	4225
Cl		2759	1383	6145	1746	3350	2451	6958	11,960	1263	9135	3212	12,551
Ca	212	1252	1364	4816	517	2216	5584	4498	3535	831	1992	3854	
K		503				412				216			1537
Fe				997									7395
Cu				2289			1006						
Ag													
Zr													
Br													

Table B.3. EDX Spectroscopic Data from Membrane Swatches and Feed Spacers Exposed to Stage 2 Feedwater

	COUNTS 10%				COUNTS 20%				COUNTS 50%		
Element	**ESPA 2 (1)**	**ESPA 2 (2)**	**Spacer (1)**	**Spacer (2)**	**ESPA 2 (1)**	**ESPA 2 (2)**	**Spacer (1)**	**Spacer (2)**	**ESPA 2 (1)**	**ESPA 2 (2)**	**Spacer (1)**
C	250,723	245,719	374,077	675,777	269,952	245,710	410,043	795,181	204,309	180,372	1,594,606
O	34,672	33,570	1619		21,305	31,642	3714		59,254	41,695	
N											
F	1595	1608	1786		1791	1365	1315	5330			
Na	2439	2633	9256	9023	1540	1257	2149	2434	10,897	8178	1518
Mg	987	1243	1808	1522			1657	2343	2991	1787	1879
Al			537	1695			635	3205	3263	1859	
Si	1191	1826	1709	3984	3035	2211	3154	5196	15,132	5502	
P									5528		
S	46,449	48,191			36,652	44,296			634,826	650,509	
Cl	2890	3343	3931	13,367	1953	1857		2443	35,227	24,739	2228
Ca	2092	1846	1752	3502	1492	1409	2711	4768	13,841	10,881	1241
K			1133	1369				1103	2688		
Fe				2040			2178	1472	2674	1775	
Cu				1978							
Ag											
Zr											
Br											

Table B.4. EDX Spectroscopic Data from Membrane Swatches and Feed Spacers Exposed to Stage 3 Feedwater

	COUNTS 10%			COUNTS 20%				COUNTS 50%			COUNTS 70%			
Element	**ESPA 2 (1)**	**Spacer (1)**	**Spacer (2)**	**ESPA 2 (1)**	**ESPA 2 (2)**	**Spacer (1)**	**Spacer (2)**	**ESPA 2 (1)**	**ESPA 2 (2)**	**Spacer (1)**	**ESPA 2 (1)**	**ESPA 2 (2)**	**Spacer (1)**	**Spacer (2)**
C	32,777	95,278	103,899	256,195	284,364	995,363	736,411	184,710	188,005	1,276,259	285,685	213,905	482,438	419,508
O	3046			44,902	49,007	61,809	4198	38,436	36,832		45,287	35,194		
N														
F						3621	3824	2756		17,134	2746	1361	5100	3112
Na	574	565	667	7554	5488	76,157	15,800	6397	6338		4543	2768	1136	1898
Mg	208	284		1534	1469	8803	2474	2048	1804		950	818		632
Al		189			1288	7794	2690	3495	2970	2736	2647	574		668
Si			541	36,734	51,017	43,661	10,679	5141	3788	3982	7827	4470	1726	2930
P						3671								
S	6164			366,113	352,905	29,662	4800	587,635	596,203		361,451	44,258		
Cl	746	736	572	7430	6553	82,422	14,096	17,417	16,622	2951	3069	3890	1775	1545
Ca	298	302	320	4974	4338	27,677	7743	8896	7373	2245	3776	2397	1038	878
K						6677	1186	1687						
Fe						3611		2134	1192			1014		
Cu				1260	1324	1305	1121	3207	2785	2118				
Ag														
Zr														
Br														

Table B.5. EDX Spectroscopic Data from Membrane Swatches and Feed Spacers from Stage 3 RO Brine (ROC)

	COUNTS 10%			COUNTS 20%		COUNTS 50%			COUNTS 70%		100%			
Element	**ESPA 2 (1)**	**Spacer (1)**	**Spacer (2)**	**ESPA 2 (1)**	**Spacer (1)**	**ESPA 2 (1)**	**ESPA 2 (2)**	**Spacer (1)**	**ESPA 2 (1)**	**Spacer (1)**	**ESPA2 (1)**	**ESPA2 (2)**	**ESPA2 (3)**	**Spacer (1)**
C	20,481	6341	35,834	62,671	923,373	52,420	42,133	80,008	25,702	518,166	122,516	134,641	177,661	540,296
O	9921	23,796	9815	112,664	133,441	104,045	124,359	80,153	10,860	33,684	66,284	68,118	61,995	21,844
N		560												
F	400			5950	10,472	4914	6657	5252	1430	6717	11,411	10,537	8929	6469
Na	1339	21,035	6712	5688	12,559	7022	10,495	8673	1180	4158	7705	9241	8758	11,626
Mg	430	3320	1282	1711	2998	1848	2111	2165		1595	2501	3588	1826	2159
Al		1655	1375	16,144	40,116	12,294	16,922	17,015	966	14,059	9725	15,071	8455	8681
Si	5383	13,374	5285	95,272	146,827	143,356	155,561	76,320	5840	56,080	44,753	73,030	37,139	37,570
P					453						4588			
S	5908	7222	2580	16,971		21,984	17,513		46,633		31,930	540,803	590,605	
Cl	1147	12232	2272	4094	3886	3805	2113	2363	2331	4008	4675	16369	15667	5794
Ca	851	1025		3146	8204	2603	4381	2920	566	4545	7290	20906	7752	4392
K	152	432	1191	1682	5276	1699	2279	2200		2978	1772	5405	2958	1928
Fe					1611							2351		
Cu										1906		2736	3238	2712
Ag														
Zr														
Br	742													

B.1 RO Unit E01 Stage 1 Feedwater Membranes

Plots of linear regression analysis for membranes receiving Unit E01 Stage 1 feedwater are displayed in Figures B.1 through B.6.

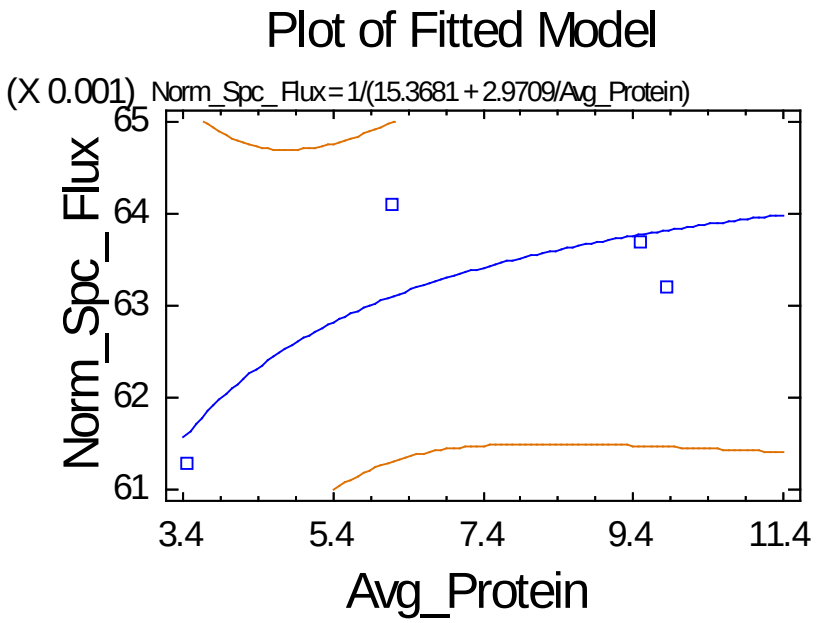

Figure B.1. Membranes receiving E01 Stage 1 feedwater. Normalized specific water flux (gfd/psi @ 25 °C) plotted as function of average total protein (µg/cm^2) accumulated on the membrane surface.

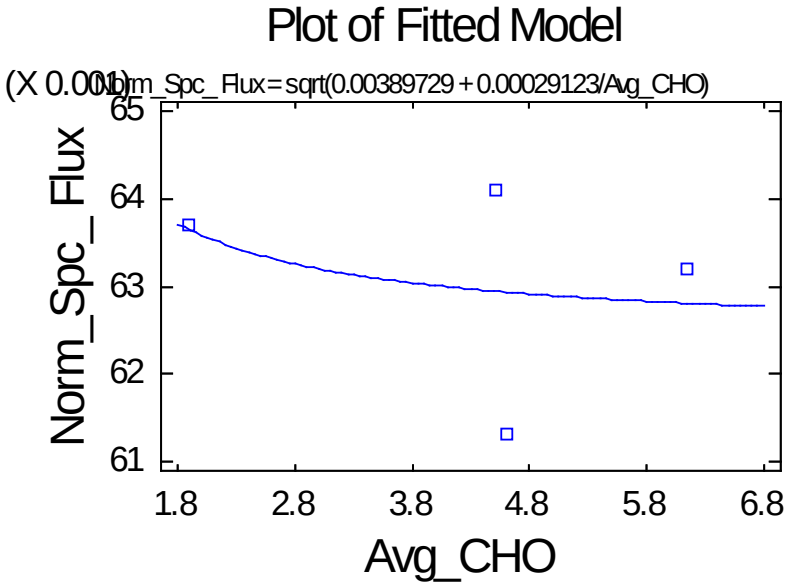

Figure B.2. Membranes receiving Unit E01 Stage 1 feedwater. Normalized specific water flux (gfd/psi @ 25 °C) plotted as a function of average carbohydrate (µg/cm^2) accumulated on the membrane surface.

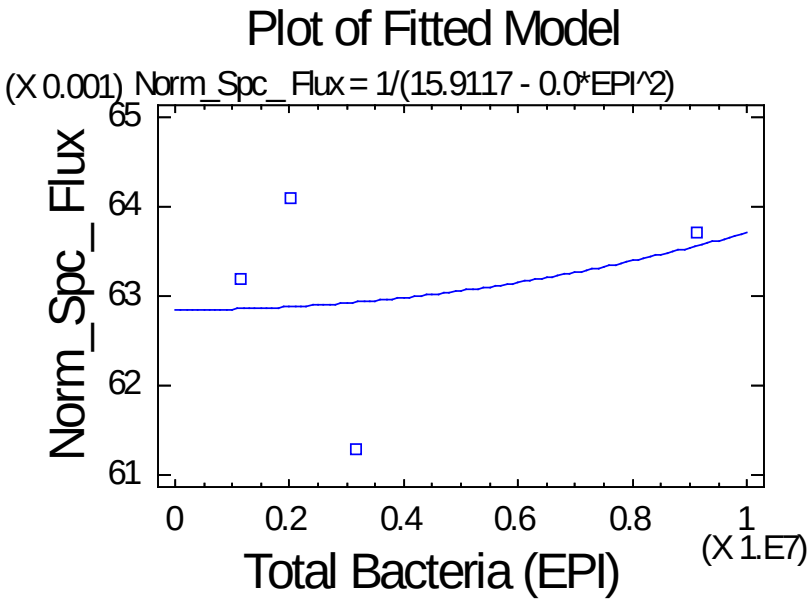

Figure B.3. Membranes receiving Unit E01 Stage 1 feedwater. Normalized specific water flux (gfd/psi @ 25 °C) plotted as a function of total bacteria (cells/cm^2) accumulated on the membrane surface.

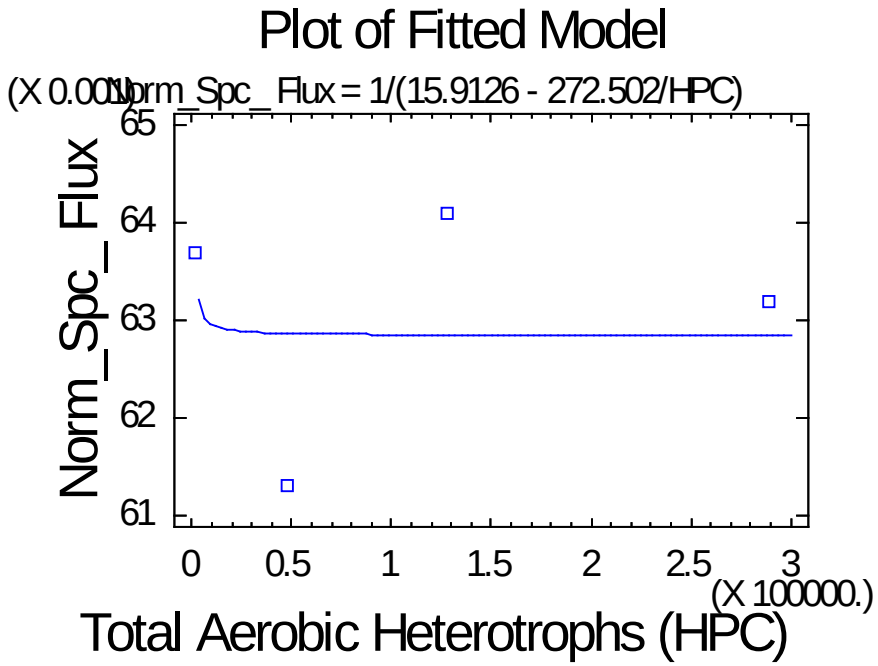

Figure B.4. Membranes receiving Unit E01 Stage 1 feedwater. Normalized specific water flux (gfd/psi @ 25 °C) plotted as a function of total aerobic heterotrophic bacteria (cells/cm^2) accumulated on the membrane surface.

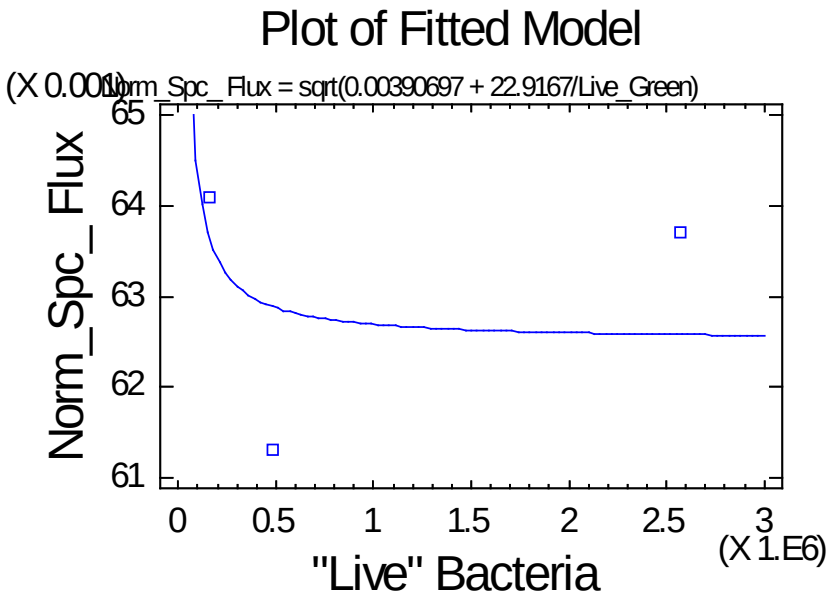

Figure B.5. Membranes receiving Unit E01 Stage 1 feedwater. Normalized specific water flux (gfd/psi @ 25 °C) plotted as a function of "live" bacteria (cells/cm^2) accumulated on the membrane surface.

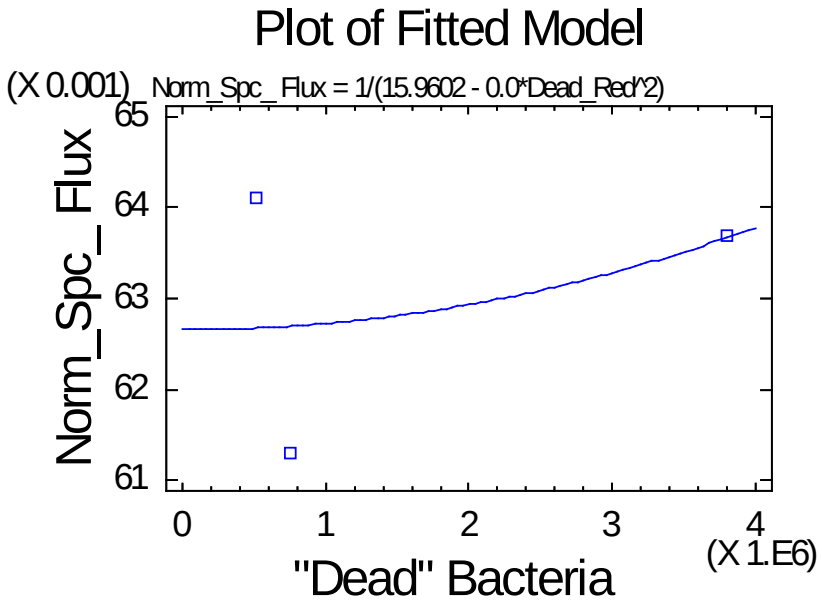

Figure B.6. Membranes receiving Unit E01 Stage 1 feedwater. Normalized specific water flux (gfd/psi @ 25 °C) plotted as function of "dead" bacteria (cells/cm^2) accumulated on the membrane surface.

B.2 RO Unit E01 Stage 2 Feedwater Membranes

Plots of linear regression analysis for membranes receiving Unit E01 Stage 2 feedwater are displayed in Figures B.7 through B.10.

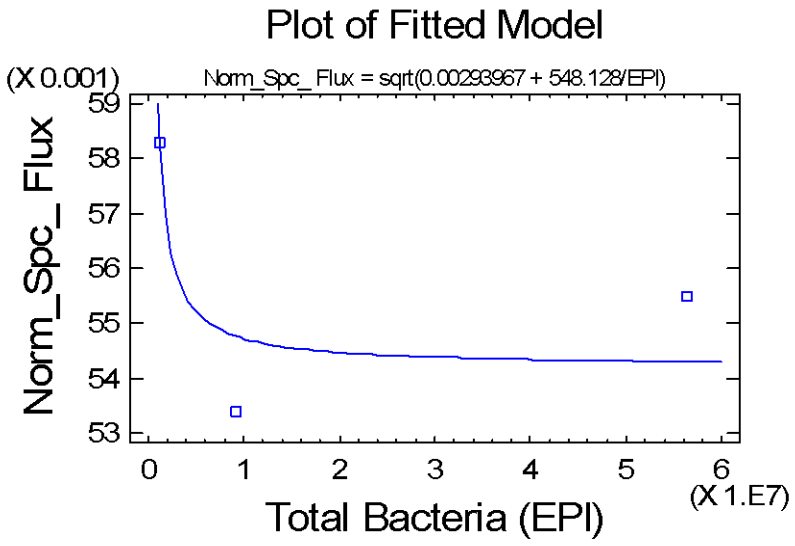

Figure B.7. Membranes receiving Unit E01 Stage 2 feedwater. Normalized specific water flux (gfd/psi @ 25 °C) plotted as function of total bacteria (cells/cm^2) accumulated on the membrane surface.

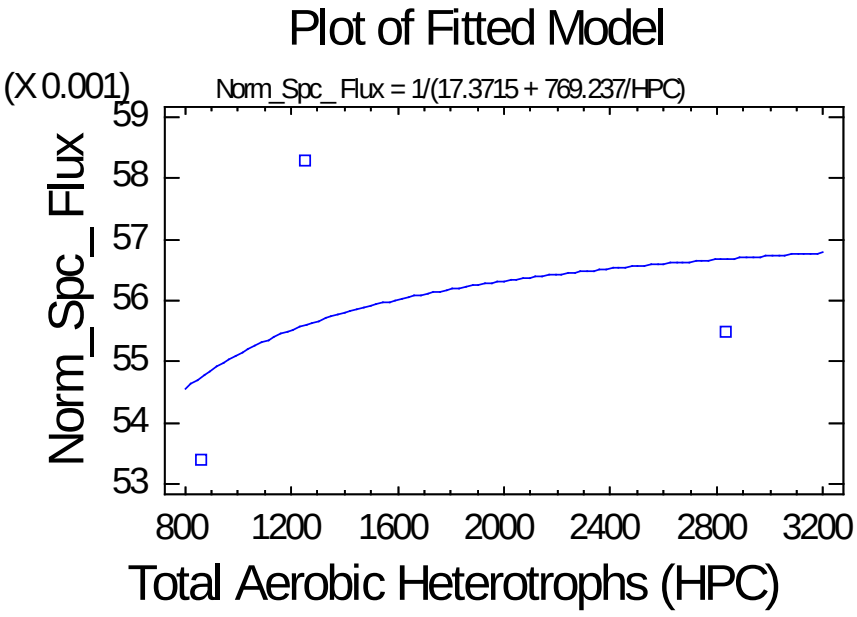

Figure B.8. Membranes receiving Unit E01 Stage 2 feedwater. Normalized specific water flux (gfd/psi @ 25 °C) as a function of total aerobic heterotrophic bacteria (cells/cm^2) accumulated on the membrane surface.

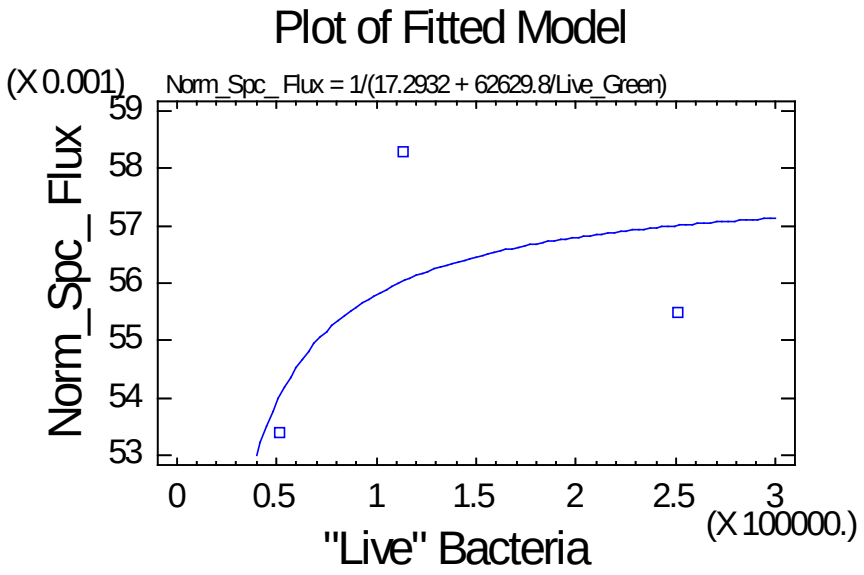

Figure B.9. Membranes receiving Unit E01 Stage 2 feedwater. Normalized specific water flux (gfd/psi @ 25 °C) plotted as function of "live" bacteria (cells/ cm^2) accumulated on the membrane surface.

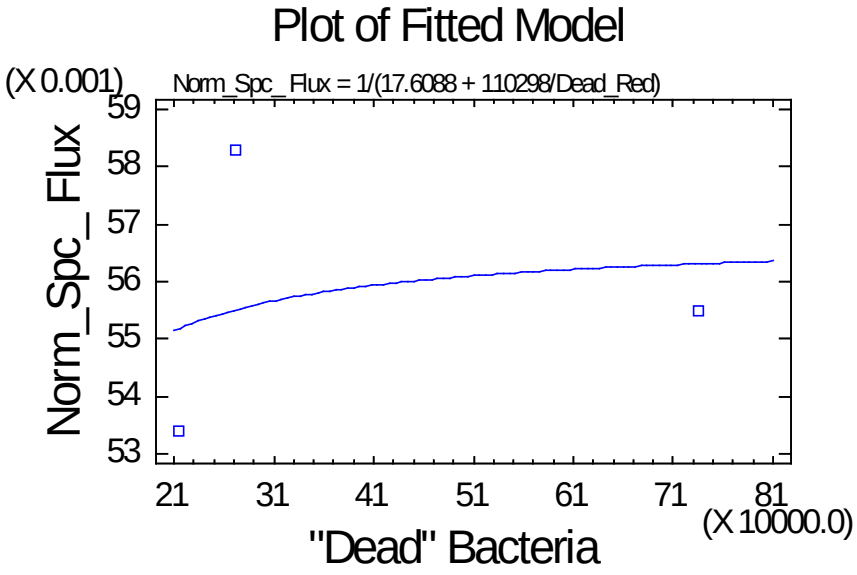

Figure B.10. Membranes receiving Unit E01 Stage 2 feedwater. Normalized specific water flux (gfd/psi @ 25 °C) plotted as a function of "dead" bacteria (cells/cm^2) accumulated on the membrane surface.

B.3 RO Unit E01 Stage 3 Feedwater Membranes

Plots of linear regression analyses for membrane swatches exposed to RO Unit E01 Stage 3 feedwater are shown in Figures B.11 through B.14.

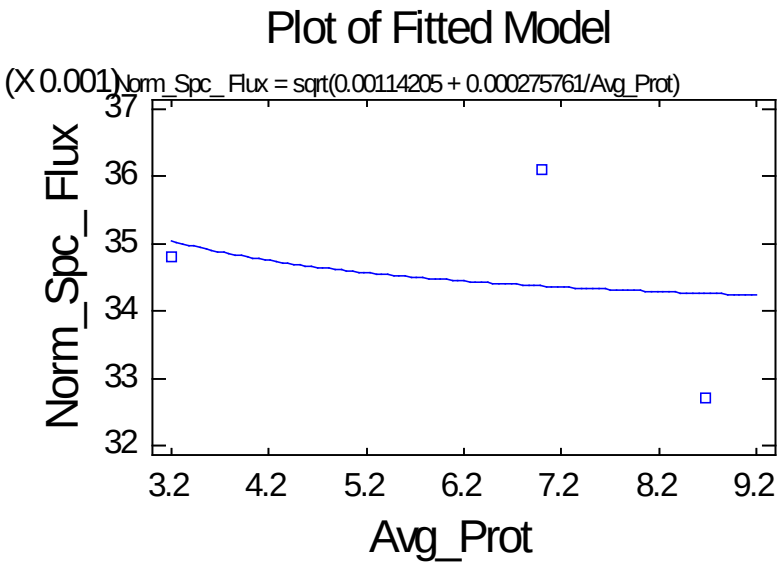

Figure B.11. Membranes receiving Unit E01 Stage 3 feedwater. Normalized specific water flux (gfd/psi @ 25 °C) plotted as function of average total protein (µg/cm^2) accumulated on the membrane surface.

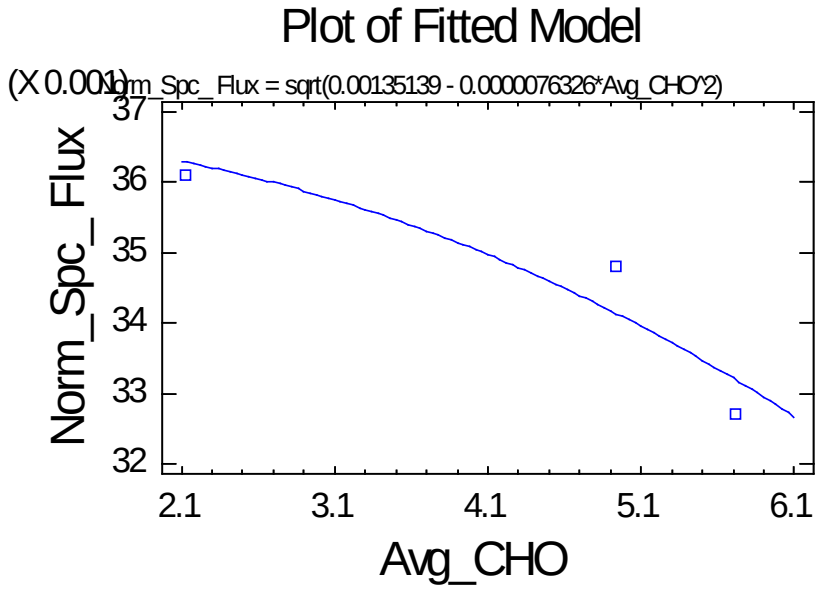

Figure B.12. Membranes receiving Unit E01 Stage 3 feedwater. Normalized specific water flux (gfd/psi @ 25 °C) plotted as function of average carbohydrate (µg/cm^2) accumulated on the membrane surface.

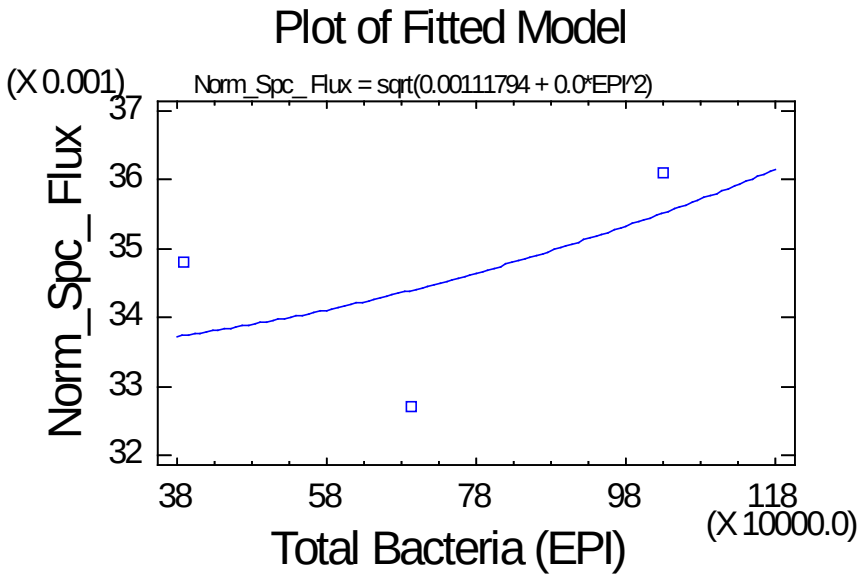

Figure B.13. Membranes receiving Unit E01 Stage 3 feedwater. Normalized specific water flux (gfd/psi @ 25 °C) plotted as function of total bacteria (cells/cm^2) accumulated on the membrane surface.

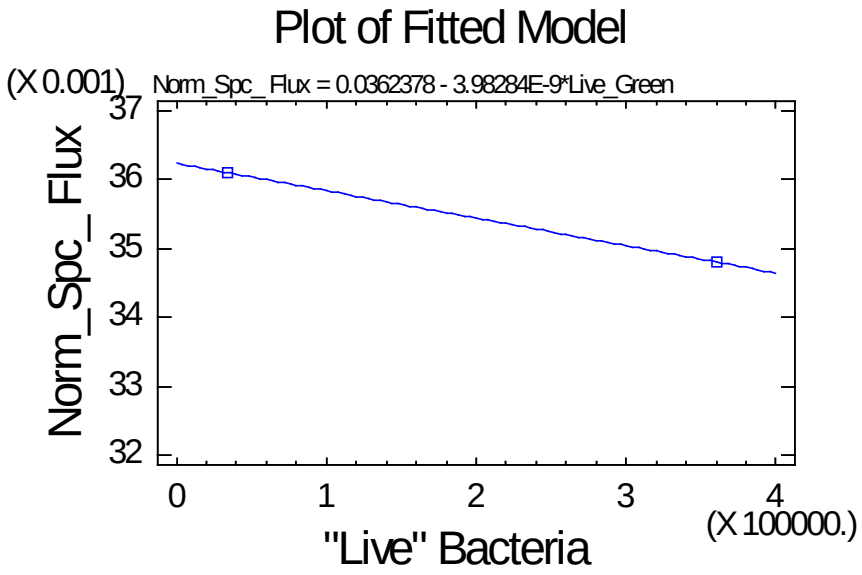

Figure B.14. Membranes receiving Unit E01 Stage 3 feedwater. Normalized specific water flux (gfd/psi @ 25 °C) plotted as function of "live" bacteria (cells/cm^2) accumulated on the membrane surface.

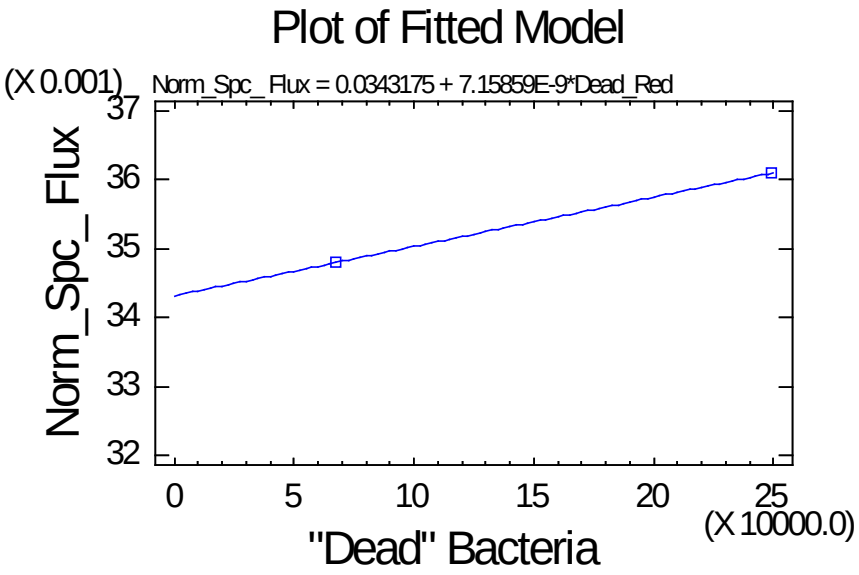

Figure B.15. Membranes receiving Unit E01 Stage 3 feedwater. Normalized specific water flux (gfd/psi @ 25 °C) plotted as function of "dead" bacteria (cells/cm^2) accumulated on the membrane surface.

B.4 RO Unit E01 Stage 3 Brine (ROC) Membranes

Plots of linear regression analyses for membrane swatches exposed to RO Unit E01 Stage 3 brine (ROC) are shown in Figures B.16 through B.19.

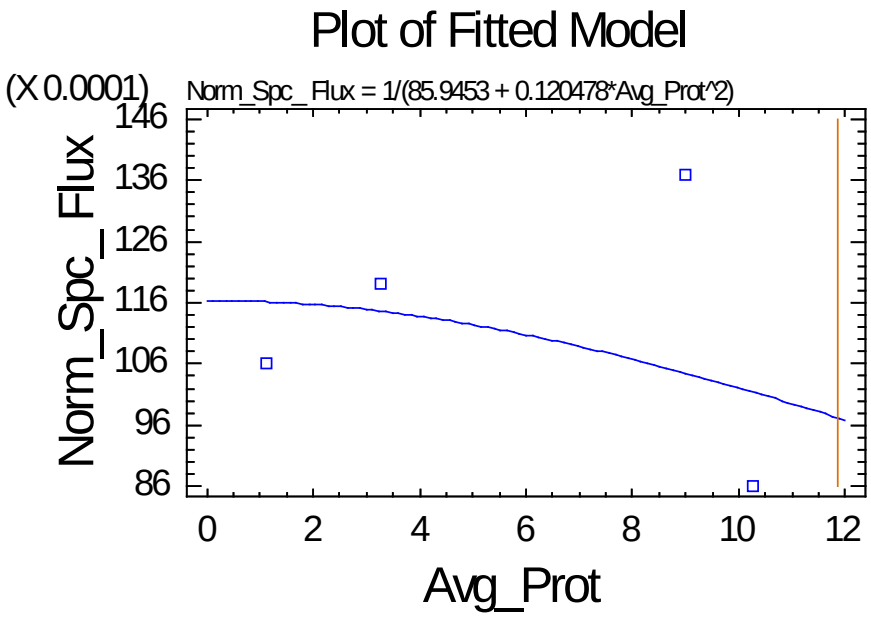

Figure B.16. Membranes receiving Unit E01 Stage 3 brine (ROC). Normalized specific flux (gfd/psi @ 25 °C) as a function of average total protein (µg/cm^2) accumulated on the membrane surface.

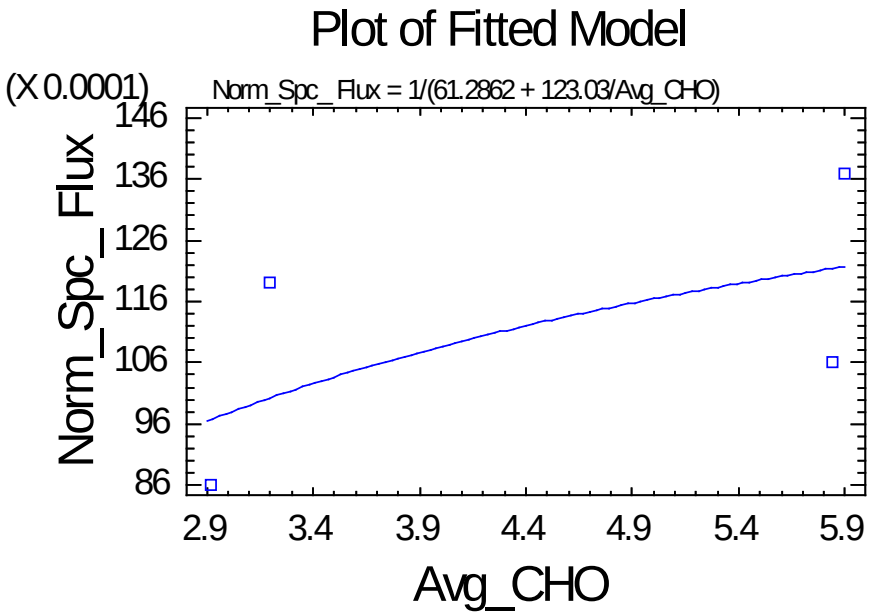

Figure B.17. Membranes receiving Unit E01 Stage 3 brine (ROC). Normalized specific flux (gfd/psi @ 25 °C) as a function of average carbohydrate (µg/cm^2) accumulated on the membrane surface.

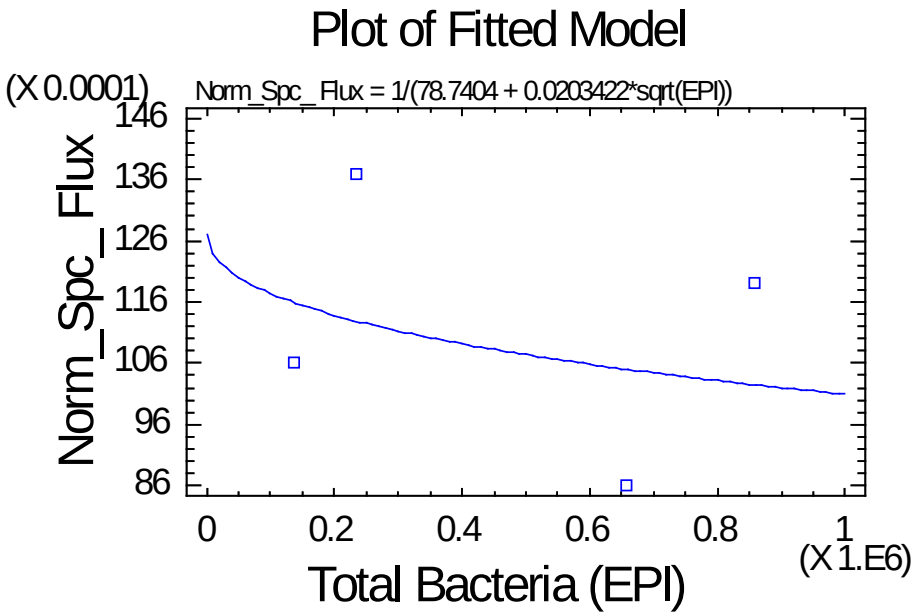

Figure B.18. Membranes receiving Unit E01 Stage 3 brine (ROC). Normalized specific flux (gfd/psi @ 25 °C) as a function of total bacteria (cells/cm^2) accumulated on the membrane surface.

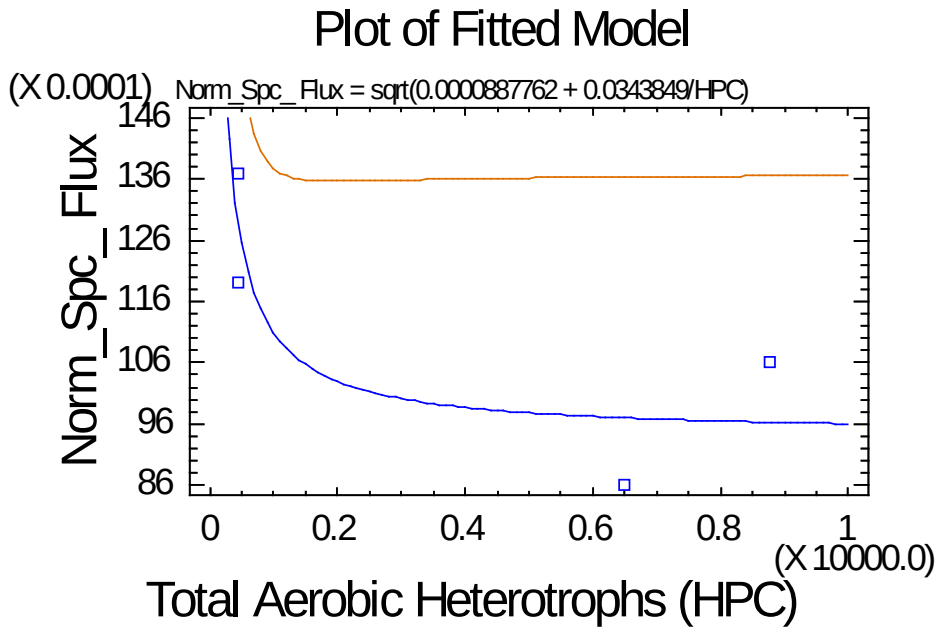

Figure B.19. Membranes receiving E01 Stage 3 brine (ROC). Normalized specific flux (gfd/psi @ 25 °C) as a function of total aerobic heterotrophic bacteria (cells/cm^2) accumulated on the membrane surface.

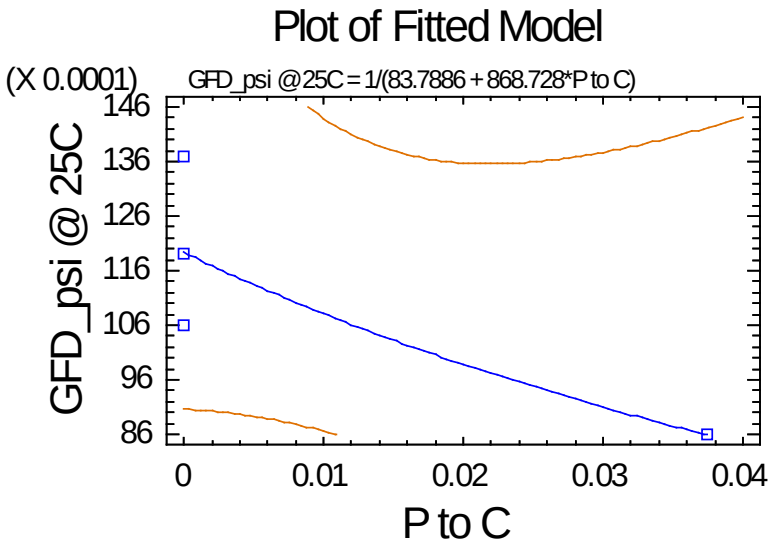

Figure B.20. Best linear regression model describing loss of normalized specific water flux of membranes at the end of RO Stage 3 as a function of the P/C EDX signal (% R^2 = 77.65%, p = 0.1188).

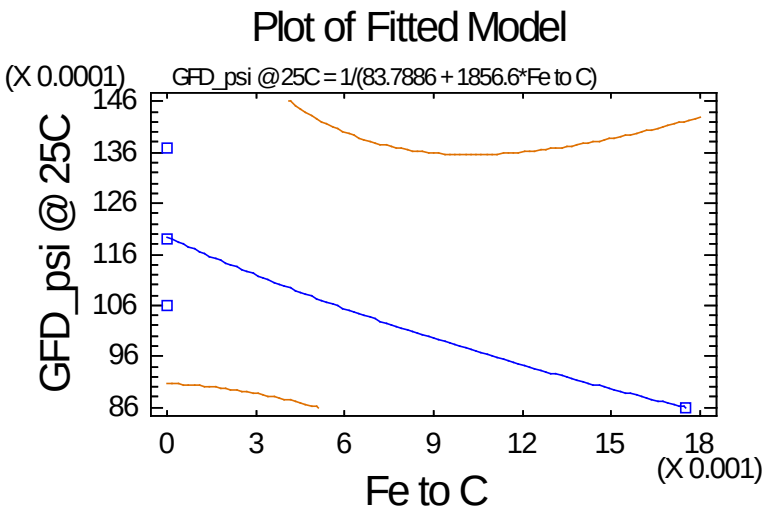

Figure B.21. Best linear regression model describing loss of normalized specific water flux of membranes at the end of RO Stage 3 as a function of the Fe/C EDX signal (% R^2 = 77.65%, p = 0.1188).

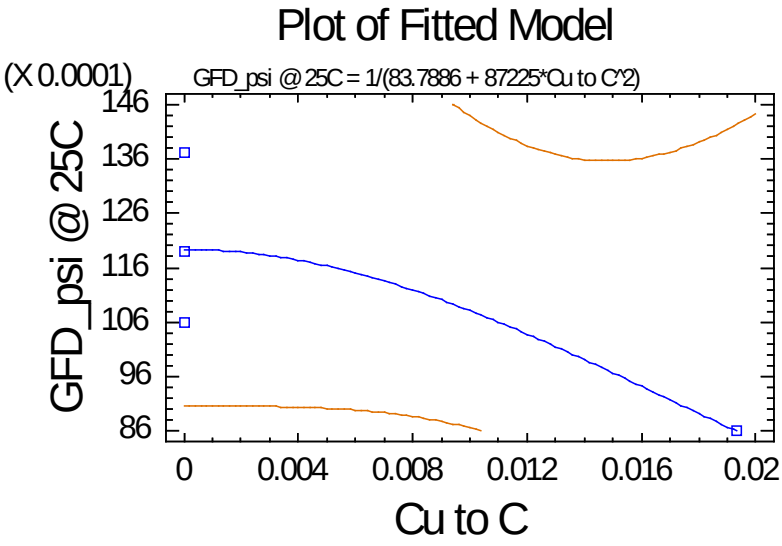

Figure B.22. Best linear regression model describing loss of normalized specific water flux of membranes at the end of RO Stage 3 as a function of the Cu/C EDX signal (% R^2 = 77.65%, p = 0.1188).

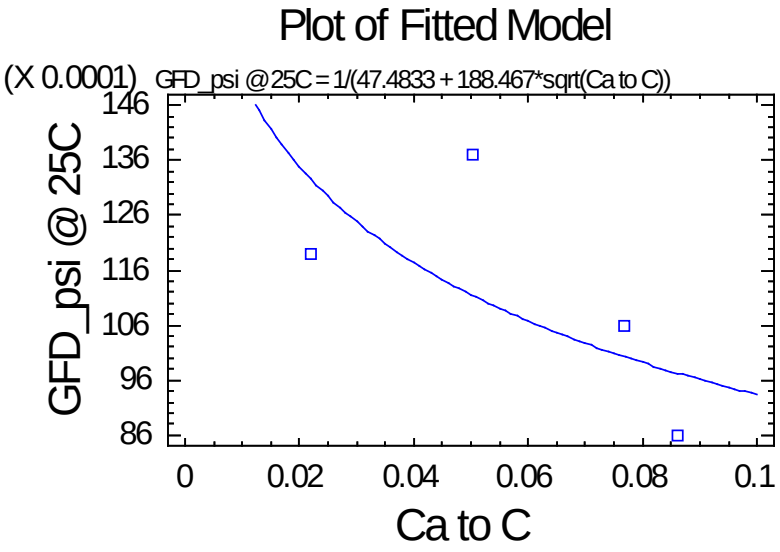

Figure B.23. Best linear regression model describing loss of normalized specific water flux of membranes at the end of RO Stage 3 as a function of the Ca/C EDX signal (% R^2 = 67.79%, p = 0.1766).

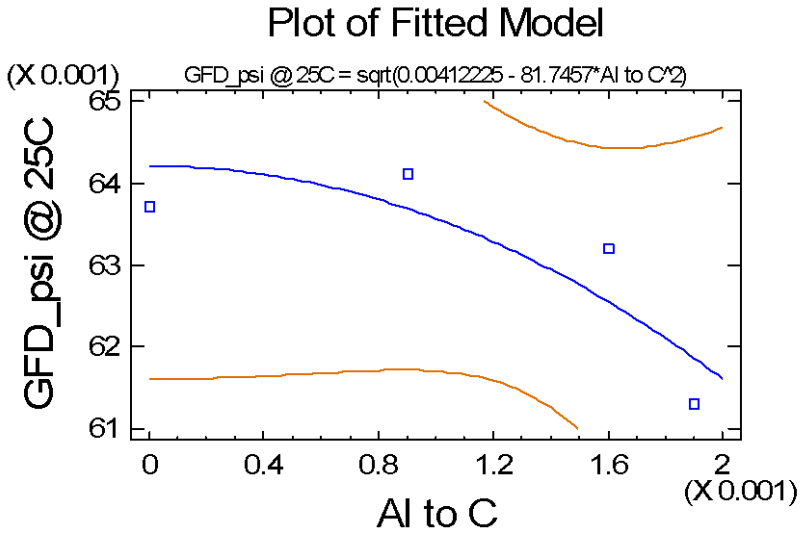

Figure B.24. Best linear regression model describing loss of normalized specific water flux of membranes at the beginning of RO Stage 1 as a function of the Al/C EDX signal on the membrane spacer (% R^2 = 74.56%, p = 0.1365).

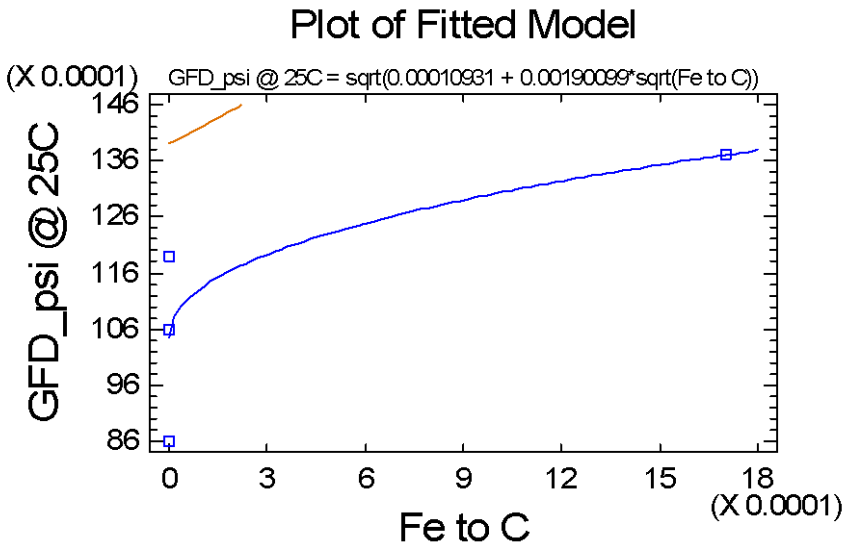

Figure B.25. Best linear regression model describing loss of normalized specific water flux of membranes at the end of RO stage 3 as a function of the Fe/C EDX signal on the membrane spacer (% R^2 = 66.68%, p = 0.1834).

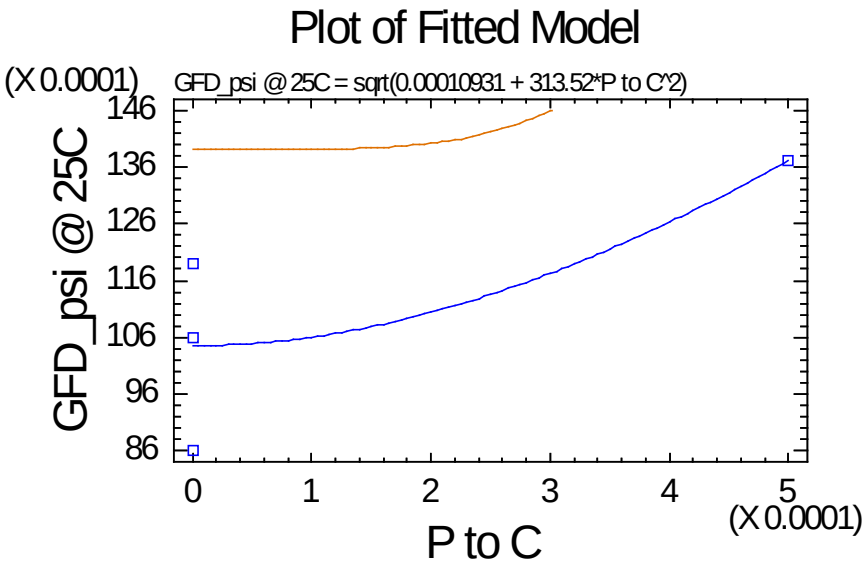

Figure B.26. Best linear regression model describing loss of normalized specific water flux of membranes at the end of RO stage 3 as a function of the P/C EDX signal on the membrane spacer (% R^2 = 66.68%, p = 0.1834).

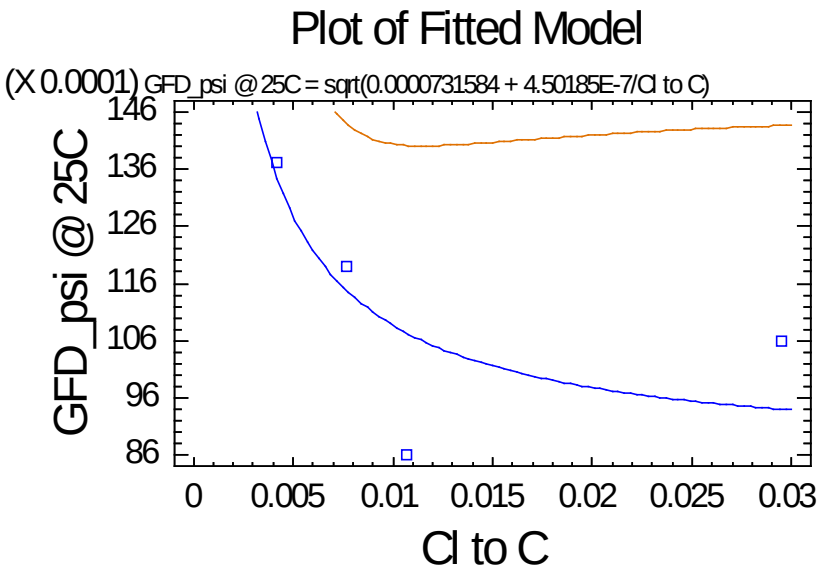

Figure B.27. Best linear regression model describing loss of normalized specific water flux of membranes at the end of RO stage 3 as a function of the Cl/C EDX signal on the membrane spacer (% R^2 = 64.83%, p = 0.1948).

Appendix C

UV Ballast and LPHO Lamp Performance

C.1 Introduction

The UV/AOP facility of the AWPF utilizes a three-chamber six-reactor UVPhox train manufactured by Trojan Technologies (London, ON, Canada). The 257-watt, low-pressure, high-output (LPHO) mercury amalgam lamp in the single-lamp pilot reactor is powered by the same ballast used to power the lamps in the UV/AOP facility of the AWPF. The output characteristics of the ballast and UV lamp associated with the single-lamp reactor were unknown and not available from Trojan Technologies. Therefore, a study was undertaken to acquire accurate data associated with the performance of the ballast and UV lamp.

The objectives of the study are outlined as follows.

- Measure the electrical power consumption of the 257-watt LPHO mercury amalgam lamp used in the AWPF at different ballast power or percentage levels.
- Simultaneously measure the 245-nm UV power output of the pilot reactor lamp at the wall of the reactor with a radiometer.
- Measure the power consumption of the pilot unit ballast.
- Determine the UV lamp performance in terms of
    - Lamp electrical power consumption at various ballast power levels (BPLs)
    - Ballast electrical power consumption recorded by the programmable logic controller (PLC) at various power levels
    - Lamp UV output at various ballast power levels
    - Lamp UV % efficiency (UV power out/Electrical power consumed * 100).

C.2 Materials and Methods

A true RMS RF ammeter was purchased (Weston Model 507) that operates by the thermal dissipation principal and capable of accurately measuring currents at radio frequencies. Frequency measurement of the output of the lamp ballast confirmed 60 kHz, which was too high for measurement by conventional ammeters. Voltage was measured using an oscilloscope with a floating ground; later measurements using a Fluke Model 87 DVM confirmed accuracy at 60 kHz. This meter was used for all test voltage measurements due to increased accuracy over the oscilloscope. Electrical power was calculated as “total power” (volt × amps, VA) as opposed to “real power” (watts).

- Real power (watts) = total power (VA) × power factor (PF).
- The power factor ranges from 0.5–1.0, and presumably is closer to 1.0 for high power factor electronic ballasts, but the exact value for the Trojan ballasts was unavailable.
- The Trojan UVPhox PLC registers total power (as kVA)

Once the instruments were in place, voltage and amperage measurements were collected at BPLs of 60, 66, 70, 76, 80, 86, 90, 96, and 100% as determined by the power module panel indicator. UV intensity was measured with a radiometer (Model 1400A, International Light Technologies, Peabody, MA) equipped with QND neutral density and TD integrating filters attached.

C.3 Results and Discussion

The electrical and UV output data were tabulated and are summarized and displayed in six plots as follows:

- **Lamp voltage and lamp amperage curves at varying power settings** were generated and are displayed in Figure C.1 as a function of BPL and in Figure C.2 as a function of electrical power consumption.

- **Lamp electrical power consumption was measured at varying ballast power percentages or levels (BPLs)** and is displayed in Figure C.3. The data are displayed as a percentage of the measured power in Figure C.4 and indicate a linear relationship between applied BPL percentage and the electrical power consumption by the lamp.

- **The radiometer measured UV lamp power output at 254 nm (watts)** is displayed in Figure C.5 as a function of measured UV lamp total electrical power consumption (VA). The same data are displayed as a function of indicated ballast power percentage in Figure C.6.

- **The UV lamp power output efficiency is plotted as function of measured UV lamp total electrical power consumption** in Figure C.7. The measurements indicate that the 257-watt LPHO UV lamp is ~27% to 28% efficient at converting electrical power into UV power at 254 nm.

- **A plot of UV output (in watts) as a function of lamp ballast power consumption** is displayed in Figure C.8, and a plot of the UV output as function of lamp ballast percentage is displayed in Figure C.9.

- Finally, a measure of the **UV lamp electrical power conversion efficiency to UV 254 nm** power is displayed in Figure C.10 as a function of lamp ballast total electrical power consumption.

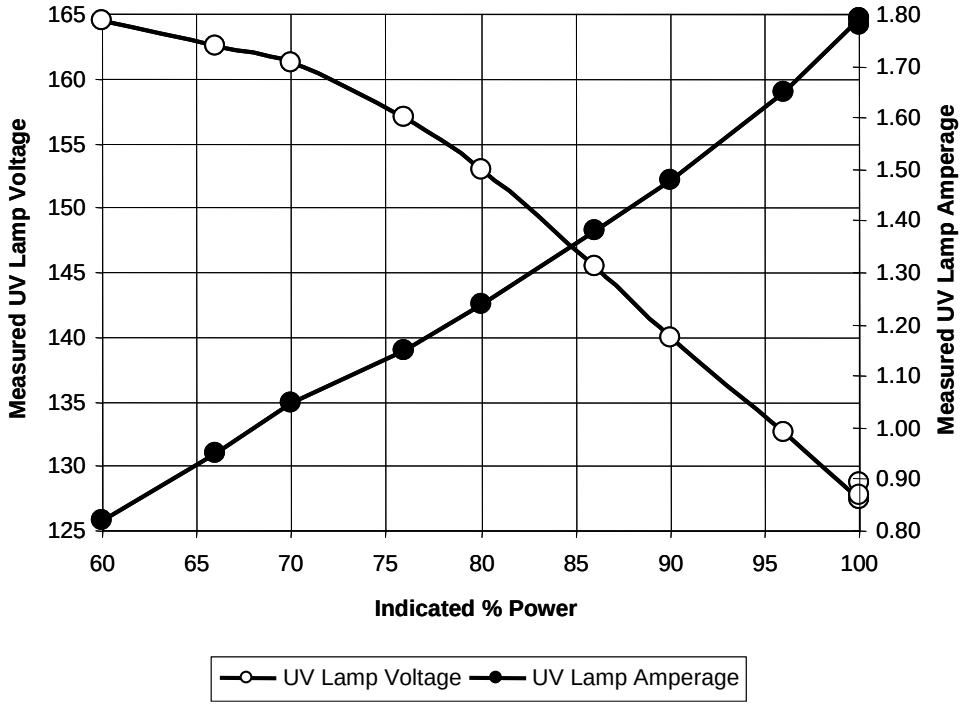

Figure C.1. Plot of measured UV lamp voltage and current as function of indicated BPL percentage.

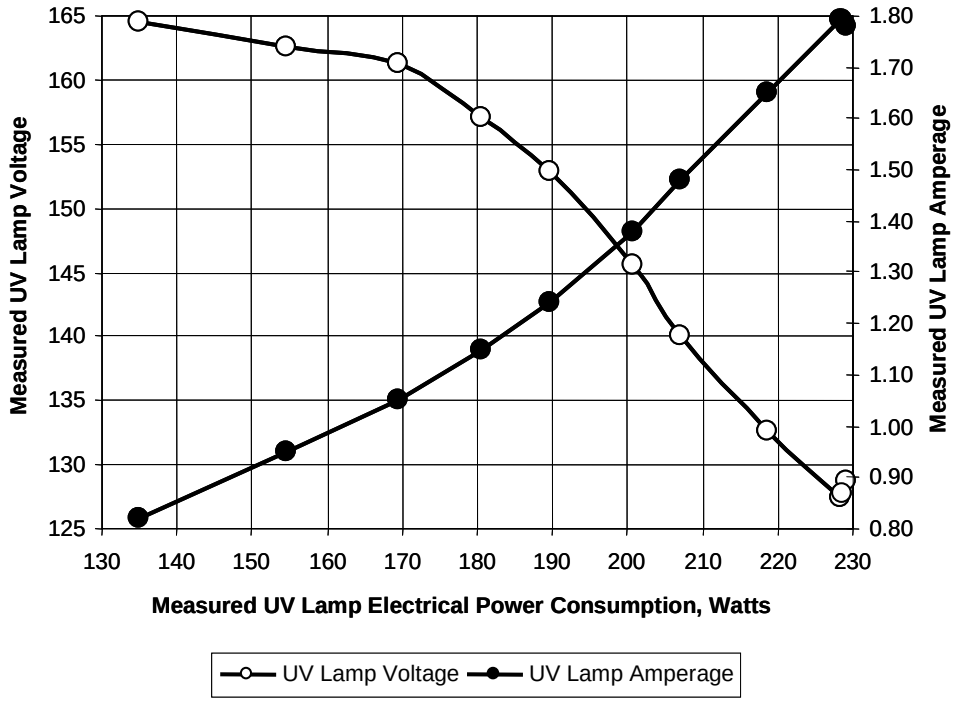

Figure C.2. Plot of measured UV lamp voltage and current as function of the measured lamp power consumption.

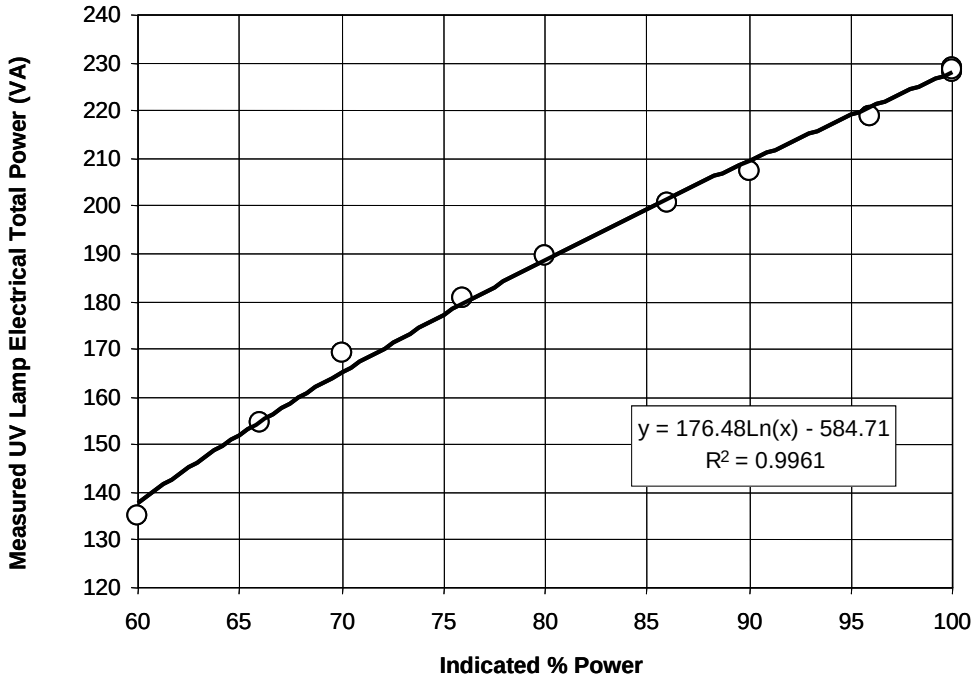

Figure C.3. Plot of the measured UV lamp total electrical power (VA) as a function of indicated BPL.

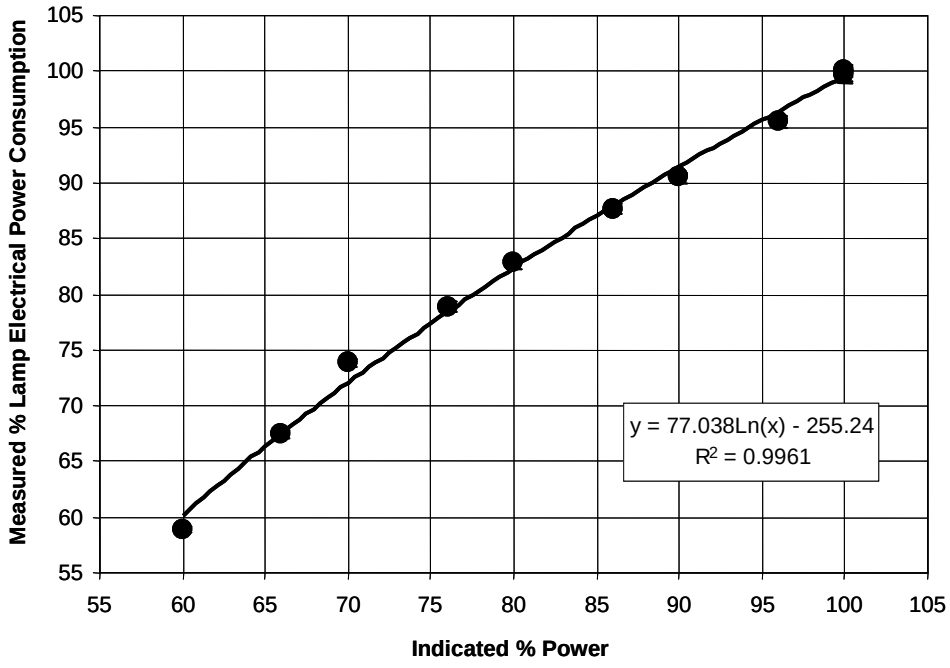

Figure C.4. Plot of the measured percentage lamp electrical power consumption as function of the BPL.

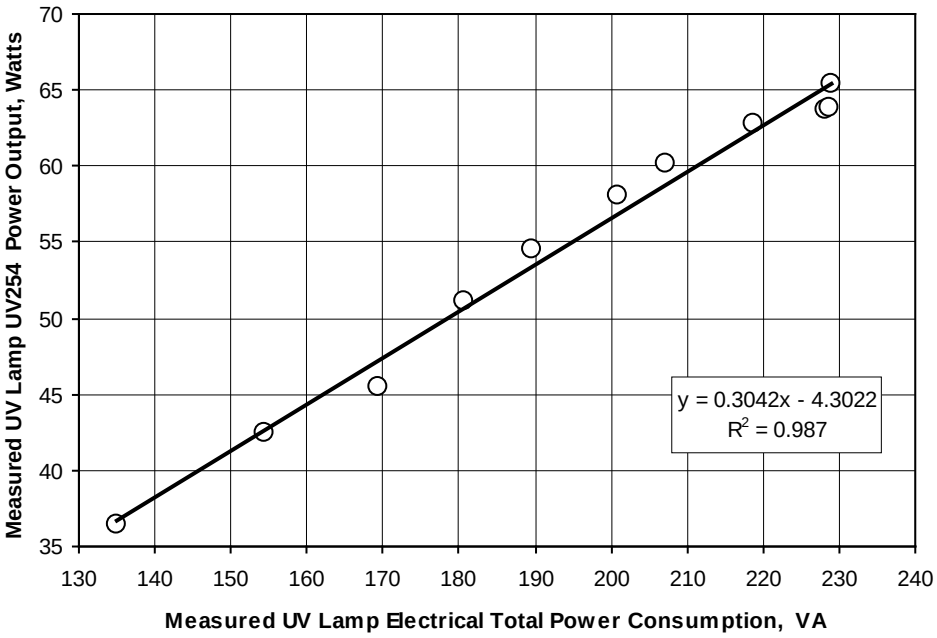

Figure C.5. Plot of measured UV lamp 254 nm output as function of measured UV lamp total power consumption (VA).

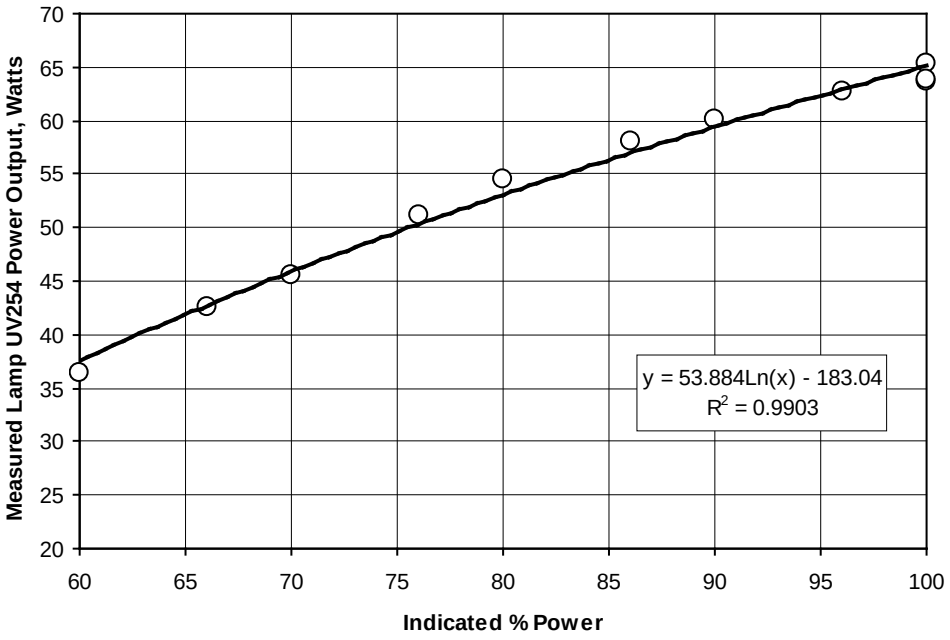

Figure C.6. Plot of measured UV lamp 254 nm power output as function of indicated BPL.

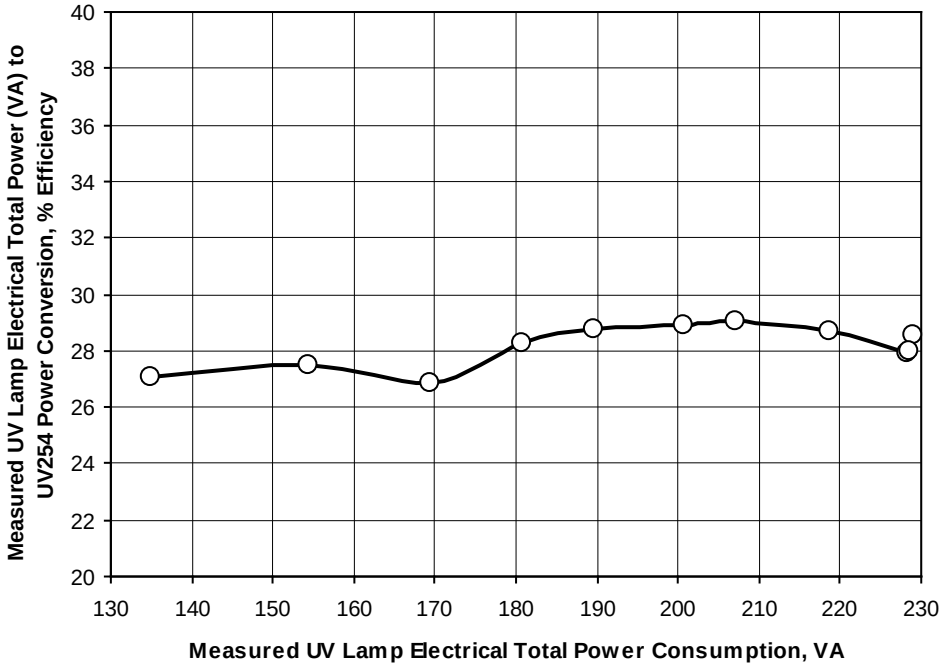

Figure C.7. Plot of the lamp UV output power efficiency as a function of lamp electrical power consumption.

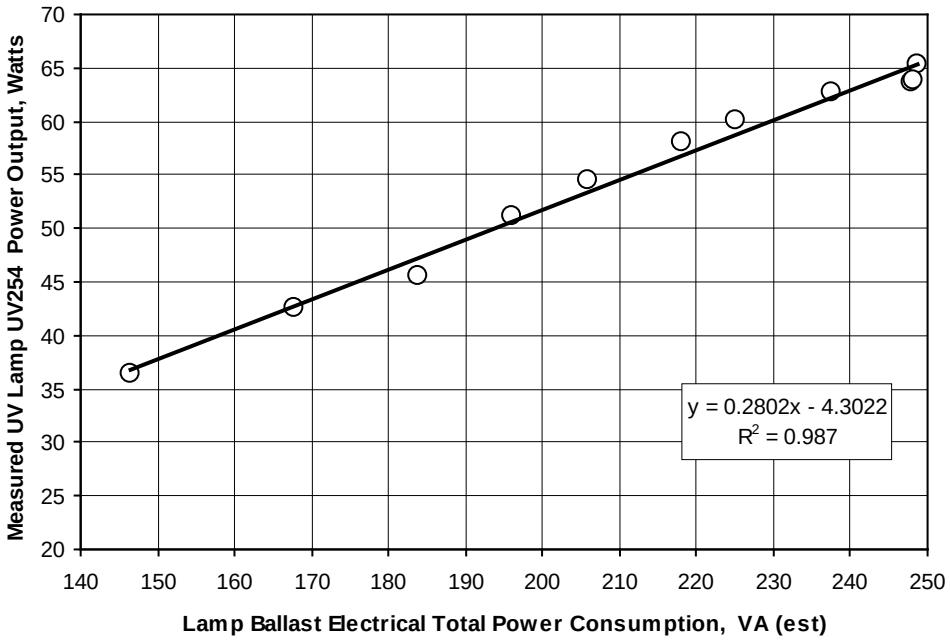

Figure C.8. Plot of the UV output as a function of lamp ballast power consumption.

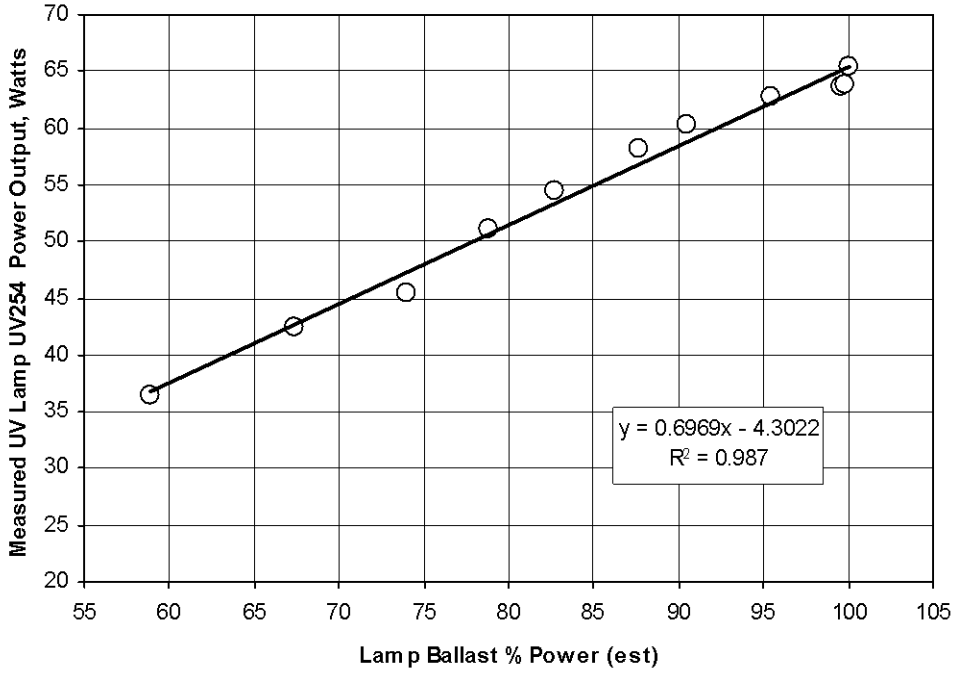

Figure C.9. Plot of the UV 254 nm output as a function of lamp ballast power percentage.

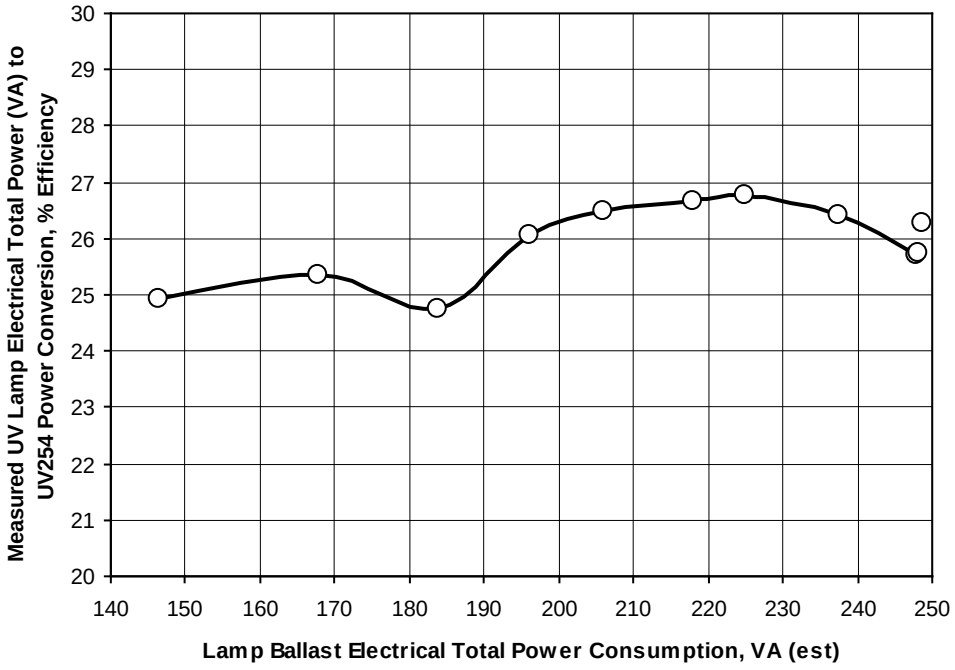

Figure C.10. Plot of the lamp UV 254 nm output power efficiency as a function of lamp ballast electrical power consumption.

C.4 Conclusions

The pilot UV reactor utilizes the same ballast–lamp pairing used in the Trojan UVPhox, so it is reasonable to presume the power behavior are parallel and scalable to the full-scale system.

Measurements of the lamp total electrical power (VA) revealed that

- The UV lamp ballast excites the gas in the lamp using a 60 kHz near-sawtooth AC waveform.
- The lamp ballast controls lamp power by varying both voltage and amperage.
- At full power the UV lamp consumes about 229 VA.
- At full power the UV lamp ballast consumes about 249 VA.
- The UV ballast is 92.1% efficient, and most of the lamp power reaches the lamp.

Measurement of UV lamp efficiency revealed that

- Lamp efficiency is relatively independent of lamp total power levels.
- About 26% of the total electrical power (VA) consumed by the ballast is converted to UV 254 nm power (watts) by the lamp (measured at the reactor sidewalls).
- At full power, the single 257-watt LPHO lamp and ballast combination consumes about 249 VA of electrical total power and produces about 65 watts of UV 254 power.

A full UVPhox system with 72 × 6 lamps would consume ~107.6 kVA of total electrical power and generate ~28 kW of UV power.

Appendix D

Autopsy of Clouded Quartz Sleeve

D.1 Introduction

Routine servicing of the UVPhox reactors revealed repeated incidences of "clouding" of the inside of the quartz sleeves. Concern existed over the possible impact of the sleeve clouding on the performance of the UV and UV/AOP processes. An autopsy was preformed to identify the material responsible for clouding of the inner surface. A used sleeve was broken into small pieces and the UV transmittance measured at 254 nm through a clouded area. Quartz pieces (new and clouded) and the Teflon o-rings used to secure electrical leads to the lamp were analyzed by SEM.

D.2 Materials and Methods

A "clouded" quartz sleeve and a new one were broken into pieces with a hammer. A piece of quartz was secured to a piece of cardboard with a whole cut to allow light to pass through. The UV transmittance was measured between 200 and 450 nm with a CCD array UV-visible spectrophotometer (S.I. Photonics, Tucson, AZ). Other samples were taken to University of California Irvine Materials Characterization Center (MC2) for analysis by SEM and EDX spectroscopy.

D.3 Results and Discussion

The average percent transmittance between 200 and 450 nm is displayed in Figure D.1. The average percent transmittance of the new quartz sleeve at 254 nm was approximately 84 %T compared to 23 %T for the clouded sleeve. This amounted to a 73% reduction of UV passing straight through the quartz material (Figure D.2). The spectrometer is only able to measure light passing directly through the sleeve and, thus, it is not known if absorption or scattering of UV light has occurred. A similar study conducted by Trojan Technologies with an integrating sphere revealed scattering of the UV light and no adsorption (data not shown).

SEM images of a virgin and clouded sleeve are displayed in Figure D.3. The clouded sleeve has a distinct egg-shell pockmarked appearance compared to the smooth appearance of the unused quartz sleeve. However, the elemental composition of the two sleeves was not significantly different, consisting of 4% to 5% carbon, 57% to 59% oxygen, and 35% to 39% silicon (Table D.1).

SEM images of a virgin Teflon o-ring and an o-ring that had been exposed to UV light are displayed in Figure D.4. As expected, both were composed of carbon and fluorine. However, the o-ring that was exposed to UV light contained 8% oxygen by weight, whereas the new o-ring did not contain any measurable oxygen. It is believed that the Teflon had undergone oxidation by the UV light.

Studies have shown that thermal degradation (200–382 °C) of Teflon leads to the breakdown of the fluorinated polymer and generation of toxic fumes including TFE (tetrafluoroethylene), HFP (hexafluoropropene), OFCB (octafluorocyclobutane), PFIB (perfluoroisobutane),

carbonyl fluoride, CF4 (carbon tetrafluoride), TFA (trifluoroacetic acid), trifluoroacetic acid fluoride, perfluorobutane, SiF4 (silicon tetrafluoride), HF (hydrofluoric acid), and particulate matter (Seidel et al., 1991; Ellis et al., 2001). However, the surface of the 257-watt LPHO UV lamps only reach a temperature between 100 and 120 °C (Brown, 2013). The impact of 254 nm UV light on Teflon is unknown.

The same cloudiness (etching) does not occur on the UV lamps, only on the sleeves, suggesting more robust composition of quartz material or possibly that inorganic acids condense on the surface of the quartz sleeves, which are cooled by the flow of water through the reactors.

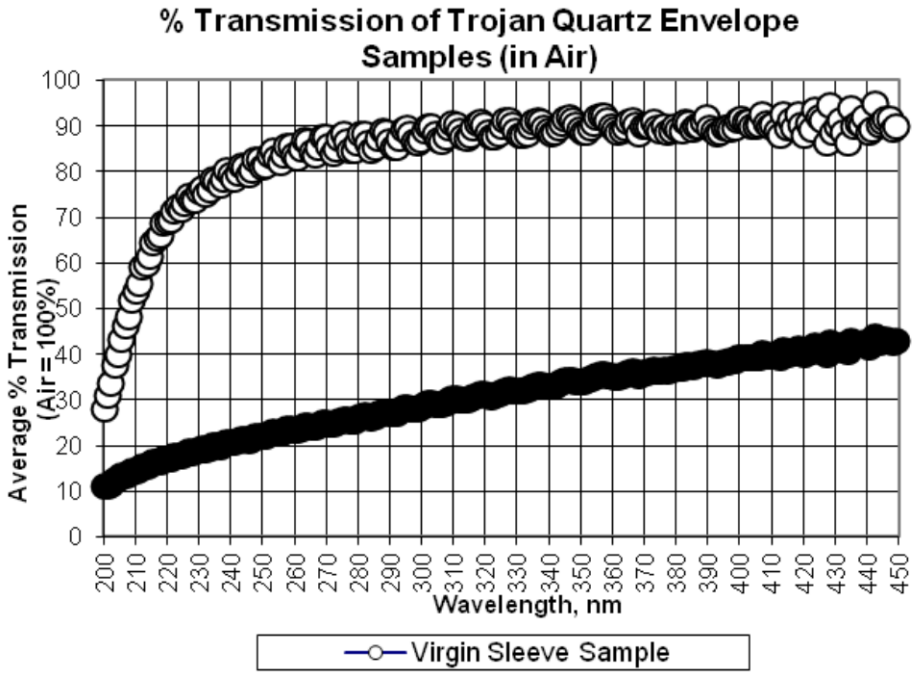

Figure D.1. Average percentage transmittance through new quartz sleeve (open circles) and clouded quartz sleeve (solid circles) across the UV spectrum from 200 to 450 nm.

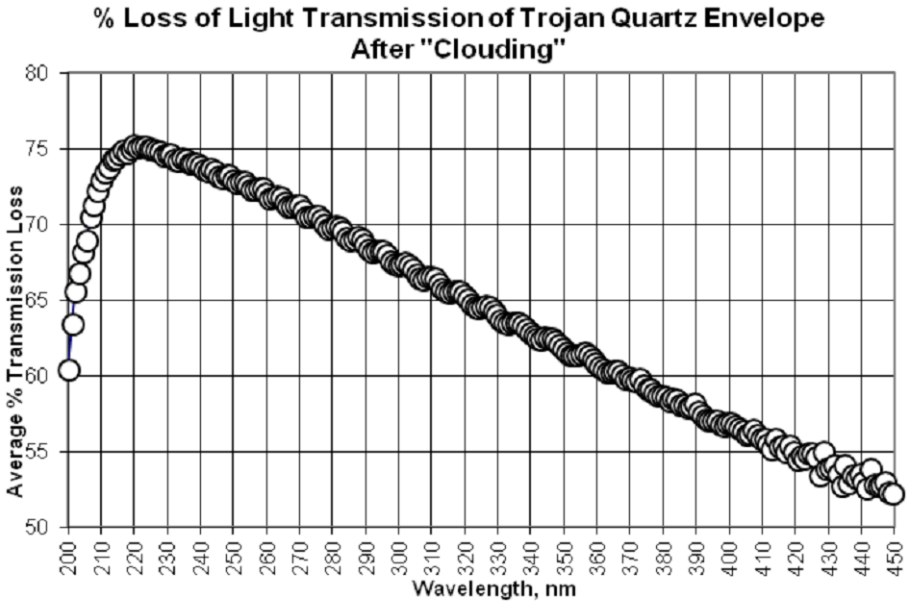

Figure D.2. Percentage loss of transmission through a clouded quartz sleeve across the UV spectrum from 200 to 450 nm.

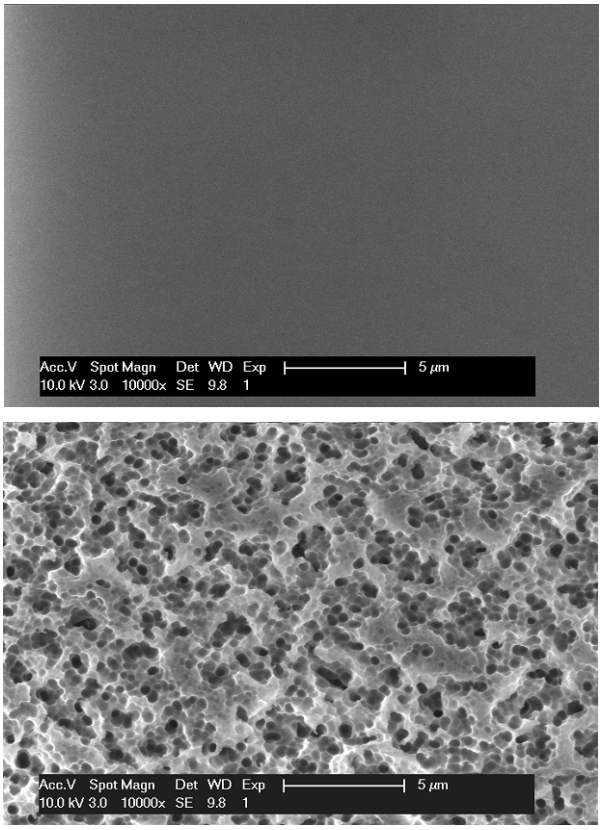

Figure D.3. SEM images of virgin quartz sleeve (top) and clouded quartz sleeve (bottom).

Table D.1. EDS Elemental Analyses of Virgin and Clouded Quartz Sleeves

	Virgin Quartz Sleeve			Cloudy Quartz Sleeve		
Element	Element Wt%	Wt% Error	Atom%	Element Wt%	Wt% Error	Atom%
C	2.39	±0.39	4.09	3.12	±0.42	5.22
O	44.59	±0.58	57.18	47.46	±0.62	59.50
Si	53.01	±0.68	38.73	49.41	±0.68	35.28
Total	100.0		100.0	100.0		100.0

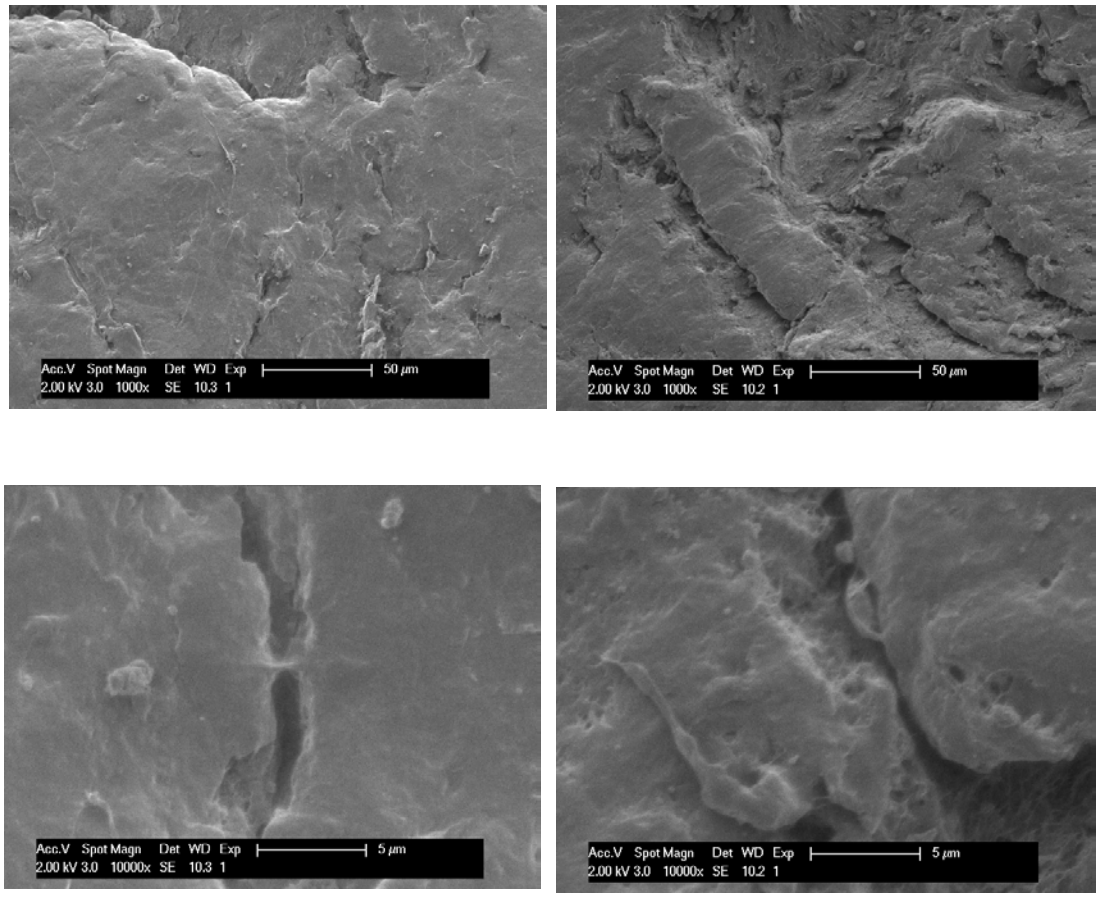

Figure D.4. SEM images virgin (top and bottom, left) and UV-exposed (top and bottom, right) Teflon o-rings.

D.4 Conclusions

The SEM showed significant degradation of the cloudy quartz surface. The cloudy quartz had an egg-shell appearance with large pores. The virgin quartz was very smooth with no discernible topography. Elemental analysis showed only silicon and oxygen and a small amount of carbon on both virgin and cloudy quartz. No particulate deposits were identified on either the virgin or cloudy quartz surface. The final conclusion is that the cloudy quartz is *etched*. EDX spectroscopic analysis of the UV-exposed Teflon o-ring showed oxygen incorporated into surface, presumably due to oxidation of the polymer. The production of hydrofluoric acid (HF) from Teflon oxidation during UV operation could explain the etching

observed on the quartz sleeve. The quartz was etched and not coated with nanoparticulates; therefore, the UV emitted by the lamp was mostly scattered rather than absorbed. The percent transmittance (%T) of a single beam through the quartz sleeve was significantly reduced in the etched quartz sleeve, but the cumulative transmittance was presumably not significantly affected. The etching results in UV scattering, not absorbance, and therefore, the UV still enters the bulk flow, although not as directly as in the virgin sleeve. The direction from which the UV comes from does not matter as long as it reaches the bulk flow (Trojan Technologies, data not shown).

Appendix E

Pilot UV Reactor Experimental Data

Table E.1. Pilot UV Reactor Experimental Data

Feed H_2O_2 (mg/L)	H_2O_2 Used (mg/L)	Flow (gpm)	Feed 14DIOX (µg/L)	Product 14DIOX (µg/L)	Log 14DIOX Removed	Conc. 14DIOX Removed (µg/L)	Feed Cl_2 (mg/L)	Product Cl_2 (mg/L)	Conc Cl2 Removed (mg/L)	Log Cl_2 Removed (mg/L)	Feed Fluorescence	Product Fluorescence	Fraction Fluorescence Removed	Control Feed Fluorescence	Control Product Fluorescence	Feed NH_3-N (mg/L)	Feed HCO_3 (mg/L)	Feed NO_3-N (mg/L)	Feed pH	Product pH	Feed UVT	Product UVT	Total Alkalinity (mg/L)	Feed TOC (mg/L)
0	0	3.0	29.33	18.27	0.21	11.06	2.3	0.3	2.0	0.88	578	282	0.51	640	648	0.6	12.3	1.00	5.73	5.49	96.7	101.3	10.1	0.15
3.12	0.63	3.0	22.03	3.59	0.79	18.44	3.4	0.4	3.0	0.93	611	231	0.62	740	528	0.6	9.6	1.13	5.60	5.22	96.9	98.4	7.8	0.09
1.05	0.19	3.1	12.49	4.75	0.42	7.74	3.0	0.5	2.5	0.78	578	271	0.53	552	555	0.4	7.7	1.15	5.70	5.26	95.9	97.8	6.3	0.09
4.99	0.80	3.0	14.47	0.75	1.29	13.72	2.2	0.1	2.1	1.34	636	240	0.62	586	617	0.6	8.3	0.96	5.83	5.55	96.3	98.8	6.8	0.15
2.86	0.57	3.0	5.68	1.07	0.72	4.61	2.6	0.2	2.4	1.11	664	218	0.67	765	801	0.7	11.3	1.30	5.75	5.56	96.3	99.5	9.3	0.14
0	0	4.0	24.80	16.95	0.17	7.85	2.3	0.5	1.8	0.66	685	218	0.68	679	718	0.5	11.2	1.35	5.74	5.38	98.1	99.0	9.2	0.17
0.96	0.19	4.0	27.95	11.85	0.37	16.10	2.1	0.5	1.6	0.62	592	252	0.57	919	672	0.7	12.0	1.31	5.79	5.47	96.2	99.9	9.8	0.16
5.08	0.71	4.0	18.55	3.30	0.79	15.25	2.9	0.6	2.3	0.68	833	232	0.72	573	609	0.6	10.9	1.00	5.69	5.40	95.3	98.3	8.9	0.16
3.45	0.71	4.0	20.40	4.80	0.63	15.60	2.4	0.5	1.9	0.68	684	231	0.66	660	830	0.6	10.9	1.19	5.81	5.54	96.2	98.7	8.9	0.17
2.61	0.25	4.0	16.25	3.40	0.68	12.85	2.2	0.4	1.8	0.74	664	734	-0.11	768	698	0.6	13.5	1.32	5.85	5.58	97.1	98.2	11.1	0.15
3.39	0.60	4.0	12.80	2.40	0.72	10.40	2.0	0.3	1.7	0.82	614	230	0.63	656	619	0.6	10.4	1.04	5.78	5.51	96.6	100.1	8.5	0.17
1.14	0.28	4.0	4.62	2.13	0.34	2.49	3.3	0.7	2.6	0.67	612	262	0.57	606	772	0.5	9.7	1.25	5.66	5.51	96.1	97.8	8.0	0.12
5.12	0.66	4.0	4.11	0.53	0.89	3.58	1.7	0.1	1.6	1.12	886	240	0.73	586	740	0.5	8.9	1.06	5.86	5.58	96.9	98.4	7.3	0.14

14DIOX = 1,4-dioxane

Table E.1. (Continued). Pilot UV Reactor Experimental Data

H_2O_2 (mg/L)	H_2O_2 Used	Flow (gpm)	Feed 14DIOX (µg/L)	Product 14DIOX (µg/L)	Log 14DIOX Removed	Conc. 14DIOX Removed (µg/L)	Feed Cl_2 (mg/L)	Product Cl_2 (mg/L)	Conc. Cl_2 Removed (mg/L)	Log Cl_2 Removed (mg/L)	Feed Fluorescence	Product Fluorescence	Fraction Fluorescence Removed	Control Feed Fluorescence	Control Product Fluorescence	Feed NH_3-N (mg/L)	Feed HCO_3 (mg/L)	Feed NO_3-N (mg/L)	Feed pH	Product pH	Feed UVT	Product UVT	Total Alkalinity (mg/L)	Feed TOC
0	0	5.2	20.50	14.90	0.14	5.60	2.6	0.7	1.9	0.57	891	910	-0.02	904	954	0.6	9.8	1.58	5.67	5.33	97.0	98.8	8.0	0.16
3.11	0.35	5.1	26.00	6.10	0.63	19.90	2.4	0.6	1.8	0.60	500	243	0.51	482	490	0.4	7.3	1.05	5.50	5.40	96.7	99.2	6.0	0.14
1.07	0.15	5.1	13.00	6.30	0.31	6.70	2.7	0.7	2.0	0.59	508	242	0.52	548	602	0.5	8.3	0.96	5.77	5.42	97.0	98.3	6.8	0.16
4.41	0.50	4.9	16.09	2.25	0.85	13.84	1.9	0.5	1.4	0.58	628	218	0.65	699	628	0.5	11.9	1.01	5.78	5.54	96.1	97.9	9.8	0.12
3.14	0.57	5.0	5.60	1.40	0.60	4.20	2.2	0.5	1.7	0.64	622	291	0.53	639	692	0.7	12.4	1.19	5.80	5.43	97.8	99.7	10.2	0.11
2.82	0.23	6.0	22.03	6.53	0.53	15.50	2.8	1.1	1.7	0.41	501	218	0.56	501	644	0.5	8.8	0.82	5.86	5.56	97.8	99.5	7.2	0.18
4.68	0.44	6.1	16.75	2.48	0.83	14.27	2.1	0.8	1.3	0.42	536	218	0.59	529	562	0.3	9.8	0.89	5.64	5.37	97.1	99.1	8.1	0.16
1.03	0.04	6.1	19.95	8.18	0.39	11.77	2.2	0.8	1.4	0.44	516	268	0.48	505	535	0.3	9.8	1.02	5.64	5.33	97.4	98.8	8.1	0.18
0	0	6.0	17.1	15.9	0.03	1.20	2.3	0.8	1.5	0.46	625	341	0.45	598	830	0.3	11	1.12	5.61	5.39	97.92	99.53	9.0	0.25

14DIOX = 1,4-dioxane




WATEREUSE

1199 North Fairfax Street, Suite 410
Alexandria, VA 22314 USA
703.548.0880
703,548.5085 (fax)
foundation@watereuse.org
www.WateReuse.org